

DEPARTMENT OF THE ARMY
U.S. Army Corps of Engineers
441 G Street, NW
Washington, DC 20314-1000

EM 1110-2-3402

CECW-EC

Manual
No. 1110-2-3402

1 August 2022

Engineering and Design
BARGE IMPACT FORCES FOR HYDRAULIC STRUCTURES

1. Purpose. This engineer manual (EM) provides guidance and information for design and evaluation of barge impact forces on inland and coastal navigation structures. This EM is applicable to glancing and head-on barge impacts and for both rigid, semi-rigid and flexible structural systems. This EM also covers case studies and examples for coastal and inland riverine floodwall structures, timber lock wall structures and lock dewatering structures. This EM does not include guidance on ship impacts to inland or coastal navigation structures.

2. Applicability. This manual applies to all Headquarters, U.S. Army Corps of Engineers (HQUSACE) commands having responsibilities for the planning, design, evaluation, repair, and rehabilitation of civil works projects. The user of this EM is responsible for seeking opportunities to incorporate the Environmental Operating Principles (EOPs) wherever possible. A listing of the EOPs is available at:

<http://www.usace.army.mil/Missions/Environmental/EnvironmentalOperatingPrinciples.aspx>.

3. Distribution Statement. Approved for public release; distribution is unlimited.

FOR THE COMMANDER:

9 Appendixes



JAMES J. HANDURA
COL, EN
Chief of Staff

CECW-EC

Manual
No. 1110-2-3402

1 August 2022

Engineering and Design
BARGE IMPACT FORCES FOR HYDRAULIC STRUCTURES

TABLE OF CONTENTS

	Paragraph	Page
Chapter 1 Introduction		
Purpose.....	1.1	1
Applicability.....	1.2	1
Distribution Statement.....	1.3	1
References.....	1.4	1
Records Management (Recordkeeping) Requirements.....	1.5	1
Discussion.....	1.6	1
Introduction.....	1.7	2
Scope.....	1.8	2
Manual Organization.....	1.9	2
General Requirements.....	1.10	3
Mandatory Requirements Criterion.....	1.11	3
Chapter 2 Design Guidance for Barge Impact		
Introduction.....	2.1	4
Design Table.....	2.2	6
Preliminary Design Impact Loads.....	2.3	7
Deterministic Analysis.....	2.4	8
Probabilistic Analysis.....	2.5	8
Return Periods and Load Factors for Barge Impact.....	2.6	8
Risks from Barge Impacts.....	2.7	10
Chapter 3 Barge Model Description and Calibration		
Introduction.....	3.1	11
Single Jumbo Hopper Barge Model.....	3.2	12
Barge Flotilla Model.....	3.3	21
Model Calibration and Validation.....	3.4	38
Summary.....	3.5	48

Chapter 4 Wall Structures – Empirical Approach

General.....	4.1	50
Approach Wall Modeling.....	4.2	51
Unified Load Model.....	4.3	56
Considerations for Hurricane and Inland Riverine Protection		
Floodwalls.....	4.4	66
Examples Using the Empirical Models for Impacts on Approach		
Walls	4.5	68
Complete Design Example – Concrete Approach Wall.	4.6	71

Chapter 5 Wall Structures – Dynamic

General.....	5.1	74
Low-Order Dynamic Model for Impact Load Prediction.	5.2	74
Typical Application Cases.	5.3	101
Deterministic Examples.	5.4	102
Complete Design Example – LODM.....	5.5	110

Chapter 6 Pier Structures

General.....	6.1	119
Semi-Circular Bullnose Structures.	6.2	119
Sloped-V Bullnose Structures.	6.3	130
Dam Piers.....	6.4	137
Examples Using Empirical Equations.	6.5	139
Complete Design Example for Semi-Circular Bullnose.....	6.6	145

Chapter 7 Steel Structures

General.....	7.1	148
Miter Gates.....	7.2	149
Vertically Framed Miter Gates – Full-Scale Experiments.....	7.3	174
Tainter Gates.	7.4	177

Appendixes

A. References and Unit Conversion Factors	201
B. Prototype Field Experiments	207
C. Data from Previous Studies	211
D. Examples of Probabilistic Barge Impact Analysis.....	241
E. Rigid Wall Historical Model (ETL 1110-2-563).....	251
F. Damage Model – Coastal and Inland Riverine Floodwalls.....	255
G. Hurricane and Storm Damage Risk Reduction Systems	278
H. Flexible Timber Guide Walls.....	298
I. Lock Dewatering Structures	309

Table List

Table 2.1 Level of Analysis Required (ER 1110-2-1150)6

Table 2.2 Preliminary Design Barge Impact Forces (ONLY for Reconnaissance stage).....7

Table 2.3 Design Return Periods for Barge Impact.....9

Table 2.4 Load Factors for Usual, Unusual and Extreme Events (Reference is made to Paragraph 2.6.3)..... 10

Table 4.1 Peak Force Results for Flotilla Collisions on Rigid Walls58

Table 4.2 Peak Force Results for Flotilla Collisions on Semi-Flexible Walls..... 59

Table 4.3 Peak Force Results for Flotilla Collisions on Pile-Founded Guide Walls.....61

Table 4.4 System Parameters for Deterministic (Usual) Impact Scenario.....68

Table 4.5 System Parameters for Deterministic (Unusual) Impact Scenario.....69

Table 4.6 System Parameters for Deterministic (Extreme) Impact Scenario.....71

Table 4.7 Design Load Cases from Deterministic Calculations72

Table 4.8 Design Example – Probabilistic Inputs.....73

Table 4.9 Design Load Cases from Probabilistic Calculations73

Table 5.1 Weights, Masses, and Mass Moments-of-Inertia of Fully Loaded Individual Barges92

Table 5.2 System Parameters for Deterministic (Usual) Impact Scenario..... 103

Table 5.3 System Parameters for Deterministic (Unusual) Impact Scenario..... 106

Table 5.4 System Parameters for Deterministic (Extreme) Impact Scenario..... 109

Table 5.5 Usual Load Case – Inputs to LODM..... 111

Table 5.6 Usual Load Case – LODM Example..... 111

Table 5.7 Usual Load Case – Inputs to LODM..... 113

Table 5.8 Unusual Load Case – LODM Example 113

Table 5.9 Usual Load Case – Inputs to LODM..... 115

Table 5.10 Unusual Load Case – LODM Example 115

Table 5.11 Design Load Cases from Deterministic Calculations..... 117

Table 5.12 Design Example – Probabilistic Inputs..... 117

Table 5.13 Design Example – LODM Constants 118

Table 5.14 Design Load Cases from Probabilistic Calculations 118

Table 6.1 Peak Impact Force Results for 35-ft Semi-Circular Bullnose (17 cases) 125

Table 6.2 Peak Impact Force Results for 10-ft Semi-Circular Bullnose (11 cases) 125

Table 6.3 Peak Impact Force Results for Sloped-V (2:1) Bullnose (18 Cases) 134

Table 6.4 Comparison of Head-On Dam Pier Impact Forces (Consolazio and Han 2018) and Semi-Circular Bullnose Load Prediction Model 139

Table 6.5 System Parameters for Deterministic (Usual) Impact Scenario on Semi-Circular Bullnose..... 140

Table 6.6 System Parameters for Deterministic (Unusual) Impact Scenario on Semi-Circular Bullnose..... 141

Table 6.7 System Parameters for Deterministic (Extreme) Impact Scenario on Semi-Circular Bullnose..... 142

Table 6.8 System Parameters for Deterministic (Usual) Impact Scenario on Sloped-V (2:1) Bullnose..... 143

Table 6.9 System Parameters for Deterministic (Unusual) Impact Scenario on Sloped-V (2:1)	144
Table 6.10 System Parameters for Deterministic (Extreme) Impact Scenario on Sloped-V (2:1) Bullnose.....	145
Table 6.11 Design Load Cases from Deterministic Calculations.....	147
Table 6.12 Design Load Cases from Deterministic Calculations.....	147
Table 6.13 Design Load Cases from Probabilistic Calculations	147
Table 7.1 Miter Gate Impact Conditions and Results (27 Cases).....	161
Table 7.2 System Parameters for Deterministic (Usual) Impact Scenario on Miter Gate	170
Table 7.3 System Parameters for Deterministic (Unusual) Impact Scenario on Miter Gate	171
Table 7.4 System Parameters for Deterministic (Extreme) Impact Scenario on Miter Gate	172
Table 7.5 Design Load Cases from Deterministic Calculations.....	173
Table 7.6 Probabilistic Parameters for Ohio River Example	174
Table 7.7 Design Load Cases from Probabilistic Calculations	174
Table 7.8 Impact Force Results (Chasten (1991))	176
Table 7.9 Tainter Gate Impact Conditions and Results (36 Cases)	190
Table 7.10 System Parameters for Deterministic (Usual) Impact Scenario on Tainter Gate.....	197
Table 7.11 System Parameters for Deterministic (Unusual) Impact Scenario on Tainter Gate	198
Table 7.12 System Parameters for Deterministic (Extreme) Impact Scenario on Tainter Gate	200

Figure List

Figure 2.1. Barge Impact Due to Loss of Control at Smithland L&D.....	4
Figure 3.1. Jumbo Hopper Barge FE Model (Mesh Not Shown for Clarity): (a) Schematic Plan and Elevation View; (b) Perspective View; (c) Exploded View	13
Figure 3.2. Barge Bow Zone FE Model Details (Partial Mesh Shown for Clarity): (a) Elevation View of Configuration; (b) Elevation View of Mesh; (c) Isometric View of Transition from Bow Zone to Hopper Zone.....	14
Figure 3.3. Barge Hopper Zone FE Model Details (Mesh Not Shown for Clarity)	14
Figure 3.4. Barge Stern Region FE Model Details (Partial Mesh Shown for Clarity): (a) Isometric View of Configuration; (b) Isometric View of Mesh.....	15
Figure 3.5. Barge Structural Steel Material Parameters.....	16
Figure 3.6. Barge Payload Modeling Schematic: (a) Elevation View; (b) Plan View	17
Figure 3.7. Barge and Payload FE Model Details (Mesh Not Shown for Clarity).....	18
Figure 3.8. Buoyancy Spring System: (a) Conceptual Schematic; (b) Elevation Schematic (with Dimensions).....	19
Figure 3.9. Illustrative Schematic of Contact and Rigid Zones: (a) Plan View; (b) Elevation View	20
Figure 3.10. Partial Rigidization of Impacting Barge FE Model.....	21
Figure 3.11. Typical Barge Flotilla in Transit.....	21
Figure 3.12. Finite Element Model of a 3x3 Flotilla Configuration (Mesh Not Shown for Clarity).....	22
Figure 3.13. Illustrative Schematic of 3x3 Flotilla Collision with Rigid Wall	22

Figure 3.14. Examples of Jumbo Hopper Barge Flotilla Configurations Considered: 1x3, 1x5, 2x3, 2x5, 3x3, 3x5.....	23
Figure 3.15. Bitt and Cavel Locations (Shown for Port Side Only).....	24
Figure 3.16. Exterior Fore/Aft Wires (Rated at 90-kip Break Strength).....	25
Figure 3.17. Interior Fore/Aft Wires (Rated at 120-kip Break Strength).....	25
Figure 3.18. Breast Wires (Rated at 90-kip Break Strength).....	26
Figure 3.19. Scissor Wires (Rated at 120-kip Break Strength).....	27
Figure 3.20. Lashing Configuration Combinations on a 3x3 Flotilla.....	28
Figure 3.21. Non-Impacting, Reduced Resolution Jumbo Hopper Barge FE Models: (a) Single Raked; (b) Double-Raked.....	30
Figure 3.22. Barge-to-Barge Contact Types (Illustrated within a 3x5 Flotilla).....	31
Figure 3.23. Bow-to-Stern Crush Simulation (Partial Mesh Shown for Clarity): (a) Before Crush; (b) During Crush; (c) Force-Penetration Relationship.....	32
Figure 3.24. Conceptual Lashing Configuration Schematics: (a) Physical Components; (b) FE Model Components.....	34
Figure 3.25. Behavior of Slipping Elements at Each Timestep: (a) Real Lashing Equivalent; (b) $T_2 > T_1$; (c) Material Transfer until $T_1 = T_2$; (d) Remeshed to Move Element Across Slipping.....	36
Figure 3.26. Close-Up View of Tensioning Cable and Failure Spring.....	37
Figure 3.27. Failure Sequence of Lashing Model: (a) Prior to Failure; (b) Failure Spring Is Deleted; (c) Lashing Material Is Pulled through Slipping; (d) Lashing Elements Are Remeshed.....	37
Figure 3.28. Load-Measurement System (Beam, Shear Pins, and Clevis Mounts) Attached to Bow Corner of Barge (Patev 2003).....	39
Figure 3.29. Finite Element Model of Load-Measurement System: (a) Overview and Attachment to Barge; (b) Elevation View of Clevis and Shear Pin Model; (c) Plan View of Clevis and Shear Pin Model.....	40
Figure 3.30. Schematic of Flotilla Impact Against Rigid Wall.....	41
Figure 3.31. Flotilla Impacts on Semi-Flexible Wall: (a) Schematic Diagram, (b) Experiments Conducted at Winfield.....	42
Figure 3.32. Semi-Flexible Wall FE Model: (a) Overall Configuration (Mesh Not Shown for Clarity); (b) Cross Section of Semi-Flexible Wall Beam.....	43
Figure 3.33. Time Histories of Normal Impact Force for Rigid Wall Experiments 41 and 42 and Corresponding FE Simulations with Load Beam Included.....	44
Figure 3.34. Time Histories of Normal Impact Force for Semi-Flexible Wall Experiments 10 and 20 and Corresponding FE Simulations with Load Beam Included.....	45
Figure 3.35. Comparison of Force Time Histories for FE Simulations of Experiments 10 and 20 with Load Beam (Instrumented) and without (Un-instrumented).....	46
Figure 3.36. Comparison of Reduced-Scale (40%) Experimental and Analytical Backbone Curves for Impacts on Rounded Surfaces (Surface Width = 1/6th of Barge Width).....	47
Figure 3.37. Comparison of Reduced-Scale (40%) Experimental and Analytical Backbone Curves for Impacts on Flat-Faced Surfaces (Surface Width = 1/6th of Barge Width).....	48
Figure 4.1. Mississippi River Lock and Dam No. 2 (MRLD2).....	53

Figure 4.2. Finite Element Model of Pile-Founded Guide Wall for MRLD2 (Pile Element “Prisms” Rendered at 12-in. Thickness; Soil Resistance Springs Not Shown for Clarity)	53
Figure 4.3. Isometric View of Concrete Portions of Finite Element Model for MRLD2.....	54
Figure 4.4. Elevation View of Pile Group at MRLD2 (Beam Elements Rendered as “Prisms” for Illustration).....	55
Figure 4.5. Peak Force Results for Flotilla Collisions on Rigid Walls (20 Cases).....	58
Figure 4.6. Peak Force Results for Flotilla Collisions on Semi-Flexible Walls (34 Cases)	59
Figure 4.7. Peak Force Results for Flotilla Collisions on Pile-Founded Guide Walls (57 Cases)	62
Figure 4.8. Peak Force Results for All Flotilla Collisions on Concrete Guide Walls (111 Cases)	62
Figure 4.9. General Form of Unified Bilinear Curve Fit Used for Concrete Walls	63
Figure 4.10. Comparison of All Concrete Wall Data and Unified Bilinear Curve Fit (the Latter Evaluated Using the Appropriate Stiffnesses, k , of the Associated Walls)	65
Figure 4.11. Comparison of Rigid Wall Data and Unified Load Prediction Model (the Latter Evaluated Using Wall Stiffness, $k = 1,000$ kip/in.)	65
Figure 4.12. Comparison of Semi-Flexible Wall Data and Unified Load Prediction Model (the Latter Evaluated Using Wall Stiffness, $k = 767$ kip/in.)	65
Figure 4.13. Comparison of Pile-Founded Guide Wall Data and Unified Load Prediction Model (the Latter Evaluated Using Wall Stiffness, $k = 592$ kip/in.)	66
Figure 4.14. Deterministic (Usual) Impact Scenario	68
Figure 4.15. Deterministic (Unusual) Impact Scenario.....	69
Figure 4.16. Deterministic (Extreme) Impact Scenario	70
Figure 5.1. Barge Flotillas: (a) Approaching Guide Wall; (b) In Transit; (c) Example Configurations	75
Figure 5.2. Examples of Navigation Wall Structures: (a) Rigid Concrete Guide Wall Impacted by Barge (in Cut-Away View); (b) Semi-Flexible Concrete Guide Wall Supported on Rigid Cells; (c) Concrete Guide Wall Founded on Timber Piles; (d) Flexible Timber Guide Wall.....	76
Figure 5.3. Overview of Low-Order Modeling of Barge Flotilla Impacts on Wall Structures....	78
Figure 5.4. Conceptual Collision Scenarios: (a) Flexible Timber Guide Wall; (b) Rigid Wall.....	79
Figure 5.5. Conceptual Barge Flotilla Impact on Wall Structures: (a) At the Onset of Impact; (b) Redirection of Lead Row Upon Generation of Maximum Impact Force; (c) Lumped Mass and Mass Moment-of-Inertia for Each Barge Row.....	81
Figure 5.6. Flotilla-Wall Collision Modeling Approaches: (a) High-Resolution FE Simulation (Mesh Not Shown for Clarity); (b) Low-Order Dynamic Analysis.....	82
Figure 5.7. Angle Dependency of Barge Bow Corner Crushing During Flotilla-Wall Impacts	84
Figure 5.8. Barge Bow Corner Crushing Simulation for a 30° Impact Angle (Not to Relative Scale): (a) Barge-Wall and Prescribed Motions; (b) Normal and Frictional Impact Forces; (c) Barge Bow at Crush Depth of 60 in.; (d) Barge Bow Plastic Strains (Blue Signifies No Plastic Strain; Red Signifies Plastic Strain 10 Times Greater than Yield Strain); (e) Inset of Bow Corner Prior to Crushing; (f) Inset of Bow Corner at Crush Depth of 60 in.....	85

Figure 5.9. Compressive Force-Deformation Relationships (Crush-Curves) Used in Low-Order Modeling of Barge Bow Corner Stiffness.....	86
Figure 5.10. Barge Flotilla Inter-Row Stiffness Simulations for a Three-Column (3x) Configuration: (a) Flexural; (b) Shear; (c) Axial (Lashing Tensile Stiffness During Separation Between Rows).....	87
Figure 5.11. Inter-Row Stiffness Curves for 1x, 2x, and 3x Flotillas: (a) Flexural; (b) Shear; (c) Axial (Inter-Row Separations Correspond to Positive Displacements)	89
Figure 5.12. Conceptual Illustration of Laterally Loaded Navigation Wall for Use in Low-Order Analysis.....	91
Figure 5.13. Overall Dimensions and Positioning of Centroidal Properties for Fully Loaded Barges (Payloads Not Shown): (a) Single-Raked; (b) Double-Raked.....	92
Figure 5.14. Arrangements of Single-Raked and Double-Raked Barges in Multi-Row Flotillas.....	92
Figure 5.15. Free-Body Diagrams of Impacted Wall and Barge Flotilla: (a) Impacted Wall; (b) Lead Flotilla Row; (c) Interior Flotilla Row; (d) Trailing Flotilla Row.....	94
Figure 5.16. Comparisons of Impact-Force Time Histories Obtained from High-Resolution FE Impact Simulation and Low-Order Analysis: (a) Rigid Wall: 3x3 – 20° – 3 ft/sec; (b) Semi Flexible Wall: 2x3 – 20° – 3 ft/sec; (c) Pile-Founded Guide Wall: 3x3 – 15° – 4 ft/sec; (d) Flexible Timber Guide Wall: 2x2 – 25° – 4 ft/sec.....	98
Figure 5.17. Comparisons of Peak Impact Forces Obtained from High-Resolution FE Impact Simulation and Low-Order Analysis; (a) Rigid Wall; (b) Semi-Flexible Wall; (c) Pile-Founded Guide Wall; (d) Flexible Timber Guide Wall.....	100
Figure 5.18. Deterministic (Usual) Impact Scenario	102
Figure 5.19. Wall Stiffness for Deterministic (Usual) Impact Scenario	103
Figure 5.20. Impact Force Time History for Deterministic (Usual) Impact Scenario.....	104
Figure 5.21. Wall Displacement Time History for Deterministic (Usual) Impact Scenario.....	104
Figure 5.22. Deterministic (Unusual) Impact Scenario.....	105
Figure 5.23. Wall Stiffness for Deterministic (Unusual) Impact Scenario	106
Figure 5.24. Impact Force Time History for Deterministic (Unusual) Impact Scenario	107
Figure 5.25. Wall Displacement Time History for Deterministic (Unusual) Impact Scenario	107
Figure 5.26. Deterministic (Extreme) Impact Scenario	108
Figure 5.27. Wall Stiffness for Deterministic (Extreme) Impact Scenario	109
Figure 5.28. Impact Force Time History for Deterministic (Extreme) Impact Scenario.....	110
Figure 5.29. Wall Displacement Time History for Deterministic (Extreme) Impact Scenario	110
Figure 5.30. Force Time History for Usual Load Case – Rigid Wall.....	112
Figure 5.31. Force Time History for Usual Load Case – Flexible	112
Figure 5.32. Displacement Time History for Usual Load Case – Flexible.....	112
Figure 5.33. Force Time History for Usual Load Case – Rigid Wall.....	114
Figure 5.34. Force Time History for Usual Load Case – Flexible	114
Figure 5.35. Displacement Time History for Usual Load Case – Flexible.....	114
Figure 5.36. Force Time History for Usual Load Case – Rigid Wall.....	116
Figure 5.37. Force Time History for Usual Load Case – Flexible	116

Figure 5.38. Displacement Time History for Usual Load Case – Flexible	116
Figure 6.1. Semi-Circular Bullnose Structure	120
Figure 6.2. Finite Element Modeling of 35-ft Diameter Semi-Circular Bullnose: (a) Plan-View Schematic; (b) Plan View of Mesh;(c) Isometric View of Mesh.....	123
Figure 6.3. Finite Element Modeling of 10-ft Diameter Semi-Circular Bullnose: (a) Plan-View Schematic; (b) Plan View of Mesh; (c) Isometric View of Mesh.....	124
Figure 6.4. Peak Impact Force Results for 35-ft Semi-Circular Bullnose (17 Cases)	126
Figure 6.5. Peak Impact Force Results for 10-ft Semi-Circular Bullnose (11 Cases)	126
Figure 6.6. Peak Impact Force Results for 10-ft and 35-ft Semi-Circular Bullnoses (28 Cases)	127
Figure 6.7. General Form of Bilinear Curve Fit Used for Semi-Circular Bullnoses	128
Figure 6.8. Comparisons of Semi-Circular Bullnose Data and Bilinear Curve Fits (Load Predictions Evaluated Using Respective Diameters).....	129
Figure 6.9. Comparison of 35-ft Semi-Circular Bullnose Data and Bilinear Curve Fit (Load Predictions Evaluated Using 35-ft Diameter).....	130
Figure 6.10. Comparison of 10-ft Semi-Circular Bullnose Data and Bilinear Curve Fit (Load Predictions Evaluated Using 10-ft Diameter).....	130
Figure 6.11. Example Sloped-V (Mississippi) Bullnose Structure.....	131
Figure 6.12. Finite Element Modeling of Sloped-V (2:1) Bullnose: (a) Plan-View Schematic; (b) Plan View of Mesh; (c) Isometric View of Mesh	133
Figure 6.13. Peak Impact Force Results for Sloped-V Bullnose (18 Cases).....	134
Figure 6.14. General Form of Bilinear Curve Fit Used for Sloped-V Bullnoses	136
Figure 6.15. Comparison of Sloped-V (2:1) Bullnose Data and Load Prediction Model.....	137
Figure 6.16. Cannelton Locks and Dam on the Ohio River (Source: Wikimedia Commons, Photo by Sarah Ewart).....	138
Figure 6.17. Deterministic (Usual) Impact Scenario on Semi-Circular Bullnose	140
Figure 6.18. Deterministic (Unusual) Impact Scenario on Semi-Circular Bullnose	141
Figure 6.19. Deterministic (Extreme) Impact Scenario on Sloped-V (2:1) Bullnose.....	142
Figure 6.20. Deterministic (Usual) Impact Scenario on Sloped-V (2:1) Bullnose.....	143
Figure 6.21. Deterministic (Unusual) Impact Scenario on Sloped-V (2:1) Bullnose.....	144
Figure 6.22. Deterministic (Extreme) Impact Scenario on Sloped-V (2:1) Bullnose.....	145
Figure 7.1. (a) Horizontal Framing (b) Vertical Framing (Chasten 1991).....	150
Figure 7.2. Greenup Locks and Dam on the Ohio River: (a) Overview Photo; (b) Miter Gates: Three in Closed Position, One in Open Position (Source: Google Maps)	151
Figure 7.3. Replacement of Greenup Miter Gates in 2012: (a) Gate Leaf Being Lifted; (b) Gate Leaves Installed in Lock Chamber.....	151
Figure 7.4. Constitutive Relationship for A572 Grade 50 Steel Used in Miter Gate Components	153
Figure 7.5. Strain-Rate Sensitivity of A572 Grade 50 Steel Used in Miter Gate Components (Based on Cowper-Symonds Model with $C = 40.4 \text{ sec}^{-1}$ and $P = 5$).....	153
Figure 7.6. Miter Gate Modeling Stages: (a) Horizontal Girders, Elevation; (b) Horizontal Girders, Isometric View; (c) Vertical Girders, Elevation; (d) Vertical Girders, Isometric View; (e) Skin Plate, Elevation; (f) Skin Plate, Isometric View; (g) Intercostals, Prestressing	

Anchorage, Diagonals, Fenders, and Contact Blocks, Elevation; (h) Intercostals, Prestressing Anchorage, Diagonals, Fenders, and Contact Blocks, Isometric View.....	154
Figure 7.7. Isolated Cut-Out Portion of Miter Gate Model Showing Primary Structural Components	155
Figure 7.8. Skin Plate and Intercostal Plates: (a) Finite Element Model with Intercostal Lines; (b) Finite Element Model with Skin Plate Mesh.....	155
Figure 7.9. Sectional Views of Single Miter Gate Leaf Model Showing Mesh Resolution: (a) Upper Portion of Leaf, Viewed from Above; (b) Upper Portion of Leaf, Viewed from Below; (c) Upper Portion of Leaf, Viewed from Upstream Side; (d) Cross-Sectional View of Leaf, Viewed from Downstream Side	156
Figure 7.10. Prestressing Diagonals: (a) Structural Plans with Added Notes on Bar Sizes and Prestressing Forces; (b) Finite Element Model	157
Figure 7.11. Two-Leaf Miter Gate Finite Element Model: (a) Geometry, with Mesh Resolution Omitted for Clarity; (b) High-Resolution Mesh of Approximately 380,000 Elements.....	158
Figure 7.12. Boundary Conditions on Miter Gate Leaf FE Model: (a) Locations of Pintle Ball, Gudgeon Pin, and Quoin Contact; (b) Simplified Boundary Conditions	159
Figure 7.13. Plan View Renderings of System Models: (a) 1x3 Leaf Impact; (b) 1x3 Miter Impact; (c) 2x3 Miter Impact; (d) 3x3 Miter Impact; (e) 3x5 Miter Impact (Note: At Different Scale).....	162
Figure 7.14. Model Used to Simulate Leaf Impact, 1x3 Barge Flotilla, 2 ft/sec.....	163
Figure 7.15. Simulation Results for Leaf Impact, 1x3 Barge Flotilla, 2 ft/sec.....	163
Figure 7.16. Plastic Strains for 1x3 – 2.0 ft/sec – Leaf Impact (Blue Signifies No Plastic Strain, Red Signifies Plastic Strain): (a) Barge Bow Plastic Strains; (b) Miter Gate Plastic Strains.....	164
Figure 7.17. Model Used to Simulate Miter Impact, 3x5 Barge Flotilla, 2 ft/sec	165
Figure 7.18. Simulation Results for Miter Impact, 3x5 Barge Flotilla, 2 ft/sec	165
Figure 7.19. Plastic Strains for 3x5 – 2.0 ft/sec – Miter Impact (Blue Signifies No Plastic Strain, Red Signifies Plastic Strain): (a) Barge Bow Plastic Strains; (b) Miter Gate Plastic Strains.....	166
Figure 7.20. Relationship Between Flotilla Momentum and Maximum Miter Gate Impact Force (27 Cases)	167
Figure 7.21. General Form of Bilinear Impact Force Prediction Model for Miter Gates	168
Figure 7.22. Comparison of Impact Forces from Dynamic Simulations and Miter Gate Impact Load Prediction Model (Equation 7.3).....	169
Figure 7.23. Deterministic (Usual) Impact Scenario on Miter Gate.....	170
Figure 7.24. Deterministic (Unusual) Impact Scenario on Miter Gate.....	171
Figure 7.25. Deterministic (Extreme) Impact Scenario on Miter Gate.....	172
Figure 7.26. Load Beam Configuration on Lead Barge (Chasten (1991)).....	175
Figure 7.27. Strain Transducer Locations (Chasten (1991)).....	175
Figure 7.28. Force Time History – Impact #3 (Chasten (1991)).....	176
Figure 7.29. Stress Flow (ksi), 573 kips – Impact #3 (Chasten (1991)).....	177
Figure 7.30. Cannelton Locks and Dam on the Ohio River (Source: Wikimedia Commons, Photo by Sarah Ewart).....	179

Figure 7.31. Constitutive Relationships for A36 and A441 Grade 42, 46, 50 Steels in Tainter Gate	180
Figure 7.32. Strain-Rate Sensitivity of A36 and A441 Steels in Tainter Gates (Based on Cowper-Symonds Model with $C = 40.4 \text{ sec}^{-1}$ and $P = 5$).....	180
Figure 7.33. Partial Tainter Gate Finite Element Model (Note: Downstream Skin Plate Removed to Reveal Internal Structural Details): (a) Surface Geometry; (b) Mesh.....	182
Figure 7.34. Side Frame Finite Element Model: (a) Surface Geometry; (b) Mesh	182
Figure 7.35. Trunnion Finite Element Model: (a) Surface Geometry; (b) Mesh	182
Figure 7.36. Tainter Gate Finite Element Model: (a) Geometry (Mesh Omitted for Clarity); (b) High-Resolution Mesh of Approximately 160,000 Elements.....	183
Figure 7.37. Dam Pier Finite Element Model: (a) Surface Geometry; (b) Finite Element Mesh.....	184
Figure 7.38. Finite Element Model of Single Module Partial-Dam: (a) Surface Geometry; (b) Surface Geometry with Gate.....	185
Figure 7.39. Tainter Gate States: (a) Gate Open (Up); (b) Gate Closed (Down).....	186
Figure 7.40. Barge-Tainter Gate Impact Conditions Investigated: (a) 1x1, Head-On; (b) 1x1, Oblique; (c) 2x1, Head-On; (d) 2x1, Oblique	189
Figure 7.41. Sensitivity of Barge Impact Forces to Angle of Obliquity (36 Cases): (a) Maximum Impact Forces; (b) Maximum Impact Forces Normalized by Corresponding Head-on ($\theta = 0^\circ$) Impact Forces	192
Figure 7.42. Comparison of Equation 4.2 and Normalized Force Data.....	192
Figure 7.43. Maximum Forces Divided by R, to Adjust for Angle of Obliquity (36 Cases): (a) Angle-Adjusted Maximum Barge Impact Forces; (b) Angle-Adjusted Maximum Trunnion Reaction Forces	193
Figure 7.44. General Form of Bilinear Force Prediction Model for Tainter Gates	194
Figure 7.45. Comparison of Angle-Adjusted Force Data from Dynamic Simulations and Empirical Tainter Gate Force Prediction Equations, Equation 7.10 and Equation 7.13 (Note: I—Impact Load, and T—Trunnion Load).....	195
Figure 7.46. Comparison of Angle-Adjusted Force Data from Impact Simulations and Empirical Tainter Gate Force Prediction Equations (a) Maximum Barge Impact Forces and Equation 7.10; (b) Maximum Trunnion Reaction Forces and Equation 7.13 (Note: I—Impact Load, and T—Trunnion Load).....	196
Figure 7.47. Deterministic (Usual) Impact Scenario on Tainter Gate	197
Figure 7.48. Deterministic (Unusual) Impact Scenario on Tainter Gate	198
Figure 7.49. Deterministic (Extreme) Impact Scenario on Tainter Gate	199

Chapter 1 Introduction

1.1. Purpose. This engineering manual (EM) provides guidance and information for design and evaluation of barge impact forces on inland and coastal navigation structures. This EM is applicable to glancing and head-on barge impacts and for rigid, semi-rigid, and flexible structural systems. This EM also covers case studies and examples for coastal and inland riverine floodwall structures, timber lock wall structures, and lock dewatering structures. This EM does not include guidance on ship impacts to inland or coastal navigation structures.

1.2. Applicability. This manual applies to all Headquarters, U.S. Army Corps of Engineers (HQUSACE) commands having responsibilities for the planning, design, evaluation, repair, and rehabilitation of civil works projects. The user of this EM is responsible for seeking opportunities to incorporate the Environmental Operating Principles (EOPs) wherever possible. A listing of the EOPs is available at:

<http://www.usace.army.mil/Missions/Environmental/EnvironmentalOperatingPrinciples.aspx>.

1.3. Distribution Statement. Approved for public release; distribution is unlimited.

1.4. References. Appendix A lists required and related publications.

1.5. Records Management (Recordkeeping) Requirements. The records management requirement for all record numbers, associated forms, and reports required by this regulation is addressed in the Army's Records Retention Schedule – Army (RRS-A). Detailed information for all related record numbers is located in Army Records Information Management System (ARIMS)/RRS-A at <https://www.arims.army.mil>. If any record numbers, forms, and reports are not current, addressed, and/or published correctly in ARIMS/RRS-A, see Department of the Army Pamphlet 25-403, Guide to Recordkeeping in the Army.

1.6. Discussion.

1.6.1. Previous guidance and design of USACE hydraulic structures for barge impact were limited to only lock approach walls. These values were based data from the full-scale impact experiments at Gallopis Lock and Dam (L&D) (Patev 2001) and capped to a maximum force of 800 kips. Based on the need to better define barge impact forces for many critical USACE navigation structures, nonlinear dynamic finite element models (DFEM) using the LS-DYNA computer program were first calibrated to data from a series of USACE full-scale barge impact experiments and then applied to a wide range of hydraulic structures at USACE navigation projects.

1.6.2. The DFEM analyses are the basis of the empirical models and case studies developed and presented in this EM. Unfortunately, this EM does not include all of the types of hydraulic structures in the USACE inventory, but the width and breadth of the EM does cover a valuable range of information to allow engineers to better estimate barge impact forces in their designs.

1.7. Introduction. This document will furnish engineering guidance for the development of barge impact forces to be used in the design of structures at USACE navigation projects. This guidance is based on the results from both the full-scale experiments and nonlinear degree conducted by USACE over the past 20 years. Empirical equations for each structure type have been developed to estimate the barge impact forces for use in the design and evaluation of these structures. A low-order dynamic analysis method is also available to estimate the force and displacement time histories for use in design and evaluation.

1.8. Scope.

1.8.1. The barge impact loads that were defined in previously expired USACE guidance are very limited in application as they applied only to rigid walls, loads less than 800 kips, and impact angles less than 30 degree. Therefore, from 2004 to 2009, the design of USACE navigation structures had been evaluated using this very limited empirical method. However, since 2009 there has been no guidance in place to assist design engineers. Based on the need to better define barge impact loads for critical USACE navigation structures, the development of nonlinear DFEMs for specific types of navigation structures have been completed and peer reviewed.

1.8.2. These DFEMs were first calibrated to data from a series of USACE full-scale barge impact experiments and then applied to a wide range of structures at USACE navigation projects. Based on these analyses, empirical equations have been developed to assist in the design and analysis of many common structural components. In addition, a low-order dynamic analysis method has also been calibrated to the finite element models (FEM) and developed to provide the additional capability to calculate impact force and displacement time histories for the design of navigation structures.

1.9. Manual Organization. Chapter 2 provides design guidance for this manual, and Chapter 3 provides the background and calibration for the DFEMs for barge impact analysis. Chapters 4 through 7 cover empirical and dynamic models for critical navigation structures. Chapter 8 presents an empirical approach to ship impact for ocean-going vessels. The appendixes in this manual are listed below.

1.9.1. Appendix A: References and Units Conversion Factors.

1.9.2. Appendix B: Prototype Field Experiments.

1.9.3. Appendix C: Data from Previous Studies.

1.9.4. Appendix D: Example of Probabilistic Barge Impact Analysis.

1.9.5. Appendix E: Rigid Wall Historical Model (Engineer Technical Letter (ETL) 1110-2-563).

1.9.6. Appendix F: Damage Model – Coastal and Inland Riverine Floodwalls.

1.9.7. Appendix G: Hurricane and Storm Damage Risk Reduction Systems

1.9.8. Appendix H: Flexible Timber Guide Walls.

1.9.9. Appendix I: Lock Dewatering Structures.

1.10. General Requirements. Design of navigation projects must be performed to ensure acceptable performance due to barge impact loads. The performance of the structure must satisfy the structural and operational (navigation) requirements for three load categories with expected range of recurrence (usual, unusual, and extreme) with appropriate load factors used in design.

1.11. Mandatory Requirements Criterion. In this manual, the term “must” denotes a mandatory requirement for compliance with this manual, and the term “will” requires future action. The term “should” indicates a strong preference for a given criterion. The term “may” indicates a criterion that is usable. Other suitable documented, verified, and approved criterion may also be used as long as it is in a manner consistent with this engineering manual.

Chapter 2 Design Guidance for Barge Impact

2.1. Introduction.

2.1.1. Inland navigation structures are subjected to impact loads due to transiting flotillas. Barge impact forces for rare events such as operator error, loss of power, or loss of control have dramatically influenced the overall costs of navigation structures. Figure 2.1 shows the results of a barge impact on a guard wall bullnose due to a loss of control (extreme) event at Smithland L&D.

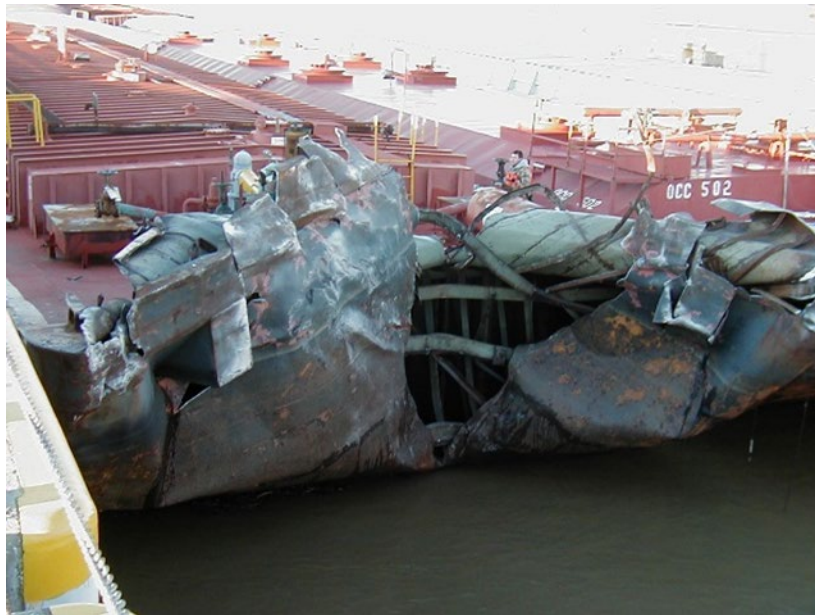


Figure 2.1. Barge Impact Due to Loss of Control at Smithland L&D

2.1.2. With the current emphasis to lower project first costs, innovative navigation structures that can be lifted or floated into place are now being designed and an accurate estimate of barge impact forces is critical in their design. Additionally, many inland navigation projects are now or have recently been designed with floating guide walls. Many coastal hurricane protection projects have been or are currently being designed with floating gates to close openings where barge and ship traffic transit through the hurricane barrier structures. In all of these cases, an accurate estimate of barge impact forces is critical in their design.

2.1.3. By accepting some reasonable risk over the service life of a project, the initial and long-term construction costs can be lowered, and the structure design can be optimized to maintain a safe and economical navigation structure. A better understanding of the risks could be gained through decision analyses that include developing tradeoffs between the stakeholders' costs, safety, and operational requirements for the navigation projects.

2.1.4. In addition, project delivery teams conducting dam or levee safety risk assessments may utilize this manual to estimate barge impact forces to conduct semi-quantitative risk assessments.

2.1.5. This EM provides the following guidance:

2.1.5.1. A design table as shown in Table 2.1 to assist an engineer on what level of analysis for barge impact is required for the design level of their structure. The goal of the table is to ensure that the correct level of analysis is used to capture realistic impact forces for use in the design. Past USACE experience has found that using the extreme values for the design has led to significant overdesign of structures and hence increased costs for structures. Careful review of the barge impact forces needs to be accounted for to ensure that the structure is not subject to total collapse and failure shutting down navigation traffic at a lock facility or leading to inundation of a coastal area in the event of a hurricane storm surge.

2.1.5.2. Preliminary design impact forces are defined in Table 2.2 to assist with the initial structural analysis and to see if the performance criteria can be met based on all return period events (usual, unusual, and extreme) that are defined in section 2.6.

2.1.5.3. Deterministic barge impact analysis is defined as a scenario-based impact analysis that uses an empirical model from Chapters 4, 6, and 7 with data from Appendix D for impact angle, velocity, and mass to reflect the usual, unusual, and extreme load cases. These values are analyzed in a structural model to see how they compare to the performance criteria in section 2.6.

2.1.5.4. Probabilistic barge impact analysis (PBIA) (Patev 2000) is defined by using probability density functions (pdf) for impact angle, velocity, and mass to find the full range of statistical combinations for impact force (pdf) and the estimate of return period (cumulative density function, CDF) for the structure. The statistical information for estimating the masses, approach velocities, and approach angles are discussed in Appendix D where examples of data and distributions for mass, angle, and velocity from past designs of USACE navigation projects structures are shown. The results from the probabilistic impact force and return periods are analyzed in the structural model to see how they compare to the performance criteria in section 2.6. Appendix D also provides information on return periods for use in probabilistic design of lock walls or coastal navigation structures for barge impact loads.

2.1.6. Empirical models have been developed to assist with the estimation of barge impact forces for several critical navigation structures. Complete deterministic and probabilistic design examples are given for each empirical model described in chapters below. These models have been calibrated to USACE full-scale experiments and then further developed using high-order, nonlinear DFEM modeling using LS-DYNA.

2.2. Design Table.

2.2.1. The level of analysis required for the design level is shown in Table 2.1. This must be followed to ensure that the designer can insure a safe and economical design for the structure. The flowchart shows the process from preliminary design forces to assist with the initial structural analysis out to both deterministic and probabilistic methods for estimating impact forces to meet the performance criteria for return periods defined in section 2.6.

2.2.2. These values for velocity and angles are for the designer to estimate based on site knowledge or information from scale model testing at the Engineer Research and Development Center (ERDC). Examples for these are given in deterministic or probabilistic calculations at the end of Chapters 4, 5, 6, and 7. Recommended values are given in Table D.2 and Table D.3 in Appendix D for deterministic, and examples for probabilistic distributions are defined in Appendix C. Values for mass of the design vessel(s) should be determined from Lock Performance Monitoring System (LPMS) database as discussed in Appendix C and D.

2.2.3. For barge impact loads on hydraulic steel structures, reference is made to EM 1110-2-2107. For hydraulic structures not covered by an empirical model in this EM, consultation with Inland Navigation Design Center (INDC) and CECW-EC is required to determine design impact loads.

Table 2.1
Level of Analysis Required (ER 1110-2-1150)

Project Stage	Sections for Design	Angle/Velocity Data (Note: Mass use LPMS data)
Reconnaissance	<ul style="list-style-type: none"> • Preliminary Forces Section 2.3/Table 2.2 <p style="text-align: center;">OR</p> <ul style="list-style-type: none"> • Deterministic Section 2.4/Appendix D • Use empirical models in Chapters 4, 6, and 7 	<p style="text-align: center;">None</p> <p style="text-align: center;">See Appendix D Table D.2, Table D.3</p>
Feasibility	<ul style="list-style-type: none"> • Deterministic with sensitivity Section 2.4/Appendix D • Use empirical models in Chapters 4, 6, and 7 <p style="text-align: center;">OR</p>	<p style="text-align: center;">See Appendix D Table D.2, Table D.3</p>

Project Stage	Sections for Design	Angle/Velocity Data (Note: Mass use LPMS data)
	<ul style="list-style-type: none"> • Probabilistic (using best estimates for probability distributions) Section D.3.3/D.3.4 • Use empirical models in Chapters 4, 6, and 7 	See Appendix D for examples
PED	<ul style="list-style-type: none"> • Deterministic with sensitivity Section D.3.3/D3.4 • Use empirical models in Chapters 4, 6, and 7 <p style="text-align: center;">OR</p> <ul style="list-style-type: none"> • Probabilistic using distributions from scale model testing at project or Appendix D estimations • Use empirical models in Chapters 4, 6, and 7 	<p>See Appendix D Table D.2, Table D.3</p> <p>See Appendix D for examples</p>

2.3. Preliminary Design Impact Loads. The impact forces for a preliminary design and analysis of a structure are shown in Table 2.2. These values are based on both historical design values used in previous barge impact designs or using the empirical models (e.g., concrete walls, bulkheads) defined in this EM. The values reported in this table are not median impact forces but values that are in the 84th percentile (or one standard deviation) to account for some conservative values of impact forces.

Table 2.2
Preliminary Design Barge Impact Forces (ONLY for Reconnaissance stage)

Hydraulic Structure	Barge Impact Forces		
	Usual (kips)	Unusual (kips)	Extreme (kips)
Lock			
Concrete guide/guard walls – upper approach	500	700	1,050
Concrete guide/guard walls – lower approach	250	350	525
Timber guide/guard walls	200	300	450
Bulkheads	NA	300	450
Concrete bulkheads	1,200	1,600	2,500
Dam			
Concrete dam pier	NA	1,600	2,500
Flood Risk Management			

Hydraulic Structure	Barge Impact Forces		
	Usual (kips)	Unusual (kips)	Extreme (kips)
Pile-Founded T-wall	400	600	900
I-wall	250	350	525
Shallow-Founded T-wall	250	350	525

2.4. Deterministic Analysis. The deterministic analysis for barge impact is very beneficial to assist with the initial design concepts and sizing of navigation structures to withstand impact loads. This type of scenario analysis is generally performed at the expected values for mass, impact angle, and velocities for each load case event defined in section 2.6. Sensitivity analysis can be conducted to examine the potential range of impact forces for use in design. Varying ranges of velocity and mass should be examined. This sensitivity should be checked at the upper bounds of velocity and angles for the extreme load case. However, this check may overestimate the extreme design impact loads when compared to a probabilistic analysis.

2.5. Probabilistic Analysis.

2.5.1. The ability to define the loads to which a structure will be subjected during its service life is critical in the design of navigation structures. A method of defining load conditions due to barge impacts needs to be defined on a basis equivalent with other loading conditions such as pool levels or seismic events. To accomplish this, the use of the return period or probability of exceedance has been adopted to design the structure to maintain a certain level of structural performance.

2.5.2. The design or evaluation navigation structures should be based on a range of barge impact angles and approach velocities that can be realistically expected to occur during its service life. PBIA affords the ability to define the return period based on the probability of possible impact events. The variables used in barge impact analysis require numerous combinations of events that cannot be modeled as a discrete event.

2.5.3. The PBIA method requires that distributions be determined for mass, impact angle, and approach velocities, as well as the uncertainties in the empirical models. The uncertainties in mass, velocity, and impact angle can be related to the variations of impact load and the likelihood of occurrence of loading conditions by using Monte Carlo Simulation software as described in Appendixes C and D.

2.5.4. PBIA accounts for the variations of the random variables and empirical model in barge impact design. Coefficients of variations for barge impact forces range from around 10% up to 30%, depending on the load condition being considered. The selection of return periods as defined in Table 2.3 needs to be tied to the variation of the uncertainties incorporated in the PBIA. The higher the variations in the input for a load condition the higher range of the return period should be selected accordingly.

2.5.5. Appendix D shows a PBIA example and how to select return periods for design. Examples of data and distributions for mass, angle, and velocity from recent designs of USACE navigation projects structures are shown in Appendix C.

2.6. Return Periods and Load Factors for Barge Impact.

2.6.1. The return periods and performance criteria for barge impact for normal structures can be defined using the following three load condition categories:

2.6.1.1. Usual. These loads can be expected to occur frequently during the service life of a structure, and no damage will occur to the structure.

2.6.1.2. Unusual. These loads can be expected to occur infrequently during the service life of a structure, and minor damage can occur to the structure. This damage is easily repairable without loss of function for the structure or disruption of service to navigation traffic.

2.6.1.3. Extreme. These loads are due to rare events and can be regarded as an emergency condition, and that moderate to extreme damage can occur to structures without complete collapse (i.e., structure is repairable but with a loss of function or with an extended disruption of service to navigation traffic).

2.6.2. From these definitions of load condition categories, Table 2.3 shows a guideline for probabilities of exceedance (P(E)) and return periods (RT) for barge impact scenarios. Extreme barge impacts do occur on inland waterways, and they are correlated with the following three conditions: (1) high water elevations; (2) high flow velocities, and (3) outdraft conditions. The combination of any of these three conditions can be expected to occur quite frequently and these events should be captured in the selection of the return period.

2.6.3. Barge impact should be included into the proper design load cases for every navigation structure. Load factors are given in Table 2.4 to meet the performance requirement in section 2.6. Refer to current versions of EM 1110-2-2104, EM 1110-2-2107 or appropriate EM for correct load factors. Use Table 2.4 if not covered by an existing EM.

Table 2.3
Design Return Periods for Barge Impact

Load Condition Categories	Probability of Exceedance (P(E))	Return Period (RT = 1/P(E))
Usual	Less than or equal to 0.1	Less than or equal to 10 years
Unusual	Greater than 0.10 but less than or equal to 0.0033	Greater than 10 years but less than or equal to 300 years
Extreme	Greater than 0.0033 but less than 0.00033 for normal structures	Greater than 300 years but less than 3000 years for normal structures

Table 2.4
Load Factors for Usual, Unusual and Extreme Events (Reference is made to Paragraph 2.6.3)

Usual	2.2
Unusual	1.6
Extreme	1.3

2.7. Risks from Barge Impacts.

2.7.1. This EM only assists the designer on loads to be applied to navigation structures. The risks from barge impacts should be addressed in the proper design guidance for the navigation structures (e.g., EM 1110-2-2104 Design of Concrete Hydraulic Structures, EM 1110-2-2107 Design of Hydraulic Steel Structures).

2.7.2. For a risk assessment of a navigation structure, failure of a gate as a result of a barge impact frequently rises to the level of a risk driving failure mode. A risk cadre or project delivery team can utilize this manual to estimate barge (and/or vessel) impact loads, which can then be employed to estimate the likelihood of a structure's failure or breach.

Chapter 3 Barge Model Description and Calibration

3.1. Introduction. Due to severe consequences of barge impact hazards on USACE infrastructure, quantifying barge impact loads on hydraulic structures is necessary. Physical testing of barge impacts proves useful in characterizing design loads but is often cost prohibitive. As an alternative, high-resolution dynamic finite element (FE) analysis is utilized to characterize barge impact forces on hydraulic structures. This chapter documents development of single barge models, extension to groups of barge models, and model calibration for impact simulations.

3.1.1. Background.

3.1.1.1. Most navigable waterways in the United States (U.S.) have the capacity to support transit of materials through use of barges. During transit, barges often navigate within proximity to hydraulic structures, thus posing potential collision risks. As a result, infrastructure such as lock walls, gates, and floodwalls are designed to resist barge impact loading. The most common type of barge traversing U.S. waterways is the jumbo hopper barge. These barges have a width of 35 ft and length of 195 ft. However, other barge types like tanker barges or deck barges may be wider (52 or 54 ft) and longer (210 or 215 ft) and are often configured differently on the waterway. However, the impacting corner structure of most inland barges are designed very similar so any difference in estimated forces would be minimal.

3.1.1.2. Development and calibration of jumbo hopper barge FE models (single, groups) are the focus of this chapter. The documented modeling techniques and calibration efforts constitute a culmination of previously conducted research. Single jumbo hopper barge FE modeling is based on Consolazio et al. (2010) and Getter et al. (2015). Modeling of groups of barges is based on Consolazio et al. (2012) and Walters et al. (2017). Calibration is based on physical barge impact tests at reduced-scale (Kantales et al., 2016) and full-scale (Patev et al., 2003). A finite element analysis (FEA) package, LS-DYNA (LSTC 2014), is used for modeling and impact simulations.

3.1.2. Scope. The material in this chapter is organized to reflect three major thrusts in developing and calibrating barge FE models for impact simulations:

3.1.2.1. Section 3.2 documents the first major thrust, which pertains to the development of a single jumbo hopper barge FE model.

3.1.2.2. Section 3.3 reports on the second major thrust, which extends the FE modeling efforts to include groups of barges.

3.1.2.3. Section 3.4 documents the validation and calibration efforts as a third major thrust.

3.1.2.4. Section 3.5 summarizes the findings and outcomes from the three major thrusts.

3.2. Single Jumbo Hopper Barge Model.

3.2.1. Structural Configuration. Jumbo hopper barges measuring 195 ft long and 35 ft wide are used for all impact simulations. The model barges are based on actual plans and site visits between two of the largest U.S. fabricators (Trinity and Jeffboat). The designs were so similar in structural designs in the areas critical to impact that any difference would be very minimal in terms of impact forces. For modeling purposes, the jumbo hopper barge (Figure 3.1) is divided lengthwise into three zones: bow, hopper, and stern. See section 3.3 for modeling considerations of other configurations (e.g., double-raked). Watertight bulkheads, spaced at 40.5-ft intervals along the hopper region, act to compartmentalize the barge. The entire barge structure is modeled using more than 900,000 elements (nonlinear quadrilateral shell elements). Individual shell element dimensions are typically 3 in. square (Figure 3.1b–c).

3.2.1.1. Throughout the three barge zones, internal and external plate thicknesses vary between 5/16 in. and 5/8 in. Internal stiffening members consist primarily of steel channel and single angle members. Shell elements located across the widths of structural member components (e.g., angle legs) are sufficiently discretized to allow local buckling. For structural shapes within the barge, three or more element divisions are modeled across member widths (legs, flanges).

3.2.1.2. The barge bow zone includes 14 internal rake trusses, frames, transverse bracing members, and external hull plates (Figure 3.2). The hopper zone contains a barge bottom plate and hopper bottom plate (Figure 3.3). These two plates are connected by closely spaced transverse stiffener plates. Additionally, the hopper zone contains 24 port and 24 starboard sidewall units (referred to as sidewall modules). Each sidewall module is stiffened by closely spaced longitudinal plates and angles. Longitudinal plates in the hopper zone terminate at watertight bulkheads, which bound each group of six modules.

3.2.1.3. The stern zone (Figure 3.4) contains 14 internal trusses and frames. Stiffening plates are closely spaced (vertically) at the port and starboard corners of the stern. Both transverse and longitudinal stiffening angles are attached to the corner stiffening plates. See Consolazio et al. (2010), Getter et al. (2015) for additional configuration and meshing details.

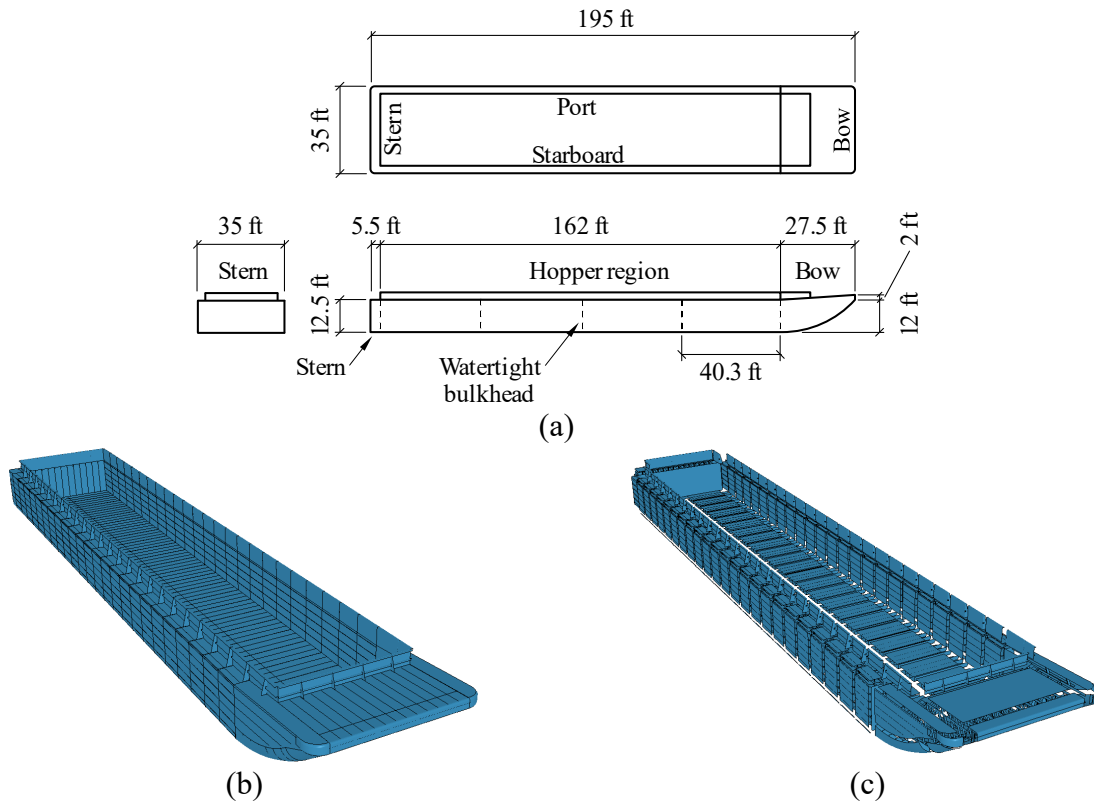


Figure 3.1. Jumbo Hopper Barge FE Model (Mesh Not Shown for Clarity):
 (a) Schematic Plan and Elevation View; (b) Perspective View; (c) Exploded View

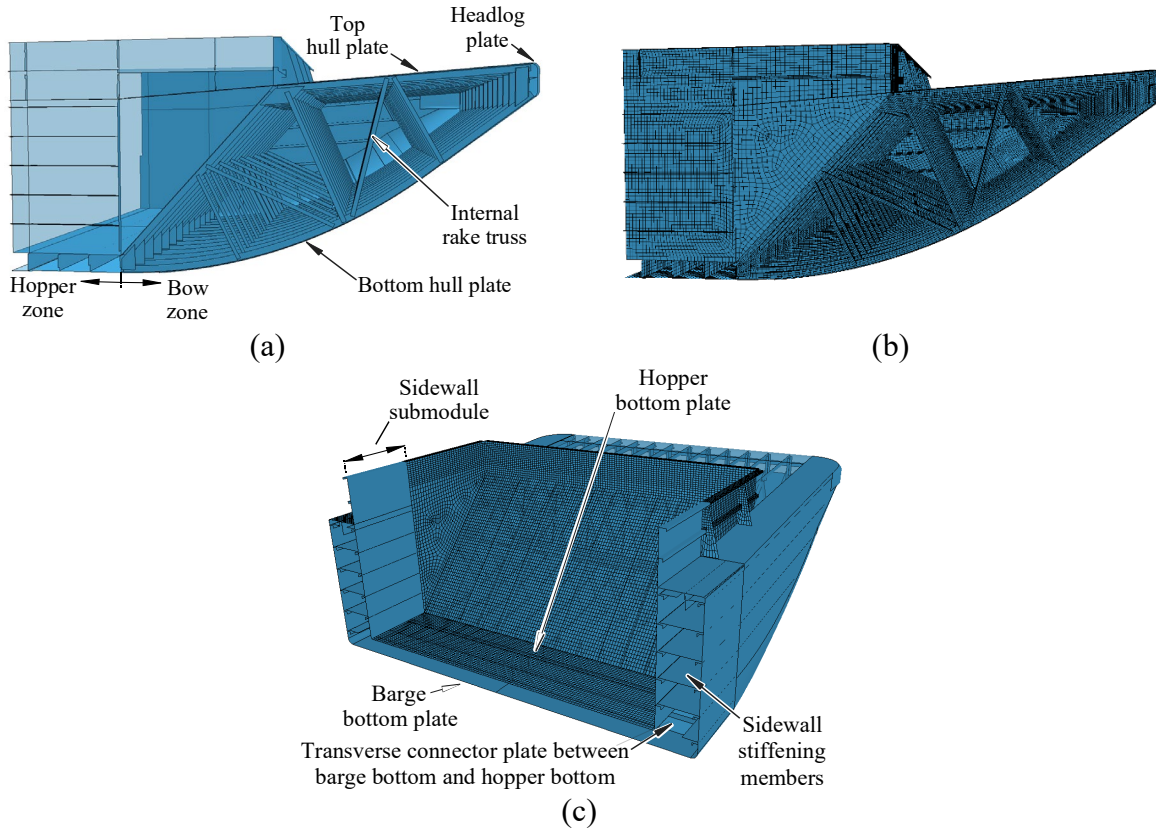


Figure 3.2. Barge Bow Zone FE Model Details (Partial Mesh Shown for Clarity):
 (a) Elevation View of Configuration; (b) Elevation View of Mesh; (c) Isometric View of Transition from Bow Zone to Hopper Zone

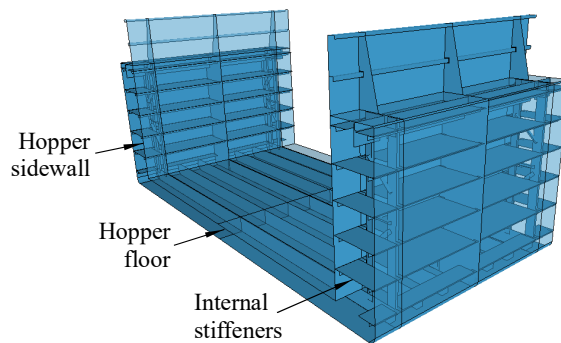


Figure 3.3. Barge Hopper Zone FE Model Details (Mesh Not Shown for Clarity)

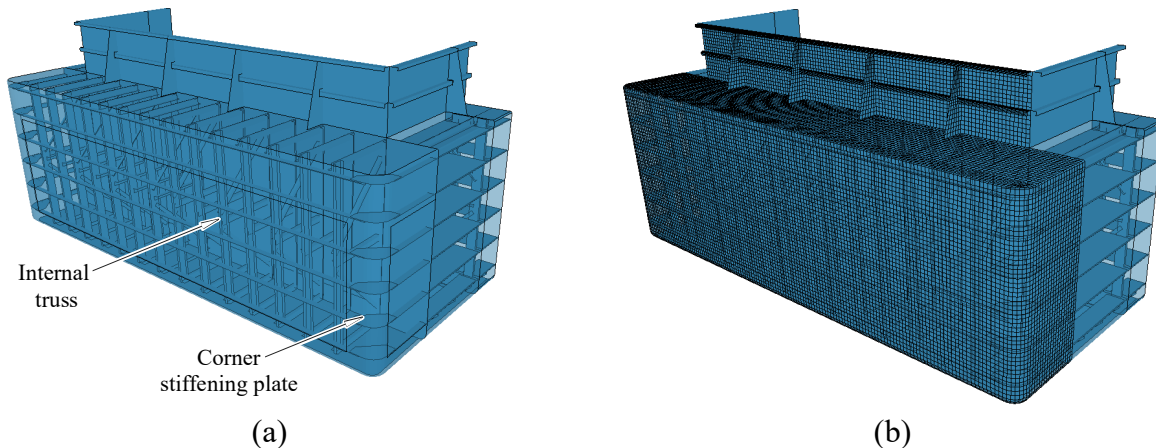


Figure 3.4. Barge Stern Region FE Model Details (Partial Mesh Shown for Clarity):
 (a) Isometric View of Configuration; (b) Isometric View of Mesh

3.2.2. Constitutive Modeling. U.S. barges are typically constructed from A36 structural steel, which has a specified minimum uniaxial tensile yield stress of 36 ksi. For modeling purposes, an elasto-plastic material model (i.e., constitutive relationship) representing the nonlinear behavior of A36 steel is used. The constitutive relationship is defined using the *MAT_PIECEWISE_LINEAR_PLASTICITY material model in LS-DYNA (LSTC 2014a). Further, the material model includes both linear elastic and nonlinear plastic components.

3.2.2.1. Determination of whether material behavior is elastic or plastic depends on the outcome of evaluating the Von Mises yield criterion. When the Von Mises stress (effective stress) is less than the uniaxial tensile yield stress, linear elastic behavior is modeled. In this context, elastic behavior signifies an elastic modulus of 29,000 ksi and Poisson's ratio of 0.33. Otherwise, yielding is deemed to have occurred and plasticity is used to compute incremental effective plastic strains.

3.2.2.2. Material hardening is described using a piecewise linear relationship between effective true stress and effective plastic strain. For the A36 material used in the barge model, a piecewise linear curve (Figure 3.5) is used to describe hardening. Material failure (rupture) occurs at a strain of 0.2 in./in. and at an effective true stress of 69.8 ksi. This material model is utilized by the more than 900,000 four-node, fully integrated shell elements that make up the barge model. See Consolazio et al. (2009) for additional details.

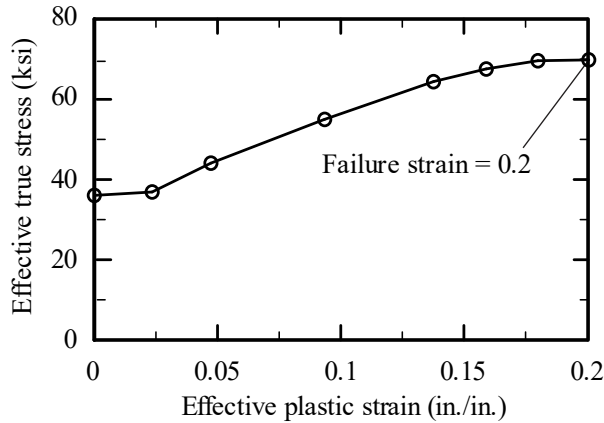


Figure 3.5. Barge Structural Steel Material Parameters

3.2.2.3. Strain-rate effects are modeled using the Cowper-Symonds model:

$$\frac{\sigma_{\text{dynamic}}^y}{\sigma_{\text{static}}^y} = \left[1 + \left(\frac{\dot{\epsilon}_{\text{eff}}^p}{C} \right)^{\frac{1}{P}} \right] \quad (3.3.1)$$

where $\sigma_{\text{dynamic}}^y$ is dynamic yield stress, σ_{static}^y is static yield stress, and $\dot{\epsilon}_{\text{eff}}^p$ is effective plastic strain rate. For mild steel, the two material parameters (C and P) are taken as 40.5 sec⁻¹ and 5, respectively, per Jones (1997).

3.2.2.4. Use of shell elements and the elasto-plastic material model (Figure 3.5) allows for complex plate and member behaviors to occur. For example, during impact, plate and member buckling can occur (as appropriate) at locations throughout the barge model. Structural shapes are modeled with sufficient mesh density to allow for curvature reversal in the event of member local buckling. Additionally, using shell elements to model internal structural members allows for barge components to undergo local material failure (fracture). In LS-DYNA (Livermore Software Technology Corp (LSTC) 2014b), fracture can be approximated through element deletion (when the failure strain is reached within an element).

3.2.2.5. Steel components in barges are joined together by localized welds. In the FE model, structural members are joined by “spot welds” which are rigid beams that connect two nodes together. The *CONSTRAINED_SPOTWELD keyword in LS-DYNA is utilized (LSTC 2014b). Connection failure is accounted for through element deletion upon failure of the joined shell elements. The base material is assumed to reach failure strain, 0.2 in./in., prior to spot weld failure. Spot welds are distributed at a sufficient density to emulate the types of welds present in physical barge configurations.

3.2.3. Barge Weight and Payload. A typical empty jumbo hopper barge possesses a displacement tonnage of 200 tons (American Association of State Highway and Transportation Officials (AASHTO) 2017). However, barge weights vary by manufacturer. Based on available structural drawings, the bare steel weight of jumbo hopper barges is taken as 285 tons. Additionally, field observations of barges and draft levels indicate that “empty” barges often retain residual transported material in the hopper. To account for residual payload, an additional 77 tons is distributed throughout hopper zones (Figure 3.6) for modeling empty conditions.

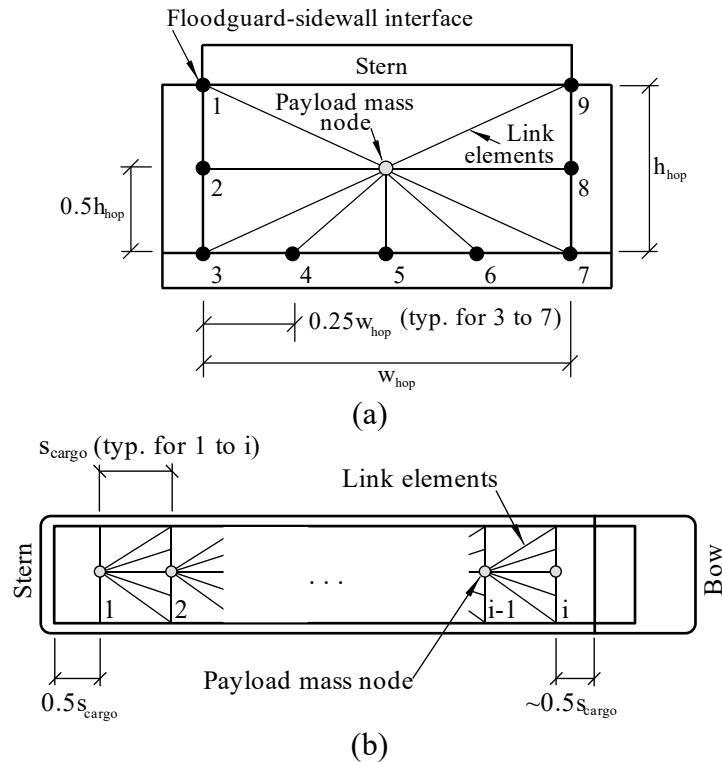


Figure 3.6. Barge Payload Modeling Schematic: (a) Elevation View; (b) Plan View

3.2.3.1. AASHTO (2017) defines a fully loaded barge as having a displacement tonnage of 1,900 tons. However, variabilities in payload weights warrant consideration of a range of “loaded” displacement tonnage conditions. Displacement tonnages up to 2,000 tons are modeled to account for maximum payload and hydrodynamic mass (Walters et al., 2017). As delineated in subsequent chapters, payloads ranging from 1,360 tons to 1,715 tons are modeled for simulating loaded barge conditions.

3.2.3.2. As a summary of the above considerations, the following displacement tonnages (per barge) are modeled:

3.2.3.2.1 Empty barge: 362 tons (bare steel weight, residual payload); and,

3.2.3.2.2 Loaded barge: 1,645 tons to 2,000 tons (bare steel weight, payload, and hydrodynamic mass).

3.2.3.3. Payload is modeled using a series of mass nodes, distributed along the hopper zone centerline (Figure 3.6, Figure 3.7). Specifically, 27 payload mass nodes are placed at a height ($0.5h_{hop}$) of 5.4 ft above the hopper bottom plate. Payload mass nodes are spaced (s_{cargo}) at 6 ft intervals (Figure 3.6b). See Consolazio et al. (2010) for listings of barge centroidal coordinates and moments of inertia.

3.2.3.4. A three-dimensional network of link elements acts to transfer forces between payload mass nodes and the surrounding barge model. For each payload mass node, link elements are attached to the sidewall top, bottom, and mid-height locations. Furthermore, link elements span between each payload mass node and five locations across the hopper bottom plate. Attachment locations across the hopper bottom plate are spaced ($0.25w_{hop}$) at 7.13 ft (Figure 3.6a).

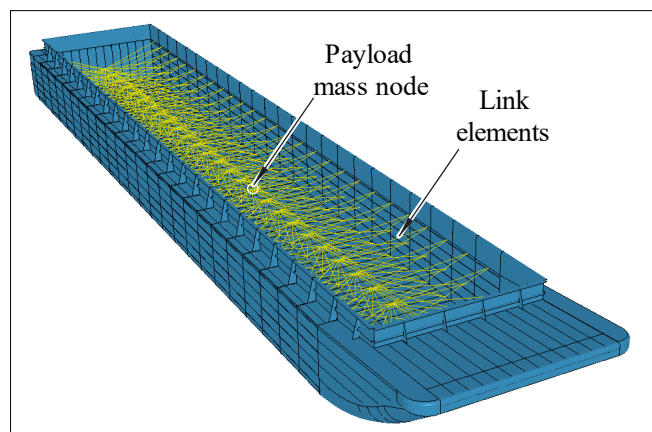


Figure 3.7. Barge and Payload FE Model Details (Mesh Not Shown for Clarity)

3.2.4. Buoyancy Effects. Buoyant effects of water surrounding the barge are modeled using distributed springs connected along the bottom surface of the barge. Specifically, more than 26,000 discrete springs are attached to barge bottom (outer surface) nodes (Figure 3.8). The springs are anchored at nodes located above the corresponding barge bottom nodes. Because barges undergo significant horizontal motions during collisions, roller support conditions were specified at the tops of the springs. This approach maintains vertical spring alignment during motion and ensures integrity of the buoyancy forces acting on the barge.

3.2.4.1. The FE model is configured such that barge bottom surfaces in hopper and stern zones remain submerged during collision simulations. However, as detailed in Consolazio et al. (2010), this is not the case for portions of the bow zone. Gaps are incorporated into the force-deformation definitions for springs attached to nodes in the bow zone. The “gapped springs” ensure that nodal buoyancy forces are generated only during times when the respective nodes are submerged.

3.2.4.2. Buoyancy springs are defined as nonlinear elastic (tension-only) elements. The stiffness of a given buoyancy spring is determined by first calculating tributary barge surface area supported by the spring. Then, the tributary area is multiplied by the density of water. Consequently, stiffness values for each spring vary in proportion to the (tributary) surface area of barge bottom being supported. Stiffness values for buoyancy springs formed in this manner are small, ranging from 0.001 to 0.004 kip/in. Such small stiffness values preclude development of unrealistically concentrated buoyant forces acting on the barge hull.

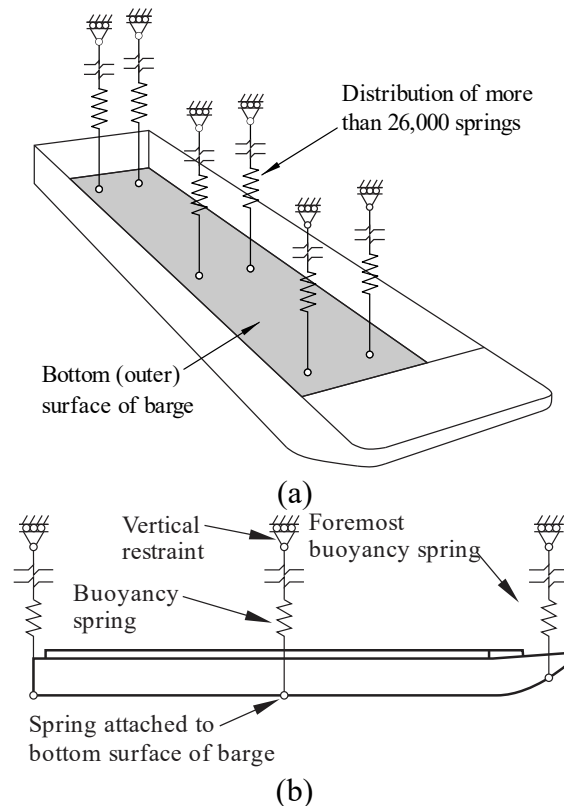


Figure 3.8. Buoyancy Spring System:
 (a) Conceptual Schematic; (b) Elevation Schematic (with Dimensions)

3.2.5. Contact Definitions for Impact on Hydraulic Structures.

3.2.5.1. For all collision simulations conducted, barge collision forces are quantified using contact-impact algorithms in LS-DYNA (LSTC 2014). An illustration of how contact definitions are implemented for an example impact scenario is given in Figure 3.9. Here, forces generated between impacting barge(s) and hydraulic structures develop based on interactions between any of a set of specified:

- 3.2.5.1.1 Nodes on the barge model, and;
- 3.2.5.1.2 Element faces (shell, solid) on the impacted structure.

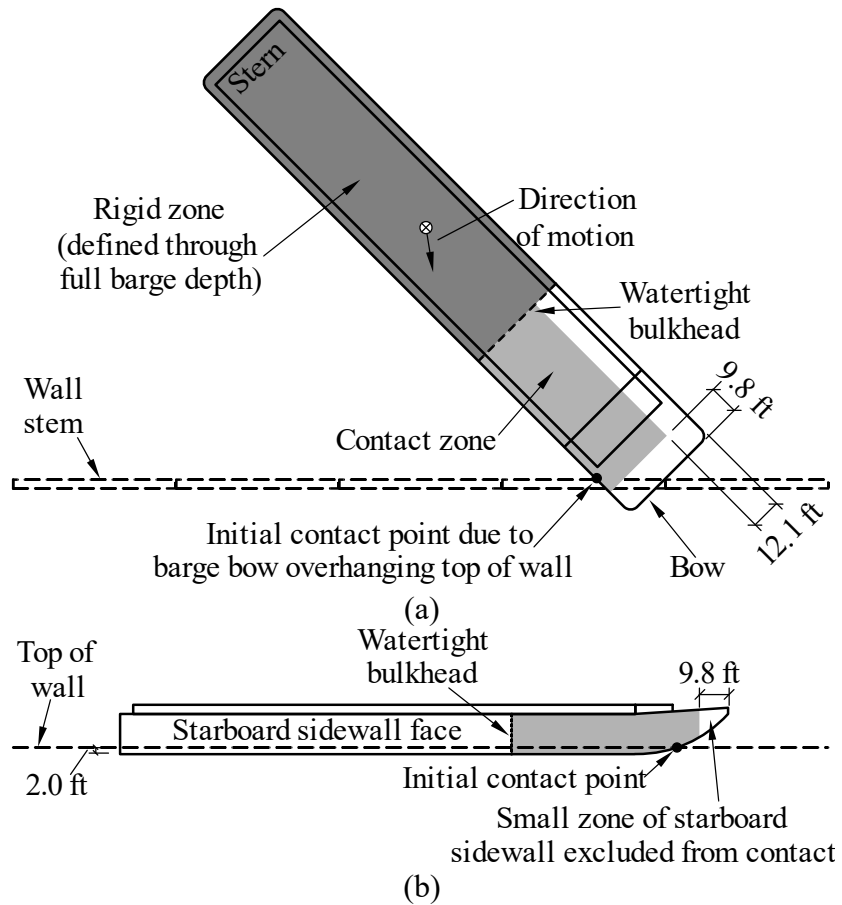


Figure 3.9. Illustrative Schematic of Contact and Rigid Zones:
 (a) Plan View; (b) Elevation View

3.2.5.2. Computational efficiency is achieved by specifying only those nodes on the barge that could potentially come into contact with the hydraulic structure (e.g., wall) during collision. An additional contact definition is employed for monitoring self-contact between specified internal and external barge components. Only nominal stresses occur in barge portions where neither barge-to-structure contact nor self-contact (internal contact) are applicable. To further improve computational efficiency, these portions of the barge are assigned a rigid material model (Figure 3.10). For each impact condition simulated (bow impact, stern impact, side impact), analogous schemes (similar to Figure 3.9) are used. In turn, the approach efficiently incorporates barge-wall contact, barge self-contact, and rigid element zones into the FE barge model.

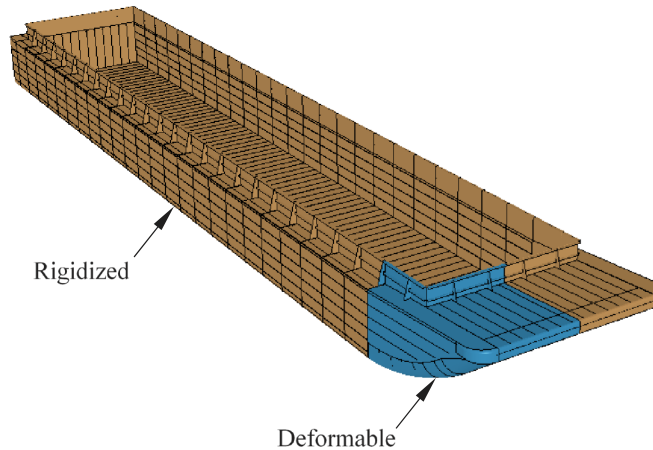


Figure 3.10. Partial Rigidization of Impacting Barge FE Model

3.3. Barge Flotilla Model.

3.3.1. Overview. A barge “flotilla” is a group (collection) of individual barges, typically arranged end-to-end in one or more columns. Inter-barge lashings, commonly consisting of steel wire rope cables, secure the individual barges together into an integral unit. The assemblage of barges can then be efficiently propelled along navigable waterways using a single (trailing) push boat. An example three-column, five-row (3x5) barge flotilla (and tug) is depicted in Figure 3.11.



Figure 3.11. Typical Barge Flotilla in Transit

3.3.1.1. The extension of the single-barge FE model (section 3.2) to allow for simulation of flotilla impacts is documented in this section. Flotilla components that tie barges together are identified and corresponding model entities (e.g., inter-barge lashings, Figure 3.12) are detailed. Further, FE modeling of contact that occurs between barges during collisions (i.e., inter-barge interactions) is documented.

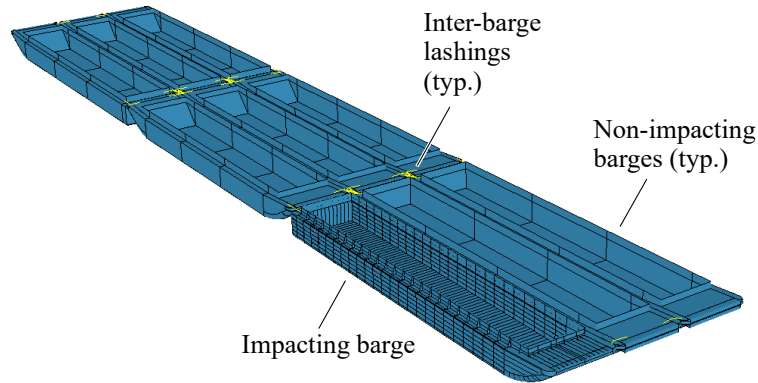


Figure 3.12. Finite Element Model of a 3x3 Flotilla Configuration (Mesh Not Shown for Clarity)

3.3.1.2. In the following, for computational efficiency, a major distinction is maintained for modeling of the impacting barge versus non-impacting barges. During impacts between flotillas and hydraulic structures, only certain flotilla portions come into direct contact with impacted structures. Typically, only one barge from the flotilla makes direct contact that results in generation of design-relevant impact forces.

3.3.1.3. Figure 3.13 depicts a 3x3 flotilla (with velocity V_0) impacting a wall at an oblique angle (θ). The frontmost (lead-row) barge on the flotilla starboard side directly impacts the wall and is designated as the impacting barge. Other barges are designated as non-impacting barges.

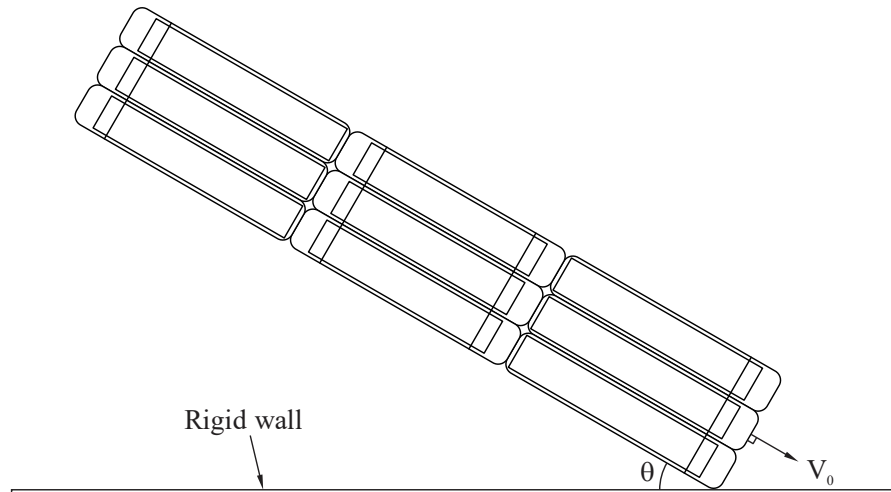


Figure 3.13. Illustrative Schematic of 3x3 Flotilla Collision with Rigid Wall

3.3.2. Structural Configuration. Flotillas are composed of multiple, individual jumbo hopper barges (single barges are detailed in section 3.2). To develop barge impact loads for design, a wide range of flotilla sizes (typical of U.S. waterways) are considered (Figure 3.14).

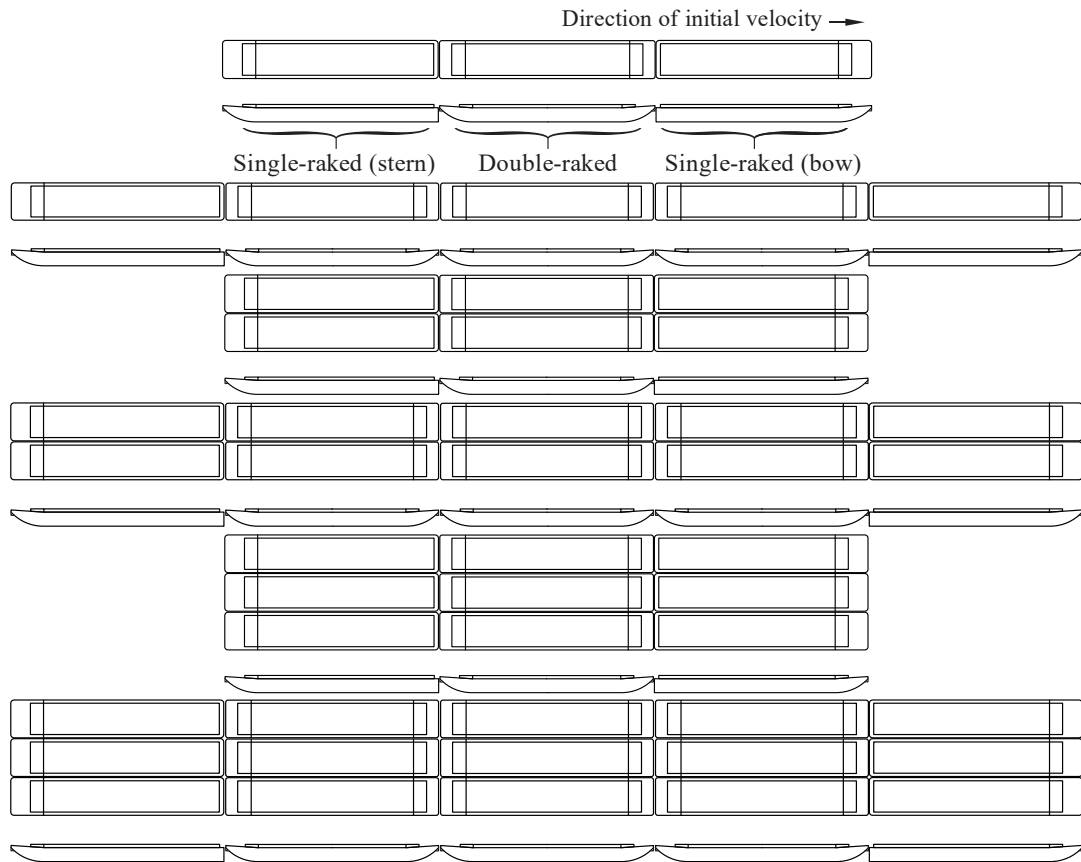


Figure 3.14. Examples of Jumbo Hopper Barge Flotilla Configurations Considered:
1x3, 1x5, 2x3, 2x5, 3x3, 3x5

3.3.2.1. Flotilla sizes are selected from the following list, based on operational feasibility for the specific type of hydraulic structure considered:

3.3.2.1.1 Single column (1x) flotillas: 1x2, 1x3, 1x5.

3.3.2.1.2 Double column (2x) flotillas: 2x1, 2x2, 2x3, 2x5.

3.3.2.1.3 Triple column (3x) flotillas: 3x3, 3x4, 3x5.

3.3.2.2. Regardless of configuration, within each flotilla, two types of jumbo hopper barge (structural) configuration are present. One configuration is that of single-raked barges, which are raked (tapered in depth) only at one end (Figure 3.14). The other configuration is that of double-raked barges, which are raked at both the bow and stern (Figure 3.14). Single-raked barges are positioned at lead and trailing rows of each flotilla, while double-raked barges occupy interior rows.

3.3.2.3. Together with application of a vertical gravity field, vertical buoyancy forces are incorporated into the flotilla FE models. Recalling Figure 3.8, each barge is suspended by vertical, tension-only springs, which attach to all bottom-surface nodes. To ensure that nodal buoyancy forces are only generated when nodes are submerged, gaps are incorporated into the buoyancy springs. See Consolazio et al. (2010) for details regarding gap spring calibration and initialization. Including both gravity and buoyancy effects permits the barges to emulate pitching and rolling motions that may occur during impact.

3.3.2.4. Bitt Locations. Every barge has multiple structures affixed to the deck that act as connection points for wire rope lashings (Figure 3.15). For example, bitts are cylindrical posts around which a lashing can be wrapped or pivoted. Cavels are smaller handle-shaped structures to which the end of a lashing can be secured. These structures are ubiquitous to barges, but the exact locations are not standardized and tend to vary by barge manufacturer. Photographs of barges aid in estimation of representative bitt and cavel locations (e.g., from Patev et al., 2003). Based on photographic review, two bitts and one cavel are placed symmetrically at barge corners throughout the flotilla FE models.

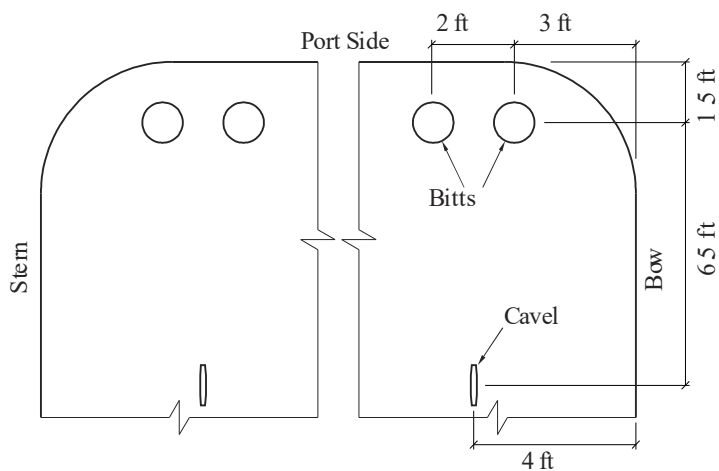


Figure 3.15. Bitt and Cavel Locations (Shown for Port Side Only)

3.3.2.5. Lashing Configurations. Each pair of adjacent barges in a flotilla is lashed together by wrapping the barge bitts in a specific pattern. In this context, a given pattern is referred to as a lashing configuration. Different configurations are used to lash different types of barge pairs (end-to-end, side-to-side, or diagonal). Lashings also allow the flotilla to remain intact during common flotilla maneuvers. When more than one configuration is required at the same location, the lashings are layered on top of each other.

3.3.2.5.1 Seven distinct lashing configurations are modeled and are divided into groups according to their function. Note that the configurations are presented as they appear on the port side of the flotilla. Starboard lashings are similar but mirrored about the flotilla centerline.

3.3.2.5.2 Fore/aft wires (Figure 3.16, Figure 3.17) secure end-to-end barge pairs together at shared corners, providing longitudinal rigidity to each barge column. The configuration used along flotilla exterior edges (L1) employs a 1-in. diameter wire rope, rated at 90-kip break strength. Other lashing configurations, including fore/aft wires along interior edges (L2–L3), use a 1¼-in. diameter wire rope rated at 120 kip.

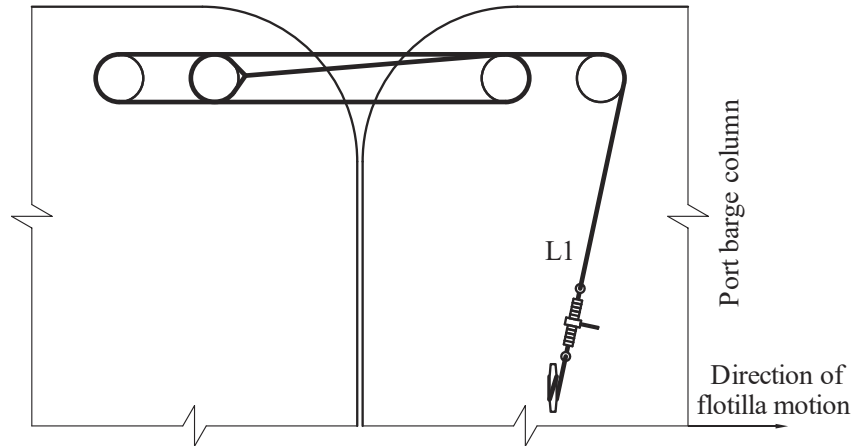


Figure 3.16. Exterior Fore/Aft Wires (Rated at 90-kip Break Strength)

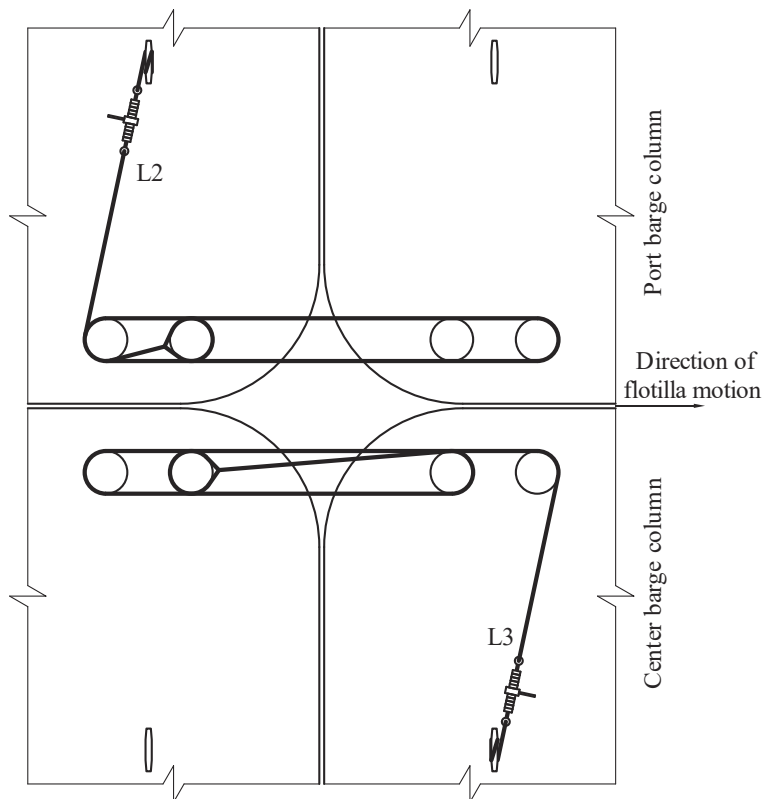


Figure 3.17. Interior Fore/Aft Wires (Rated at 120-kip Break Strength)

3.3.2.5.3 Breast wires (Figure 3.18) are used to connect side-to-side barge pairs together at shared corners. This configuration prevents port and starboard columns from lagging behind the center column during flotilla travel. Towing wires (L4) are engaged when the center column is pushed forward. Backing wires (L5) are engaged when the center column is pulled backward.

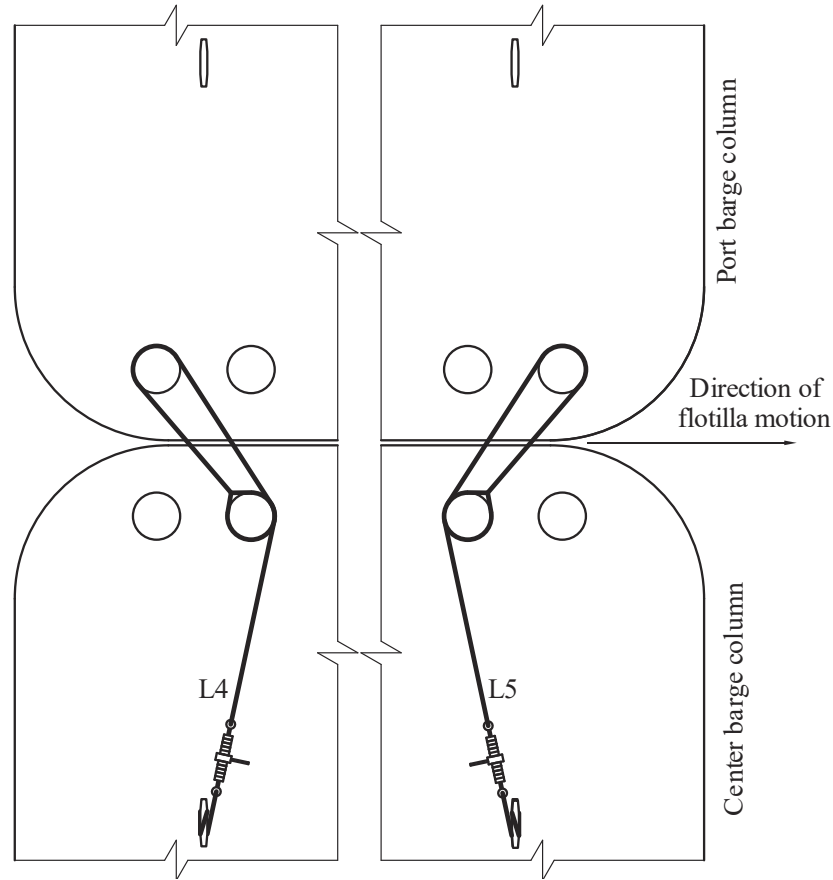


Figure 3.18. Breast Wires (Rated at 90-kip Break Strength)

3.3.2.5.4 Scissor wires (L6–L7, Figure 3.19) connect diagonal barge pairs together at every four-corner interface. This configuration straightens out the flotilla and increases flexural rigidity. Also, scissor wires maintain flotilla integrity when steered from behind.

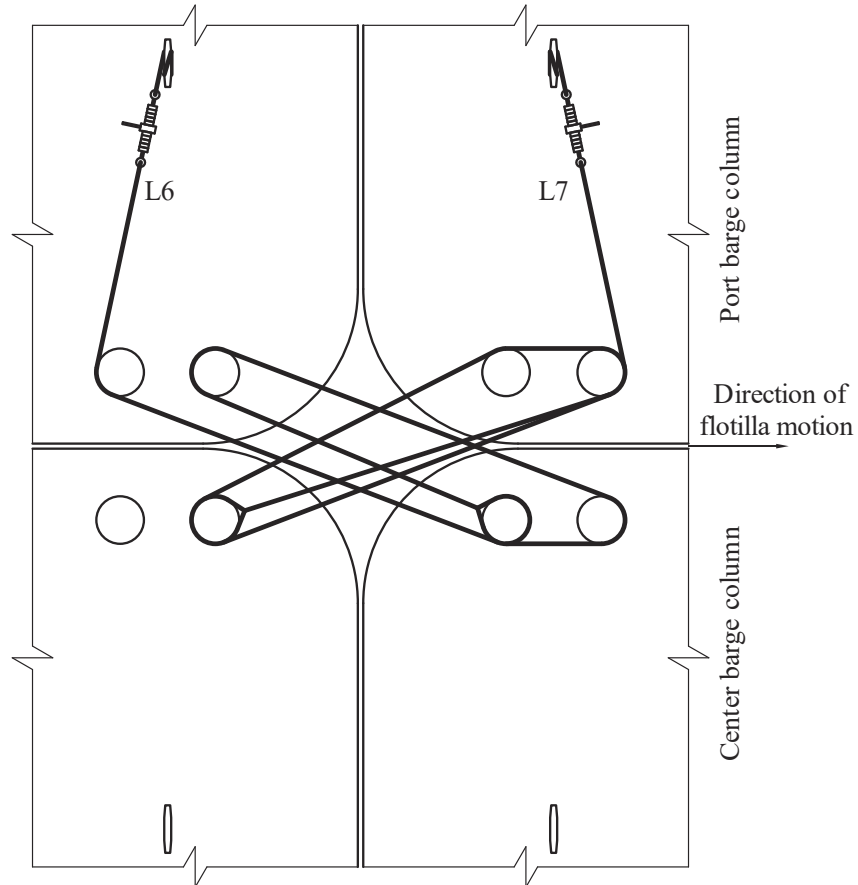


Figure 3.19. Scissor Wires (Rated at 120-kip Break Strength)

3.3.2.5.5 In a fully lashed flotilla, there are four unique combinations of lashing configurations (shown on a 3x3 flotilla in Figure 3.20). These lashings may be repeated or deleted, based on the size of the flotilla under consideration. For example, 3x5 flotillas are analogous to those of 3x3 flotillas, but with additional “A” and “C” regions inserted. Only the four-corner interface (“C” region) requires multiple layers of lashings.

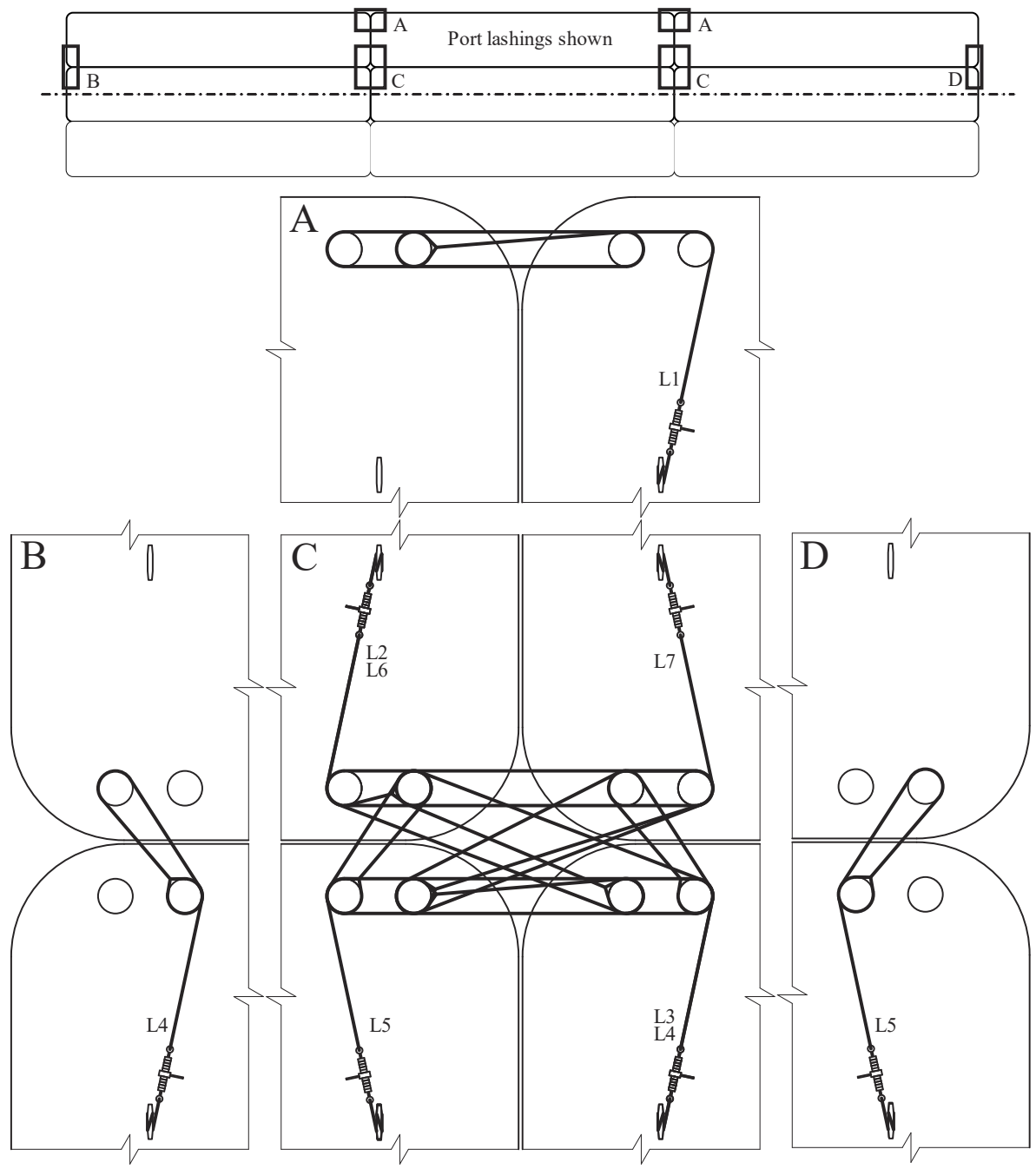


Figure 3.20. Lashing Configuration Combinations on a 3x3 Flotilla

3.3.3. Finite Element Modeling of the Impacting Barge. For typical flotilla collision scenarios, one lead-row barge (recall Figure 3.13) will make initial contact with the hydraulic structure. Lead-row barges are often single-raked. Therefore, a single-raked jumbo hopper barge is designated as the impacting barge in flotilla models. Modeling considerations for the impacting barge (throughout the barge, between the barge and impacted structure) are documented in section 3.2. Considerations for FE modeling of non-impacting barges and interactions between barges are reported in the remainder of section 3.3.

3.3.4. Finite Element Modeling of Non-Impacting Barges. Non-impacting barges in flotilla FE models provide a means of representing mass-related barge inertial properties. In addition, non-impacting barges are used to model dynamic interactions between barges. However, using a finely discretized (e.g., 900,000 element) barge model at each position within a multi-barge flotilla is computationally inefficient. This is because the impacting barge is the only unit in the flotilla expected to undergo concentrated, inelastic deformations. Limited insights would be gained by including detailed geometric and constitutive modeling of non-impacting barges. Non-impacting barges are modeled as being similar to the impacting barge in terms of external geometry. However, the internal structural configurations are wholly modified to improve numerical efficiency.

3.3.4.1. Structural Model. Flotilla models include two variations of non-impacting barges: a single-raked barge (Figure 3.21a) and a double-raked barge (Figure 3.21b). Note that the double-raked (non-impacting) barge maintains the same overall dimensions as the non-impacting single-raked barge. However, the headlog of the double-raked model is more finely discretized than that of the (non-impacting) single-raked model. Here, the increased level of discretization ensures robust detection of contact for both bow-to-bow and bow-to-stern interactions.

3.3.4.1.1 In each non-impacting barge model, all shell elements are sized at approximately 36 in. by 36 in. Exterior surfaces of non-impacting barges are rigidized (i.e., made rigid). Deformability of barge perimeters, as related to interactions between contacting barges, is modeled using nonlinear force-penetration contact definitions (discussed later). This approach improves computational efficiency relative to detailed modeling of the barge perimeter with deformable shell elements.

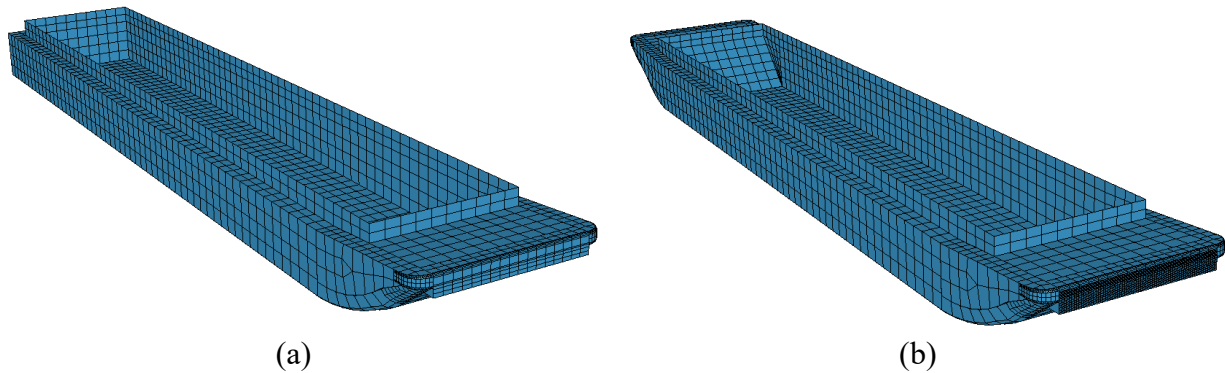


Figure 3.21. Non-Impacting, Reduced Resolution Jumbo Hopper Barge FE Models:
 (a) Single-Raked; (b) Double-Raked

3.3.4.1.2 Given that deformability is managed through contact definitions (rather than deformable shell elements), internal structural shell elements serve no purpose. Therefore, internal shell elements that would otherwise represent structural shapes, plates, and frames are removed from the model. Despite simplifications for computational efficiency, all non-impacting barges mimic the global mass- and stiffness-related attributes of the deformable, impacting barge. As examples, all barges possess equivalent mass moments of inertia (Consolazio et al., 2010), translational mass, and nonlinear perimeter stiffness.

3.3.4.2. Payload.

3.3.4.2.1 Barge and payload weights (and masses) for non-impacting barges are equal to those of the impacting barge (recall section 3.2.3. However, modeling of weight (and mass) in non-impacting barges is handled differently than in the (high-resolution) impacting barge model. In the non-impact barge models, all internal components are removed (i.e., they no longer contribute mass). Consequently, the correct mass-related properties must be specified through a different modeling mechanism to ensure correct dynamic response during impact. Because non-impacting barges are rigid, mass-related inertial properties of the entire barge models can be specified at a single point.

3.3.4.2.2 For each non-impacting barge model, a node is added at the location of the center of gravity (c.g.) and rigidly attached to the rest of the barge model (rigid outer shell). Next, translational mass and inertial tensor quantities are derived from corresponding highly discretized (~900,000 elements) models of single- and double-raked barges. Properties derived from high-resolution models are then specified as c.g. properties in respective low-resolution (~4,000 elements) non-impacting barge models.

3.3.4.3. Buoyancy Effects. Buoyancy for the non-impacting barges is, overall, modeled in the same manner as that used for the impacting barge. The exception is that fewer discrete buoyancy springs (~900) are used due to the lower mesh resolution of non-impacting barge models. Buoyancy springs in non-impacting barges use the same force-deformation relationships, offsets, and calibration schemes as those discussed in section 3.2.4.

3.3.5. Inter-Barge Contact Definitions. Barge-to-barge contact definitions are assigned based on the row and column position of a barge within the flotilla. Available contact surface is also considered. The various barge-to-barge contact definitions (types) assigned are illustrated in Figure 3.22, and include side-to-side, bow-to-bow, or bow-to-stern.

3.3.5.1. Barge-to-barge contact definitions in the flotilla FE model are included for each anticipated instance of barge-to-barge adjacency. In contrast, and to promote computational efficiency, contact types are intentionally excluded for non-adjacent barges. For example, barges in flotilla lead rows are not expected to make direct contact with barges in the trailing row. So, no contact type is defined between a barge in the lead row and barge in the trailing row.

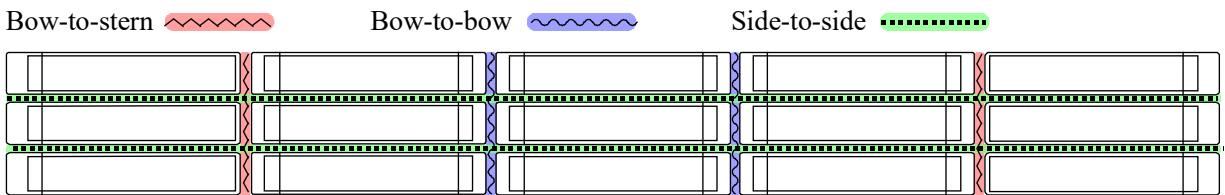


Figure 3.22. Barge-to-Barge Contact Types (Illustrated within a 3x5 Flotilla)

3.3.5.2. Rigid Contact Crush Curves. Nonlinear contact deformations that arise between rigidized portions of two adjacent barges are represented using a special-purpose rigid body contact algorithm. In particular, the `*CONTACT_RIGID_BODY_ONE_WAY_TO_RIGID_BODY` option in LS-DYNA is utilized (LSTC 2014). Accordingly, objects that are otherwise treated as being perfectly rigid are instead permitted to penetrate each other during contact interactions. As a result, when two barges come into contact, a restoring force is applied to each penetrating node. The restoring force increases as penetration increases, until sufficient force has been generated to eliminate the nodal penetration. This approach mimics the contact interactions that would normally occur between deformable objects.

3.3.5.2.1 A nonlinear force-penetration relationship is used to quantify nodal (normal) force versus penetration through designated rigid surfaces (along barge perimeters). Definitions are supplied on a per-node basis, specific to the barge-to-barge contact type being modeled (bow-to-stern, bow-to-bow, side-to-side). The process of generating force-penetration relationships is illustrated for bow-to-stern impact in Figure 3.23.

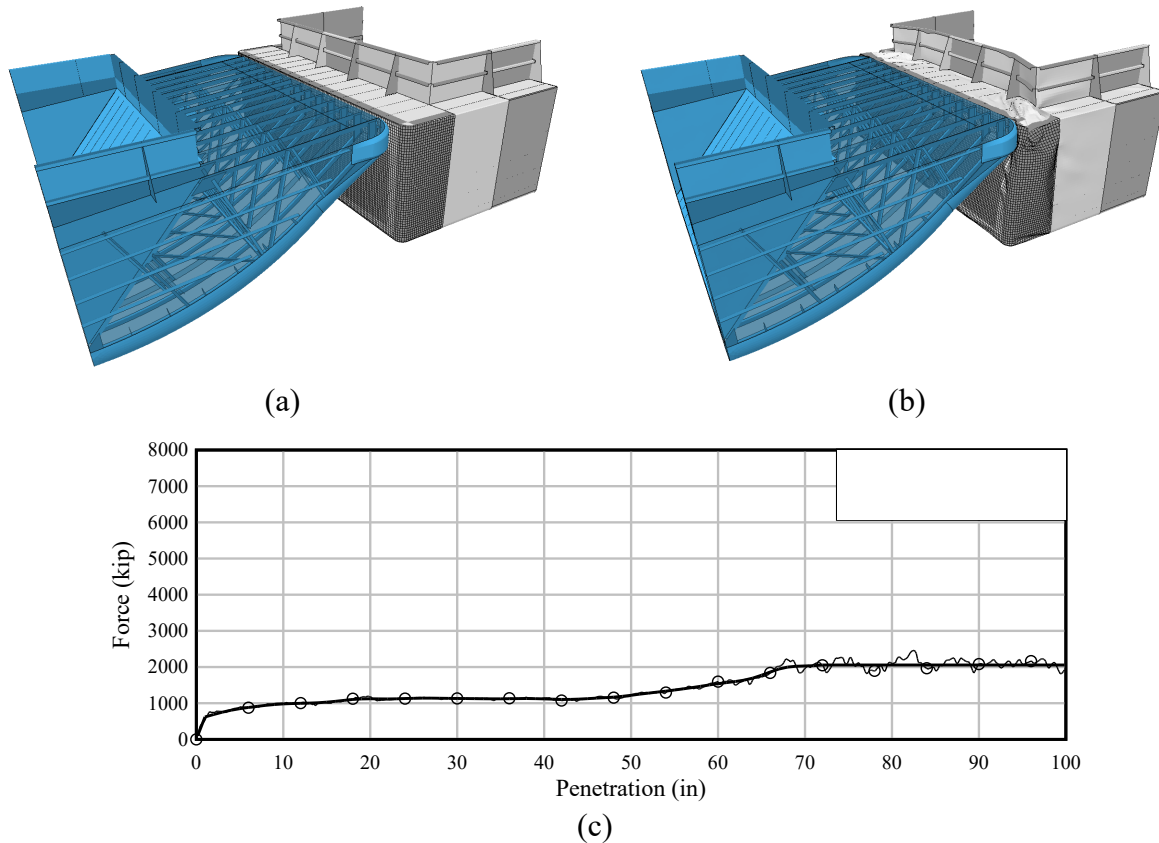


Figure 3.23. Bow-to-Stern Crush Simulation (Partial Mesh Shown for Clarity):
 (a) Before Crush; (b) During Crush; (c) Force-Penetration Relationship

3.3.5.2.2 Force-penetration relationships for each barge-to-barge contact type are derived from deformable (high-resolution) barge crush simulations. For impact simulations involving barge flotillas, the relationships are then assigned to appropriate contact zones (recall Figure 3.22). For example, bow-to-stern interactions utilize a force-penetration relationship obtained from crushing a fully deformable bow and stern (Figure 3.23). Due to the greater bow (versus stern) stiffness, the majority of deformation occurs in the stern (Figure 3.23b). However, low-level deformation also occurs in the bow. Regardless, these phenomena are accounted for in the curve of Figure 3.23c.

3.3.5.2.3 After carrying out the bow-to-stern barge crush simulation, the total contact force attributable to crushing is paired with penetration distance. A smoothed curve (Figure 3.23c) is then utilized for that type of interaction in the flotilla FE model (recall Figure 3.22). Additionally, corresponding simulations are carried out to characterize barge-to-barge interactions for the bow-to-bow and side-to-side types (Consolazio et al., 2012). Hence, deformations arising as a result of barge-to-barge interactions are accounted for through the use of rigid body contact definitions. This is despite the use of rigid shell elements for modeling non-impacting barges.

3.3.6. Bitt and Lashing Modeling.

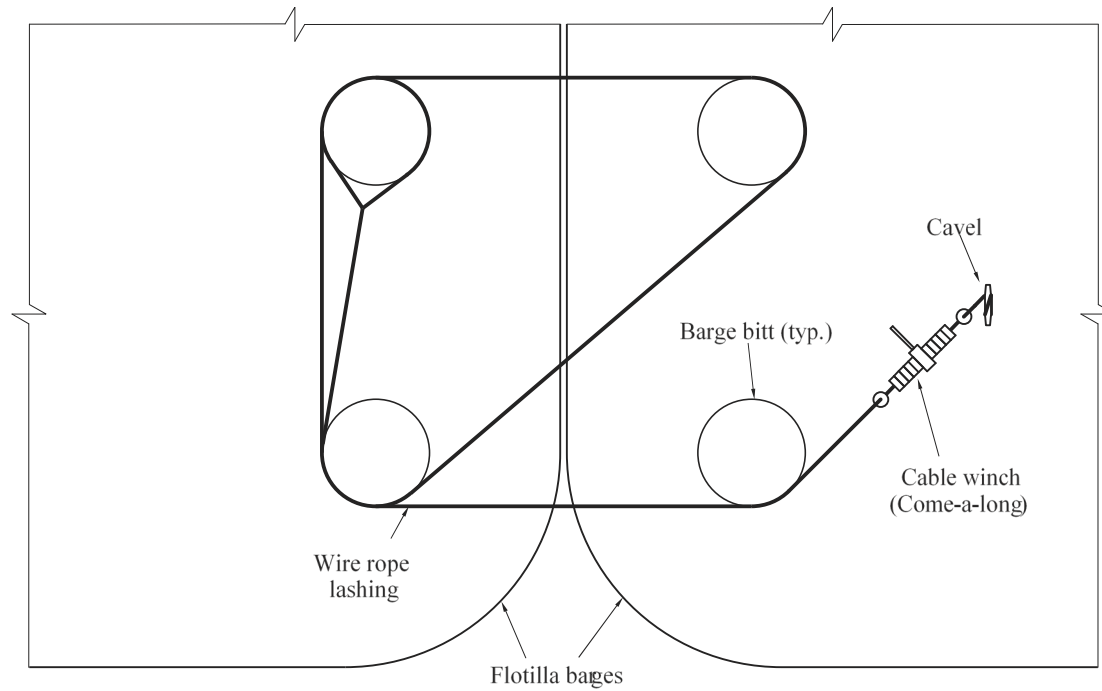
3.3.6.1. Introduction. Varying configurations of lashings are used to introduce inter-barge stiffnesses into flotilla units (recall section 3.3.2.5). With a lashing system in place, barges no longer act independently of one another. Rather, forces that arise (for example) due to impact on hydraulic structures are distributed throughout the entire barge flotilla. FE representation of lashings requires that the lashing model be capable of modeling material-level behavior of wire rope. In addition, physical-level behavior (e.g., lashing pretension, slip of lashings around barge bitts, and lashing failure) must be incorporated.

3.3.6.1.1 The lashing FE model captures the following key aspects of lashing behavior:

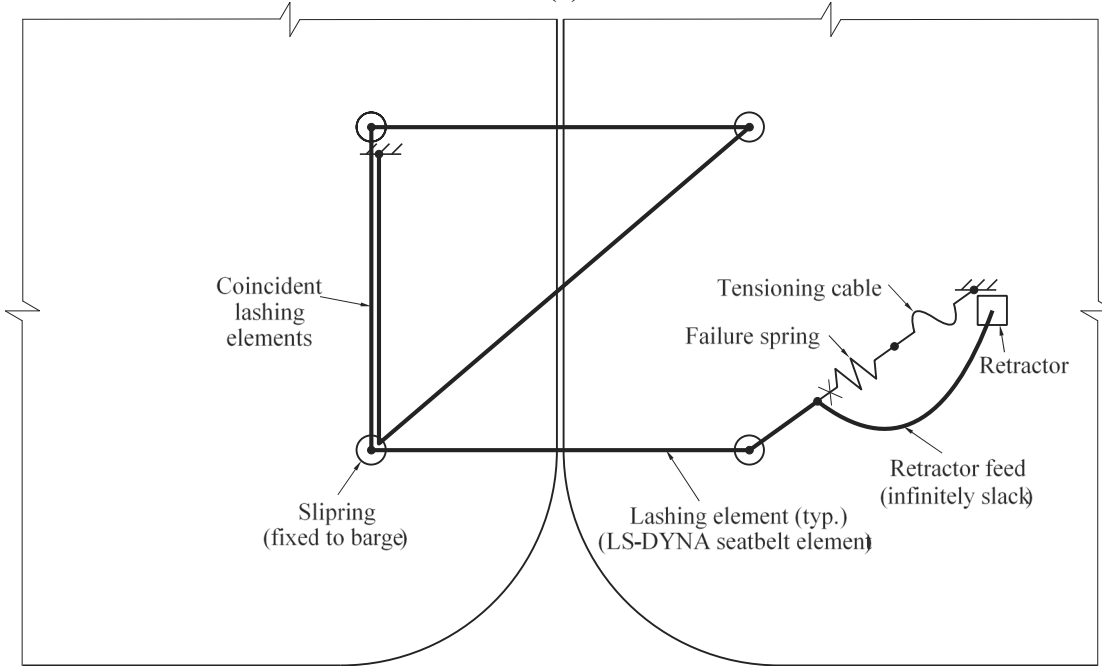
- Material model: The lashing has a nonlinear stiffness in tension (only).
- Continuity: Equilibrium is maintained throughout the total length of the lashing.
- Slippage: The lashing is able to slip around the bitts.
- Pretensioning: Tension is gradually initialized until the target initial tension is reached.
- Lashing failure: When the breaking strength is exceeded, the lashing fails.
- Layers: Layers of lashings can act independently while occupying the same location.

3.3.6.1.2 All (physical) lashings are tensioned to hold two adjacent barges together. Therefore, development of a suitable FE representation of lashings requires both geometric and constitutive considerations. A demonstrative, conceptual lashing configuration is shown in Figure 3.24a, where commonly used configurations are given in section 3.2.2.2. Figure 3.24b shows the FE model entities that correspond to the physical components of Figure 3.24a.

3.3.6.1.3 The lashing model (Figure 3.24b) brings together “seatbelt” elements (LSCT 2014b), failure spring, tensioning cable, and slack-ended retractor. Each bitt acts as a pivot point for the lashing, while still allowing the lashing to undergo slippage. Resultant forces on the bitts vary based on the tension force developed in each straight (bitt-to-bitt) segment of the lashing. If the flotilla lashing system is perturbed, slippage around the bitts is often required to maintain equilibrium.



(a)



(b)

Figure 3.24. Conceptual Lashing Configuration Schematics:
 (a) Physical Components; (b) FE Model Components

3.3.6.2. Lashing Material Model.

3.3.6.2.1 Physically, a single flotilla lashing consists of a length of wire rope that is wrapped around a sequence of barge bitts. Wire rope is composed of steel strands arranged in a helical pattern in layer(s) around an inner core. Steel wires that make up wire rope strands are required to have tensile failure stresses between 227-284 ksi (American Society for Testing and Materials (ASTM) 2009).

3.3.6.2.2 In addition to variations in wire rope material properties, varying geometric configurations are encountered (in practice) for linking barges together. Tensile breaking strengths, or ultimate strengths, for several wire rope configurations are listed in ASTM (2009). Consolazio et al. (2012) details lashing cable constitutive models (stress-strain, pretensioning, failure), constraints, relative motions (e.g., slippage, retraction).

3.3.6.3. Lashing Elements. In order to accurately model wire rope lashings, an element must be able to simulate the physical behaviors described above. An appropriate choice is a specialized type of LS-DYNA (LSTC 2014b) cable element (*ELEMENT_SEATBELT). Each bitt-to-bitt lashing segment is represented by one element with the nonlinear tension-only stiffness that is characteristic of wire rope. Sliprings (described below) can interface with these elements to simulate the slippage and continuity of physical lashings in flotillas.

3.3.6.4. Sliprings.

3.3.6.4.1 During flotilla motions, lashings (at times) undergo slippage around cylindrical bitts. Such slippage requires the physical lashing chain to deform along (or contour around) sharp angles. Barge bitts are modeled with sliprings (*ELEMENT_SEATBELT_SLIPRING), which are nodal entities that act as pivot points for the lashing chain. Further, lashing elements are permitted to be remeshed at every timestep during collision simulations. Together, these model components enable the slipring to, in turn, allow the lashing chain to slide smoothly through sharp angles. Figure 3.25 demonstrates how slipring elements are modeled using LS-DYNA (LSTC 2014b).

3.3.6.4.2 Each slipring is constrained to a single node in the lashing chain. At each timestep, the tensile forces in the two elements that meet at the slipring (T_1 and T_2) are evaluated (Figure 3.25b). An equivalent amount of unstressed length (ΔL) is then subtracted from one element and added to the other. This ensures that T_1 remains equal to T_2 (Figure 3.25c). However, it is possible that an element becomes shorter than the minimum length, L_{\min} , during the subtraction process. When this occurs, the lashing (seatbelt) element is remeshed to move that element across the slipring (Figure 3.25d).

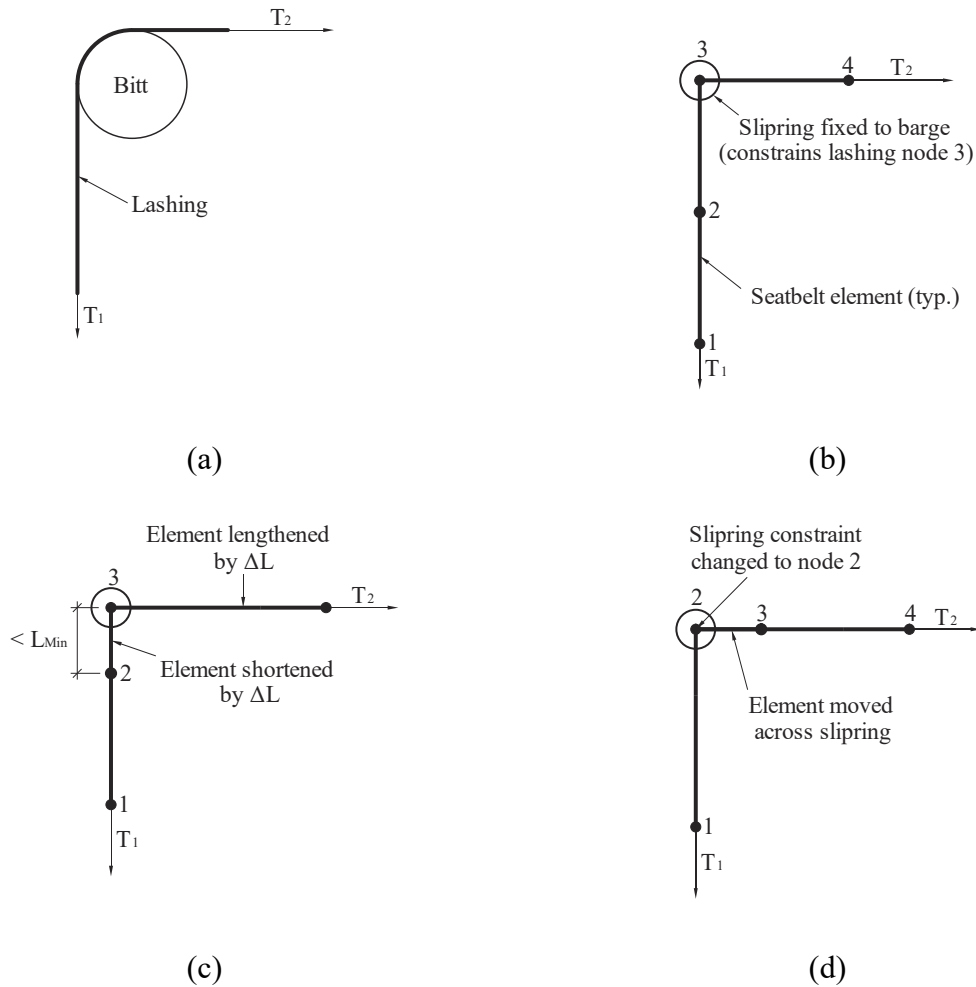


Figure 3.25. Behavior of Slipping Elements at Each Timestep:
 (a) Real Lashing Equivalent; (b) $T_2 > T_1$; (c) Material Transfer until $T_1 = T_2$;
 (d) Remeshed to Move Element Across Slipping

3.3.6.5. Tensioning Cable.

3.3.6.5.1 The lashing model includes an LS-DYNA cable element (LSTC 2014b) that simulates the effect of a cable winch (Figure 3.26). During the initialization stage of collision simulations involving flotillas, the element internal force ramps from zero to the desired pretension. The element tension is then held constant while the flotilla reaches equilibrium. Note that constant tension is maintained regardless of elastic shortening effects caused by small deformations of the barges.

3.3.6.5.2 The FE model tensioning process is analogous to the manner in which lashings are tensioned in a physical flotilla. Physically, lashings are tightened manually until the desired tension is reached. Once initialization of the FE model is complete, the computed length of each element becomes the reference for subsequent strain calculations. Additionally, the tensioning cable behaves like a normal lashing element with the same nonlinear stiffness.

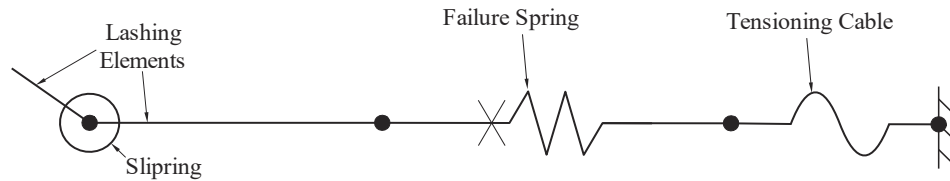


Figure 3.26. Close-Up View of Tensioning Cable and Failure Spring

3.3.6.6. Failure Spring. Lashing failure is modeled by means of a dedicated failure spring. The spring is connected in series between the tensioning cable and the chain of lashing elements (Figure 3.26). Similar to the rest of the lashing, the spring has the equivalent nonlinear stiffness of wire rope. When the spring is subjected to a critical elongation (which corresponds to the ultimate breaking strength), it fails. In this context, “fails” denotes that the spring is deleted from the analysis. This occurrence severs the continuity of the load path of the lashing. Consequently, the lashing becomes unable to carry tension and is therefore unable to prevent the connected barges from drifting apart.

3.3.6.7. Retractor.

3.3.6.7.1 When the failure spring is deleted, absent further considerations, the connected lashing element is left with a free node. Free nodes generated in this manner are not permitted in LS-DYNA (LSTC 2014b). To prevent this scenario, an additional lashing element is added to the model. The additional lashing element connects the free node to a retractor (Figure 3.27a). When a tension force is applied to the element, the retractor freely adds material to lengthen the element. In this way, this precludes the element from carrying load. Effectively, the element has zero stiffness, so it does not affect the total stiffness of the lashing system.

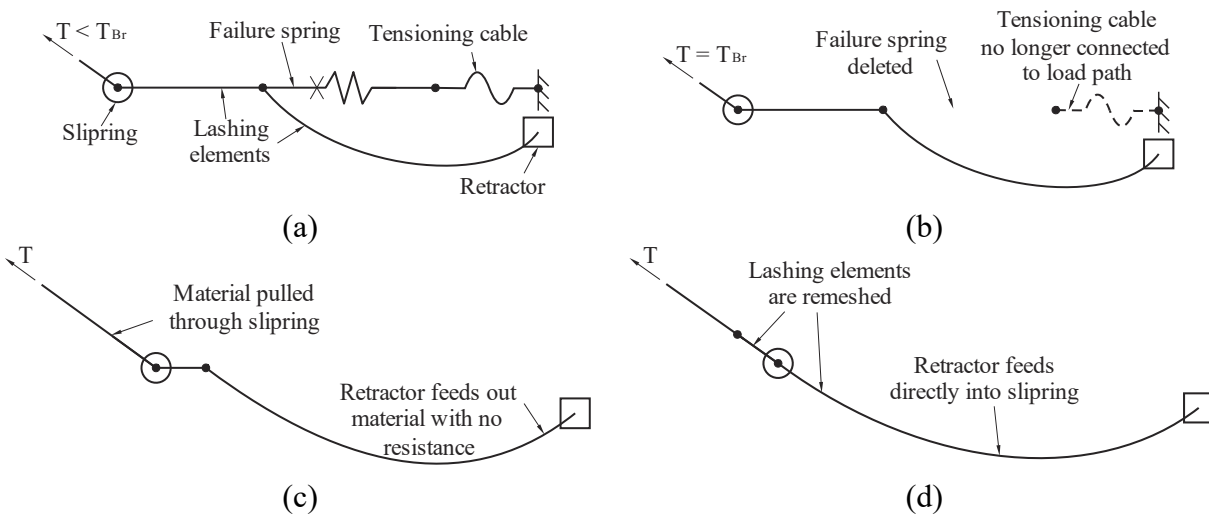


Figure 3.27. Failure Sequence of Lashing Model: (a) Prior to Failure; (b) Failure Spring Is Deleted; (c) Lashing Material Is Pulled through Slipring; (d) Lashing Elements Are Remeshed

3.3.6.7.2 With the addition of a retractor, deletion of the failure spring no longer creates a free node (Figure 3.27b). As barges separate, lashing material is pulled through the sliprings and the retractor freely feeds out replacement material (Figure 3.27c). Once the lashing is pulled far enough, the elements are remeshed (Figure 3.27d). This leaves the retractor feeding directly into the slipring. Although the barges remain connected throughout the process, the stiffness of the connection is effectively zero-valued. Therefore, previously connected barges are free to move apart.

3.4. Model Calibration and Validation.

3.4.1. Overview.

3.4.1.1. Barge and flotilla FE modeling techniques discussed throughout this chapter are presented for the purposes of:

3.4.1.1.1 Enabling comparisons between simulation data and experimental data.

3.4.1.1.2 Observing dynamic effects in flotillas.

3.4.1.1.3 Quantifying impact forces for design of hydraulic structures.

3.4.1.1.4 Characterizing barge force-deformation behaviors (e.g., for barge bows).

3.4.1.2. Two previously conducted studies are drawn upon in validating the FE modeling techniques detailed in section 3.2 and section 3.3. Specifically, forces measured during a previously conducted (full-scale) barge flotilla impact study at the Gallipolis Locks are considered. Model calibrations (Walters et al., 2017), based on results from the full-scale experiments (Patev et al., 2003), are also documented. Further, reduced-scale impacts between barge bows and surfaces of various geometries are considered (as reported in Kantrales et al., 2016).

3.4.2. Full-Scale Testing of Barge Flotilla Impacts. Patev et al. (2003) conducted 42 full-scale 3x5 flotilla impact experiments against a rigid wall structure. These USACE tests were carried out at the Gallipolis Locks and Dam (subsequently renamed Robert C. Byrd Locks and Dam). Later, in 2008, USACE conducted 23 full-scale 3x3 flotilla impact experiments against a semi-flexible wall structure. The latter set of impact tests were conducted (by Ebeling et al., 2010) at the Winfield L&D. Data from two rigid wall experiments and two semi-flexible wall experiments are used to validate accuracy of the flotilla models.

3.4.2.1. Load-Measurement System. In both series of experiments, a custom-designed load-measurement system was utilized (Figure 3.28). In particular, the measurement system was affixed to the bow corner of the impacting barge in the test flotilla. As a result, the experiments were able to measure impact forces for both the 3x5 and 3x3 configurations. The load-measurement system consisted of a solid curved steel beam 9 in. x 5 in. in cross section. Positioned at each beam end were two 6-in. diameter bi-axial 400-kip clevis pin load cells, and two clevis mounts.

3.4.2.1.1 Each clevis pin shear load cell was inserted through one end of the load beam and through a clevis mount. The base of each clevis mount was welded to the barge bow. Upon impact, force was transmitted from the load beam into the instrumented shear pins (where forces were measured). Then, forces passed into the clevis mounts, and finally, into the corner of the barge bow.



Figure 3.28. Load-Measurement System (Beam, Shear Pins, and Clevis Mounts) Attached to Bow Corner of Barge (Patev 2003)

3.4.2.1.2 The configuration, stiffness, and impact force distributions associated with the load-measurement system differ from those of un-instrumented barge bow corners. Furthermore, impact forces measured through use of the load beam differ from impact forces generated during collisions involving un-instrumented barges. Such differences were demonstrated in Walters et al. (2017). In the following, validation of the flotilla FE model is documented, which requires direct incorporation of the load-measurement system. As model calibration, the validated flotilla model, excluding the load-measurement system, is then made use of in subsequent chapters.

3.4.2.2. Finite Element Model of Load-Measurement System. An FE model of the load-measurement system (Figure 3.29a) is developed and integrated with the overall flotilla model. Three-dimensional solid elements are used to model the geometry of the load beam and the two clevis mounts. Recall the strain-rate-dependent nonlinear steel material model (section 3.2.2) that is used to model the barge. This same material model is also used to represent the steel in the load beam and steel clevis mounts.

3.4.2.2.1 As a measure of computational efficiency, nodal rigid bodies are used to emulate the function of the pins. In LS-DYNA, a nodal rigid body consists of multiple nodes that are constrained to move as a single rigid entity. Distances between nodes within the rigid body remain constant, even as the overall body translates and rotates.

3.4.2.2.2 A nodal rigid body is defined at each end of the load beam (Figure 3.29b–c). Each nodal rigid body ties (constrains) nodes within the footprint of the clevis pin to a single line of nodes. In turn, each single line of nodes lies inside the clevis mount. Each nodal line inside the clevis mounts corresponds to the hypothetical longitudinal axis of the corresponding shear pin.

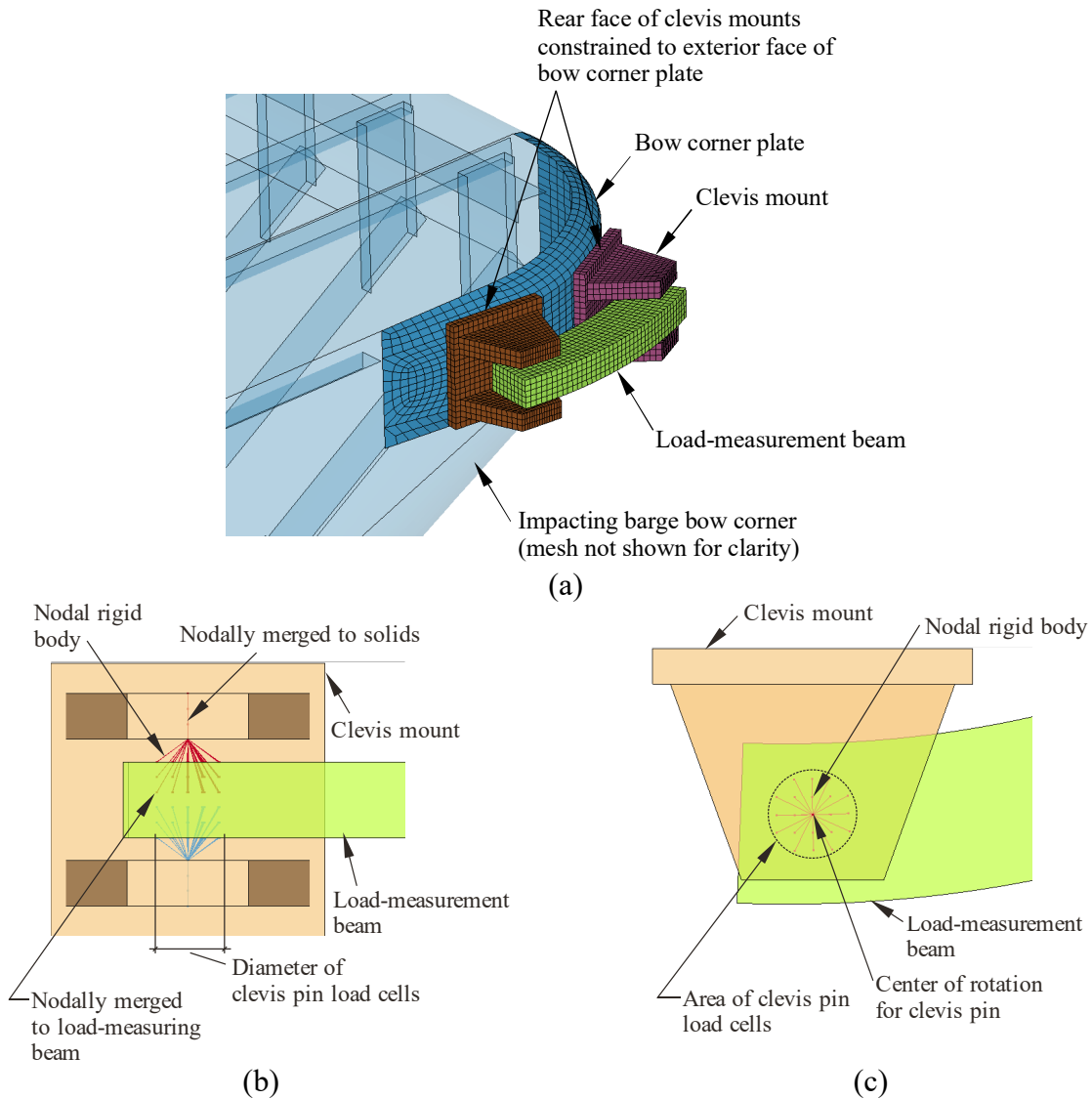


Figure 3.29. Finite Element Model of Load-Measurement System:
 (a) Overview and Attachment to Barge; (b) Elevation View of Clevis and Shear Pin Model;
 (c) Plan View of Clevis and Shear Pin Model

3.4.2.2.3 This approach is computationally efficient and allows the end of the load beam to rotate within the clevis mesh. In particular, rotation can occur in a manner that emulates the rotation that would be (physically) permitted by the pin. Both clevis mounts are attached to the corner of the barge bow model (Figure 3.29a). These attachments are achieved using translational constraints between nodes on the rear faces of the clevis mounts and corresponding nodes on the barge bow.

3.4.2.3. Rigid Wall Structure and FE Model. For rigid wall simulations, the flotilla is positioned (Figure 3.30) to impact the wall at angle of obliquity, θ . Additionally, the barge is assigned an initial velocity (V_0). The rigid wall FE model is composed of rigid 8-node solid elements. Each solid (or brick) element possesses a characteristic length of 36 in. All nodes in the wall FE model are fully restrained from motion. The barge-wall contact zone is sized to preclude barge penetration on wall portions located outside of the defined contact surface.

3.4.2.3.1 Computational efficiency is achieved by only designating for contact the barge nodes that can potentially impact the wall during collision. Contact nodes are assigned only for the barge that makes primary (initial) contact with the wall. More specifically, shell elements located within the starboard half of the bow are included in the barge-wall contact definition. Contact forces that are generated possess both normal and transverse (frictional) components with respect to the rigid wall contact face. Friction parameters for the barge-to-wall contact definition are 0.50 and 0.45 for static and dynamic coefficients of friction, respectively.

3.4.2.3.2 Further considerations for modeling or rigid walls, as well as design guidance, are provided in Chapter 4. Historical context and former approaches to the design of rigid wall navigation structures can be found in ETL 1110-2-563 (USACE 2004). Additionally, a summary of ETL 1110-2-563 is provided in Appendix E.

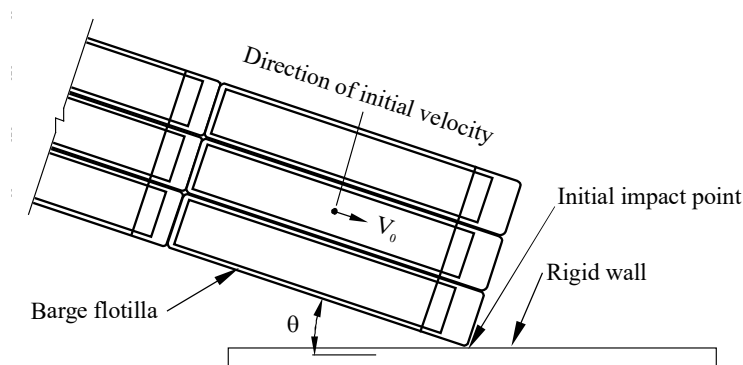


Figure 3.30. Schematic of Flotilla Impact Against Rigid Wall

3.4.2.4. Semi-Flexible Wall Structure and FE Model. The semi-flexible wall structure spans 118 ft from rigid cell to rigid cell (Figure 3.31). The single span derives from the Winfield L&D approach wall (Ebeling et al., 2010, Ebeling et al., 2011).

3.4.2.4.1 The segmental post-tensioned span is divided longitudinally into three match-cast segments of equal length. Each segment possesses a unique cross-sectional shape. Solid, hollow, and transition cross sections are present within the two outer segments of the semi-flexible wall. The central segment is hollow. Essentially rigid concrete cell foundations are located at each end of the three-segment span. The top of each rigid cell is fitted with a concrete thrust block, tieback anchors, and bearing pads.

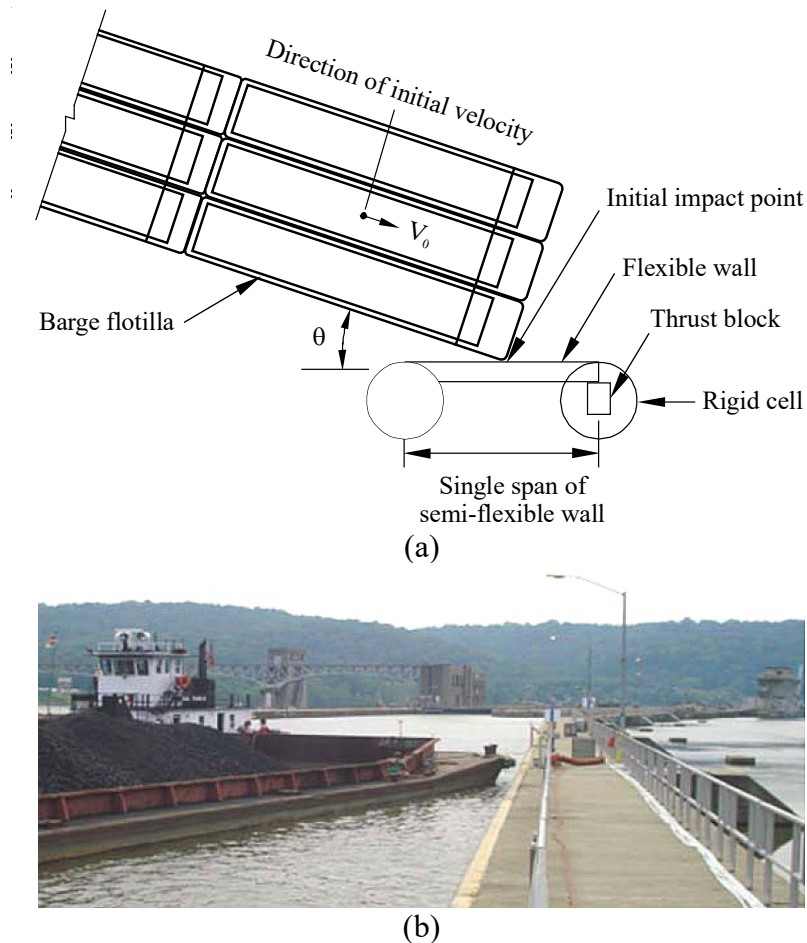


Figure 3.31. Flotilla Impacts on Semi-Flexible Wall:
 (a) Schematic Diagram, (b) Experiments Conducted at Winfield

3.4.2.4.2 Nonlinear beam elements are used to model the majority of the semi-flexible wall (Figure 3.32). However, solid elements are used near the ends of the span. Solid elements are also used to model the rigid cell foundations and the thrust blocks. Longitudinal mild steel bars and prestressing tendons are modeled along the span length using discrete beam elements. Elements representing reinforcement are positioned according to structural plan sets.

3.4.2.4.3 Bearing pads and tieback anchors are modeled using beam elements. All mild steel rebar details, prestressing tendon details, and concrete cross-sectional shapes are listed in Consolazio and Walters (2012). Nonlinear flexural behavior of the semi-flexible wall model is verified with respect to moment-curvature. Specifically, model moment-curvature data are found to compare favorably with data obtained from cross-sectional analysis software (Consolazio et al., 2004).

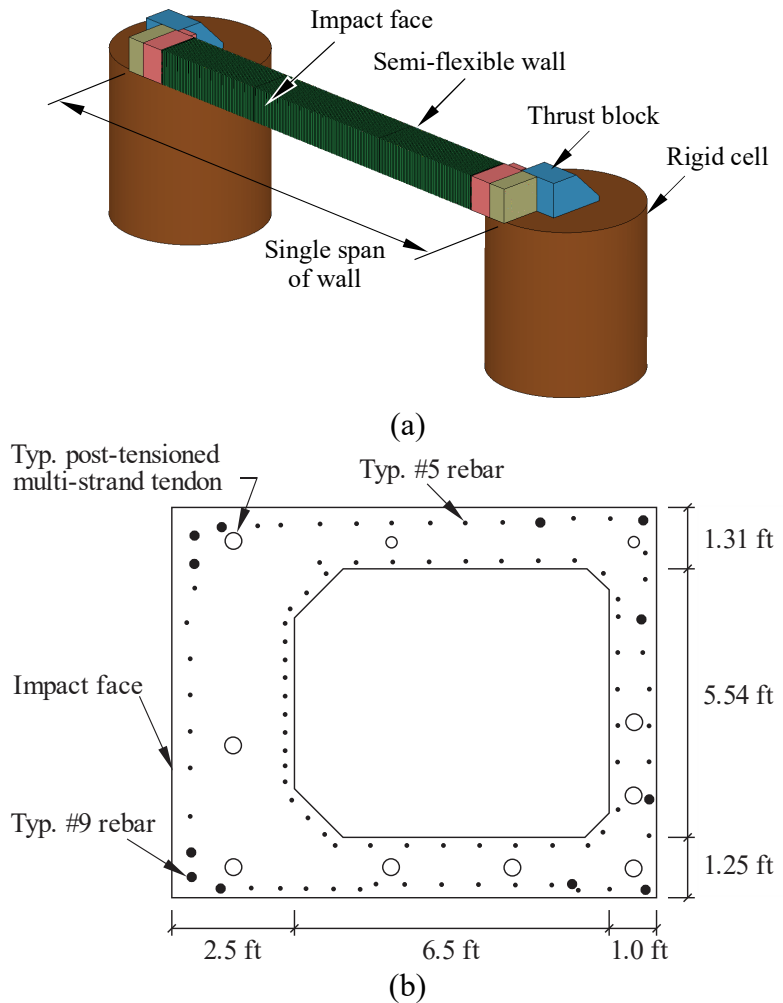


Figure 3.32. Semi-Flexible Wall FE Model: (a) Overall Configuration (Mesh Not Shown for Clarity); (b) Cross Section of Semi-Flexible Wall Beam

3.4.2.5. Model Validation Using Data from Rigid Wall Impact Experiments.

3.4.2.5.1 To assess the accuracy of the flotilla modeling procedures, two tests are selected from Patev et al. (2003). The following tests from the Robert C. Byrd Locks and Dam rigid wall test program are simulated:

- Experiment 41 (3x5 flotilla, 9° angle, 0.88 m/sec, 2.9 ft/sec, impact velocity); and,
- Experiment 42 (3x5 flotilla, 18° angle, 0.55 m/sec, 1.8 ft/sec, impact velocity).

3.4.2.5.2 Each experiment is simulated with the load beam attached to the impacting barge to enable direct comparison between experiment and simulation. Experimental and simulated impact forces acting perpendicular to the longitudinal axis of the wall are compared in Figure 3.33. The peak impact force measured during Experiment 41, using the load-measurement system, is 417 kip. Numerical impact simulation of the same condition, with inclusion of the load-measurement system, predicts an impact force of 360 kip. The two values differ by approximately 14%, with the experimentally measured force being the larger of the two.

3.4.2.5.3 Regarding Experiment 42, the peak experimental impact force is 579 kip. The simulation predicts a force of 539 kip—approximately 7% less than the experimental value. Observed differences between the experimental test data and simulation results are attributed to several physical phenomena and features. Examples include hydrodynamic effects acting on the flotilla; variability of lashing pretension levels; and variability of barge surface (friction) conditions. However, the level of agreement between the experimental forces and corresponding simulation results is considered acceptable for determining design impact forces.

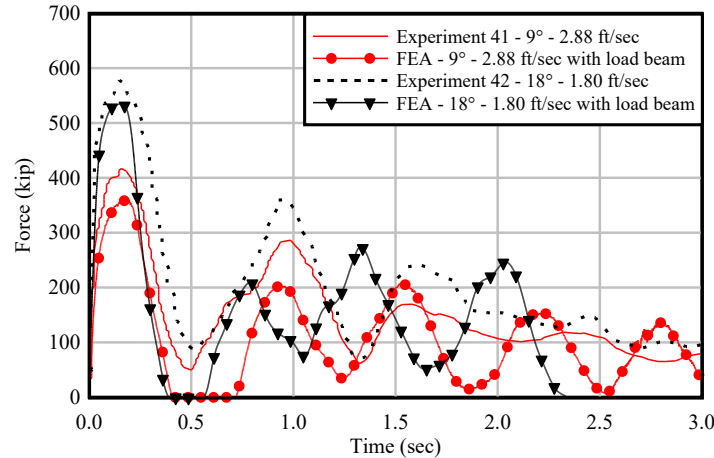


Figure 3.33. Time Histories of Normal Impact Force for Rigid Wall Experiments 41 and 42 and Corresponding FE Simulations with Load Beam Included

3.4.2.6. Model Validation Using Data from Semi-Flexible Wall Impact Experiments.

3.4.2.6.1 To further assess the accuracy of the flotilla modeling procedures, two tests are selected from Ebeling et al. (2010). The following two tests from the Winfield L&D semi-flexible wall test program are simulated:

- Experiment 10 (3x3 flotilla, 17° angle, 0.88 m/sec, 2.88 ft/sec, impact velocity); and,
- Experiment 20 (3x3 flotilla, 13.6° angle, 0.82 m/sec, 2.69 ft/sec, impact velocity).

3.4.2.6.2 Each experiment is simulated with the load beam attached to the impacting barge to enable direct comparison between experiment and simulation. Experimental and simulated impact forces acting perpendicular to the longitudinal axis of the wall are compared in Figure 3.34. The peak impact force measured during Experiment 10, using the load-measurement system, is 517 kip. Numerical impact simulation of the same condition, with inclusion of the load-measurement system, predicts an impact force of 571 kip. The two values differ by approximately 10%, with the experimentally measured force being of smaller magnitude.

3.4.2.6.3 Regarding Experiment 20, the peak experimental impact force is 411 kip. The simulation predicts a force of 448 kip, which is approximately 10% greater than the experimental value. In Consolazio and Walters (2012), additional comparisons of experimentally measured wall deflection data and corresponding FE deflection data are compared. The deflections data and frequency of oscillation are shown to be in comparable agreement relative to the force comparisons.

3.4.2.6.4 Observed differences between the experimental test data and simulation results are attributed to similar phenomena as described in section 3.4.3. In addition, deviations are attributed to differences between structural damping in the physical semi-flexible wall tested and the as-modeled wall. In the numerical model, motions of the semi-flexible wall are assumed to be damped at 5% of critical damping. Overall, the level of agreement between the experimental data and simulation results is considered acceptable for quantifying design impact forces.

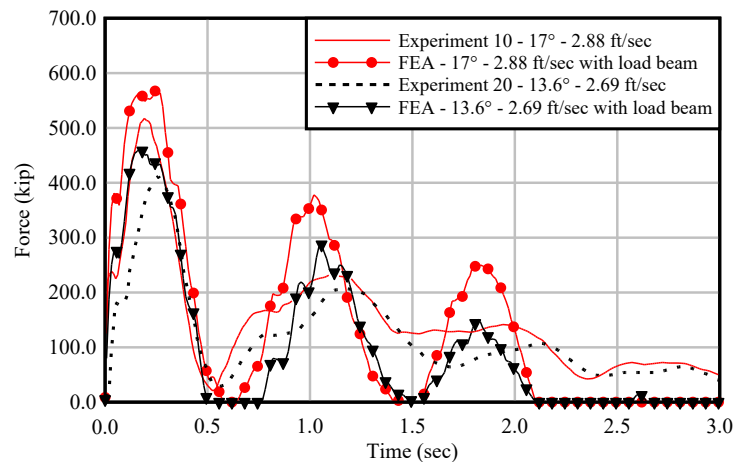


Figure 3.34. Time Histories of Normal Impact Force for Semi-Flexible Wall Experiments 10 and 20 and Corresponding FE Simulations with Load Beam Included

3.4.2.7. Influence of Load Beam on Measured and Computed Impact Forces. In the following, the test conditions from sections 3.4.2.5 and 3.4.2.6 are revisited. As a key difference, for each collision simulation, the load beam is excluded from the flotilla FE model. Consequently, the un-instrumented bow corner of the impacting barge FE model, rather than the load beam, directly contacts the wall. Forces computed in this manner are more representative of typical (i.e., un-instrumented) barge impact conditions.

3.4.2.7.1 In Figure 3.35, FE impact forces computed with and without the load-measurement beam are compared. For the Experiment 10 conditions, the peak impact force is 426 kip (compared to 571 kip without the load beam). For the Experiment 20 conditions, the peak impact force is 353 kip (no load beam) versus 448 kip (load beam).

3.4.2.7.2 For both impact conditions, peak impact forces determined using an instrumented barge are found to exceed those generated by an un-instrumented barge. For the Experiment 10 and 20 conditions, forces increase by approximately 20% to 25% when the load-measurement system is included. These differences arise because the load beam stiffness is greater than the stiffness of a typical un-instrumented barge bow corner.

3.4.2.7.3 Importantly, this finding indicates that unnecessary conservatism can be avoided when designing hydraulic structures to resist impact loads. In particular, design guidance developed based on un-instrumented barges is more representative of actual (real-world) conditions. Therefore, collision simulations involving un-instrumented barges are utilized for determining design loads in the remainder of this document.

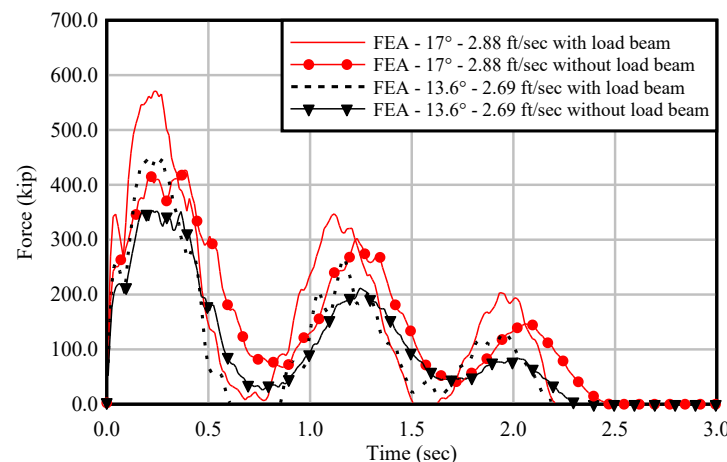


Figure 3.35. Comparison of Force Time Histories for FE Simulations of Experiments 10 and 20 with Load Beam (Instrumented) and without (Un-instrumented)

3.4.3. Impact Testing of Scaled Barge Bows. From section 3.3, the impacting barge for collisions between flotillas and hydraulic structures is selected from the (flotilla) lead row. Further, the lead-row barges in flotillas are typically single-raked, where the barge bow makes direct contact with the impacted structure. Therefore, it is important that FE modeling of barges leads to accurate characterizations of barge bow force-deformation (crushing) behaviors. A previous Florida Department of Transportation study is drawn upon to validate crushing behaviors of barge bow FE models.

3.4.3.1. Using controlled (laboratory) conditions, reduced-scale (40%), pendulum-impact tests were performed on barge bows (Consolazio et al., 2014, Kantrales et al., 2016). The reduced-scale tests were performed to experimentally characterize barge force-deformation behavior representative of high-energy, high-deformation, barge collision events. Two series of tests were conducted: rounded impactor tests and flat-faced (e.g., rectangular) impactor tests.

3.4.3.2. Impact surfaces used during testing in Kantrales et al. (2016) were of widths equal to 1/6th of the barge bow width. Both of the impacted surface geometries (round, flat-faced) are relevant to hydraulic structures maintained by USACE. Examples of flat-faced impact surfaces include those within lock walls and floodwalls, while rounded surfaces are found among bullnose structures.

3.4.3.3. Validation of Barge Bow Crushing Behavior.

3.4.3.3.1 FE modeling and analysis procedures involving barge bow crushing (at full scale) were developed in Consolazio et al. (2008). Kantrales et al. (2016) used the same procedures to model and predict barge bow crushing behaviors at reduced scale (40%). The predicted crushing behaviors were then compared to measured force-deformation relationships obtained from pendulum-impact experiments.

3.4.3.3.2 Experimentally measured versus FE predictions of barge bow crushing behavior (40% scale) are shown in Figure 3.36 (round), Figure 3.37 (flat-faced). Agreement between results from simulations of reduced-scale tests and corresponding experimental test data validate the accuracy of the analytical techniques. The same FE modeling methods were utilized in developing full-scale FE barge bow models in Consolazio et al. (2008). Kantrales et al. (2016) concluded (by extension) that the analytical basis for the full-scale barge bow load deformation model is valid.

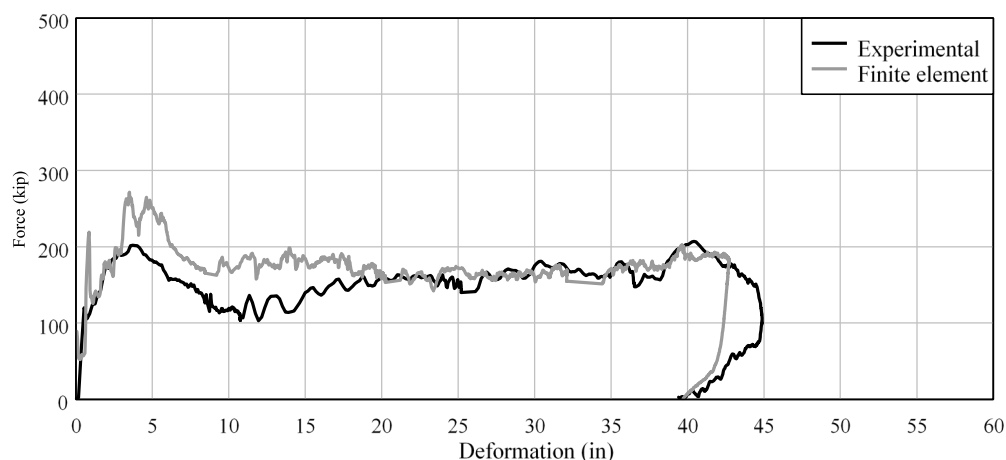


Figure 3.36. Comparison of Reduced-Scale (40%) Experimental and Analytical Backbone Curves for Impacts on Rounded Surfaces (Surface Width = 1/6th of Barge Width)

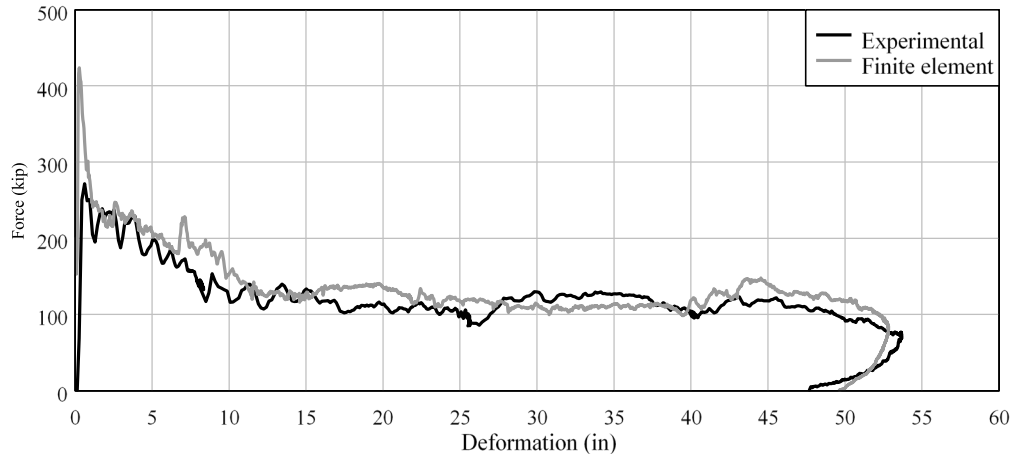


Figure 3.37. Comparison of Reduced-Scale (40%) Experimental and Analytical Backbone Curves for Impacts on Flat-Faced Surfaces (Surface Width = 1/6th of Barge Width)

3.5. Summary.

3.5.1. Single Barge Model.

3.5.1.1. To perform contact-impact analyses of collision conditions involving individual barges, FE models of a typical jumbo hopper barge were developed. The single barge FE model was developed based on detailed structural drawings, which were obtained from a barge manufacturer. To validate barge bow crushing behaviors, results from impact tests involving reduced-scale replicates of jumbo hopper barge bows were used. These tests involved impacted surface geometries (round, flat) relevant to hydraulic structures maintained by USACE.

3.5.1.2. Selected portions of design guidance provided in this document derive from simulations of single barge collisions with hydraulic structures. Such portions of the design considerations relate primarily to hurricane protection structures and inland riverine floodwalls, as discussed in section 4.4. Additionally, use of single jumbo hopper barge FE models is applicable to considerations presented in Appendixes F and G.

3.5.2. Barge Flotilla Model.

3.5.2.1. As an extension to the single jumbo hopper barge model, multi-barge flotilla FE models were also developed in varying sizes. Each flotilla model included numerical representations of key structural members, member connections, inter-barge contact interactions, and inter-barge wire rope lashings. To validate impact loads determined from simulations of multi-barge flotilla collisions, rigid and semi-flexible concrete wall structures were modeled. These wall structures corresponded to those used in full-scale impact experiments previously conducted by USACE at two different sites. Data gathered during the USACE impact experiments were used to:

3.5.2.1.1 Characterize the influence of load-measurement systems used during the physical tests.

3.5.2.1.2 Validate peak impact forces computed from FE simulations of barge flotilla collisions with rigid walls and semi-flexible walls.

3.5.2.1.3 Validate peak wall deflections computed from FE simulations of barge flotilla collisions with semi-flexible walls.

3.5.2.2. Design guidance provided in this document for determining impact forces derives from FE simulations of flotilla collisions on hydraulic structures.

Chapter 4 Wall Structures – Empirical Approach

4.1. General.

4.1.1. This chapter presents a method for empirically assessing barge impact loads on concrete wall structures. Oblique (i.e., glancing blow) flotilla-wall collisions are focused on, and pertinent wall types are identified. More specifically, an empirical load prediction model is presented that facilitates impact-resistant design of rigid, semi-flexible, and pile-founded guide walls. The load prediction model is referred to as a unified model. In this context, the term “unified” signifies simultaneous applicability to multiple types of concrete wall structures. Further, the associated empirical equations incorporate dependency on wall stiffness in the load calculation process.

4.1.2. This chapter reviews FE model components for rigid, semi-flexible, pile-founded walls, and flood walls. Additionally, summaries are provided of simulated (oblique) collision forces that factor into development of the empirical load prediction equations. Derivation of the load prediction equations (via curve fitting of simulated collision forces) is then provided. Bilinear curve fits are formulated to relate (normal-to-wall) impact force to the lead-row momentum of the impacting flotilla. To illustrate use of the empirical equations in design applications, both deterministic and probabilistic design examples are included as well.

4.1.3. Scope.

4.1.3.1. The material in this chapter has been organized into the following sections as:

4.1.3.1.1 Section 4.2 includes brief reviews of major FE model components for applicable types of wall structures.

4.1.3.1.2 Section 4.3 documents the unified load prediction model, including listings of simulated collision forces and the curve fit procedure.

4.1.3.1.3 Section 4.4 summarizes flotilla collisions on hurricane protection wall and inland riverine structures with references to materials found in Appendix G.

4.1.3.1.4 Section 4.5 gives examples of empirical model calculations for impacts on approach walls.

4.1.3.1.5 Section 4.6 gives a complete design example that follows the methodology presented in Chapter 2. This design example performs both deterministic and probabilistic calculations and compares the difference between the results.

4.1.3.2. Additional considerations for collisions on riverine floodwalls and hurricane protection walls are documented in Appendix F and Appendix G. The examples in Appendix F and G are not guidance but show the load-carrying capacity of floodwall structures. Navigation structures susceptible to loadings from direct, head-on impacts (e.g., bullnose structures) are discussed in Chapter 6. Further, considerations for flotilla-wall collisions involving relatively flexible navigation structures, such as timber guide walls, are provided in Appendix H.

4.2. Approach Wall Modeling.

4.2.1. Overview. During flotilla-wall collisions, both the structural characteristics of the flotilla and (impacted) wall influence the generation of impact forces. Component descriptions and FE modeling techniques attributed to barge flotillas are given in Chapter 3. Also found in Chapter 3 are discussions of FE modeling for rigid and semi-flexible wall structures. Modeling considerations for rigid and semi-flexible guide walls are briefly revisited below in section 4.2.3 and section 4.2.4, respectively. Introduced in section 4.2.5 are FE modeling considerations pertaining to pile-founded guide walls. Collectively, these wall modeling considerations provide a contextual backdrop for the collision-force summaries and curve fitting procedure presented in section 4.3. The calculations of wall stiffness are discussed in section 4.5.2.

4.2.2. Background. Numerous barge impact studies, encompassing both experimental and numerical efforts, were previously carried out under USACE auspices. For example, full-scale experimental barge impact tests were performed against a rigid concrete lock wall. Impact tests were also conducted on a semi-flexible concrete approach wall at Winfield L&D in West Virginia. Additional physical-testing details are found in Chapter 3, or respectively, in Patev et al. (2003) and Ebeling et al. (2010).

4.2.2.1. Computational studies were subsequently carried out using nonlinear dynamic FE analysis techniques to simulate barge impacts on various navigation structures. The analytical studies involved development of high-resolution barge flotilla FE models and simulation of collisions on various wall types. Flotillas impacting rigid and semi-flexible concrete guide walls were focused on in Walters et al. (2017). Similarly, flotilla collisions (simulated) on pile-founded guide walls were detailed in Consolazio et al. (2014). Still other studies focused on (for example) hurricane protection structures (Getter et al., 2015; Davidson et al., 2020).

4.2.2.2. Overall, several types of navigation structures and hundreds of collision scenarios were investigated. Furthermore, those navigation structures that possessed commonalities (overall structural configuration; conceivable range of collision scenarios) were identified. Only oblique (or glancing blow) impacts were deemed of interest for flotilla collisions on rigid, semi-flexible, and pile-founded guide walls. In addition, practical ranges of stiffness associated with these wall types were found to be amenable to a common load prediction methodology. Accordingly, overarching (unified) empirical load prediction equations were developed for impacts on the three wall types (rigid, semi-flexible, pile-founded guide walls).

4.2.3. Rigid Walls.

4.2.3.1. Monolithic wall structures, including some portion of concrete lock approach walls, can be characterized as effectively rigid (see Figure 3.30). Walls designated as rigid typically possess considerable stiffness relative to multi-barge flotilla stiffness. Further, rigid walls (in a practical sense) are capable of exhibiting nearly full restraint against lateral motions. Alternatively stated, the generation of impact forces during collision events is not limited by overall displacements of the wall structure.

4.2.3.2. A historical approach to impact-resistant design of rigid walls (from ETL 1110-2-563, USACE 2004) is summarized in Appendix E. Subsequent efforts involving FE modeling of rigid walls are discussed in Chapter 3 (and Walters et al., 2017). Modeling of rigid walls, as described in Chapter 3, is necessary for characterizing ranges of associated collision forces. In turn, such force data are utilized when forming the (empirical) unified load prediction model.

4.2.4. Semi-Flexible Walls.

4.2.4.1. A sizable portion of approach walls near locks can be characterized as semi-flexible (see Figure 3.32). In this context, semi-flexible wall structures possess significant stiffness relative to multi-barge flotilla stiffness. However, semi-flexible walls may undergo measurable lateral displacements when subjected to dynamic barge impact loading.

4.2.4.2. The semi-flexible wall FE model considered herein is based on an approach wall from the Winfield L&D, West Virginia. This segmental post-tensioned wall configuration is the same as that investigated during full-scale impact experiments (Ebeling et al., 2010). Validation of corresponding collision simulations involving the semi-flexible wall model are given in Walters et al. (2017). See Chapter 3 for details of the wall FE model and validation of high-resolution FE impact simulations using full-scale experimental data.

4.2.5. Pile-Founded Guide Walls. USACE maintains a significant inventory of large-mass concrete walls supported by timber piling foundations. Navigation wall structures of this type are referred to as pile-founded guide walls. A finite element model is formed for a representative configuration using the general-purpose FEA software LS-DYNA (LSTC 2014). The pile-founded guide wall FE model is developed from an upper-pool interior monolith system (Figure 4.1). More specifically, the pile-founded guide wall is located at Mississippi River Lock and Dam No. 2 (MRLD2) near Hastings, Minnesota.



Figure 4.1. Mississippi River Lock and Dam No. 2 (MRLD2)

4.2.5.1. The interior guide wall located at the aforementioned lock structure is representative of typical pile-founded guide wall structures for collision simulation purposes. Specifically, the MRLD2 configuration is representative of pile-founded guide walls supported on plumb and battered timber pilings with typical spacings. Extensive structural configuration details and structural drawings for this and other wall configurations are given in Consolazio et al. (2014).

4.2.5.2. The FE wall model representing the selected configuration (MRLD2) is shown in Figure 4.2. The MRLD2 structure includes a plain concrete wall supported on timber piles. In the corresponding FE model, the concrete wall is modeled with three-dimensional solid brick elements. Timber piles are modeled using beam elements, including both plumb and battered orientations. Soil resistance is modeled using distributed nonlinear springs (not shown).

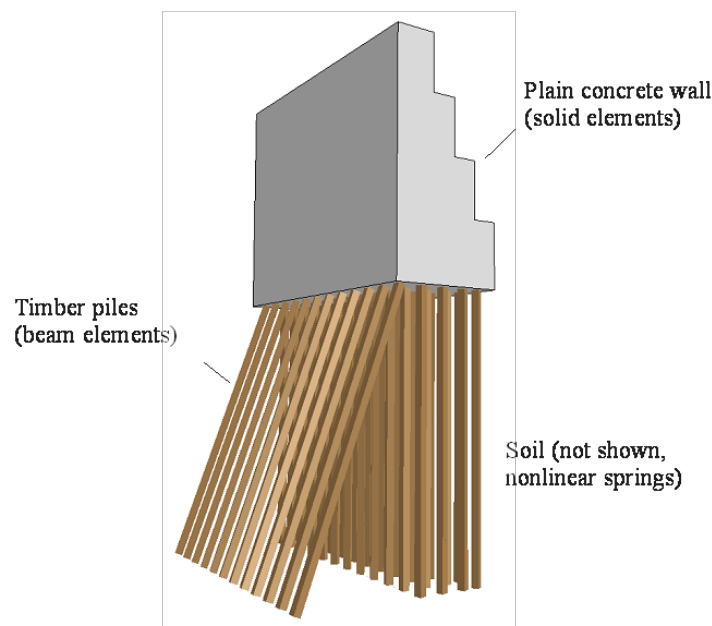


Figure 4.2. Finite Element Model of Pile-Founded Guide Wall for MRLD2 (Pile Element “Prisms” Rendered at 12-in. Thickness; Soil Resistance Springs Not Shown for Clarity)

4.2.5.3. Linear elastic material properties are used for both the concrete wall and underlying timber piles. This approach facilitates generation of conservative impact loads since the materials of impacted structural members cannot undergo softening behaviors. Further, adoption of linear elastic behaviors ensures that individual structural components do not limit the forces quantified during simulation. Nonlinear spring elements are used to represent stiffness contributions (lateral, vertical) from soil surrounding the piles. Additional details are provided in Consolazio et al. (2014) regarding characterization of soil resistance springs.

4.2.5.4. Modeling of Plain Concrete Walls. The plain concrete guide wall, with overall dimensions shown in Figure 4.3, is modeled with 8-node solid brick elements. Individual element dimensions are 6 in. x 6 in. x 6 in. In comparison, length dimensions of the smallest impacting shell elements on the surface of the deformable barge bow are approximately 3 in. Therefore, an element size ratio of approximately 2:1 is maintained between wall and barge elements that may come into contact. Maintaining a size ratio no greater than 2:1 for elements in contact is desirable for numerical impact simulations. The accuracy of detecting contact is compromised if too much size disparity exists between the barge and wall elements.

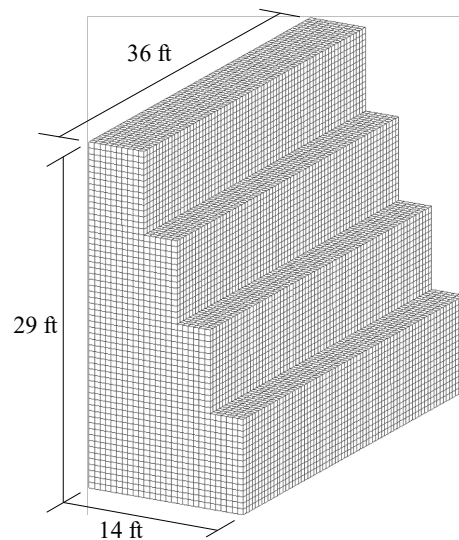


Figure 4.3. Isometric View of Concrete Portions of Finite Element Model for MRLD2

4.2.5.4.1 Excerpts from as-built plans (see Consolazio et al., 2014) indicate that the guide walls at MRLD2 were constructed in 1947. Limited information, beyond a class “B” designation, is available regarding concrete material specifications (e.g., minimum strength, aggregate size, sieve testing). As such, reasonably conservative material properties are selected for use in the MRLD2 FE model.

4.2.5.4.2 For example, increasing the density of pile-founded guide wall components corresponds to increased mass, thereby potentially increasing peak impact force. Thus, a reasonably high material density is understood to be conservative for impact load prediction. Consequently, concrete with weight density of 145 pcf is selected for modeling purposes.

4.2.5.4.3 Given practices at the time of construction of MRLD2, a compressive strength of approximately 2,000 psi is selected. The modulus of elasticity is determined to be approximately 2,500 ksi based on present-day specifications (American Concrete Institute (ACI) 2011). A Poisson's ratio of 0.16 is selected based on McCormac and Nelson (2005).

4.2.5.5. Modeling of Timber Piles. All timber piles are modeled using resultant beam elements, to which gross cross-sectional properties are assigned. As such, the beam elements (and nodes) are positioned along the pile centerlines. Pile element nodes are evenly spaced at 18-in. vertical intervals throughout the length of each pile. Thus, the longitudinal lengths of beam elements representing plumb piles are 18 in. Longitudinal element lengths for battered piles are approximately 19.2 in. (at 20° batter).

4.2.5.5.1 Replicated along the length of the MRLD2 FE model is a group consisting of one battered and four plumb piles. The pile group presented in Figure 4.4 is replicated longitudinally at 3-ft intervals along the wall. All piles vertically extend 34.5 ft below the base of the guide wall. Also, all pile spacings are center of pile to center of pile.

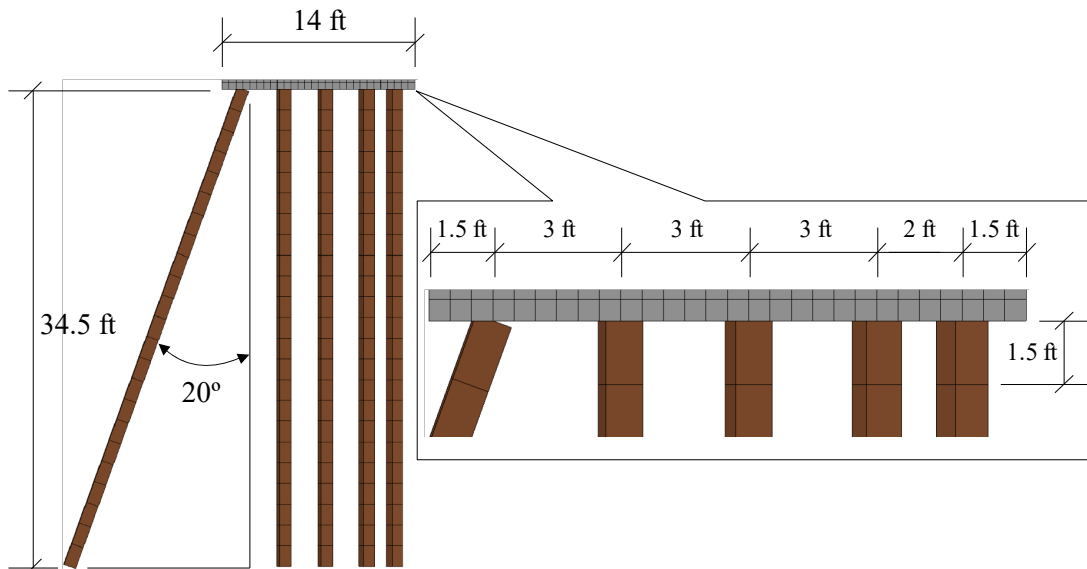


Figure 4.4. Elevation View of Pile Group at MRLD2
(Beam Elements Rendered as “Prisms” for Illustration)

4.2.5.5.2 Section stiffnesses for all timber pile beam elements are specified by defining a cross-sectional area and moments of inertia. Although, physically, the timber piling is tapered, all piles are modeled using a constant cross section. In particular, a 12 in. diameter is selected from the physical pile cross section at 3 ft from the pile butt end.

4.2.5.5.3 As with concrete walls, selection of a reasonably high material density for timber piling is conservative for impact force prediction. However, limited data are available regarding the materials properties of the timber pilings at MRLD2. Timber pilings at sites such as Mississippi River L&D 6, Wisconsin, include mixtures of eight timber species (USACE 2012).

4.2.5.5.4 Lacking additional information, it is assumed that use of a wide range of wood species for timber pilings is typical. As such, a relatively high-magnitude density of 50.0 pcf is selected for pile modeling. Also, an elastic modulus of 1,000 ksi and Poisson's ratio of 0.10 are selected for modeling purposes.

4.2.5.6. Additional Modeling Considerations. Extensive documentation for FE modeling of pile-founded guide walls is provided in Consolazio et al. (2014). Included therein are considerations for modeling of the connection between the plain concrete walls and timber piles. Also discussed is use of supporting software packages such as FB-MultiPier (Bridge Software Institute (BSI) 2014) for characterization of nonlinear soil resistance springs. Furthermore, details are provided concerning a combined discrete element, finite element approach (LSTC 2014) for modeling of rock-filled timber cribbings. Still further, analytical techniques for initializing the wall configurations under gravitational loads are discussed.

4.3. Unified Load Model.

4.3.1. Introduction. Several previous studies involving simulation of flotilla-wall collisions are drawn upon to develop the unified load prediction model. For example, barge flotillas impacting rigid concrete guide walls are studied in Consolazio et al. (2012). Also, barge flotilla collisions on semi-flexible concrete guide walls are investigated in Consolazio and Walters (2012). Validation of high-resolution collision simulations on both rigid and semi-flexible concrete guide walls is presented in Walters et al. (2017). Simulation of flotillas colliding with pile-founded guide walls is detailed in Consolazio et al. (2014).

4.3.1.1. Each of the aforementioned studies led to numerous computations of impact forces, spanning a wide range of collision scenarios. Peak forces, and the associated impact condition parameters, from these analytical studies form data populations used for development of the unified load prediction model. By merging oblique impact force results from these prior studies together, a comprehensive impact force database is produced. In the following, the impact force data most relevant to collisions involving rigid, semi-flexible, and pile-founded guide walls are cataloged.

4.3.1.2. The selected, cataloged data obtained from the collision simulations are then incorporated into an error minimization curve fitting process. In this way, empirical relationships are formed, constituting a unified load prediction model for concrete guide walls. Empirical relationships making up the unified load prediction model are functions of select, key parameters for a given collision scenario. Only the flotilla lead-row momentum and lateral wall stiffness at the impact location are required for computing impact forces.

4.3.2. Oblique Impacts on Walls. Among the aforementioned studies, impact force data from more than 300 collision simulations (involving USACE waterway structures) are available. Results from the dataset are categorized into three impact categories: oblique, head-on, and aberrant single-barge impacts under hurricane (wind-driven) conditions. The oblique impact category is of greatest relevance to formation of the unified load prediction model. More specifically, the USACE navigation structures most susceptible to oblique flotilla impacts include: rigid, semi-flexible, and pile-founded guide walls.

4.3.2.1. A significant number of FE simulations conducted in previous studies pertain to oblique flotilla impacts against inland waterway structures. Impact force data from more than 100 oblique collision simulations are drawn from in forming the unified load prediction model. Accompanying the collected data are variations in wall configuration, flotilla size (rows, columns), impact velocity, and relative flotilla-wall orientation.

4.3.2.2. Impact data encompasses flotilla sizes ranging from 1x1, or a single barge, to a 3x5 (three rows, five columns). Three distinct FE wall models, covering a range of USACE navigation structures, are also included. The three FE models consist of a rigid wall, semi-flexible wall, and a representative configuration of a pile-founded guide wall.

4.3.2.3. Impact simulation results are compiled into a merged database with maximum values of impact force retained from each collision scenario. In turn, force data are used in developing a unified approach to load prediction for oblique flotilla impacts on concrete wall structures.

4.3.2.4. Force components in the normal (lateral) direction are typically of principal interest in structural design. Accordingly, forces tabulated in sections 4.3.3–4.3.5 consist of peak forces normal to (perpendicular to) the surface of the wall structure. Frictional forces along the longitudinal axis of impacted walls can be approximated using a constant dynamic friction coefficient of 0.45. Vertical forces are not reported, as the associated magnitudes are generally small relative to normal forces.

4.3.2.5. In addition to the tabulated force results in the following sections, peak forces are also plotted with respect to lead-row momentum. Components of momenta of lead-row barge(s) normal to the surface of the impacted wall structure are focused on. Emphasis on lead-row momentum (correlated to maximum, normal-to-wall impact force) is based on findings from Walters et al. (2017).

4.3.3. Peak Impact Forces on Rigid Walls.

4.3.3.1. Listed in Table 4.1 are results from 20 unique, oblique impact simulations between barge flotillas and a rigid wall. Results from specialized sensitivity studies (e.g., lead-row barges with no payload) are not included in the interest of conservatism. Consolazio and Walters (2012) provides further discussion regarding impact-force influences from payload and other phenomena (e.g., pretensioning levels in lashings).

Table 4.1
Peak Force Results for Flotilla Collisions on Rigid Walls

Flotilla	Speed (ft/sec)	Angle (°)	Normal Lead-Row Momentum (kip-sec)	Peak Normal Force (kip)	Flotilla	Speed (ft/sec)	Angle (°)	Normal Lead-Row Momentum (kip-sec)	Peak Normal Force (kip)
3 x 3	1.0	10	65	143	3 x 5	4.0	20	510	603
3 x 3	3.0	20	383	352	3 x 5	5.0	20	638	639
3 x 5	1.0	10	65	164	3 x 5	3.0	25	473	622
3 x 5	2.0	10	130	240	3 x 5	0.5	30	93	266
3 x 5	3.0	10	194	279	3 x 5	1.0	30	186	349
3 x 5	4.0	10	259	315	3 x 5	2.0	30	373	546
3 x 5	5.0	10	324	351	3 x 5	3.0	30	559	768
3 x 5	1.0	20	128	295	3 x 5	4.0	30	746	818
3 x 5	2.0	20	255	383	3 x 5	5.0	30	932	833
3 x 5	3.0	20	383	475	3 x 5	8.0	30	1,492	1,198

4.3.3.2. Analysis of results from the rigid wall study reveal that peak impact force is meaningfully correlated to momentum of the lead-row barges. As emphasis, and consistent with Walters et al. (2017), these quantities are taken normal to the impacted wall surface. Thus, the tabulated (normal) force results (Table 4.1) are plotted with lead-row momentum normal to the rigid wall (Figure 4.5.).

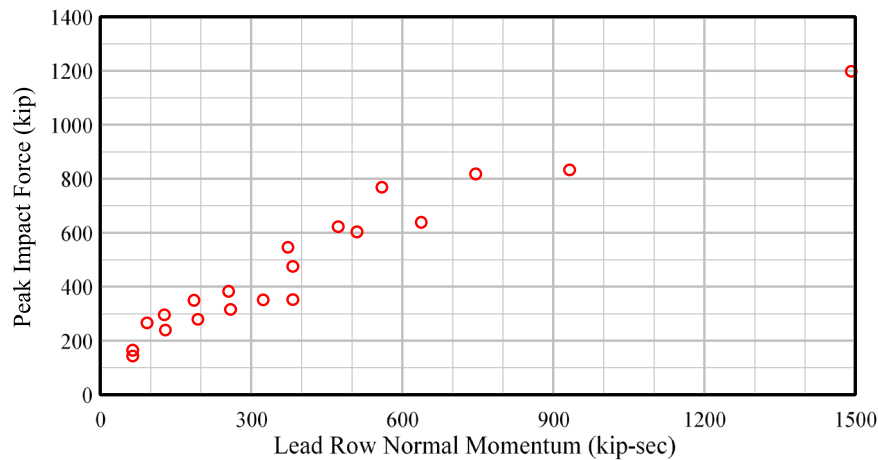


Figure 4.5. Peak Force Results for Flotilla Collisions on Rigid Walls (20 Cases)

4.3.4. Peak Impact Forces on Semi-Flexible Walls.

4.3.4.1. Results from 34 impact simulations against a semi-flexible wall (Winfield) are listed in Table 4.2. Specialized simulations expressly dedicated to studying peak force sensitivity to various phenomena are excluded in the interest of conservatism. See Consolazio and Walters (2012) for additional details.

Table 4.2
Peak Force Results for Flotilla Collisions on Semi-Flexible Walls

Flotilla	Speed (ft/sec)	Angle (°)	Normal Lead-Row Momentum (kip-sec)	Peak Normal Force (kip)
1 x 3	0.5	20	21	82
1 x 3	1.0	20	43	142
1 x 3	1.5	20	64	202
1 x 3	2.0	20	85	230
1 x 3	2.5	20	106	287
1 x 3	3.0	20	128	308
2 x 3	3.0	20	255	405
3 x 1	3.0	20	383	432
3 x 2	3.0	20	383	461
3 x 3	2.0	10	130	224
3 x 3	3.0	10	194	267
3 x 3	4.0	10	259	306
3 x 3	2.7	14	237	348
3 x 3	2.9	17	316	418
3 x 3	3.0	20	383	471
3 x 3	4.0	20	510	579
3 x 3	5.0	20	638	639
3 x 3	8.0	20	1,021	670
3 x 3	1.0	30	186	338
3 x 3	3.0	30	559	757
3 x 3	5.0	30	932	883
3 x 3	5.0	30	932	853
3 x 3	6.0	30	1,119	960
3 x 3	7.0	30	1,305	998
3 x 3	8.0	30	1,492	1,028
3 x 5	2.0	10	130	222
3 x 5	3.0	10	194	267
3 x 5	2.0	20	255	365
3 x 5	3.0	20	383	467
3 x 5	4.0	20	510	579
3 x 5	4.0	30	746	815
3 x 5	5.0	30	932	859
3 x 5	6.0	30	1,119	959
3 x 5	7.0	30	1,305	1,038

4.3.4.2. Analysis of peak force results pertaining to the semi-flexible wall reveal a correlation to (wall normal) momentum of the lead-row barges. Further discussion of various aspects (and significance) of the correlative relationship are found in Consolazio and Walters (2012). Plotted in Figure 4.6 are the tabulated force results (Table 4.2) versus lead-row momentum normal to the semi-flexible (Winfield) wall.

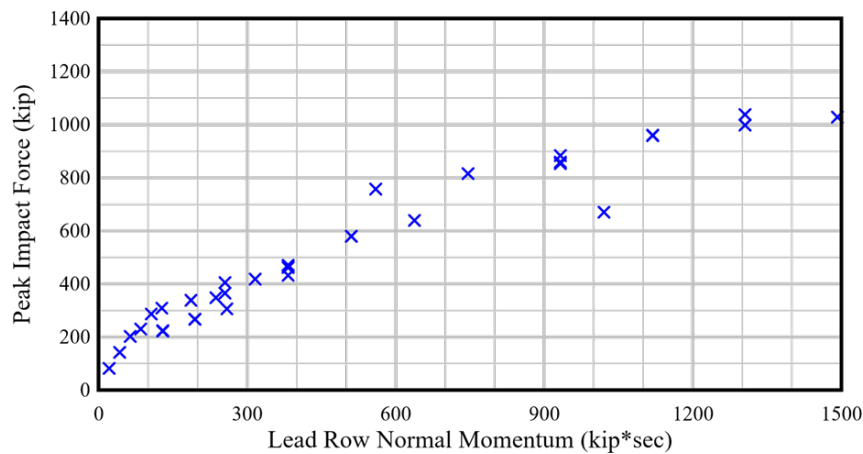


Figure 4.6. Peak Force Results for Flotilla Collisions on Semi-Flexible Walls (34 Cases)

4.3.5. Peak Impact Forces on Pile-Founded Guide Walls.

4.3.5.1. Peak impact forces obtained from 57 impact simulations against a pile-founded guide wall are listed in Table 4.3. Results from specialized simulations performed to study peak force sensitivity to several modeling parameters are not included in the interest of conservatism. See Consolazio et al. (2014) for additional documentation concerning the multifaceted sensitivity study.

4.3.5.2. Peak impact forces listed in Table 4.3 exhibit a correlative relationship with lead-row barge momentum normal to the guide wall. The tabulated results are plotted against lead-row momentum normal to the pile-founded (MRLD2) guide wall (Figure 4.7). Additional force listings (e.g., for other wall configurations) are provided in Consolazio et al. (2014).

4.3.6. Unified Load Prediction Model. The unified load prediction model involves empirically relating maximum impact forces to flotilla momentum. Specifically, the component of lead-row momentum oriented normal to the impacted wall is considered. An empirical expression relating force and momentum is formed, as presented below, through an error-minimization curve fitting process.

4.3.6.1. The empirical curve-fitting approach is applicable to flotilla impacts on concrete guide walls (rigid, semi-flexible, and pile-founded guide walls). In contrast, other types of navigation structures (e.g., flexible timber guide walls) typically possess far less stiffness and mass. Consequently, a separate, case-specific empirical load prediction model is provided in Appendix H for flexible timber guide walls. Further, an alternative load prediction methodology, which is robust over a wide variety of wall types, is presented in Chapter 5.

4.3.6.2. General Form of Empirical Load Prediction Curve. Impact force data described previously for rigid, semi-flexible, and pile-founded guide walls are plotted together in Figure 4.8. The data plotted in Figure 4.8 appear amenable to representation via a linear segment for low-momentum impacts. Likewise, moderate to high momentum impacts appear to adhere to a second reduced-slope linear trend.

Table 4.3
Peak Force Results for Flotilla Collisions on Pile-Founded Guide Walls

Flotilla	Speed (ft/sec)	Angle (°)	Normal Lead-Row Momentum (kip-sec)	Peak Normal Force (kip)	Flotilla	Speed (ft/sec)	Angle (°)	Normal Lead-Row Momentum (kip-sec)	Peak Normal Force (kip)
1 x 3	1.0	5	11	29	2 x 3	2.0	25	210	216
1 x 3	2.0	5	22	70	2 x 3	4.0	25	420	314
1 x 3	4.0	5	43	130	3 x 3	1.0	5	33	61
1 x 3	1.0	10	22	84	3 x 3	2.0	5	65	126
1 x 3	2.0	10	43	145	3 x 3	4.0	5	130	222
1 x 3	6.0	10	130	343	3 x 3	1.0	10	65	146
1 x 3	1.0	15	32	114	3 x 3	2.0	10	130	256
1 x 3	2.0	15	64	225	3 x 3	4.0	10	259	379
1 x 3	4.0	15	129	357	3 x 3	6.0	10	389	443
1 x 3	1.0	20	43	163	3 x 3	1.0	15	97	228
1 x 3	2.0	20	85	290	3 x 3	4.0	15	386	494
1 x 3	4.0	20	170	424	3 x 3	6.0	15	579	596
1 x 3	1.0	25	53	169	3 x 5	1.0	5	33	62
1 x 3	2.0	25	105	300	3 x 5	2.0	5	65	128
1 x 3	4.0	25	210	439	3 x 5	4.0	5	130	227
1 x 3	6.0	25	315	523	3 x 5	1.0	10	65	147
2 x 3	1.0	5	22	39	3 x 5	2.0	10	130	259
2 x 3	2.0	5	43	73	3 x 5	4.0	10	259	382
2 x 3	4.0	5	87	149	3 x 5	6.0	10	389	446
2 x 3	1.0	10	43	105	3 x 5	1.0	15	97	229
2 x 3	2.0	10	86	190	3 x 5	4.0	15	386	496
2 x 3	6.0	10	259	388	3 x 5	6.0	15	579	596
2 x 3	1.0	15	64	154	3 x 3	4.0	20	510	621
2 x 3	2.0	15	129	281	3 x 3	6.0	20	765	786
2 x 3	4.0	15	257	417	3 x 3	8.0	20	1,021	814
2 x 3	1.0	20	85	212	3 x 3	4.0	25	630	751
2 x 3	2.0	20	170	360	3 x 3	6.0	25	946	886
2 x 3	4.0	20	340	496	3 x 3	8.0	25	1,261	902
2 x 3	1.0	25	105	155					

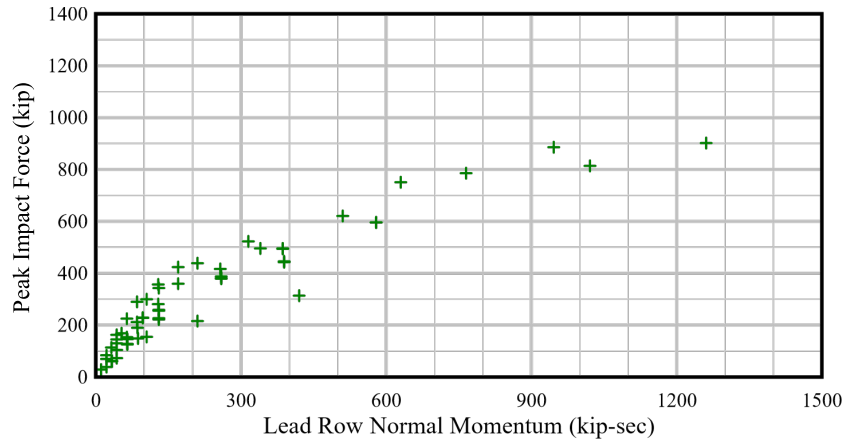


Figure 4.7. Peak Force Results for Flotilla Collisions on Pile-Founded Guide Walls (57 Cases)

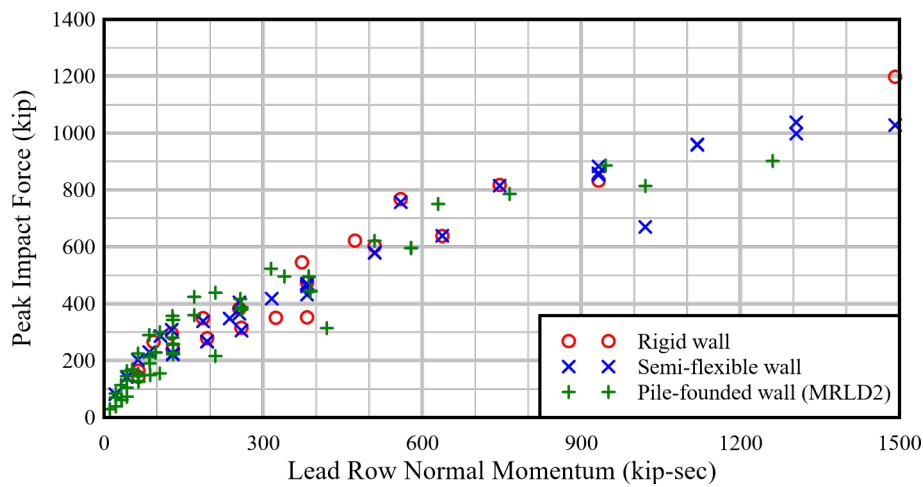


Figure 4.8. Peak Force Results for All Flotilla Collisions on Concrete Guide Walls (111 Cases)

4.3.6.2.1 Such trends suggest that a bilinear curve fit is appropriate for representing the relationship between impact force and momentum. Prior studies also demonstrated correlations between impact force and the stiffness of the impacted structure. Particularly, for sustained contact-impact events, increases in lateral wall stiffness have been found to increase the magnitudes of impact force generated.

4.3.6.2.2 Consequently, the unified empirical load prediction model developed for concrete walls adopts a bilinear representation with dependence on wall stiffness. As shown in the plot schematic of Figure 4.9, the slope (S_1) of the first segment (low-momentum impacts) is constant. The slope (S_2) of the second linear segment (moderate to high momentum impacts) is itself a linear function of wall stiffness. Functionally, the bilinear curve has the form:

$$F = \begin{cases} S_1 \cdot (m_{LR} \cdot v \cdot \sin \theta) & \text{if } m_{LR} \cdot v \cdot \sin \theta \leq (F_{12}/S_1) \\ F_{12} + \frac{(S_{2A} + S_{2B} \cdot k)}{S_2} \cdot (m_{LR} \cdot v \cdot \sin \theta - (F_{12}/S_1)) & \text{otherwise} \end{cases} \quad (4.1)$$

where F is the impact force normal to the wall. The terms F_{12} , S_{2A} , and S_{2B} are bilinear curve fitting parameters. Also, k is the lateral stiffness of the wall at the impact point. The m_{LR} term is the mass of all barges in the lead row of the flotilla. Flotilla impact velocity is given as v , and θ is the angle between the flotilla transit direction and wall longitudinal axis.

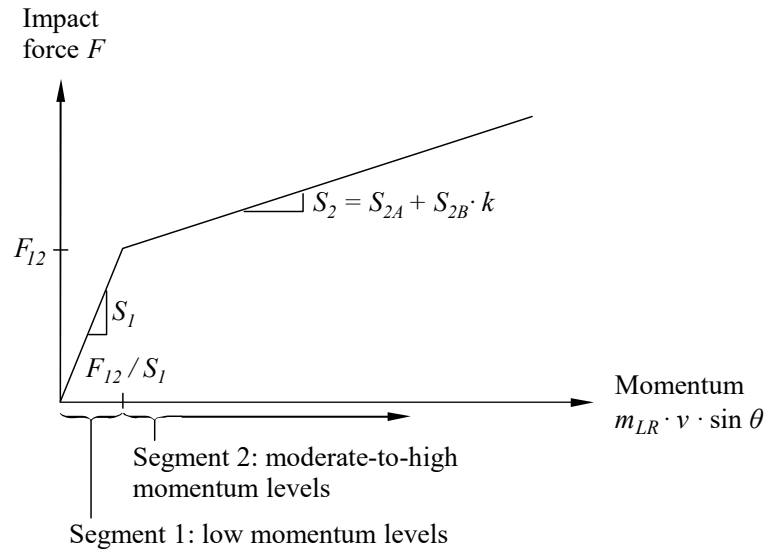


Figure 4.9. General Form of Unified Bilinear Curve Fit Used for Concrete Walls

4.3.6.3. Empirical Curve Fitting. An error function minimization process is used to optimally compute best-fit parameter values across three concrete wall types. The error function is defined as the sum of the squares of the load prediction errors. Load prediction errors are taken as differences between impact simulation force-momentum data (Figure 4.8) and predictions from Equation 4.1. For a given candidate set of coefficients, Equation 4.1 is repeatedly evaluated and errors accumulated across all three concrete wall datasets. In total, the three force-momentum datasets entail 111 unique points (or paired values). Candidate coefficient sets are iterated until a minimum error is quantified.

4.3.6.3.1 As indicated above, the bilinear load prediction model (Equation 4.1) is a function of lateral wall stiffness (k). Consequently, determination of prediction errors requires that a stiffness value be assigned for evaluation of each point in the dataset. For rigid walls, lateral stiffness is hypothetically infinity. However, beyond a certain threshold, maximum impact forces tend to be limited by impacting barge stiffness (not wall stiffness). A lateral wall stiffness of 1,000 kip/in. constitutes a practical threshold for use with rigid walls (Consolazio et al., 2014). Note that limited utility may be achieved through use of stiffness values exceeding 1,000 kip/in.

4.3.6.3.2 For semi-flexible walls, a lateral stiffness of 767 kip/in. is assigned a representative quantity. This stiffness value corresponds to the lateral stiffness at the mid-span of the waterway wall at Winfield L&D. For pile-founded guide walls, a lateral stiffness of 592 kip/in. is assigned. This stiffness value is based on results from quasi-static lateral load analysis of the wall FE model (recall Figure 4.2).

4.3.6.3.3 Using (in part) the aforementioned wall stiffnesses, minimization of the cumulative square error function produces the best fit parameters. Values for slope S_I and fitting parameters F_{I2} , S_{2A} , and S_{2B} , are determined. In turn, the following mean-value unified load prediction model is established for concrete walls:

$$F = \begin{cases} 2.266 \cdot m_{LR} \cdot v \cdot \sin \theta & \text{if } m_{LR} \cdot v \cdot \sin \theta \leq 143 \text{ kip-sec} \\ 325 + (0.491 + 0.000173 \cdot k) \cdot (m_{LR} \cdot v \cdot \sin \theta - 143) & \text{otherwise} \end{cases} \quad (4.2)$$

where $m_{LR} \cdot v \cdot \sin \theta$ is the lead-row momentum normal to the wall in units of kip-section. Here, F is the (normal to wall) impact force (kip), and k is the lateral wall stiffness in units of kip/in. The maximum value of k recommended for use in evaluating Equation 4.2 is limited to 1,000 kip/in.

4.3.6.3.4 The confidence bounds are also established at confidence levels of 1-standard deviation (84.1%) and 2-standard deviations (97.7%) from the mean. Functionally, these bounds are given by:

$$F_{84.1\%} = \begin{cases} 3.152 \cdot m_{LR} \cdot v \cdot \sin \theta & \text{if } m_{LR} \cdot v \cdot \sin \theta \leq 116 \text{ kip-sec} \\ 366 + (0.533 + 0.000205 \cdot k) \cdot (m_{LR} \cdot v \cdot \sin \theta - 116) & \text{otherwise} \end{cases} \quad (4.3)$$

and:

$$F_{97.7\%} = \begin{cases} 3.771 \cdot m_{LR} \cdot v \cdot \sin \theta & \text{if } m_{LR} \cdot v \cdot \sin \theta \leq 111 \text{ kip-sec} \\ 418 + (0.621 + 0.000186 \cdot k) \cdot (m_{LR} \cdot v \cdot \sin \theta - 111) & \text{otherwise} \end{cases} \quad (4.4)$$

4.3.6.3.5 A summary plot of mean-value best fits curves and force-momentum data is presented in Figure 4.10. The load prediction model is plotted with normal-to-wall force and lead-row momentum data for rigid walls in Figure 4.11. Similar plots are provided in Figure 4.12 and Figure 4.13, respectively, for semi-flexible and pile-founded guide walls.

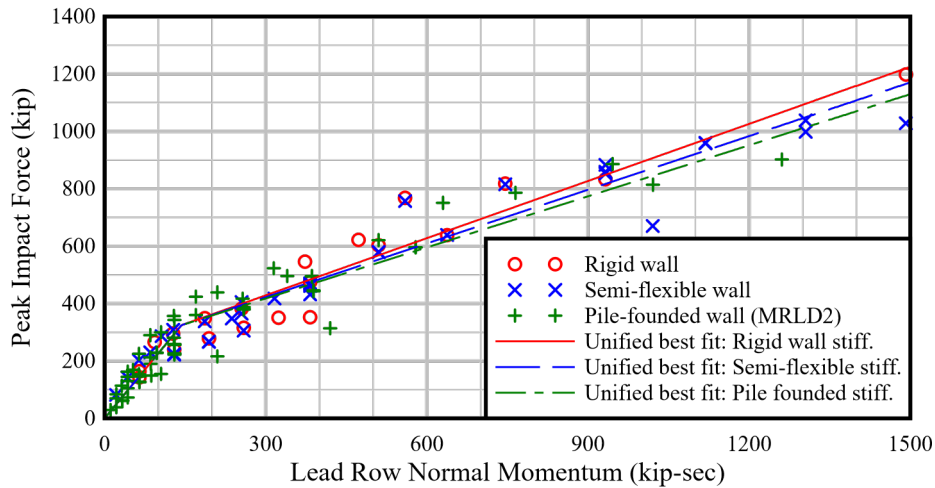


Figure 4.10. Comparison of All Concrete Wall Data and Unified Bilinear Curve Fit (the Latter Evaluated Using the Appropriate Stiffnesses, k , of the Associated Walls)

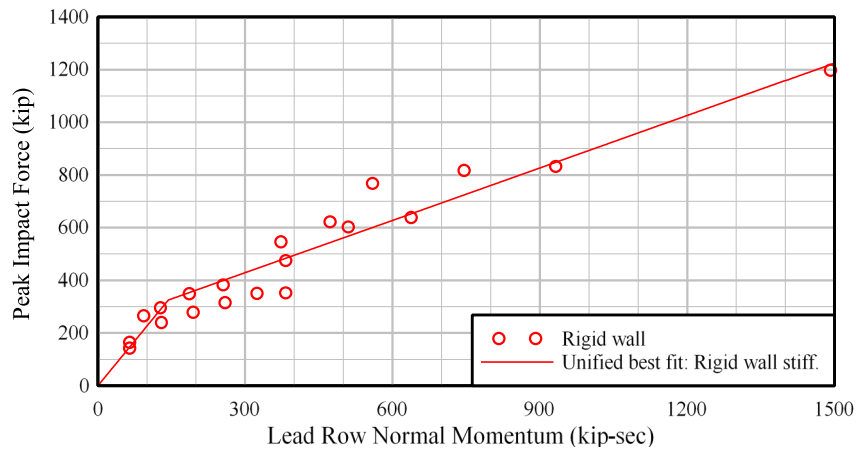


Figure 4.11. Comparison of Rigid Wall Data and Unified Load Prediction Model (the Latter Evaluated Using Wall Stiffness, $k = 1,000$ kip/in.)

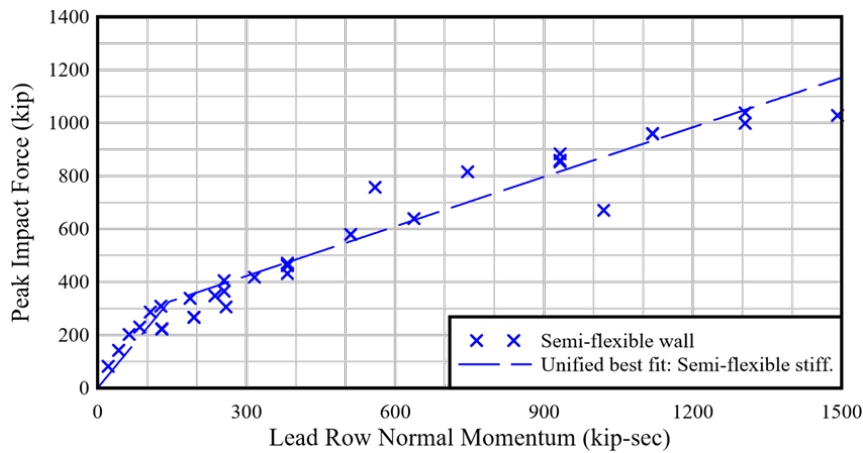


Figure 4.12. Comparison of Semi-Flexible Wall Data and Unified Load Prediction Model (the Latter Evaluated Using Wall Stiffness, $k = 767$ kip/in.)

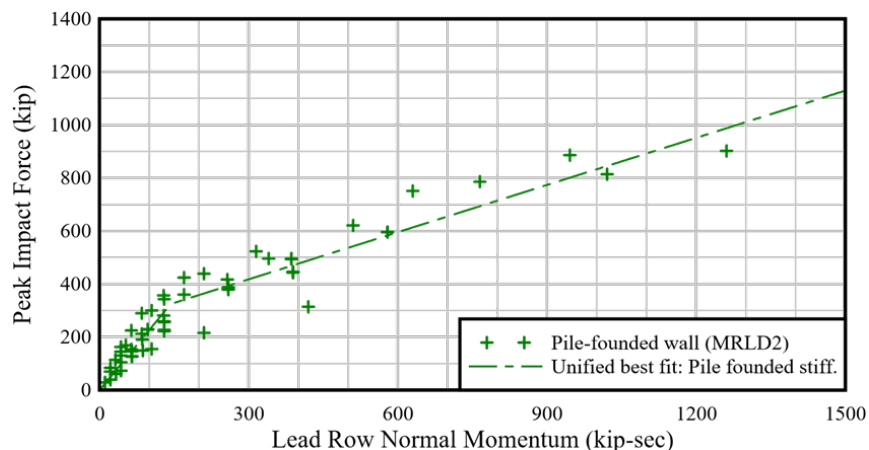


Figure 4.13. Comparison of Pile-Founded Guide Wall Data and Unified Load Prediction Model (the Latter Evaluated Using Wall Stiffness, $k = 592$ kip/in.)

4.4. Considerations for Hurricane and Inland Riverine Protection Floodwalls.

4.4.1. Background. The empirical load prediction model presented in section 4.3.6 applies to both concrete approach walls as well as hurricane and inland riverine protection floodwalls. Moreover, the dynamic load prediction procedure described later in Chapter 5 also applies to both classifications of walls. However, protection walls may also require additional considerations relating to potential damage modes, hurricane-stage or river-stage impact conditions, and probabilistic design. Such considerations are not completely addressed by either the empirical load method of section 4.3.6 or by the dynamic procedure of Chapter 5. Additional considerations specific to hurricane protection walls and inland riverine floodwalls are therefore addressed in the following sections and in the corresponding Appendixes F and G.

4.4.2. Damage Modes and Failure. The potential consequences of hurricane protection walls sustaining structural damage due to barge impact loads are greater than those of lock approach walls. Significant structural damage in protection walls has the potential to lead to widespread flooding of adjacent low-lying areas.

4.4.2.1. For structural design purposes, loads computed per section 4.3.6 are compared to corresponding static wall capacities (flexural or otherwise). However, barge impacts are dynamic rather than static loading events. In Consolazio and Han (2018), concrete wall failure (damage) modes were investigated under both static and barge impact loading conditions.

4.4.2.2. In static design, wall capacity associated with flexural damage and flexural failure typically governs. By investigating both static and dynamic loading conditions, it was possible to determine whether changes in governing wall damage mode occurred. Of interest was assessing whether a transition from flexural failure to punching failure might occur as a result of inertial forces. Such a transition could potentially render static wall flexural capacity calculation methods underconservative.

4.4.2.3. However, for the barge impact conditions and wall configurations that were investigated in Consolazio and Han (2018), flexural patterns of damage were still primarily observed. Study results indicated that designing static flexural wall capacity to exceed peak impact load will generally produce adequate designs. Peak barge impact loads used in such design processes may be computed via either section 4.3.6 or Chapter 5. Additional details of wall damage modes under static and dynamic barge impact loading conditions are provided in Appendix F.

4.4.3. Hurricane Protection Walls Considerations. During hurricanes, strong winds can cause barges to break loose from moorings and be propelled into hurricane protection walls. Impact speeds and angles of barges driven by wind and waves may differ significantly from those of barges carried by river currents. Hurricane-driven barge orientation angles may vary widely, leading to bow, side, or stern impacts on protection walls. Also, impact velocities may not align with the longitudinal axis of impacting barges, as is assumed for river flow impacts.

4.4.3.1. Further, during storm surge, the water level may be at or near the top-of-wall elevation. Conditions are then possible where the headlog of a barge overtops the protection wall and results in an under-rake impact. In contrast, the load prediction model of section 4.3.6 was developed from data corresponding to oblique barge bow (headlog) impacts. Stern, side, and under-rake barge impacts are not directly addressed by section 4.3.6, nor were they addressed by ETL 1110-2-563.

4.4.3.2. Consequently, to complement the studies presented in section 4.3, additional investigations were carried out under USACE auspices. These studies considered barge bow, side, stern, and under-rake impact conditions at hurricane-driven barge impact speeds. USACE (2010) and Davidson et al. (2020) document the resulting risk assessment procedure for barge impacts on the Hurricane and Storm Damage Risk Reduction System (HSDRRS). Components of the risk assessment procedure bring together findings from forensic, experimental, and numerical modeling investigations.

4.4.3.3. Further, the risk assessment procedure encompasses both probability of failure and consequence of failure assessments. Use of the procedure is demonstrated in the aforementioned studies for critical floodwall infrastructure located throughout New Orleans, Louisiana. Also provided are recommendations for improved design of hurricane and storm damage risk reduction systems. Additional details are supplied in Appendix G.

4.4.4. Inland Riverine Flood Walls Considerations. During high flow events on the river, winds and current can cause barges to break loose from moorings and be propelled downstream toward inland riverine floodwalls. These impact speeds and angles of aberrant barges driven by wind and waves on the river may differ significantly from those of barges moved by hurricane events. The barge orientation at impact into these flood walls will have angles that may vary widely, leading to bow, side, or stern impacts on flood walls. Also, impact velocities may not align with the longitudinal axis of impacting barges, as barges may find varying current close to the flood walls depending upon river bathymetries.

4.5. Examples Using the Empirical Models for Impacts on Approach Walls.

4.5.1. Overview. Section 4.5 presents three deterministic examples of collision scenarios on concrete wall structures. The examples progress from less severe to more severe with respect to both flotilla size (mass) and impact velocity. Although the examples are deterministic, they do represent increasingly rare collision events. An impact scenario associated with usual conditions is presented in section 4.5.2. Unusual and extreme impact scenarios are focused on in section 4.5.3 and section 4.5.4, respectively.

4.5.2. Usual.

4.5.2.1. Figure 4.14 shows a plan-view schematic of the deterministic example for usual impact conditions. A fully loaded 1x1 flotilla (i.e., single barge) is selected for this scenario, weighing 2,000 short tons (10.4 kip-sec²/in. mass). The initial barge velocity is 2 ft/sec and impacts a concrete wall at an angle of 25°. Wall stiffness is defined as 767 kip/in., which is approximately representative of a semi-flexible guide wall. The wall stiffness is determined by using a static FE model and performing a pushover analysis with incremental loads resulting in deflections. This force-deflection data is plotted, and a linear line is approximated to reflect the stiffness of the structure typically focused on the upper end of the forces.

4.5.2.2. A summary of relevant parameters associated with the deterministic (usual) impact scenario are listed in Table 4.4. Lead-row mass (m_{LR}), impact velocity (v), impact angle (θ), and wall stiffness (k) are used in evaluating Equation 4.2. Lead-row momentum normal to the wall ($m_{LR} \cdot v \cdot \sin \theta$) is 105 kip-sec in this example. The momentum is less than the proportional threshold of 143 kip-sec in Equation 4.2. Therefore, the deterministic design force, associated with segment 1 of Figure 4.9, for this usual impact condition is 238 kip.

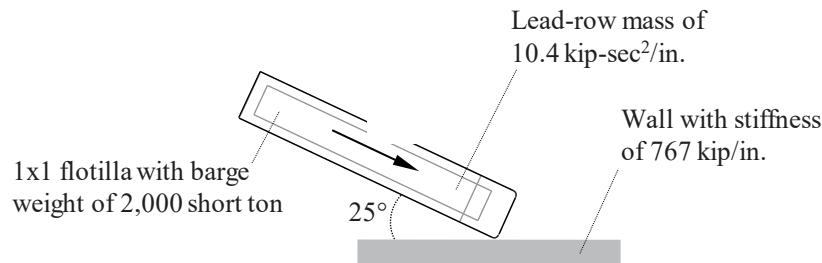


Figure 4.14. Deterministic (Usual) Impact Scenario

Table 4.4
System Parameters for Deterministic (Usual) Impact Scenario

Parameter Description	Value	Units
Flotilla columns	1	N/A
Weight per barge	2,000	short tons
Lead-row mass, m_{LR}	10.4	kip-sec ² /in.
Impact velocity, v	2	ft/sec

Parameter Description	Value	Units
Impact angle, θ	25	$^{\circ}$
Wall stiffness, k	767	kip/in.
Usual Empirical Impact Result	238	kips

4.5.3. Unusual.

4.5.3.1. Figure 4.15 shows a plan-view schematic of the deterministic example for unusual impact conditions. A fully loaded 3x3 flotilla is selected for this scenario, with each barge weighing 2,000 short tons. Correspondingly, the lead-row mass (3 barges) is 31.1 kip-sec²/in. The initial velocity of the flotilla is 3 ft/sec, and the flotilla impacts the wall at an angle of 20°. Wall stiffness is defined as 767 kip/in., which is approximately representative of a semi-flexible guide wall.

4.5.3.2. Relevant parameters for this (unusual) collision scenario are listed in Table 4.5, and are used in evaluating Equation 4.2. Lead-row momentum normal to the wall ($m_{LR} \cdot v \cdot \sin \theta$) is 383 kip-sec, which is greater than the 143 kip-sec listed in Equation 4.2. Therefore, the deterministic design force, associated with segment 2 of Figure 4.9, for this unusual impact condition is 474 kip.

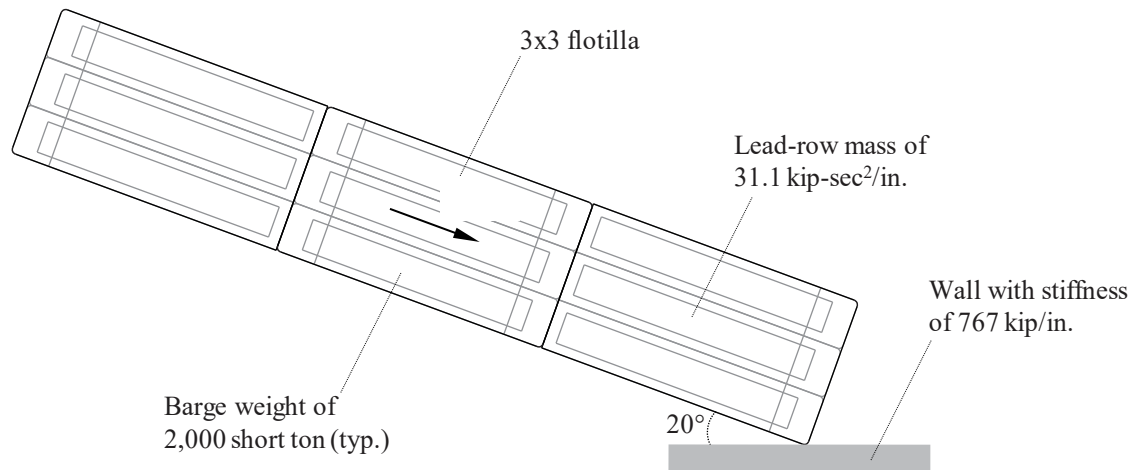


Figure 4.15. Deterministic (Unusual) Impact Scenario

Table 4.5
System Parameters for Deterministic (Unusual) Impact Scenario

Parameter Description	Value	Units
Flotilla columns	3	N/A
Weight per barge	2,000	short tons
Lead-row mass, m_{LR}	31.1	kip-sec ² /in.
Impact velocity, v	3	ft/sec

Parameter Description	Value	Units
Impact angle, θ	20	°
Wall stiffness, k	767	kip/in.
Unusual Empirical Impact Result	474	kips

4.5.4. Extreme.

4.5.4.1. Figure 4.16 shows a plan-view schematic of the deterministic example for extreme impact conditions. A fully loaded 3x5 flotilla is selected for this scenario, with each barge weighing 2,000 short tons. The lead-row mass for this collision scenario (that of 3 fully loaded barges) is 31.1 kip-sec²/in. An initial velocity of 8 ft/sec is assigned to the flotilla. Impact occurs on the wall at an angle of 30°. Wall stiffness is defined as 767 kip/in., which is approximately representative of a semi-flexible guide wall.

4.5.4.2. Unified load model parameters for the extreme (deterministic) collision scenario are listed in Table 4.6. The associated impact force is determined using Equation 4.2. Lead-row momentum normal to the wall ($m_{LR} \cdot v \cdot \sin \theta$) is 1,492 kip-sec, which exceeds the 143 kip-sec listed in Equation 4.2. Therefore, the deterministic design force, associated with segment 2 of Figure 4.9, for this extreme impact condition is 1,166 kip.

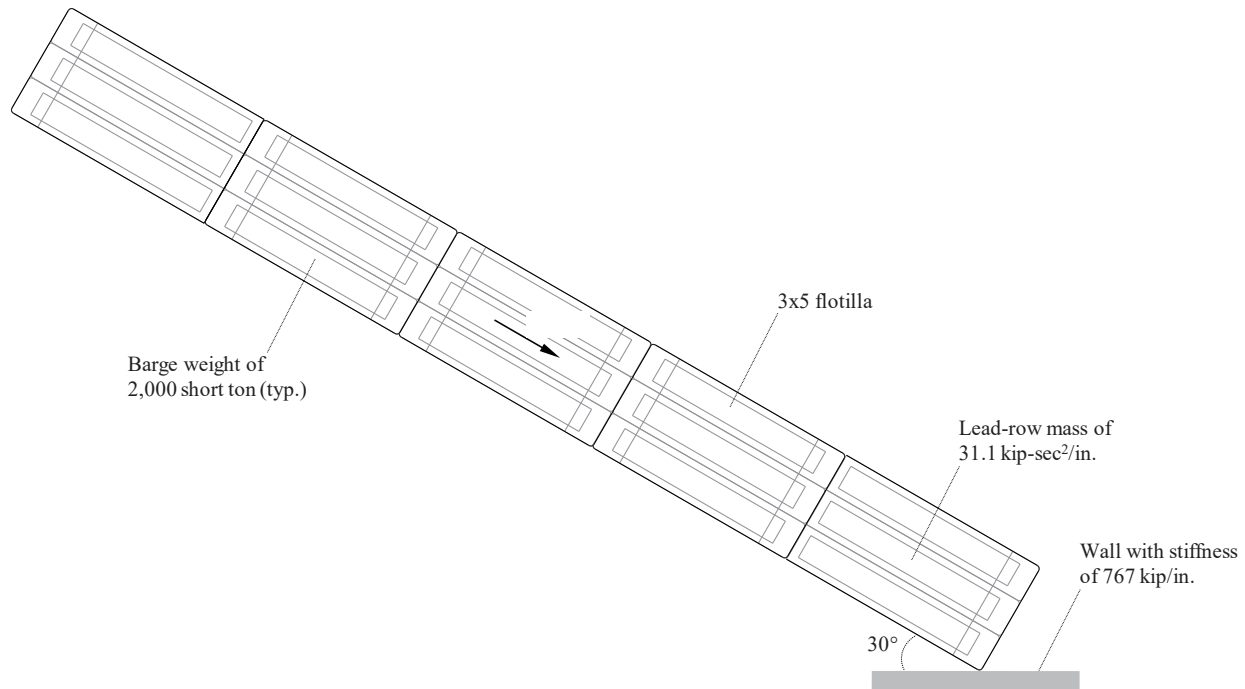


Figure 4.16. Deterministic (Extreme) Impact Scenario

Table 4.6
System Parameters for Deterministic (Extreme) Impact Scenario

Parameter Description	Value	Units
Flotilla columns	3	N/A
Weight per barge	2,000	short tons
Lead-row mass, m_{LR}	31.1	kip-sec ² /in.
Impact velocity, v	8	ft/sec
Impact angle, θ	30	°
Wall stiffness, k	767	kip/in.
Unusual Empirical Impact Result	1,166	kips

4.6. Complete Design Example – Concrete Approach Wall.

4.6.1. Deterministic Example. This example is for the design of a rigid approach wall for a new lock on the Ohio River. Based on present traffic predictions and navigation model testing at ERDC, a 15-barge tow and input parameters selected for the usual, unusual, and extreme load cases are as follows:

4.6.1.1. Usual load case:

$$V = 2 \text{ ft/sec}$$

$$\theta = 10 \text{ degrees}$$

$$K = 1,000 \text{ kip/in}$$

$$W_{\text{barge}} = 30,000 \text{ short tons (Lead row} = 6,000 \text{ short tons} = 12,000 \text{ kips)}$$

Checking, $M_{LR} * v * \sin \theta = 12,000 / 32.2 * 2 * \sin (10) = 129.43 \text{ kip-sec}$

Since $129.43 \text{ kip-sec} < 143 \text{ kip-sec}$, use first line segment

$$F = 2.266 * M_{LR} * v * \sin \theta = 2.266 * 129.43 = 293.28 \text{ kips}$$

4.6.1.2. Unusual load case:

$$V = 4 \text{ ft/sec}$$

$$\theta = 20 \text{ degrees}$$

$$K = 1,000 \text{ kip/in}$$

$$W_{\text{barge}} = 30,000 \text{ short tons (Lead row} = 6,000 \text{ short tons} = 12,000 \text{ kips)}$$

Checking, $M_{LR} * v * \sin \theta = 12,000 / 32.2 * 4 * \sin (20) = 509.84 \text{ kip-sec}$

Since $509.84 > 143 \text{ kip-sec}$, use second line segment

$$\begin{aligned}
F &= 325 + (0.491 + 0.000173k) * (M_{LR} * v * \sin \theta - 143) \\
&= 325 + (0.491 + 0.000173 * 1,000) * (509.84 - 143) \\
&= 325 + (0.664) * (366.84) \\
&= 568.25 \text{ kips}
\end{aligned}$$

4.6.1.3. Extreme load case:

$$\begin{aligned}
V &= 6 \text{ ft/sec} \\
\theta &= 30 \text{ degrees} \\
K &= 1,000 \text{ kip/in} \\
W_{\text{barge}} &= 30,000 \text{ short tons (Lead row} = 6,000 \text{ short tons} = 12,000 \text{ kips)}
\end{aligned}$$

Checking, $M_{LR} * v * \sin \theta = 12,000 / 32.2 * 6 * \sin (30) = 1,118.01 \text{ kip-sec}$

Since $1,118.01 \text{ kip-sec} > 143 \text{ kip-sec}$, use second line segment

$$\begin{aligned}
F &= 325 + (0.491 + 0.000173k) * (M_{LR} * v * \sin \theta - 143) \\
&= 325 + (0.491 + 0.000173 * 1,000) * (1,118.01 - 143) \\
&= 325 + (0.664) * (975.01) \\
&= 972.4 \text{ kips}
\end{aligned}$$

4.6.1.4. Table 4.7 below shows a summary based on calculating the deterministic calculations defined in the flowchart in Chapter 2.

Table 4.7
Design Load Cases from Deterministic Calculations

Load Case	Force (kips)
Usual	293
Unusual	568
Extreme	972

4.6.2. Probabilistic Example. This example is for the design of a concrete approach wall ($k = 1,000 \text{ k-in.}$) for a new lock on the Ohio River. Based on present traffic predictions and navigation model testing at ERDC, a 15-barge tow and input parameters selected for probabilistic analysis are shown in Table 4.8.

Table 4.8
Design Example – Probabilistic Inputs

Parameter	Distribution	E(x)	$\sigma(x)$	Min(x)	Max(x)
Velocity (ft/sec)	Lognormal	2	1	0.1	7
Angle (degs)	Lognormal	8	4	1	30
Weight – lead row (short tons)	Constant	6,000	-	-	-
Stiffness – k (kip/in)	Constant	1,000			

4.6.2.1. The probabilistic model run is made using Monte Carlo Simulation for 50,000 iterations. Return periods for this site were selected for the usual (2 year), unusual (150 year), and extreme (1000 year) load cases.

Table 4.9
Design Load Cases from Probabilistic Calculations

Load Case	Force (kips)
Usual – 2 year	187
Unusual – 150 year	515
Extreme – 1000 year	627

4.6.2.2. Note: The difference in the extreme load case in Table 4.7 and Table 4.9 is due to the true frequency of the extreme load in the probabilistic calculations. Deterministic calculations may sometimes overestimate for forces in the extreme events since this combination of upper bound has a low frequency that is accounted for in the simulation results.

Chapter 5 Wall Structures – Dynamic

5.1. General.

5.1.1. This chapter focuses on dynamic analysis techniques for assessing barge impact loads on wall structures. A fast-running dynamic analysis method is presented that uses straightforward characterizations of flotilla-wall systems for rapidly calculating dynamic response quantities. The method simplifies many aspects of contact-impact interactions between flotillas and walls yet remains suitably accurate for use in design applications. The streamlined analysis method (and collective, underlying techniques) is referred to as low-order dynamic model (LODM) analysis. This LODM method may be used, if the appropriate inputs are available, to estimate impact forces for comparison to empirical models in Chapter 4 of this EM or for application to structures not covered in this EM.

5.1.2. Discussed herein are key aspects of the low-order analysis development, model components, and verification against high-resolution impact simulations. Low-order analysis is demonstrated to be sufficiently robust for assessing impact loads across various wall structures and collision scenarios. To illustrate use of the dynamic analysis method in design applications, both deterministic and probabilistic design examples are also provided.

5.1.3. Scope. The material in this chapter has been organized into the following sections as:

5.1.3.1. Section 5.2 documents key aspects (e.g., development, verification) of the method.

5.1.3.2. Section 5.3 contains additional considerations and resources for analyzing selected types of navigation wall structures (bullnose structures, flexible timber guide walls).

5.1.3.3. Section 5.4 documents deterministic design examples, with use of low-order analysis under usual, unusual, and extreme collision scenarios.

5.1.3.4. Section 5.5 gives probabilistic design examples.

5.2. Low-Order Dynamic Model for Impact Load Prediction.

5.2.1. Introduction. USACE is responsible for ensuring impact-resistant design of navigation infrastructure along U.S. waterways. As context, a barge-and-tug and example structure (approach wall near a lock) is shown in Figure 5.1a. To aid in characterizing impact loads associated with waterway vessels (e.g., barge flotillas, Figure 5.1b–c), USACE previously conducted impact testing. The experiments (Patev et al., 2003) were performed against rigid and semi-flexible wall structures. Subsequent analytical studies (Arroyo et al., 2003) were carried out to quantify shallow angle (oblique) barge impact loads on navigation structures.

5.2.1.1. Findings from experimental and analytical efforts led to design guidance for estimating impact loads on wall structures (Patev 2000). Impact force data collected from the previous full-scale impact studies were correlated to the momentum of the impacting barge flotilla. Further, forces were resolved normal (perpendicular) to the longitudinal axis of the impacted wall to form empirical load prediction equations. In some cases, empirical equations were formed by treating navigation walls as rigid (Arroyo et al., 2003). In other cases, simplified approximations of wall stiffness were directly factored into the empirical formulations (e.g., Consolazio et al., 2014).

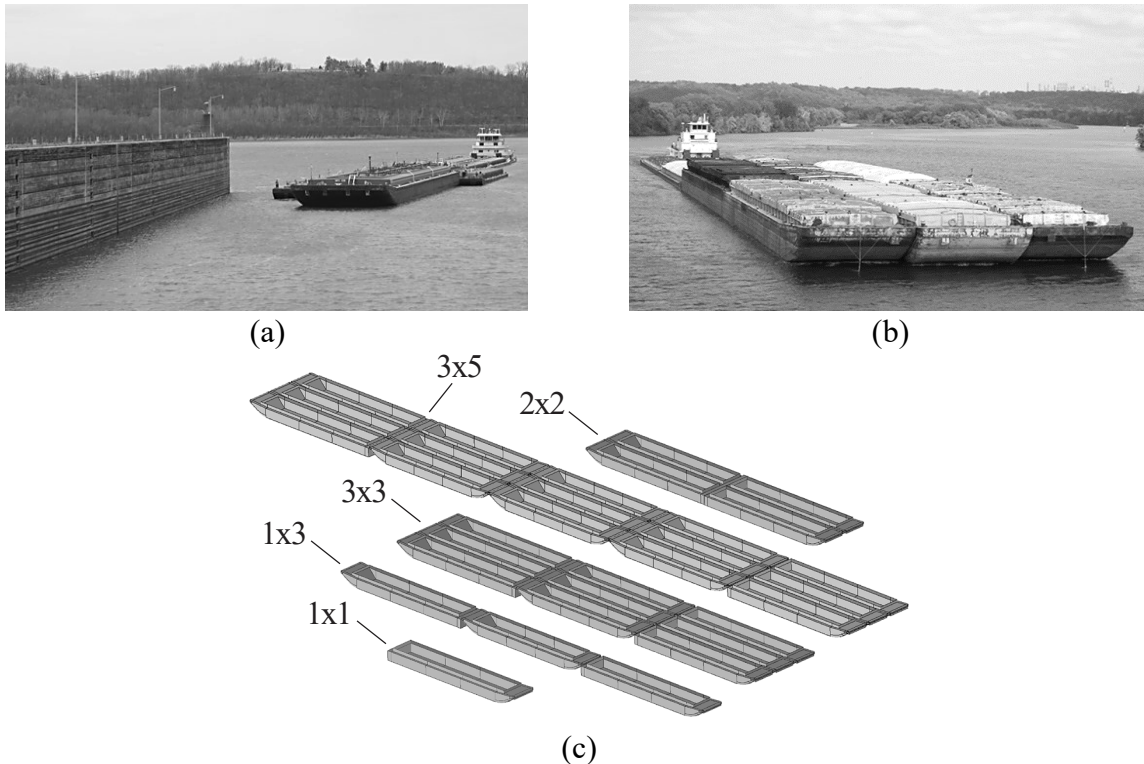


Figure 5.1. Barge Flotillas: (a) Approaching Guide Wall; (b) In Transit; (c) Example Configurations

5.2.1.2. Several types of navigation structures are distributed along navigable U.S. waterways. Due to cost and logistical constraints, physical testing of impacts on myriad wall types was deemed impractical for impact-load characterization. High-resolution FE impact simulations were subsequently conducted as an alternative to characterization via physical testing. A range of wall structures were considered, spanning high-stiffness, high-mass configurations (Figure 5.2a) to low-stiffness, low-mass configurations (Figure 5.2d). Special considerations for low-stiffness, low-mass configurations are discussed in section 5.3 and Appendix H.

5.2.1.3. Flotilla impacts on rigid and semi-flexible concrete walls (Figure 5.2a–b) were investigated in Walters et al. (2017). Collision simulations on monolithic concrete walls founded on timber piles (Figure 5.2c) were carried out in Consolazio et al. (2014). Flexible timber guide walls were investigated in Consolazio and Wilkes (2013). Still other wall types (hurricane protections structures) were investigated in Getter et al. (2015) and Consolazio et al. (2010).

5.2.1.4. Collectively, the above analytical studies revealed that several parameters influence impact load generation during flotilla-wall collisions. Regarding barge flotillas: impact speed, barge flotilla mass, inter-barge motions (Kantales et al., 2019), and inter-barge stiffness were of significance. In addition, impacted wall stiffness (including soil resistance), mass, and damping were shown to influence dynamic collision forces. These analytical studies demonstrated the merit of high-resolution FE modeling approaches. However, the associated (computationally expensive) FE modeling schemes were deemed impractical for routine use in design.

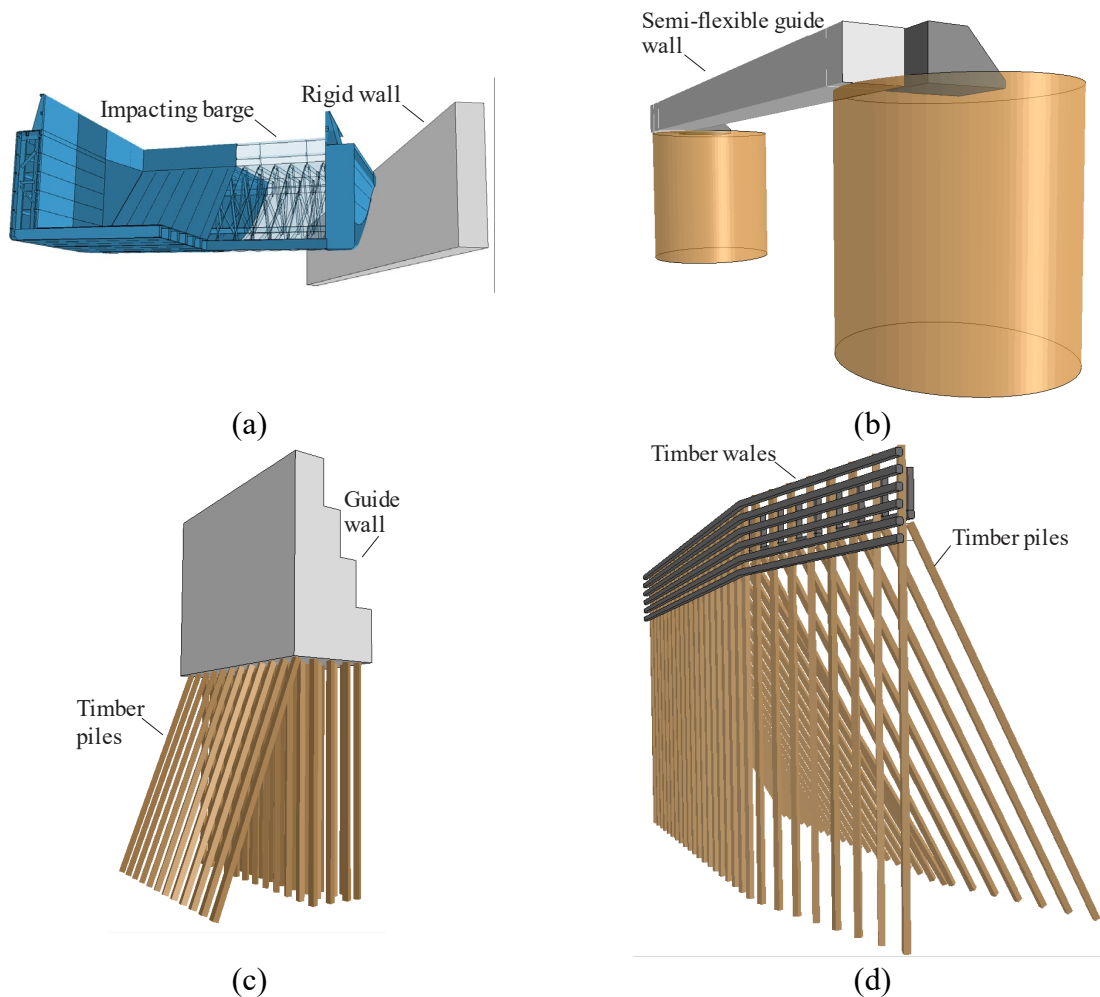


Figure 5.2. Examples of Navigation Wall Structures: (a) Rigid Concrete Guide Wall Impacted by Barge (in Cut-Away View); (b) Semi-Flexible Concrete Guide Wall Supported on Rigid Cells; (c) Concrete Guide Wall Founded on Timber Piles; (d) Flexible Timber Guide Wall

5.2.1.5. Limitations associated with routine use of high-resolution FE modeling in design motivated development of a design-oriented dynamic analysis procedure. As detailed below, the low-order analysis procedure was created to facilitate dynamic analysis of flotilla-wall impacts. Low-order analysis was implemented as an efficient, simple to use, and suitably accurate (i.e., not overly conservative) design method. See Consolazio and Han (2015a) and Consolazio and Han (2015b), respectively, for comprehensive accounts of the low-order analysis development and implementation.

5.2.2. Overview. The low-order dynamic analysis method employs simplified flotilla-wall models to compute dynamic collision response quantities without requiring external FE methods. The procedure accounts for dynamic characteristics of walls (mass, damping, nonlinear elastic stiffness), barge contact-impact stiffness, and inter-barge motions. Computed results include time-varying impact forces and wall displacements. An overview is given in Figure 5.3.

5.2.2.1. The low-order analysis method is rooted in validated, high-resolution FE models of barge flotillas (Figure 5.3, top left to center left). See Chapter 3 (and Walters et al., 2017) for details of requisite modeling techniques, components, element types, and constitutive relationships. As shown in Figure 5.3 (center left), the validated flotilla models allow for verification of the low-order analysis method. Verification of low-order analyses is discussed in section 5.2.8.

5.2.2.2. A simplified flotilla representation is contained in the low-order approach (Figure 5.3, bottom). Rigid beams span the fore-aft flotilla centerline to efficiently permit propagation of dynamic forces and motions during flotilla-wall collision analysis. Barge model components are concentrated at the centers of flotilla rows (masses, inertias) and inter-row interfaces (connection stiffnesses).

5.2.2.3. Inter-row stiffnesses are based on data from specialized simulations using the high-resolution flotilla FE models (Figure 5.3, top right). Three forms of stiffness are included in the simplified flotilla representation: shear, axial, and flexural. See section 5.2.6 for details regarding the specialized simulations and corresponding characterizations of inter-row stiffnesses.

5.2.2.4. Contact-impact interactions at the interface between the impacting barge bow and impacted wall are encapsulated into a nonlinear elastic spring. Constitutive relationships are dependent on flotilla-wall orientation (Figure 5.3, center right), and based on data obtained from high-resolution bow-corner crushing simulations. For a given flotilla-wall orientation, the force-deformation relationship of the compression-only impact spring is automatically determined by the low-order method. Additional details are provided in section 5.2.5.

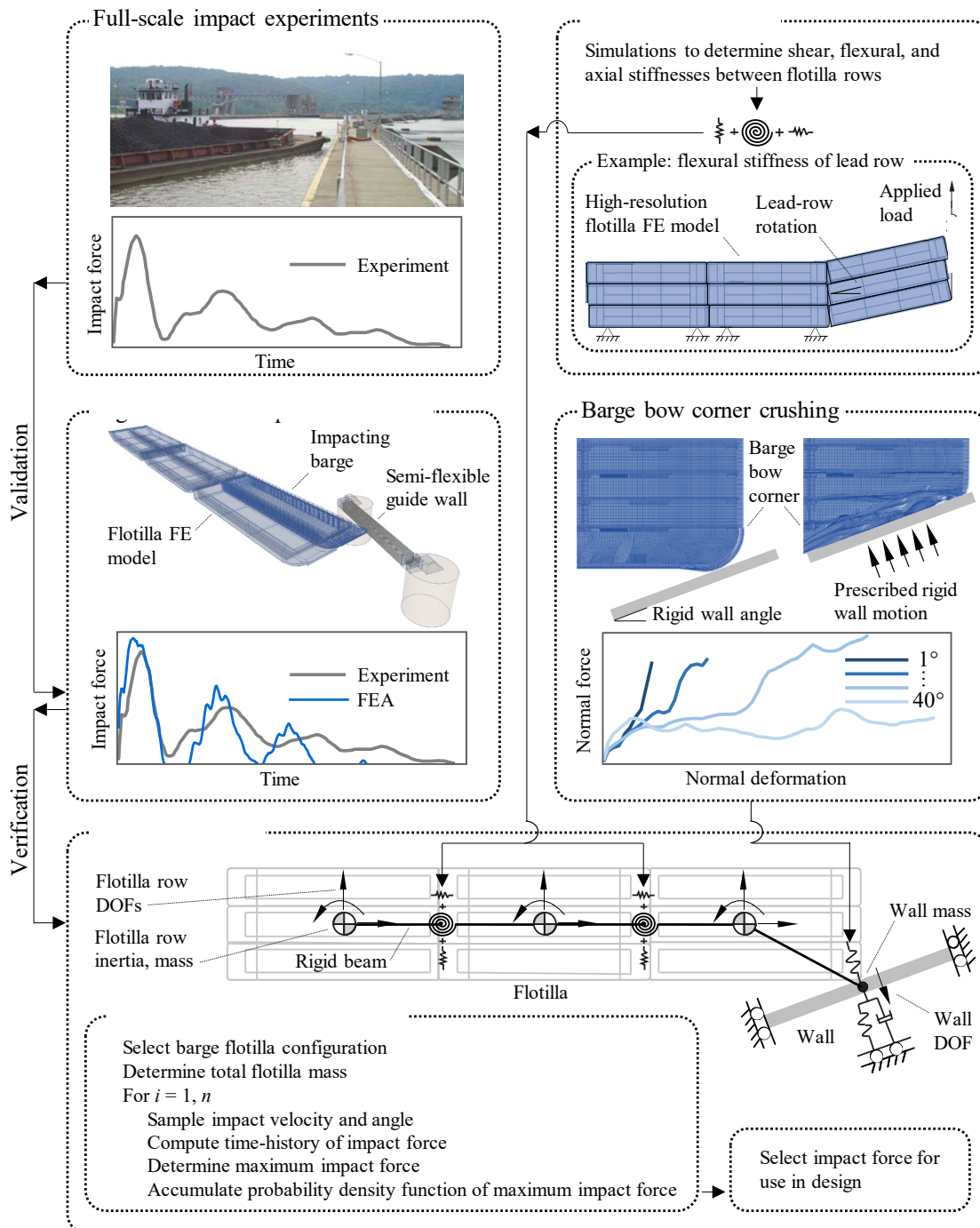


Figure 5.3. Overview of Low-Order Modeling of Barge Flotilla Impacts on Wall Structures

5.2.2.5. Wall structures are distilled into a single degree-of-freedom (SDOF) spring-mass-dashpot system (Figure 5.3, bottom right). Here, a nonlinear elastic spring permits unique force-displacement curve portions for motions directed toward (versus away from) the impacting flotilla. As discussed further in section 5.2.7, a wide range of physical wall configurations can be compactly represented in the low-order approach.

5.2.2.6. Numerically efficient procedures are adopted for assembling the low-order model components into a time integration scheme. Response quantities throughout the multiple degree-of-freedom (MDOF) flotilla and SDOF wall representations are computed using the central difference method (CDM). See section 5.2.7. for derivation of the underlying equations of motion.

5.2.2.7. Importantly, the low-order analysis approach is amenable to use in probabilistic design applications (see section 5.5 for design examples). A conceptual probabilistic design procedure is summarily listed in Figure 5.3 (bottom). In probabilistic design involving n collision analyses, flotilla-wall orientation and impact velocity are sampled, and the low-order analysis methodology is employed. For collision analysis i , the maximum computed impact force is identified from the time history of computed impact forces. Maximum impact forces are then accumulated across n analyses to form a probability density function. The design impact force is then selected based on the desired probability of exceedance.

5.2.2.8. Presented in the remainder of section 5.2 are details of low-order model components, underlying equations, and verification of computed results.

5.2.3. Barge Flotilla Behavior. A wide range of barge flotilla impact scenarios could conceivably occur on navigation infrastructure. Barge flotilla impacts against walls often involve shallow angle glancing impacts, as illustrated for two conceptual wall structures in Figure 5.4. Contributing to the range of conceivable scenarios are variations in flotilla configurations (number of columns, rows, mass). Impact angle (θ) and impact velocity (V_0) contribute to this range of scenarios as well. Consequently, flotilla momenta in directions normal to impacted walls may not be proportional to dynamic forces generated during collision.

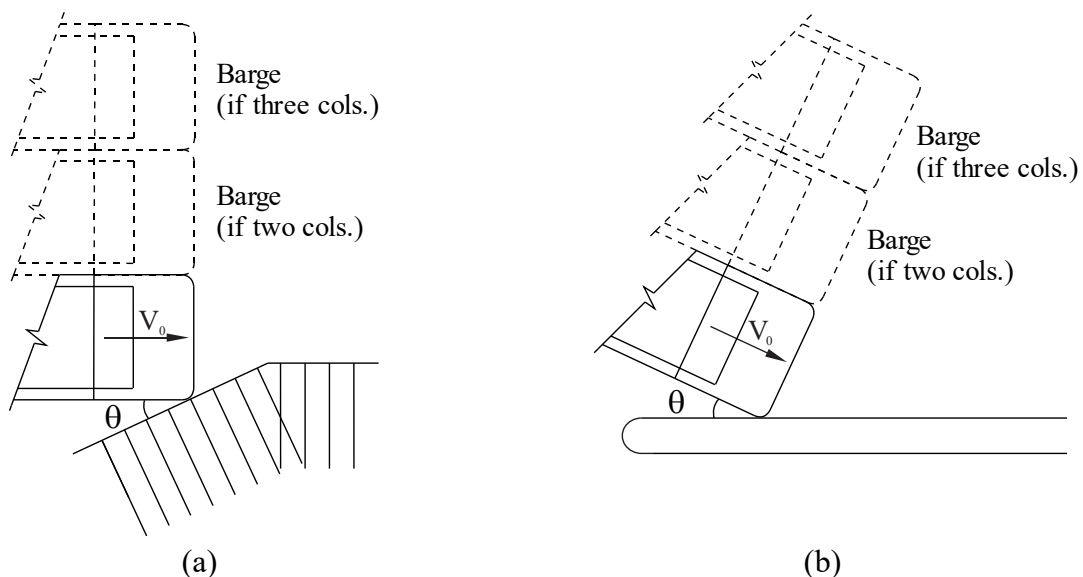


Figure 5.4. Conceptual Collision Scenarios: (a) Flexible Timber Guide Wall; (b) Rigid Wall

5.2.3.1. Barges within flotillas possess mass-related properties, including mass attributed to inertia (and momenta) during sudden translations. Included among these intrinsic properties is rotational (plan view) mass moment-of-inertia (Figure 5.5). As discussed in Chapter 3, adjacent rows of barges are physically integrated together via wire rope lashings (Figure 5.5a). Inter-row flotilla stiffnesses in flexural, shear, and axial modes of deformation are primarily functions of lashing properties. Wire rope stiffness and geometric configurations influence the stiffnesses associated with flexural, shear, and axial motions.

5.2.3.2. For the illustrative collision depicted in Figure 5.5a–b, the flotilla initial velocity is oblique relative to the impacted wall face. After the onset of impact between the starboard bow corner of the impacting barge and wall, transient impact forces develop. Time-varying impact forces normal to the wall (F_{impact}) are determined by deformation (crushing) of the barge bow. Frictional forces (μF_{impact}), oriented parallel to the impacted wall face, dissipate system kinetic energy as the impacting barge undergoes sliding.

5.2.3.3. Peak impact forces are primarily a function of dynamic properties of the lead row of barges in a flotilla. The relevant properties include row mass, velocity (i.e., momentum, Walters et al., 2017) and mass moment-of-inertia. Dynamic impact forces are also influenced by flexural stiffness between flotilla lead and trailing rows (Consolazio and Wilkes 2013). Therefore, the lead row is rotationally redirected (Figure 5.5b) as the resultant dynamic impact force reaches maximum magnitude. However, during this stage of the collision, interior rows and trailing rows undergo only relatively minor changes in orientation.

5.2.3.4. The low-order approach accounts for the influences of mass-related barge flotilla inertial properties on dynamic impact force. Flotilla rows are divided into one of three categories: lead row, LR ; interior row, IR ; and, trailing row, TR . Lumped translational masses are then assigned to lead, interior, and trailing rows (m_{LR} , m_{IR} , and m_{TR} , respectively). Additionally, rotational (plan view) mass moments-of-inertia are assigned to lead, interior, and trailing rows (I_{LR} , I_{IR} , and I_{TR} , respectively). Both the lumped masses and mass moments-of-inertia are concentrated at the corresponding flotilla row centers of mass (Figure 5.5c).

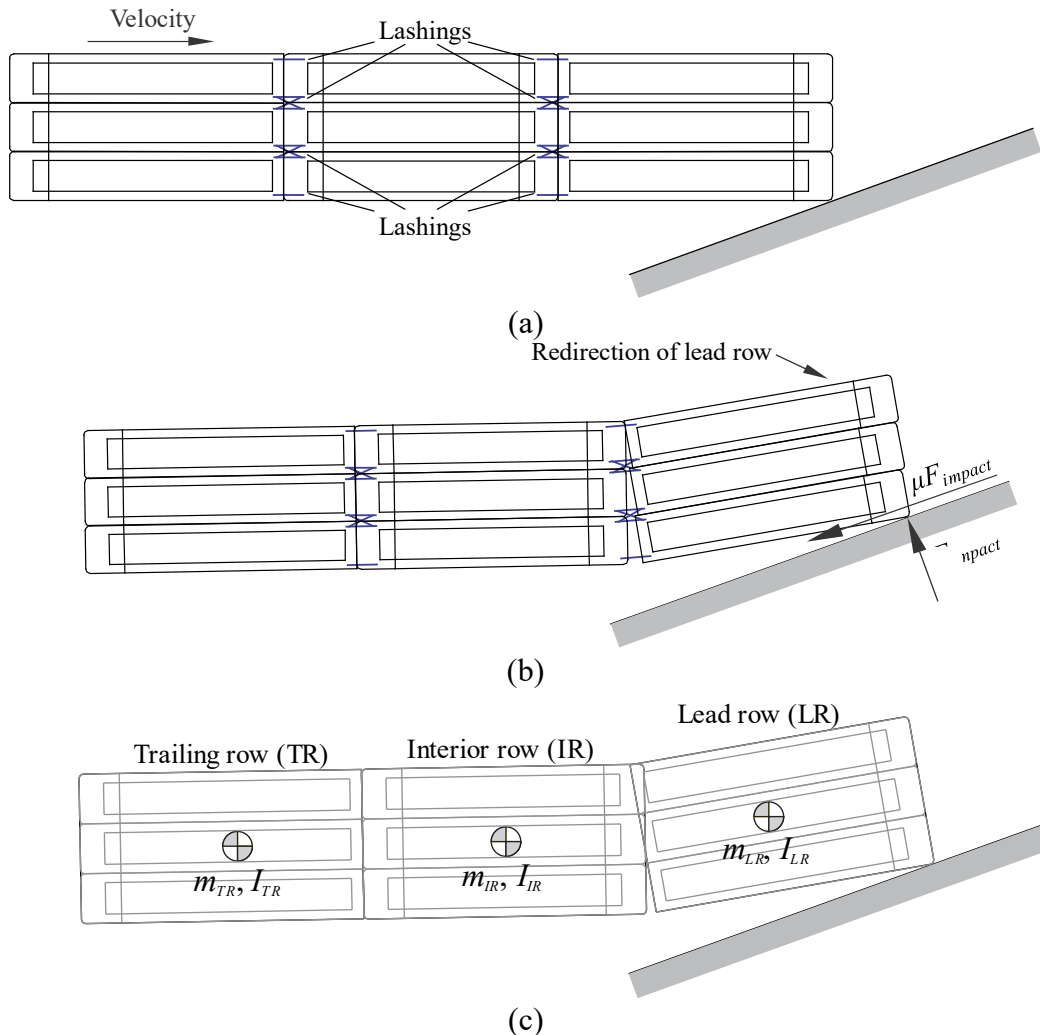


Figure 5.5. Conceptual Barge Flotilla Impact on Wall Structures: (a) At the Onset of Impact; (b) Redirection of Lead Row Upon Generation of Maximum Impact Force; (c) Lumped Mass and Mass Moment-of-Inertia for Each Barge Row

5.2.4. Modeling Approaches. The low-order analysis method is standalone; it does not require separate FE software for use. Two distinct approaches for modeling flotilla-wall collisions factor into the method development. High-resolution nonlinear FE modeling (Figure 5.6a) pertaining to development of stiffness relationships used during low-order analysis is discussed in section 5.4.2.1. Considerations leading to simplified model representations of flotilla-wall components in the low-order method (Figure 5.6b) are presented in section 5.4.2.2.

5.2.4.1. High-Resolution Nonlinear Finite Element Modeling.

5.2.4.1.1 Recall that Chapter 3 details high-resolution FE models of flotilla-wall systems for conducting dynamic impact simulations. Major components of these models (e.g., Figure 5.6a) are essential to forming stiffness relationships that describe collision-related flotilla and wall behaviors. For example, determination of flotilla inter-row stiffnesses is relevant to the low-order method. The formation of barge bow corner crushing (i.e., force-deformation) curves is also relevant. In addition, results obtained from the high-resolution collision simulations serve as a basis for verifying low-order analysis results.

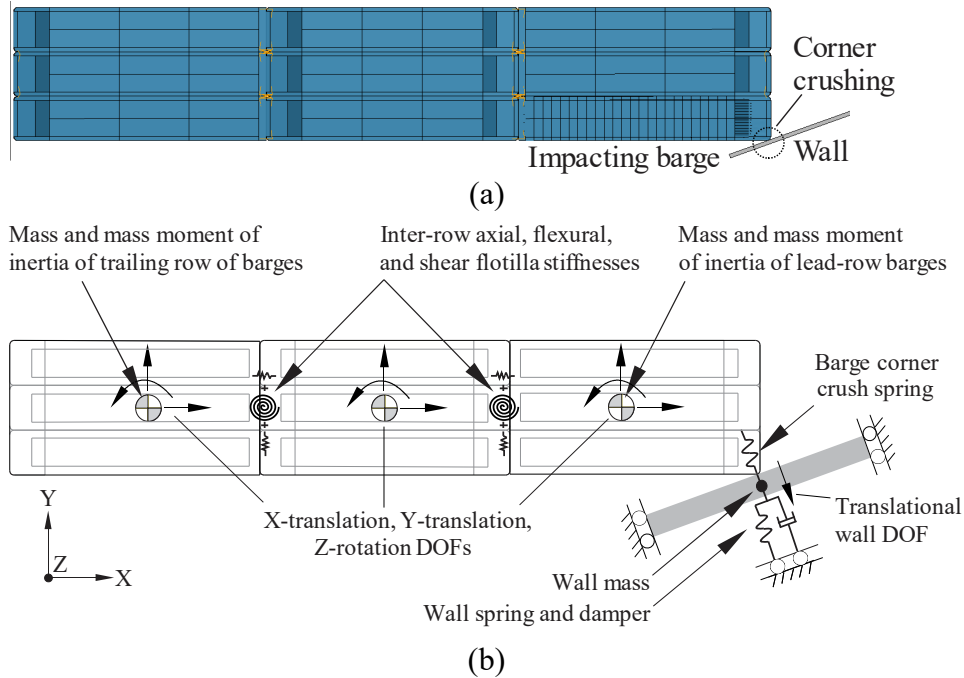


Figure 5.6. Flotilla-Wall Collision Modeling Approaches: (a) High-Resolution FE Simulation (Mesh Not Shown for Clarity); (b) Low-Order Dynamic Analysis

5.2.4.1.2 For determination of the necessary stiffness relationships, the impacting barge is modeled in LS-DYNA (LSTC 2014) using approximately 900,000 elements. To efficiently represent mass-related inertial properties of barges throughout flotillas, each non-impacting barge is modeled using approximately 4,000 rigid shell elements. Within each flotilla FE model, individual barges are connected together through nonlinear lashing elements. Contact definitions are defined between each set of adjacent barges. Contact detections were also defined for potential contact regions between the flotilla and wall model. Additional details of the high-resolution flotilla model components are given in Chapter 3.

5.2.4.2. Low-Order Dynamic Analysis Model. Simulations involving high-resolution flotilla-wall FE models are not feasible for routine use in design. The low-order approach retains key representations of dynamic flotilla and wall behaviors, and thereby permits rapid execution of dynamic analysis. Discussed below are considerations and simplifications associated with the low-order (low degree-of-freedom (DOF)) dynamic analysis procedure, relative to high-resolution FE modeling.

5.2.4.2.1 In the low-order approach, all model DOFs and mechanical components are defined in a single horizontal plane (or 2D space). As shown in Figure 5.6b, three DOFs are used for each flotilla row (X-translation, Y-translation, and Z-rotation). The three DOFs are concentrated at the center of mass of each row of barges within the flotilla. Masses and mass moments-of-inertia of respective flotilla rows are attached to these locations. Further, flotilla inter-row stiffnesses (axial, flexural, and shear springs) are concentrated at fore- and aft interfaces of interior flotilla rows.

5.2.4.2.2 One translational DOF is retained for the wall structure (a spring-mass-dashpot element, with nonlinear elastic spring). A barge bow corner crush spring is included to efficiently couple together the flotilla-wall model components. For example (Figure 5.6b), 10 DOFs are required for low-order modeling of impact between a 3x3 barge flotilla and wall. Here, the flotilla contains 9 DOFs (3 DOFs per row) and the wall contains a single DOF.

5.2.5. Angle-Dependent Barge Bow Corner Crushing. Compressive force-deformation relationships of impacting barge bow corners (Figure 5.7) are represented in the low-order approach as nonlinear elastic springs. This type of spring represents bow crushing stiffness and is oriented normal to the impacted wall surface. A range of design-relevant orientations may occur between impacting barges and wall structures. Correspondingly, variations may arise among initial contact locations, contact areas, and stiffnesses at the corner of the impacting barge bow.

5.2.5.1. Crushing stiffness of the barge bow corner, in particular, varies with respect to relative barge-wall orientation (θ_1 , θ_2 ; Figure 5.7). Therefore, the low-order analysis procedure utilizes a family of compressive force-deformation curves (resolved normal to the impacted wall face). These curves draw upon high-resolution barge bow corner crushing simulations (discussed below). The family of force-deformation relationships encompasses a wide range of practical impact angles (spanning 1° to 40°).

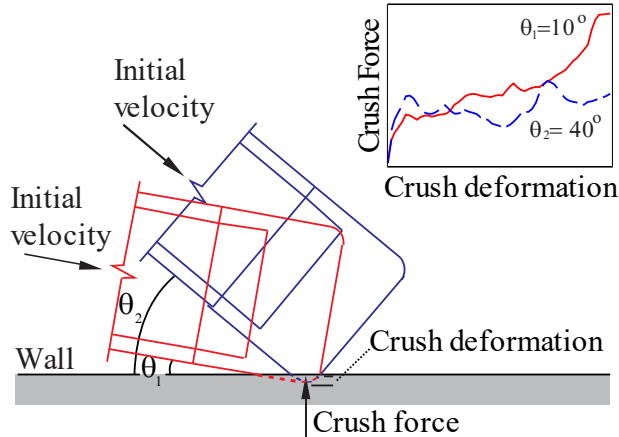


Figure 5.7. Angle Dependency of Barge Bow Corner Crushing During Flotilla-Wall Impacts

5.2.5.2. As illustration of the types of barge bow corner crushing simulations conducted, consider a relative flotilla-wall impact angle of 30° (Figure 5.8). For these simulations, the rear extents of the high-resolution bow FE model are restrained from motion (i.e., fixed in space using boundary conditions). For numerical efficiency, velocities are imposed on the wall (rather than the barge) so that the wall actively crushes the bow corner. Prescribed normal and tangential velocity components are assigned as 4 ft/sec and 7 ft/sec, respectively (Figure 5.8a).

5.2.5.3. The prescribed velocities are based on measurements from full-scale impact experiments (Patev et al., 2003). More specifically, the velocities approximate barge-wall motions and dynamic strain-rate effects that physically occur during oblique impact. Accompanying crushing motions (Δ) and tangential sliding are, respectively, normal (F_{impact}) and frictional (μF_{impact}) forces (Figure 5.8a).

5.2.5.4. Crush simulations are terminated after yielding and damage of the bow corner (Figure 5.8c–e) exceed levels typical of wall design. An example of the deformed state of the barge bow corner upon halting the simulation is shown in Figure 5.8f.

5.2.5.5. Barge bow force-deformation (crush) curves for each angle (Figure 5.9) are formed by pairing normal forces and normal deformations. That is, normal components of force (F_{impact}) and normal components of barge deformation (Δ) are extracted from the crushing simulations. Note that tangential friction forces (μF_{impact}) are directly included in the low-order analysis algorithm, as discussed later.

5.2.5.6. When used in low-order analysis, crush curves for intermediate angles are formed by interpolating between the curves plotted in Figure 5.9. For very small impact angles between 0° and 1° , interpolation is performed between two curves. The barge side-to-side (i.e., 0°) crush-curve provided in Consolazio and Walters (2012) is utilized together with the 1° curve (Figure 5.9).

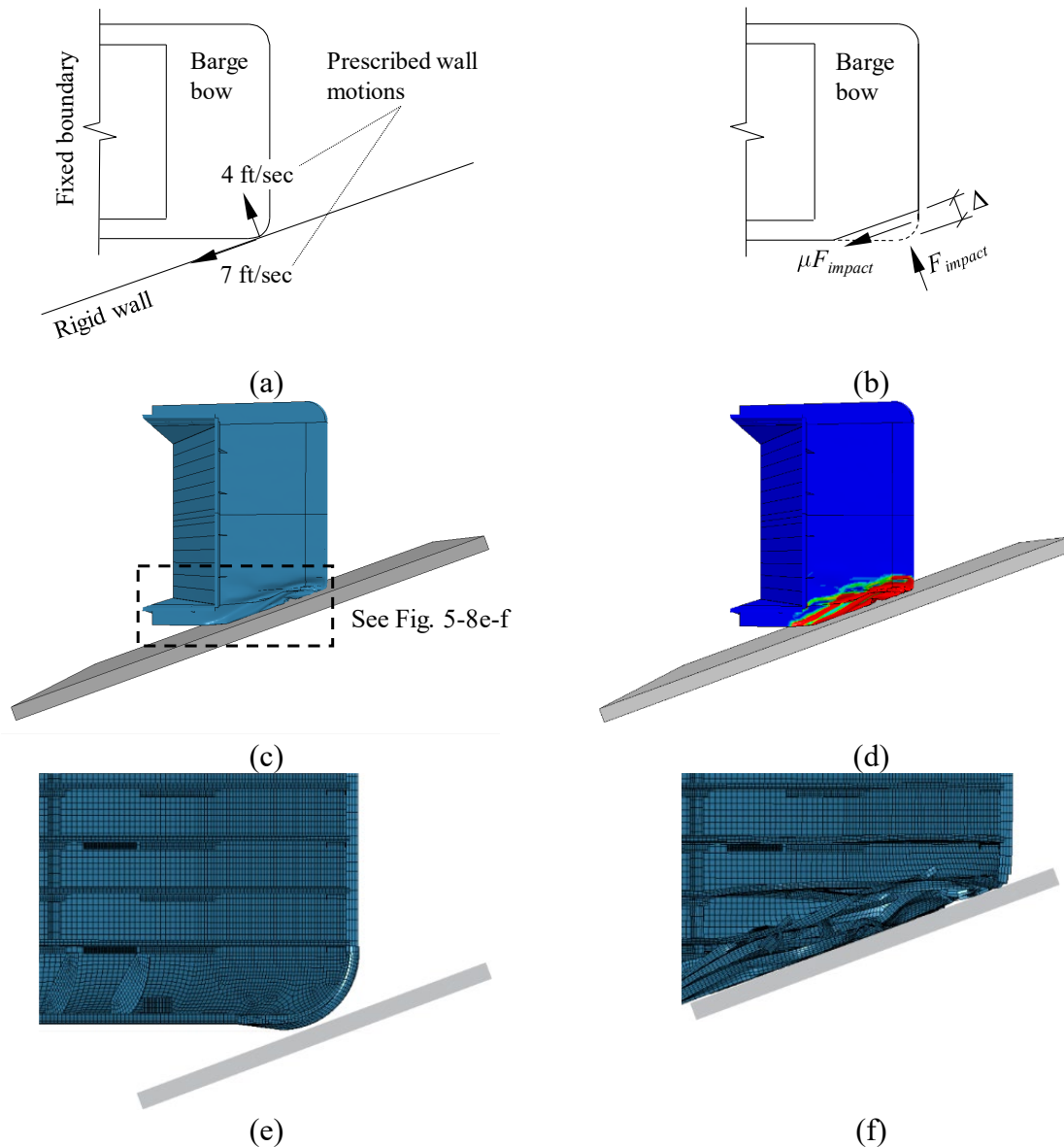


Figure 5.8. Barge Bow Corner Crushing Simulation for a 30° Impact Angle (Not to Relative Scale): (a) Barge-Wall and Prescribed Motions; (b) Normal and Frictional Impact Forces; (c) Barge Bow at Crush Depth of 60 in.; (d) Barge Bow Plastic Strains (Blue Signifies No Plastic Strain; Red Signifies Plastic Strain 10 Times Greater than Yield Strain); (e) Inset of Bow Corner Prior to Crushing; (f) Inset of Bow Corner at Crush Depth of 60 in.

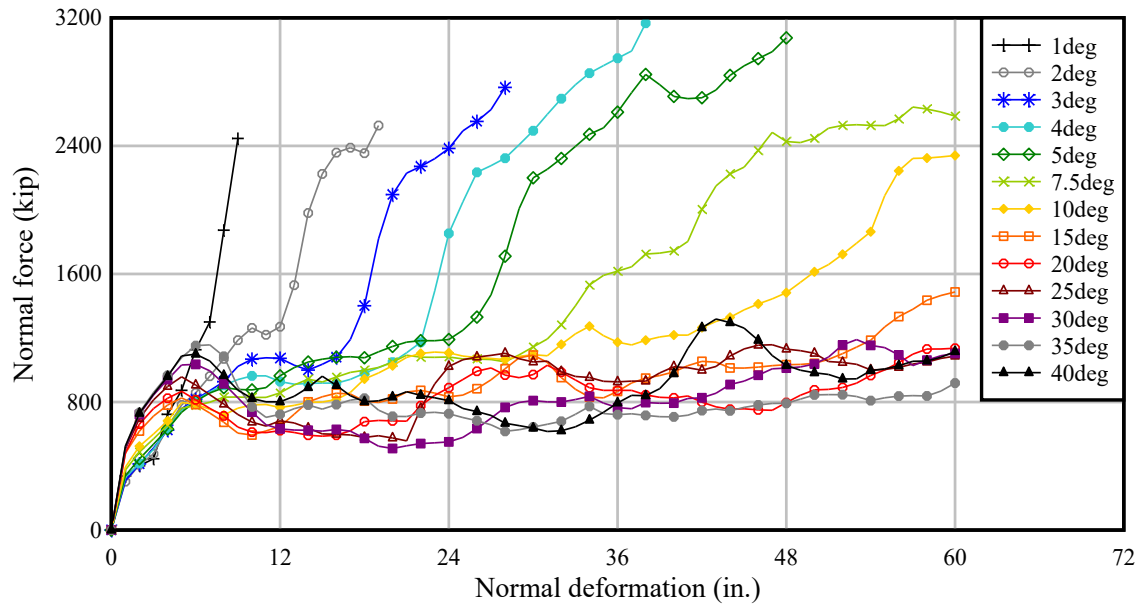


Figure 5.9. Compressive Force-Deformation Relationships (Crush-Curves) Used in Low-Order Modeling of Barge Bow Corner Stiffness

5.2.6. Barge Flotilla Inter-Row Stiffnesses. In the low-order model, translational and rotational springs are used to account for interactions between rows of barges in flotillas. Specifically, flexural, axial, and shear modes of deformation are represented by nonlinear springs between adjacent rows of barges. Force-deformation relationships of flotilla inter-row stiffnesses derive from FE simulations of one-column (1x), two-column (2x), and three-column (3x) barge flotillas. Example schematics of the flexural, axial, and shear stiffness formation processes are provided for a 3x configuration in Figure 5.10.

5.2.6.1. For inter-row motions, resisting forces are dictated by the stiffness and geometric configurations of lashings tying barges together (Consolazio and Han 2015b). Therefore, lashing modeling techniques developed in Walters et al. (2017) are incorporated into the flotilla models when determining inter-row flotilla stiffnesses.

5.2.6.2. In the high-resolution FE models, the external geometry of each barge is modeled using approximately 4,000 rigid shell elements. This precludes the need to model barge-internal structural members. Due to use of rigid shell elements, the appropriate structural stiffness of the barge model is not automatically generated. Instead, structural stiffness is introduced into the barge model through contact definitions.

5.2.6.3. Barge models formed in this way mimic appropriate resistances to relative barge motions (within a flotilla) that arise during barge-barge contact interactions. Additional details are provided in Walters et al. (2017).

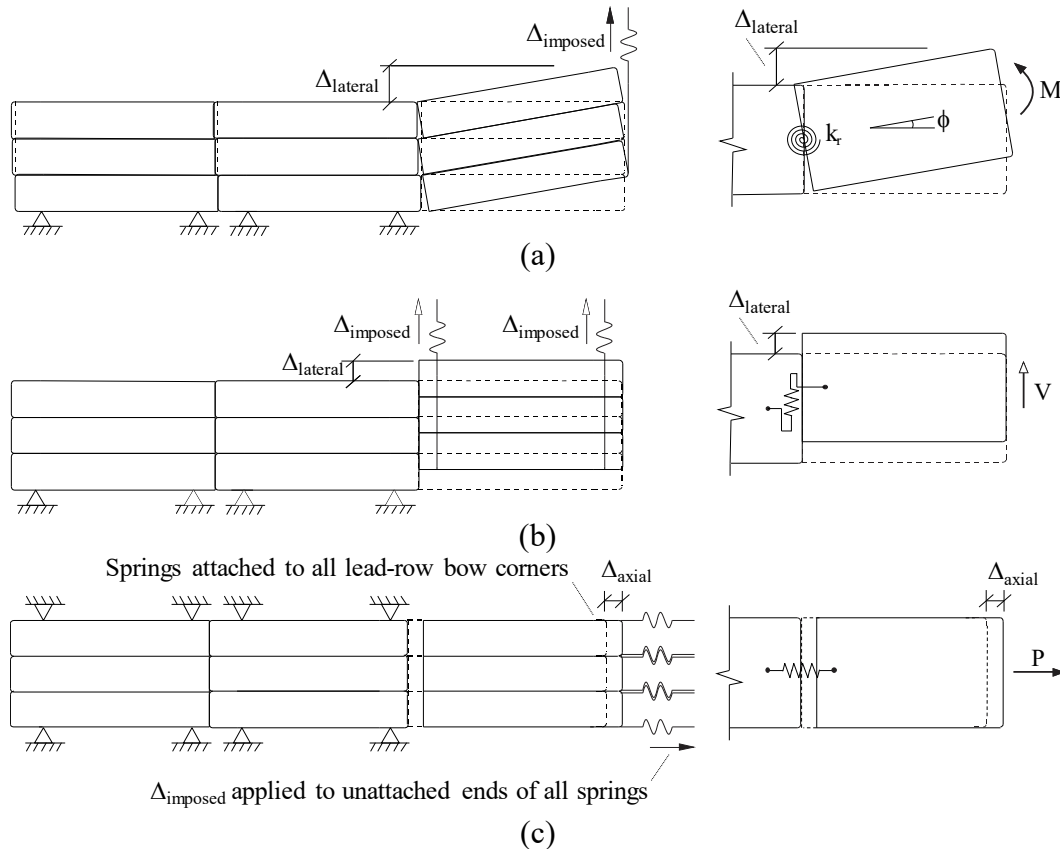


Figure 5.10. Barge Flotilla Inter-Row Stiffness Simulations for a Three-Column (3x) Configuration: (a) Flexural; (b) Shear; (c) Axial (Lashing Tensile Stiffness During Separation Between Rows)

5.2.6.4. Flexural Stiffness. Regarding evaluation of inter-row flexural stiffness, boundary conditions are applied to the models as shown in Figure 5.10a. To prevent over-constraint of relative motions, only those barges located in the starboard column are restrained from translation. All other barges in the flotilla are permitted to move within the horizontal plane. This distribution of boundary conditions permits relative sliding between columns (in the 2x and 3x cases).

5.2.6.4.1 To apply flexural moment to the lead row of barges, a stiff axial-load monitoring spring is incorporated into the model. The spring is attached to the starboard corner of the lead-row barge bow. A slow, constant rate of displacement ($\Delta_{imposed}$) is subsequently imposed on the unattached end of the spring. As a result, the lead row of barges undergoes lateral displacements.

5.2.6.4.2 As axial forces develop in the spring, flexural moment is calculated at the stern end of the lead row of barges. Also, rotation is calculated from the differential lateral displacements (Δ_{lateral}) between the bow and stern ends of the lead row. Moment-rotation curves are shown in Figure 5.11a for 1x, 2x, and 3x flotilla configurations. For each simulation conducted, the calculated moment and rotation values are paired together.

5.2.6.5. Shear Stiffness. For evaluation of inter-row shear stiffness, boundary conditions are defined as illustrated in Figure 5.10b for a 3x flotilla. To generate shear forces between the lead and interior barge rows, two stiff-load monitoring springs are also defined. These springs are attached to the starboard side bow and stern corners of a lead-row barge (Figure 5.10b). Further, constant rates of displacement are imposed (Δ_{imposed}) on the unattached spring ends. In turn, the imposed displacements induce lateral displacements (Δ_{lateral}) in the lead row of barges. Shear-displacement curves are formed by pairing the total force generated in the monitoring springs with lateral displacements (Δ_{lateral}), Figure 5.10b). Plotted in Figure 5.11b are the nonlinear, inter-row shear stiffness curves obtained for 1x, 2x, and 3x flotilla configurations.

5.2.6.6. Axial Stiffness. Axial stiffness at flotilla row interfaces is characterized in two respects. Tensile lashing elongation during separation between barge rows (i.e., tensile stiffness) is considered. Compressive barge-barge contact stiffness during relative row motions toward one another is also taken into consideration.

5.2.6.6.1 Regarding characterizations pertaining to inter-row tensile stiffness, boundary conditions are defined as illustrated in Figure 5.10c. Here, only barges in the lead row remain free to undergo longitudinal translations. Also, stiff axial-load monitoring springs are attached to both port and starboard corners of each lead-row barge bow. Then, displacements are imposed (Δ_{imposed}) at the unattached ends of the springs. Consequently, the lead row of barges undergoes separating motions relative to the other flotilla rows (at a slow, constant rate).

5.2.6.6.2 Tension forces in the load monitoring springs, versus axial displacement (Δ_{axial}), are paired to form tensile axial stiffness curves. The Figure 5.11c plot contains tensile portions of axial stiffness relationships for 1x, 2x, and 3x flotilla configurations.

5.2.6.6.3 Inter-row compression (axial) stiffness is characterized using nonlinear crush deformations associated with two rows of barges translating toward one another. Quasi-static crushing simulations of high-resolution FE models of barge bows and sterns are drawn on for this purpose. Associated model components and simulation techniques are detailed in Walters et al. (2017). Among the variations considered are those involving crushing of bow-stern, bow-bow, and stern-stern barge portions.

5.2.6.6.4 Compressive force-deformation relationships reported in Walters et al. (2017) are directly adopted when conducting low-order analyses involving 1x flotilla configurations. For two-column (2x) and three-column (3x) flotillas, ordinates associated with the 1x curve (i.e., the forces) are scaled. Scale factors of two and three are employed, respectively, for 2x and 3x configurations (relative to the 1x configuration). Combining together nonlinear stiffnesses across the tensile and compressive domains, axial force-displacement relationships are formed (Figure 5.11c).

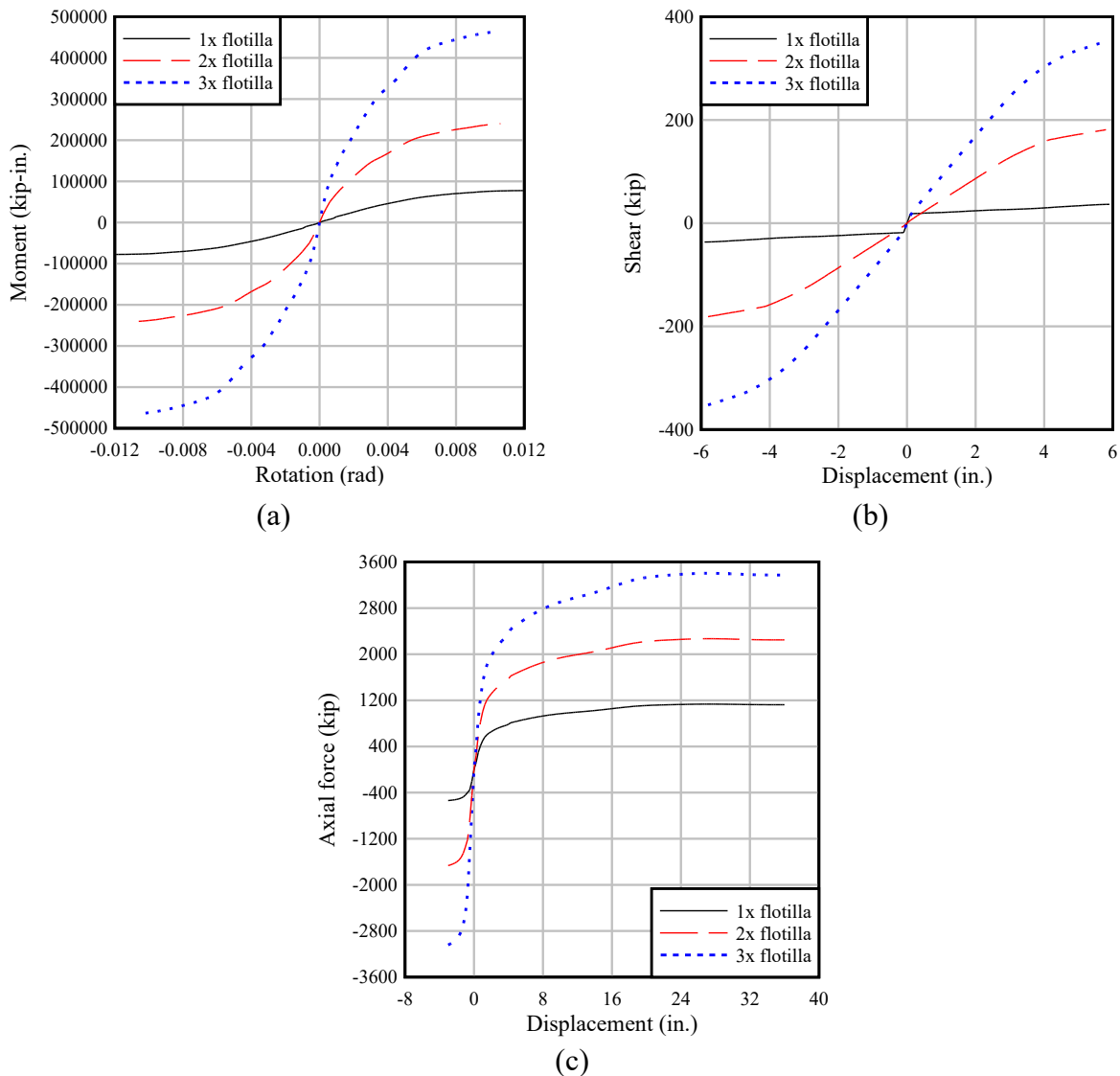


Figure 5.11. Inter-Row Stiffness Curves for 1x, 2x, and 3x Flotillas: (a) Flexural; (b) Shear; (c) Axial (Inter-Row Separations Correspond to Positive Displacements)

5.2.6.6.5 For some design scenarios, flotillas possessing greater than three columns may need to be considered. Therefore, the low-order approach is formulated to consider inter-row stiffnesses of flotilla configurations possessing more than three columns. Inter-row stiffnesses are approximated in the low-order approach by scaling up ordinates of the stiffness curves associated with 3x configurations. The scale factor is determined by dividing the number of columns in a flotilla by that of a 3x flotilla (three).

5.2.7. Characterization of Impacted Wall. Wall structures in the low-order formulation are modeled as a single-DOF system (spring-mass-dashpot). This enables collision analysis of a wide variety of wall structures, while requiring definition of only three model characteristics. Included in the wall definition are participating mass (m_{wall}), damping (c_{wall}), and nonlinear stiffness.

5.2.7.1. Participating mass (m_{wall}) is defined as the effective wall mass that dynamically responds during flotilla-wall collisions. Wall model components relevant to low-order analysis are illustrated schematically in Figure 5.12 for a laterally loaded pile-founded guide wall.

5.2.7.2. Wall stiffness characterizations in low-order analyses are based on the pushover concept. In this context, a separate structural model of the wall structure (wall-pile-soil system) is created. A detailed example of the associated multi-DOF modeling process is found in Consolazio et al. (2014). Subsequent to creating the model, a linearly increasing lateral load (F_{wall}) is applied to the wall. It is assumed that the center of mass of the wall structure serves as a representative impact location. Also, the lateral load (F_{wall}) is oriented normal to the vertical face of the wall.

5.2.7.3. Across a range of lateral loads, the corresponding lateral displacement (w_{wall}) of the wall is computed and cataloged. A force-displacement relationship for the wall structure is then obtained (Figure 5.12, top right) by pairing together F_{wall} and w_{wall} . The pushover concept is robust to characterization of wall stiffness with respect to both negative-direction and positive-direction lateral loads. Curves obtained from separate analyses of this type are used to represent lateral wall stiffness in the low-order dynamic methodology.

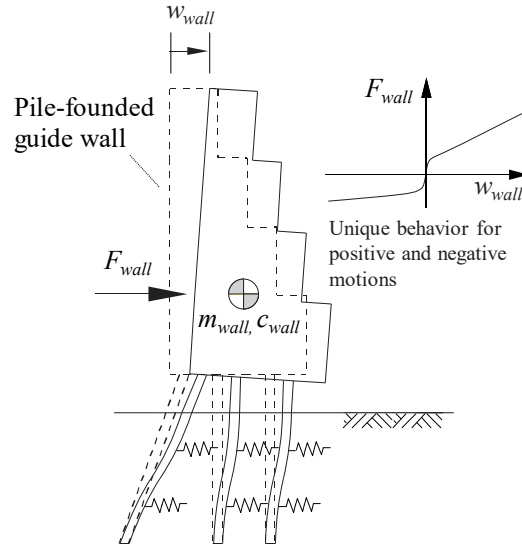


Figure 5.12. Conceptual Illustration of Laterally Loaded Navigation Wall for Use in Low-Order Analysis

5.2.8. Analysis Algorithm. In the low-order model, dynamic behavior of the single-DOF wall (Equation 5.1) is modeled via an expression of dynamic equilibrium:

$$m_{wall}\ddot{w}_{wall} + c_{wall}\dot{w}_{wall} + F_{wallspring} - F_{impact} = 0 \quad (5.1)$$

where \ddot{w}_{wall} is wall lateral acceleration and \dot{w}_{wall} is wall lateral velocity (both normal to the impacted wall vertical face). $F_{wallspring}$ represents the time-varying stiffness-related wall resistance (i.e., the product of F_{wall} and w_{wall}). Acting in opposition to these dynamic wall resistance forces is the time-varying barge impact force, F_{impact} . The impact force is generated by the bow corner of the (impacting) lead-row barge. Calculation of F_{impact} requires use of barge flotilla properties and additional dynamic equilibrium equations as described below.

5.2.8.1. Barge Types and Physical Properties. Two common types of barges are considered in the low-order approach (Figure 5.13). The barge types considered include single-raked (single) and double-raked (double) jumbo hopper barges. Both types share overall lengths of 195 ft and widths of 35 ft. Barge masses ($m_{bargeFull}$) are defined consistent with full payload conditions: 2,000 short tons, as listed in Table 5.1. Masses and mass moments-of-inertia ($I_{singleFull}$ and $I_{doubleFull}$, for single-raked and double-raked, respectively) are concentrated at respective barge centers of mass.

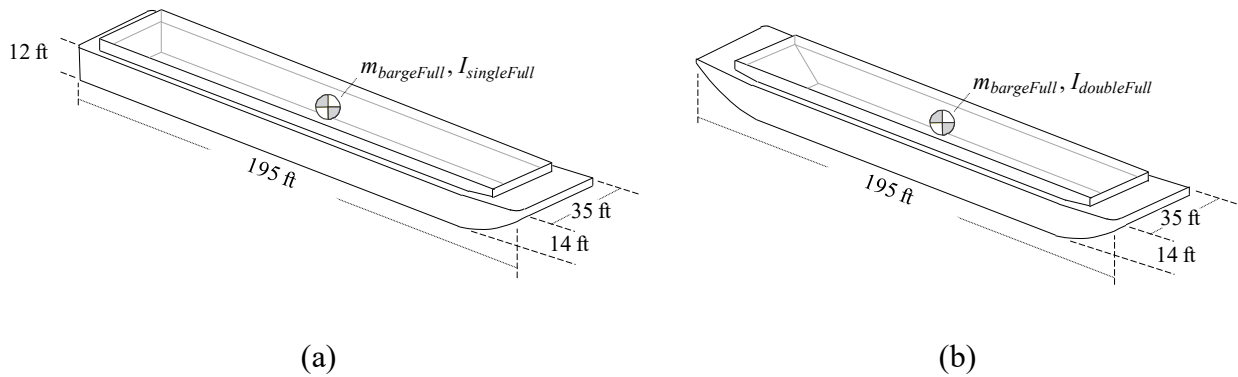


Figure 5.13. Overall Dimensions and Positioning of Centroidal Properties for Fully Loaded Barges (Payloads Not Shown): (a) Single-Raked; (b) Double-Raked

5.2.8.1.1 The positions, orientations, and types of individual barges within various flotilla configurations are shown in Figure 5.14. Single-raked barges are used at the lead rows of flotillas. Single-raked barges in reverse orientation (with stern pointing forward) are used at trailing rows. For flotillas consisting of three or more barge rows, all interior rows are composed of double-raked barges.

Table 5.1
Weights, Masses, and Mass Moments-of-Inertia of Fully Loaded Individual Barges

Property of fully loaded barge	Single-raked	Double-raked
Weight (short ton)	2,000	2,000
Mass (kip-sec ² /in.)	11.6	11.6
Mass moment-of-inertia about vertical axis (kip-in.-sec ²)	3.53E+06	2.71E+06

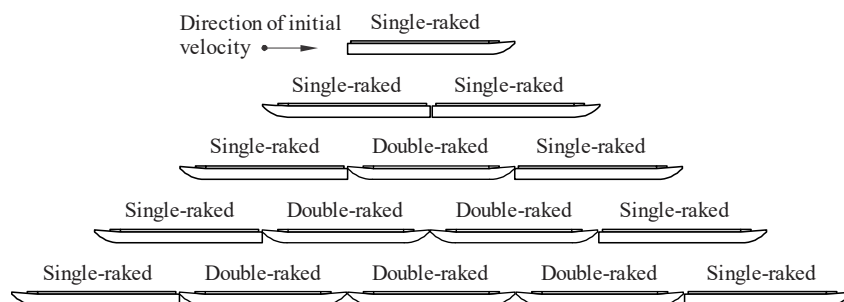


Figure 5.14. Arrangements of Single-Raked and Double-Raked Barges in Multi-Row Flotillas

5.2.8.1.2 To account for the number of columns present within a flotilla, approximate mass and mass moment-of-inertia scaling expressions are adopted. Additionally, the scaling expressions facilitate analysis of barges possessing tonnages lighter than those of full-payload conditions. For lead rows of barges in flotillas, the mass (m_{LR}) and mass-moment-of-inertia (I_{LR}) terms are defined using single-raked barge properties:

$$m_{LR} = m_{barge} \cdot n_{col} \quad (5.2)$$

$$I_{LR} = \frac{m_{barge} \cdot I_{doubleFull} \cdot n_{col}}{m_{bargeFull}} \quad (5.3)$$

where m_{barge} is the specified mass of an individual barge in the flotilla; n_{col} is the number of flotilla columns. For flotilla configurations that include interior rows, the row mass (m_{IR}) and mass moment-of-inertia (I_{IR}) are similarly defined using double-raked properties:

$$m_{IR} = m_{barge} \cdot n_{col} \quad (5.4)$$

$$I_{IR} = \frac{m_{barge} \cdot I_{doubleFull} \cdot n_{col}}{m_{bargeFull}} \quad (5.5)$$

5.2.8.1.3 For trailing rows of flotillas, row mass (m_{TR}) and mass moment-of-inertia (I_{TR}) are defined using single-raked properties (with forward-facing sterns):

$$m_{TR} = m_{barge} \cdot n_{col} \quad (5.6)$$

$$I_{TR} = \frac{m_{barge} \cdot I_{singleFull} \cdot n_{col}}{m_{bargeFull}} \quad (5.7)$$

5.2.8.2. Dynamic Equilibrium of the Barge Flotilla. For each type of barge row considered (lead, interior, trail) three equilibrium equations are defined (Figure 5.15). These equilibrium equations correspond to X translation (u), Y translation (v), and Z rotation (θ) DOFs for each barge row. The equations augment the expression of wall dynamic equilibrium and thereby form a complete collection of dynamic equilibrium equations. Consequently, the expression of dynamic equilibrium for flotilla-wall systems (Equation 5.1) is expanded into a series of simultaneous equations.

5.2.8.2.1 Each barge row is condensed into a single node. The associated translational masses and rotational mass moments-of-inertia are concentrated at respective nodes. Eccentricities between barge centers of mass and bows, as well as between centers of mass and sterns, are defined in Figure 5.15b–d. For single-raked barges, unique values of eccentricity are assigned with respect to bow ($e_{singleBow}$) versus stern ($e_{singleStern}$). The same value of eccentricity is applicable for both ends of double-raked barges (e_{double}), Figure 5.15c.

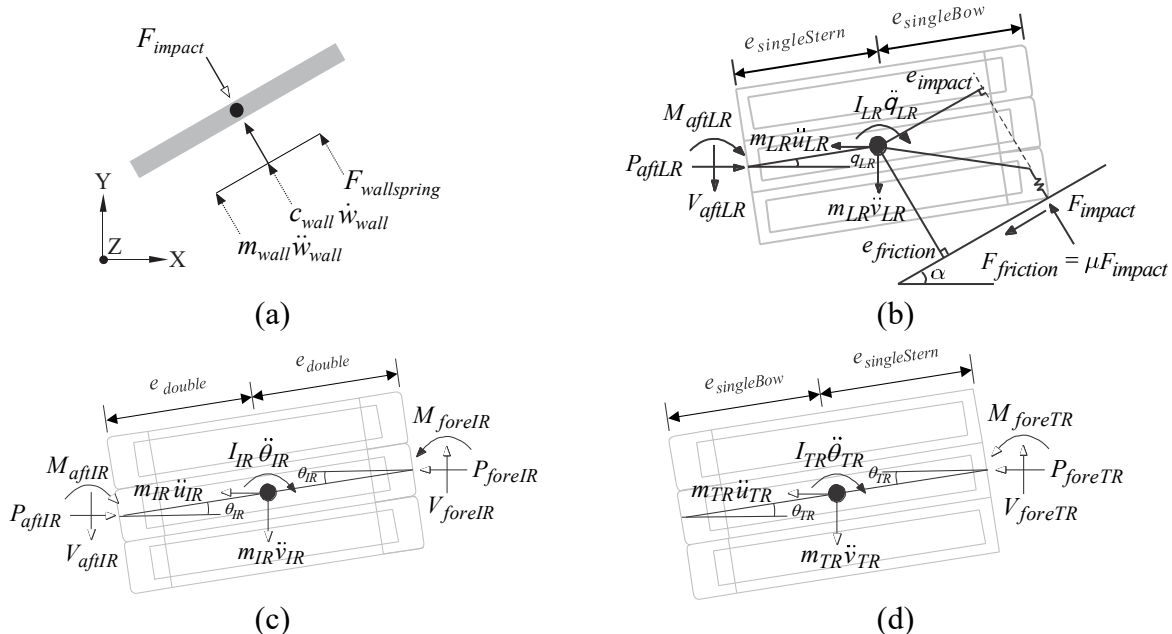


Figure 5.15. Free-Body Diagrams of Impacted Wall and Barge Flotilla: (a) Impacted Wall; (b) Lead Flotilla Row; (c) Interior Flotilla Row; (d) Trailing Flotilla Row

5.2.8.2.2 From Figure 5.15b, for impact angle α , the dynamic equilibrium equations pertaining to the lead row are defined as:

$$m_{LR}\ddot{u}_{LR} + F_{impact} \sin \alpha + \mu F_{impact} \cos \alpha - P_{aftLR} = 0 \quad (5.8)$$

$$m_{LR}\ddot{v}_{LR} - F_{impact} \cos \alpha + \mu F_{impact} \sin \alpha + V_{aftLR} = 0 \quad (5.9)$$

$$I_{LR}\ddot{\theta}_{LR} - F_{impact}e_{impact} + \mu F_{impact}e_{friction} + M_{aftLR\Sigma} = 0 \quad (5.10)$$

where P_{aftLR} is the X-direction (axial) force at the aft end of the lead row of barges. Additionally, V_{aftLR} is the Y-direction (shear) force at the aft end of the lead row of barges. Regarding eccentricities, e_{impact} is the eccentricity between the line of action of the (wall-normal) impact force and the lead-row center of mass. Also, $e_{friction}$ is the eccentricity between the line of action of the friction force (parallel to wall) and lead-row center of mass. The summation of moments term, $M_{aftLR\Sigma}$, is defined as:

$$M_{aftLR\Sigma} = M_{aftLR} - V_{aftLR} \cdot e_{singleStern} \cdot \cos \theta_{LR} - P_{aftLR} \cdot e_{singleStern} \cdot \sin \theta_{LR} \quad (5.11)$$

where M_{aftLR} , V_{aftLR} , and P_{aftLR} are moment, shear (Y-direction), and axial (X-direction) forces. Each of M_{aftLR} , V_{aftLR} , and P_{aftLR} are caused by the remainder of the flotilla, and act on the aft end.

5.2.8.2.3 Similar expressions for interior barge rows (Figure 5.15c) are developed with consideration of forces at both fore and aft locations:

$$m_{IR}\ddot{u}_{IR} + P_{foreIR} - P_{aftIR} = 0 \quad (5.12)$$

$$m_{IR}\ddot{v}_{IR} - V_{foreIR} + V_{aftIR} = 0 \quad (5.13)$$

$$I_{IR}\ddot{\theta}_{IR} + M_{foreIR\Sigma} + M_{aftIR\Sigma} = 0 \quad (5.14)$$

where P_{foreIR} is the X-direction force at the fore end of the interior row of barges. Further, V_{foreIR} is the Y-direction force at the fore end of the interior row of barges. Terms for summation of fore ($M_{foreIR\Sigma}$) and aft ($M_{aftIR\Sigma}$) moments (about the Z-direction) attributed to interior rows are defined as:

$$M_{foreIR\Sigma} = -M_{foreIR} - V_{foreIR} \cdot e_{double} \cdot \cos \theta_{IR} - P_{foreIR} \cdot e_{double} \cdot \sin \theta_{IR} \quad (5.15)$$

$$M_{aftIR\Sigma} = M_{aftIR} - V_{aftIR} \cdot e_{double} \cdot \cos \theta_{IR} - P_{aftIR} \cdot e_{double} \cdot \sin \theta_{IR} \quad (5.16)$$

5.2.8.2.4 As shown in Figure 5.15d, equilibrium equations attributed to the trailing row of barges during collision are expressed as:

$$m_{TR}\ddot{u}_{TR} + P_{foreTR} = 0 \quad (5.17)$$

$$m_{TR}\ddot{v}_{TR} - V_{foreTR} = 0 \quad (5.18)$$

$$I_{TR}\ddot{\theta}_{TR} + M_{foreTR\Sigma} = 0 \quad (5.19)$$

where $M_{foreTR\Sigma}$ is the moment summation term corresponding to the fore location of the trailing row of barges, given by:

$$M_{foreTR\Sigma} = -M_{foreTR} - V_{foreTR} \cdot e_{singleStern} \cdot \cos \theta_{TR} - P_{foreTR} \cdot e_{singleStern} \cdot \sin \theta_{TR} \quad (5.20)$$

5.2.8.3. Assembly of Equations.

5.2.8.3.1 Equations of motion for all flotilla rows and the wall are assembled to form the system-level (matrix) dynamic equilibrium equation:

$$[M]\{\ddot{d}\} + [C]\{\dot{d}\} + [K]\{d\} = \{F_{ext}\} \quad (5.21)$$

where $[M]$ is the mass matrix and $\{\ddot{d}\}$ is the vector of system accelerations (at the DOF). $[C]$ is the damping matrix, which is only considered for the wall, and $\{\dot{d}\}$ is the vector of system velocities (at the DOF). The product of nonlinear stiffness $[K]$ and displacements $\{d\}$ is represented by the internal force vector, $\{F_{int}\}$. The term on the right-hand side of the equation, $\{F_{ext}\}$, is the vector of external forces. Replacing the quantity $\{d\}$ (and associated time derivatives) with direction-specific, time-dependent terms introduced earlier ($\{u\}$, $\{v\}$, and $\{w\}$) results in:

$$[M]\{\ddot{d}\} = \begin{bmatrix} m_{wall} & 0 & 0 & 0 & 0 & 0 & 0 & \dots & 0 & 0 & 0 \\ 0 & m_{LR} & 0 & 0 & 0 & 0 & 0 & \dots & 0 & 0 & 0 \\ 0 & 0 & m_{LR} & 0 & 0 & 0 & 0 & \dots & 0 & 0 & 0 \\ 0 & 0 & 0 & I_{LR} & 0 & 0 & 0 & \dots & 0 & 0 & 0 \\ 0 & 0 & 0 & 0 & m_{IR} & 0 & 0 & \dots & 0 & 0 & 0 \\ 0 & 0 & 0 & 0 & 0 & m_{IR} & 0 & \dots & 0 & 0 & 0 \\ 0 & 0 & 0 & 0 & 0 & 0 & I_{IR} & \dots & 0 & 0 & 0 \\ \vdots & \ddots & \vdots & \vdots & \vdots \\ 0 & 0 & 0 & 0 & 0 & 0 & 0 & \dots & m_{TR} & 0 & 0 \\ 0 & 0 & 0 & 0 & 0 & 0 & 0 & \dots & \vdots & m_{TR} & 0 \\ 0 & 0 & 0 & 0 & 0 & 0 & 0 & \dots & 0 & 0 & I_{TR} \end{bmatrix} \begin{bmatrix} \ddot{w}_{wall} \\ \ddot{u}_{LR} \\ \ddot{v}_{LR} \\ \ddot{\theta}_{LR} \\ \ddot{u}_{IR} \\ \ddot{v}_{IR} \\ \ddot{\theta}_{IR} \\ \vdots \\ \ddot{u}_{TR} \\ \ddot{v}_{TR} \\ \ddot{\theta}_{TR} \end{bmatrix} \quad (5.22)$$

$$[C]\{\dot{d}\} = \begin{bmatrix} C_{wall} & 0 & 0 & 0 & 0 & 0 & 0 & \dots & 0 & 0 & 0 \\ 0 & 0 & 0 & 0 & 0 & 0 & 0 & \dots & 0 & 0 & 0 \\ 0 & 0 & 0 & 0 & 0 & 0 & 0 & \dots & 0 & 0 & 0 \\ 0 & 0 & 0 & 0 & 0 & 0 & 0 & \dots & 0 & 0 & 0 \\ 0 & 0 & 0 & 0 & 0 & 0 & 0 & \dots & 0 & 0 & 0 \\ 0 & 0 & 0 & 0 & 0 & 0 & 0 & \dots & 0 & 0 & 0 \\ 0 & 0 & 0 & 0 & 0 & 0 & 0 & \dots & 0 & 0 & 0 \\ \vdots & \ddots & \vdots & \vdots & \vdots \\ 0 & 0 & 0 & 0 & 0 & 0 & 0 & \dots & 0 & 0 & 0 \\ 0 & 0 & 0 & 0 & 0 & 0 & 0 & \dots & \vdots & 0 & 0 \\ 0 & 0 & 0 & 0 & 0 & 0 & 0 & \dots & 0 & 0 & 0 \end{bmatrix} \begin{bmatrix} \dot{w}_{wall} \\ 0 \\ 0 \\ 0 \\ 0 \\ 0 \\ 0 \\ \vdots \\ 0 \\ 0 \\ 0 \end{bmatrix} \quad (5.23)$$

$$[K]\{d\} = [F_{int}] = \begin{bmatrix} -F_{impact} + F_{wallspring} \\ F_{impact} \sin \alpha + \mu F_{impact} \cos \alpha - P_{aftLR} \\ -F_{impact} \cos \alpha + \mu F_{impact} \sin \alpha - V_{aftLR} \\ -F_{impact} d_{impact} + \mu F_{impact} d_{friction} + M_{aftLR\Sigma} \\ P_{foreIR} - P_{aftIR} \\ -V_{foreIR} + V_{aftIR} \\ M_{foreIR\Sigma} - M_{aftIR\Sigma} \\ \vdots \\ P_{foreTR} \\ -V_{foreTR} \\ M_{foreTR\Sigma} \end{bmatrix} \quad (5.24)$$

5.2.8.3.2 Solution of the above equations is initiated through the introduction of non-zero initial conditions. Specifically, the impact speed under consideration is assigned to the initial X-direction translational velocity of each barge row. Note that external forces are not present, therefore $\{F_{ext}\} = \{0\}$.

5.2.8.4. Time-Step Integration. Computing time-varying barge impact loads and wall displacements using dynamic analysis requires an accompanying time integration scheme. To accommodate nonlinearities present in model components, a nonlinear adaptation of the CDM (Tedesco et al., 1999) is adopted. A time-step size of 0.001 sec is recommended for conducting low-order analyses. This value ensures both stability of the time integration scheme and accurate modeling of system nonlinearities.

5.2.9. Verification. High-resolution FE simulation results for flotilla impacts on navigation structures are used to verify the low-order modeling approach (Figure 5.16). Collision scenarios involving flotilla impacts on four distinct types of wall structure are considered. The four verification cases encompass a spectrum of high-to-low masses and high-to-low stiffnesses.

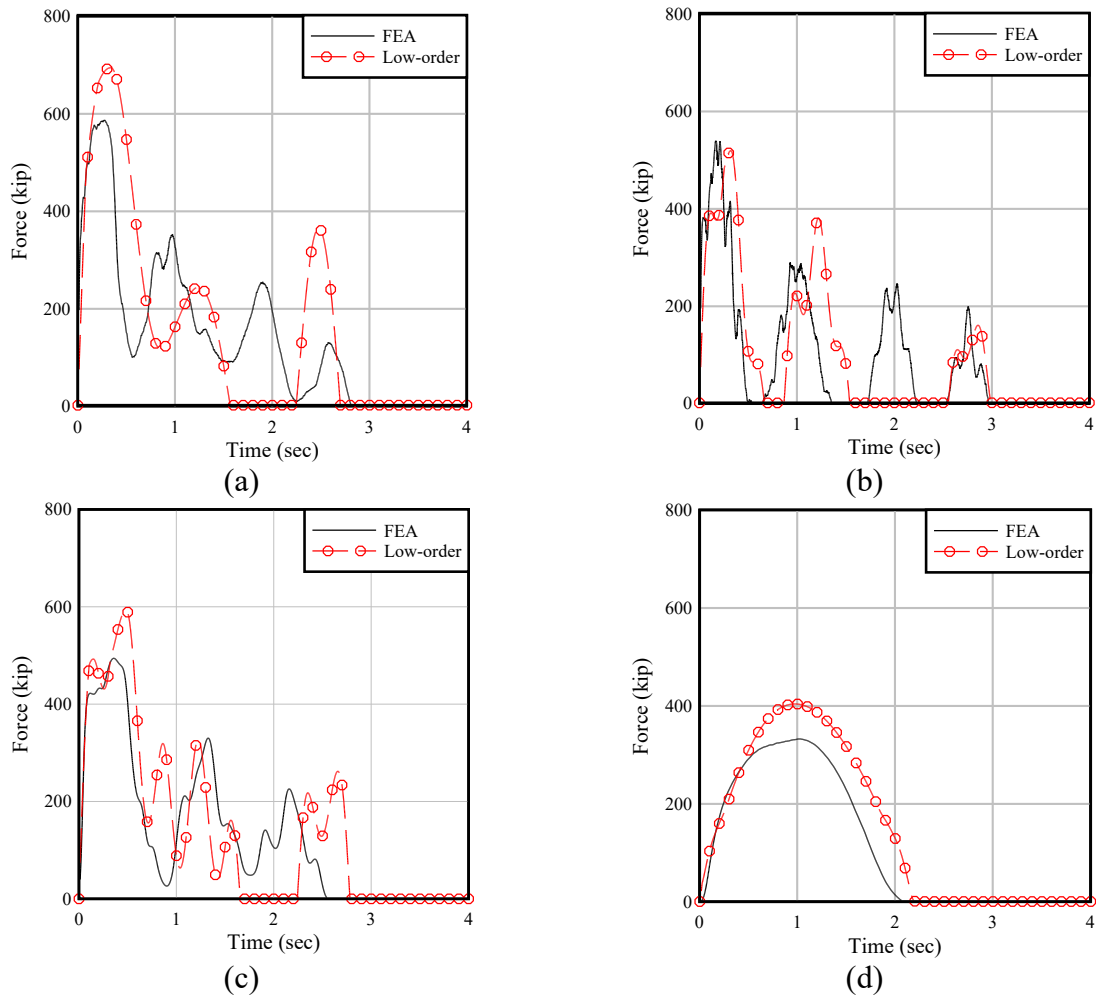


Figure 5.16. Comparisons of Impact-Force Time Histories Obtained from High-Resolution FE Impact Simulation and Low-Order Analysis: (a) Rigid Wall: $3 \times 3 - 20^\circ - 3$ ft/sec; (b) Semi-Flexible Wall: $2 \times 3 - 20^\circ - 3$ ft/sec; (c) Pile-Founded Guide Wall: $3 \times 3 - 15^\circ - 4$ ft/sec; (d) Flexible Timber Guide Wall: $2 \times 2 - 25^\circ - 4$ ft/sec

5.2.9.1. Collectively, the cases include flotilla impacts on rigid walls, semi-flexible walls, pile-founded guide walls, and flexible timber guide walls. Collision scenarios involve flotillas of 2×2 , 2×3 , and 3×3 configurations. Impact angles considered range from 15° to 25° . Flotilla impact speeds considered lie between 3 ft/sec and 4 ft/sec.

5.2.9.2. Figure 5.16 plots impact-force time histories obtained from high-resolution FE simulations and from corresponding low-order analyses. Of note, peak impact forces are important for the design of navigation wall structures. Among the four cases considered, peak impact forces calculated using the low-order model show favorable agreement to FE results. In particular, low-order results are either approximately equal to or only moderately greater than those computed using high-resolution FE impact simulations.

5.2.9.3. Such results demonstrate that the low-order analysis approach provides an accurate, yet fast-running, method of computing peak design impact loads. The approach additionally avoids introducing excess conservatism as may be associated with the use of empirical load prediction equations. Further assessment of accuracy is investigated using six additional scenarios for each of the four wall structures (totaling 24 additional scenarios). The extended verification set includes flotilla sizes from 1x1 (single barge) up to 3x5. Impact angles range from 10° to 30° and initial flotilla speeds range from 1 ft/sec to 8 ft/sec.

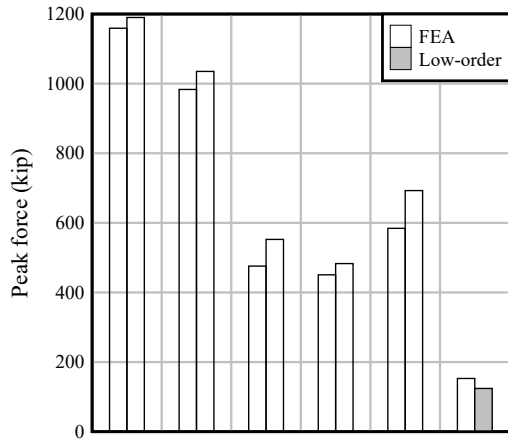
5.2.9.4. Figure 5.17 compares peak impact forces obtained from the 24 high-resolution FE simulations and 24 respective low-order analyses. For 18 cases, maximum impact forces computed using low-order analysis equal or only moderately exceed those from high-resolution FE simulations. For the remaining six cases, low-order analysis produces design-level impact forces that differ by less than 20% relative to benchmark FE values.

5.2.10. Implementation. The low-order model is intended for use in rapidly predicting design-level (i.e., maximum-magnitude) barge flotilla impact loads on wall structures. This includes analysis and design over a wide range of wall masses and stiffnesses. The fast-running code module can be called on thousands of times to compute impact loads within probabilistic analysis frameworks. An example probabilistic framework for analyzing barge impacts on navigation structures is found in Patev (2005).

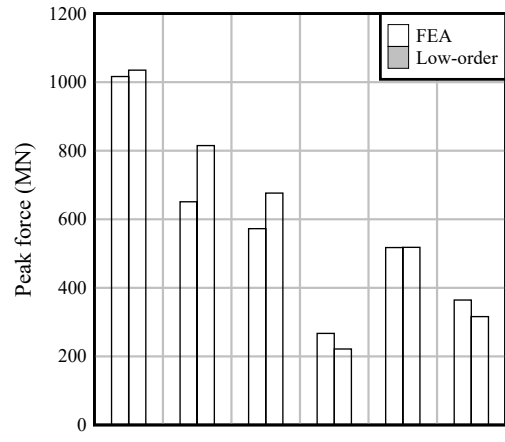
5.2.10.1. The low-order dynamic analysis method is packaged into a code module (software package) that can be invoked from Excel. The low-order code module computes barge impact loads by both constructing the required system equations and dynamically solving said equations. Also computed are the time-varying displacements of the impacted wall structure, as well as peak values of force and displacements. The low-order impact analysis is carried out without dependency on separate structural analysis software.

5.2.10.2. For ease of use, only minimal input parameters need be specified to construct a complete low-order system model. All required barge (and flotilla) force-deformation relationships are encoded within the module. As a result, such data do not have to be provided (or specified) by the engineer. Walls structures may be modeled as being rigid, flexible with linear stiffness, or flexible with nonlinear stiffness.

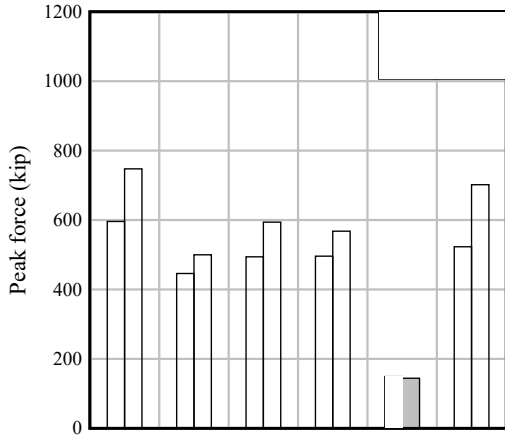
5.2.10.3. To maximize execution speed, the low-order dynamic analysis algorithm is implemented using the C programming language. Furthermore, strategies used in coding the algorithm targeted fast execution speed as a goal. Encoded data such as the barge corner crushing relationships, and the flotilla stiffness relationships (axial, shear, flexure), are pre-embedded within the code module. A numerically efficient implementation CDM based nonlinear time integration is also included. Additional implementation details are provided in Consolazio and Han (2015), in association with a wider implementation by Palisade (2015).



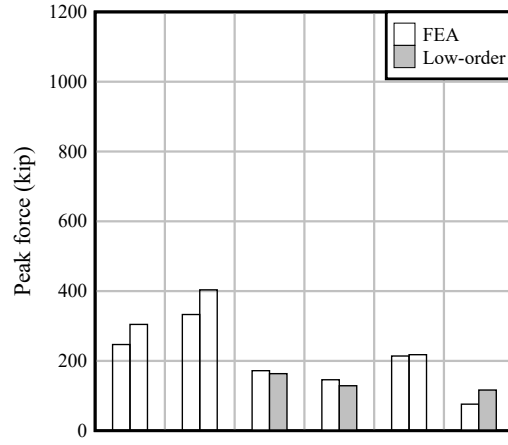
(a)



(b)



(c)



(d)

Figure 5.17. Comparisons of Peak Impact Forces Obtained from High-Resolution FE Impact Simulation and Low-Order Analysis; (a) Rigid Wall; (b) Semi-Flexible Wall; (c) Pile-Founded Guide Wall; (d) Flexible Timber Guide Wall

5.3. Typical Application Cases.

5.3.1. Concrete Walls. As introduced in section 5.2, the low-order analysis method is applicable to concrete walls of varying structural configuration. Impact loads for concrete guide walls that are treated as rigid (Figure 5.2a) can be efficiently computed via low-order analysis. For such cases, wall stiffness and mass need not be specified, however barge deformations and dynamics are included in load determination. Semi-flexible concrete guide walls with high mass and moderate stiffness (Figure 5.2b) can be dynamically analyzed by providing suitable structural characteristics.

5.3.1.1. Pile-founded concrete guide walls (Figure 5.2c) with high mass and low stiffness are also appropriate for low-order analysis. The timber pile footings used under such walls may require nonlinear descriptions of stiffnesses. Moreover, the stiffnesses in the positive and negative displacement directions may be unique, due to asymmetrical pile configuration. Such conditions can be analyzed by the low-order method through appropriate specification of stiffness data.

5.3.1.2. Concrete walls that provide flood protection are also suitable candidates for application of low-order dynamic analysis. Examples include both coastal floodwalls and inland riverine floodwalls. Through suitable approximation of wall stiffness and mass, T-wall and I-wall configurations can be analyzed. Foundation characteristics such as soil stiffness and sheet piling stiffness may be approximated through suitable specification of nonlinear wall stiffness.

5.3.2. Flexible Timber Guide Walls. Flexible timber guide walls are often constructed from a combination of timber elements and composite materials (recycled plastic, fiberglass, rebar). Such walls are constructed by framing together piles, wales, and girts using an assortment of connection components. In contrast to stiff slab-like concrete walls, framed walls constructed from lower-modulus materials (timber, plastic) are much more flexible. Additionally, materials such as timber and plastic are much less dense (lower mass) than concrete.

5.3.2.1. Therefore, flexible timber guide walls tend to be characterized by both low-stiffness and low-mass. In contrast to concrete walls, mass-related inertial (dynamic) wall forces are less influential in the analysis of timber guide walls. Barge flotilla deformations and dynamic responses are, however, still pertinent. As demonstrated in section 5.2.9, impact forces on timber guide walls can be efficiently quantified using low-order dynamic analysis.

5.3.2.2. As an alternative to low-order dynamic analysis, an empirical load prediction model is also developed in Appendix H. Data used in development of the empirical model are derived from high-resolution FE impact simulations (described in Appendix H). Timber piles, fiberglass-reinforced plastic wales, and various configurations of steel barge flotillas are represented in the FE simulations. The resulting empirical model is intended specifically for application to flexible timber guide walls and involves approximation through curve fitting.

5.4. Deterministic Examples.

5.4.1. Overview. Section 5.4 presents three deterministic examples of collision scenarios on wall structures. The examples progress from less severe to more severe with respect to both flotilla size (mass) and impact velocity. Although these examples are deterministic, they do represent increasingly rare collision events. An impact scenario associated with usual conditions is presented in section 5.4.2. Unusual and extreme impact scenarios are focused on in section 5.4.3 and section 5.4.4, respectively.

5.4.2. Usual.

5.4.2.1. Figure 5.18 shows a plan-view schematic of the deterministic example for usual impact conditions. A fully loaded 1x1 flotilla (i.e., single barge) is selected for this scenario, weighing 2,000 short tons. The initial barge velocity is 2 ft/sec and impacts a concrete wall weighing 904 kip at an angle of 25°. Impact-induced wall motions are assumed as being damped at 5% of critical damping. Nonlinear wall stiffness (Figure 5.19) is approximately representative of a flexible concrete guide wall (recall Figure 5.2b). Frictional effects generated during impact are characterized by a barge-wall friction coefficient of 0.45.

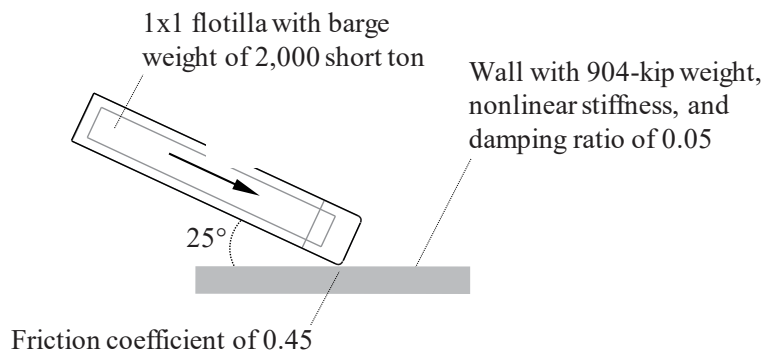


Figure 5.18. Deterministic (Usual) Impact Scenario

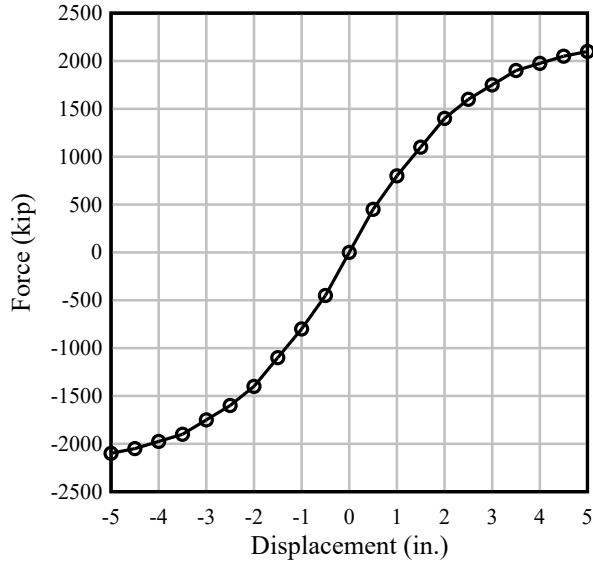


Figure 5.19. Wall Stiffness for Deterministic (Usual) Impact Scenario

5.4.2.2. Table 5.2 lists the input parameters supplied to the low-order code module for analyzing the usual design example. The wall force-displacement curve plotted in Figure 5.19 is supplied as input data to describe the nonlinear wall stiffness. The computed time history of impact force is plotted in Figure 5.20, and indicates a single pulse. Maximum impact force (278 kip) is attained within 1 sec. Regarding the impacted wall response (Figure 5.21), the maximum displacement (0.52 in.) also occurs within 1 sec.

Table 5.2
System Parameters for Deterministic (Usual) Impact Scenario

Parameter Description	Value	Units
Flotilla columns	1	N/A
Flotilla rows	1	N/A
Weight per barge	2,000	short tons
Impact speed	2	ft/sec
Impact angle	25	°
Weight of wall	904	kip
Barge-wall friction coefficient	0.45	N/A
Wall damping ratio	0.05	N/A
Time-step size	0.001	sec
Impact duration	10	sec

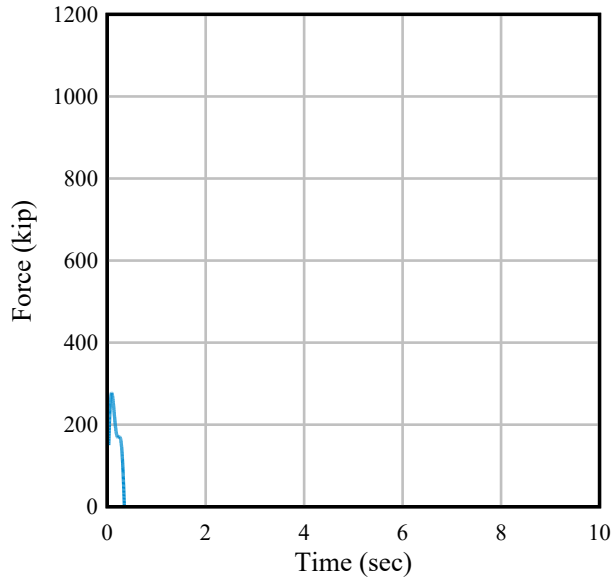
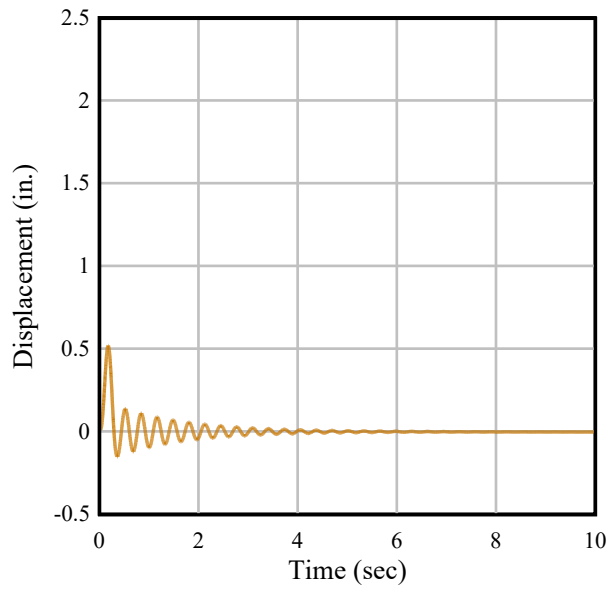


Figure 5.20. Impact Force Time History for Deterministic (Usual) Impact Scenario



F
Figure 5.21. Wall Displacement Time History for Deterministic (Usual) Impact Scenario

5.4.3. Unusual.

5.4.3.1. Figure 5.22 depicts a plan-view schematic of a deterministic example for unusual impact conditions. A fully loaded 3x3 flotilla is selected for the collision scenario, with each barge weighing 2,000 short tons. The flotilla impact velocity is 3 ft/sec. Impact occurs on a concrete wall weighing 904 kip at an angle of 20°. Impact-induced wall motions are assumed to be damped at 5% of critical damping. Nonlinear wall stiffness (Figure 5.23) is approximately representative of a concrete flexible guide wall. Frictional effects generated during impact are characterized by a barge-wall friction coefficient of 0.45.

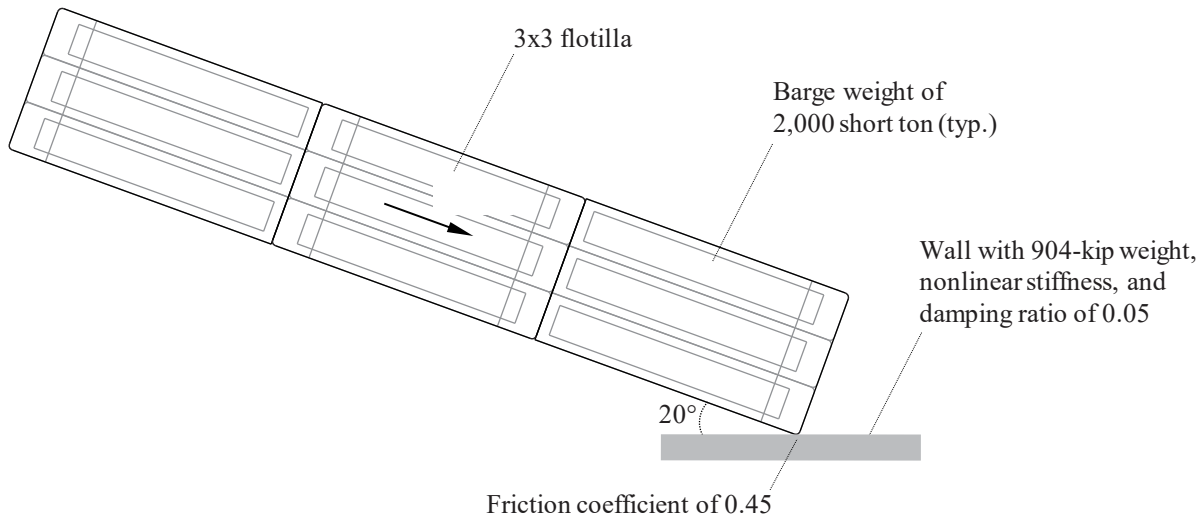


Figure 5.22. Deterministic (Unusual) Impact Scenario

5.4.3.2. Table 5.3 lists the input parameters supplied to the low-order code module for analyzing the unusual design example. The wall force-displacement curve plotted in Figure 5.19 is supplied as input data to describe the nonlinear wall stiffness. The computed time history of impact force is plotted in Figure 5.24 and indicates two distinct pulses. Maximum impact force (676 kip) is attained within 1 sec. Regarding the impacted wall response (Figure 5.25), the maximum displacement (0.95 in.) also occurs within 1 sec.

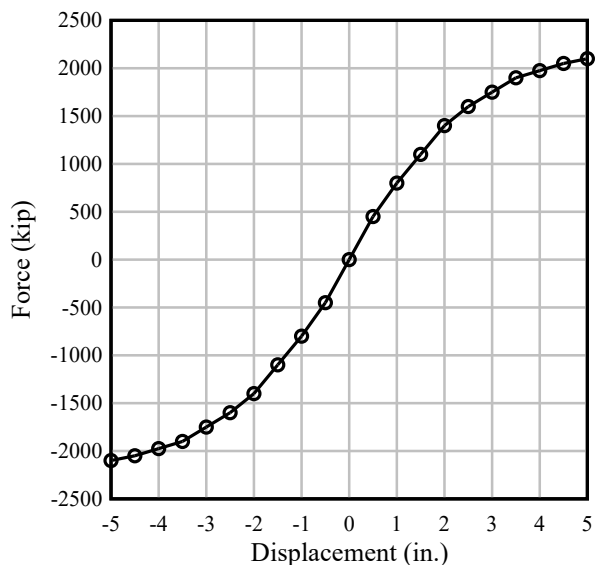


Figure 5.23. Wall Stiffness for Deterministic (Unusual) Impact Scenario

Table 5.3
System Parameters for Deterministic (Unusual) Impact Scenario

Parameter Description	Value	Units
Flotilla columns	3	N/A
Flotilla rows	3	N/A
Weight per barge	2,000	short tons
Impact speed	3	ft/sec
Impact angle	20	°
Weight of wall	904	kip
Barge-wall friction coefficient	0.45	N/A
Wall damping ratio	0.05	N/A
Time-step size	0.001	sec
Impact duration	10	sec

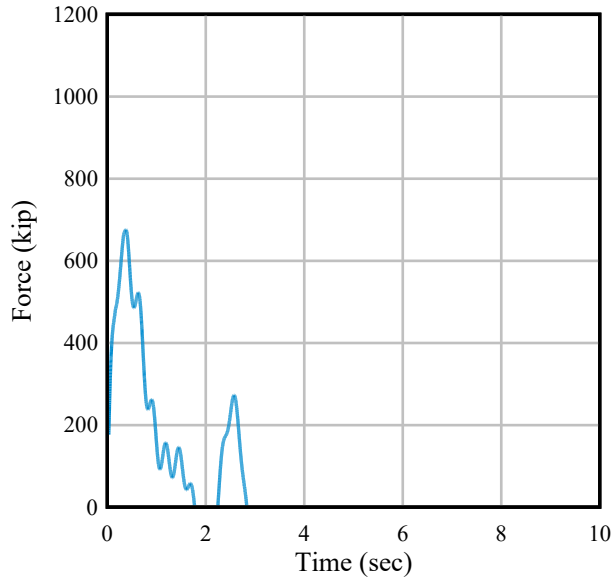


Figure 5.24. Impact Force Time History for Deterministic (Unusual) Impact Scenario

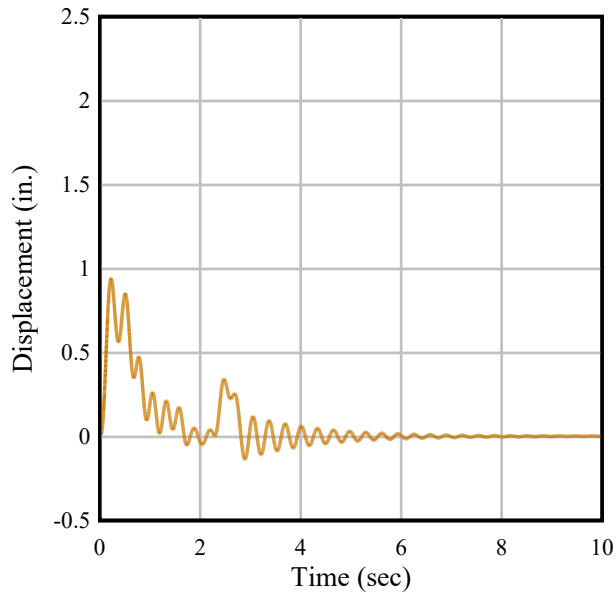


Figure 5.25. Wall Displacement Time History for Deterministic (Unusual) Impact Scenario

5.4.4. Extreme.

5.4.4.1. A plan-view schematic of the deterministic example for extreme impact conditions is shown in Figure 5.26. Here, a fully loaded 3x5 flotilla (three columns, five rows) is selected for the collision scenario. Further, each barge in the flotilla is at full payload (i.e., weighs 2,000 short tons). The initial barge velocity is 8 ft/sec and impacts a wall weighing 904 kip at an angle of 30°. Impact-induced wall motions are assumed as being damped at 5% of critical damping. In addition, the wall stiffness (Figure 5.27) is approximately representative of a flexible concrete guide wall. Frictional effects generated during impact are characterized by a barge-wall friction coefficient of 0.45.

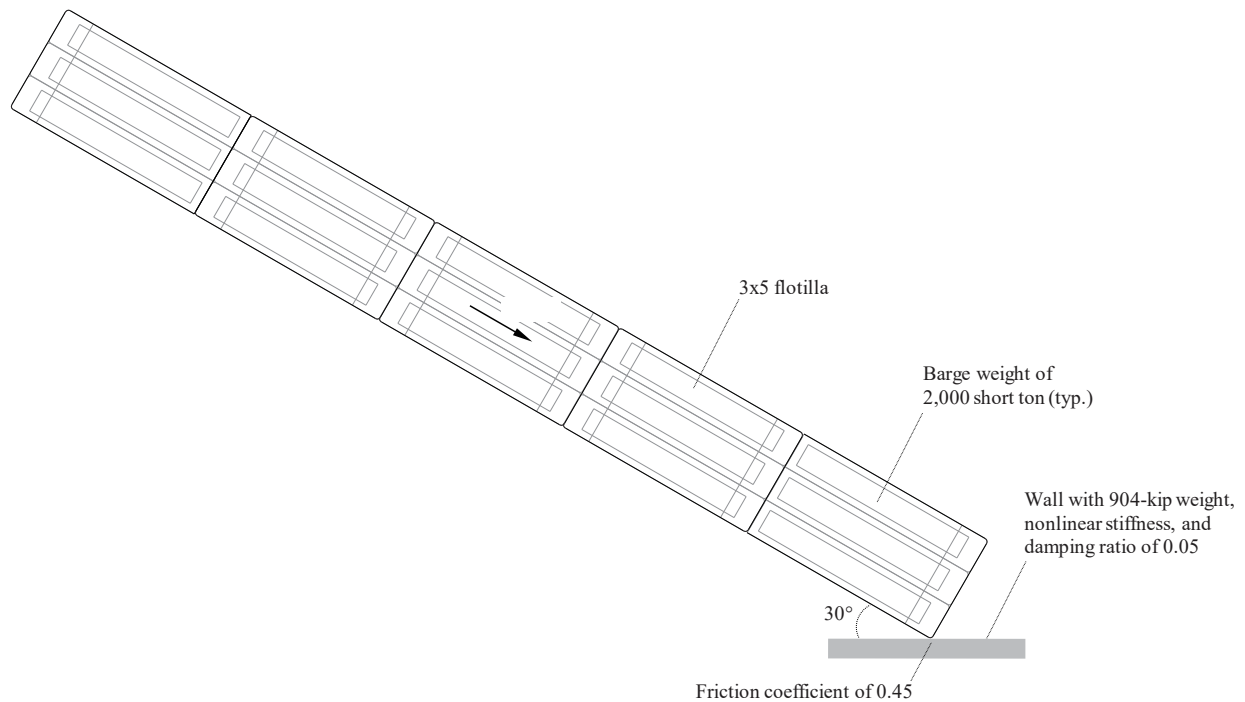


Figure 5.26. Deterministic (Extreme) Impact Scenario

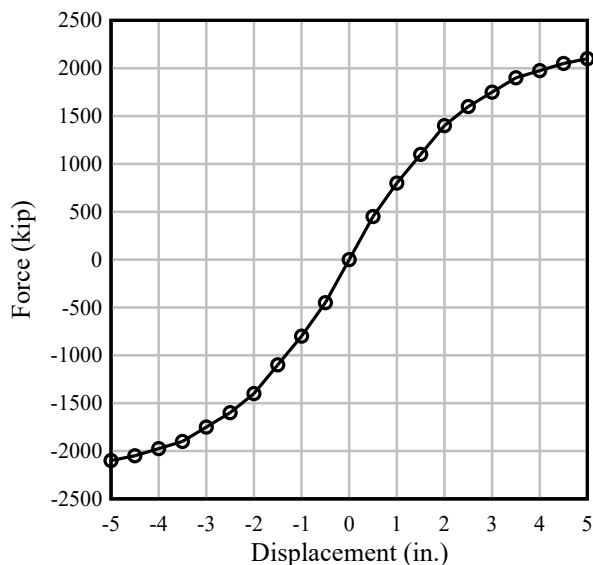


Figure 5.27. Wall Stiffness for Deterministic (Extreme) Impact Scenario

5.4.4.2. Table 5.4 lists the input parameters supplied to the low-order code module for analyzing the extreme design example. The wall force-displacement curve plotted in Figure 5.27 is supplied as input data to describe the nonlinear wall stiffness. The computed time history of impact force is plotted in Figure 5.28, and indicates several distinct pulses. Maximum impact force (1,190 kip) is attained at approximately 2 sec after the onset of impact. However, regarding the impacted wall response (Figure 5.29), the maximum displacement (2.4 in.) occurs within 1 sec.

Table 5.4
System Parameters for Deterministic (Extreme) Impact Scenario

Parameter Description	Value	Units
Flotilla columns	3	N/A
Flotilla rows	5	N/A
Weight per barge	2,000	short tons
Impact speed	8	ft/sec
Impact angle	30	°
Weight of wall	904	kip
Barge-wall friction coefficient	0.45	N/A
Wall damping ratio	0.05	N/A
Time-step size	0.001	sec
Impact duration	10	sec

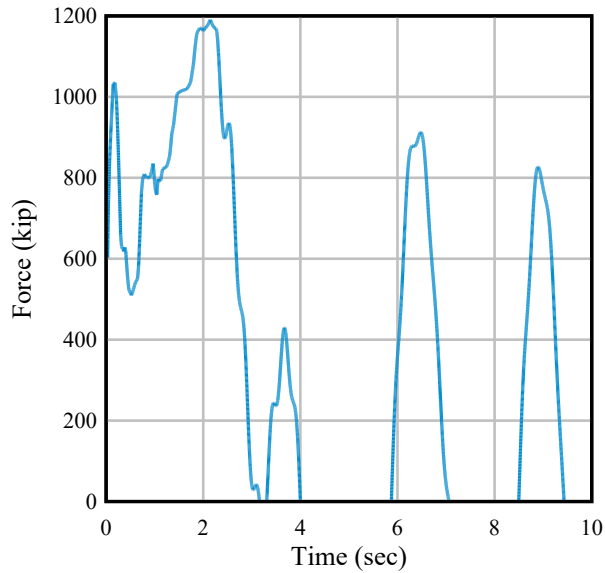


Figure 5.28. Impact Force Time History for Deterministic (Extreme) Impact Scenario

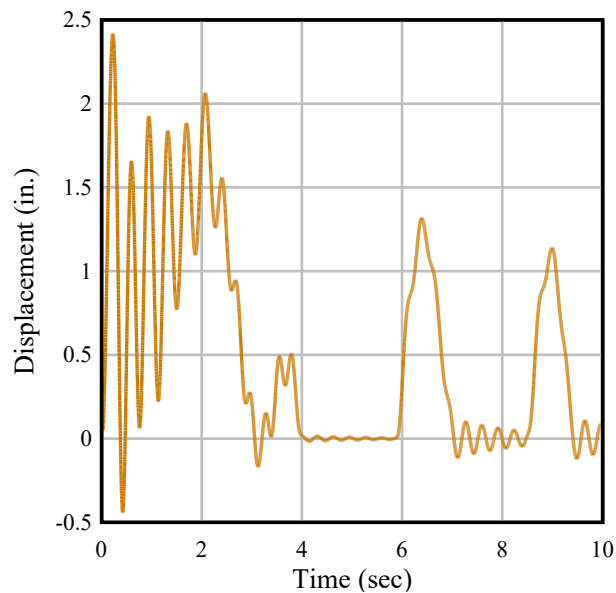


Figure 5.29. Wall Displacement Time History for Deterministic (Extreme) Impact Scenario

5.5. Complete Design Example – LODM.

5.5.1. Deterministic Example. This example is for the design of a rigid approach wall for a new lock on the Ohio River. Based on present traffic predictions and navigation model testing at ERDC, a 15-barge tow and input parameters selected for the usual, unusual, and extreme load cases are as follows:

5.5.1.1. Usual Load Case. The LODM input parameters for the rigid and flexible approach wall calculations are shown in Table 5.5. The flexible wall stiffness for this load case is shown above in Figure 5.27. The results for a rigid and flexible approach wall are shown in Table 5.6 and in Figures 5.30 to 5.32.

Table 5.5
Usual Load Case – Inputs to LODM

Inputs	Value
Velocity	2 ft/sec
θ	10 degrees
W_{barge}	2,000 short tons (per barge)
Barge columns	3
Barge rows	5
Wall weight	904 kips
Wall damping ratio	0.05
Friction coefficient	0.45
Time end	5 Sec
Time sample	0.01 sec

Table 5.6
Usual Load Case – LODM Example

Wall Type	Force (kips)	Displacement (inches)
Rigid	248	N/A
Flexible	217	0.5

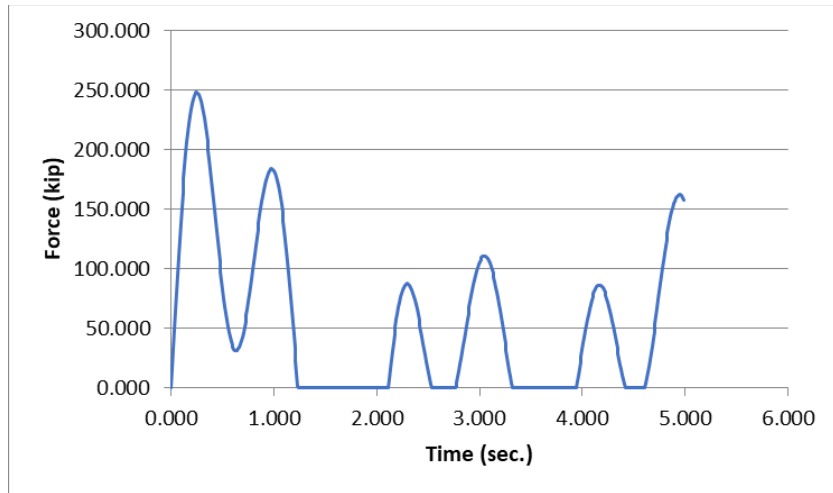


Figure 5.30. Force Time History for Usual Load Case – Rigid Wall

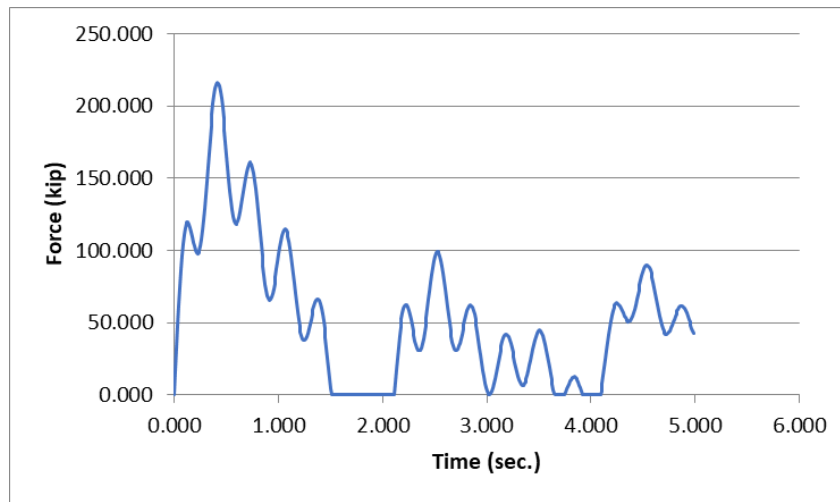


Figure 5.31. Force Time History for Usual Load Case – Flexible

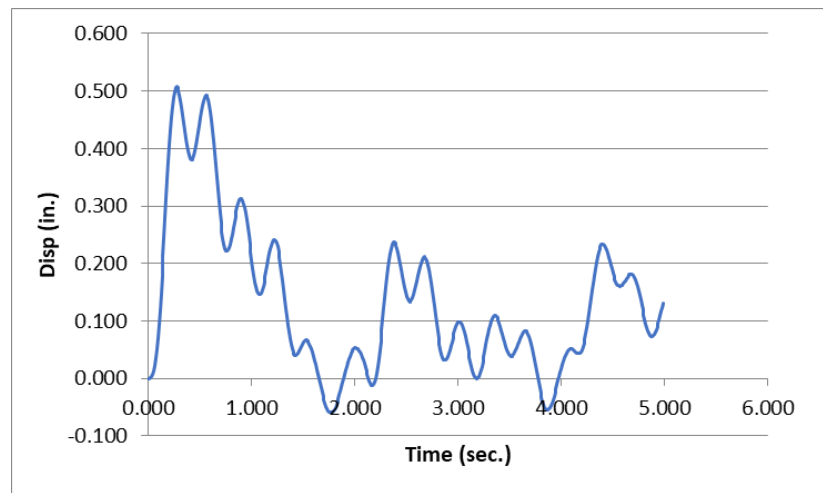


Figure 5.32. Displacement Time History for Usual Load Case – Flexible

Unusual Load Case. The LODM input parameters for the rigid and flexible approach wall are shown in Table 5.7. The flexible wall stiffness for this load case is shown above in Figure 5.27. The results for a rigid and flexible approach wall are shown in Table 5.8 and in Figures 5.33 to 5.35.

Table 5.7
Usual Load Case – Inputs to LODM

Inputs	Value
Velocity	4 ft/sec
θ	20 degrees
W_{barge}	2,000 short tons (per barge)
Barge columns	3
Barge rows	5
Wall weight	904 kips
Wall damping ratio	0.05
Friction coefficient	0.45
Time end	5 Sec
Time sample	0.01 sec

Table 5.8
Unusual Load Case – LODM Example

Wall Type	Force (kips)	Displacement (inches)
Rigid	773	N/A
Flexible	770	2.2

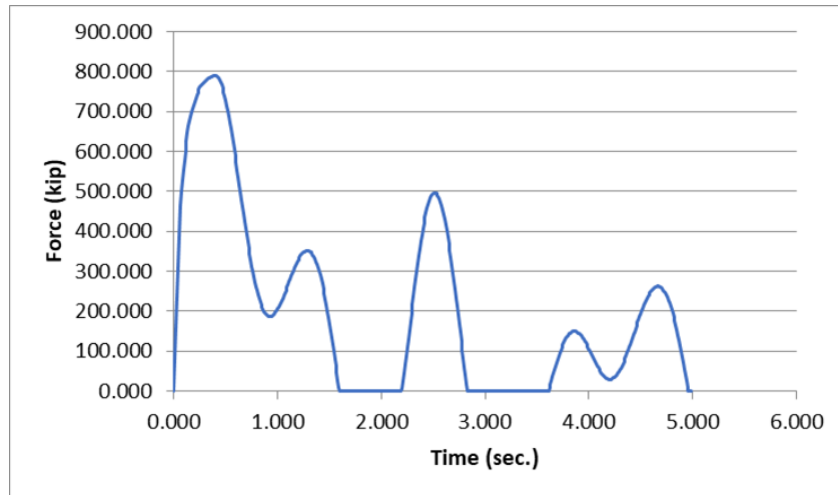


Figure 5.33. Force Time History for Usual Load Case – Rigid Wall

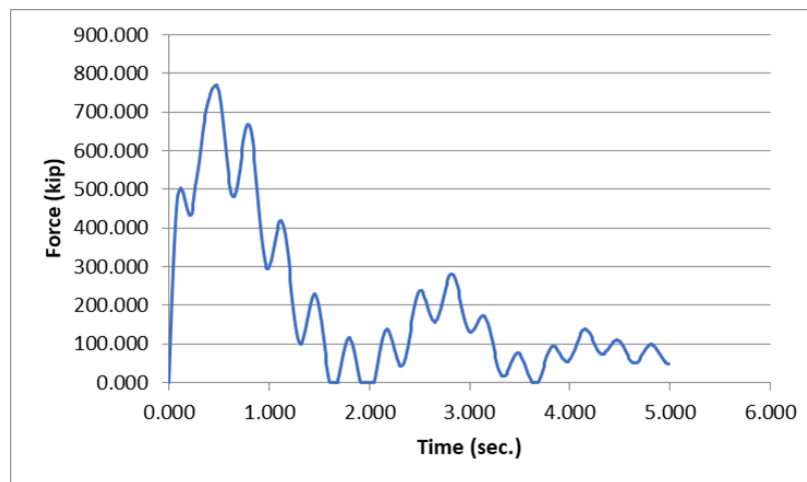


Figure 5.34. Force Time History for Usual Load Case – Flexible

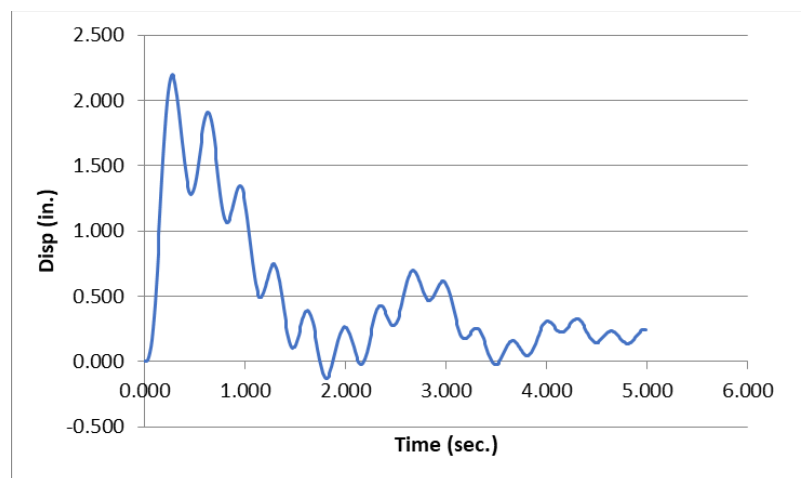


Figure 5.35. Displacement Time History for Usual Load Case – Flexible

5.5.1.2. Extreme Load Case.

5.5.1.2.1 The LODM input parameters for the rigid and flexible approach walls are shown in Table 5.9. The flexible wall stiffness for this load case is shown above in Figure 5.27. The results for a rigid and flexible wall are shown in Table 5.12 and in Figures 5.36 to 5.38.

Table 5.9
Usual Load Case – Inputs to LODM

Inputs	Value
Velocity	6 ft/sec
θ	30 degrees
W_{barge}	2,000 short tons (per barge)
Barge columns	3
Barge rows	5
Wall weight	904 kips
Wall damping ratio	0.05
Friction coefficient	0.45
Time end	5 Sec
Time sample	0.01 sec

Table 5.10
Unusual Load Case – LODM Example

Wall Type	Force (kips)	Displacement (inches)
Rigid	1035	N/A
Flexible	1035	4.0

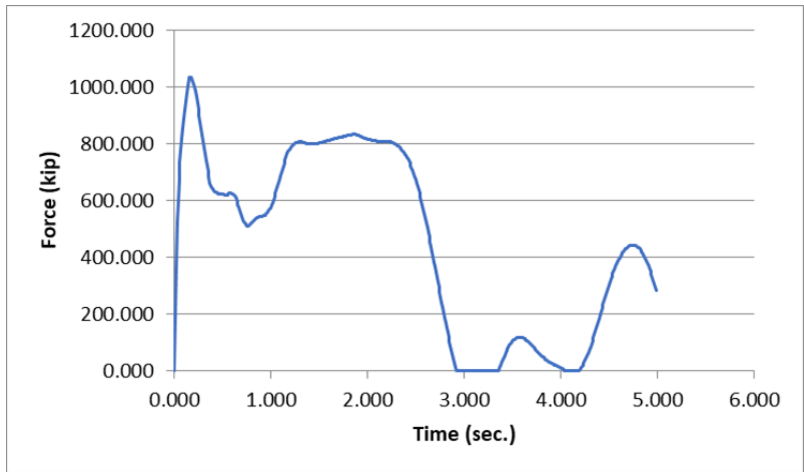


Figure 5.36. Force Time History for Usual Load Case – Rigid Wall

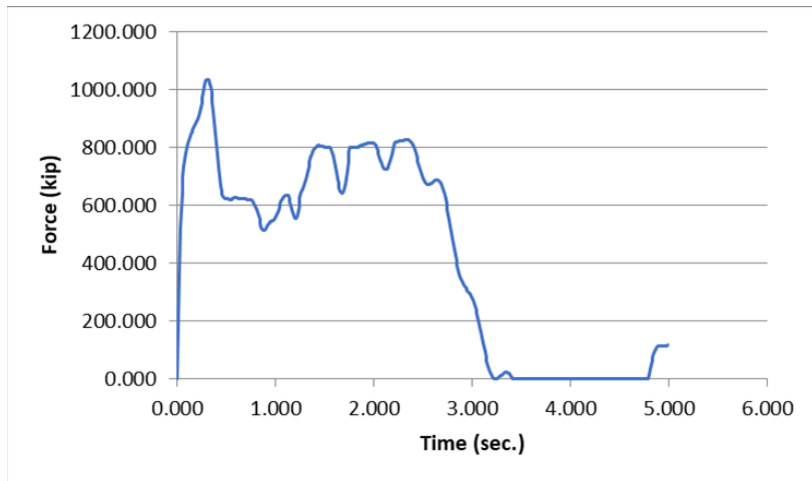


Figure 5.37. Force Time History for Usual Load Case – Flexible

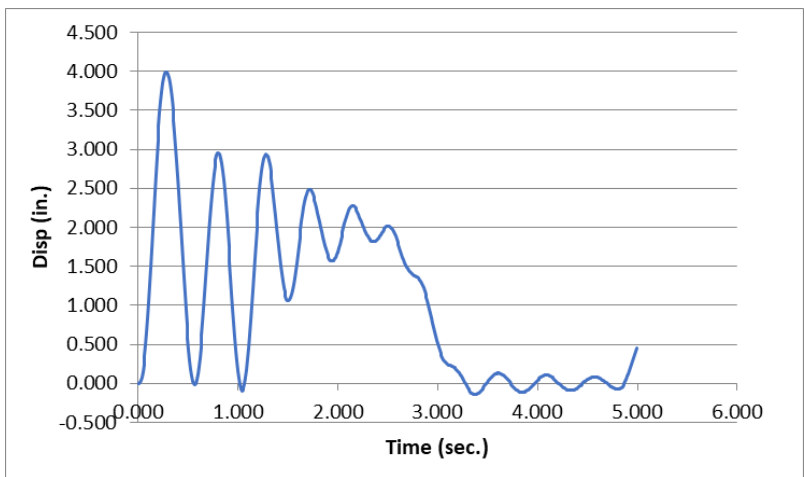


Figure 5.38. Displacement Time History for Usual Load Case – Flexible

5.5.1.2.2 Table 5.13 shows a summary of the barge impact forces using the LODM and calculating the deterministic method defined in the flowchart in Chapter 2 as:

Table 5.11
Design Load Cases from Deterministic Calculations

Load Case	Rigid Force (kips)	Flexible Force (kips)	Displacement Flexible (inches)
Usual	248	217	0.5
Unusual	773	770	2.2
Extreme	1,035	1035	4.0

5.5.2. Probabilistic Example.

5.5.2.1. This example is for the design of a concrete approach wall ($k = 1,000$ k-in) for a new lock on the Ohio River. Based on present traffic predictions and navigation model testing at ERDC, a 15-barge tow and input parameters selected for probabilistic analysis are shown in Table 5.12. The LODM constants are defined in Table 5.13.

Table 5.12
Design Example – Probabilistic Inputs

Parameter	Distribution	$E(x)$	$\sigma(x)$	Min(x)	Max(x)
Velocity (ft/sec)	Lognormal	2	1	0.1	7
Angle (degs)	Lognormal	8	4	1	30
Weight – single barge (short tons)	Constant	2,000	-	-	-
Wall weight	Constant	904			

Table 5.13
Design Example – LODM Constants

Inputs	Value
Barge columns	3
Barge rows	5
Wall weight	904 kips
Wall damping ratio	0.05
Friction coefficient	0.45
Time end	5 Sec
Time sample	0.01 sec

5.5.2.2. A probabilistic model run is completed using Monte Carlo Simulations for 50,000 iterations. Return periods for this site were selected for the usual (2 year), unusual (150 year), and extreme (1000 year) load cases and are shown in Table 5.14.

Table 5.14
Design Load Cases from Probabilistic Calculations

Load Case	Force (kips)
Usual – 2 year	134
Unusual – 150 year	662
Extreme – 1000 year	849

Chapter 6 Pier Structures

6.1. General.

6.1.1. This chapter focuses on methods for empirical assessment of barge impact loads on pier portions of waterway navigation structures. Direct, head-on impacts of barge flotillas are considered for multiple types of piers. Particular emphasis is placed on impact forces that arise during collision between flotillas and bullnose structures.

6.1.2. A wide range of flotilla-pier collision scenarios are considered, where flotilla size, impact speed, and bullnose configuration are all varied. For various bullnose configurations (e.g., semi-circular, sloped-V), impact force data are obtained from high-resolution FE simulations. Correlations between impact force and impacted pier diameter (and/or flotilla momentum) are used to form empirical load prediction equations.

6.1.3. Both deterministic and probabilistic design examples are provided for usual, unusual, and extreme barge impact conditions involving bullnose structures. In addition, discussion is included in this chapter to facilitate design of other types of pier structures. These other types of pier structures include piers positioned along dam walls (dam piers) and mooring cells.

6.1.4. Scope. The material in this chapter has been organized into the following sections as:

6.1.4.1. Section 6.2 contains configuration details, FE model components, simulated impact force listings, and load prediction equations for semi-circular bullnose piers.

6.1.4.2. Section 6.3 discusses sloped-V bullnose configuration details, model components, impact force data, and load prediction equations.

6.1.4.3. Section 6.4 details the empirical model for dam piers.

6.1.4.4. Section 6.5 gives examples using the empirical models for semi-circular and V-shaped bullnoses.

6.1.4.5. Section 6.6 gives a complete design example that follows the methodology presented in Chapter 2. This design example performs both deterministic and probabilistic calculations and compares the difference between the results.

6.2. Semi-Circular Bullnose Structures.

6.2.1. Overview.

6.2.1.1. Bullnose structures are included among the inventory of navigation structures for which USACE is responsible. A significant portion of lock systems feature a circular bullnose

structure, such as that shown in Figure 6.1. Bullnose structures with a semi-circular impact face may be followed by a wall with a width equal to the bullnose diameter. Alternatively, a semi-circular bullnose structure may be attached to a wall that is narrower than the bullnose diameter. In section 6.2, focus is given to quantifying impact forces exerted on semi-circular bullnose structures from flotillas of varying sizes.

6.2.1.2. Semi-circular impact faces followed by walls of equal width are used in all circular bullnose cases considered. From the perspective of predicting conservatively large impact forces, this equal-width layout is appropriate. However, semi-circular bullnose configurations vary across the inventory of navigation structures. To represent the general range of USACE bullnoses that are constructed, diameters of 10 ft and 35 ft are considered.



Figure 6.1. Semi-Circular Bullnose Structure

6.2.2. Modeling Considerations. Reinforced concrete bullnose structures are typically much stiffer than the bow or stern (structural steel) components of hopper barges. Accordingly, FE models of the two semi-circular bullnose structures utilize non-deformable, materially rigid entities. This simplification upholds conservatism with respect to the calculation of impact forces for use in design of bullnose structures.

6.2.2.1. Soil deformation is also conservatively ignored (i.e., soil is treated as rigid) in the FE model portions of the semi-circular bullnose structures. More specifically, fixed boundary conditions are applied to the base nodes of all semi-circular bullnose structural models.

6.2.2.2. These simplifying approximations are motivated by the relative stiffnesses between an impacting barge and a typical USACE concrete bullnose structure. Also, the approximations are consistent with direct observations from high-energy collision incidents that have occurred at various USACE bullnose installations. See Consolazio and Wilkes (2013) for additional details regarding selected historical incidents.

6.2.2.3. All bullnose structures are modeled with 8-node solid brick elements (LSTC 2014) and a mathematically rigid material definition. The 8-node solid brick elements are meshed to be approximately 6 in. x 6 in. x 6 in. (wherever possible). In this way, the bullnose FE models accurately reflect the exterior geometry of the concrete bullnoses. Accurate modeling of the impacted surface contours is important for determining representative impact forces during flotilla-pier contact interactions.

6.2.2.4. Use of 8-node elements with characteristics of 6 in. (in this context) is consistent with desirable modeling practices. That is, element sizes in the bullnose model are less than twice that of the smallest elements in the impacting barge. These relative proportions of element sizes in the flotilla-bullnose models help ensure integrity of contact detection during impact simulation. Details regarding barge flotilla FE modeling are provided in Chapter 3, Getter et al. (2015), and Walters et al. (2017).

6.2.2.5. Friction Coefficients. During impact simulations, contact forces are generated at the interface between the steel barge model and rigid concrete bullnose model. Contact forces possess both normal (perpendicular) and transverse (frictional) components with respect to the impacted face of the bullnose structure. Consequently, friction coefficients constitute an important part of the contact definition between steel barge and rigid concrete bullnose model portions. Frictional parameters are assigned as 0.55 and 0.45 for static and dynamic coefficients of friction, respectively. Selection of these parameter values is consistent with Consolazio and Walters (2012).

6.2.2.6. Thirty-Five-Foot Diameter Bullnose. The 35-ft diameter bullnose FE model (Figure 6.2) is representative of large-width concrete bullnose structures in the USACE structural inventory. The 35-ft diameter is also chosen as it corresponds to the full width of a jumbo hopper barge. As indicated in Figure 6.2a, the 10-ft wall length extending beyond the semi-circular portion is also 35 ft wide.

6.2.2.6.1 The total length of the bullnose model (in the direction of head-on impacts considered) is 27.5 ft (Figure 6.2a). More than 137,000 (rigid) solid elements are included in the 35-ft diameter bullnose model (Figure 6.2b, Figure 6.2c). All nodes distributed across the base of the model are fully restrained against translation.

6.2.2.6.2 A 20-ft vertical height is assigned to prevent overtopping of the impacting barge over the range of collision scenarios considered. In this context, overtopping signifies the barge passing over the top surface of the bullnose structure. This phenomenon could occur due to steel plate folding and fracturing, or buoyant uplift motion of the barge during impact.

6.2.2.6.3 Physically, partial overtopping may or may not occur depending on the bullnose height, water level, and the barge tow draft. However, in conducting flotilla-bullnose collision simulations, preventing overtopping ensures that conservatively high predictions of impact force are obtained. Per Consolazio and Wilkes (2013), a 20-ft model height is sufficient to prevent overtopping.

6.2.2.7. Ten-Foot Diameter Bullnose.

6.2.2.7.1 The FE model of the 10-ft diameter bullnose configuration is presented in Figure 6.3. The configuration is intended to represent smaller diameter semi-circular concrete bullnose structures in the USACE structural inventory. As annotated in Figure 6.3a, the wall length extends 10 ft beyond the semi-circular portion and is also 10 ft wide.

6.2.2.7.2 The total length of the 10-ft diameter bullnose FE model is 15 ft (Figure 6.3a). Approximately 22,000 solid elements (8-node, rigid) are dispersed throughout the 10-ft diameter bullnose model (Figure 6.3b, Figure 6.3c). Nodes of the 10-ft bullnose model that are positioned at the model base are fully restrained against translation. A 20-ft vertical height is assigned to prevent overtopping of the impacting barge over the range of collision scenarios considered.

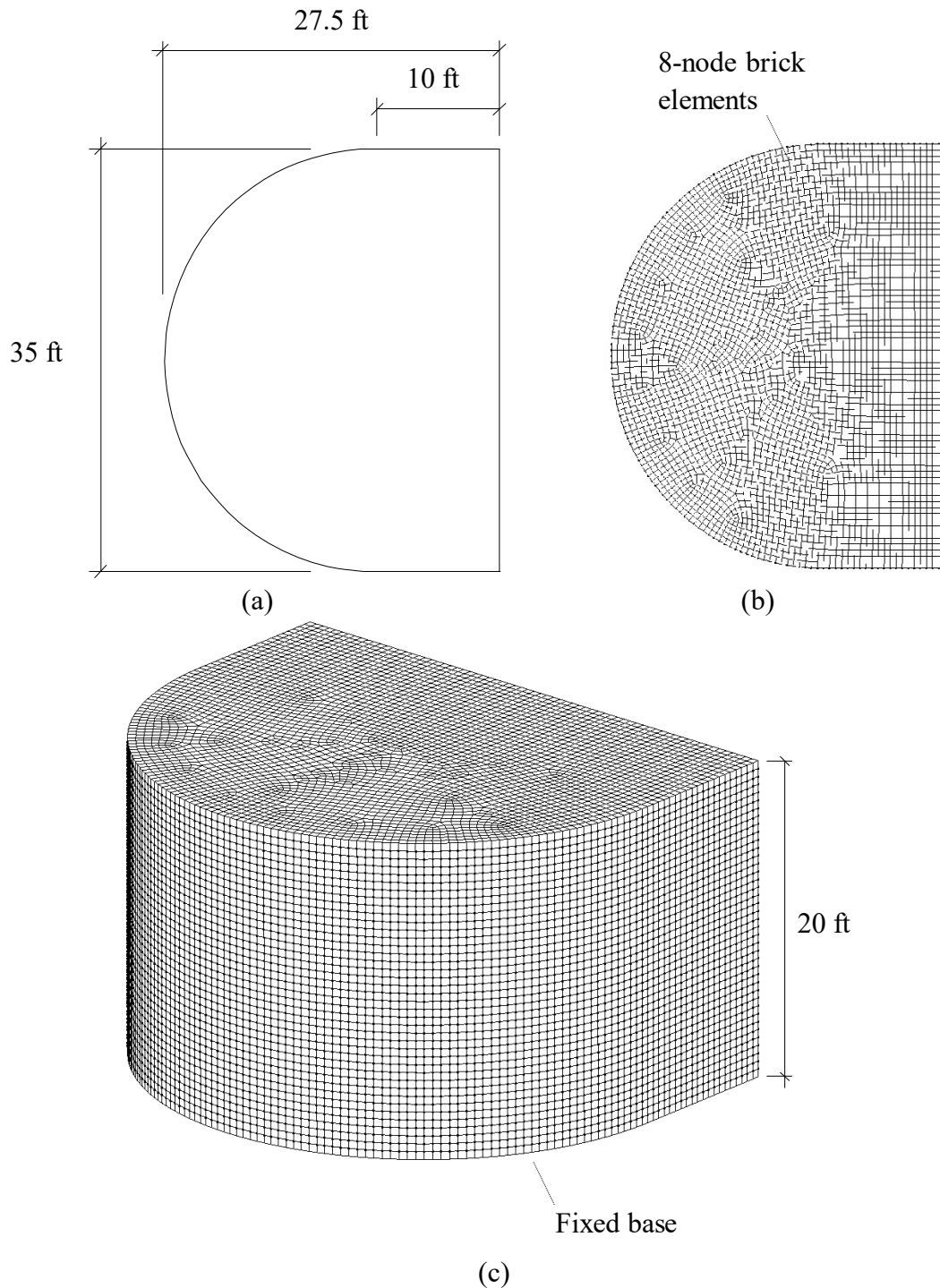


Figure 6.2. Finite Element Modeling of 35-ft Diameter Semi-Circular Bullnose: (a) Plan-View Schematic; (b) Plan View of Mesh; (c) Isometric View of Mesh

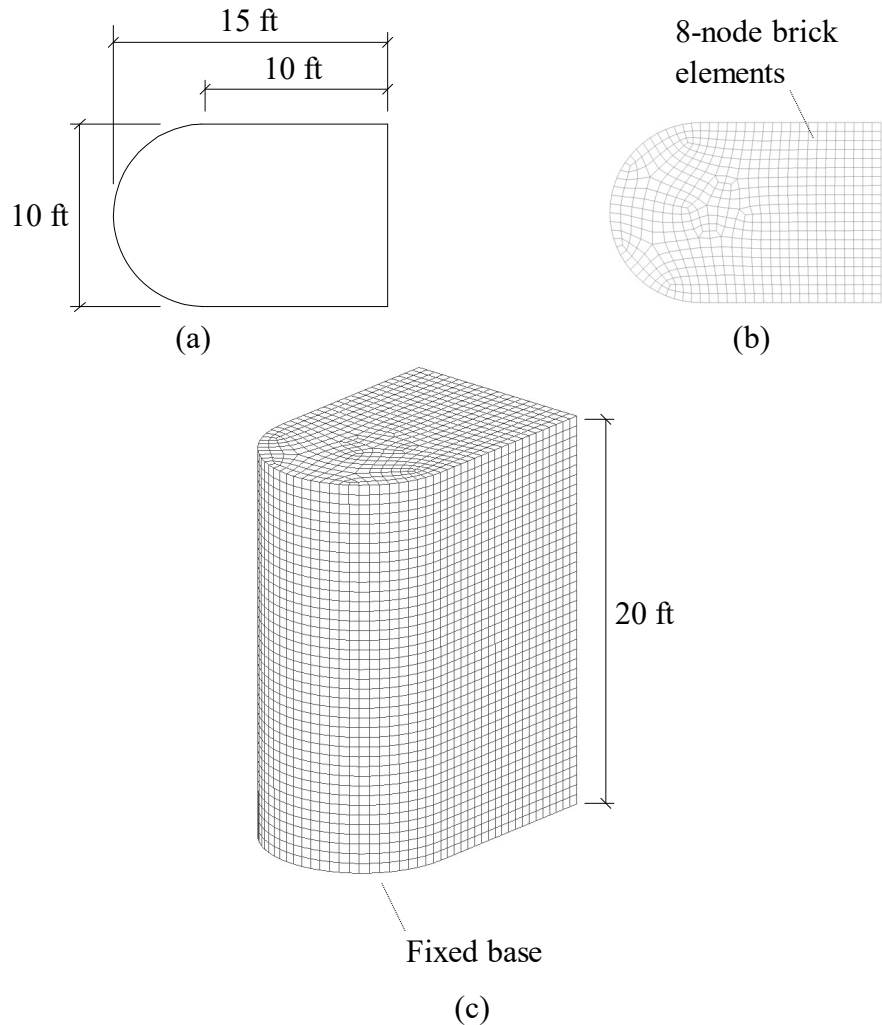


Figure 6.3. Finite Element Modeling of 10-ft Diameter Semi-Circular Bullnose: (a) Plan-View Schematic; (b) Plan View of Mesh; (c) Isometric View of Mesh

6.2.3. Peak Impact Forces. Barge flotilla models of varying sizes are combined with FE models of bullnose structures to conduct collision simulations. See Chapter 3 for additional details regarding FE modeling of barge flotillas. For collision simulations involving bullnose structures, both the 10-ft and 35-ft diameter are subjected to a variety of collision conditions.

6.2.3.1. All collision simulation results that are utilized in forming empirical load relationships pertain to head-on impact conditions. Basic parameters that are varied include flotilla configuration (number of strings, number of rows), flotilla mass, and impact speed. Peak impact forces for selected cases are listed in Table 6.1 (35-ft diameter) and Table 6.2 (10-ft diameter).

6.2.3.2. Additional variations are investigated in Consolazio and Wilkes (2013), including impacting barge end (bow, stern) and impacting string (exterior, interior). Furthermore, simulations involving impact angle and lateral impact offset are explored in Consolazio and Wilkes (2013). A subset of the overall collection of simulation results is focused on to bring about conservative load prediction equations.

6.2.3.3. Peak impact forces obtained from 28 (total) dynamic barge-bullnose impact simulations are listed among Table 6.1 and Table 6.2. The forces correspond to maximums (through-time) of dynamic contact forces between the deformable barge and the bullnose impact surface. All impact forces are resultant forces in the horizontal plane. Further, the forces are low-pass filtered at approximately 10 Hz. In this way, the quantified impact forces are not unduly influenced by higher frequency oscillations present in the simulation results.

Table 6.1
Peak Impact Force Results for 35-ft Semi-Circular Bullnose (17 cases)

Flotilla	Speed (ft/sec)	Flotilla Momentum (kip-sec)	Peak Impact Force (kip)
3 x 5	6.0	11,189	1,983
3 x 5	6.0	11,189	1,996
3 x 5	2.0	3,730	1,586
3 x 5	2.0	3,730	1,604
3 x 3	2.0	2,238	1,341
3 x 3	6.0	6,713	1,836
3 x 3	2.0	2,238	1,601
2 x 5	2.0	2,486	1,326
2 x 3	2.0	1,492	1,323

Flotilla	Speed (ft/sec)	Flotilla Momentum (kip-sec)	Peak Impact Force (kip)
1 x 3	6.0	3,730	1,642
2 x 3	6.0	7,459	1,816
2 x 3	6.0	4,476	1,669
1 x 3	2.0	1,243	1,317
1 x 3	2.0	746	1,260
1 x 3	6.0	2,238	1,637
1 x 3	2.0	249	1,022
1 x 3	6.0	746	1,610

Table 6.2
Peak Impact Force Results for 10-ft Semi-Circular Bullnose (11 cases)

Flotilla	Speed (ft/sec)	Flotilla Momentum (kip-sec)	Peak Impact Force (kip)
3 x 5	6.0	11,189	1,653
3 x 5	2.0	3,730	1,249
3 x 5	6.0	11,189	1,477
3 x 5	2.0	3,730	1,480
3 x 3	4.0	4,476	1,413
3 x 3	2.0	2,238	1,304

Flotilla	Speed (ft/sec)	Flotilla Momentum (kip-sec)	Peak Impact Force (kip)
2 x 5	4.0	4,973	1,427
2 x 3	4.0	2,984	1,429
1 x 5	4.0	2,486	1,335
1 x 3	4.0	1,492	1,313
1 x 1	4.0	497	1,119

6.2.3.4. Peak Impact Force Plots. Peak impact forces associated with flotillas impacting semi-circular bullnose collisions are plotted in Figure 6.4, Figure 6.5, and Figure 6.6. Specifically, peak (maximum) impact forces versus flotilla momentum, for impacts involving the 35-ft bullnose structure, are presented in Figure 6.4. Similarly, impact force versus flotilla momentum is plotted for impacts on the 10-ft bullnose structure in Figure 6.5. Combined results are plotted in Figure 6.6. The plotted results consistently indicate correlation between peak impact force and flotilla momentum. Note that in this context, the momentum of the entire flotilla is considered.

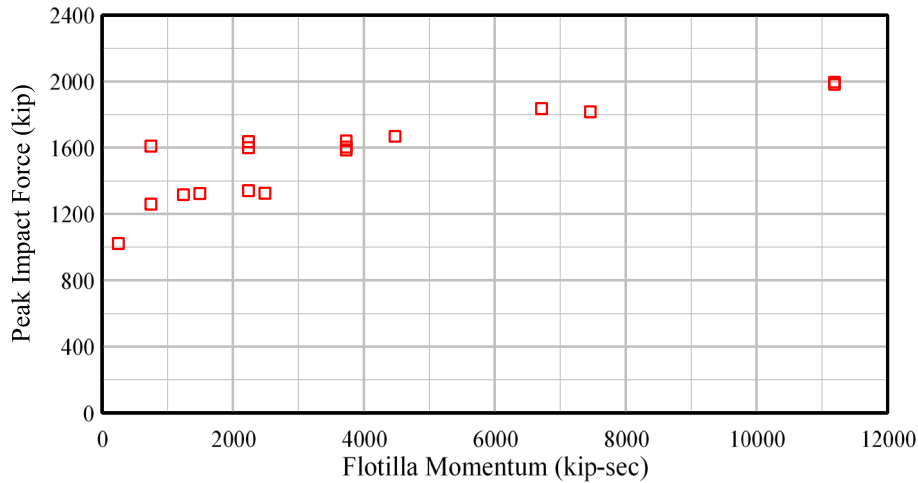


Figure 6.4. Peak Impact Force Results for 35-ft Semi-Circular Bullnose (17 Cases)

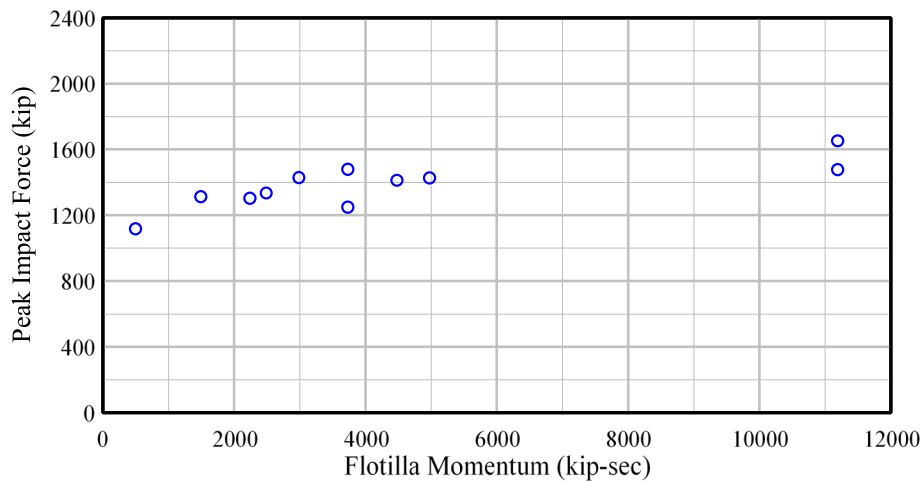


Figure 6.5. Peak Impact Force Results for 10-ft Semi-Circular Bullnose (11 Cases)

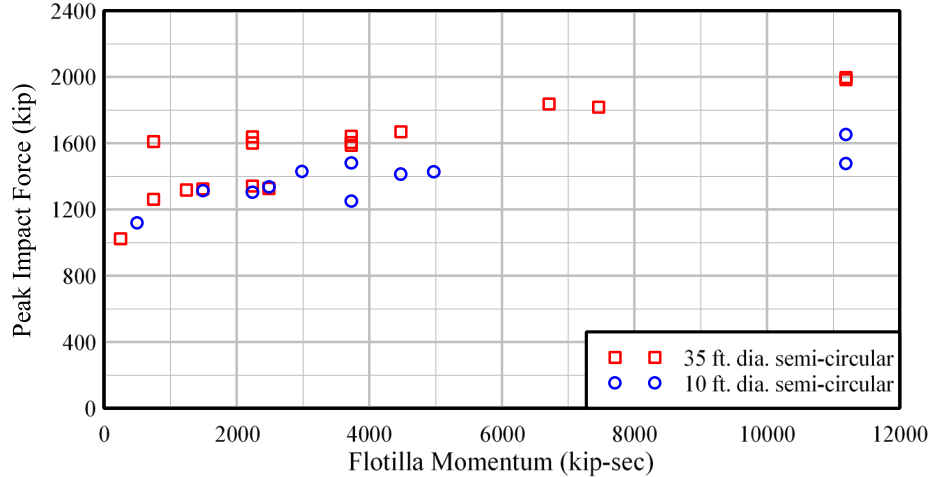


Figure 6.6. Peak Impact Force Results for 10-ft and 35-ft Semi-Circular Bullnoses (28 Cases)

6.2.4. Empirical Load Prediction Model. As is evident from Figure 6.6, increasing the bullnose diameter tends to produce an increase in impact force. This phenomenon is more prominent at moderate to high levels of flotilla impact momentum. Furthermore, this finding is consistent with prior analytical studies (Consolazio et al., 2009, Getter and Consolazio 2011). Prior studies found that magnitudes of barge impact forces for circular bridge piers are approximately linearly correlated to pier diameter. Therefore, impact forces for moderate to high momentum impact conditions on bullnoses are assumed to be linearly dependent on diameter (ϕ).

6.2.4.1. The empirical load prediction model developed for semi-circular bullnose structures adopts a bilinear representation. As shown in the plot schematic of Figure 6.7, the slope (S_1) of the first segment (low momentum impacts) is constant. The slope (S_2) of the second linear segment (moderate to high momentum impacts) is a linear function of bullnose diameter. Functionally, the bilinear curve has the form:

$$F = \begin{cases} S_1 \cdot (m \cdot v) & \text{if } m \cdot v \leq (F_{12}/S_1) \\ F_{12} + \underbrace{(S_{2A} + S_{2B} \cdot \phi)}_{S_2} \cdot (m \cdot v - (F_{12}/S_1)) & \text{otherwise} \end{cases} \quad (6.1)$$

where F is the horizontal impact force. The terms F_{12} , S_{2A} , and S_{2B} are bilinear curve fitting parameters. The m term is the mass of all barges in the flotilla. As emphasis, the associated flotilla momentum ($m \cdot v$) is the total flotilla momentum. Flotilla impact velocity is given as v and is assumed to pertain to head-on impact conditions.

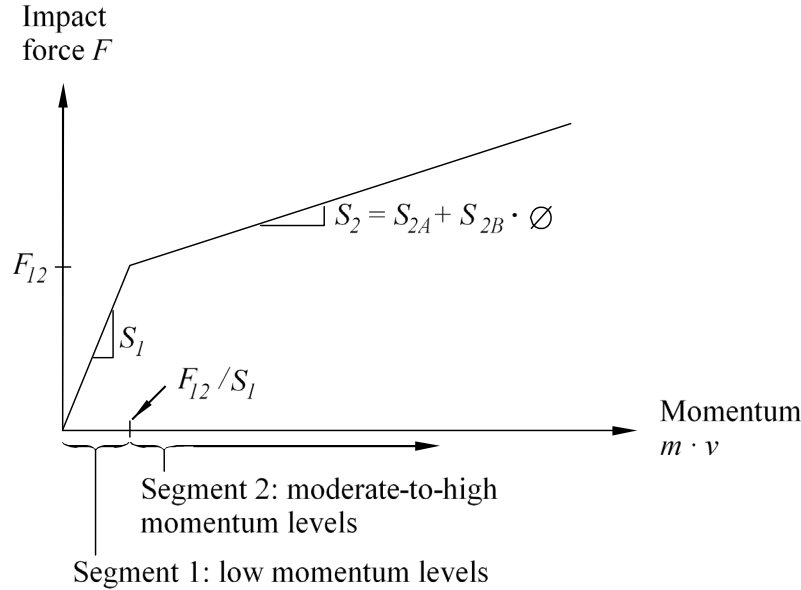


Figure 6.7. General Form of Bilinear Curve Fit Used for Semi-Circular Bullnoses

6.2.4.2. Numerical values for F_{I2} , S_{2A} , and S_{2B} in Equation 6.1 are determined via an error minimization (least-square error) fitting procedure (recall section 4.3.6.3). The curve fitting process consists of repeatedly evaluating Equation 6.1 using candidate coefficient values, flotilla mass, velocity, and bullnose diameter. Expression evaluations (or impact force) are then compared to respective (benchmark) data points from Table 6.1 and Table 6.2.

6.2.4.3. The candidate coefficients are iteratively modified until minimum error is achieved between Equation 6.1 evaluations and the benchmark data. Accordingly, numerical values are obtained for F_{I2} , S_1 , S_{2A} , and S_{2B} , result in the bilinear expression:

$$F = \begin{cases} 4.128 \cdot m \cdot v & \text{if } m \cdot v \leq 320 \text{ kip-sec} \\ 1321 + (0.003 + 0.001863 \cdot \phi) \cdot (m \cdot v - 320) & \text{otherwise} \end{cases} \quad (6.2)$$

6.2.4.4. For impacts involving semi-circular bullnose structures, low levels of momentum are distinguished from medium and high levels of momentum. For impacts involving momentum values of 320 kip-sec or smaller, the impact is characterized as having low momentum. Correspondingly, the initial linear curve segment from Figure 6.7 (with Slope S_1) is utilized to estimate impact force. Elsewhere, the relatively softer second linear segment depicted in Figure 6.7 (with slope, S_2) is utilized for evaluating impact force.

6.2.4.5. The confidence bounds are also established at confidence levels of 1-standard deviation (84.1%) and 2-standard deviations (97.7%) from the mean. Functionally, these bounds are given by:

$$F_{84.1\%} = \begin{cases} 4.433 \cdot m \cdot v & \text{if } m \cdot v \leq 319 \text{ kip-sec} \\ 1417 + (0.003 + 0.002015 \cdot \phi) \cdot (m \cdot v - 319) & \text{otherwise} \end{cases} \quad (6.3)$$

and:

$$F_{97.7\%} = \begin{cases} 4.781 \cdot m \cdot v & \text{if } m \cdot v \leq 317 \text{ kip-sec} \\ 1514 + (0.001 + 0.002224 \cdot \phi) \cdot (m \cdot v - 317) & \text{otherwise} \end{cases} \quad (6.4)$$

6.2.4.6. Comparisons of Simulated and Predicted Impact Forces. Use of the load prediction model is illustrated (Figure 6.8 to Figure 6.10) for impacts on 10-ft and 35-ft bullnose structures. Here, peak impact forces from Table 6.1 and Table 6.2 are compared to respective evaluations of the mean-value best fit curve Equation 6.2. The combined set of comparisons (for both bullnose diameters considered) is presented in Figure 6.8. Comparisons between only the 35-ft and 10-ft diameter force-momentum pairs are plotted in Figure 6.9 and Figure 6.10, respectively.

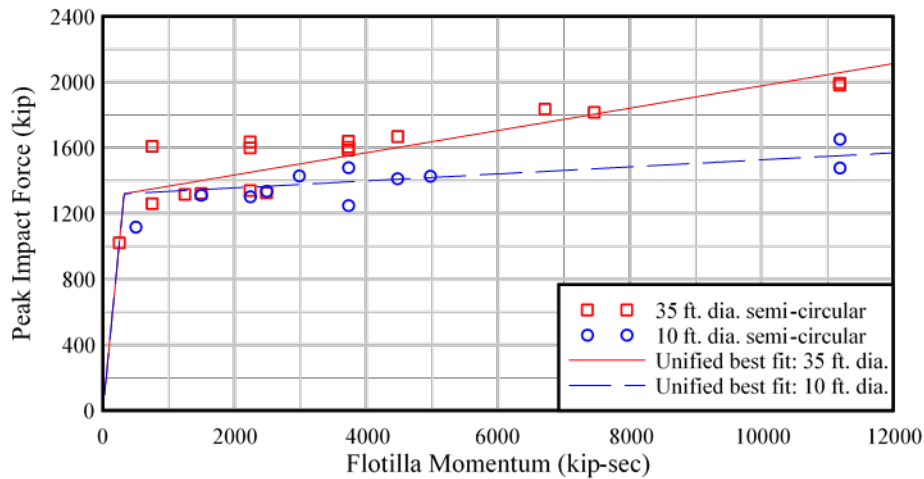


Figure 6.8. Comparisons of Semi-Circular Bullnose Data and Bilinear Curve Fits (Load Predictions Evaluated Using Respective Diameters)

6.2.4.7. Reasonable agreement is found between the empirical load prediction model and simulation-based force data across all cases considered. Further, the necessity of accounting for impacted bullnose diameter is made evident. In particular, the second-segment slope associated with impacts on the 35-ft bullnose is steeper than that of the 10-ft bullnose. Additional comparisons of the load prediction model to various bullnose impact datasets are provided in Consolazio et al. (2014).

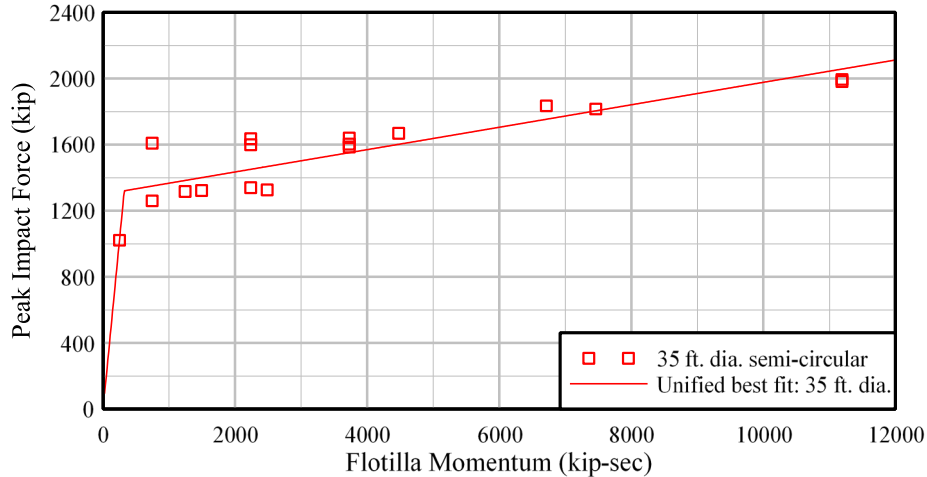


Figure 6.9. Comparison of 35-ft Semi-Circular Bullnose Data and Bilinear Curve Fit (Load Predictions Evaluated Using 35-ft Diameter)

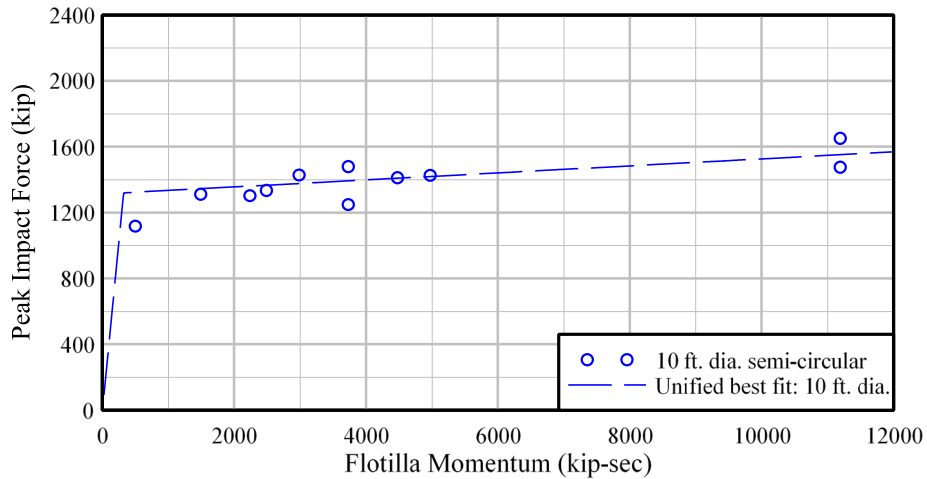


Figure 6.10. Comparison of 10-ft Semi-Circular Bullnose Data and Bilinear Curve Fit (Load Predictions Evaluated Using 10-ft Diameter)

6.3. Sloped-V Bullnose Structures.

6.3.1. Overview. In addition to circular bullnoses (see section 6.2), the sloped-V bullnose shape is commonly utilized along the Mississippi River. An example sloped-V configuration (at a lock located on the Mississippi River) is shown in Figure 6.11. Impact interactions between impacting barge flotillas and vertical faces of semi-circular bullnoses differ from those involving sloped-V bullnoses. In the latter instance, the bow of the impacting barge tends to ride partially up the sloped face of the bullnose. As a result, impact force relationships (relative to flotilla momentum) differ when considering impacts on semi-circular versus sloped-V bullnoses.

6.3.1.1. Given the above, it is necessary to separate vertical face semi-circular bullnose impact conditions from sloped-V impact conditions. As such, the approach adopted in section 6.3 is to develop a separate load prediction model for impacts on sloped-V bullnose structures. Accordingly, a sloped-V bullnose pier shape is modeled using FEs and utilized in forming empirical load prediction equations.

6.3.1.2. The sloped-V bullnose geometry considered herein possesses a 2:1 (vertical-to-horizontal) slope on the impact face. FE modeling of the sloped-V configuration derives from construction plans for the Mississippi River L&D No. 7. The selected sloped-V geometry is considered to be reasonably representative of similar structures contained in the USACE inventory. Relevant construction plans and additional variations on the sloped-V geometry are documented in Consolazio and Wilkes (2013). In addition, sensitivity analysis to pier features such as slope (e.g., 2:1 vs. 1:1) are investigated in Consolazio and Wilkes (2013).

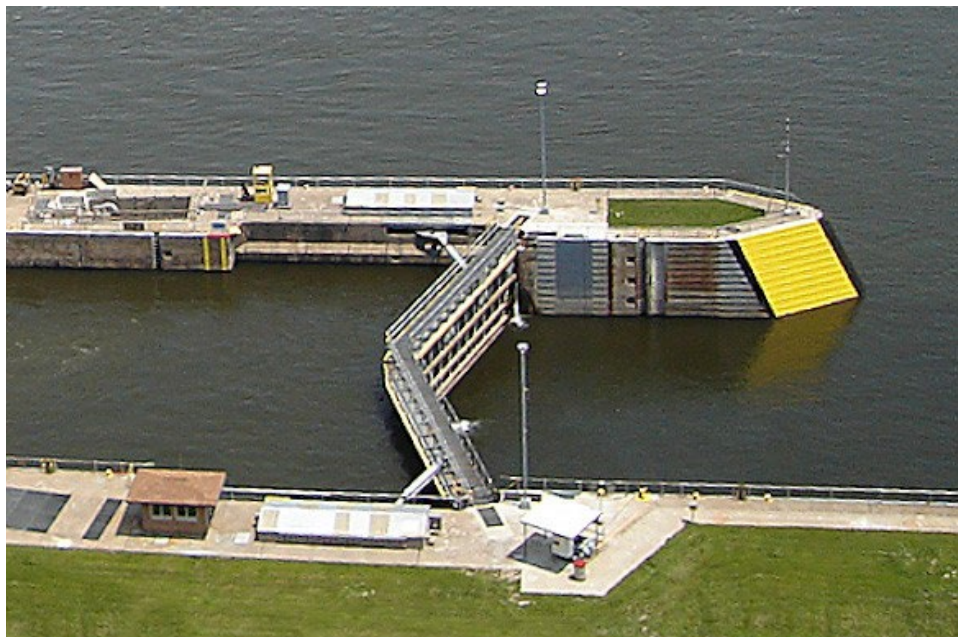


Figure 6.11. Example Sloped-V (Mississippi) Bullnose Structure

6.3.2. Modeling Considerations. In plan view, the sloped-V bullnose shape is approximately triangular in form (Figure 6.12a, Figure 6.12b). The ridge of the slope-V, which comes into direct contact with barges during collisions, features a 4 ft diameter radial nose.

6.3.2.1. The base and sidewalls of the sloped-V FEM possess widths of 28 ft. More than 16,000 8-node solid brick elements (LSTC 2014) are distributed throughout the sloped-V model. All solid elements are approximately 6-in. x 6-in. x 6-in. in size and are assigned a rigid material definition. Soil resistance is ignored (i.e., assumed to be rigid) as a conservative assumption with respect to impact force generation. Consequently, nodes located at the base of the FE model are fully restrained against translation (Figure 6.12c).

6.3.2.2. Given the 2:1 slope of the sloped-V impact face, barges may slide (or ride) partially up the structure during collision. A 33-ft height is assigned to the sloped-V model to prevent barges from sliding beyond the topmost bullnose surface. In this way, conservatism is upheld with respect to estimating maximum impact forces. The effects of pronounced sliding of barges upward along the impacted bullnose face are documented in Consolazio and Wilkes (2013).

6.3.2.3. Friction Coefficients. Friction coefficients constitute an important part of the contact definition when simulating flotilla-bullnose collisions that involve sliding. Frictional parameters are assigned as 0.55 and 0.45 for static and dynamic coefficients of friction, respectively. Use of these values in simulating collisions between steel barges and concrete structures is consistent with Consolazio and Walters (2012).

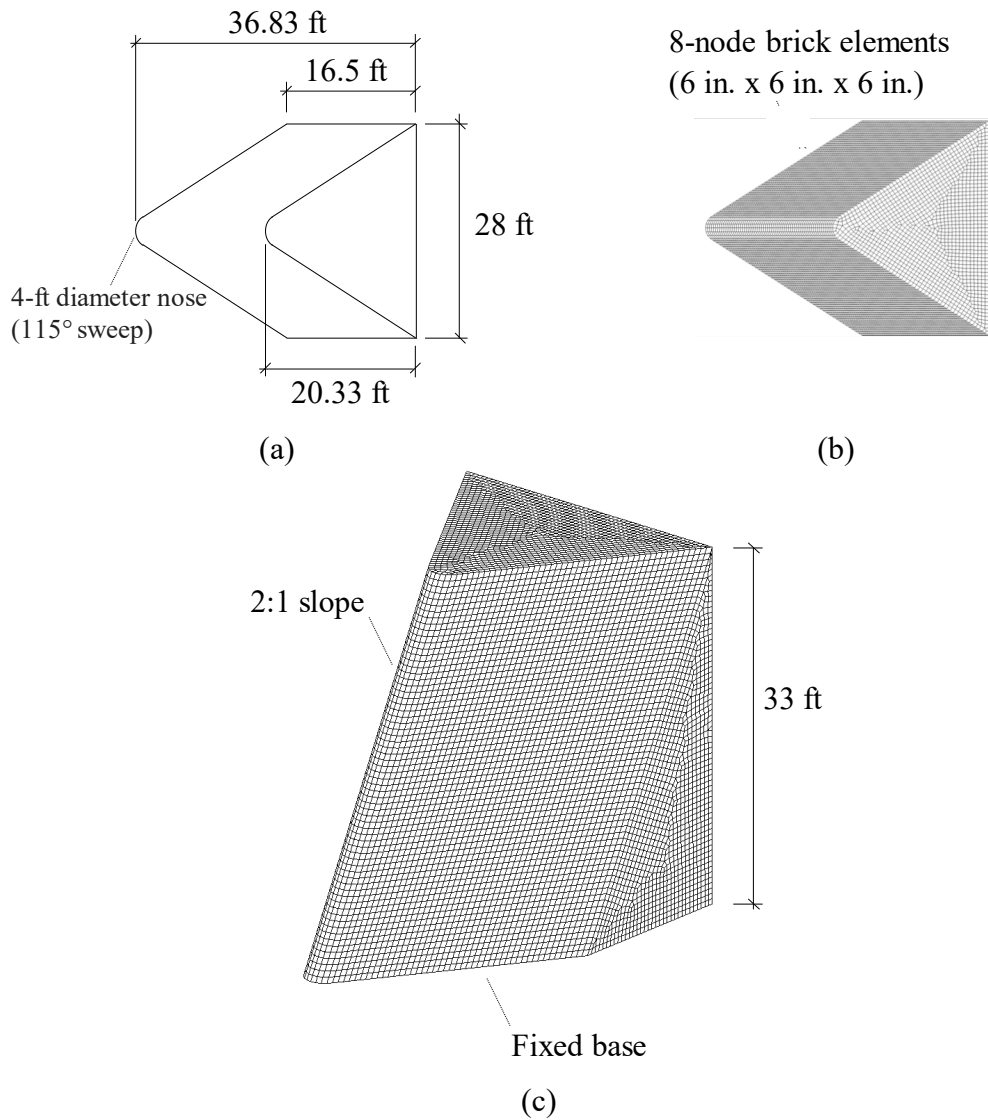


Figure 6.12. Finite Element Modeling of Sloped-V (2:1) Bullnose: (a) Plan-View Schematic; (b) Plan View of Mesh; (c) Isometric View of Mesh

6.3.3. Peak Impact Forces. Barge flotilla models of varying sizes are combined with FE models of sloped-V structures to conduct collision simulations. Details regarding flotilla FE modeling are provided in Chapter 3, Getter et al. (2015) and Walters et al. (2017). For the sloped-V bullnose collision simulations presented here, the configuration shown in Figure 6.12 is subjected to varying collision conditions.

6.3.3.1. All collision simulation results that are utilized in forming empirical load prediction equations pertain to head-on impact conditions. The conditions that are varied include flotilla configuration (number of strings, number of rows), flotilla mass, and impact speed. Peak impact forces for selected cases are listed in Table 6.3.

6.3.3.2. Peak impact forces obtained from additional variations are provided in Consolazio and Wilkes (2013), in which the effects of bullnose slope are documented, along with variations in impact angle and lateral offset. A subset of simulation results is focused on below to bring about conservative load prediction equations.

6.3.3.3. Peak impact forces obtained from 18 dynamic barge-bullnose impact simulations are listed in Table 6.3. The maximum (through-time) dynamic contact forces are taken as resultant forces in the horizontal plane. All forces listed in Table 6.3 reflect low pass filtering at approximately 10 Hz. Use of filtering prevents undue influence by higher frequency (purely numerical) oscillations present among the simulation results.

Table 6.3
Peak Impact Force Results for Sloped-V (2:1) Bullnose (18 Cases)

Flotilla	Speed (ft/sec)	Flotilla Momentum (kip-sec)	Peak Impact Force (kip)	Flotilla	Speed (ft/sec)	Flotilla Momentum (kip-sec)	Peak Impact Force (kip)
3 x 5	2.0	3,730	991	3 x 3	2.0	2,238	902
3 x 5	6.0	11,189	1,935	2 x 5	2.0	2,486	910
3 x 5	2.0	3,730	994	1 x 5	2.0	1,243	789
3 x 5	6.0	11,189	1,351	1 x 5	6.0	3,730	1,192
3 x 4	5.0	7,459	1,210	2 x 3	2.0	1,492	890
3 x 3	6.0	6,713	1,336	1 x 3	2.0	746	629
2 x 5	6.0	7,459	1,362	1 x 3	6.0	2,238	1,204
2 x 3	6.0	4,476	1,221	1 x 1	2.0	249	488
3 x 3	2.0	2,238	900	1 x 1	6.0	746	937

6.3.3.4. Peak Impact Force Plots. Peak impact forces obtained from simulating flotillas colliding with sloped-V bullnose structures are plotted in Figure 6.13. Peak impact forces are paired with flotilla momentum, as listed in Table 6.3. The plotted results indicate an evident correlation between peak impact force and total flotilla momentum.

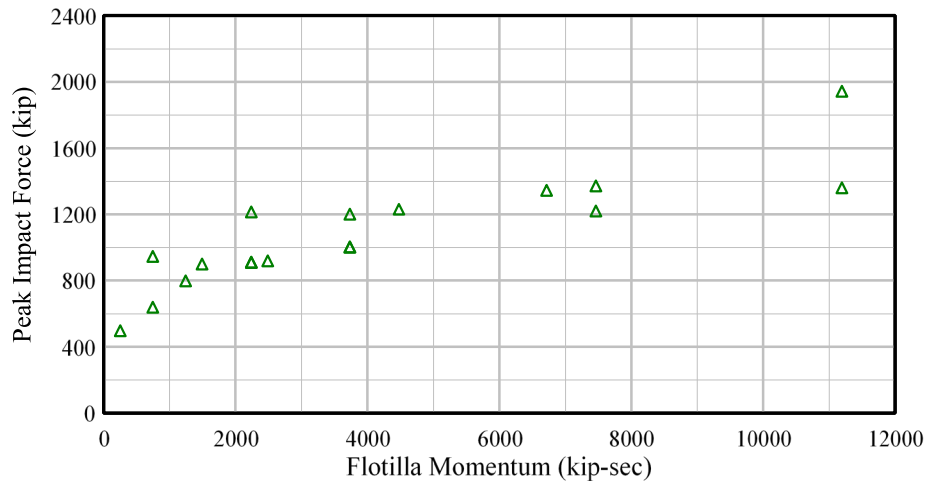


Figure 6.13. Peak Impact Force Results for Sloped-V Bullnose (18 Cases)

6.3.4. Empirical Load Prediction Model. The mechanics of barge impacts with vertical face semi-circular bullnoses differ significantly from impacts against the 2:1 sloped-V bullnose. As noted in section 6.3.1, the sloped face of the bullnose allows the impacting barge bow to partially slide up the structure. Sliding reduces the abruptness with which the barge flotilla is halted during collision and simultaneously dissipates energy. Both effects tend to lead to reductions in impact force.

6.3.4.1. Further, sloped-V bullnoses induce deformation zones in impacting barge bows that differ from those produced during impacts with semi-circular bullnoses. Consequently, relationships between momentum, bow deformation, and impact force for the sloped-V differ from those associated with semi-circular bullnoses.

6.3.4.2. For these reasons, independent empirical load prediction expressions are developed for sloped-V bullnoses using the data summarized in Figure 6.13. For consistency with semi-circular bullnoses, the sloped-V impact load prediction model is formulated as a bilinear function (Figure 6.14). However, since only a single slope-V configuration is considered, the bilinear fit is defined as independent of ridge diameter.

6.3.4.3. This leads to the following bilinear functional form:

$$F = \begin{cases} S_1 \cdot (m \cdot v) & \text{if } m \cdot v \leq (F_{12}/S_1) \\ F_{12} + S_2 \cdot (m \cdot v - (F_{12}/S_1)) & \text{otherwise} \end{cases} \quad (6.5)$$

where F is the horizontal impact force. The terms F_{12} , S_1 , and S_2 are bilinear curve fitting parameters. The m term is the total mass of all barges in the flotilla. Flotilla impact velocity is given as v .

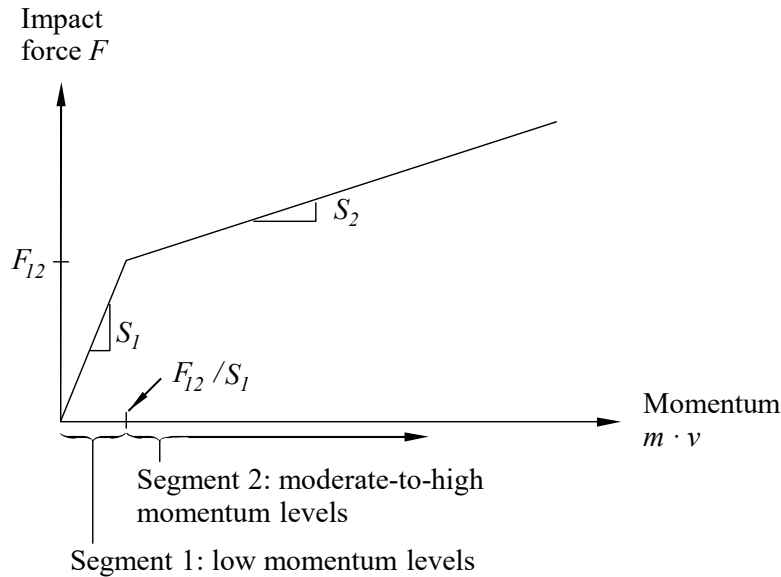


Figure 6.14. General Form of Bilinear Curve Fit Used for Sloped-V Bullnoses

6.3.4.4. As indicated in Figure 6.14, slope (S_1) of the first (low momentum) segment is considered constant for sloped-V bullnoses. Likewise, slope (S_2) of the second linear (moderate to high momentum) segment is also considered constant. An error minimization curve fitting procedure is employed to determine optimal values of F_{12} , S_1 , and S_2 in Equation 6.5. The curve fitting process consists of repeatedly evaluating Equation 6.5 using candidate coefficient values, flotilla mass, and velocity. Evaluations of impact force are then compared to respective (benchmark) data points from Table 6.3.

6.3.4.5. Candidate values for coefficients are iteratively modified until minimum error is achieved. In this way, numerical values are obtained for F_{12} , S_1 , and S_2 , result in the bilinear expression:

$$F = \begin{cases} 1.963 \cdot m \cdot v & \text{if } m \cdot v \leq 407 \text{ kip-sec} \\ 799 + 0.078 \cdot (m \cdot v - 407) & \text{otherwise} \end{cases} \quad (6.6)$$

where the threshold between low and medium to high levels of total flotilla momentum is identified as 407 kip-sec.

6.3.4.6. The confidence bounds are also established at confidence levels of 1-standard deviation (84.1%) and 2-standard deviations (97.7%) from the mean. Functionally, these bounds are given by:

$$F_{84.1\%} = \begin{cases} 2.197 \cdot m \cdot v & \text{if } m \cdot v \leq 410 \text{ kip-sec} \\ 900 + 0.087 \cdot (m \cdot v - 410) & \text{otherwise} \end{cases} \quad (6.7)$$

and:

$$F_{97.7\%} = \begin{cases} 2.394 \cdot m \cdot v & \text{if } m \cdot v \leq 414 \text{ kip-sec} \\ 991 + 0.099 \cdot (m \cdot v - 414) & \text{otherwise} \end{cases} \quad (6.8)$$

6.3.4.7. Comparisons of Simulated and Predicted Impact Forces. Use of the load prediction model for impacts on sloped-V bullnoses is illustrated in Figure 6.15. Specifically, peak impact forces listed in Table 6.3 are compared to respective evaluations of the mean-value best fit curve Equation 6.6. Reasonable agreement is found between the empirical load prediction model and simulated force data regardless of the associated flotilla momentum. Additional comparisons of the load prediction model to various sloped-V bullnose impact datasets are provided in Consolazio et al. (2014).

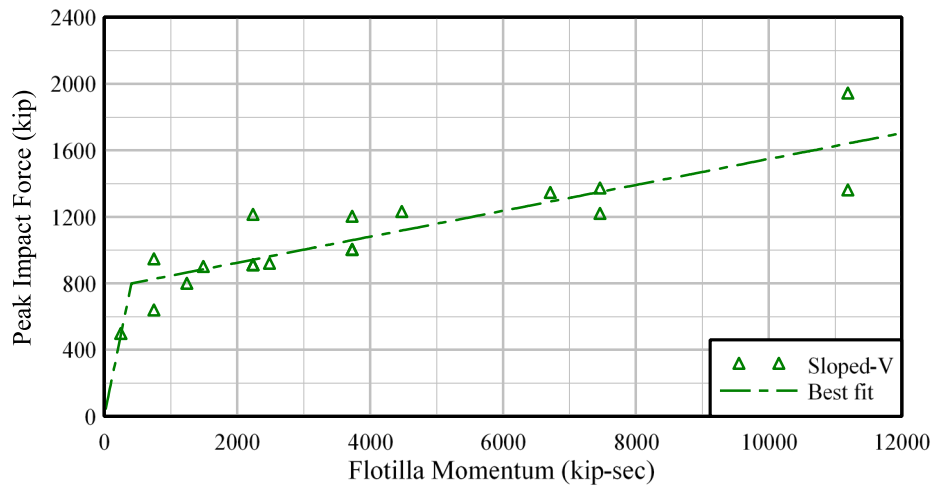


Figure 6.15. Comparison of Sloped-V (2:1) Bullnose Data and Load Prediction Model

6.4. Dam Piers.

6.4.1. Overview.

6.4.1.1. USACE maintains a substantial inventory of dam structures that are vulnerable to barge impacts, particularly during flood-stage flow conditions. An example dam structure (including dam piers) is shown in Figure 6.16. Impacts on other dam portions such as Tainter gates are focused on in Chapter 7. Past incidents involving barge flotillas losing control, breaking up, and impacting dam piers have also led to extensive (and costly) damage. Collisions with dam piers therefore pose potential risks with respect to the structural integrity of dam structures.



Figure 6.16. Cannelton Locks and Dam on the Ohio River
(Source: Wikimedia Commons, Photo by Sarah Ewart)

6.4.1.2. Estimating impact loads for structural design of dam piers is thus an important component of risk management for USACE. Quantifying such loads using full-scale experimental testing would be costly, complex, and potentially impractical. High-resolution FE modeling and collision simulations are alternatively used to efficiently assess relevant impact forces encompassing various conditions.

6.4.2. Background. In Consolazio and Han (2018), high-resolution FE models of barge flotillas were merged with a representative dam pier model. An extensive set of collision simulations were subsequently conducted. Included among the set of simulations were head-on and oblique barge bow-pier impacts for various flotilla sizes (1x1, 2x1 in side-by-side). Also, perfectly side-on impact simulations (barge sidewall to dam pier) were conducted. Impact velocities ranging from 4 ft/sec to 6 ft/sec were included across the range of collision scenarios investigated.

6.4.2.1. The barge bow-pier simulations revealed—for impact at angles of 0° , 30° , and 60° —that the head-on (0°) condition produced maximum impact forces. For non-zero (oblique) impact angles, a portion of the flotilla kinetic energy was consumed in rotationally accelerating the impacting barge. Consequently, less energy was available to deform the barge bow and generate impact load. Also, for head-on cases, increasing the number of barges from 1x1 to 2x1 (side-by-side) had negligible effect on peak force.

6.4.2.2. Supplementary barge-pier sidewall (90°) impact analyses produced force levels that were within 10% of those produced by head-on (0°) conditions. Producing maximum sidewall impact forces, however, required careful and improbable barge positioning. Specifically, to prevent rotation, the barge center of gravity had to be positioned along the axis of the pier. Such positioning was deemed statistically unlikely to occur. Further, any deviation from this critical positioning would tend to reduce the magnitude of sidewall (90°) impact force generated.

6.4.2.3. Moreover, with only moderate deviations from the critical position, the barge would simultaneously contact multiple adjacent piers, resulting in load-sharing. Thus, among all collision scenarios considered, head-on conditions were found to produce controlling levels of impact force.

6.4.3. Empirical Load Prediction Model.

6.4.3.1. Consolazio and Han (2018) noted that head-on barge-pier impact scenarios were very similar to head-on barge-bullnose impact scenarios. Specifically, similarities are expected between maximum impact forces obtained from head-on collisions on dam piers and semi-circular bullnoses (from section 6.2).

6.4.3.2. In Table 6.4, impact forces from head-on barge-pier simulations are compared to predictions from the semi-circular bullnose empirical model (Equation 6.2). As expected, the comparisons indicate favorable agreement. Consequently, it is recommended that the empirical semi-circular bullnose impact load prediction equations be utilized to quantify dam pier impact forces. This recommendation pertains to dam piers with approximately semi-circular impact surface geometry.

Table 6.4
Comparison of Head-On Dam Pier Impact Forces (Consolazio and Han 2018) and Semi-Circular Bullnose Load Prediction Model

Impact speed (ft/sec)	Impact momentum (kip-sec)	Peak force from dam-pier impact simulation (kip)	Force from semi-circular bullnose Equation 6.2 (kip)	Differences of impact force
4	497	1,172	1,326	13%
6	746	1,401	1,334	5%

6.5. Examples Using Empirical Equations.

6.5.1. Overview. Section 6.6 presents six deterministic examples of collision scenarios on a bullnose structure. Three examples pertain to flotilla collisions on semi-circular bullnose structures (section 6.5.2), and three pertain to sloped-v configurations (section 6.5.3). The examples progress from less severe to more severe with respect to both flotilla size (mass) and impact velocity. Although these examples are deterministic, the scenarios represent increasingly rare collision events.

6.5.2. Semi-Circular Bullnose Structures. A deterministic impact scenario, associated with usual conditions, is presented for semi-circular bullnose structures in section 6.5.2.1. Unusual and extreme impact scenarios involving semi-circular bullnose structures are focused on in section 6.5.2.2 and section 6.5.2.3, respectively.

6.5.2.1. Usual.

6.5.2.1.1 Figure 6.17 shows a plan-view schematic of the deterministic example for usual impact conditions. A fully loaded 1x1 flotilla (single barge) is selected for this scenario, weighing 2,000 short tons (10.4 kip-sec²/in. mass). The barge has an initial velocity of 2 ft/sec and impacts a 35-ft semi-circular bullnose in a head-on manner.

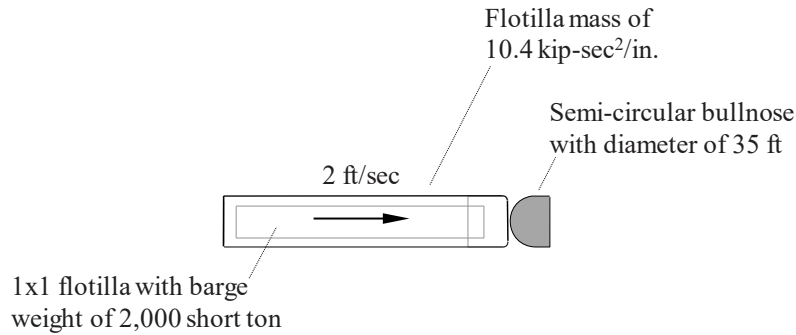


Figure 6.17. Deterministic (Usual) Impact Scenario on Semi-Circular Bullnose

6.5.2.1.2 Relevant parameters associated with the deterministic (usual) impact scenario are listed in Table 6.5. Flotilla (single barge) mass (m), impact velocity (v), and bullnose diameter (35 ft) are used in evaluating Equation 6.2. Total flotilla momentum ($m \cdot v$) is 249 kip-sec in this example. The momentum is less than the 320 kip-sec listed in Equation 6.2. Therefore, the design impact force, associated with segment 1 of Figure 6.7, for the (deterministic) usual impact condition is 1,026 kip.

Table 6.5
System Parameters for Deterministic (Usual) Impact Scenario on Semi-Circular Bullnose

Parameter Description	Value	Units
Flotilla columns	1	N/A
Flotilla rows	1	N/A
Weight per barge	2,000	short tons
Flotilla mass, m	10.4	kip-sec ² /in.
Impact velocity, v	2	ft/sec
Impacted surface diameter	35	ft
Usual Impact Force	1,026	kip

6.5.2.2. Unusual.

6.5.2.2.1 Figure 6.18 depicts a plan-view schematic of the deterministic example for unusual impact conditions. A fully loaded 3x3 flotilla is selected for this scenario, with each barge weighing 2,000 short tons (10.4 kip-sec²/in. mass). The total flotilla mass is 93.2 kip-sec²/in, and the flotilla is assigned an initial velocity of 2 ft/sec. Impact occurs in a head-on manner on a 35-ft semi-circular bullnose structure.

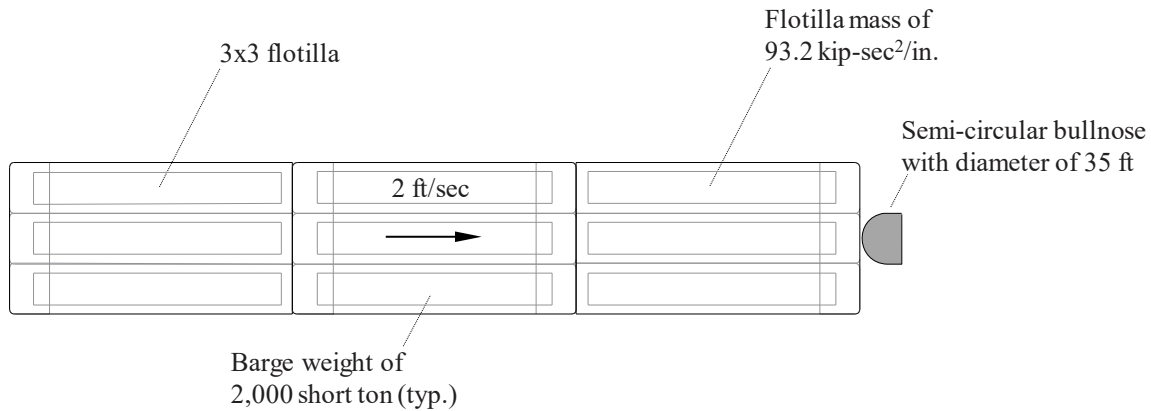


Figure 6.18. Deterministic (Unusual) Impact Scenario on Semi-Circular Bullnose

6.5.2.2.2 Parameters associated with the deterministic (unusual) impact scenario are given in Table 6.6. The 3x3 flotilla mass (m), impact velocity (v), and impacted bullnose diameter (35 ft) are used in evaluating Equation 6.2. Total flotilla momentum ($m \cdot v$) for this scenario is 2,238 kip-sec. This level of momentum exceeds the 320 kip-sec from Equation 6.2. Therefore, the design impact force, associated with segment 2 of Figure 6.7, for the (deterministic) unusual impact condition is 1,452 kip.

Table 6.6
System Parameters for Deterministic (Unusual) Impact Scenario on Semi-Circular Bullnose

Parameter Description	Value	Units
Flotilla columns	3	N/A
Flotilla rows	3	N/A
Weight per barge	2,000	short tons
Flotilla mass	93.2	kip-sec ² /in.
Impact velocity	2	ft/sec
Impacted surface diameter	35	ft
Unusual Impact Force	1,452	kip

6.5.2.3. Extreme.

6.5.2.3.1 A plan-view schematic of the deterministic example for extreme impact conditions is given in Figure 6.19. Here, a fully loaded 3x5 flotilla is considered, with each barge weighing 2,000 short tons (10.4 kip-sec²/in. mass). Total flotilla mass in this case is 155.4 kip-sec²/in, and the flotilla is assigned an initial velocity of 6 ft/sec. Head-on impact occurs against a 35-ft semi-circular bullnose structure.

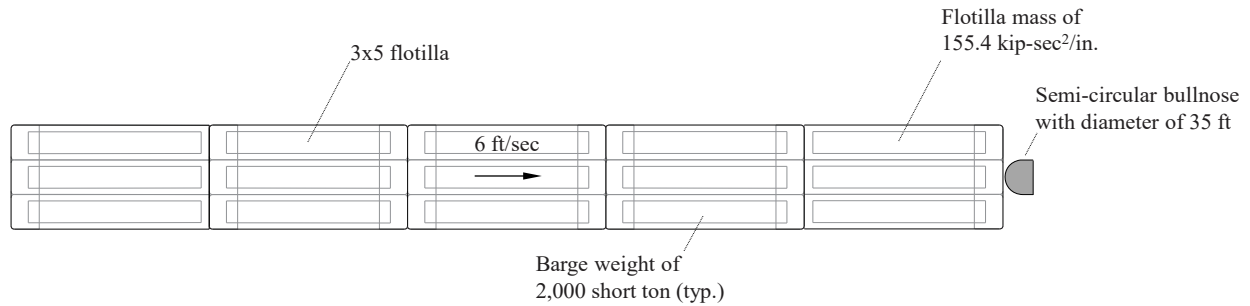


Figure 6.19. Deterministic (Extreme) Impact Scenario on Sloped-V (2:1) Bullnose

6.5.2.3.2 Parameters associated with the deterministic (extreme) impact scenario are given in Table 6.7. Flotilla mass (m), impact velocity (v), and impacted bullnose diameter (35 ft) are all used in evaluating Equation 6.2. The total flotilla momentum ($m \cdot v$) for this scenario is 11,189 kip-sec. This level of momentum exceeds the 320 kip-sec from Equation 6.2. Therefore, the design impact force, associated with segment 2 of Figure 6.7, for the (deterministic) extreme impact condition is 2,062 kip.

Table 6.7
System Parameters for Deterministic (Extreme) Impact Scenario on Semi-Circular Bullnose

Parameter Description	Value	Units
Flotilla columns	5	N/A
Flotilla rows	3	N/A
Weight per barge	2,000	short tons
Flotilla mass	155.4	kip-sec ² /in.
Impact velocity	6	ft/sec
Impacted surface diameter	35	ft
Extreme Impact Force	2,062	kip

6.5.3. Sloped-V Bullnose Structures. A deterministic impact scenario pertaining to sloped-V bullnose structures, under usual conditions, is presented in section 6.5.3.1. Counterparts for unusual and extreme impact conditions are focused on in section 6.5.3.2 and section 6.5.3.3, respectively.

6.5.3.1. Usual.

6.5.3.1.1 Figure 6.20 shows a plan-view schematic of the deterministic example for usual impact conditions. A fully loaded 1x1 flotilla (single barge) is selected for this scenario, weighing 2,000 short tons (10.4 kip-sec²/in. mass). The barge has an initial velocity of 2 ft/sec and impacts a sloped-V (2:1) bullnose in a head-on manner.

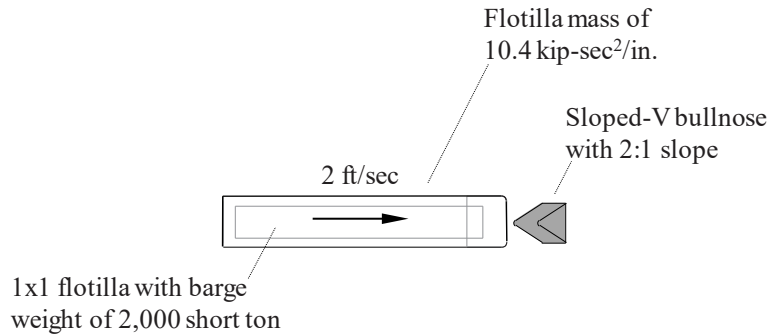


Figure 6.20. Deterministic (Usual) Impact Scenario on Sloped-V (2:1) Bullnose

6.5.3.1.2 Relevant parameters associated with the deterministic (usual) impact scenario are listed in Table 6.8. Flotilla (single barge) mass (m) and impact velocity (v), and no other parameters, are used in evaluating Equation 6.6. Total flotilla momentum ($m \cdot v$) is 249 kip-sec in this example. The momentum is less than the 407 kip-sec listed in Equation 6.6. Therefore, the design impact force, associated with segment 1 of Figure 6.14, for the (deterministic) usual impact condition is 488 kip.

Table 6.8
System Parameters for Deterministic (Usual) Impact Scenario on Sloped-V (2:1) Bullnose

Parameter Description	Value	Units
Flotilla columns	1	N/A
Flotilla rows	1	N/A
Weight per barge	2,000	short tons
Flotilla mass	10.4	kip-sec ² /in.
Impact velocity	2	ft/sec
Usual Impact Force	448	kip

6.5.3.2. Unusual.

6.5.3.2.1 Figure 6.21 shows a plan-view schematic of the deterministic example for unusual impact conditions. A fully loaded 3x3 flotilla is selected for this scenario, with each barge weighing 2,000 short tons (10.4 kip-sec²/in. mass). The total flotilla mass is 93.2 kip-sec²/in, and the flotilla is assigned an initial velocity of 2 ft/sec. Impact occurs in a head-on manner on a sloped-V (2:1) bullnose structure.

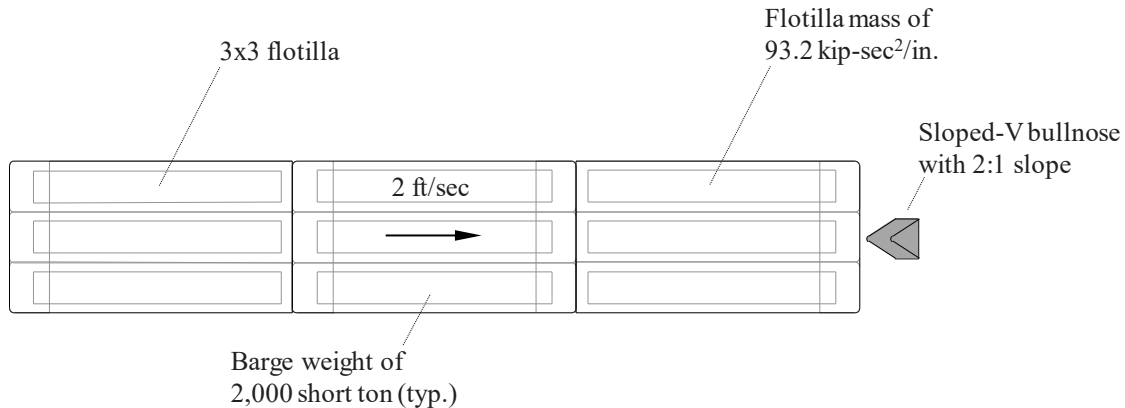


Figure 6.21. Deterministic (Unusual) Impact Scenario on Sloped-V (2:1) Bullnose

6.5.3.2.2 Parameters associated with the deterministic (unusual) impact scenario are given in Table 6.9. The 3x3 flotilla mass (m) and impact velocity (v) are used in evaluating Equation 6.6. Total flotilla momentum ($m \cdot v$) for this scenario is 2,238 kip-sec. This level of momentum exceeds the 407 kip-sec from Equation 6.6. Therefore, the design impact force, associated with segment 2 of Figure 6.14, for the (deterministic) unusual impact condition is 942 kip.

Table 6.9
System Parameters for Deterministic (Unusual) Impact Scenario on Sloped-V (2:1)

Parameter Description	Value	Units
Flotilla columns	3	N/A
Flotilla rows	3	N/A
Weight per barge	2,000	short tons
Flotilla mass	93.2	kip-sec ² /in.
Impact velocity	2	ft/sec
Unusual Impact Force	942	kip

6.5.3.3. Extreme.

6.5.3.3.1 A plan-view schematic of the deterministic example for extreme impact conditions is given in Figure 6.22. Here, a fully loaded 3x5 flotilla is considered, with each barge weighing 2,000 short tons (10.4 kip-sec²/in. mass). Total flotilla mass in this case is 155.4 kip-sec²/in, and the flotilla is assigned an initial velocity of 6 ft/sec. Head-on impact occurs against a sloped-V (2:1) bullnose structure.

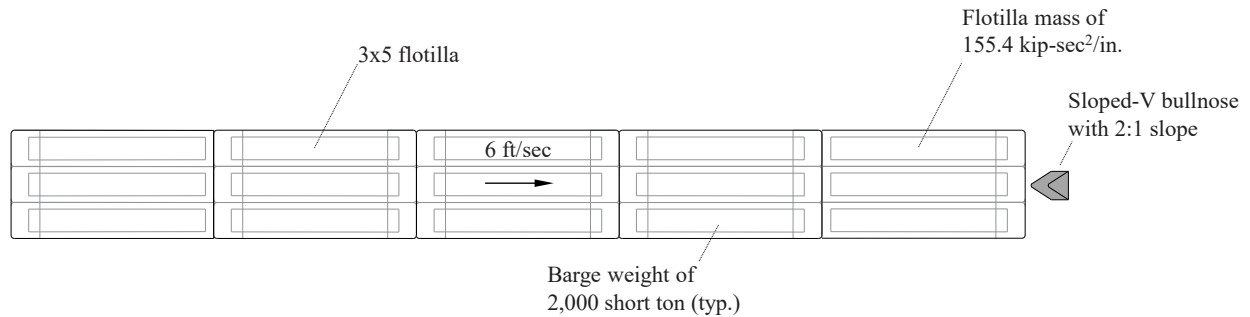


Figure 6.22. Deterministic (Extreme) Impact Scenario on Sloped-V (2:1) Bullnose

6.5.3.3.2 Parameters associated with the deterministic (extreme) impact scenario are given in Table 6.10. Flotilla mass (m) and impact velocity (v) are used in evaluating Equation 6.6. The total flotilla momentum ($m \cdot v$) for this scenario is 11,189 kip-sec. This level of momentum exceeds the proportional threshold of 407 kip-sec from Equation 6.6. Therefore, the design impact force, associated with segment 2 of Figure 6.14, for the (deterministic) extreme impact condition is 1,640 kip.

Table 6.10
System Parameters for Deterministic (Extreme) Impact Scenario on Sloped-V (2:1) Bullnose

Parameter Description	Value	Units
Flotilla columns	3	N/A
Flotilla rows	5	N/A
Weight per barge	2,000	short tons
Flotilla mass	155.4	kip-sec ² /in.
Impact velocity	6	ft/sec
Extreme Impact Force	1,640	kips

6.6. Complete Design Example for Semi-Circular Bullnose. This example is for the design of a 35-ft diameter bullnose structure for a new lock on the Ohio River. Based on present traffic predictions and navigation model testing at ERDC, a 15-barge tow and input parameters selected for the usual, unusual, and extreme load cases are as follows:

6.6.1. Deterministic Load Cases.

6.6.1.1. Usual load case:

$$\begin{aligned}
 V &= 2 \text{ ft/sec} \\
 \text{Diameter} &= 35 \text{ ft} \\
 W_{\text{barge}} &= 30,000 \text{ short tons} \\
 &= 60,000 \text{ kips}
 \end{aligned}$$

Checking, $M^*v = 60,000/32.2 * 2 = 3,726.71$ kip-sec

Since $3,726.71$ kip-sec $>$ 320 kip-sec, use second line segment

$$\begin{aligned} F &= 1,321 + (0.003 + 0.001863D) * (M^*v - 320) \\ &= 1,321 + (0.003 + 0.001863*35) * (3,726.71 - 320) \\ &= 1,321 + (0.068) * (3,406.71) \\ &= 1,552.66 \text{ kips} \end{aligned}$$

6.6.1.2. Unusual load case:

$$V = 4 \text{ ft/sec}$$

$$\text{Diameter} = 35 \text{ ft}$$

$$W_{\text{barge}} = 30,000 \text{ short tons}$$

Checking, $M^*v = 60,000/32.2 * 4 = 7,453.42$ kip-sec

Since $7,453.42$ kip-sec $>$ 320 kip-sec, use second line segment

$$\begin{aligned} F &= 1,321 + (0.003 + 0.001863D) * (M^*v - 320) \\ &= 1,321 + (0.003 + 0.001863*35) * (7,453.42 - 320) \\ &= 1,321 + (0.068) * (7,133.42) \\ &= 1,806.07 \text{ kips} \end{aligned}$$

6.6.1.3. Extreme load case:

$$V = 6 \text{ ft/sec}$$

$$\text{Diameter} = 35 \text{ ft}$$

$$W_{\text{barge}} = 30,000 \text{ short tons}$$

Checking, $M^*v = 60,000/32.2 * 6 = 11,180.12$ kip-sec

Since $11,180.12$ kip-sec $>$ 320 kip-sec, use second line segment

$$\begin{aligned} F &= 1,321 + (0.003 + 0.001863D) * (M^*v - 320) \\ &= 1,321 + (0.003 + 0.001863*35) * (11,180.12 - 320) \\ &= 1,321 + (0.068) * (10,860.12) \\ &= 2,059.49 \text{ kips} \end{aligned}$$

6.6.1.4. Table 6.11 shows a summary based on calculating the deterministic calculations defined in the flowchart in Chapter 2.

Table 6.11
Design Load Cases from Deterministic Calculations

Load Case	Force (kip)
Usual	1553
Unusual	1806
Extreme	2059

6.6.2. Probabilistic Example.

6.6.2.1. This example is for the design of a 35-ft diameter bullnose for a new lock on the Ohio River. Based on present traffic predictions and navigation model testing at ERDC, a 15-barge tow and input parameters selected for probabilistic analysis are shown in Table 6.12.

Table 6.12
Design Load Cases from Deterministic Calculations

Parameter	Distribution	E(x)	$\sigma(x)$	Min(x)	Max(x)
Velocity (ft/sec)	Lognormal	2	1	1	7
Weight – entire flotilla (kips)	Constant	60,000	-	-	-
Diameter – (ft)	Constant	35	-	-	-

6.6.2.2. The probabilistic model run was completed using Monte Carlo Simulation with 50,000 iterations. Return periods for this site were selected for the usual (2 year), unusual (150 year), and extreme (1000 year) load cases and are shown in Table 6.13.

Table 6.13
Design Load Cases from Probabilistic Calculations

Load Case	Force (kip)
Usual – 2 year	1541
Unusual – 150 year	1752
Extreme – 1000 year	1900

Chapter 7 Steel Structures

7.1. General.

7.1.1. This chapter focuses on numerical modeling and empirical load predictions for collisions between barges and steel gates in the USACE navigation infrastructure. Collisions involving flotillas and two types of steel gate structures are addressed. Miter gates, which are generally constructed at the terminating ends of lock chambers are considered. In addition, documentation is provided for steel gate structures that span between dam piers (i.e., Tainter gates).

7.1.2. Please note that the barge impact loads estimated in this chapter are for unusual and extreme loading as defined in Chapter 2. Usual impacts to both miter gates, Tainter gates, and lock dewatering structures may be considered at reduced levels if justification is warranted.

7.1.3. Discussed herein are high-resolution FE model components comprising horizontally framed miter gate, and separately, Tainter gate structures. Experimental impacts to vertically framed miter gates are discussed as well. Representative gate configurations are selected from existing USACE navigation infrastructure, and key aspects of the physical configurations are documented. In the following, high-resolution barge flotilla FE models (recall Chapter 3) are combined with each of the gate FE models. A range of impact simulations are then conducted. Numerous collision scenarios are analyzed, with variations in flotilla size, impact velocity, and flotilla-gate orientations.

7.1.4. Empirical load prediction models are developed for each type of gate structure by correlating collision-scenario parameters with peak impact forces. Deterministic design examples are provided for usual, unusual, and extreme barge impact conditions involving both horizontally framed miter and Tainter gate structures. Analogous, probabilistic design examples are reported as well.

7.1.5. Scope. The material in this chapter has been organized into following sections as:

7.1.5.1. Section 7.2 documents physical configuration details and FE model components of horizontally framed miter gates. Also, listings of peak impact forces obtained from a collection of collision simulations are provided. Further, an empirical load prediction model is detailed. Deterministic and probabilistic design examples for miter gates (three examples per structure type) are provided in section 7.2.

7.1.5.2. Section 7.3 discusses the full-scale experiment conducted on vertically framed miter gates and the resulting impact forces.

7.1.5.3. Section 7.4 includes physical and numerical (FE) representations of Tainter gates. Relevant listings of peak-force results and an empirical load model are presented for flotilla impacts on Tainter gates. Here, both the peak impact forces and the associated forces arising within Tainter gate trunnions are addressed. Deterministic design examples for Tainter gates (three examples per structure type) are provided in section 7.3.

7.1.5.4. For additional reference, Appendix I also gives lock dewatering examples for barge impact (center posts and bulkheads) and covers the FE analysis and application of the LODM defined in Chapter 5 to estimate accidental barge impact loads.

7.2. Miter Gates.

7.2.1. Overview.

7.2.1.1. Barge impacts on miter gates are focused on throughout section 7.2. In particular, modeling considerations for miter gates are documented in section 7.2.2. Section 7.2.3 introduces peak impact force results obtained from collision simulations between barge flotillas and miter gates. Observations related to the listings of peak impact forces are provided in section 7.2.4. Gate modeling and collision forces summaries provide context for development (via curve fitting) of the empirical load prediction model presented in section 7.2.5. Section 7.3 discusses the full-scale barge impact experiments at L&D 26 on vertically framed miter gates.

7.2.1.2. Background. A significant fraction of navigational locks operated by USACE use steel miter gates as hydraulic control structures. Horizontally framed gates resist water pressure by a series of horizontal girders that are supported by vertical posts at each end. The USACE inventory of miter gates currently in service are primarily horizontally framed in terms of structural configuration. However, vertically framed gates are still present at many older locks and these gates resist water pressure by a series of vertical girders supported at the top and bottom by horizontal girders. In these systems shown in Figure 7.1, hydrostatic and barge impact loads are transmitted from point(s) of application along miter gates and into lock walls. Loads applied directly to miter gates typically progress through horizontal girders, then to quoin blocks, and finally into the lock walls.

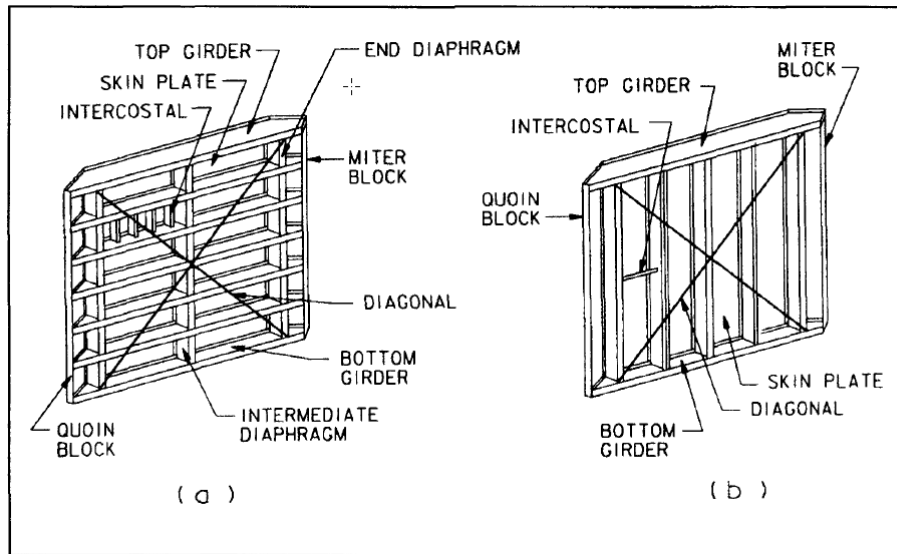


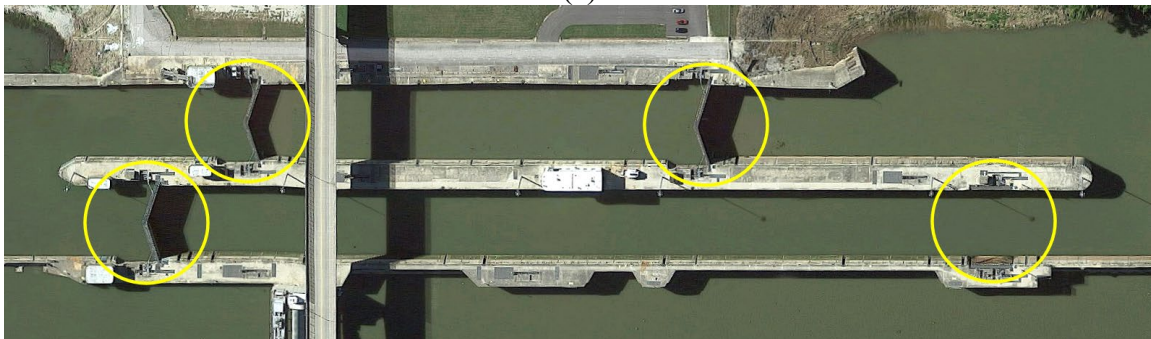
Figure 7.1. (a) Horizontal Framing (b) Vertical Framing (Chasten 1991)

7.2.1.2.1 When in the closed position, the two leaves of a miter gate form a three-hinged arch structure. Also, when closed, horizontal miter gates possess significant stiffness and strength compared to vertically framed miter gates, especially in terms of impact resistance. Chasten (1991) states that due to the greater rigidity, comparable cost, and superior resistance to barge impact of horizontally framed miter gates, vertically framed miter gates will not be used for future construction under normal circumstances.

7.2.1.2.2 To facilitate characterization of maximum barge impact forces that arise during barge-gate collisions, representative FE models of horizontal framed gates are developed in this chapter. Configurations modeled are selected from in-service USACE miter gates, namely, the horizontally framed gates at the Greenup Locks and Dam (Figure 7.2) on the Ohio River are modeled. In 2012, a construction project was completed in which the Greenup miter gates were replaced (Figure 7.3). Structural plans corresponding to the newly installed replacement miter gates were used for modeling and simulation purposes. Additional resources, such as excerpts of structural drawings and comprehensive details of the FE gate models, are provided in Consolazio and Han (2015).



(a)



(b)

Figure 7.2. Greenup Locks and Dam on the Ohio River: (a) Overview Photo; (b) Miter Gates: Three in Closed Position, One in Open Position (Source: Google Maps)



(a)



(b)

Figure 7.3. Replacement of Greenup Miter Gates in 2012: (a) Gate Leaf Being Lifted; (b) Gate Leaves Installed in Lock Chamber

7.2.2. Horizontally Framed Miter Gates.

7.2.3. Modeling Considerations. Modern miter gates found within USACE navigation structures are typically constructed as three-dimensional structural steel systems. Horizontally framed gates consist of steel girders, an array of stiffening diaphragms, intercostals, prestressed diagonals, and skin plates.

7.2.3.1. Concerning impacts between barge flotillas and miter gates, various impact conditions may be realized. For example, impact conditions may vary depending on the arrangement of barges in an impacting flotilla. Depending on the flotilla configuration, various points along the leading edge of the flotilla may contact impacted miter gates. Associated with points of contact are dynamic loads, which induce structural demands throughout gate components.

7.2.3.2. An FE model of the Greenup Locks and Dam miter gate is developed for assessing practical ranges of conceivable impact conditions. The high-resolution FE model of the gate structure, developed using LS-DYNA (LSTC 2014), contains approximately 380,000 shell elements. In this way, discrete representations of steel flanges, webs, vertical diaphragms, skin plates, stiffeners, intercostals, and fenders are included. All flanges, webs, diaphragms, and skin plates are meshed with sufficient resolution that local buckling can be properly represented. An inelastic, nonlinear material model corresponding to 50 ksi steel (A572 Grade 50) is used throughout the model.

7.2.3.3. Material Model. Per structural plans (see Consolazio and Han 2015), most of the miter gate is fabricated from A572 Grade 50 structural steel. A nonlinear constitutive relationship for A572 Grade 50 steel is therefore adopted (Figure 7.4) for use in FE gate modeling. Strain-rate sensitivity effects in constitutive modeling of the miter gate steel are also included.

7.2.3.3.1 Strain-rate effects are modeled in the same manner as previously described for the barge steel in Chapter 3. The Cowper-Symonds model is employed:

$$\frac{\sigma_{dynamic}^y}{\sigma_{static}^y} = \left[1 + \left(\frac{\dot{\epsilon}_{eff}^p}{C} \right)^{\frac{1}{P}} \right] \quad (7.1)$$

7.2.3.3.2 For mild steel, the terms C and P are taken as 40.4 sec^{-1} and 5.0 , respectively (Jones 1997). Figure 7.5 illustrates the relationship between effective plastic strain rate ($\dot{\epsilon}_{eff}^p$) and increase of dynamic yield stress, $\sigma_{dynamic}^y$. Here, the ordinate axis is normalized by the static yield stress, σ_{static}^y , which is assigned a magnitude of 50 ksi.

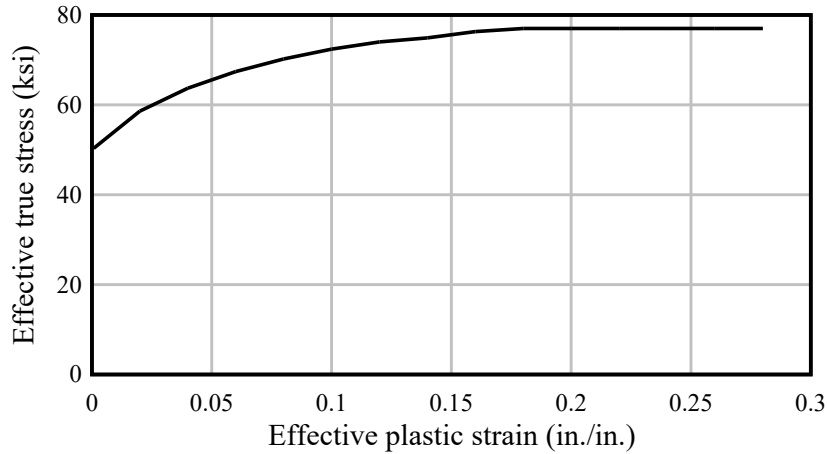


Figure 7.4. Constitutive Relationship for A572 Grade 50 Steel Used in Miter Gate Components

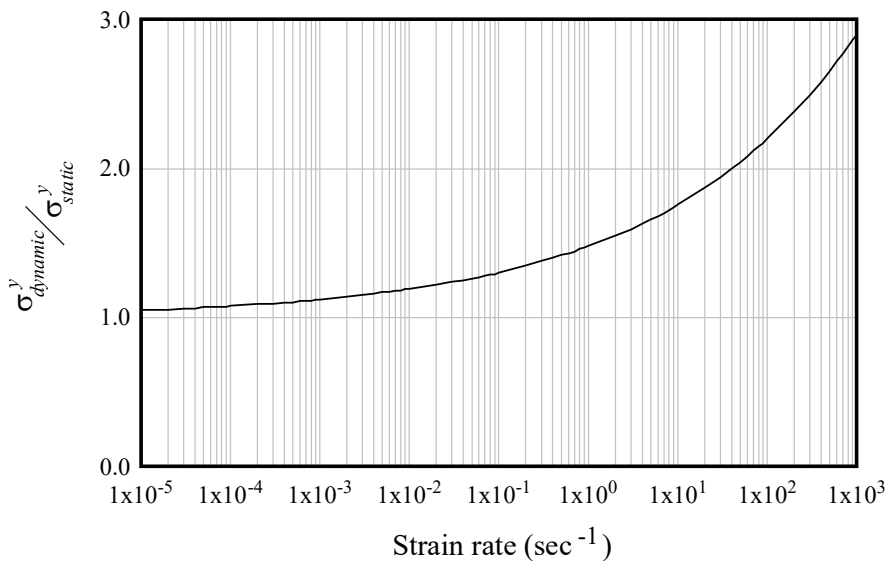


Figure 7.5. Strain-Rate Sensitivity of A572 Grade 50 Steel Used in Miter Gate Components (Based on Cowper-Symonds Model with $C = 40.4 \text{ sec}^{-1}$ and $P = 5$)

7.2.3.4. Component Modeling. The miter gate model developed in this study includes horizontal steel girders, vertical diaphragms, and an array of stiffening elements. Also included are skin plates, diagonals, intercostals, fender (protection) elements, and prestressed diagonals. Parametric modeling techniques are leveraged to build the model component-wise. Key stages comprising the model development process are visually presented in Figure 7.6.

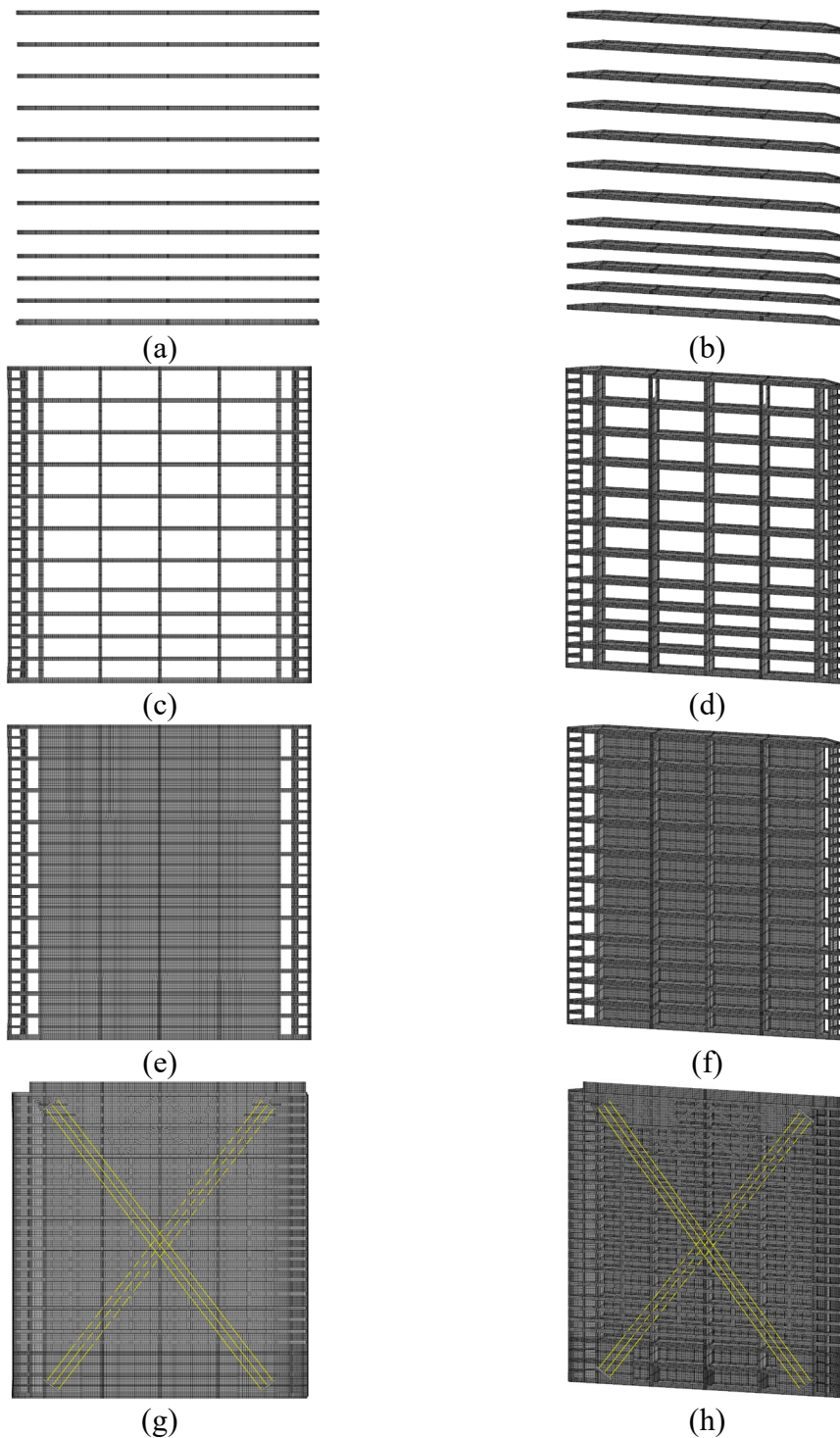


Figure 7.6. Miter Gate Modeling Stages: (a) Horizontal Girders, Elevation; (b) Horizontal Girders, Isometric View; (c) Vertical Girders, Elevation; (d) Vertical Girders, Isometric View; (e) Skin Plate, Elevation; (f) Skin Plate, Isometric View; (g) Intercostals, Prestressing Anchorage, Diagonals, Fenders, and Contact Blocks, Elevation; (h) Intercostals, Prestressing Anchorage, Diagonals, Fenders, and Contact Blocks, Isometric View

7.2.3.4.1 Structural components in the model are generally modeled using high-resolution meshes of 4-node fully integrated shell elements. Exceptions include the prestressing diagonal bars and fender elements, which are discussed later. Horizontal girders (Figure 7.7) are modeled using individual meshes (subsequently nodally merged together) for the flanges, webs, and stiffening elements. Similarly, vertical diaphragms (Figure 7.7), skin plates (Figure 7.8), and intercostals (Figure 7.8) are modeled using high-resolution shell element meshes.

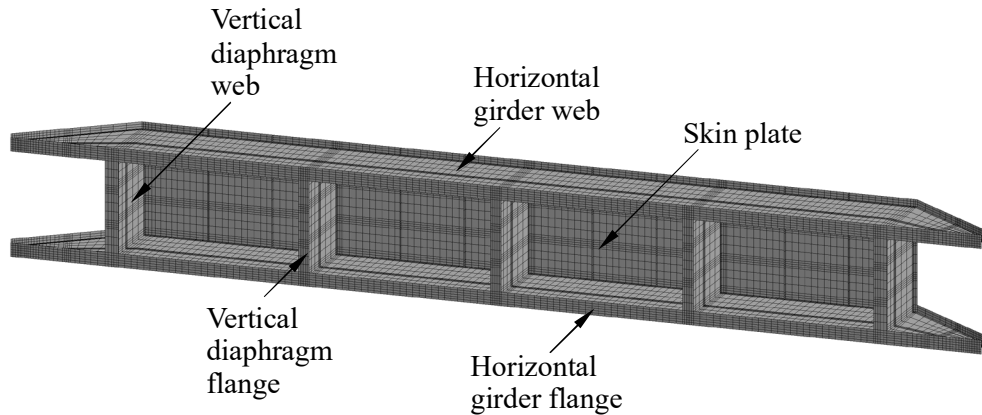
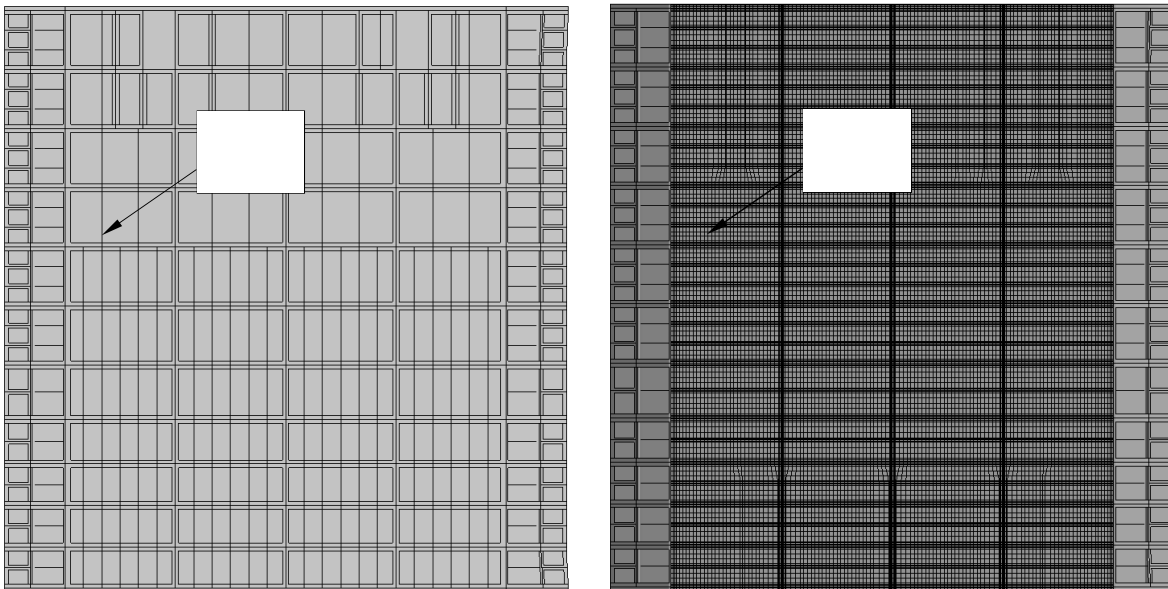


Figure 7.7. Isolated Cut-Out Portion of Miter Gate Model Showing Primary Structural Components



(a)

(b)

Figure 7.8. Skin Plate and Intercostal Plates: (a) Finite Element Model with Intercostal Lines; (b) Finite Element Model with Skin Plate Mesh

7.2.3.4.2 The mesh resolution of each primary structural component (Figure 7.9) is sufficiently refined for simulation of highly nonlinear behaviors. For example, localized inelastic buckling can occur in any component model portions during barge impact simulation.

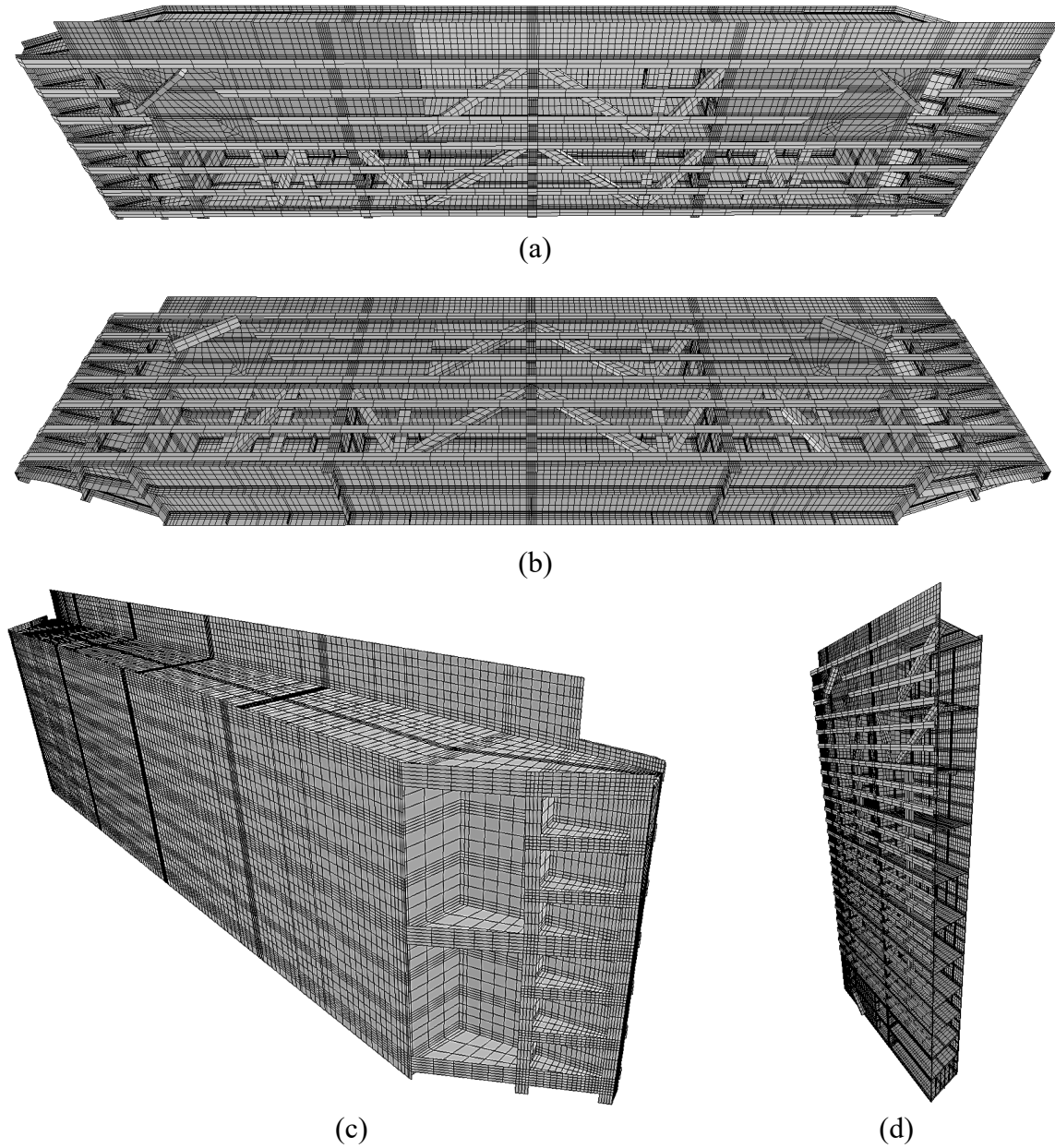


Figure 7.9. Sectional Views of Single Miter Gate Leaf Model Showing Mesh Resolution:
(a) Upper Portion of Leaf, Viewed from Above; (b) Upper Portion of Leaf, Viewed from Below;
(c) Upper Portion of Leaf, Viewed from Upstream Side; (d) Cross-Sectional View of Leaf,
Viewed from Downstream Side

7.2.3.5. Diagonal Prestressing Bars and Anchorages. Diagonal prestressing bars within miter gates serve both to resist gravity loads and facilitate gate alignment. Therefore, prestressing bars are included in each leaf of the miter gate model. On each leaf, and in each diagonal direction, three individual bars (Figure 7.10) are modeled. Each bar is fabricated from A572 Grade 60 steel and is rectangular in cross section. Bar cross-section dimensions are either 7 in. x 1.25 in. or 6 in. x 1.25 in.

7.2.3.5.1 Each prestressing bar is modeled using a single beam/cable element (LSTC 2014). This particular element formulation permits prestressing forces to be applied in a controlled, time-varying manner. The formulation also enables structural deformations due to prestressing to be automatically considered during the prestressing process.

7.2.3.5.2 For the practical range of collision scenarios considered, localized failure of the prestressing anchorage assemblies is not expected to occur. Consequently, such components are represented in the FE model using a simplified approach rather than the typical detailed meshing approach. At each end of each group of three diagonal bars, a single nodal rigid body (NRB) is used. The NRB acts to distribute prestressing forces over an appropriately sized portion of the gate mesh. The extent, or coverage, of each NRB is configured to approximate the footprint of the anchorage component plates. These include the associated end, stiffening, and gusset plate(s).

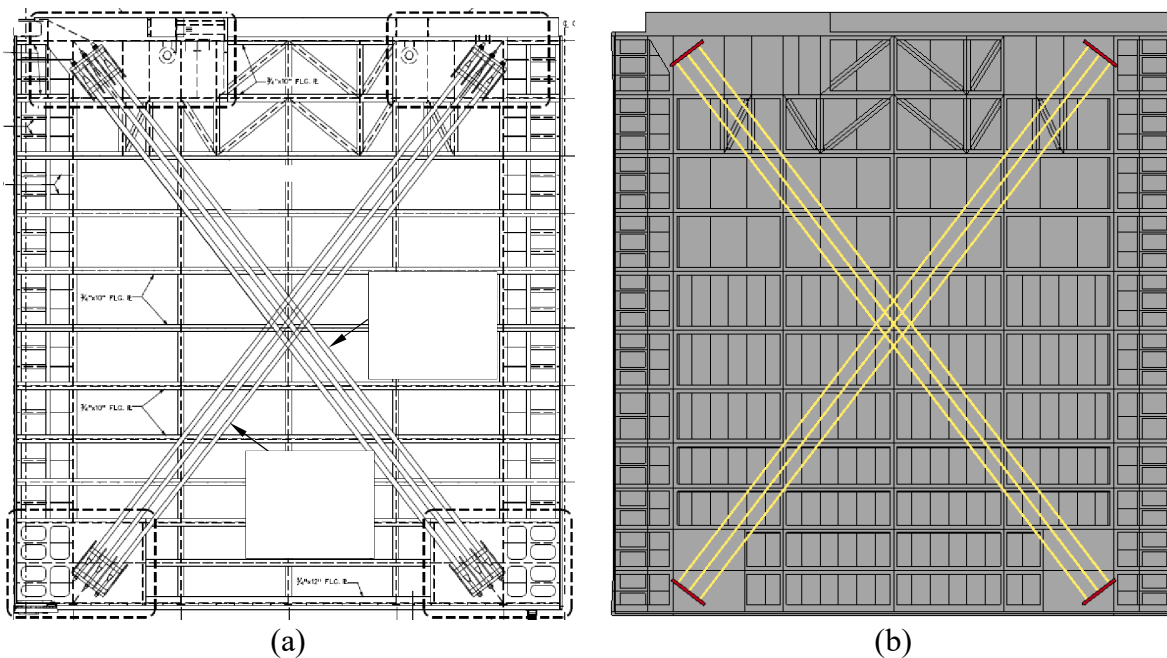


Figure 7.10. Prestressing Diagonals: (a) Structural Plans with Added Notes on Bar Sizes and Prestressing Forces; (b) Finite Element Model

7.2.3.6. Two-Leaf Miter Gate Model: Mirroring and Contact.

7.2.3.6.1 To efficiently construct the two-leaf miter gate model, one leaf is first modeled, and then mirrored. Stated alternatively, a copy of the first leaf is reflected to produce the majority of the required second leaf components. Adjustments in shell element normal vectors and contact segments are then made to the second leaf as needed. In total, the completed high-resolution two-leaf miter gate model (Figure 7.11a) consists of approximately 380,000 shell elements (Figure 7.11b).

7.2.3.6.2 Transmission of contact forces is modeled across the miter joint where the two leaves meet. More specifically, contact detection is defined between the miter blocks (i.e., steel plates) present at the miter ends of each leaf. Static and dynamic coefficients of friction of 0.55 and 0.45, respectively, are assigned. These values are assigned to represent frictional effects during the steel-to-steel contact.

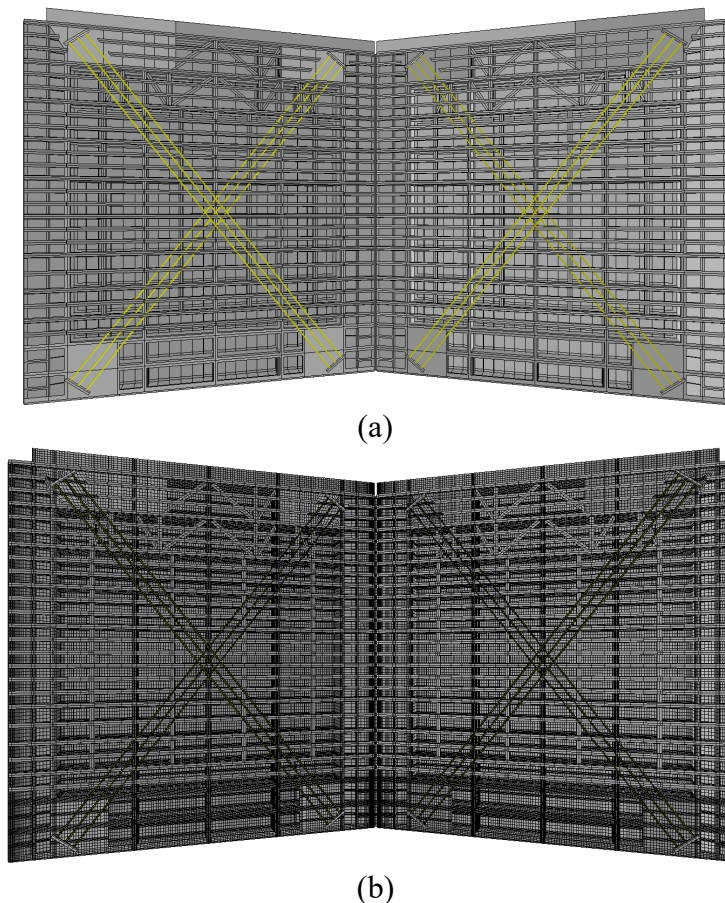


Figure 7.11. Two-Leaf Miter Gate Finite Element Model: (a) Geometry, with Mesh Resolution Omitted for Clarity; (b) High-Resolution Mesh of Approximately 380,000 Elements

7.2.3.7. Contact Detection Between Barge Model and Miter Gate Model. To quantify barge impact loads on the miter gate, the barge flotilla models described in Chapter 3 are utilized. That is, the miter gate and barge flotilla FE models are merged together. Contact detection is defined between the deformable bow of the impacting barge and appropriate zones of the miter gate. Only portions of the gate model that may potentially interact with the barge are included in the defined contact detection zones. Static and dynamic coefficients of friction of 0.55 and 0.45, respectively, are assigned. These values are selected to represent frictional forces that develop at the barge-to-gate (i.e., steel-to-steel) contact interfaces.

7.2.3.8. Boundary Conditions at Lock Wall. Miter gates can be positioned in closed, partially open, and fully open configurations. For open configurations, each gate leaf is attached to, and supported by, the lock wall through two mechanisms: a pintle ball at the base, and a gudgeon pin at the top (Figure 7.12a). The pintle ball restrains translation of the base of the leaf in all three directions (plan view, and vertical). Also, the pintle ball supports the leaf vertically and allows rotation about the vertical axis.

7.2.3.8.1 Similarly, the gudgeon pin restrains translation of the top of the leaf in two directions (plan view) rather than three. However, the gudgeon pin does not support the leaf vertically, and allows rotation about the vertical axis. Gravity loading acting on the gate is carried through vertical and horizontal forces at the pintle ball and gudgeon pin. In the closed configuration, hydrostatic and barge impact loads are carried into the lock wall through quoin contact (Figure 7.12a). Contact occurs between the quoin post of the miter gate leaf and quoin block embedded within the lock wall.

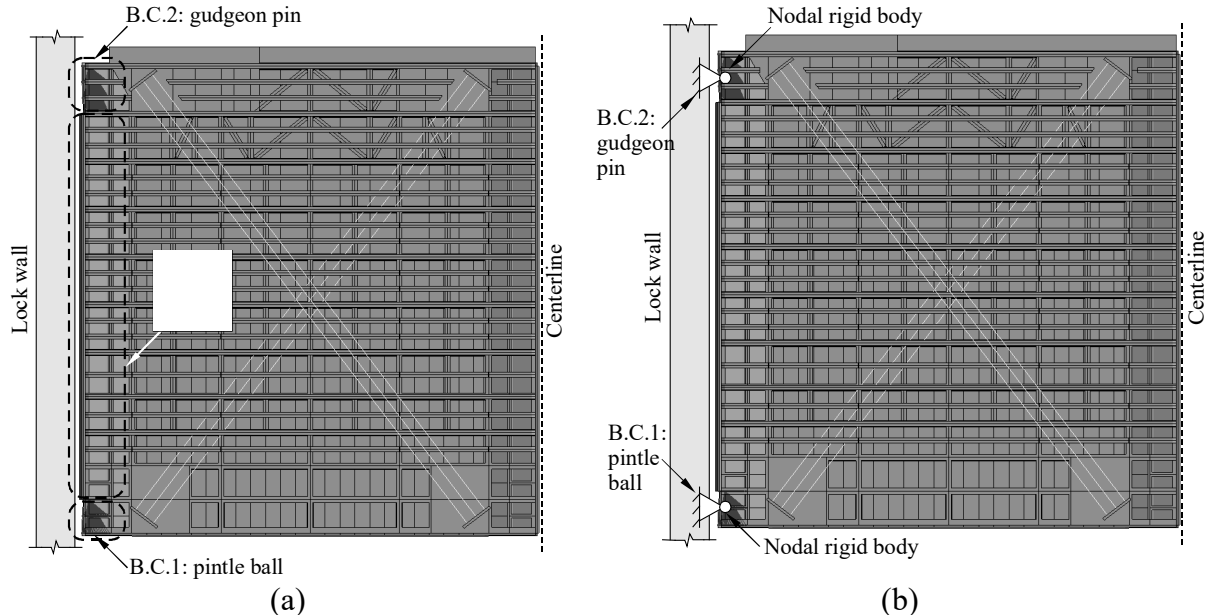


Figure 7.12. Boundary Conditions on Miter Gate Leaf FE Model: (a) Locations of Pintle Ball, Gudgeon Pin, and Quoin Contact; (b) Simplified Boundary Conditions

7.2.3.8.2 Boundary conditions (BCs) are applied to the FE model (Figure 7.12b) at the pintle ball and gudgeon pin. NRBs and suitable translational restraints (plan view: x-direction, y-direction, and vertical: z-direction) are utilized for these purposes. In particular, NRBs are utilized because detailed meshes of pintle balls and gudgeon pins are unnecessary for simulating flotilla-gate collisions.

7.2.3.8.3 Coverage areas for respective NRBs (pintle ball, gudgeon pin) are configured to approximately represent zones of influence of each component. Consolazio and Han (2015) reported that quoin contact between the gate and lock wall did not influence computed barge impact forces. As such, boundary conditions on the miter gate are further simplified (Figure 7.12a). More specifically, detection of quoin contact is omitted except for purposes of explicitly quantifying impact force sensitivity to such contact.

7.2.3.9. Additional Modeling Considerations. Additional considerations and techniques specific to modeling of the miter gate are detailed in Consolazio and Han (2015). Included therein is the manner by which pre-impact loading conditions are applied to the model. These include gravity, hydrostatic pressure, and diagonal prestressing. Also, verification of the high-resolution FE miter gate model under idealized lateral pressures is documented.

7.2.4. Impact Forces on Miter Gates. Listed in Table 7.1 are peak forces obtained from collision simulations between barge flotillas and miter gates. The simulations enable characterization of barge impact forces on miter gate structures and identification of factors that influence such forces. In total, barge flotilla models of varying sizes are combined with the miter gate FE model in 27 unique configurations. Results obtained from additional simulations are reported in Consolazio and Han (2015).

Table 7.1
Miter Gate Impact Conditions and Results (27 Cases)

Flotilla size	Impact speed (ft/sec)	Horizontal impact point	Vertical impact point	Max. impact force (kip)
1x3	0.2	Unsymmetric on leaf	Girder web	223
1x3	0.7	Unsymmetric on leaf	Girder web	572
1x3	1.2	Unsymmetric on leaf	Girder web	797
1x3	2.0	Unsymmetric on leaf	Girder web	1,109
1x3	4.0	Unsymmetric on leaf	Girder web	1,599
1x3	6.0	Unsymmetric on leaf	Girder web	1,503
1x3	1.2	Unsymmetric on leaf	Between webs	827
1x3	2.0	Unsymmetric on leaf	Between webs	1,202
1x3	1.2	Unsymmetric on leaf at mid-width	Girder web	818
1x3	2.0	Miter	Girder web	1,306
1x3	0.2	Unsymmetric on leaf	Top girder	120
1x3	0.7	Unsymmetric on leaf	Top girder	573
1x3	1.2	Unsymmetric on leaf	Top girder	809
1x3	2.0	Unsymmetric on leaf	Top girder	1,161
2x3	0.2	Miter	Girder web	396
2x3	0.7	Miter	Girder web	796
2x3	1.2	Miter	Girder web	1,111
2x3	2.0	Miter	Girder web	1,335
3x3	0.2	Miter	Girder web	472
3x3	0.7	Miter	Girder web	981
3x3	1.2	Miter	Girder web	1,425
3x3	2.0	Miter	Girder web	1,856
3x3	2.0	Miter	Between webs	1,578
3x5	0.2	Miter	Girder web	538
3x5	0.7	Miter	Girder web	1,132
3x5	1.2	Miter	Girder web	1,731
3x5	2.0	Miter	Girder web	2,086

7.2.4.1. Basic parameters varied include flotilla configuration (number of strings, rows; and thus, flotilla mass). Also varied are impact speed and impact point on the miter gate (varied horizontally and vertically). Each analyzed system model (i.e., each combined barge flotilla and miter gate model) is displayed (in plan view) in Figure 7.13.

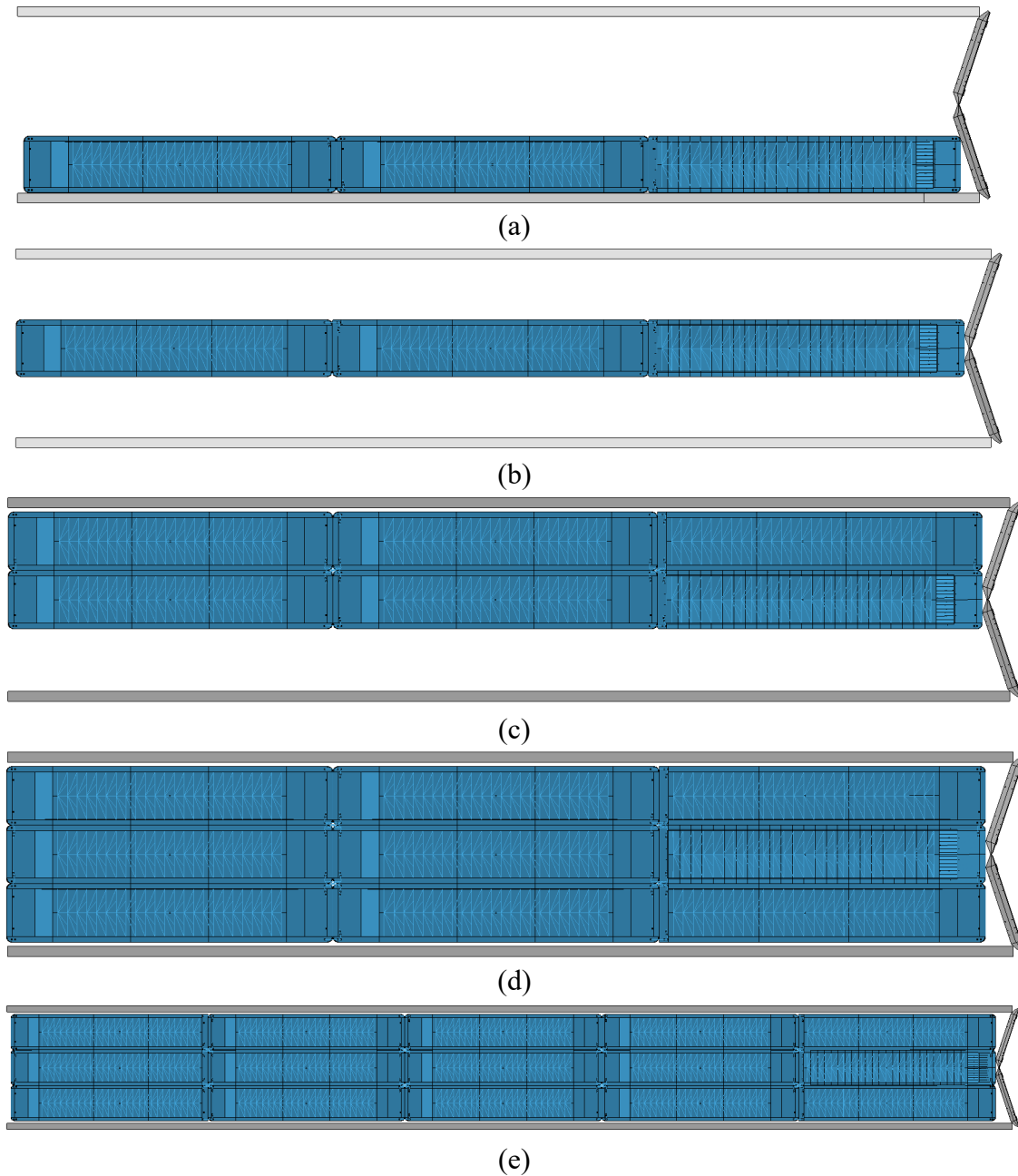


Figure 7.13. Plan View Renderings of System Models: (a) 1x3 Leaf Impact;
 (b) 1x3 Miter Impact; (c) 2x3 Miter Impact; (d) 3x3 Miter Impact;
 (e) 3x5 Miter Impact (Note: At Different Scale)

7.2.4.2. Peak forces (Table 7.1) are extracted from dynamic contact forces between the deformable impacting barge and the miter gate surface. As a precursor, all dynamic forces are low-pass filtered at approximately 10 Hz. The filter process ensures that impact forces are not unduly influenced by higher frequency oscillations present in the FE results. Also, all forces are resolved in the direction of barge travel.

7.2.5. Observations. Consider the unsymmetric, leaf impact of a 1x3 flotilla (Figure 7.14) at a practical upper-bound impact speed (2 ft/sec). Impact force results obtained from this simulation are plotted in Figure 7.15. After rising relatively rapidly initially, the impact force plateaus at approximately 0.5 sec. Zones of plastic strain are rendered for the barge and miter gate at various points in time in Figure 7.16. Propagation of plasticity dissipates at approximately 0.5 sec, consistent with the plateau in force level from Figure 7.15.

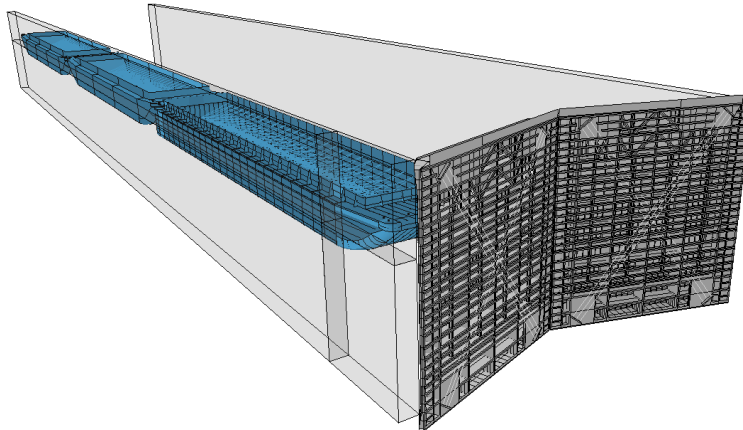


Figure 7.14. Model Used to Simulate Leaf Impact, 1x3 Barge Flotilla, 2 ft/sec

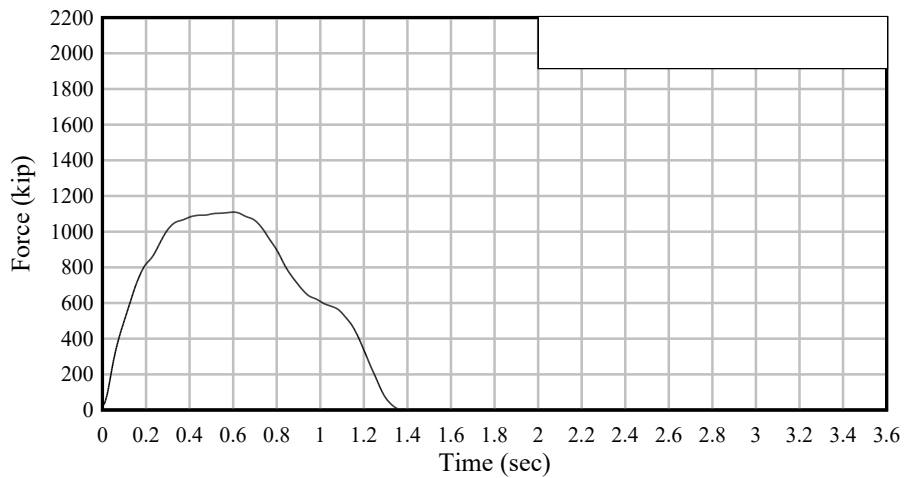


Figure 7.15. Simulation Results for Leaf Impact, 1x3 Barge Flotilla, 2 ft/sec

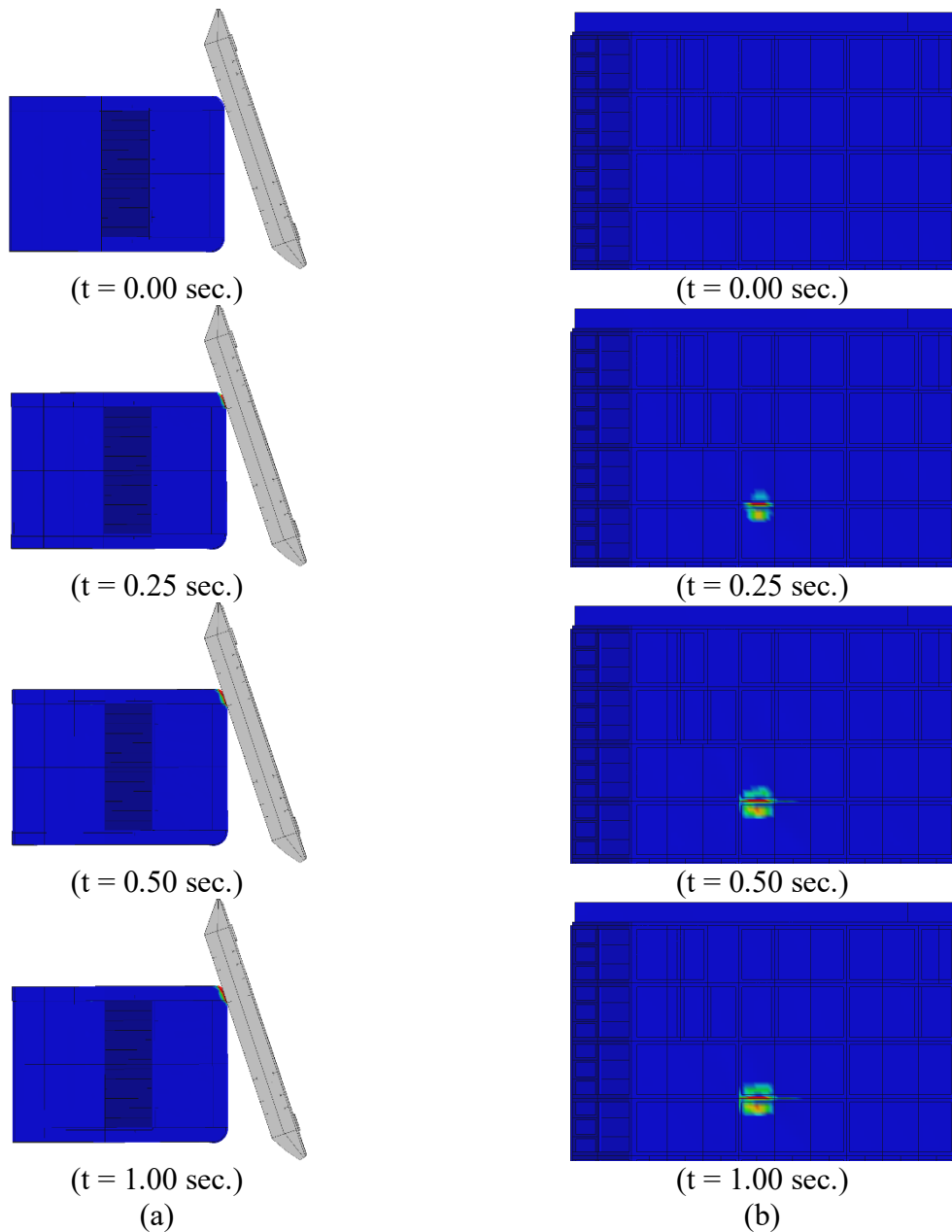


Figure 7.16. Plastic Strains for 1x3 – 2.0 ft/sec – Leaf Impact (Blue Signifies No Plastic Strain, Red Signifies Plastic Strain): (a) Barge Bow Plastic Strains; (b) Miter Gate Plastic Strains

7.2.5.1. Figure 7.17 shows a similar system model, but for a simulation of much higher momentum. Specifically, impact occurs symmetrically on a miter gate from a 3x5 flotilla, at an impact speed of 2 ft/sec. Impact force results obtained from this simulation are shown in Figure 7.19. The momentum level in this latter case is five times larger than that of the 1x3 leaf impact presented above. Even so, the maximum force level achieved (Figure 7.18) is only two times the force level reached in Figure 7.15.

7.2.5.2. Comparing results from these two cases reveals that flotilla-gate impact forces are not linearly correlated to momentum. This phenomenon is partially explained by examining the plastic strains generated during the 3x5 miter point impact (Figure 7.19). For the 3x5 miter impact, the zone of significant plastic deformation is at least 10 times wider than that of Figure 7.16. Additionally, significantly greater level of miter gate penetration into the barge bow is apparent for the 3x5 impact scenario. Conversely, gate plastic strains are not significantly greater in the 3x5 impact (Figure 7.19) versus the 1x3 impact (Figure 7.16).

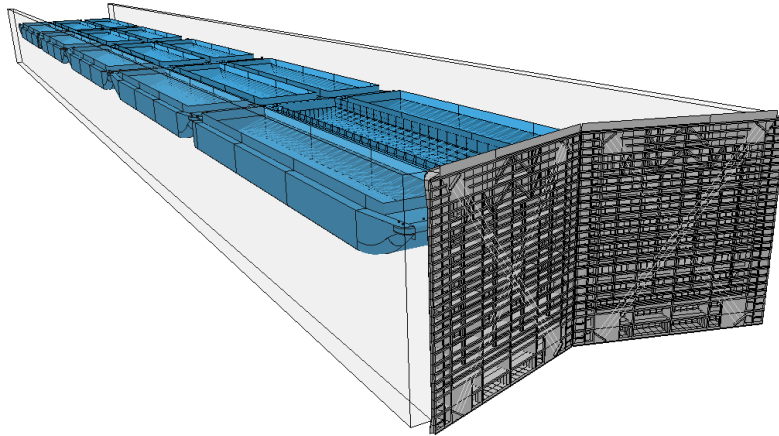


Figure 7.17. Model Used to Simulate Miter Impact, 3x5 Barge Flotilla, 2 ft/sec

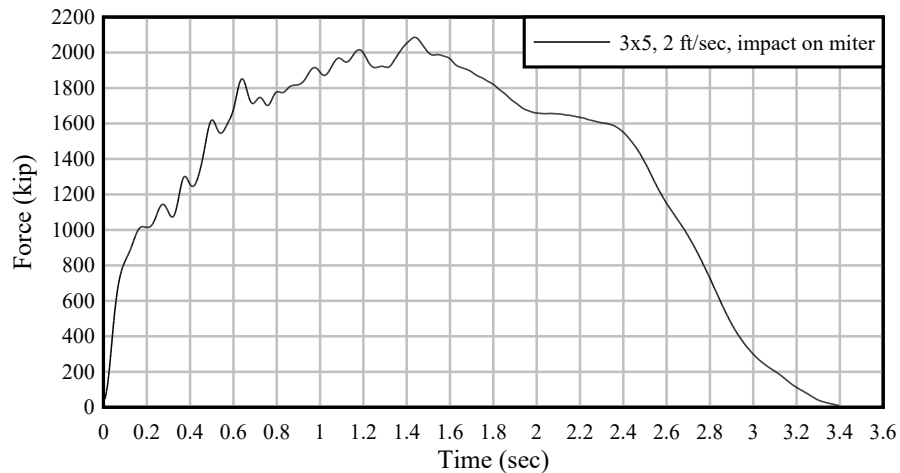


Figure 7.18. Simulation Results for Miter Impact, 3x5 Barge Flotilla, 2 ft/sec

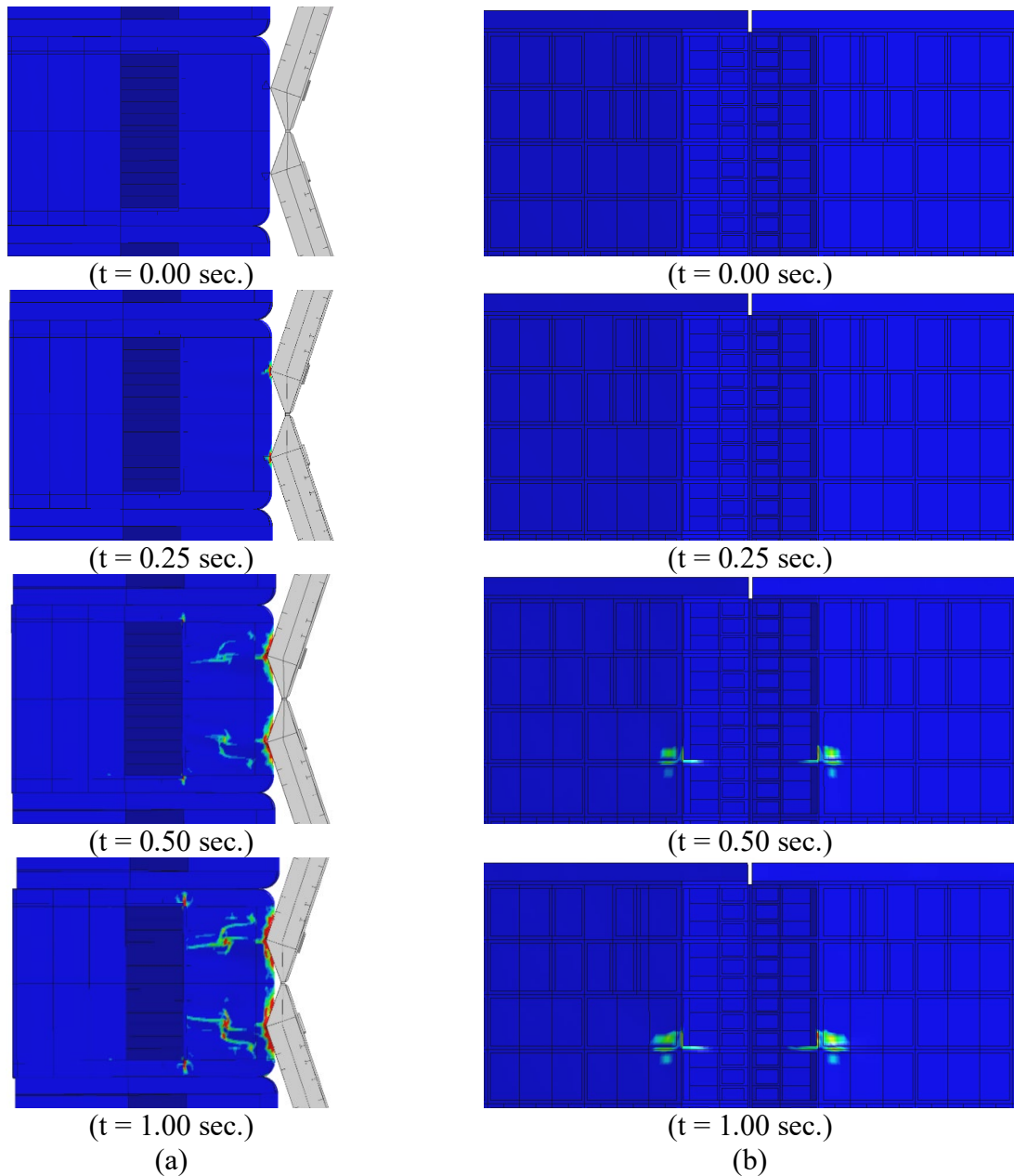


Figure 7.19. Plastic Strains for 3x5 – 2.0 ft/sec – Miter Impact (Blue Signifies No Plastic Strain, Red Signifies Plastic Strain): (a) Barge Bow Plastic Strains; (b) Miter Gate Plastic Strains

7.2.5.3. Damage renderings (e.g., Figure 7.19) reveal that the barge bow possesses less stiffness and strength than the miter gate. Consequently, for impacts of sufficient momentum, time-varying impact forces are limited by plastic crushing strength of the barge bow. In such instances, the barge bow acts as a force limiter, in comparison to the stiffer miter gate structure.

7.2.5.4. This observation is consistent with prior analytical (e.g., Consolazio et al., 2009) and experimental (e.g., Consolazio et al., 2005) studies. Therein, relationships between impact momentum and barge bow deformation are shown to be either elastic-perfectly plastic, or elastic-plastic with hardening, but not linear. Results obtained for barge impacts on miter gates indicate an approximately elastic-plastic (with hardening) relationship between momentum and impact force. Section 7.2.5 presents an empirical impact load prediction model. The prediction model employs a bilinear relationship between impact momentum and peak impact force.

7.2.5.5. In general, increasing the flotilla impact momentum increases both the maximum forces generated and the force durations. Maximum force levels achieved at relatively high levels of momentum tend to be relatively sustained (Consolazio and Han 2015). Accordingly, applying such forces as static impact loads in miter gate design processes is considered appropriate.

7.2.6. Empirical Load Prediction Model. An empirical procedure for predicting miter gate impact loads incorporates maximum force data from the 27 cases of Table 7.1. All utilized maximum force data are plotted as a function of barge flotilla momentum in Figure 7.20. It is evident that maximum impact forces are generally well correlated to flotilla momentum. However, such correlation does not maintain a single linear proportionality factor. A trend is apparent in which one slope (proportionality factor) is evident at momentums less than approximately 800 kip-sec. A second, reduced slope is evident at higher momentum levels.

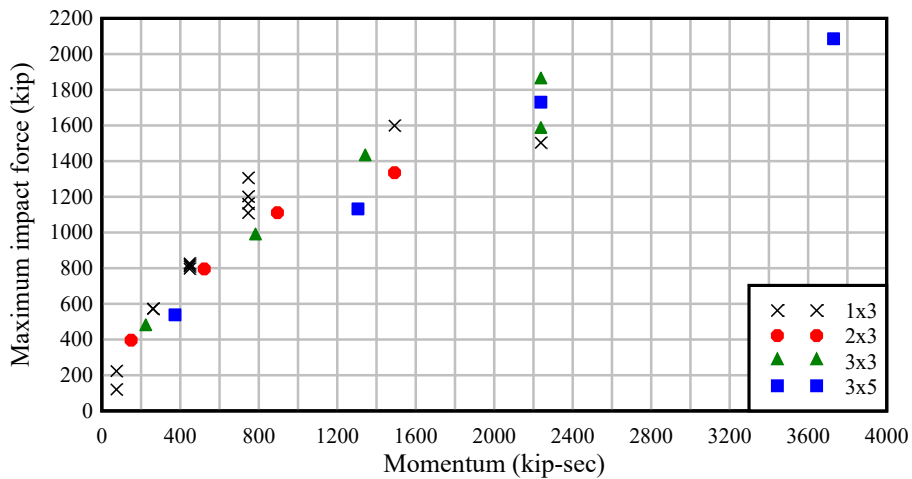


Figure 7.20. Relationship Between Flotilla Momentum and Maximum Miter Gate Impact Force (27 Cases)

7.2.6.1. A variety of different functional forms (e.g., power models) could be used to fit the data in Figure 7.20. However, a bilinear form is both consistent with empirical models documented in Chapter 4 and Chapter 6, and mathematically simple. Consequently, a bilinear functional form (Figure 7.21) is adopted for development of a barge impact load prediction model for miter gates.

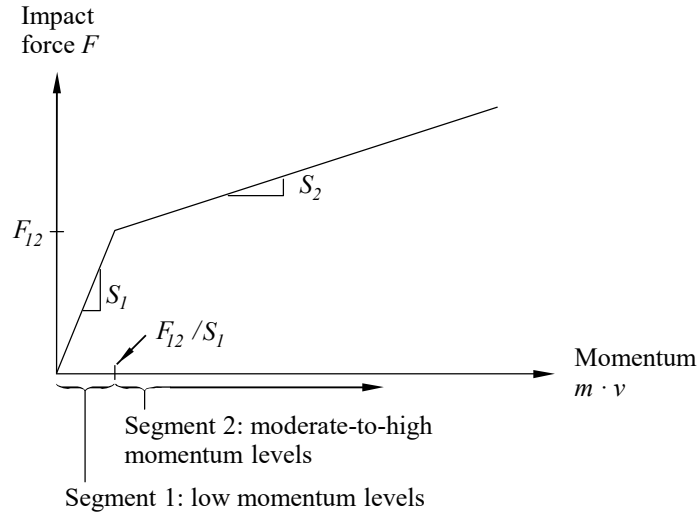


Figure 7.21. General Form of Bilinear Impact Force Prediction Model for Miter Gates

7.2.6.2. Three parameters define the bilinear fitting function. These include slopes of the two segments (S_1 and S_2), and a transition force level, F_{12} . Functionally, the bilinear curve fit may be expressed in the form:

$$F = \begin{cases} S_1 \cdot (m \cdot v) & \text{if } m \cdot v \leq (F_{12}/S_1) \\ F_{12} + S_2 \cdot (m \cdot v - (F_{12}/S_1)) & \text{otherwise} \end{cases} \quad (7.2)$$

where F is the impact force on the miter gate (resolved in the direction of barge flotilla travel). The m term is the total mass of all barges in the flotilla. Flotilla impact velocity is given as v .

7.2.6.3. Values of S_1 , S_2 , and F_{12} that optimally fit the force data are determined using an error function minimization process. An error function is defined as the sum of the squares of the load prediction errors. The function is used to accumulate differences between the impact simulation force data (Table 7.1) and predictions from Equation 7.2. Differences are accumulated across all considered impact cases (27 data points in total). The cumulative square error function with respect to the fitting parameters is then minimized. As a result, the following empirical load prediction model is established for miter gates:

$$F = \begin{cases} 1.80 \cdot m \cdot v & \text{if } m \cdot v \leq 611 \text{ kip-sec} \\ 1100 + 0.330 \cdot (m \cdot v - 611) & \text{otherwise} \end{cases} \quad (7.3)$$

where $m \cdot v$ is the total flotilla momentum in units of kip-sec. Also, F is the impact force in the direction of barge flotilla travel, in units of kip.

7.2.6.4. Confidence bounds are also established at confidence levels of 1-standard deviation (84.1%) and 2-standard deviations (97.7%) from the mean. Functionally, these bounds are given by:

$$F_{84.1\%} = \begin{cases} 2.20 \cdot m \cdot v & \text{if } m \cdot v \leq 619 \text{ kip-sec} \\ 1360 + 0.420 \cdot (m \cdot v - 619) & \text{otherwise} \end{cases} \quad (7.4)$$

and:

$$F_{97.7\%} = \begin{cases} 2.60 \cdot m \cdot v & \text{if } m \cdot v \leq 605 \text{ kip-sec} \\ 1570 + 0.480 \cdot (m \cdot v - 605) & \text{otherwise} \end{cases} \quad (7.5)$$

7.2.6.5. Comparison of Simulated and Predicted Impact Forces. In Figure 7.22, the mean-value empirical load prediction model (Equation 7.3) is compared to flotilla-gate maximum impact forces. Simulation results are plotted based on values listed in Table 7.1. Overall good agreement is observed between the mean-value empirical load prediction model and the benchmark simulation results.

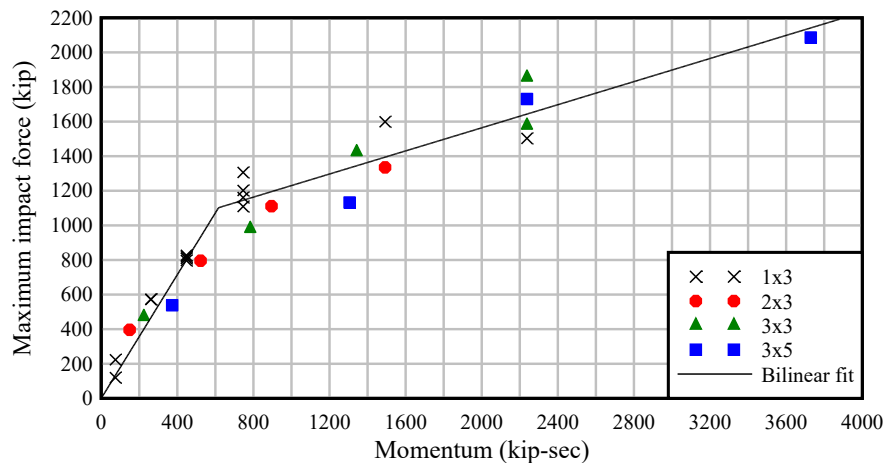


Figure 7.22. Comparison of Impact Forces from Dynamic Simulations and Miter Gate Impact Load Prediction Model (Equation 7.3)

7.2.7. Deterministic Design Example.

7.2.7.1. A deterministic impact scenario, associated with usual conditions, is presented for miter gates in section 7.2.6.5. Unusual and extreme impact scenarios involving miter gates are focused on in section 7.4.2.4 and section 7.4.2.5, respectively.

7.2.7.2. Usual.

7.2.7.2.1 Figure 7.23 shows a plan-view schematic of the deterministic example for usual impact conditions on a miter gate. A fully loaded 1x3 flotilla is selected for this scenario, with each barge weighing 2,000 short tons (10.4 kip-sec²/in. mass). The initial flotilla velocity is 0.2 ft/sec and impacts the centerline of the miter gate structure in a head-on manner.

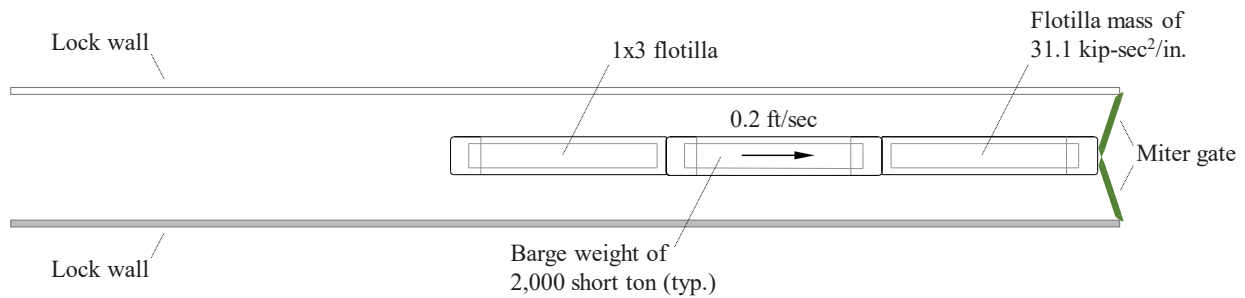


Figure 7.23. Deterministic (Usual) Impact Scenario on Miter Gate

7.2.7.2.2 Relevant parameters associated with the deterministic (usual) impact scenario are listed in Table 7.2. Flotilla mass (m) and impact velocity (v) are used in evaluating Equation 7.3. Total flotilla momentum ($m \cdot v$) is 74.6 kip-sec in this example. The momentum is less than the 611 kip-sec listed in Equation 7.3. Therefore, the design impact force, associated with segment 1 of Figure 7.21, for the (deterministic) usual impact condition is 134 kip.

Table 7.2
System Parameters for Deterministic (Usual) Impact Scenario on Miter Gate

Parameter Description	Value	Units
Flotilla columns	1	N/A
Flotilla rows	3	N/A
Weight per barge	2,000	short tons
Flotilla mass	31.1	kip-sec ² /in.
Impact speed	0.2	ft/sec
Flotilla momentum	74.6	kip-sec
Usual Impact Force	134	kip

7.2.7.3. Unusual.

7.2.7.3.1 Figure 7.24 shows a plan-view schematic of the deterministic example for unusual impact conditions on a miter gate. A fully loaded 3x3 flotilla is selected for this scenario, with each barge weighing 2,000 short tons (10.4 kip-sec²/in. mass). The initial flotilla velocity is 0.7 ft/sec and impacts the centerline of the miter gate structure in a head-on manner.

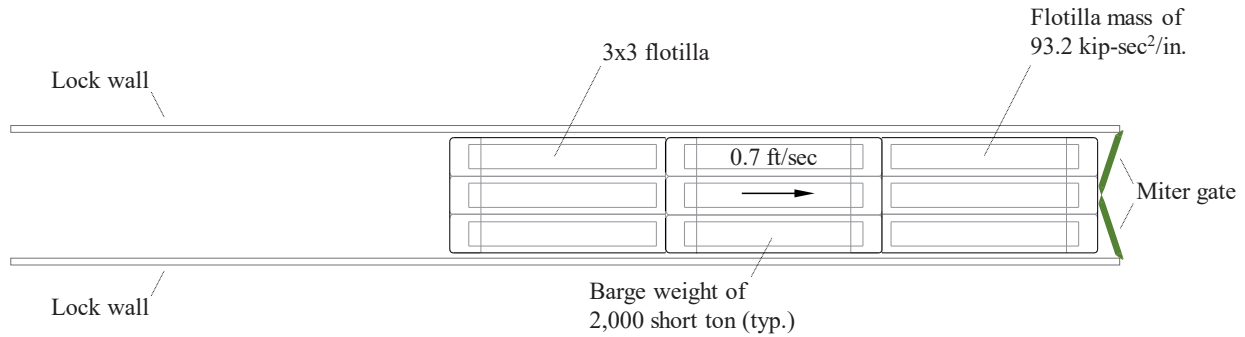


Figure 7.24. Deterministic (Unusual) Impact Scenario on Miter Gate

7.2.7.3.2 Relevant parameters associated with the deterministic (unusual) impact scenario are listed in Table 7.3. Flotilla mass (m) and impact velocity (v) are used in evaluating Equation 7.3. Total flotilla momentum ($m \cdot v$) is 783.2 kip-sec in this example. The momentum exceeds the 611 kip-sec listed in Equation 7.3. Therefore, the design impact force, associated with segment 2 of Figure 7.21, for the (deterministic) unusual impact condition is 1157 kip.

Table 7.3
System Parameters for Deterministic (Unusual) Impact Scenario on Miter Gate

Parameter Description	Value	Units
Flotilla columns	3	N/A
Flotilla rows	3	N/A
Weight per barge	2,000	short tons
Flotilla mass	93.2	kip-sec ² /in.
Impact speed	0.7	ft/sec
Flotilla momentum	783.2	kip-sec
Unusual Impact Force	1,157	kip

7.2.7.4. Extreme.

7.2.7.4.1 Figure 7.25 shows a plan-view schematic of the deterministic example for extreme impact conditions on a miter gate. A fully loaded 3x5 flotilla is selected for this scenario, with each barge weighing 2,000 short tons (10.4 kip-sec²/in. mass). The initial flotilla velocity is 1.2 ft/sec and impacts the centerline of the miter gate structure in a head-on manner.

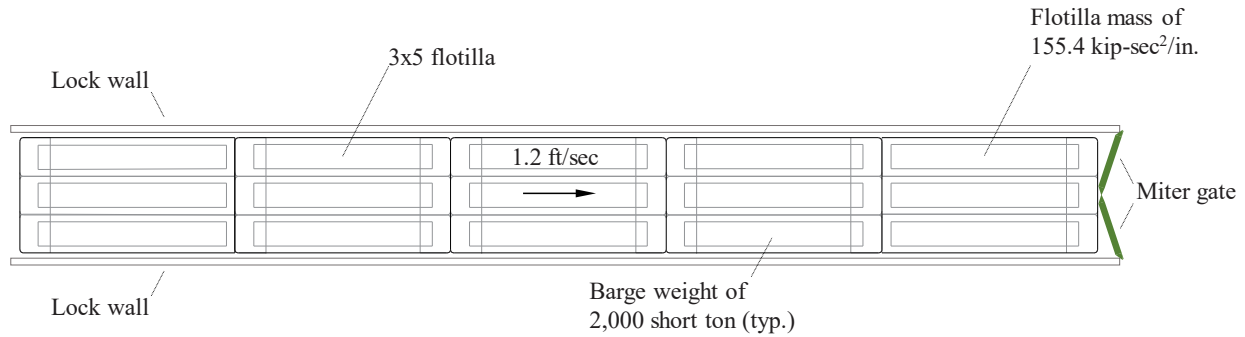


Figure 7.25. Deterministic (Extreme) Impact Scenario on Miter Gate

7.2.7.4.2 Relevant parameters associated with the deterministic (extreme) impact scenario are listed in Table 7.4. Flotilla mass (m) and impact velocity (v) are used in evaluating Equation 7.3. Total flotilla momentum ($m \cdot v$) is 2,237.8 kip-sec in this example. The momentum exceeds the 611 kip-sec listed in Equation 7.3. Therefore, the design impact force, associated with segment 2 of Figure 7.21, for the (deterministic) extreme impact condition is 1,637 kip.

Table 7.4
System Parameters for Deterministic (Extreme) Impact Scenario on Miter Gate

Parameter Description	Value	Units
Flotilla columns	3	N/A
Flotilla rows	5	N/A
Weight per barge	2,000	short tons
Flotilla mass	155.4	kip-sec ² /in.
Impact speed	1.2	ft/sec
Flotilla momentum	2,237.8	kip-sec
Extreme Impact Force	1,637	kip

7.2.8. Complete Design Example. This example is for the design of a horizontally framed miter gate for a new lock on the Ohio River. Based on present traffic predictions and navigation model testing at ERDC, a 15-barge tow and input parameters selected for the unusual and extreme load cases. Design load cases are shown in Table 7.5. There is no usual load case since these impacts are infrequent load cases or rare events for a barge impacting miter gates.

7.2.8.1. Unusual load case:

$$V = 1.0 \text{ ft/sec}$$

$$W_{\text{barge}} = 30,000 \text{ short tons} = 60,000 \text{ kip}$$

$$\text{Checking, } M^*v = 60,000/32.2 * 1.0 = 1,863.35 \text{ kip-sec}$$

Since 1,863.35 kip-sec > 611 kip-sec, use second line segment

$$\begin{aligned} F &= 1,100 + 0.33 * (M^*v - 611) \\ &= 1,110 + 0.33 * (1,863.35 - 611) \\ &= 1,100 + 0.33 * (1,252.35) \\ &= 1,513.28 \text{ kip} \end{aligned}$$

7.2.8.2. Extreme load case:

$$V = 2.0 \text{ ft/sec}$$

$$W_{\text{barge}} = 30,000 \text{ short tons} = 60,000 \text{ kip}$$

$$\text{Checking, } M^*v = 60,000/32.2 * 2.0 = 3,726.71 \text{ kip-sec}$$

Since 3,726.71 kip-sec > 611 kip-sec, use second line segment

$$\begin{aligned} F &= 1,100 + 0.33 * (M^*v - 611) \\ &= 1,110 + 0.33 * (3,726.71 - 611) \\ &= 1,100 + 0.33 * (3,115.71) \\ &= 2,128.18 \text{ kip} \end{aligned}$$

Table 7.5
Design Load Cases from Deterministic Calculations

Load Case	Force (kip)
Usual	NA
Unusual	1,513
Extreme	2,128

7.2.9. Probabilistic Example.

7.2.9.1. This example is for the design of a horizontally framed miter gate for a new lock on the Ohio River. Based on present traffic predictions and navigation model testing at ERDC, a 15-barge tow and input parameters selected for probabilistic analysis are:

Table 7.6
Probabilistic Parameters for Ohio River Example

Parameter	Distribution	E(x)	$\sigma(x)$	Min(x)	Max(x)
Velocity (ft/sec)	Lognormal	0.5	0.3	0.1	2
Weight – entire flotilla (short tons)	Constant	30,000	-	-	-

7.2.9.2. The probabilistic model run is made using Monte Carlo Simulations for 50,000 iterations. Return periods for this site were selected for the usual (Not applicable), unusual (150 year), and extreme (1000 year) load cases and the results are shown in Table 7.7.

Table 7.7
Design Load Cases from Probabilistic Calculations

Load Case	Force (kips)
Usual	NA
Unusual – 150 year	1390
Extreme – 1000 year	1479

7.3. Vertically Framed Miter Gates – Full-Scale Experiments.

7.3.1. Background. Prior to the removal of L&D 26 on the Mississippi River, Chasten et al (1991) performed four full-scale barge impact experiments on vertically framed miter gates. These experiments utilized a nine-barge tow that was composed of jumbo hopper barges (35 ft by 195 ft) each with a weight of 1,700 tons when loaded. The total weight of the configuration including the towboat was 31,900 kips.

7.3.2. Impact Sequence for Full-Scale Experiments. A series of four progressively increasing impact loads were applied to the downstream miter gates. The first two experiments were kept within the elastic range of the miter gate, and the third and fourth experiments were designed to cause local damage to the miter girder. The front of the barge did not experience any damage during any impacts.

7.3.3. Instrumentation. These experiments used instrumentation on both the gates and barge to record data during each of the four tests. The barge contained a load transfer beam configuration with load cells to measure the force with time curve for each test. This setup on the lead barge is shown in Figure 7.26. The gates were instrumented with strain gauges on critical members at the top of the gates, including the top girder and miter point. This setup on the miter gate leaf is shown in Figure 7.27.

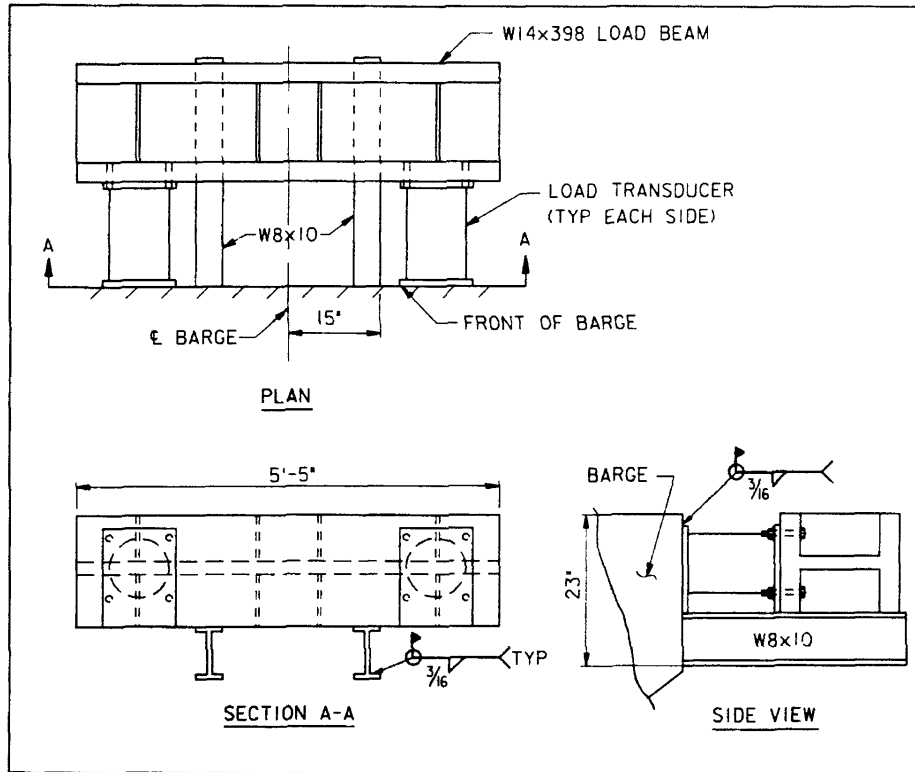


Figure 7.26. Load Beam Configuration on Lead Barge (Chasten (1991))

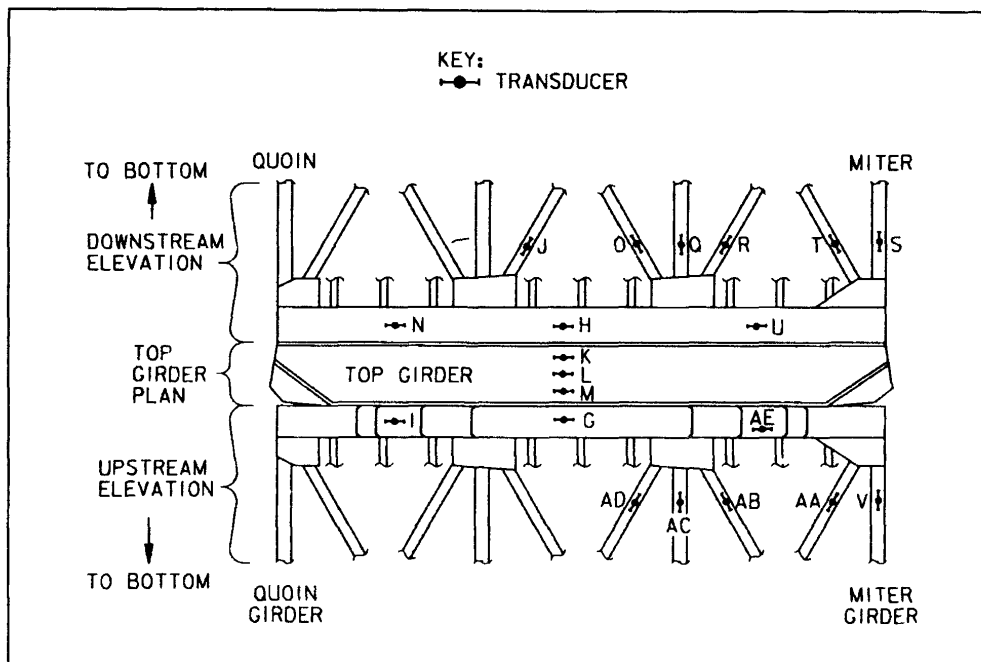


Figure 7.27. Strain Transducer Locations (Chasten (1991))

7.3.4. Results. The results from the experiments are shown in the Table 7.8. This table also shows the resulting impact to the gate and barge during each experiment. The force time history is shown for Impact #3 in Figure 7.28. These are very similar to the time histories in Figure 7.15 and Figure 7.18 for horizontally framed miter gates. The stress flow shown in Figure 7.29 is determined from the strain gauge data and shows that the location of the yielding of the top girder during Impact #3.

Table 7.8
Impact Force Results (Chasten (1991))

Impact	Approach Velocity (ft per second)	Impact Force (kips)	Damage to Gate
1	0.36	442	None
2	0.59	443	None
3	0.94	605	Local damage to miter girders and cracks in welds that attached load transducers to barge
4	0.73	488	Load transducers to barge welds fractured and test was stopped

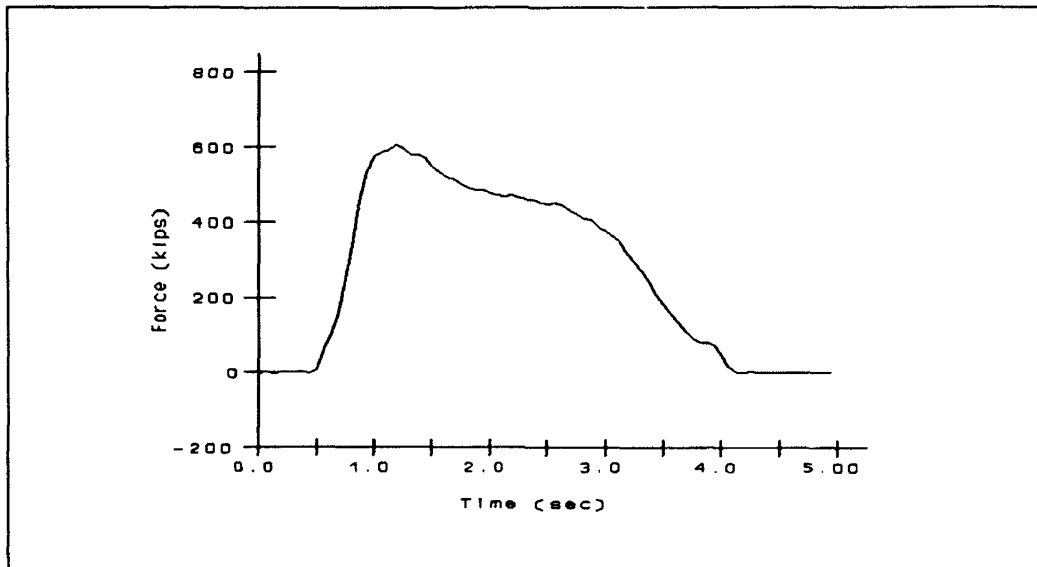


Figure 7.28. Force Time History – Impact #3 (Chasten (1991))

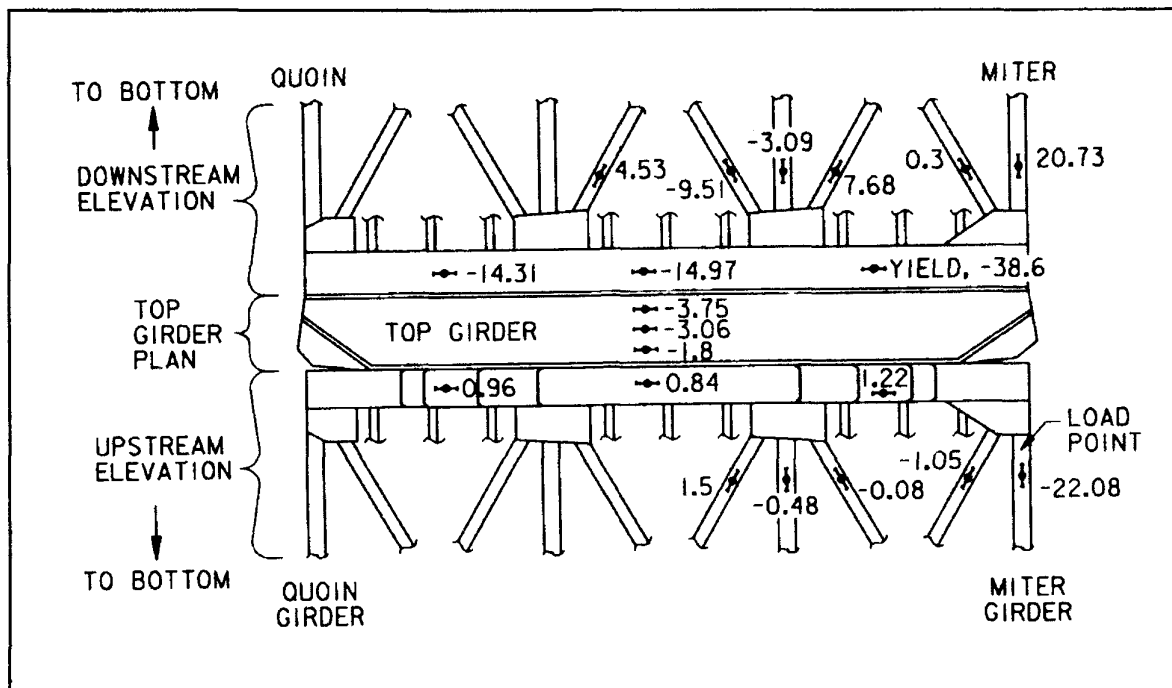


Figure 7.29. Stress Flow (ksi), 573 kips – Impact #3 (Chasten (1991))

7.3.5. Conclusions. Chasten (1991) concluded that, in general, vertically framed miter gates are relatively fragile when compared to horizontally framed miter gates. The vertically framed configuration is rather flexible and will likely have a lower stiffness and coefficient of restitution compared to horizontally framed configuration. Horizontally framed gates will absorb the impact in a much stiffer fashion, and under moderate impacts will most likely not be damaged. This difference between gate types is directly shown in the FE modeling of a horizontal framed miter gate in section 7.2 above. EM 1110-2-2107 discusses the design considerations for both types of miter gates.

7.4. Tainter Gates.

7.4.1. Overview.

7.4.1.1. Barge impacts on Tainter gates, which span between dam piers, are the focus of section 7.4. Modeling considerations for Tainter gates are provided in section 7.4.2. Section 7.4.3 documents peak impact force results obtained from collision simulations between barge flotillas and Tainter gates. Observations associated with a parametric study of 36 simulations are discussed in section 7.4.4. The gate modeling considerations and collision forces summaries facilitate formation of the empirical load prediction expressions given in section 7.4.5.

7.4.1.2. Background. USACE maintains a substantial inventory of dam structures that are vulnerable to barge impacts, particularly during flood-stage flow conditions. Past incidents have involved barge flotillas losing control, breaking up, and impacting dam piers and/or Tainter gates. Whereas collisions with dam piers were addressed in Chapter 6, impacts on dam Tainter gates are focused on below.

7.4.1.2.1 Tainter gates are steel hydraulic control structures that are anchored to adjacent concrete dam piers. Alternatively stated, a Tainter gate is a radial arm floodgate that can be rotated upward or downward. The rotated position allows for control of water elevation and flow rate. Tainter gates may be subjected to hydrostatic loads and barge impact loads, as well as other load types. During impact events, collision forces are dynamically transmitted from the point of application on the gate outward to adjacent piers. Within the Tainter gate, forces flow into side frames and then into trunnions that connect the gate to dam piers.

7.4.1.2.2 Past impact events demonstrate that extensive and costly damage can result from barge impacts on dam gate components. Direct impacts against Tainter gates often leave such systems inoperable. Thus, potential risk exists for uncontrolled flow and the inability to control pool elevation. Estimating impact loads for structural design of Tainter gates is, therefore, an important component of risk management.

7.4.1.2.3 Quantifying impact loads using full-scale experimental testing would be costly, complex, and potentially impractical. However, FE modeling and impact simulation techniques can be used to efficiently assess relevant impact forces over numerous conditions. In the following, FE modeling and simulation techniques are employed to simulate barge collisions on Tainter gates. Variations in collision scenarios considered include barge size, impact speed, impact location, and impact angle. Results from the impact simulations are used in developing design loads for use in structural design of Tainter gates.

7.4.1.2.4 A FE dam model is developed based on a representative, in-service USACE dam structure. The dam piers and Tainter gates at the Cannelton Locks and Dam (Figure 7.30) are modeled. Structural plans corresponding to the Cannelton dam and gate structures are used for model development. Relevant excerpts of the structural drawings are provided in Consolazio and Han (2018). Making use of the model, impact simulations are conducted to quantify impact loads and trunnion reaction forces.



Figure 7.30. Cannelton Locks and Dam on the Ohio River
(Source: Wikimedia Commons, Photo by Sarah Ewart)

7.4.2. Modeling Considerations. Modeling contact interactions between an impacting barge model and the representative Tainter gate model requires careful attention to meshing details. Accordingly, high-resolution mesh densities and nonlinear steel material models are utilized. Localized plate bending, buckling, and yielding in the gate have the potential to influence the quantified impact loads. Moreover, given the possibility of simulating catastrophic gate damage under barge impact loading, a high-fidelity gate model is necessary.

7.4.2.1. In Consolazio and Han (2018), simulations of barge impacts against dam piers and dam gates were separately conducted. A summary of impact force results obtained from simulations of flotilla impacts on dam piers is given in section 6.4.2. Also provided in that section are recommended procedures for computing design impact loads for dam piers. The following sections therefore focus on simulating flotilla impacts on Tainter gates and quantifying the associated forces.

7.4.2.2. Tainter gates are attached to dam piers, however, so a brief description of representation of the piers is included here. Given the size and strength of dam piers, only sufficient mesh density is modeled to achieve accurate representation of structural geometry. A simplified material model is utilized since concrete damage (e.g., spalling) is not required to compute controlling impact forces. Specific to simulations between flotillas and Tainter gates, the dam material is assumed to be rigid, but with the contact stiffness of concrete.

7.4.2.3. Steel Material Models. The Cannelton Tainter gates are fabricated from A36 steel and multiple grades of A441 steel. Constitutive modeling is based on the Tainter gate construction date and design standards that were applicable at the time. Selected yield and ultimate strengths for each of the constituent steels are plotted in Figure 7.31. Four inelastic, nonlinear material relationships are adopted for constitutive modeling, each possessing a unique yield stress. These correspond to 36 ksi, 42 ksi, 46 ksi, and 50 ksi steel (A36 and A441 Grade 42, 46, 50).

7.4.2.3.1 Strain-rate sensitivity effects (Figure 7.32) are incorporated into each steel material model using the Cowper-Symonds model:

$$\frac{\sigma_{dynamic}^y}{\sigma_{static}^y} = \left[1 + \left(\frac{\dot{\epsilon}_{eff}^p}{C} \right)^{\frac{1}{P}} \right] \quad (7.6)$$

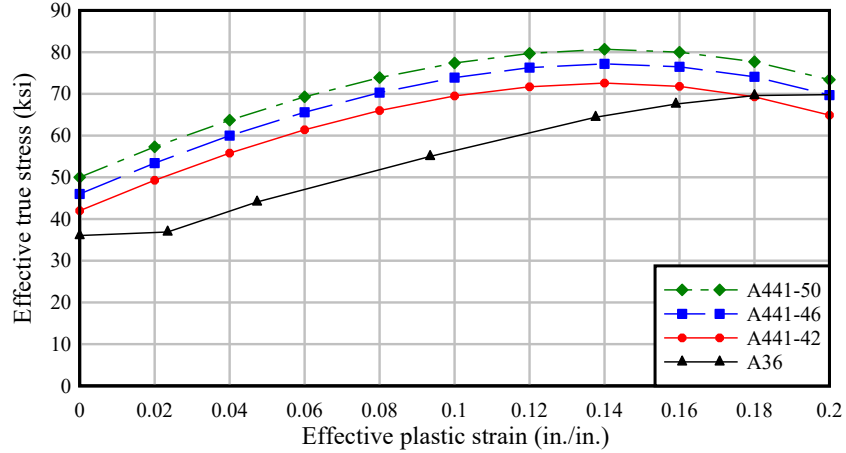


Figure 7.31. Constitutive Relationships for A36 and A441 Grade 42, 46, 50 Steels in Tainter Gate

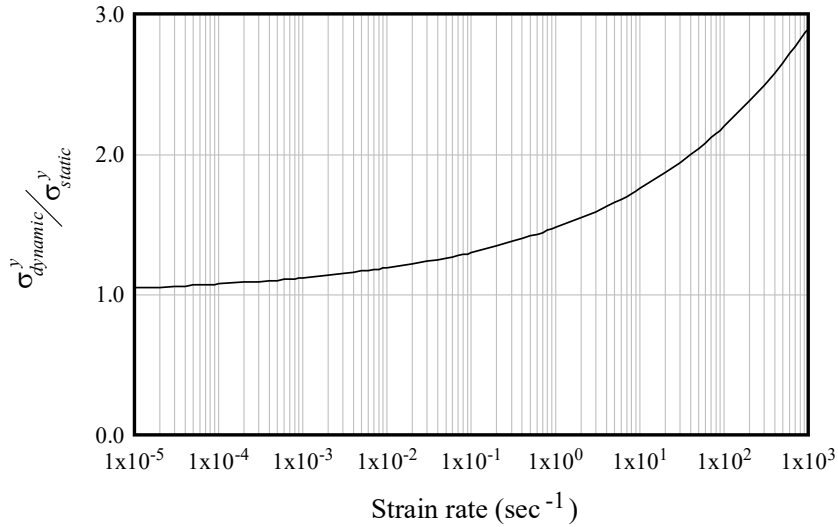


Figure 7.32. Strain-Rate Sensitivity of A36 and A441 Steels in Tainter Gates (Based on Cowper-Symonds Model with $C = 40.4 \text{ sec}^{-1}$ and $P = 5$)

7.4.2.3.2 All constituent types of steel used in the Tainter gate are considered mild strength steels. Therefore, the Cowper-Symonds C and P coefficients are taken as 40.4 sec^{-1} and 5.0 , respectively (Jones 1997). The increase of dynamic yield stress, $\sigma_{dynamic}^y$, is then quantified with respect to effective plastic strain rate, $\dot{\epsilon}_{eff}^p$. Note that the ordinate axis in Figure 7.32 is normalized by the respective static yield stress, σ_{static}^y . Values of σ_{static}^y include 36 ksi, 42 ksi, 44 ksi, and 50 ksi, depending on the steel type.

7.4.2.4. Tainter Gate Component Modeling. The Tainter gate model includes skin plates, web plates, and vertical diaphragms. Also included are stiffening elements, side frames, and trunnions (Figure 7.33a, Figure 7.34a). Structural components are generally modeled using high-resolution meshes of 4-node fully integrated shell elements. Mesh resolutions are sufficiently refined such that localized inelastic buckling are properly represented (when appropriate) during barge impact interactions. As an exception, unique considerations are given for modeling of trunnions, as discussed below. Various depictions of the mesh resolution are shown in (Figure 7.33b, Figure 7.34b).

7.4.2.4.1 Trunnion structures located at the ends of the side frames serve as reaction points for loads exerted on the gate. Trunnions additionally serve as pivot points during gate rotation. Barge impact loads applied to the upstream skin plate of the gate are carried into the trunnions through structural side frames. Quantifying the loads transmitted to the trunnions by the gate is therefore an important consideration. However, modeling trunnion failure is not required to quantify trunnion loads. Therefore, detailed meshes of the trunnions are not developed. Instead, a simplified mesh of 8-node solid elements is used to represent each trunnion (Figure 7.35).

7.4.2.4.2 Nearly all of the solid elements in the trunnion model are assigned a rigid material model. Only a small number of elements located at the core of the trunnion model are defined with an elastic material. At this location, boundary conditions are defined to restrain translations along, but permit rotations about, the trunnion axis. In total, the complete high-resolution Tainter gate model (Figure 7.33a) consists of approximately 160,000 shell elements (Figure 7.33b).

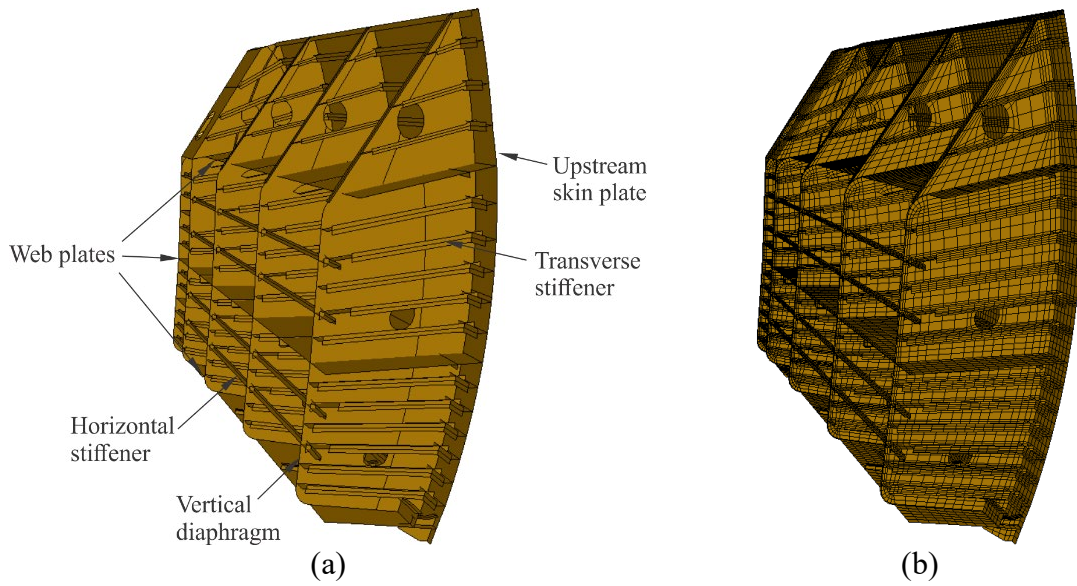


Figure 7.33. Partial Tainter Gate Finite Element Model (Note: Downstream Skin Plate Removed to Reveal Internal Structural Details): (a) Surface Geometry; (b) Mesh

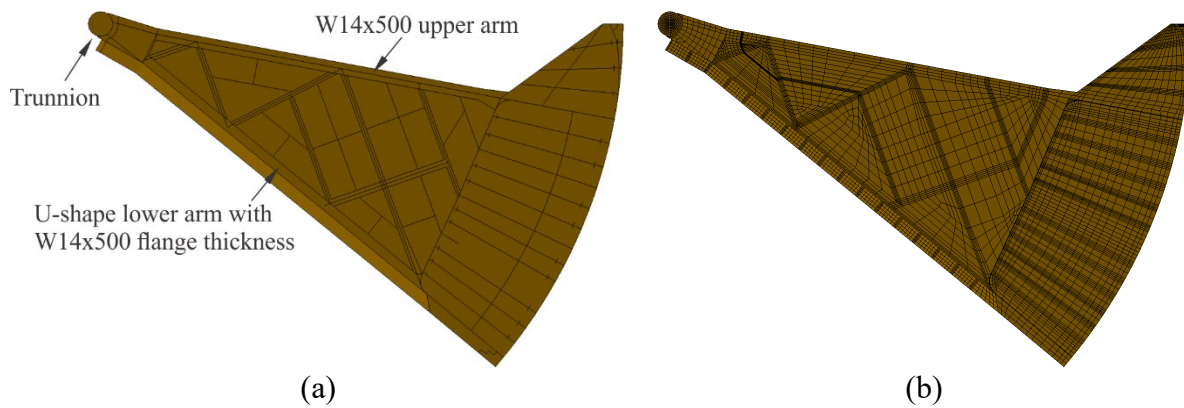


Figure 7.34. Side Frame Finite Element Model: (a) Surface Geometry; (b) Mesh

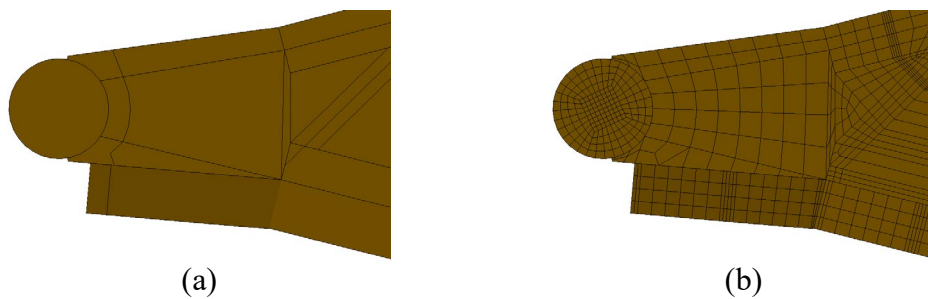
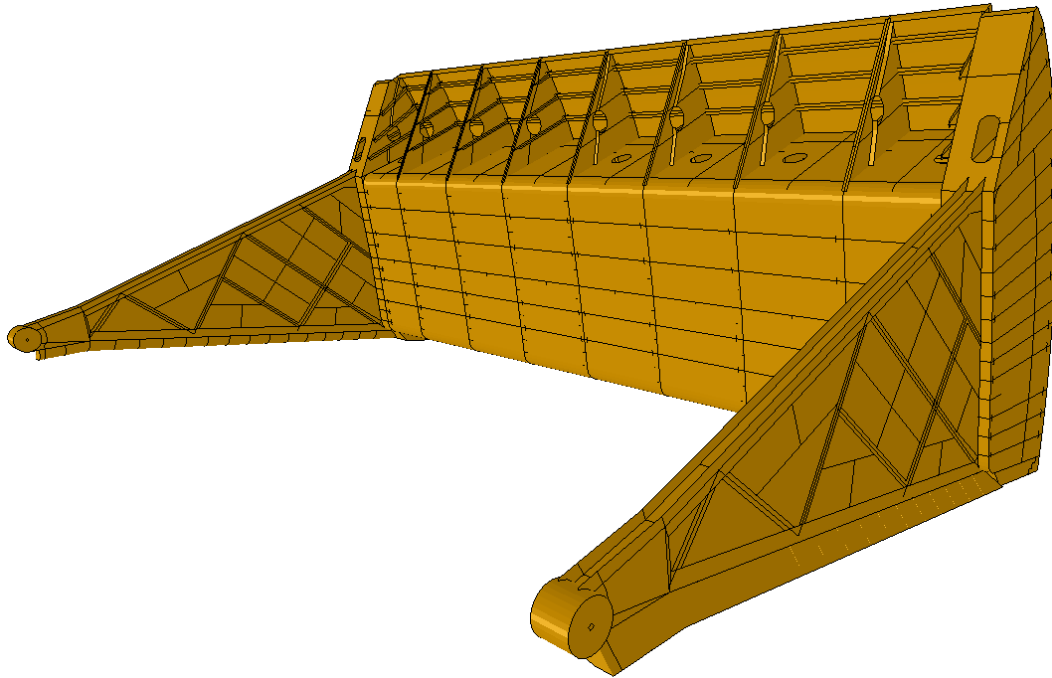
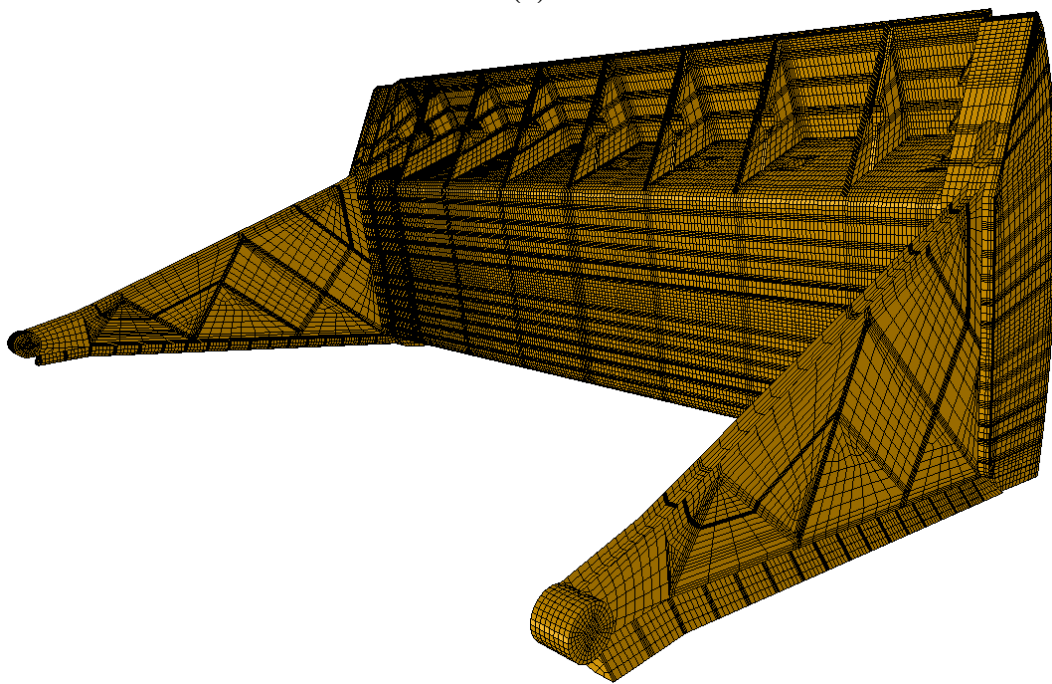


Figure 7.35. Trunnion Finite Element Model: (a) Surface Geometry; (b) Mesh



(a)



(b)

Figure 7.36. Tainter Gate Finite Element Model: (a) Geometry (Mesh Omitted for Clarity);
(b) High-Resolution Mesh of Approximately 160,000 Elements

7.4.2.5. Dam Pier Modeling.

7.4.2.5.1 A representative FEM of a typical pier at Cannelton Locks and Dam is developed (Figure 7.37). Pertinent excerpts from structural plans, used to develop the geometry of key pier surfaces, are provided in Consolazio and Han (2018). Such surfaces include the rounded upstream impact face (Figure 7.32a). Each dam pier model consists of approximately 48,500 solid elements (Figure 7.37b). To ensure robust detection of barge contact, portions of each dam are modeled with a high-resolution mesh (e.g., Figure 7.37b). In these regions, element sizes are approximately 3 in. x 3 in., which are similar to elements in the barge.

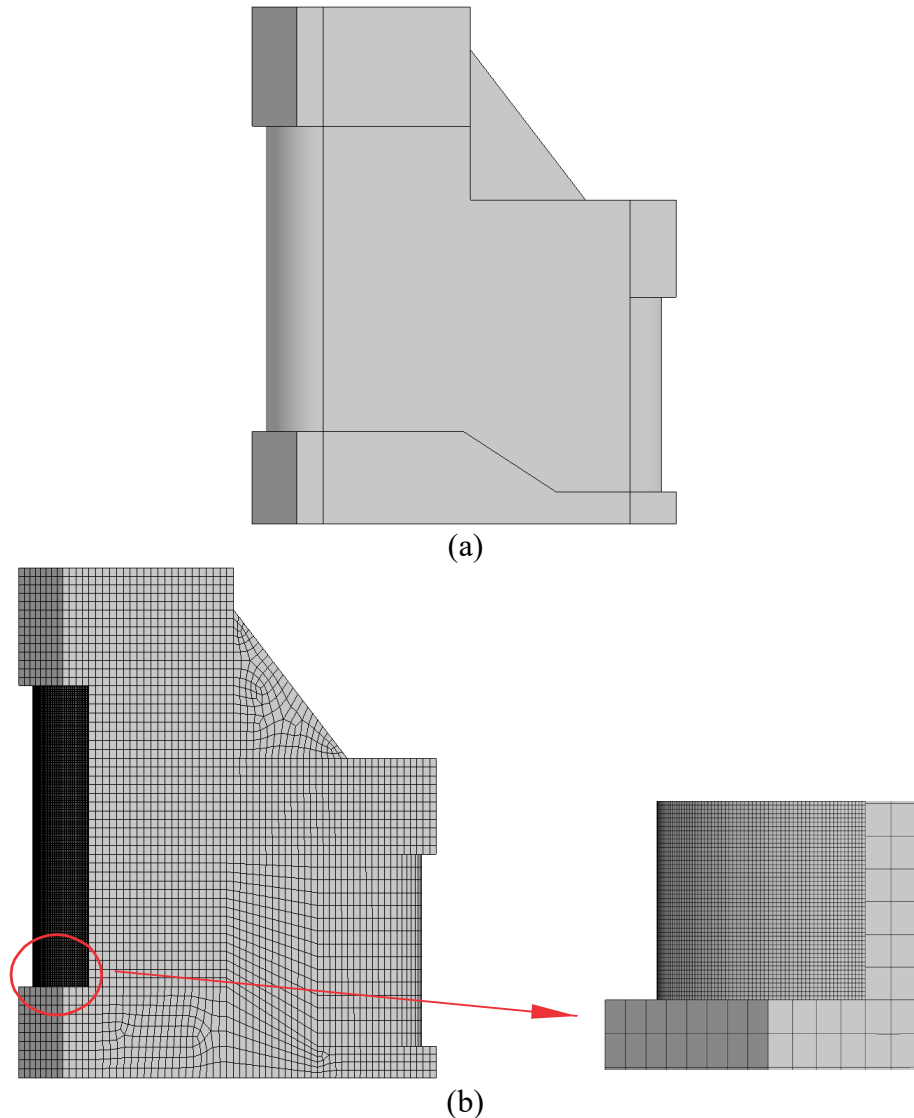
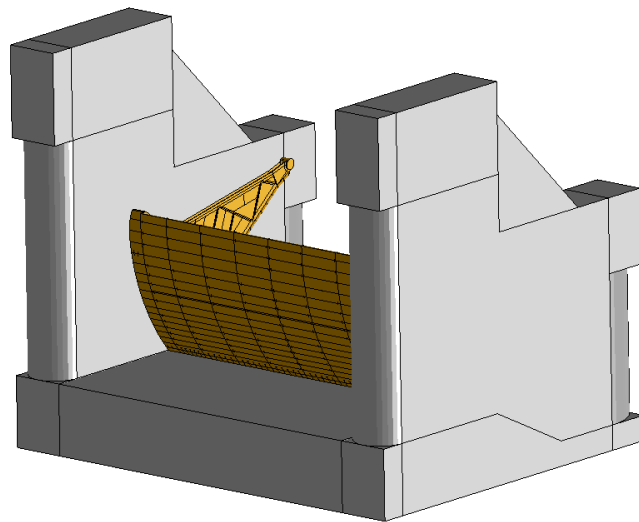
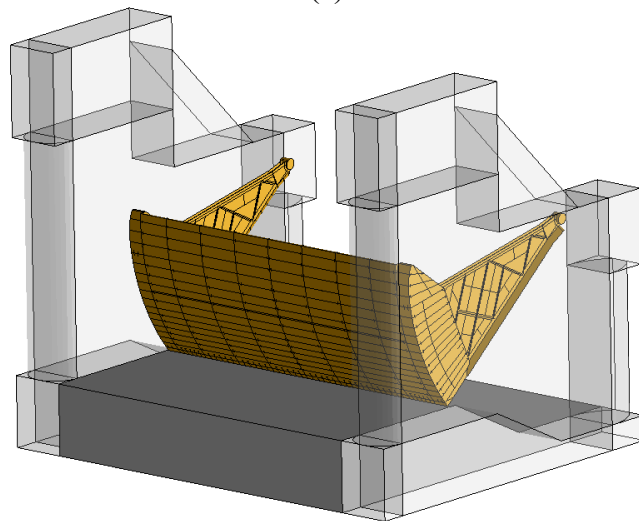


Figure 7.37. Dam Pier Finite Element Model: (a) Surface Geometry; (b) Finite Element Mesh

7.4.2.5.2 A single-module (1-gate, 2-pier) partial-dam structure is produced by merging two piers and the Tainter gate model (Figure 7.38). Barge-gate impact simulations are conducted to assess barge-gate impact loads, gate deformations, gate damage, and trunnion reaction forces. Additional dam pier and Tainter gate configurations are investigated in Consolazio and Han (2018).



(a)



(b)

Figure 7.38. Finite Element Model of Single Module Partial-Dam: (a) Surface Geometry; (b) Surface Geometry with Gate

7.4.2.6. Tainter Gate Open and Closed States. To control water flow rates through a dam, adjustments may be made in the vertical positions of individual Tainter gates. When Tainter gates are in the fully open (up) state, water flows freely from the dam upstream to downstream sides (Figure 7.39a). When gates are in the fully closed (down) state, water flow is prevented (Figure 7.39b). Intermediate positions between these two extremes are possible, but the bounding “open/up” and “closed/down” gate states are focused on.

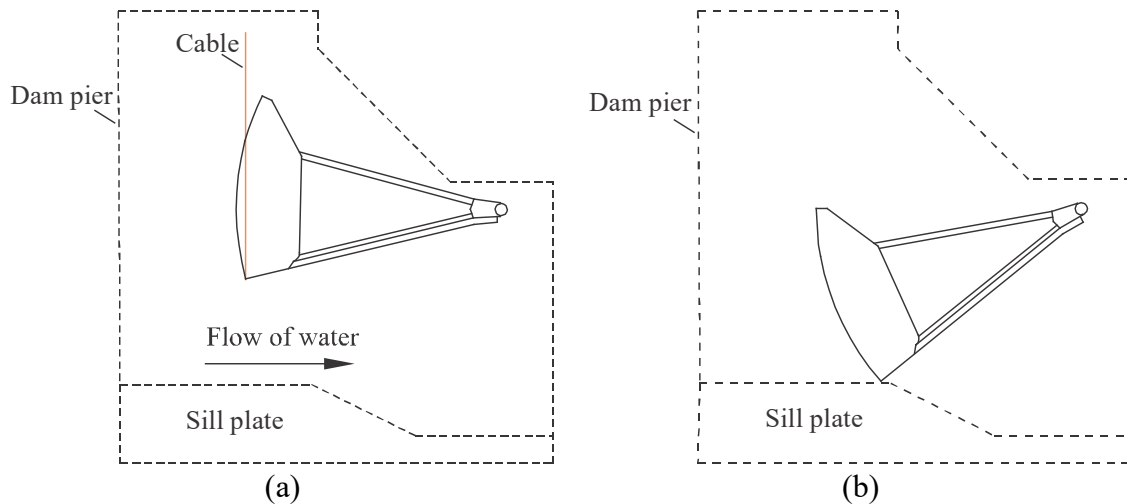


Figure 7.39. Tainter Gate States: (a) Gate Open (Up); (b) Gate Closed (Down)

7.4.2.6.1 A Tainter gate is moved between states (open, closed) by operating cable drums. Supported by the piers, cable drums lift or lower the gate using a series of cables. Per structural plans (see Consolazio and Han 2018), a total of 24 cables are connected to the Tainter gate. Each cable possesses a diameter of 1-3/8 in., and there are 12 cables on each side of each gate. To model the cables, a typical cross section is assumed of 6x25 filler wire.

7.4.2.6.2 Individual cable cross-sectional area is estimated at 1 in². This estimate is based on the approximate weight per foot of 1-3/8 in. cable (ASTM A1023-09 2009). Per Consolazio et al. (2012), the elastic modulus of the cable is selected to be 8,500 ksi. The collection of 12 cables on each side of the gate is modeled with a single effective cable. Effective cable cross-sectional areas are defined 12 times greater than that of individual 1-3/8 in. cables.

7.4.2.6.3 Lengthwise (i.e., extending from top to bottom), each effective cable is discretized into 20 individual LS-DYNA “beam/cable” elements. For purposes of distributing effective cable forces into the gate, nodal rigid bodies (i.e., multipoint constraints), or NRB, are introduced. Further, NRBs are placed at each side of the gate. In this way, the cable load is distributed across an adequately large area of shell elements in the gate.

7.4.2.6.4 When modeled and simulated in the open (up) state, the Tainter gate is suspended from two effective cables. Consequently, the weight (i.e., gravity load) of the gate is carried upward through the cables and into reaction/support nodes. During impact, small vertical motions of the gate are possible due to the flexibility of the cables. When modeled and simulated in the closed (down) state, the gate bottom edge meets the dam (concrete) sill plate. In this scenario, contact detection is defined at the interface between the gate and sill plate. As such, the gravity load of the gate is carried by the sill plate.

7.4.2.7. Contact Detection. For simulating flotilla-gate collisions, barge flotilla models developed in Chapter 3 are merged together with partial dam models. Contact detection is defined between the deformable portion(s) of the impacting barge(s) and appropriate zones of the Tainter gate. Static and dynamic coefficients of friction of 0.55 and 0.45, respectively, are assigned to the barge-to-gate (i.e., steel-to-steel) contact interfaces. For numerical efficiency, only selected portions of the gate model are included in the defined contact detection zones. In particular, only those gate portions that may potentially interact with the barge(s) are assigned as contact detection zones.

7.4.2.8. Additional Modeling Considerations. Prior to performing impact simulations, the pre-impact static-equilibrium state of the Tainter gate model is initialized. Included among the pre-impact loadings are the effects of gravity and hydrostatic upstream pressure. Hydrostatic loading only negligibly influences impact loads and impact-induced trunnion reactions (Consolazio and Han 2018). Additional details are provided in Consolazio and Han (2018).

7.4.3. Impact Forces on Tainter Gates. Flotilla models are merged together with Tainter gate models for purposes of conducting head-on and oblique impact simulations. Impact speeds considered range from approximately 4 ft/sec to 7 ft/sec, which is representative of flood-stage flow conditions. A parametric study is performed by varying barge flotilla mass, impact speed, impact angle, and impact location in the FE simulations. For each simulation conducted, impact forces and trunnion reaction forces are quantified.

7.4.3.1. To carry out collision simulations, barge flotilla models (1x1, 2x1) and the single module partial dam FE model are combined (Figure 7.40). A summary listing of 36 head-on and oblique barge impacts is provided in Table 7.2. The summary listing indicates impact conditions simulated, and force results obtained. Basic parameters that are varied include flotilla configuration (number of strings, and thus flotilla mass) and Tainter gate state (open, closed). Also varied are impact angle (0° to 45°) and impact speed (4 ft/sec to 7 ft/sec).

7.4.3.2. Impact angle is defined as the angle between the centerline of impacting barge and the centerline of the Tainter gate. Here, the centerline of the Tainter gate is taken in a direction parallel to the longitudinal axes of the dam piers. As such, an impact angle of 0° denotes head-on impact. Initial barge flotilla velocity is in the direction parallel to the gate centerline. Alternatively stated, initial flotilla motion corresponds to the direction of hypothetical water flow through the dam.

7.4.4. Observations. Examining the force results (Table 7.2), it is evident that maximum forces are correlated to barge impact velocities. As barge impact velocities increase, so do maximum computed impact forces and maximum computed trunnion reaction forces. Additionally, maximum impact forces are correlated to impact angle. As impact angles vary from 0° (head-on) to 45° (oblique), maximum impact forces and maximum trunnion reactions consistently decrease.

7.4.4.1. For both head-on and oblique impacts, an important similarity is observed among the maximum force results. In the open gate configuration, head-on and oblique impacts both produce significant amplification of trunnion reactions relative to applied load. That is, maximum trunnion reactions are larger than the barge impact loads that are applied to the gate.

7.4.4.2. Consider two illustrative cases of open gate impacts (Table 7.9). For the 1x1 head-on impact at 0° and 6 ft/sec, the maximum trunnion reaction is 53% larger than the maximum barge impact load. Similarly, for the 2x1 oblique impact at 45° and 6 ft/sec, the maximum trunnion reaction is 50% larger than the maximum barge impact load. Both cases exhibit significant amplification of trunnion reactions even though the impact load magnitudes and the impact angles differ widely. This amplification phenomenon is demonstrated in Consolazio and Han (2018) to be associated with dynamic responses of open Tainter gates.

7.4.4.3. In contrast, when the gate is in the closed (i.e., down) condition, minimal amplification is observed. When closed, frictional forces act between the gate and sill plate, and movement of the gate is more limited. Additionally, the impact location on the gate changes, possibly leading to a change of characteristic stiffness and period of oscillation. Further details are provided in Consolazio and Han (2018).

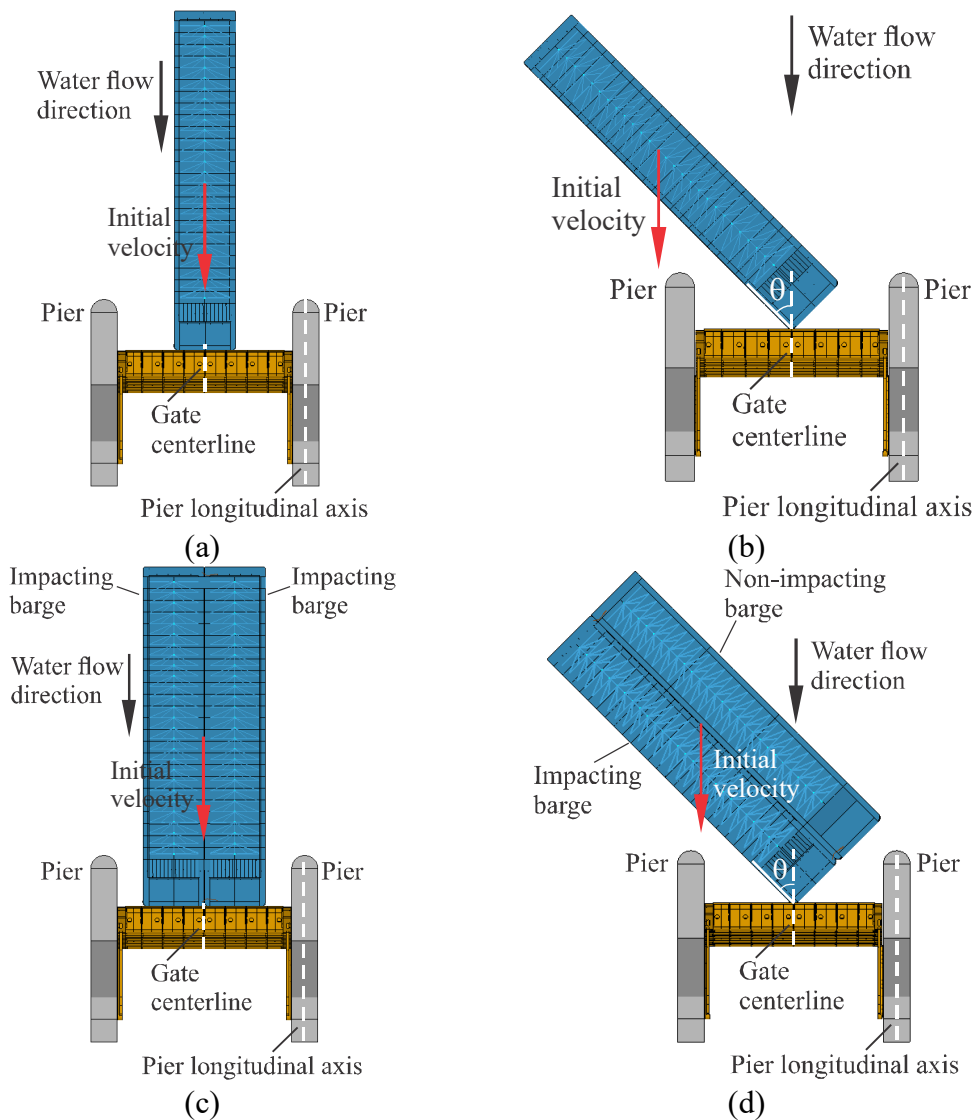


Figure 7.40. Barge-Tainter Gate Impact Conditions Investigated: (a) 1x1, Head-On; (b) 1x1, Oblique; (c) 2x1, Head-On; (d) 2x1, Oblique

Table 7.9
Tainter Gate Impact Conditions and Results (36 Cases)

Flotilla size	Gate state	Impact angle	Impact speed (ft/sec)	Max. impact force (kip)	Max. trunnion force (kip)	Max. force ratio (trunnion/impact)
1x1	Gate open	0°	4	4,290	5,330	1.24
			5	4,648	6,458	1.39
			6	4,831	7,397	1.53
			7	5,257	8,042	1.53
1x1	Gate closed	0°	4	3,877	4,356	1.12
			5	4,299	4,693	1.09
			6	4,748	5,412	1.14
			7	5,222	6,201	1.19
2x1	Gate open	0°	4	7,655	7,820	1.02
			5	8,444	9,047	1.07
			6	9,037	10,538	1.17
			7	9,372	11,847	1.26
2x1	Gate closed	0°	4	7,350	7,647	1.04
			5	8,174	8,544	1.05
			6	8,836	9,438	1.07
			7	9,276	10,156	1.09
1x1	Gate open	1°	7	4,719	5,030	1.07
		2°	7	3,641	3,990	1.10
		5°	7	2,496	3,029	1.21
		10°	7	1,888	2,648	1.40
1x1	Gate open	15°	4	1,527	1,918	1.26
			6	1,581	2,176	1.38
		30°	4	1,311	1,535	1.17
			6	1,414	2,021	1.43
		45°	4	996	1,419	1.42
			6	1,129	1,739	1.54
1x1	Gate closed	15°	4	1,440	1,425	0.99
			6	1,667	2,216	1.33
		30°	4	1,124	1,351	1.20
			6	1,337	1,814	1.36
		45°	4	947	1,074	1.13
			6	1,049	1,365	1.30
2x1	Gate open	45°	4	1,130	1,534	1.36
			6	1,139	1,705	1.50
2x1	Gate closed	45°	4	1,084	1,114	1.03
			6	1,305	1,390	1.07

7.4.4.4. As observed from summary data of the 36 parametric study cases (Table 7.9), several factors influence maximum impact forces. These factors include flotilla momentum, impact angle, and amplification of trunnion reactions. The phenomena (momentum, impact angle, trunnion reactions) are reflected in the simplified empirical prediction equations presented below.

7.4.5. Empirical Load Prediction Model. Using the barge impact forces and trunnion reactions from Table 7.9, empirical force prediction equations are developed in this section.

7.4.5.1. Sensitivity of Barge Impact Force to Angle of Obliquity. Maximum barge impact forces from Table 7.9 are plotted as a function of impact angle of obliquity in Figure 7.41. Sensitivity of force to angle of obliquity (θ) is clearly evident. Maximum forces occur when $\theta = 0^\circ$, where the entire width of the barge makes contact with the gate during impact. As the angle increases, the width of barge bow that is engaged upon impact decreases. Likewise, the magnitude of maximum force correspondingly decreases. This finding is consistent with prior published research (e.g., Getter and Consolazio 2011).

7.4.5.1.1 Beyond an angle of approximately 15° , the maximum impact forces (Figure 7.41a) tend to reach a minimum plateau level. In Figure 7.36b, maximum forces from Figure 7.41a are normalized by (divided by) the corresponding head-on maximum forces. As a result, the ordinate axis of Figure 7.41b consists of force ratios (R) less than or equal to 1.0. Consider, for example, the maximum force from the 1x1, 4 ft/sec, gate open, 15° case. To compute R , this value is normalized by the maximum force from the 1x1, 4 ft/sec, gate open, 0° case.

7.4.5.1.2 The data in Figure 7.41b strongly suggest an exponentially decaying relationship between normalized force ratio (R) and angle (θ):

$$R(\theta) = a_0 + a_1 \cdot e^{-a_2 \cdot \theta} \quad (7.7)$$

where angle θ is in $^\circ$ (degrees), a_0 is the plateau level; and a_1 and a_2 are exponential curve fitting parameters. An error minimization process is used to determine the parameters that best fit the data in a least square error sense.

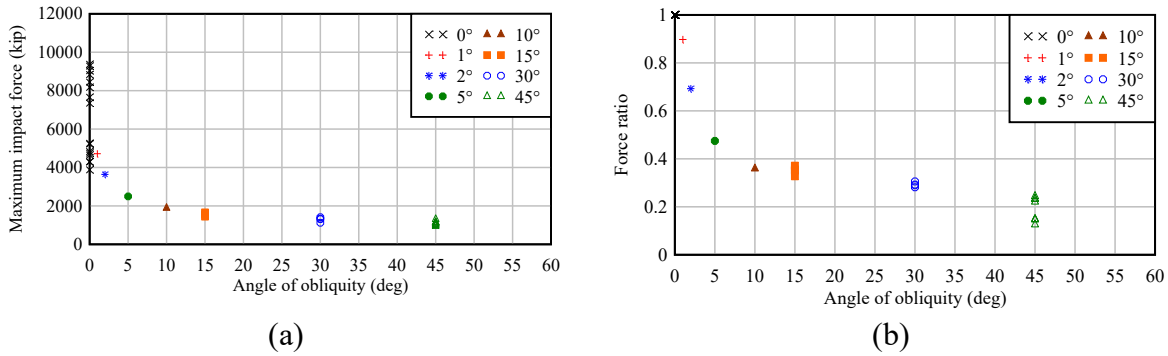


Figure 7.41. Sensitivity of Barge Impact Forces to Angle of Obliquity (36 Cases):
 (a) Maximum Impact Forces; (b) Maximum Impact Forces Normalized by
 Corresponding Head-on ($\theta = 0^\circ$) Impact Forces

7.4.5.1.3 After minimizing the cumulative square error function with respect to fitting parameters, the following relationship is established:

$$R(\theta) = 0.23 + 0.77e^{-0.168 \cdot \theta} \quad (7.8)$$

where angle θ is in $^\circ$ (degrees). Note that in Consolazio and Han (2018), angle θ was expressed in radians rather than degrees. Consequently, the numeric value of a_2 in Equation 7.8 differs from that reported in Consolazio and Han (2018). In Figure 7.42, Equation 7.8 is plotted together with the data from Figure 7.36b. Good agreement between the fitted curve and the data is observed.

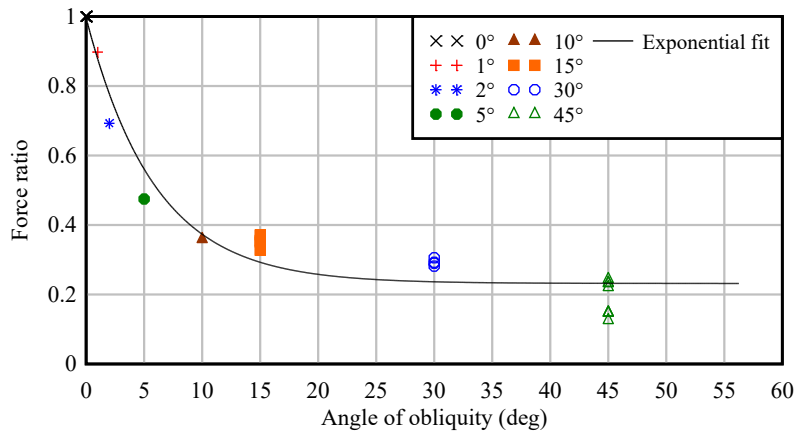


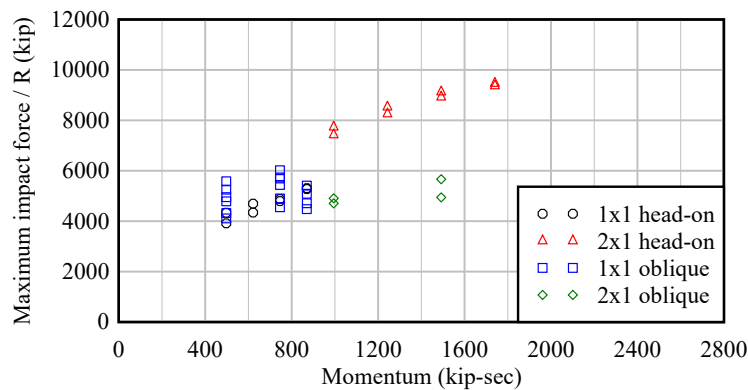
Figure 7.42. Comparison of Equation 4.2 and Normalized Force Data

7.4.5.2. Empirical Prediction of Impact Loads and Trunnion Reactions. Empirical expressions for predicting barge impact loads on Tainter gates and trunnion reactions incorporate force data from Table 7.8. To adjust for angle of obliquity (θ), maximum force data from Table 7.9 are divided by R , Equation 7.8. In Figure 7.43, adjusted maximum barge impact forces and maximum trunnion reaction forces are plotted as functions of linear impact momentum.

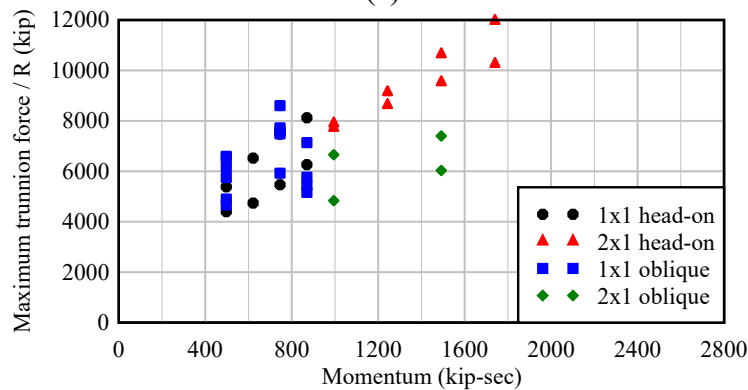
7.4.5.2.1 In Figure 7.43, the angle-adjusted maximum force data ($F/R(\theta)$) are shown to be generally well correlated to flotilla momentum. Outliers are found among the 2x1 oblique cases, which exhibit deviations from rest of the data set. Including the 2x1 oblique data would significantly reduce the overall conservatism of the empirical force prediction equations that are developed. Therefore, these data are omitted from the (empirical) curve fitting processes.

7.4.5.2.2 The curve fitting process maintains consistency of functional form with empirical force prediction models provided elsewhere in this manual. Bilinear forms are adopted elsewhere when forming empirical models for barge impact loads on other types of navigation structures. Accordingly, a bilinear form (Figure 7.44) is adopted for development of force prediction equations for flotilla-Tainter gate collisions.

7.4.5.2.3 The data in Figure 7.43 do not exhibit a clear transition between segments for low momentum and moderate to high momentum. The transition momentum level for each data set is therefore estimated as 100 kip-sec. This selection adds an initial, linear ramp to each empirical expression, applicable at low momentum levels.



(a)



(b)

Figure 7.43. Maximum Forces Divided by R , to Adjust for Angle of Obliquity (36 Cases):
 (a) Angle-Adjusted Maximum Barge Impact Forces; (b) Angle-Adjusted Maximum Trunnion Reaction Forces

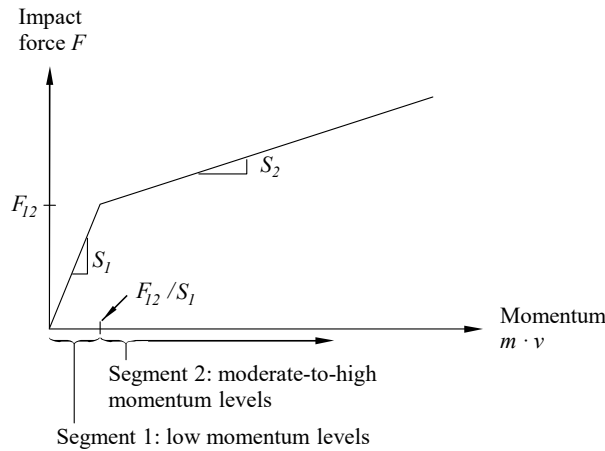


Figure 7.44. General Form of Bilinear Force Prediction Model for Tainter Gates

7.4.5.2.4 Three parameters define the bilinear fitting function. These are slopes S_1 and S_2 of the two segments, and an angle-adjusted transition force level, (F_{12}/S_1) . Functionally, the bilinear curve fit is expressed in the form:

$$\frac{F}{R(\theta)} = \begin{cases} S_1 \cdot (m \cdot v) & \text{if } m \cdot v \leq (F_{12}/S_1) \\ F_{12} + S_2 \cdot (m \cdot v - (F_{12}/S_1)) & \text{otherwise} \end{cases} \quad (7.9)$$

where $F/R(\theta)$ is the angle-adjusted barge impact force or trunnion reaction. Also, $m \cdot v$ is the total momentum of all barges in the flotilla.

7.4.5.2.5 To determine values of S_1 , S_2 , and F_{12} that optimally fit force data, error function minimization process is used. Using data in Figure 7.43a (except the 2x1 oblique data), an equation is established for impact forces on Tainter gates:

$$F_{impact} = \begin{cases} R(\theta) \cdot 25.5 \cdot m \cdot v & \text{if } m \cdot v \leq 100 \text{ kip-sec} \\ R(\theta) \cdot [2550 + 4.38 \cdot (m \cdot v - 100)] & \text{otherwise} \end{cases} \quad (7.10)$$

where $m \cdot v$ is the total flotilla momentum in units of kip-sec.

7.4.5.2.6 The confidence bounds are also established at confidence levels of 1-standard deviation (84.1%) and 2-standard deviations (97.7%) from the mean. Functionally, these bounds are given by:

$$F_{impact, 84.1\%} = \begin{cases} R(\theta) \cdot 28.7 \cdot m \cdot v & \text{if } m \cdot v \leq 100 \text{ kip-sec} \\ R(\theta) \cdot [2870 + 4.96 \cdot (m \cdot v - 100)] & \text{otherwise} \end{cases} \quad (7.11)$$

and:

$$F_{impact, 97.7\%} = \begin{cases} R(\theta) \cdot 31.6 \cdot m \cdot v & \text{if } m \cdot v \leq 100 \text{ kip-sec} \\ R(\theta) \cdot [3160 + 5.55 \cdot (m \cdot v - 100)] & \text{otherwise} \end{cases} \quad (7.12)$$

7.4.5.2.7 Using the data in Figure 7.43b (except the 2x1 oblique data), an empirical equation is established for predicting trunnion reactions:

$$F_{trunnion} = \begin{cases} R(\theta) \cdot 37.7 \cdot m \cdot v & \text{if } m \cdot v \leq 100 \text{ kip-sec} \\ R(\theta) \cdot [3770 + 4.42 \cdot (m \cdot v - 100)] & \text{otherwise} \end{cases} \quad (7.13)$$

7.4.5.2.8 The confidence bounds are also established at confidence levels of 1-standard deviation (84.1%) and 2-standard deviations (97.7%) from the mean. Functionally, these bounds are given by:

$$F_{trunnion, 84.1\%} = \begin{cases} R(\theta) \cdot 43.1 \cdot m \cdot v & \text{if } m \cdot v \leq 100 \text{ kip-sec} \\ R(\theta) \cdot [4310 + 5.08 \cdot (m \cdot v - 100)] & \text{otherwise} \end{cases} \quad (7.14)$$

and:

$$F_{trunnion, 97.7\%} = \begin{cases} R(\theta) \cdot 48.1 \cdot m \cdot v & \text{if } m \cdot v \leq 100 \text{ kip-sec} \\ R(\theta) \cdot [4810 + 5.78 \cdot (m \cdot v - 100)] & \text{otherwise} \end{cases} \quad (7.15)$$

7.4.5.2.9 Impact force and trunnion reaction force (F_{impact} , $F_{trunnion}$, respectively), in the direction of barge flotilla travel, possess units of kip. Plotted in Figure 7.45 and Figure 7.46 are the mean-value empirical load prediction models Equation 7.10 and Equation 7.13. Also included in the plots are maximum impact forces and trunnion reactions, as determined from FE impact simulations.

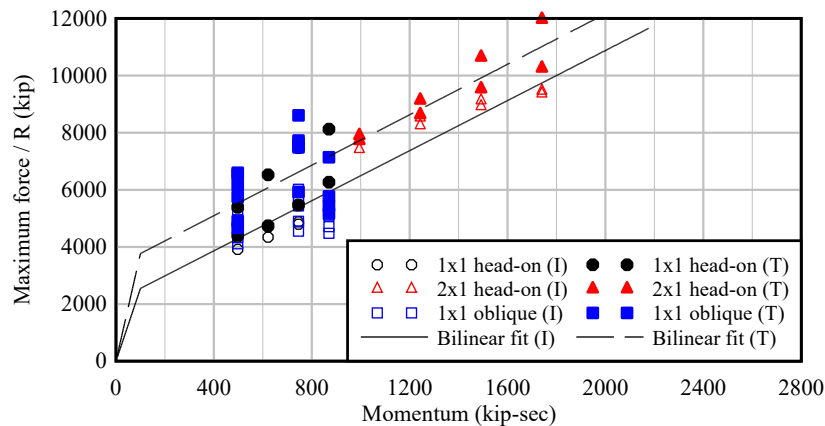


Figure 7.45. Comparison of Angle-Adjusted Force Data from Dynamic Simulations and Empirical Tainter Gate Force Prediction Equations, Equation 7.10 and Equation 7.13 (Note: I—Impact Load, and T—Trunnion Load)

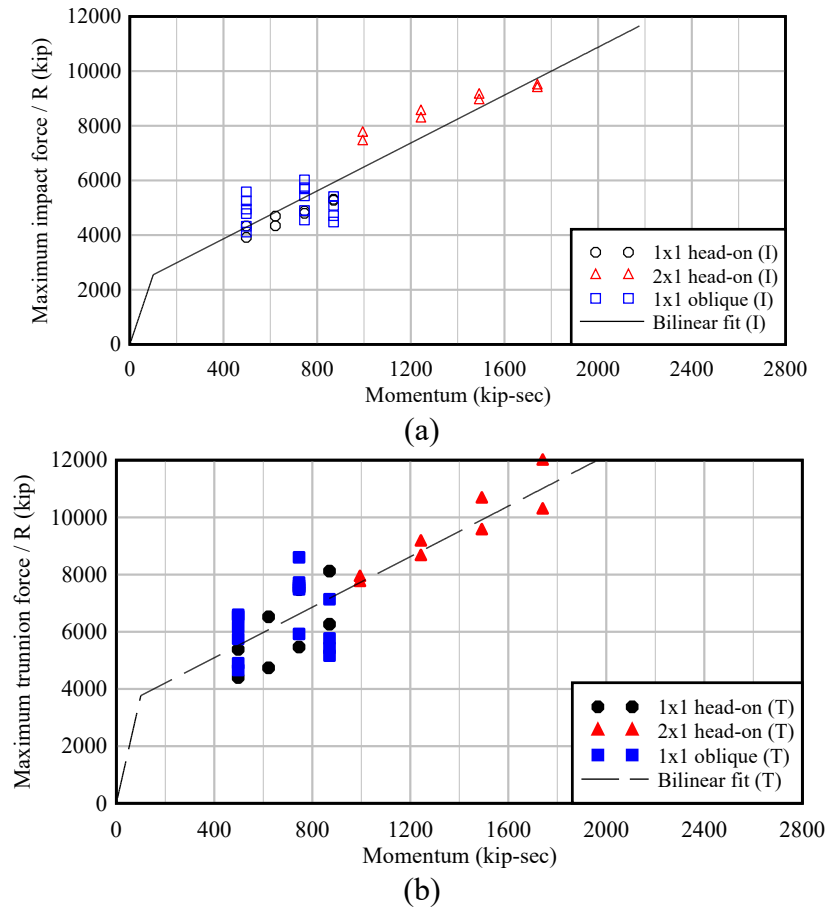


Figure 7.46. Comparison of Angle-Adjusted Force Data from Impact Simulations and Empirical Tainter Gate Force Prediction Equations (a) Maximum Barge Impact Forces and Equation 7.10; (b) Maximum Trunnion Reaction Forces and Equation 7.13 (Note: I—Impact Load, and T—Trunnion Load)

7.4.6. Deterministic Example – Tainter Gates. A deterministic impact scenario, associated with usual conditions, is presented for Tainter gates in section 7.4.6.1. Unusual and extreme impact scenarios involving Tainter gates are focused on in section 7.4.6.2 and section 7.4.6.3, respectively.

7.4.6.1. Usual. Figure 7.47 shows a plan-view schematic of the deterministic example for usual impact conditions on a Tainter gate. A fully loaded 1x1 (single-barge) flotilla is selected for this scenario, weighing 2,000 short tons (10.4 kip-sec²/in. mass). The initial barge velocity is 4 ft/sec, directed parallel to the long dimensions of the adjacent piers. However, the barge is oriented at an angle of obliquity of 45° from head-on impact conditions. Impact occurs at the centerline of the Tainter gate structure.

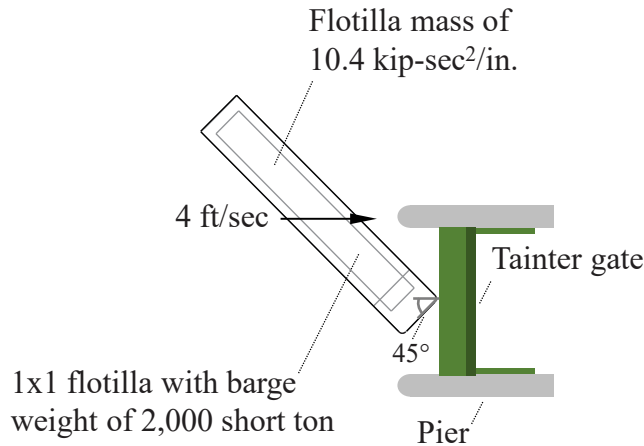


Figure 7.47. Deterministic (Usual) Impact Scenario on Tainter Gate

7.4.6.1.1 Relevant parameters associated with the deterministic (usual) impact scenario are listed in Table 7.10. Barge mass (m), angle of obliquity (θ), and impact velocity (v) are used in evaluating impact and trunnion forces. First, using the angle of 45° (degrees) the normalized impact versus trunnion force ratio, R , is calculated (as 0.23) using Equation 7.8.

7.4.6.1.2 Next, impact and trunnion forces are determined using Equation 7.10 and Equation 7.13, respectively. As used in each force calculation (impact, trunnion), barge momentum ($m \cdot v$) is 497.3 kip-sec in this example. Barge momentum exceeds the proportional threshold of 100 kip-sec, where this threshold is common to both Equation 7.10 and Equation 7.13. Therefore, the design impact and trunnion forces, associated with segment 2 of Figure 7.44 for the (deterministic) usual impact condition are, respectively, 990 kip and 1,271 kip.

Table 7.10
System Parameters for Deterministic (Usual) Impact Scenario on Tainter Gate

Parameter Description	Value	Units
Flotilla columns	1	N/A
Flotilla rows	1	N/A
Weight per barge	2,000	short tons
Flotilla mass	10.4	kip-sec ² /in.
Impact speed	4	ft/sec
Flotilla momentum	497.3	kip-sec
Angle of obliquity	45	°
Usual Impact Force	990/1,271	kip

7.4.6.2. Unusual. Figure 7.48 shows a plan-view schematic of the deterministic example for unusual impact conditions on a Tainter gate. A fully loaded 1x1 (single-barge) flotilla is selected for this scenario, weighing 2,000 short tons (10.4 kip-sec²/in. mass). The initial barge velocity is 5 ft/sec, directed parallel to the long dimensions of the adjacent piers. The barge is oriented consistent with a head-on impact condition, which corresponds to an angle of obliquity of 0°. Impact occurs at the centerline of the Tainter gate structure.

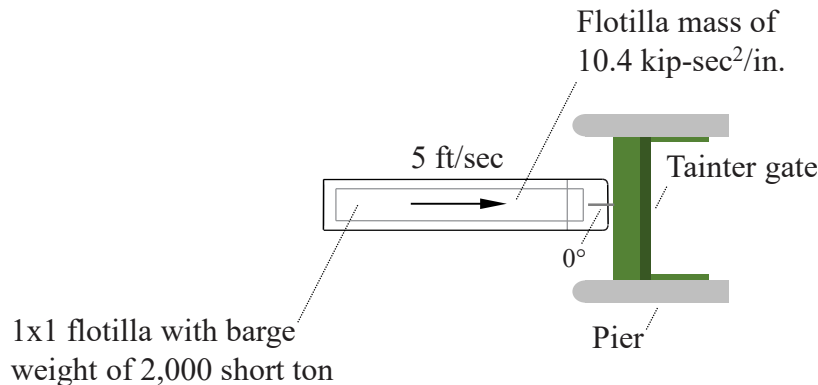


Figure 7.48. Deterministic (Unusual) Impact Scenario on Tainter Gate

7.4.6.2.1 Parameters associated with predicting impact forces for the deterministic (unusual) impact scenario are listed in Table 7.11. Barge mass (m), angle of obliquity (θ), and impact velocity (v) are used in evaluating impact and trunnion forces. First, the normalized impact versus trunnion force ratio, R , is calculated (as 1.0) using Equation 7.8.

7.4.6.2.2 Subsequently, impact and trunnion forces are quantified using Equation 7.10 and Equation 7.13, respectively. As used in each force calculation (impact, trunnion), barge momentum ($m \cdot v$) is 621.6 kip-sec in this example. Barge momentum exceeds the 100 kip-sec, where this threshold is common to both Equation 7.10 and Equation 7.13. Therefore, the design impact and trunnion forces, associated with segment 2 of Figure 7.44, for the (deterministic) unusual impact condition are, respectively, 4,797 kip and 6,004 kip.

Table 7.11

System Parameters for Deterministic (Unusual) Impact Scenario on Tainter Gate

Parameter Description	Value	Units
Flotilla columns	1	N/A
Flotilla rows	1	N/A
Weight per barge	2,000	short tons
Flotilla mass	10.4	kip-sec ² /in.
Impact speed	5	ft/sec
Flotilla momentum	621.6	kip-sec
Angle of obliquity	0	°
Unusual Impact Force	4,797/6,004	kip

7.4.6.3. Extreme. Figure 7.49 shows a plan-view schematic of the deterministic example for extreme impact conditions on a Tainter gate. A fully loaded 2x1 flotilla is selected for this scenario, with each barge weighing 2,000 short tons (10.4 kip-sec²/in. mass). The initial flotilla velocity is 6 ft/sec, directed parallel to the long dimensions of the adjacent piers. The flotilla is oriented for head-on impact, corresponding to an angle of obliquity of 0°. Impact occurs such that the centerline of the flotilla aligns with the centerline of the Tainter gate structure.

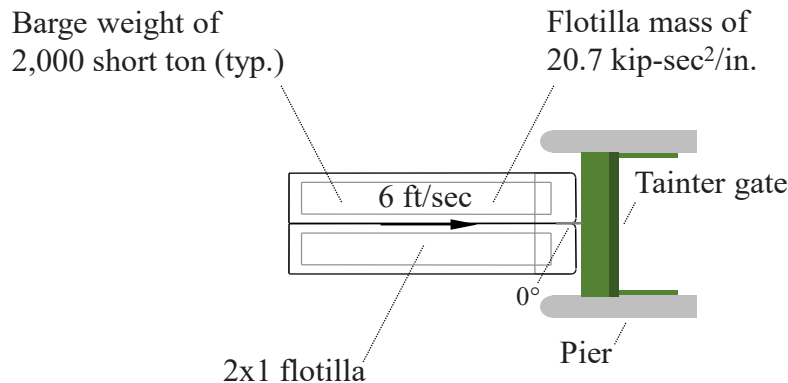


Figure 7.49. Deterministic (Extreme) Impact Scenario on Tainter Gate

7.4.6.3.1 Empirical load prediction parameters associated with the deterministic (extreme) impact scenario are listed in Table 7.12. Barge mass (m), angle of obliquity (θ), and impact velocity (v) are used in evaluating impact and trunnion forces. First, the normalized impact versus trunnion force ratio, R , is calculated (as 1.0) using Equation 7.8.

7.4.6.3.2 Afterward, impact and trunnion forces are determined using Equation 7.10 and Equation 7.13, respectively. Relevant to each force calculation (impact, trunnion), the flotilla momentum ($m \cdot v$) is 1,491.8 kip-sec in this example. Flotilla momentum exceeds the 100 kip-sec, for both Equation 7.10 and Equation 7.13. The design impact and trunnion forces, associated with segment 2 of Figure 7.44 for the (deterministic) extreme impact condition are, respectively, 8,588 kip and 9,795 kip.

Table 7.12**System Parameters for Deterministic (Extreme) Impact Scenario on Tainter Gate**

Parameter Description	Value	Units
Flotilla columns	2	N/A
Flotilla rows	1	N/A
Weight per barge	2,000	short tons
Flotilla mass	20.7	kip-sec ² /in.
Impact speed	6	ft/sec
Flotilla momentum	1,491.8	kip-sec
Angle of obliquity	0	°
Extreme Impact Force	8,588/9,795	kip

Appendix A

References and Unit Conversion Factors

A.1. Required.

1. EM 1110-2-2104, Headquarters, U.S. Army Corps of Engineers (HQUSACE), Strength Design for Reinforced Concrete Hydraulic Structures, <https://www.publications.usace.army.mil/LinkClick.aspx?fileticket=GWtYuDwRnRs%3d&tabid=16439&portalid=76&mid=43544>.
2. EM 1110-2-2107, HQUSACE, Steel Design for Hydraulic Structures, <https://www.publications.usace.army.mil/LinkClick.aspx?fileticket=GWtYuDwRnRs%3d&tabid=16439&portalid=76&mid=43545>.
3. Chasten, C and T. Ruf. (1991). “Miter Gate Barge Impact Testing, Lock and Dam 26, Mississippi River.” USACE Structural Engineering Conference, 8–12 July 1991, St John’s County, FL. <https://apps.dtic.mil/dtic/tr/fulltext/u2/a269604.pdf>.
4. Consolazio, G.R., Cowan, D.R., Biggs, A., Cook, R.A., Ansley, M., and Bollmann, H.T. (2005). “Full-Scale Experimental Measurement of Barge Impact Loads on Bridge Piers.” Transportation Research Record: Journal of the Transportation Research Board, No. 1936, pp. 81–93. <https://journals.sagepub.com/doi/pdf/10.1177/0361198105193600110>.
5. Consolazio G.R., Davidson M.T., Cowan D.R. (2009). “Barge Bow Force-Deformation Relationships for Barge-Bridge Collision Analysis.” Transportation Research Record, Vol. 2131, Issue 1: pp. 3–14. <https://doi.org/10.3141/2131-01>.
6. Consolazio, G.R., Davidson, M.T., Getter, D.J. (2010). “Development and Support of Dynamic Numerical Modeling of Aberrant Rake Barges Impacting Hurricane Protection Structures Subjected to Forces from a Hurricane Environment” Final Report. Structures Research Report 2010/83710, University of Florida, Department of Civil and Coastal Engineering. p. 112. <https://www.impact.essie.ufl.edu/wp-content/uploads/sites/176/2020/08/UF-report-2010-83710.pdf>.
7. Consolazio, G.R., Fung, J., Ansley, M. (2004). “M-f-P Diagrams for Concrete Sections Under Biaxial Flexure and Axial Compression.” American Concrete Institute (ACI) Structural Journal, Vol. 101, No. 1, pp. 114–123. <https://www.concrete.org/publications/internationalconcreteabstractsportal.aspx?m=details&i=13004&m=details&i=13004>.
8. Consolazio, G. R., Getter, D.J., Kantrales, G. C. (2014). “Validation and Implementation of Bridge Design Specifications for Barge Impact Loading.” Structures Research Report 2014/87294, University of Florida, Department of Civil and Coastal Engineering. <https://www.impact.essie.ufl.edu/wp-content/uploads/sites/176/2020/08/UF-report-2014-87294.pdf>.

9. Consolazio, G.R., Z. Han. (2015a). “Determination of Barge Impact Loads for Probabilistic Design of Miter Gates.” Structures Research Report 2015/118747, University of Florida, Department of Civil and Coastal Engineering.
<https://www.impact.essie.ufl.edu/publications/>.
10. Consolazio, G.R., Z. Han. (2015b). “Development of Low-Order Dynamic Code Module for Impact Load Prediction for Probabilistic Design and Analysis.” Structures Research Report 2015/118754, University of Florida, Department of Civil and Coastal Engineering.
<https://www.impact.essie.ufl.edu/publications/>.
11. Consolazio, G.R. and Z. Han. (2018). “Analysis of Concrete Floodwall Failure due to Impacts from Runaway Barges.” Structures Research Report 2018/126487, University of Florida, Department of Civil and Coastal Engineering.
<https://www.impact.essie.ufl.edu/publications/>.
12. Consolazio, G.R., R.A. Walters. (2012). “Development of Multi-Barge Flotilla Finite Element Models for Use In Probabilistic Barge Impact Analysis of Flexible Walls.” Structures Research Report 2012/94753, University of Florida, Department of Civil and Coastal Engineering, p. 79. <https://www.impact.essie.ufl.edu/wp-content/uploads/sites/176/2020/08/UF-report-2012-94753.pdf>.
13. Consolazio, G.R., Walters, R.A., Harper, Z.S. (2012). “Development of Finite Element Models for Studying Multi-barge Flotilla Impacts.” Structures Research Report 2010/87754, University of Florida, Department of Civil and Coastal Engineering.
<https://www.impact.essie.ufl.edu/wp-content/uploads/sites/176/2020/08/UF-report-2012-87754.pdf>.
14. Consolazio, G.R., J.R. Wilkes. (2013). “Determination of Multi-Barge Flotilla Impact Loads on Bullnose Structures and Flexible Timber Guide Walls.” Structures Research Report 2013/96918, University of Florida, Department of Civil and Coastal Engineering.
<https://www.impact.essie.ufl.edu/wp-content/uploads/sites/176/2020/08/UF-report-2013-96918.pdf>.
15. Consolazio, G.R., Wilkes, J.R., Rodrigues, C.R. (2014). “Determination of Barge Flotilla Impact Loads on Pile-Founded Concrete Guide Walls & Development of a Unified Impact Load Prediction Model for Navigational Structures.” Structures Research Report 2014/104971, University of Florida, Department of Civil and Coastal Engineering.
<https://www.impact.essie.ufl.edu/wp-content/uploads/sites/176/2020/08/UF-report-2014-104971.pdf>.
16. Davidson, M.T., Patev, R.C, Consolazio, G.R. (2020). “Probabilistic Risk Assessment of Barge Impacts on Hurricane Floodwalls.” American Society of Civil Engineers (ASCE) Journal of Performance of Constructed Facilities, Vol. 34, Issue 2, April 2020.
<https://ascelibrary.org/doi/full/10.1061/%28ASCE%29CF.1943-5509.0001412>.

17. Getter, D.J., G.R. Consolazio. (2011). “Relationships of Barge Bow Force-Deformation for Bridge Design: Probabilistic Consideration of Oblique Impact Scenarios.” Transportation Research Record: Journal of the Transportation Research Board, No. 2251, Issue 1, pp. 3–15. <https://journals.sagepub.com/doi/abs/10.3141/2251-01>.
18. Getter, D.J., Davidson, M.T., Consolazio, G.R., Patev, R.C. (2015). “Determination of Hurricane-Induced Barge Impact Loads on Floodwalls using Dynamic Finite Element Analysis.” Engineering Structures, Vol. 104, pp. 95–106. <https://www.sciencedirect.com/science/article/abs/pii/S0141029615005921>.
19. Kantrales, G.C., Consolazio, G.R., Wagner, D.R., Fallaha, S. (2016). “Experimental and Analytical Study of High-Level Barge Deformation for Barge–Bridge Collision Design.” ASCE Journal of Bridge Engineering, Vol. 21, Issue 2. <https://ascelibrary.org/doi/full/10.1061/%28ASCE%29BE.1943-5592.0000801>.
20. Kantrales, G.C., Davidson, M.T., Consolazio, G.R. (2019). “Influence of Impact-Induced Relative Motion on Effective Barge Flotilla Mass.” ASCE Journal of Bridge Engineering, Vol. 24, Issue 4. <https://ascelibrary.org/doi/full/10.1061/%28ASCE%29BE.1943-5592.0001374>.
21. Patev, R.C. (2005). “Development of U.S. Army Corps of Engineers Engineering Guidance for the Barge Impact Design of Navigation Structures.” Transportation Research Record: Journal of the Transportation Research Record, Vol. 1936, Issue 1. pp. 94–99. <https://journals.sagepub.com/doi/pdf/10.1177/0361198105193600111>.
22. Patev, Robert C. (Dec 1999). “Full-Scale Barge Impact Experiments.” Transportation Research Circular No. 491, Transportation Research Board, National Research Council, Washington, D.C. [https://www.safetylit.org/citations/index.php?fuseaction=citations.viewdetails&citationIds\[\]=journalarticle_181155_29](https://www.safetylit.org/citations/index.php?fuseaction=citations.viewdetails&citationIds[]=journalarticle_181155_29).
23. Patev, R.C. (2000). “Probabilistic Barge Impact Analysis of the Upper Guide and Guard Walls at Marmet Locks and Dam.” USACE Research and Development Center, Technical Report ERDC/ITL TR-00-4. Vicksburg, MS. USACE. <https://www.impact.essie.ufl.edu/wp-content/uploads/sites/176/2020/08/USACE-ERDC-ITL-TR-00-4.pdf>.
24. Patev, R.C., Barker, B.C., Koestler III, L.V. (2003a). “Full-Scale Barge Impact Experiments, Robert C. Byrd Lock and Dam, Gallipolis Ferry, West Virginia.” USACE Research and Development Center, Technical Report ERDC/ITL TR-03-7, Vicksburg, MS. <https://www.impact.essie.ufl.edu/wp-content/uploads/sites/176/2020/08/USACE-ERDC-ITL-TR-03-7.pdf>.

25. Patev, R.C., Barker, B.C., Koestler III, L.V. (2003b). “Prototype Barge Impact Experiments, Allegheny Lock and Dam 2, Pittsburgh, Pennsylvania.” USACE Research and Development Center, Technical Report ERDC/ITL TR-03-2, Vicksburg, MS.
<https://www.impact.essie.ufl.edu/wp-content/uploads/sites/176/2020/08/USACE-ERDC-ITL-TR-03-2.pdf>.

26. Patev, R.C., Consolazio, G.R., Hudson, P., McCormick, M., Marr, B., Walker, C.J., Hokens, K. (2010). “Aberrant Barge Impact Loads on Hurricane and Storm Damage Risk Reduction System (HSDRRS) Floodwalls.” USACE North Atlantic Division.
<https://www.mvn.usace.army.mil/Missions/Engineering/Hurricane-Design-Guidelines/Hurricane-Design-Guidelines/>.

A.2. Related.

1. USACE. “Hurricane and Storm Damage Reduction System Design Guidelines, Interim.” USACE, New Orleans District Engineering Division, October.
<https://www.mvn.usace.army.mil/Missions/Engineering/Hurricane-Design-Guidelines/Hurricane-Design-Guidelines/>.

2. American Association of State Highway and Transportation Officials (AASHTO). (2017). “LRFD Bridge Design Specifications,” 8th Edition. Washington D.C.
<https://aashtojournal.org/2020/05/08/aashto-issues-updated-lrfd-bridge-design-guide/>.

3. American Society for Testing and Materials (ASTM). (2009). “Standard Specification for Stranded Carbon Steel Wire Ropes for General Purposes.” American Society for Testing and Materials, ASTM A1023-09, West Conshohocken, PA.
<https://www.astm.org/DATABASE.CART/HISTORICAL/A1023A1023M-09.htm>.

4. ASTM A328/A328M-13a. (2013). “Standard Specification for Steel Sheet Piling.” ASTM International. <https://www.astm.org/Standards/A328.htm>.

5. Arroyo, Jose R., Ebeling, Robert M., and Barker, Bruce C. (June 2003). “Analysis of Impact Loads from Full-Scale, Low Velocity, Controlled Barge Impact Experiments, Robert C. Byrd Lock, December 1998.” USACE Research and Development Center, Technical Report ERDC/ITL-03-03, Vicksburg, MS. <https://www.impact.essie.ufl.edu/wp-content/uploads/sites/176/2020/08/USACE-ERDC-ITL-TR-11-1.pdf>.

6. Bae, R.G. (2008). “Failure of the New Orleans 17th Street Canal Levee and Floodwall During Hurricane Katrina.” Geotechnical Engineering Congress, New Orleans, LA, March 9–12. [https://ascelibrary.org/doi/abs/10.1061/40962\(325\)23](https://ascelibrary.org/doi/abs/10.1061/40962(325)23).

7. Bridge Software Institute (BSI). (2013, 2014, 2016). “FB-MultiPier User’s Manual.” Florida Bridge Software Institute, University of Florida, Gainesville, FL.
<https://bsi.ce.ufl.edu/products/overview.aspx?software=7>.

8. Ebeling, Robert M., Mohamed, Abdul, Arroyo, Jose R., White, Barry C., Strom, Ralph W., Barker, Bruce C. (August 2011). “Dynamic Structural Flexible-Beam Response to a Moving Barge Train Impact Force Time History Using Impact Beam.” USACE Research and Development Center, Technical Report ERDC/ITL TR-11-1, Vicksburg, MS. <https://www.impact.essie.ufl.edu/wp-content/uploads/sites/176/2020/08/USACE-ERDC-ITL-TR-11-1.pdf>.
9. Jones, N. (1997). “Structural Impact.” Cambridge University Press, New York, NY. <https://books.google.com/books?hl=en&lr=&id=AkGnbX4kIsEC&oi=fnd&pg=PR7&dq=structural+impact+jones&ots=SYFvCaz0B0&sig=wDmarOgldegRFJnxDSQFBrdhczA#v=onepage&q=structural%20impact%20jones&f=false>.
10. LSTC. (2014a). “LS-DYNA Keyword User’s Manual, Vol. II.” Material Models, Livermore Software Technology Corporation Livermore, CA. http://lstc.com/pdf/ls-dyna_971_manual_k.pdf.
11. LSTC. (2014b). “LS-DYNA Keyword User’s Manual, Vol. I.” Livermore Software Technology Corporation Livermore, CA. http://lstc.com/pdf/ls-dyna_971_manual_k.pdf.
12. McCormack, J.C., R.H. Brown. (2015). “Design of Reinforced Concrete, 10th Ed.,” <https://www.wiley.com/en-us/Design+of+Reinforced+Concrete,+10th+Edition-p-9781118879108>.
13. Minorsky, V.U. (1959). “An Analysis of Ship Collisions with Reference to Protection of Nuclear Power Plants.” Journal of Ship Research, Vol. 3, No. 2, pp. 1–4. <https://www.osti.gov/biblio/4257123>.
14. NOAA. (1987). “The National Hurricane Center Risk Analysis Program (HURISK).” NOAA Technical Memorandum NWS NHC 38, National Hurricane Center, Coral Gables, FL. <https://www.nhc.noaa.gov/pdf/NWS-NHC-1987-38.pdf>.
15. Palisade. (2015). @Risk: Risk Analysis and Simulation Add-In for Microsoft Excel, Version 7, Palisade Corporation, Ithaca, NY. <https://www.palisade.com/support/manuals.asp>.
16. Patev, Robert C., Mlakar, Paul F., Bryant, Larry M. (Nov. 2000) “Physical Data Collection for Lock Wall Deterioration.” USACE Research and Development Center, Technical Report ERDC/ITL-00-6, Vicksburg, MS. <https://apps.dtic.mil/sti/citations/ADA386607>.
17. Patev, Robert C., Vineuza, Gustavo, Mejia, Daniel. (March 2014). “User’s Guide for Probabilistic Barge Impact Model for Design and Analysis of Barge Impact – @Risk Excel Software.” Institute for Water Resources, Risk Management Center Technical Report, RMC-17-01, Concord, MA. <https://www.palisade.com/support/manuals.asp>.
18. STAAD.PRO [Computer software]. Bentley, Exton, PA. https://communities.bentley.com/cfs-file/_key/telligent-evolution-components-attachments/13-275895-00-00-00-24-18-54/technical_5f00_reference_5f00_v8i.pdf.

19. Tedesco, J.W., McDougal, W.G., Ross, C.A. (1999). “Structural Dynamics: Theory and Applications.” Addison Wesley Longman, Inc., Menlo Park, CA.
<https://www.scribd.com/document/426603774/STRUCTURAL-DYNAMICS-Tedesco>.

20. Tsang, Joshua, L., Lambert, James H., Patev, Robert C. (Dec. 2002). “Multiple Criteria Decision-Making in the Design of Innovative Lock Walls for Barge Impact; Phase 2, Implementation of Methodologies.” ERDC Technical Report ITL-03-8, USACE Research and Development Center, Vicksburg, MS. <https://apps.dtic.mil/sti/citations/ADA410814>.

A.3. Unit Conversion Factors.

Table A.1
Unit Conversion Factors

Multiply	By	To Obtain
cubic feet	0.02831685	cubic meters
cubic inches	1.63871E-05	cubic meters
degrees (angle)	0.01745329	radians
feet	0.3048	meters
inches	0.0254	meters
pounds (force)	4.448222	newtons
pounds (force) per square foot	47.88026	pascals
pounds (force) per square inch	6.894757	kilopascals
square feet	0.09290304	square meters
square inches	6.4516E-04	square meters
square miles	2.59E+06	square meters
cubic meters	35.31466	cubic feet
cubic meters	61023.7	cubic inches
radians	57.295788	degrees (angle)
meters	3.2808	feet
meters	39.37	inches
newtons	0.224809	pounds (force)
pascals	0.020885	pounds (force) per square foot
kilopascals	0.145038	pounds (force) per square inch
square meters	10.763910	square feet
square meters	1,550.0	square inches
square meters	3.86E-07	square miles

Appendix B

Prototype Field Experiments

B.1. Introduction. Three series of full-scale impact experiments were completed under the Innovations for Navigation Research and Development Program at the Engineer Research and Development Center – Waterways Experiment Station. These experiments have been termed prototype, full-scale, and crushing impact experiments. These experiments were conducted to help estimate actual impact loads using typical inland waterway flotillas and to develop analytical or numerical models for barge impact design of navigations structures.

B.2. Prototype Barge Impact Experiments.

B.2.1. The prototype barge impact experiments were conducted on an old lock wall at Allegheny River L&D 2 in Pittsburgh, Pennsylvania. These experiments were termed prototype because this type of full-scale experiment using an inland waterway flotilla has never before been attempted. The goals of these prototype experiments were to learn how to quantify and measure barge impact forces, as well as understand the complexity of the barge-wall system during impact. The observations and results from these prototype experiments are discussed and documented further in Patev et al 2003.

B.2.2. These experiments utilized four standard (27 ft by 195 ft) open hopper rake barges. The barges were drafting as 8 ½ ft and had a combined mass of around 4,000 short tons. Twenty-eight impact experiments were performed on a rigid massive concrete wall, and seven tests on frictionless ultra-high molecular weight (UHMW) plastic fenders. The use of the UHMW fenders was to investigate the redistribution of the barge energy and direction during impact. The experiments utilized 15 different instrumentations recorded on 28 channels on the flotilla and land wall.

B.2.3. The instrumentation included accelerometers and strain gauges on the lead corner barge as well as clevis pin load cells spliced into the lashings. These clevis pin load cells measured the changes in tensile force in the lashing parts upon impact. A multi-unit Differential Global Positioning System (DGPS) also measured the velocities (normal and tangential), impact angle, and rotation of the flotilla during impact. A high-speed camera (100 frames per second) and a video camera were set up to document the interaction of the barge-wall system upon impact.

B.2.4. Overall, these experiments were very valuable in providing a better understanding of the dynamics of the barge-wall system and contributed vital data that could be used to plan and design the full-scale barge impact experiments.

B.3. Full-Scale Barge Impact Experiments.

B.3.1. The full-scale barge impact experiments were conducted on a lock wall at Robert C. Byrd L&D (Old Gallipolis Lock) in Gallipolis Ferry, West Virginia. The primary goal of these experiments was to measure the actual impact forces normal to the wall using a load-measuring

device. The focus of these experiments was to measure the baseline response of an inland waterway barge, quantify an MDOF system during impact, and investigate the use of energy-absorbing fenders. The observations and results from these full-scale experiments are discussed further in Patev et al., 2003.

B.3.2. The full-scale experiments used a fifteen-barge commercial flotilla. The barges were jumbo open hopper rake barges (35 ft x 195 ft) and were ballasted with anthracite coal to a draft of 9 ft. The total mass of the flotilla was approximately 30,000 short tons. The use of the barges and a 2,800-horsepower towboat, the MS Jeffery V. Raike, was arranged under a partnership agreement with American Electric Power River Transportation Division of Lakin, West Virginia. A helper boat was also needed in case of emergency with the prime vessel or breakup of the flotilla during impact.

B.3.3. The helper boat, a 1,100-horsepower towboat, the MS Quaker State, was supplied by Kanawha River Towing of Point Pleasant, West Virginia. A picture of the fifteen-barge tow and helper boat is shown in Figure B.1.



Figure B.1. Picture of Flotilla Used for Full-Scale Experiments

B.3.4. Forty-four impact experiments were successfully conducted on both the rigid concrete upper guide wall (baseline and load-measuring device) and on the prototype fendering system (baseline and load-measuring device). A matrix of the required angles and velocities was assembled for the comparison between the baseline and load-measuring experiments on both the concrete and prototype fendering systems. This matrix was successfully filled for each impact case during these 44 experiments. The final matrix contained angles of impact from 5 to 25 degrees with velocities of 0.5 to 4 ft per second (fps). An example matrix for velocities and angles for the load beam experiments is shown in Figure B.2.

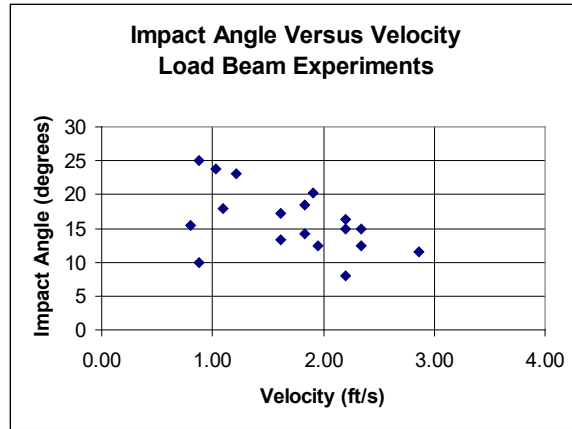


Figure B.2. Impact Angle and Velocities Matrix for Load Beam Experiments

B.3.5. Similar instrumentation used during the prototype experiments was utilized for the full-scale experiments. This included accelerometers (over 12 locations on flotilla), strain gauges, and clevis pin load cells in the lashing parts. The instrumentation data was collected using over 80 channels of instrumentation on both the barge and lock wall. These experiments also utilized DGPS on the flotilla to measure the velocity, angle, and rotation during impact as well as high-speed cameras to capture the barge-wall and barge-fender interaction. In addition, new instrumentation was developed to measure the actual load normal to the barge and wall.

B.3.6. This consisted of a load-measuring beam that had two clevis pin load cells capable of measuring up to 1,200 kips of force. In addition, a system of polyvinylidene flouride sensors was developed at the Waterways Experiment Station as part of a redundant load-measurement system on the load beam.

B.4. Full-Scale Crushing Experiments.

B.4.1. The full-scale crushing experiments were conducted in New Orleans, Louisiana, at the Halter Gulf Repair facilities during June 21–23, 2000. The experiments consisted of using two jumbo open hopper (95 ft by 135 ft) barges that were recently removed from service on the inland waterways and donated for the experiments. The barges were impacted using the 14 MN Statnamic load device owned by Applied Foundation Testing of Green Cove Springs, Florida. The Statnamic device is primarily used to test the axial and lateral capacities of piles and drilled shafts. The Statnamic device used for the experiments has the capability to deliver up to 2,400 kips of lateral force at a time duration similar to a barge impact.

B.4.2. A total of nine experiments were conducted on both the barge corners and headlogs (front face of the barge above the rake) of the two barges to determine the impact forces and deformations of the components. The experiments were conducted by incrementally loading the barge first to gain the linear response of the component and second to get the plastic or nonlinear response of the barge system.

B.4.3. The barges were instrumented with accelerometers, strain gauges, and force load cells to capture the impact data. High-speed and normal-speed video equipment was positioned above the impact zone to document the deformations and movements of the barge during impact. The impact loads on the barges ranged from 400 kips up to 1,600 kips of lateral forces. Deformations range from no observable to a foot of displacement.

B.5. Summary of Experimental Results.

B.5.1. The series of full-scale experiments conducted have been very beneficial in defining the complex behavior of a barge system during impact. These types of measurements have never been quantified before and give a better understanding of how the system works, so future modeling efforts can reflect the actual dynamics of the system.

B.5.2. While the data collected from these experiments is extremely valuable, the results do have some limitations before they can be extracted fully toward design. First, the prototype and full-scale experiments were for lower ranges of approach velocities and angles for flotillas on the inland waterway. Therefore, this data should not be extrapolated to high-speed impact events such as a loss of power or control. Second, these experiments were under controlled circumstances and included the preference of the towboat captain to maintain a safe environment during the experiments.

B.5.3. This preference does not include any unusual approach conditions due to pilot error, currents, or outdrafts that typically occur at navigation structures. Third, the crushing experiments, while more designed for head-on or side impact with structures, were only a limited number of experiments. This data set is only for typical inland waterway barges but cannot directly account for variation of the different barge types in service on the inland waterway.

Appendix C

Data from Previous Studies

C.1. Introduction.

C.1.1. This appendix will document several inland navigation studies that have performed analyses to determine the distribution of velocities and impact angles for tows for the design of their approach walls. The purpose of this appendix is to provide some basic design information on distributions for velocity and angles so that designers can gain an understanding of the scope of what needs to be developed for their own navigation study efforts.

C.1.2. The data summaries are presented for the typical design parameters (velocity, angle, and mass) used in design of approach walls at Olmsted L&D (Ohio River), Winfield L&D (Kanawha River), Kentucky L&D (Tennessee River), Marmet L&D (Kanawha River), London L&D (Kanawha River), and Greenup L&D (Ohio River). A brief description of the approach walls that were designed, plans and hydraulic flow vectors from the navigation model, if available, are presented for each project. The barge impact forces used in design of these projects are shown in Table D.11.

C.1.3. However, many of the distributions presented in these examples are documented using a Beta Subjective distribution. These distributions have been converted to a lognormal distribution with matching statistical parameters (i.e., mean, standard deviation and percentiles) since the Beta Subjective distribution is not always recommended for probabilistic analysis. Correlation coefficients for the velocity, angle, and mass are shown for the Marmet L&D project.

C.2. Project Examples.

C.2.1. Olmsted Approach Walls – Ohio River, Olmsted, Illinois.

C.2.1.1. The Louisville District began construction of the first phase of the Olmsted Locks and Dam project in 1993. The Olmsted Locks project began in 1996 and included the construction of two 1,200-ft-long lock chambers. Toward the end of the construction contract for completion of the locks, the contract to construct the approach walls began in 1999. The Olmsted Approach Walls project included four floating guard walls and one fixed guide wall; the four guard walls are aligned between the dam and the lock approaches.

C.2.1.2. Figure C.1 shows the layout of the approach walls at Olmsted L&D. The Olmsted Locks are aligned close to the Illinois shore, thus the approach angles for flotillas entering the locks are not expected to be large. The walls were designed for the Louisville District following the method described in Patev et al 2003. At the time of the design, there was not yet a set of locks at Olmsted at which the behavior of arriving flotillas could be observed.

C.2.1.3. Therefore, the design of the walls included data from model testing on a 1:120 scale model at ERDC-WES and the use of time-lapse videotape of the approaches at both Smithland Locks and Uniontown (currently called J.T. Myers) Locks since the characteristics of the barge traffic and the flow of the Ohio River were judged to be similar between these projects and Olmsted.

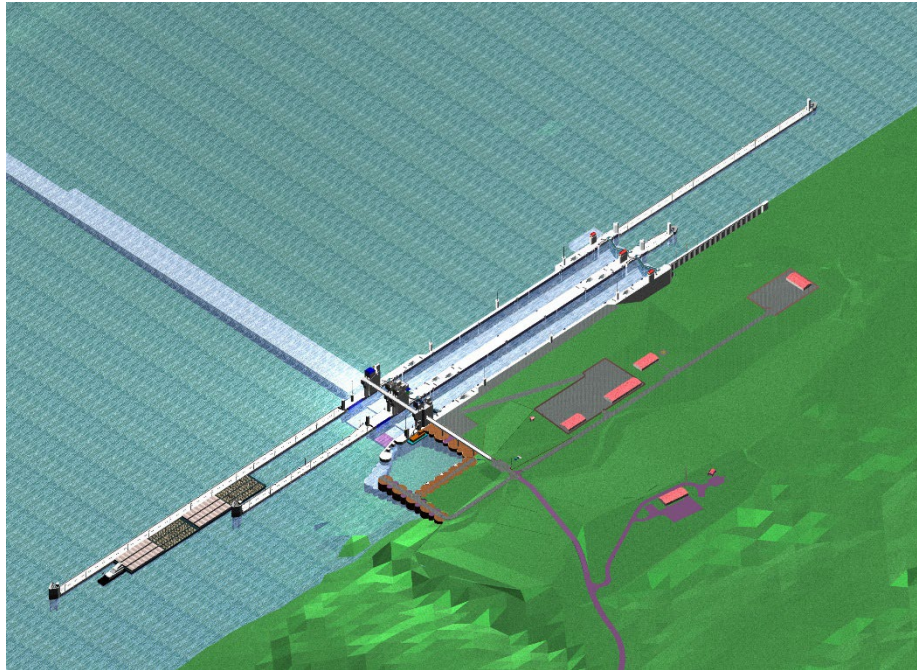


Figure C.1. Olmsted Locks and Approach Walls

C.2.1.4. The results from the scale model were primarily used to determine the barge impact parameters for the design of the approach walls. The videotape data from Smithland and J.T. Myers was used to validate the approach and landing of tows and the currents in the scale models and engineering judgment was used to combine the results of these discrete studies in development of the design parameters at Olmsted. Figure C.2 shows the velocities and flow vectors from the ERDC scale model, and Figure C.3 shows the time trace of the tow as it makes its approach to the locks under controlled landing scenario.

C.2.1.5. From the processing of the scale model experiments, the probability distribution for the impact angle is shown in Figure C.4, the probability distribution for the longitudinal velocity, V_{ox} , is shown on Figure C.5, and probability distribution for lateral velocity, V_{oy} , is in Figure C.6. The probability distribution for mass of the tows was taken from downbound traffic data at Lock 52, which is 25 miles downstream. This distribution for mass is shown in Figure C.7. A summary of the statistical parameters used for the barge impact design of the upper river guide wall is shown in Table C.1.

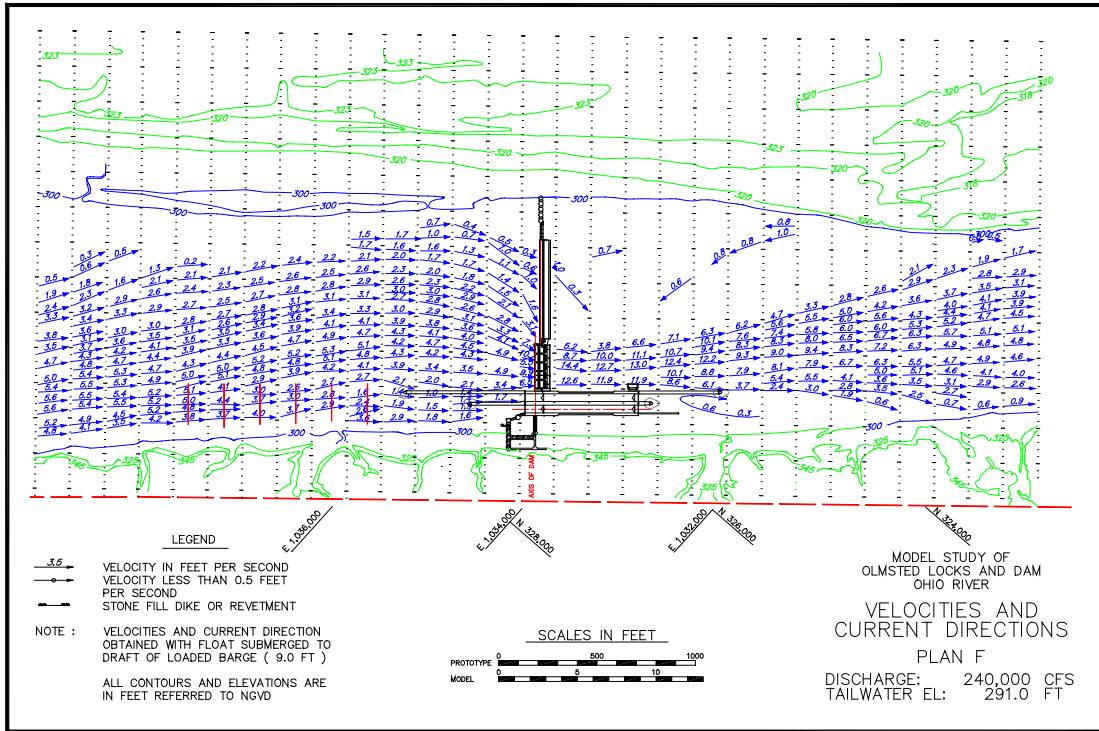


Figure C.2. Hydraulic Flow Results from Navigation Model for Olmsted Locks & Dam

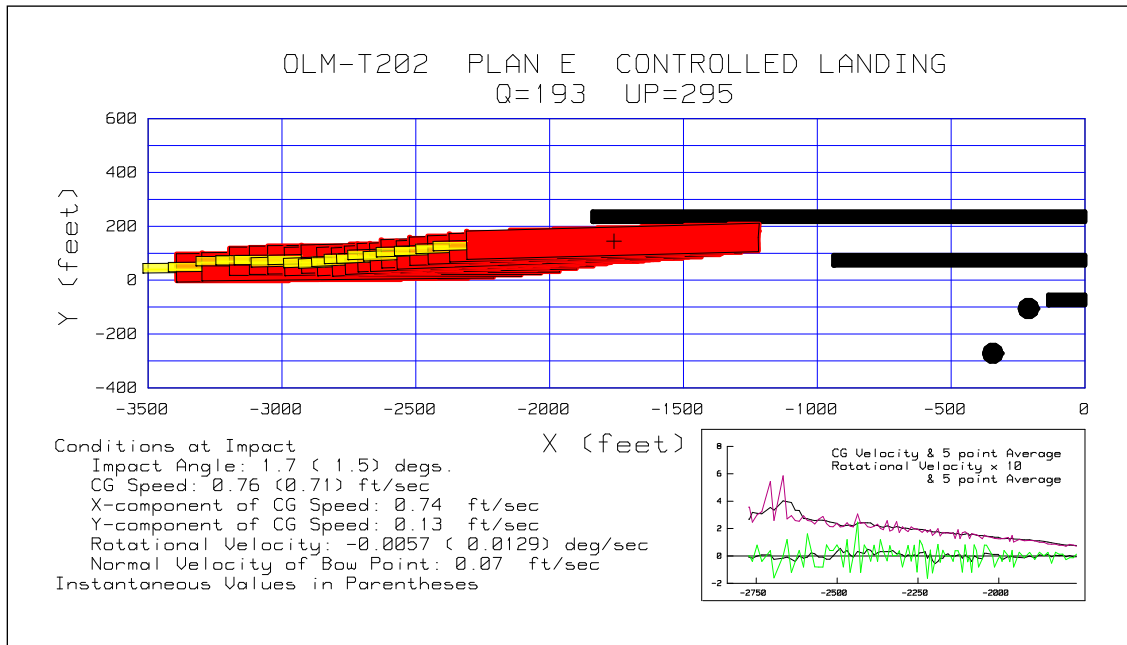


Figure C.3. Typical Trace of Experimental Barge Impacts at Olmsted Upper River Approach Wall from the ERDC-WES 1:120 Navigation Model

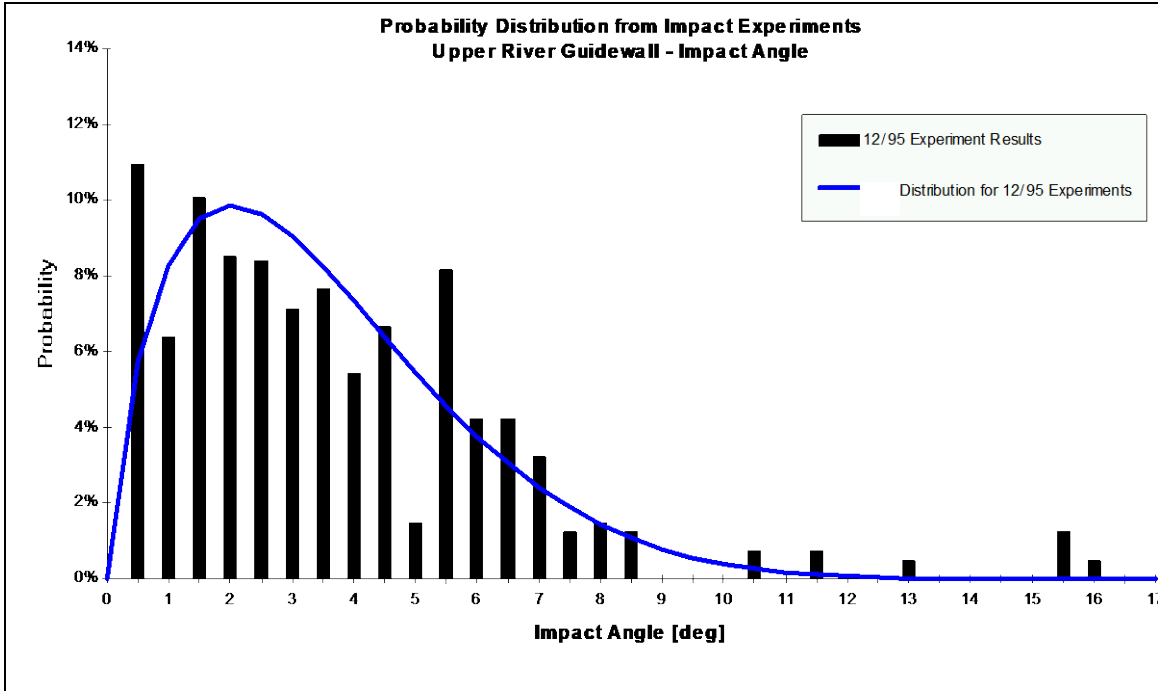


Figure C.4. Probability Distribution of Impact Angle for Olmsted Upper River Approach Wall

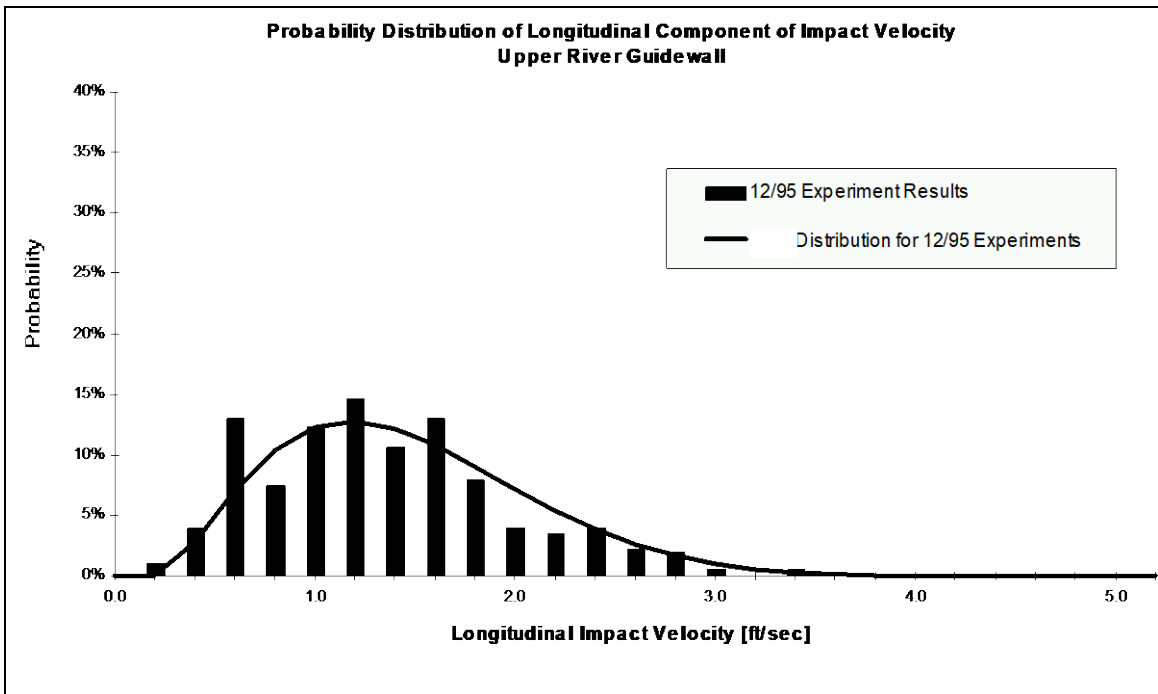


Figure C.5. Probability Distribution of Longitudinal Impact Velocity for Olmsted Upper River Approach Wall

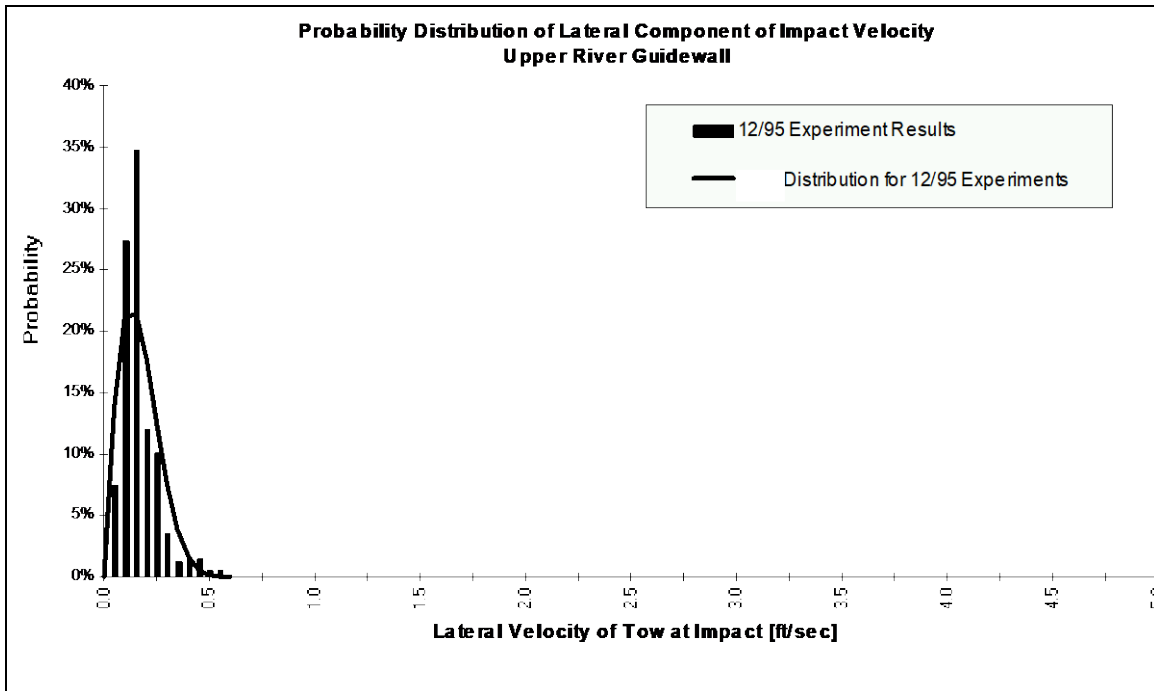


Figure C.6. Probability Distributions of Velocities and Angles for Olmsted Upper River Approach Wall

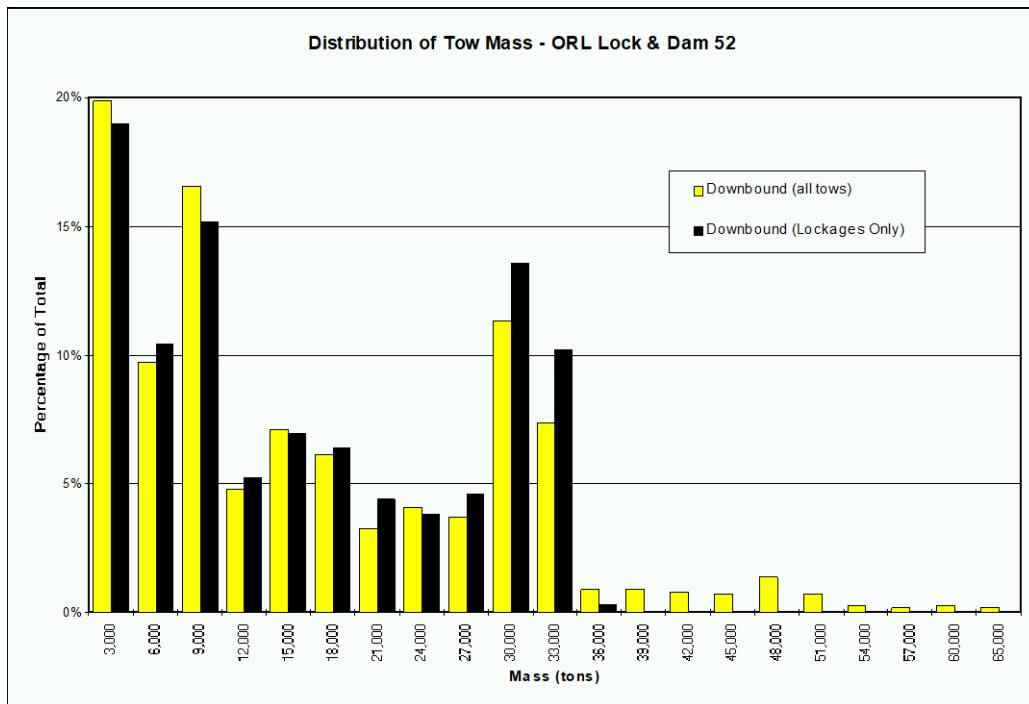


Figure C.7. Probability Distribution of Tow Mass for Olmsted Upper River Approach Wall (Data Taken from Lock 52, Located 25 Miles Upstream)

Table C.1
Lognormal Distribution Parameters for Impact Variables Olmsted Upper River Wall Approach Wall

Traffic Direction	Variable	Mean	Standard Deviation	Minimum	Maximum
Upper River Guide Wall	θ (deg)	3.3	2.2	0	17
	V_{ox} (ft/sec)	1.27	0.62	0	4.8
	V_{oy} (ft/sec)	0.07	0.092	0	1

C.2.2. Winfield Upper Approach Guard Wall – Kanawha River, Winfield, West Virginia.

C.2.2.1. The Huntington District completed construction of a new main lock chamber and upper approach guard wall at Winfield Locks in 1997. The new main lock is 110 ft wide by 800 ft long. During the construction contract for the new lock, the contractor prepared a Value Engineering proposal to reduce the number of sheet pile cells for the upper approach wall. This made the precast beams that spanned between sheet pile cells approximately three times longer as the original contract plans had designed and new barge impact analysis for the walls was required.

C.2.2.2. The barge impact design of the approach walls followed the method described in older ETLs. The Winfield site is located on the inside of a tight bend in the Kanawha River; thus, the approach angles for the upper guide wall can be expected to have a fairly wide variation. The approach for new lock at Winfield is shown in Figure C.8. To account for this fact, the 1:120 scale model included approximately 250 simulated barge impact events for both controlled experiments that used three different operators and uncontrolled or loss of power events.

C.2.2.3. For the design of the approach wall, the impact angle and forward velocity (i.e., composed of the longitudinal, V_{ox} , and transverse, V_{oy} , velocity components) data from the ERDC-WES scale navigation model was utilized. The distributions for velocity and angle are shown in Figure C.9 and Figure C.10. The data for the tow mass distribution as shown in Figure C.11 as obtained from the OMNI database by Huntington’s Navigation Planning Center. Table C.2 shows the statistical parameters from the scale model experiments used in the design of the approach walls.



Figure C.8. Upper Approach Guard Wall at Winfield L&D

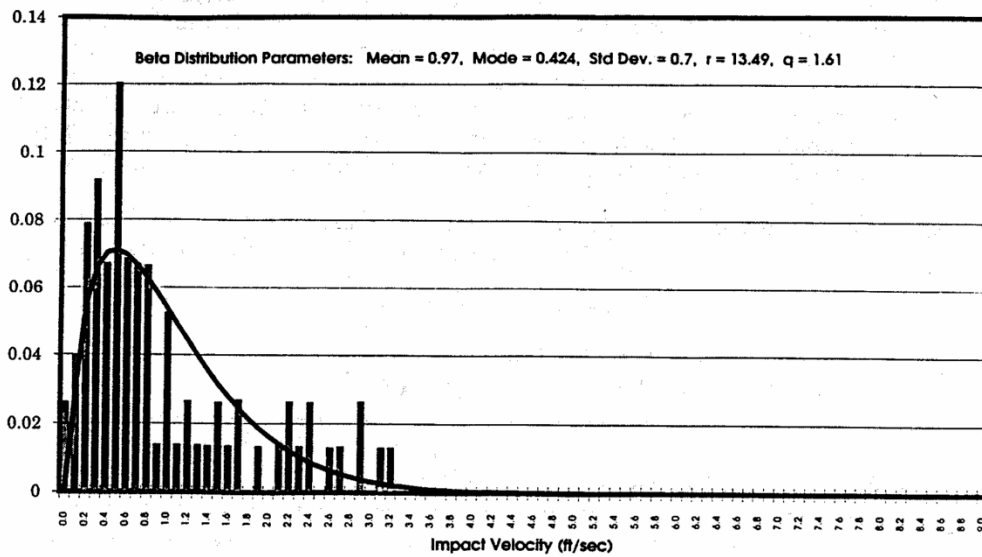


Figure C.9. Weighted Histogram and Fitted Probability Distribution Function for Forward Velocity at Winfield Upper Approach Guard Wall

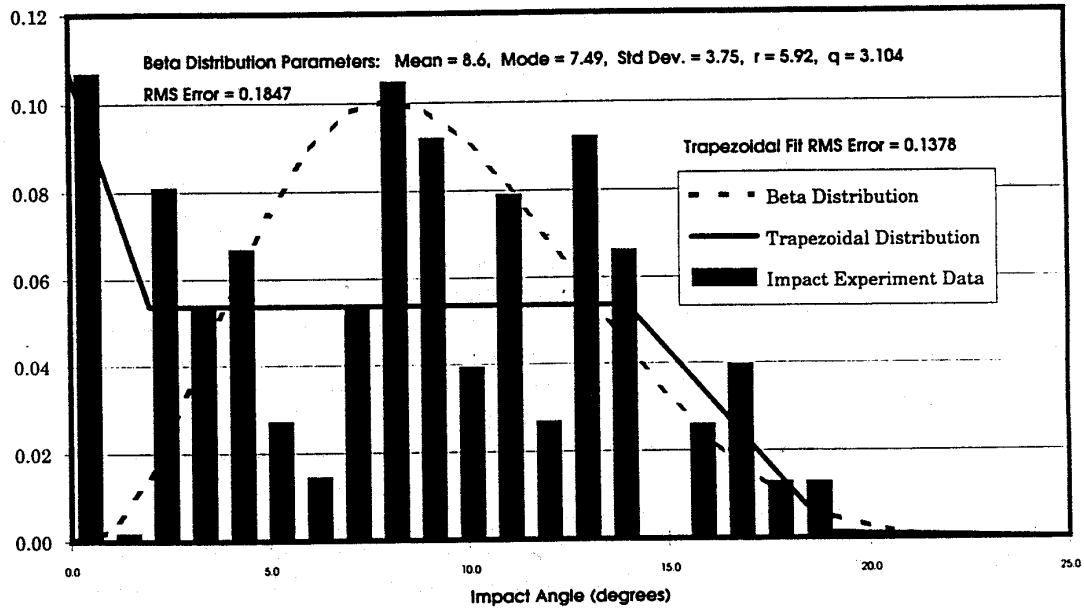


Figure C.10. Histogram and Probability Distribution Function for Impact Angle at Winfield Upper Approach Guard Wall

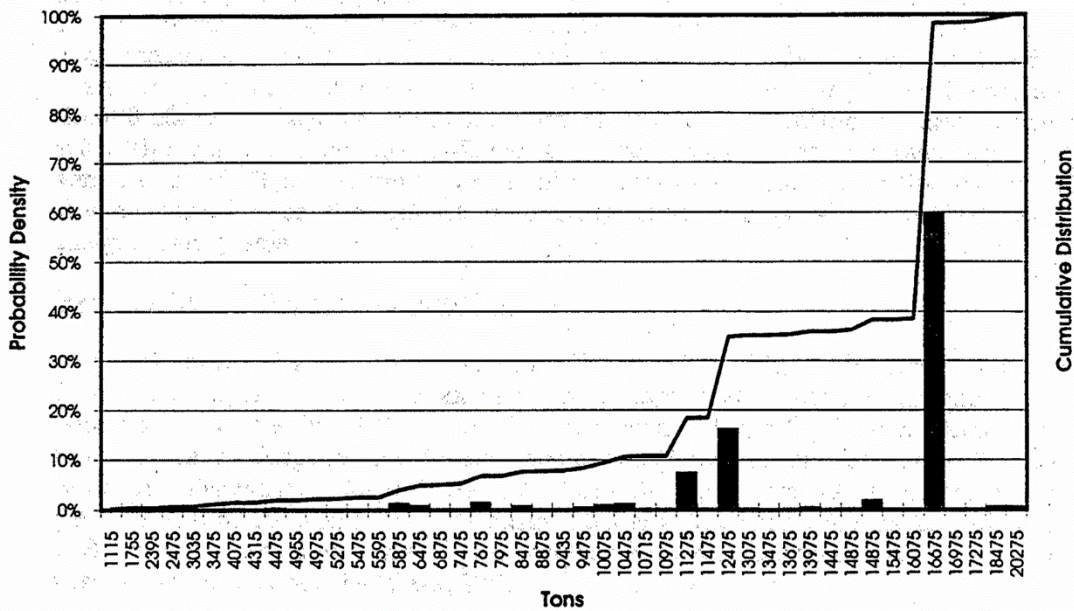


Figure C.11. Histogram and Cumulative Probability Distribution of Tow Mass for Winfield Upper Approach Guard Wall

Table C.2.
Lognormal Distribution Parameters for Impact Variables at Winfield Upper Approach Guard Wall

Traffic Direction	Variable	Mean	Standard Deviation	Minimum	Maximum
Upper Approach Guard Wall	θ (deg)	9.3	3.75	0	30
	V (ft/sec)	1.08	0.7	0	10

C.2.3. Kentucky Lock Addition Upper Approach Walls – Tennessee River, Grand Rivers, Kentucky.

C.2.3.1. Nashville District started the design for this navigation project to increase the capacity for Kentucky Locks in the 1990s. The Kentucky Lock Addition consists of a new 110-ft by 1,200-ft lock landward of the existing 110-ft by 600-ft lock. The upper land approach wall consists of a 1,300-ft-long wall that is designed as a 42-ft-wide floating guide structure. The upper middle approach wall is similar in construction and function, except that it is a 277-ft-long, 46-ft-wide wall with a 12-degree bend toward the river near the middle of the wall.

C.2.3.2. This allows the floating wall to align with the existing lock’s landward wall and to guide barge traffic into the new lock. The upper approach for this project is within Kentucky Lake, which is very wide near the locks and has minimal effects on tows from either currents or outdrafts. Figure C.12 shows the layout for the upper middle approach wall.

C.2.3.3. Therefore, from this design, it is anticipated that the approach angle can be expected to have a wider degree of variation than was estimated in either the Olmsted or Winfield examples above, but the approach velocities can be expected to be lower. A 1:120 scale navigation model was constructed at ERDC-WES, but no impact experiments of the upper approach walls were conducted as part of the modeling. Instead, the final design incorporated the use of data from the Olmsted approach walls design since both designs incorporated floating guide walls.

C.2.3.4. The experiment data from Olmsted was then adjusted based on the opinions from tow captains that utilize the locks as well as engineering judgment from District hydraulic and structural engineers. The distributions for impact and forward velocity of the barge are shown in Figure C.13 and Figure C.14. The distribution for tow weight was taken from the OMNI database and is shown in Figure C.15. Table C.3 shows the statistical parameters used for the design of the upper guide wall.

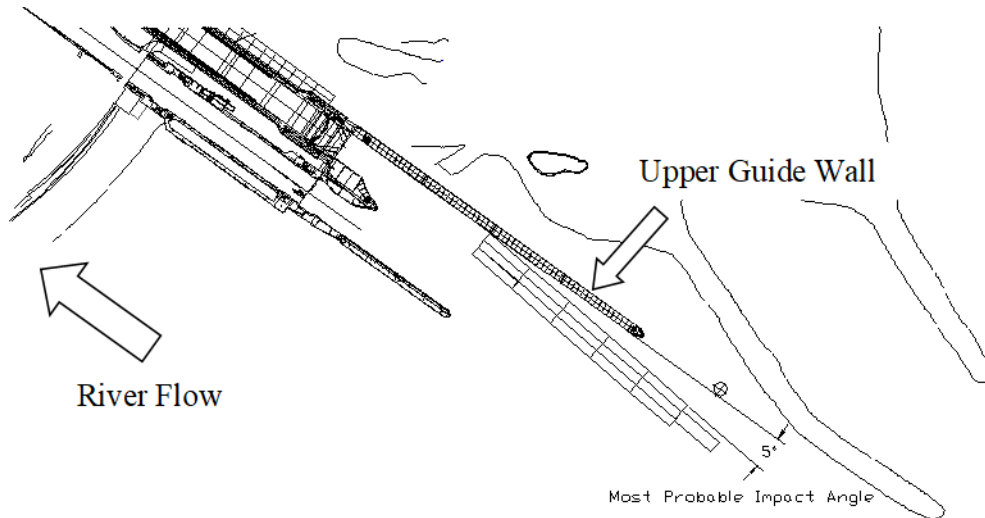


Figure C.12. Upper Landside Guide Wall at Kentucky Locks

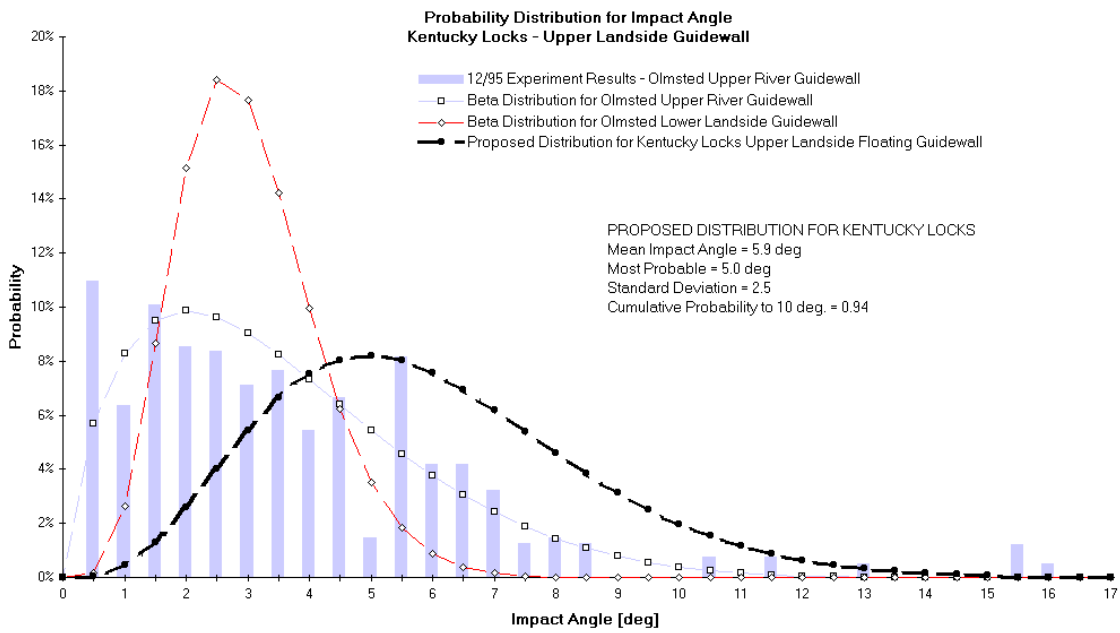


Figure C.13. Probability Distribution Function for Impact Angle at Kentucky Locks Upper Landside Guide Wall

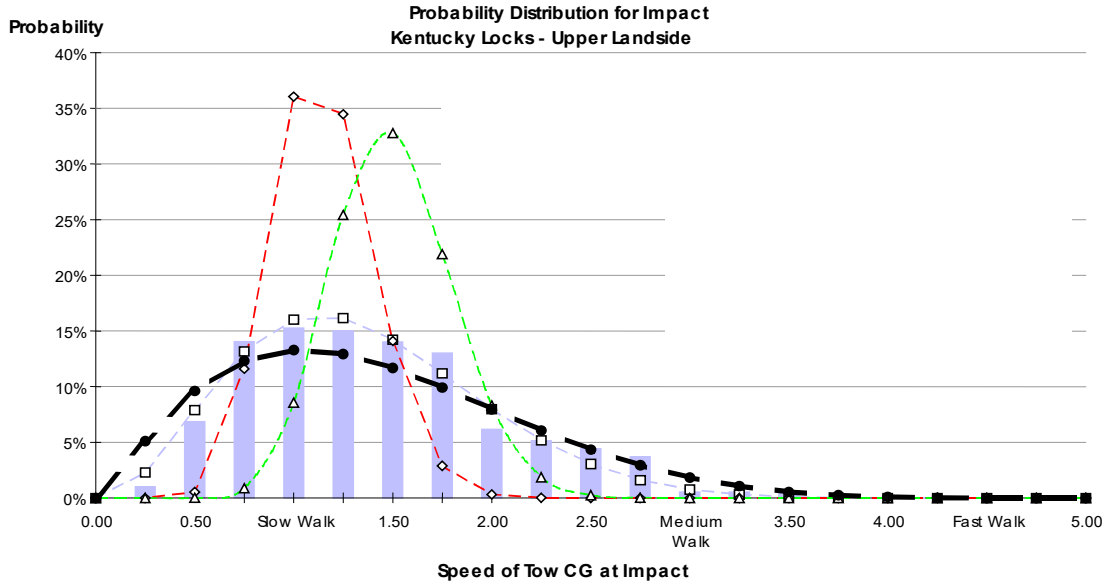


Figure C.14. Distribution Function for Forward Impact Velocity at Kentucky Locks Upper Landside Guide Wall

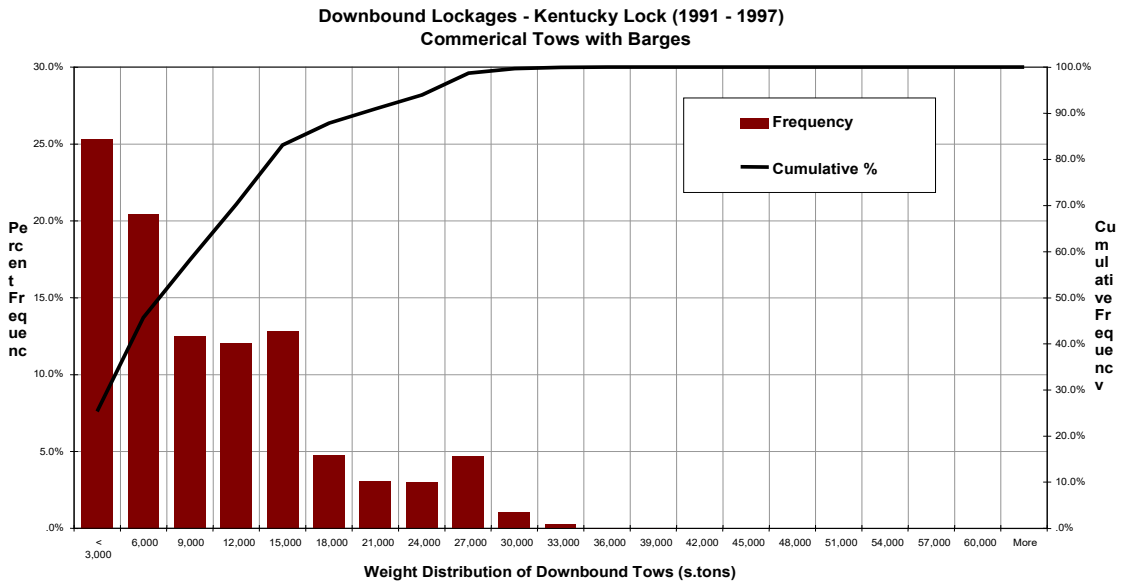


Figure C.15. Histogram of Cumulative Probability Distribution of Downbound Lockages at Kentucky Locks Upper Landside Guide Wall

Table C.3
Lognormal Distribution Parameters for Impact Variables at Kentucky L&D Upper Approach Guard Wall

Traffic Direction	Variable	Mean	Standard Deviation	Minimum	Maximum
Upper Landside Guide Wall	θ (deg)	6.15	2.5	0	27
	V (ft/sec)	1.4	0.7	0	5

C.2.4. Marmet Upstream Guide Wall, Kanawha River, Marmet, West Virginia.

C.2.4.1. The Marmet upstream guide wall structure consists of 14 concrete drilled piers spaced at 105 ft center to center and a sheet pile nose cell that supports 15 precast concrete beams. Figure C.16 shows the layout for the upper approach walls at Marmet. Each pier is constructed of two 6-ft diameter drilled shafts with cast-in-place cap beams to support the precast wall beams as shown in Figure C.17. A thrust block is provided at the cap beam to transfer barge impact from the beam into the shafts and nose cell. The hollow, rectangular beams have an outside dimension of 10 ft by 10 ft and the weight of each of the precast beams is approximately 495 tons.

C.2.4.2. Scale model experiments at 1:120 were performed at ERDC to determine the approach velocities and angles of impact for both a nine-barge jumbo tow and an existing design five-barge tow. These experiments were laid out for various flow conditions to cover a range of hydraulic conditions as well as for the loss of power condition of a nine-barge tow. The flow regime for the scale model is shown in Figure C.18.

C.2.4.3. Overall, five scale model testing sequences were recommended and are summarized in Table C.4. These testing sequences assisted in defining the annual probability distributions for a wide range of flows and events. An example of the statistical parameters for a 25,000 cubic ft per second (cfs) flow using five standard barges is shown in Table C.5. The velocities results for these experiments were determined as both normal, V_n , and tangential, V_t , velocities to the wall and are not in barge coordinates.

C.2.4.4. The correlation coefficients of the random variables from the testing data for this event are shown in Table C.6. For information on the distributions for the other testing sequences, correlation coefficients, or raw experiment data, additional details can be found in Patev et al 2003.

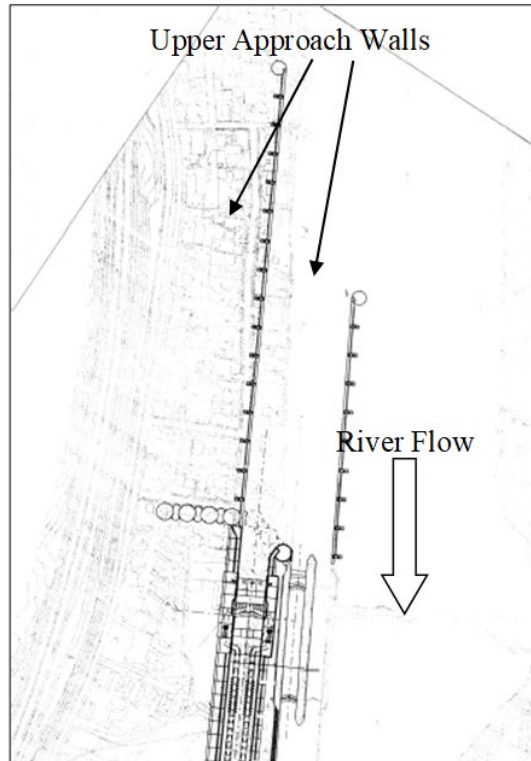


Figure C.16. Layout of Upper Approach Walls at Marmet L&D (from Patev 2000)

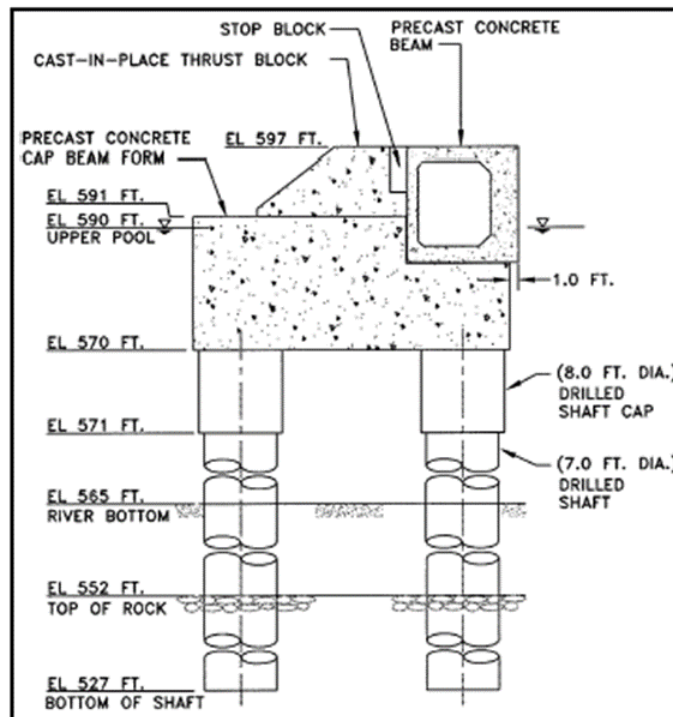


Figure C.17. Concept Design of Approach Walls at Marmet L&D (from Patev 2000)

Table C.4
Summary of Model Experiments for Marmet L&D (Patev 2000)

Flow Conditions (CFS)	Number of Model Runs	Number of Barges	Controlled	Loss of Power	Walls Affected
25,000	25	9 (jumbos)	Yes	No	Guide wall
25,000	25	5 (standards)	Yes	No	Guard wall
50,000	25	9 (jumbos)	No	Yes	Guard wall/Guide wall
106,000	25	9 (jumbos)	Yes	No	Guide wall
125,000	25	9 (jumbos)	No	Yes	Guard wall

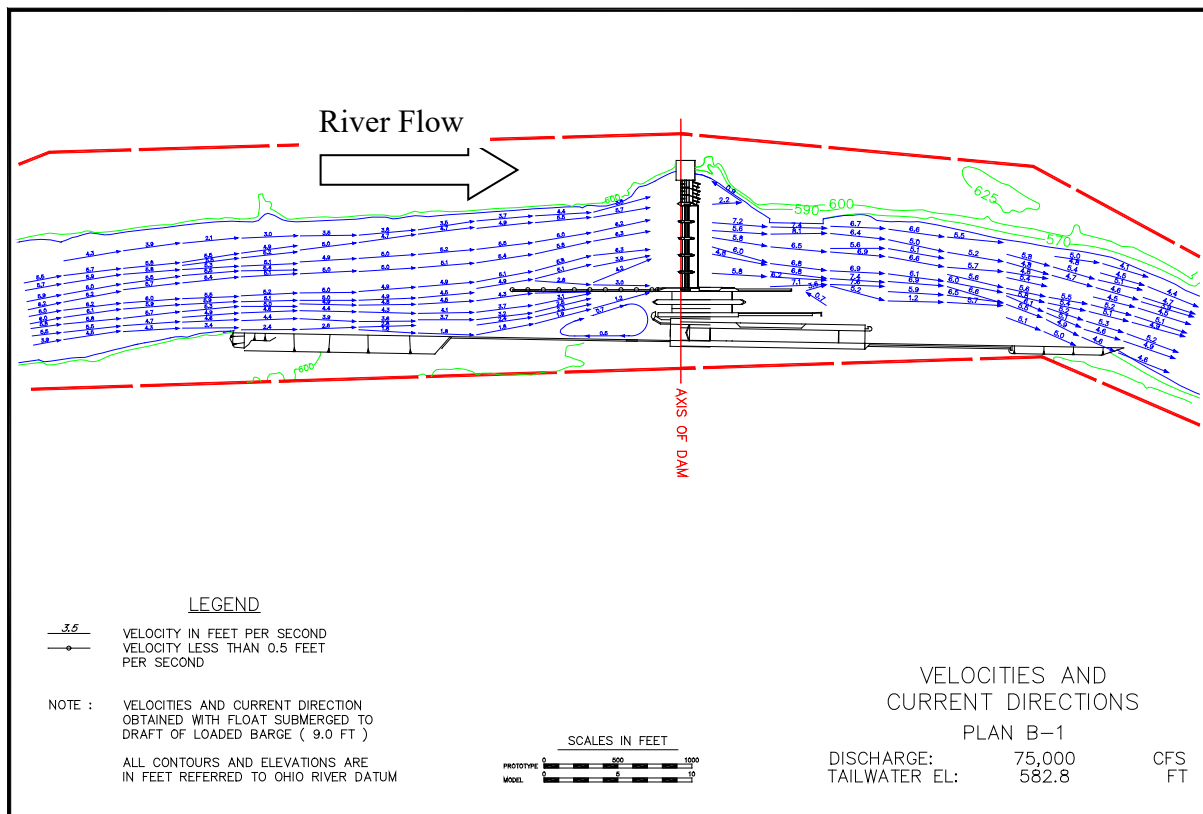


Figure C.18. Flow Vectors from Navigation Model for Marmet L&D

Table C.5
Example Lognormal Distribution Parameters for Impact Variables at Marmet L&D Upper Guide Wall

Traffic Direction	Variable	Mean	Standard Deviation	Minimum	Maximum
25,000-cfs 5-barge	V_t (ft/s)	0.94	0.4	0	5
	V_n (ft/s)	0.13	0.065	0	1
	θ (deg)	6.92	1.47	0	20

Table C.6
Example Correlation Coefficient Matrix of Distribution Parameters at Marmet L&D Upper Guide Wall (Patev 2000)

Note: Correlation values ranges from -1 (negative) to 1 (positive)				
Traffic Direction	Variable	V_t (ft/s)	V_n (ft/s)	θ (deg)
25,000-cfs 5-barge	V_t (ft/s)	-	0.6	0.08
	V_n (ft/s)	0.6	-	0.68
	θ (deg)	0.08	0.68	-

C.2.5. London Locks Upstream Guard Wall on the Kanawha River, West Virginia.

C.2.5.1. The London Locks and Dam Upstream Guard Wall is on the Kanawha River at London, West Virginia. The structure consists of five piers spaced at 105 ft center to center and a sheet pile nose cell, which supports five precast concrete beams. Each pier is constructed of two 6-ft diameter drilled shafts with cast-in-place cap beams to support the precast wall beams. A thrust block is provided at the cap beam to transfer the barge impact from the beam into the shafts.

C.2.5.2. The hollow, rectangular precast wall beams are each 105 ft long, and have an outside dimension of 10 ft by 8 ft. The weight of each of the precast beams is approximately 340 tons. The tow weights for this project design were not based on a statistical analysis of the existing distribution of tow masses but used a single value for the design tow weight in the analysis. The design tow consisted of four fully loaded jumbo barges (35 ft x 195 ft) and a towboat. The total weight was modeled as 7,000 short tons and the overall tow dimension is modeled at 920 ft long by 35 ft wide.

C.2.5.3. A 1:120 scale navigation model was developed for the London Locks project at ERDC. The flow vector from the scale model is shown in Figure C.19. A limited number of scale model experiments under controlled events were performed to assist with determining the distributions for approach angles or forward velocities to be used in the impact design. These distributions for forward velocity and impact angle from the model testing are shown in Figure C.20 and Figure C.21, respectively. Table C.7 shows the statistical parameters used in the design of the upper river guide wall.

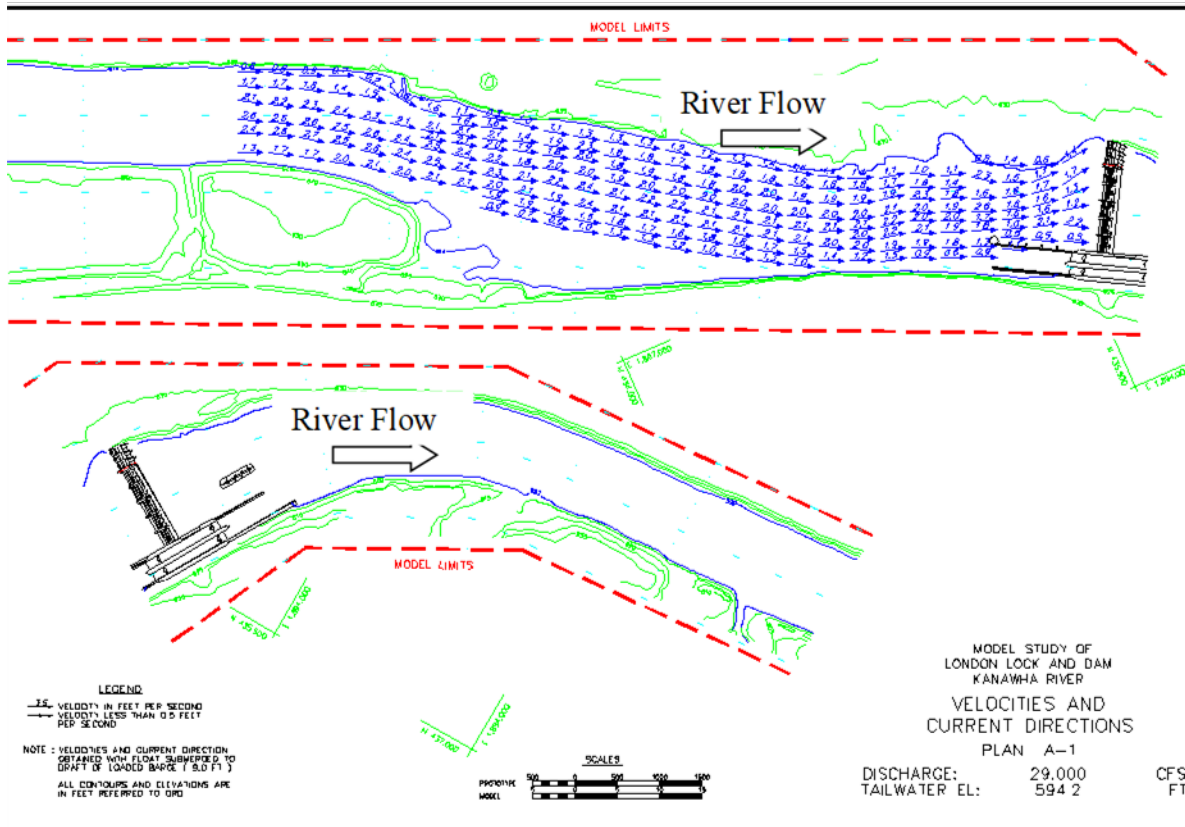


Figure C.19. Vectors from Navigation Model at London L&D

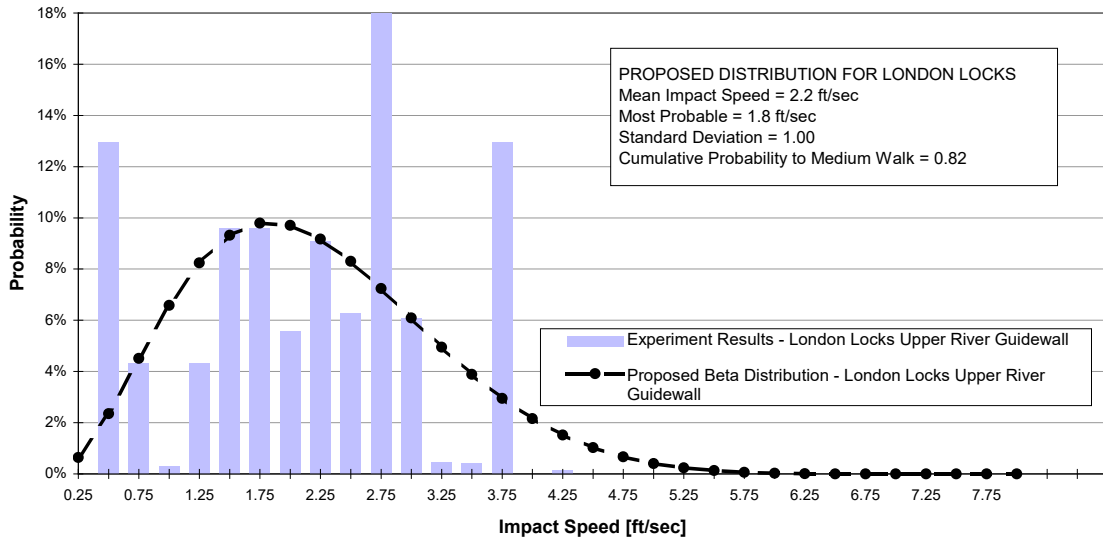


Figure C.20. Probability Distribution for Forward Impact Speed at London Locks Upper Landside Guard Wall

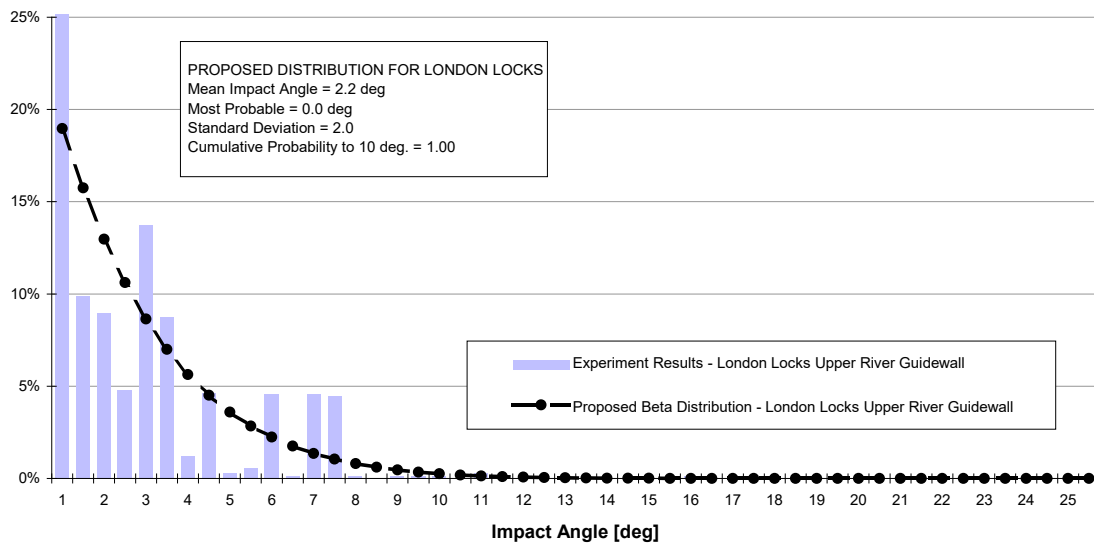


Figure C.21. Probability Distribution for Impact Angle at London Locks Upper Landside Guard Wall

**Table C.7
Lognormal Distribution Parameters for Impact Variables at London L&D Upper Landside Guard Wall**

Traffic Direction	Variable	Mean	Standard Deviation	Minimum	Maximum
Upper Landside Guard Wall	θ (deg)	2.2	1.5	0	12
	V (ft/sec)	2.2	0.6	0	10

C.2.6. Greenup Locks Approach Walls, Ohio River.

C.2.6.1. As part of the Ohio River Main Stem Systems Study, a preliminary approach wall design was completed on the extension of the guide and guard walls at Greenup Locks. Currently, the existing upstream approach conditions are less than desirable due to crosscurrent problems. These crosscurrents are encountered by tows approaching the lock, which force them to flank toward the bank while their stern is being pulled toward the river. Figure C.22 shows the flow vectors from the navigation model at Greenup.

C.2.6.2. In order to ensure an adequate landing zone for the tows, the approach walls will be lengthened and configured to allow a 1,200-ft landing zone for each chamber. In order to facilitate the new approach to Greenup Locks after the landward existing 600-ft lock chamber is extended, the following approach wall lengths were proposed for the project:

C.2.6.2.1. Extend the existing upper river wall and upper middle wall by approximately 1,345 ft.

C.2.6.2.2. Extend the existing lower land wall by approximately 1,184 ft beyond the new lower landside lock monolith causing the wall to project 1,100 ft beyond the new lower middle wall monolith.

C.2.6.2.3. Extend the existing lower river wall by approximately 295 ft. The upper approach walls are proposed to be floating pontoons, which are restrained laterally by nose piers and pylons.

C.2.6.3. These approach layouts and the constraints on impact angles are shown in Figure C.23. The distributions for the weight of both upbound and downbound tows were taken from existing OMNI data and are shown in Figure C.24 and Figure C.25. Since this design is for preliminary concept walls, navigation modeling was not completed as part of the Ohio River Mainstem System Study. However, it is anticipated that additional navigation modeling will be needed as the project rolls into the feasibility level design. As a part of the next design phase, scale model impact experiments will be conducted to better estimate the distributions for velocities and impact angle of downbound tows.

C.2.6.4. For this preliminary design, the values for velocity are based on observations made during site visits and select time-lapse video records from the lock. The values for the angle of impact were based on site constraints as discussed above. Figure C.26 and Figure C.27 present the proposed distributions for barge impact velocity and impact angles for the three floating walls at the project. Table C.8 shows the summary of the statistical parameters to be used in the preliminary design and sizing of approach walls.

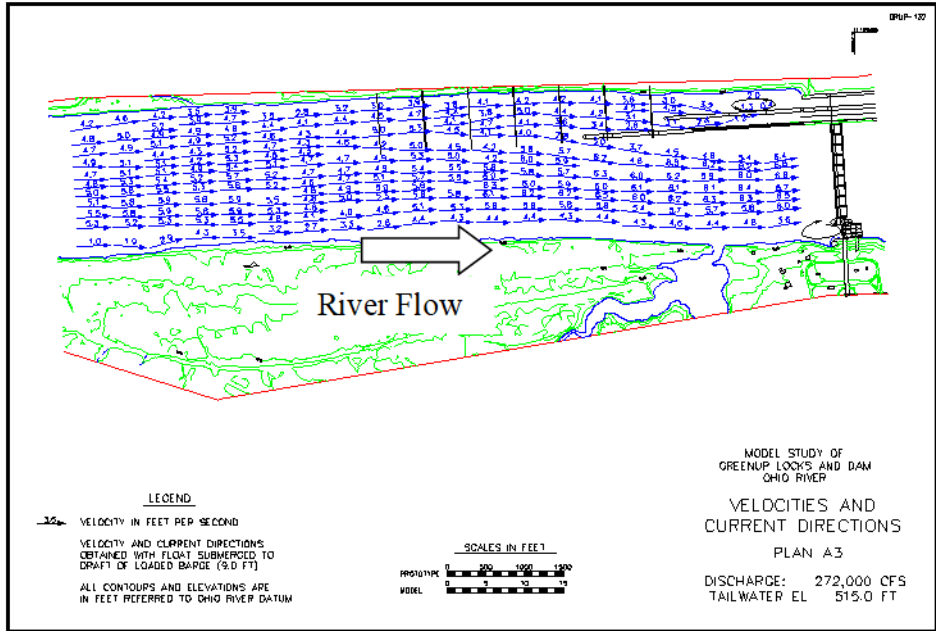


Figure C.22. Flow Vectors from Navigation Model for Greenup L&D

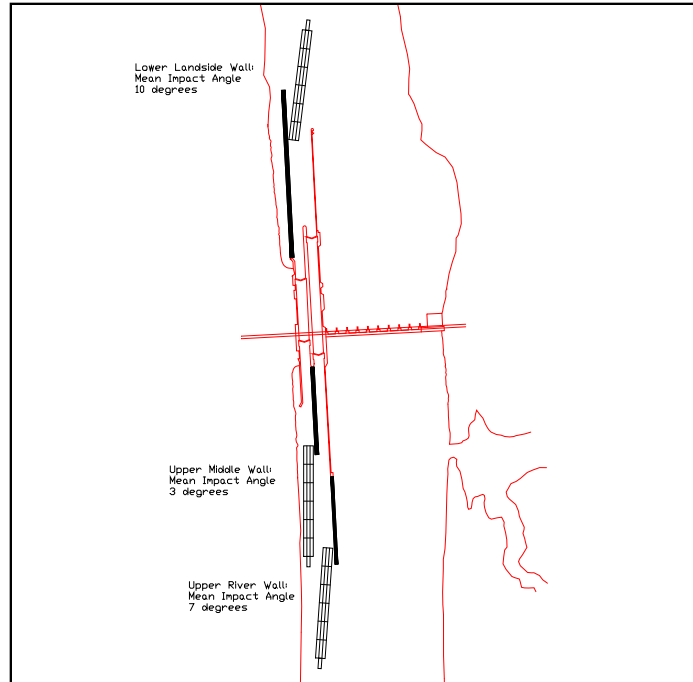


Figure C.23. Physical Constraints on Impact Angles at Greenup Locks

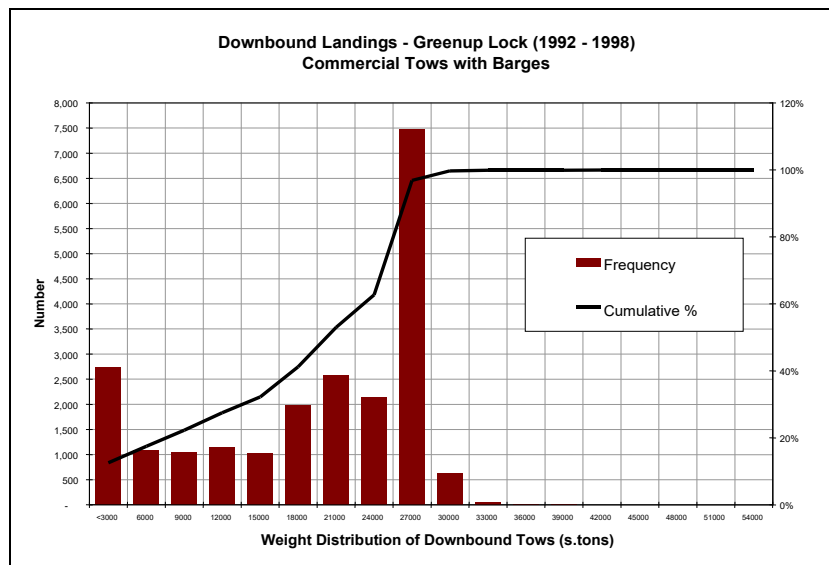


Figure C.24. Histogram of Downbound Tow Weight Distribution for Greenup L&D

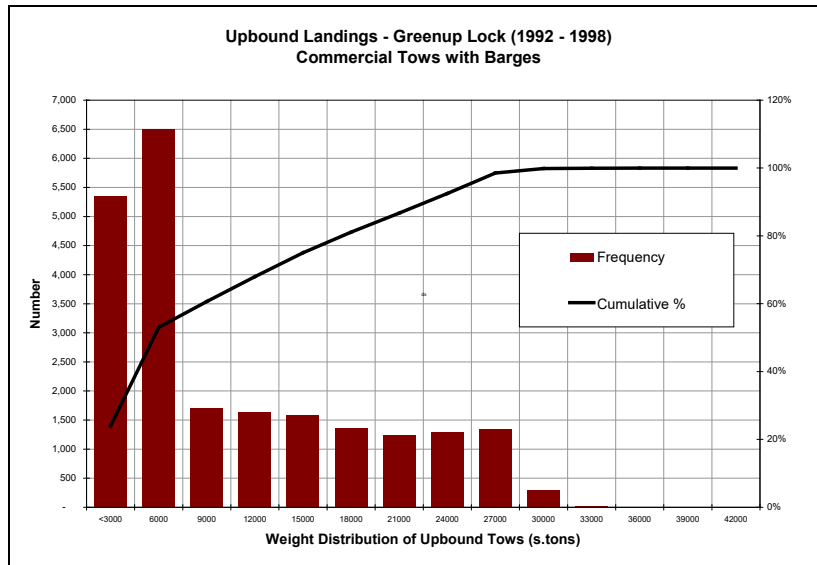


Figure C.25. Histogram of Upbound Tow Weight Distribution for Greenup L&D

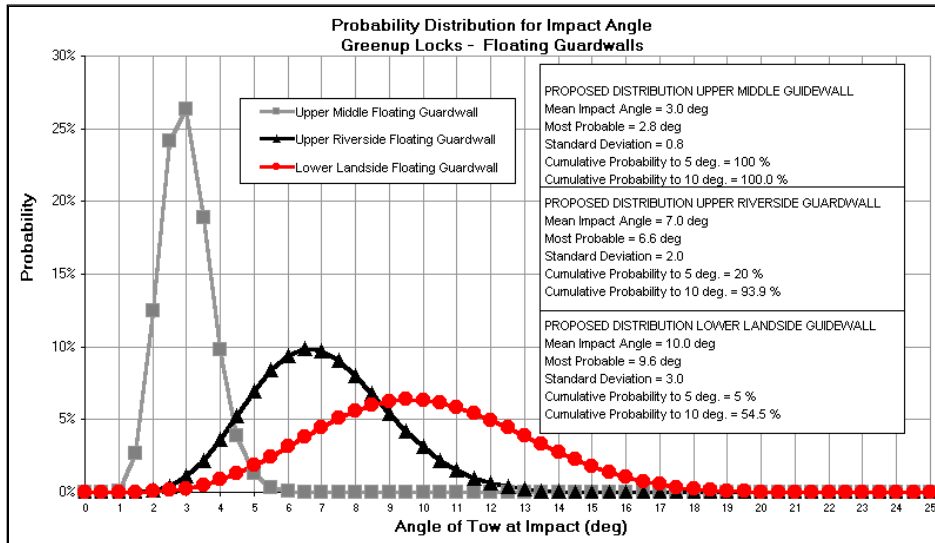


Figure C.26. Probability Distributions for Impact Angle at Greenup L&D

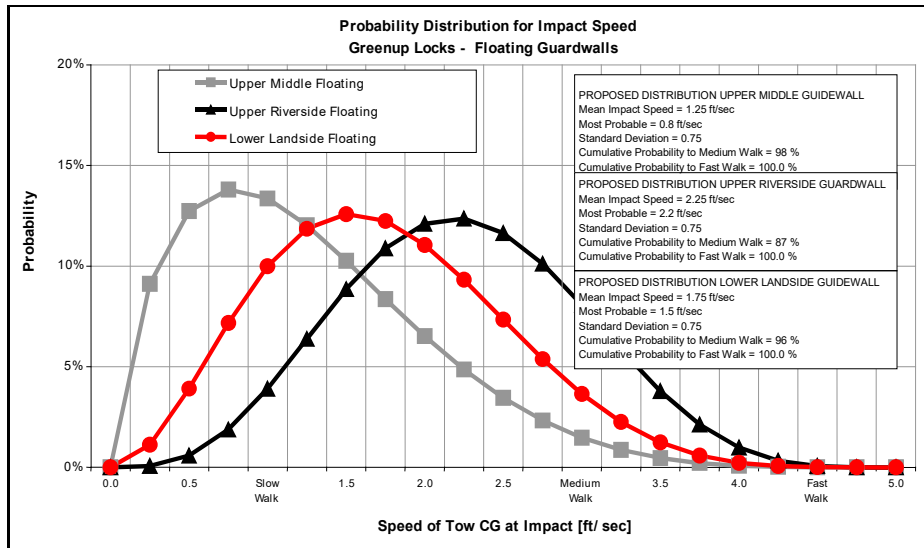


Figure C.27. Probability Distributions for Forward Velocity at Greenup L&D

Table C.8
Lognormal Distribution Parameters for Impact Variables at Greenup L&D

Traffic Direction	Variable	Mean	Standard Deviation	Minimum	Maximum
Upper Middle Wall (downbound)	θ (deg)	3.0	0.8	0	6
	V (ft/sec)	1.25	0.75	0	5
Upper Riverside Wall (downbound)	θ (deg)	7.0	2.0	0	22
	V (ft/sec)	2.25	0.75	0	5
Lower Landside Wall (upbound)	θ (deg)	10.0	3.0	0	25
	V (ft/sec)	1.75	0.75	0	5

Appendix D

Examples of Probabilistic Barge Impact Analysis

D.1. Introduction. This appendix will document information that will be required to perform a probabilistic analysis using the empirical equations in Chapters 4, 6, and 7, or the low-order dynamic model in Chapter 5. The examples shown in this appendix use typical design parameters (velocity, angle, and mass) used for design of navigation structures. The values selected also fit into the limitations of the empirical models presented in previous chapters.

D.2. Parameters for Barge Impact.

D.2.1. Background.

D.2.1.1. It is frequently difficult to estimate the range or distributions of masses, approach velocities, and angles used in the PBIA. This range should include angles and velocities caused by a loss of power and control, as well as any future anticipated changes in navigation traffic at the lock. This range of data should be compiled into a design matrix and processed with return periods for anticipated events at the particular structure. Return periods were previously discussed in Chapter 2. For preliminary or feasibility design efforts, engineering judgment should be used to formulate reasonable impact angle and velocity scenarios. For some existing locks, the designer may have information available from previous model studies or lockmaster logs.

D.2.1.2. Other ways to obtain data for feasibility level designs could be from using lockmaster's logs or towing industry records from similar existing facilities. This type of data should be utilized only during conceptual design and should not be incorporated as the only source of data for the final design. Limited data could result in an unsafe or uneconomical design of the navigation structure. As work progresses toward the final design, the range of values for impact angles and velocities should be defined with reasonable certainty. Measurements for these parameters can be made in the field using time-lapse video photography or in a laboratory scale model.

D.2.2. Site Constraints.

D.2.2.1. Approach walls are provided upstream and downstream of lock chambers. Approach walls adjacent to the dam are commonly referred to as guard walls, and the walls opposite the guard walls are usually referred to as guide walls. The walls are used by approaching barge traffic as landing or holding points prior to entering the lock chambers. Barge traffic routinely impacts the walls at ranges of velocities and angles that are constrained by the geometry of the site. This is shown in Figure D.1. Approach walls are designed to accommodate a wide variety of operating conditions that range from normal river conditions to flood events. The levels of loading that the walls resist should be consistent with a probabilistic approach where loading is classified as usual, unusual, or extreme based on a given return period of the event.

D.2.2.2. Generally, the upstream approach walls are designed for a higher impact load than the downstream walls as explained below. Upstream of the lock, river flow is distributed from bank to bank. The cross-sectional area of the lock in the river will partially block bank-to-bank flow. To improve hydraulic conditions, the upper guard wall is usually ported (a system of openings designed by hydraulic engineers) below the impact face to allow flow under the wall. Outdraft conditions or currents (see Figure D.1) toward the upstream guard wall influence both impact speed and angle in a predictable manner over the range of flow conditions.

D.2.2.3. The following fundamental differences influence the design of walls impacted by upbound or downbound traffic. Downbound traffic is moving with the current, whereas upbound traffic is moving against river current. Towboats usually have more control moving upstream against the current than moving downstream with the current. The disparity in load conditions for upstream and downstream walls becomes more pronounced as flood conditions are encountered.

D.2.2.4. Usual impact forces are based on typical river conditions and assume a controlled landing against the wall with a typical barge configuration. The usual load reflects typical operating conditions. Unusual impact forces may occur prior to navigation shut down before a flood event, when fully loaded barges attempt a lockage in fast river currents. They may also occur when approach conditions are exacerbated by outdraft currents in the upper approach.

D.2.2.5. The vessel will usually be traveling at a greater velocity and may impact the approach walls at larger angles during these conditions, resulting in higher impact forces. The conditions associated with extreme impact forces are highly unpredictable and difficult to establish. Extreme events can occur when a towboat pushing a flotilla loses power under normal conditions. They can also occur during a flood event when navigation has shut down and barges break away from moorings and float out of control downstream. Hydraulic modeling should be used to investigate various scenarios to gain insight and data for design.

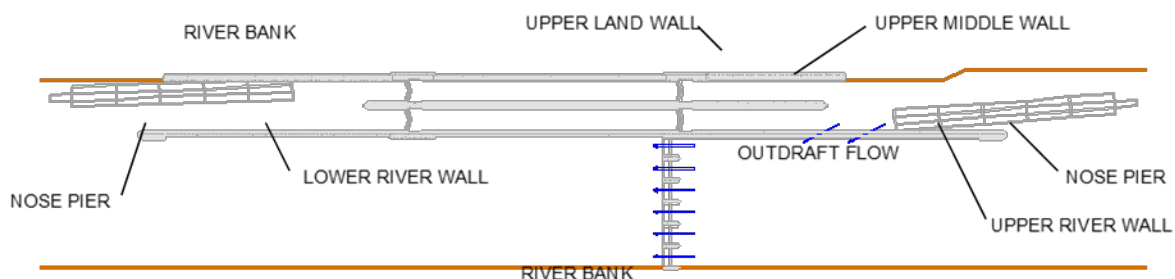


Figure D.1. Site Constraints for a Typical Lock Structure

D.2.3. Data Requirements.

D.2.3.1. Flotilla Size.

D.2.3.1.1. The dimensions of lock chambers are typically based on the sizes of flotillas that will use the lock. The most common barge on the inland waterway is the jumbo barge that is 35 ft wide and 195 ft long. Typical configurations are generally three wide by five long (105 ft by 1,175, including 200 ft for the tow boat) or three wide by three long (105 ft wide by 785 ft, including 200 ft for the tow boat).

D.2.3.1.2. On some rivers, the standard barge in service is generally 27 ft wide and 175 ft long. There are older barges in service that are 24 ft wide, however, these barges are slowly being removed from service. Another type of barge is the double-hulled oil, gas, and chemical barge. These barges are typically 52 to 54 ft wide and 200 to 300 ft long and travel the river in one wide by two long, or two wide by two long configurations, depending on the river system.

D.2.3.2. Flotilla Mass. The mass is based on the total weight of the barge and the commodity being carried in the barge hopper. Weights for inland waterway barges are generally expressed in short tons (2,000 lbs per ton). A loaded jumbo open hopper barge drafting 9 ft typically weighs between 1,500 to 1,900 tons. Typical weight of an empty barge is 200 to 270 tons. The mass ($\text{kip}\cdot\text{sec}^2/\text{ft}$) is determined by dividing the weight by the gravitational constant, g ($32.2 \text{ ft}/\text{sec}^2$). In addition, the mass of the towboat should also be included when calculating the mass of the flotilla.

D.2.3.2.1. The mass for a flotilla can be determined from a variety of sources. The USACE operations database called OMNI (also called Lock Performance Monitoring System (LPMS)) contains information about each lockage at every USACE lock across the nation. OMNI contains information on the total weight of each flotilla, type of commodity, and number of barges (loaded, unloaded), etc. However, the weights in OMNI are typically rounded by lock personnel to simplify their input to the database.

D.2.3.2.2. If more accurate weights are desired for the barge impact analysis, data from the Waterborne Commerce (WBC) Statistics Center records could be utilized. WBC data can be obtained from the USACE Navigation Data Center at the Institute for Water Resources: <http://www.iwr.usace.army.mil/ndc/index.htm>. WBC data is based on the port-to-port manifest for each flotilla and is available for individual years and most navigation waterways.

D.2.3.2.3. This manifest includes the exact weight of the commodity in each barge and the weight of an empty barge. While the WBC data is more accurate than OMNI, the format for the data will require it to be processed further for use in the analysis. Table D.1 contains examples of collected data, including a comparison for various USACE locks for the year 1999. The data shows a 3% to 4% difference existing between the two databases for higher traffic locks. Locks that have smaller chambers or less traffic tend to have less than 1% difference in the mass.

Table D.1
Comparison of OMNI Data and WBC Data for the Year 1999

	OMNI DATA			WBC DATA			Percent Diff.
	No. Loaded Barges	Weight Ktons	Avg Loading	No. Loaded Barges	Weight Ktons	Avg Loading	
Greenup	44,746	70,039	1,565	43,867	71,656	1,633	4.18%
Winfield	14,234	19,521	1,371	13,761	19,716	1,433	4.28%
L/D 1 (Green)	2,915	4,353	1,493	2,685	4,193	1,562	4.38%
Myers	44,718	71,394	1,597	44,091	72,711	1,649	3.19%
Ky Lock	26,042	40,837	1,568	25,239	40,655	1,611	2.65%
Cheatham	6,092	9,542	1,566	5,997	9,449	1,576	0.59%
Dashields	18,858	24,513	1,300	18,533	24,285	1,310	0.80%
L/D 4(All)	1,598	1,612	1,009	1,497	1,506	1,006	-0.27%
L/D 2 (Mon)	16,311	21,124	1,295	15,981	20,762	1,299	0.31%

D.2.3.2.4. The distribution for the mass of a flotilla can be determined using existing traffic information from OMNI or WBC. From data collected at various lock projects, the distribution for flotilla mass is generally dominated by a single- or double-humped (camel-backed) distributions. The reason for this is that at least one or two typical flotilla configurations (e.g., 6 or 15 barges) exist in several navigation systems. This distribution should also account for any anticipated future traffic changes. Generally, the distribution for mass is the easiest one to determine.

D.2.3.3. Hydrodynamic Added Mass.

D.2.3.3.1. Forces due to the momentum of the water associated with the moving flotilla are typically included when developing impact forces. This phenomenon is known as hydrodynamic added mass and would normally be considered in the transverse, longitudinal, and rotational directions. Equations to calculate the added mass are based on traditional ship design techniques and are discussed in Chapter 8. Generally, the added mass for flotillas has been assigned 40% in the longitudinal, 5% in the transverse, and 40% in the rotational directions.

D.2.3.3.2. It is important to recognize that the effects of hydrodynamic added mass are included in the measured force data used to develop the empirical relationship discussed in Chapters 4 to 7. Therefore, the mass term in the empirical correlation used in this EM should include only the mass of the flotilla.

D.2.3.4. Drag and Cushioning Effects on Flotillas. The drag force is the resisting force water to the momentum of the flotilla, and it can be applied as a damping coefficient or percent damping in a MDOF analysis. This is shown in Chapter 5 on the LODM. The drag force on a flotilla is not significant compared to the magnitude of the impact force. Cushioning forces between the barges and walls are usually not included but may be significant for broadside impacts. The effects of drag and cushioning forces were included in the measured force data used to develop the empirical relationship discussed in Chapters 4 to 7. Further consideration of these forces is not necessary in the empirical model calculations.

D.2.3.5. Velocity Components Normal and Parallel to the Wall.

D.2.3.5.1. Velocities for flotillas can be estimated using field and/or laboratory methods. Two components of barge velocity (forward, V_{0x} and lateral, V_{0y}) should be determined for barge impact analysis. The empirical models defined in calculated the force normal to the wall. These components of the barge motion are combined to form components normal and parallel to the rigid wall. Typically, the normal component is important since it usually contributes to the primary force used for the wall design. The parallel component will be important to structures that use end support piers to handle the shear load and for operating conditions that cause a broadside impact of the barges against the lock wall. The parallel component force is calculated using the dynamic coefficient of friction times the normal force from the empirical models.

D.2.3.5.2. For flood events, the upper limit for velocities of flotillas approaching a lock can be based on the velocities of the currents, the local flow regimes, or results from navigation models. During a major flood event, navigation ceases for safety and should be considered when selecting appropriate velocities for design. Outdraft or currents near open or ported approach walls should also be considered in selecting velocities that are used for the impact analysis. For usual events, the maximum flotilla velocities can be estimated using average daily flow velocities of the currents adjusted for the ability of the operator to control the flotilla.

D.2.3.5.3. For unusual events, the maximum velocity may be estimated using daily flow velocities of the currents adjusted for local conditions, such as an outdraft, that challenge the ability of the operator to control the flotilla. For extreme events, the maximum velocity may be estimated using flow velocities for river conditions approaching major flood stages that challenge the ability of the operator to control the flotilla.

D.2.3.5.4. Velocities can be determined in the laboratory using scale model hydraulic testing. These models are scaled at typically 1:120 but can range down to 1:50 if required. This laboratory method requires the construction of a scale navigation model at Engineer Research and Development Center (ERDC). An overhead recording system is used to track the flotilla in XYZ space on the navigation model. The data is collected by a computerized acquisition system and then processed to determine the velocities and angles during the entire approach to the lock. When performed in conjunction with a navigation study, these types of experiments are cost effective.

D.2.3.5.5. After the construction of the model is complete, testing is conducted using a scale model barge and towboat. The flotillas used for the experiments can be sized to fit the current and future trends of navigation traffic. In addition, the testing can model the approach of the flotilla at a variety of flow conditions. Obtaining impact data at different hydraulic conditions should be an integral part of any model test matrix.

D.2.3.5.6. Velocities in the approaches should cover a minimum of three flow conditions where probabilities can be defined by hydraulic curves for the site. A typical range of flows should not exceed probabilities of 2%, 50%, and 99%. The hydraulic engineer on the design team should furnish these values. A testing matrix for the project should also be developed for each flow condition that requires testing. To provide a statistically significant sample size, a minimum of 30 experiments should be conducted for each flow condition. Also, using two or more model flotilla operators for the range of experiments would yield better information on the range of impact velocities and angles.

D.2.3.5.7. Caution should be exercised when interpreting the raw data from the experiments due to the scale model effects of water near the structure. This cushioning effect of the flotilla as it approaches the lock wall creates a slowing in the velocity prior to impact into the wall. A solution to offset this effect would be to use a time-averaging scheme for the values of velocity 10 ft prior and 10 ft past (in scale) the point of impact.

D.2.3.5.8. Another method to collect data on velocities is using time-lapse videotape or Time-Lapse Data Acquisition system (TLDAQ). These systems were first developed and utilized to collect velocity and impact data for concrete deterioration models for the Upper Mississippi Illinois Waterway Navigation Study in Patev (2000). Additional research was conducted in the TLDAQ systems to develop a PC-based computer data collection system that could incorporate needed measurements (e.g., wind, flows) in the field.

D.2.3.5.9. These systems were recently developed and have been implemented in a wide variety of navigation projects including, most recently, Kentucky Lock and J.T. Myers L&D. Figure D.2 shows the installation of this TLDAQ equipment at Kentucky Lock. This type of data collection system is very useful to both document the existing approach and examine any potential future needs or design changes that might be required.

D.2.3.5.10. While this methodology is most useful if the navigation conditions are not drastically changed, it can still be applied to examine approach conditions of flotilla subjected to the effects of hazardous outdrafts and existing current conditions at the site.

D.2.3.5.11. TLDAQ systems require the installation of a video camera and computer acquisition system or time-lapse VHS recorder. The camera is mounted to either a light standard on the existing approach wall or lock chamber, or a bridge over the approach. The recording device is placed either in a weatherproof case or within a secure building. These systems are set up to record the motion of the flotilla as they navigate the approach to the lock. These systems capture a wide variety of data and information that can be processed later from the recorded media using different interpretational techniques to get velocities and angles.

D.2.3.5.12. Another method to estimate barge velocities is using an Automated Information System (AIS) velocity data obtained from USACE database at ERDC. The site location to request data is www.aisap.usacegis.us. Data may be available for a specific project or can be requested for transiting vessels at many USACE locks in the AIS system. The AIS data will need to define an Area of Interest (AOI) for both upstream and downstream approaches to process the GIS track data. The AIS data is presented using a summary of statistical data table (with histograms) and the actual GIS vessels tracks in the approaches. The background AIS data can also be exported from the website. Note that this AIS system is not recommended to obtain impact angles since the accuracy of the GIS on the vessels is limited. Impact angles should be quantified using a TLDAQ or visual observations at a project.

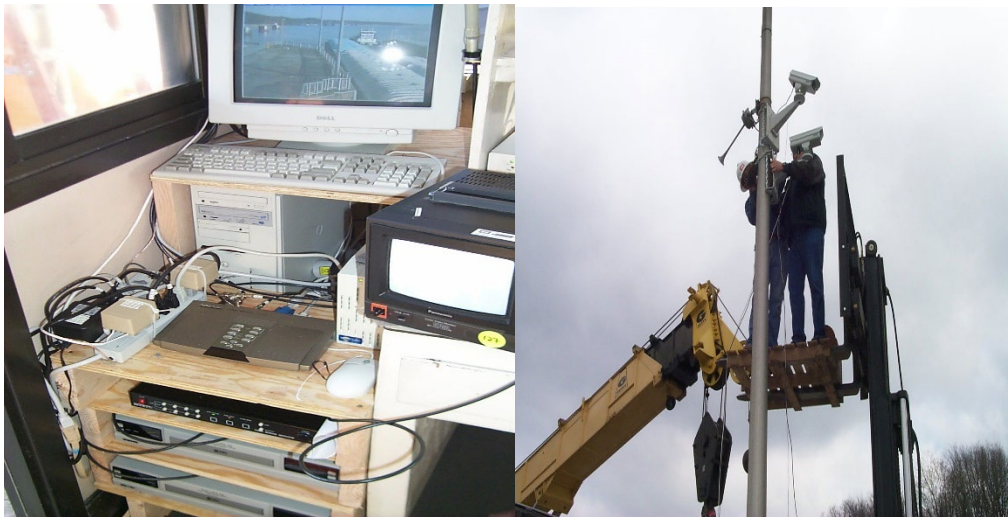


Figure D.2. Demonstrations of Time-Lapse Equipment Installed at Kentucky Lock (Computer Acquisition System on Left and Time-Lapse Camera on Right)

D.2.3.5.13. Table D.2 shows typical ranges for impact velocities for approach conditions to navigation lock walls that are appropriate for preliminary analyses only. Accurate determination of velocities for final design should be made using one of the methods presented above.

Table D.2
Typical Ranges for Impact Velocities for Preliminary Analyses

Load Condition	Velocity (ft/s)
Usual	0.5–2.0
Unusual	2.0–4.0
Extreme	4.0–7.0

D.2.3.6. Angular Velocity. Barges tend to rotate about their center of mass and not typically at the geometric center of the flotilla. If this rotation is significant, it can cause either an increase or decrease in the velocity components for the impact. For preliminary design, the angular velocities can be ignored in the impact analysis. If there is concern about outdraft currents at a navigation site, rotation of the flotilla should be investigated using a hydraulic scale model.

D.2.3.7. Angle of Impact.

D.2.3.7.1. The angle of impact for a flotilla governs the magnitude of the velocity components to the wall. It is important to define this parameter as accurately as possible. The impact angle typically may be assumed to be a function of site geometry, functional layout, and flow conditions. The angle is also heavily influenced by the towboat operator’s ability to maneuver into the lock approach under adverse operating conditions, such as high flows or stormy weather. The impact angle can be captured using either of the methods (scale models or time-lapse) as discussed. Scale model experiments may lead to less accurate angles unless special provisions are made to account for the effects of water cushioning. Caution should be exercised when using time-lapse video to measure the impact angle. A range of angles should be calibrated in the field of view and applied to the results to avoid inaccuracies that may be 10% to 20%.

D.2.3.7.2. For preliminary analyses, Table D.3 shows typical values for impact angles for approach conditions to navigation lock walls. Accurate determination of impact angles for final design should be made using one of the methods presented above.

Table D.3
Typical Ranges for Impact Angles Used in Preliminary Analyses

Load Condition	Approach Angle (degrees)
Usual	5–10
Unusual	10–20
Extreme	20–25

D.2.3.7.3. The distributions for impact angle and velocity can be based on data from either geometric constraint, scale model testing, or time-lapse video. From the results of previous PBIA, the distribution for velocities and angles are lognormally distributed. This is a reasonable observation since most of the angles and velocities that occur in the field are generally skewed to the left of the average value. These distributions may be truncated depending on certain physical limitations that exist at a navigation site.

D.2.3.7.4. The trend as shown in this appendix indicates that the average range for the mean impact velocity falls within the 0.75 to 1.5 fps range and average angles tend to be around 4 to 8 degrees. This will, however, vary greatly depending on the site-specific conditions that are being analyzed in the PBIA. Also, another item to include in the PBIA is the correlation between the mass, velocity, and angle. From previous PBIA, a direct correlation between mass, velocity, and angle has been observed. For example, a large flotilla (15 barges) will generally approach a lock wall with a slower velocity than a smaller flotilla (2 barges). These correlations should be investigated and accounted for in any PBIA.

D.3. Example of Probabilistic Barge Impact Analysis for an Upper Guide Wall.

D.3.1. Introduction. This appendix details an example of a Probabilistic Barge Impact Analysis (PBIA) for a rigid upper guide wall at a L&D project. This example is conceptual, and each chapter in this EM has probabilistic (PBIA) examples for each structure type.

D.3.1.1. The purpose of the example is to show how to implement the methods and empirical model defined in Appendix E to determine the return periods for the design of the guide wall. This example uses data for impact angle and velocity from 1:100 scale model hydraulic experiments that were conducted at ERDC. The hydraulic conditions for the experiments were conducted under a flow regime of 25,000 cfs.

D.3.1.2. The data has been processed to determine the annual distributions and statistical parameters for the random variables in the PBIA. Data for loss of power, loss of control, and higher flow events are not included in this example. The combination of various annual events needs to be carefully considered and properly applied when performing a PBIA.

D.3.2. Results and Processing of Data from Scale Model Tests.

D.3.2.1. Site-specific data for the design of the upper guide wall for the lock was taken from a 1:100 scale hydraulic modeling at ERDC. Fifty experiments were conducted using a scale model rigid flotilla (105 ft wide by 975 ft) and remote-control towboat. The experiments utilized two different operators that simulated 25 approaches to the upper guide wall. These experiments were conducted at a river flow of 25,000 cfs.

D.3.2.2. The raw data was recorded on a computer data acquisition system and post-processed to determine the x-velocity and y-velocity component of the barge, and the angle of impact to the approach wall. Due to scaling effects of the water, the data for velocity and angle were processed prior to the barge impacting the wall. The data from the 50 experiments are presented in Table D.4 and Figures D3 to D4.

Table D.4
Raw Data from Scale Model Experiments at ERDC

	Velocity (ft/sec)	Angle
Experiment 1	1.04	
Experiment 2	2.71	5.61
Experiment 3	0.05	3.17
Experiment 4	1.81	4.27
Experiment 5	1.07	3.34
Experiment 6	0.68	2.49
Experiment 7	8.32	11.31
Experiment 8	1.61	3.80
Experiment 9	0.14	7.89
Experiment 10	0.55	2.93
Experiment 11	0.62	1.95
Experiment 12	0.68	2.96
Experiment 13	0.05	3.59
Experiment 14	0.28	1.15
Experiment 15	4.02	1.16
Experiment 16	2.57	1.09
Experiment 17	0.20	3.47
Experiment 18	0.11	3.88
Experiment 19	0.48	7.12
Experiment 20	0.88	5.92
Experiment 21	0.95	2.71
Experiment 22	0.53	1.36
Experiment 23	0.23	4.49
Experiment 24	0.17	1.50
Experiment 25	0.47	2.13
Experiment 26	2.46	2.40
Experiment 27	0.04	1.86
Experiment 28	0.08	4.00
Experiment 29	1.91	3.75
Experiment 30	0.35	0.44
Experiment 31	0.80	7.47
Experiment 32	0.02	2.42
Experiment 33	2.82	2.82
Experiment 34	0.19	2.11
Experiment 35	0.28	6.46
Experiment 36	0.37	8.56
Experiment 37	1.91	1.59
Experiment 38	0.06	1.61
Experiment 39	3.01	3.41
Experiment 40	4.87	1.65
Experiment 41	0.02	5.59
Experiment 42	0.02	2.78
Experiment 43	0.62	8.23
Experiment 44	0.20	2.15
Experiment 45	0.56	2.99
Experiment 46	0.55	3.50
Experiment 47	0.05	2.29
Experiment 48	0.02	1.69
Experiment 49	0.17	4.14
Experiment 50	0.10	2.99
Experiment 50	0.18	1.54

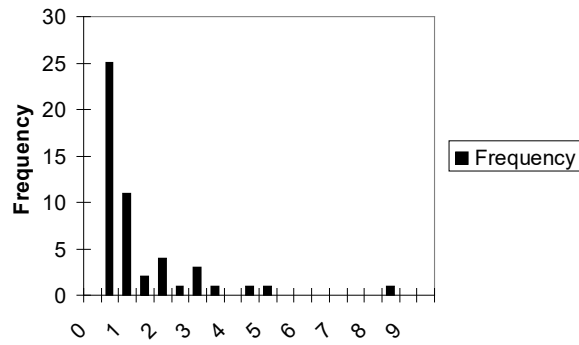


Figure D.3. Histogram for Velocity

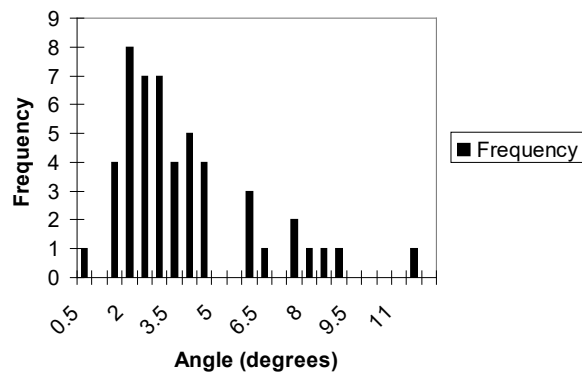


Figure D.4. Histogram for Angles

D.3.3. PBIA Data.

D.3.3.1. The data required for a PBIA are the velocity, approach angle, and the lead row mass for the flotilla. This data must be processed to define the statistical parameters (e.g., mean, standard deviation) for the input to the PBIA model. The processing of the data may be done in the form of either a discrete distribution (a probability density for a specific value) or a continuous distribution (smoothed function that fits the data). These concepts will be explained in further detail using the data for this example.

D.3.3.2. The lead row mass of the flotilla was taken from OMNI database (LPMS) records from 1984 to present for downstream loaded barges transiting the adjacent lock chambers. From this data, an annual histogram was processed using Excel to produce a distribution of the data. The annual histogram for lead row mass for the flotilla is shown in Figure D.6. This figure shows that the data illustrates that a three-barge wide configuration is typical at this lock project since the mean of lead row weight is 5100 short tons. The statistics for the PBIA for lead row mass is shown in Table D.5

D.3.3.3. From the hydraulic model data for velocity and angle, a continuous distribution and statistical parameters are fitted using a commercially available program. These statistical programs permit the fitting of data to numerous distributions and ranks them based on statistical testing procedures. For simplicity, a Pert distribution was taken for the best fit to the raw data, and the distributions are shown in Figure D.7 and Figure D.8. Table D.6 shows a summary of the statistical parameters used for velocity and angle in the PBIA.

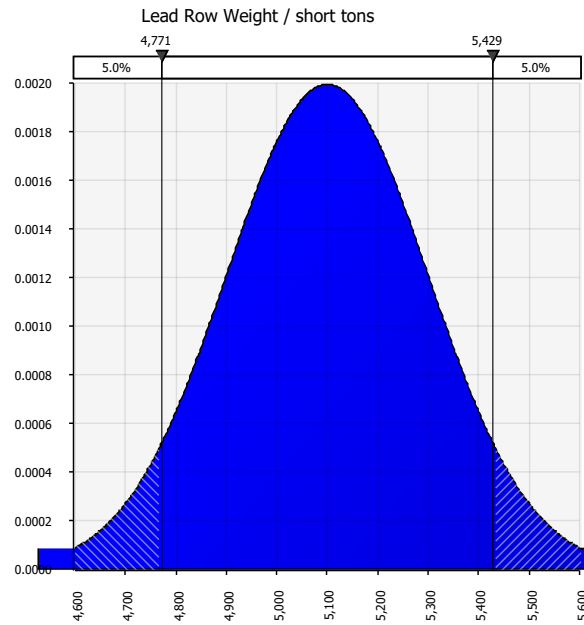


Figure D.5. pdf of Lead Row Weight

Table D.5
Probability Distribution Statistics for Lead Row Weight

Distribution	E (x)	Min((x)	Max (x)
Normal	5100	4300	5900

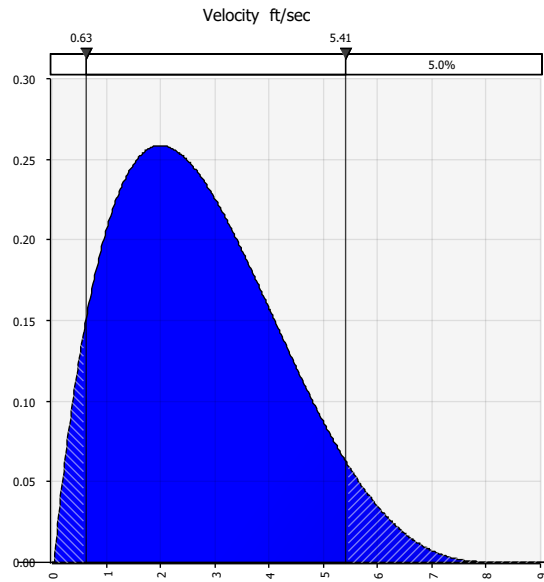


Figure D.6. pdf for Velocity

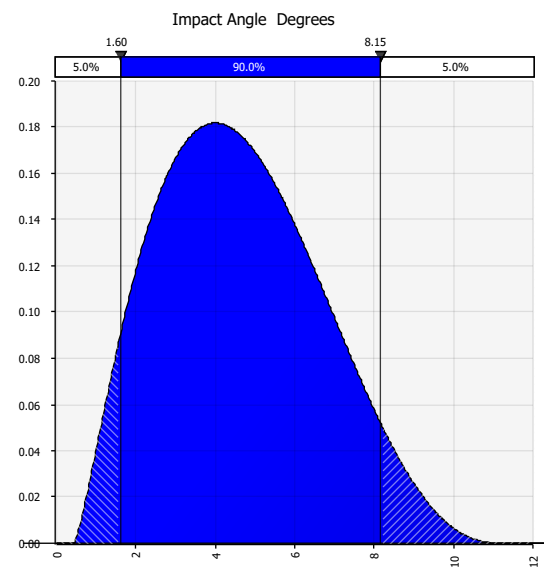


Figure D.7. pdf of Angle

Table D.6
Probability Distributions for Velocity and Angle

	Distribution Type	Most Likely (x)	Lower limit (x)	Upper limit (x)
Velocity (ft/sec)	Pert	2	0.04	8.32
Angle (degrees)	Pert	4	0.44	11.31

D.3.3.4. For this example, the PBIA model is developed in Excel using a commercial Monte Carlo Simulation program. Monte Carlo Simulations allows the easy simulation of numerous combinations of annual events, which develop an annual probability distribution for the impact loads on the upper guide wall. For this example, 25,000 iterations were run to determine the distribution for the impact load using the empirical equation in Chapter 4. This annual distribution of impact load is then used to calculate the return periods for the impact loads to be used in design.

D.3.4. PBIA Results.

D.3.4.1. The statistical results from the PBIA are shown in Table D.7. This table shows the minimum, maximum, mean, and standard deviation from the simulation data for the impact force. However, since the PBIA is performed to calculate the return periods, the output needs to be expressed in terms of either the histogram, cumulative probability distribution, or the corresponding percentiles. These are all derived from the output or graphing capabilities from with the simulation program.

Table D.7
Statistics from the PBIA Example

Statistic	Force (kips)
Minimum	0.44
Maximum	505
Mean	151.12
Std Dev	98.08

D.3.4.2. The histogram shows the range and distribution of expected annual impact forces. Figure D.11 shows the histogram for this example. The histogram shows that a majority of the impact forces (over 90% as shown in Figure D.11) from the simulation are below the mean value of 47.2 kip. From this histogram, a cumulative probability distribution of impact forces can be fit. Figure D.11 shows the cumulative probability distribution (CPD) for the PBIA. The CPD is used to determine the percentage of distribution that is below a specified level. Figure D.12 shows that there is 90% of impact values below the mean value and 10% of the distribution lies above that value.

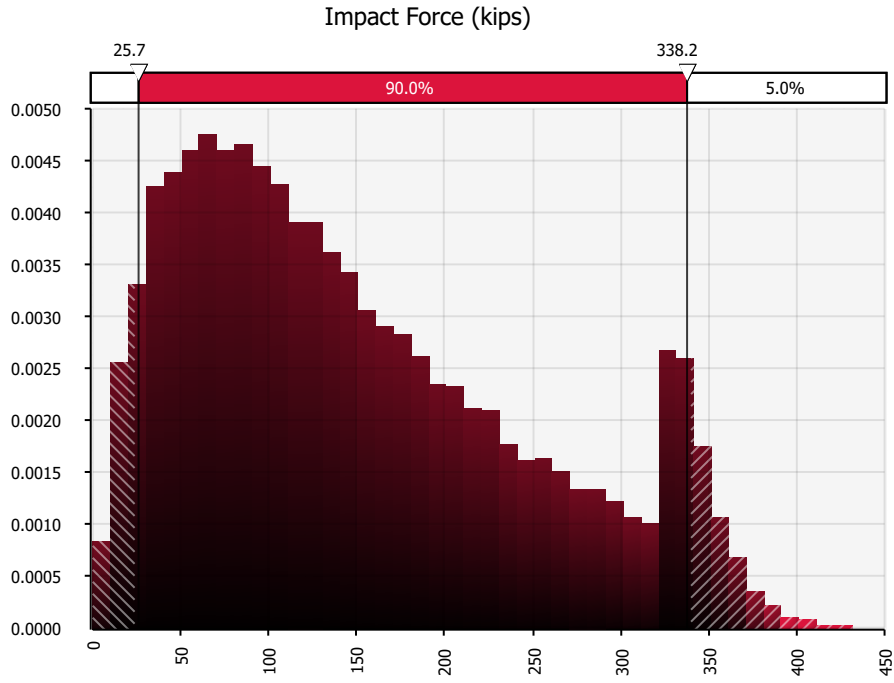


Figure D.8. Histogram of Impact Forces
 (Note: The increase in density is caused by the segment break (at 325 kips) in empirical equation)

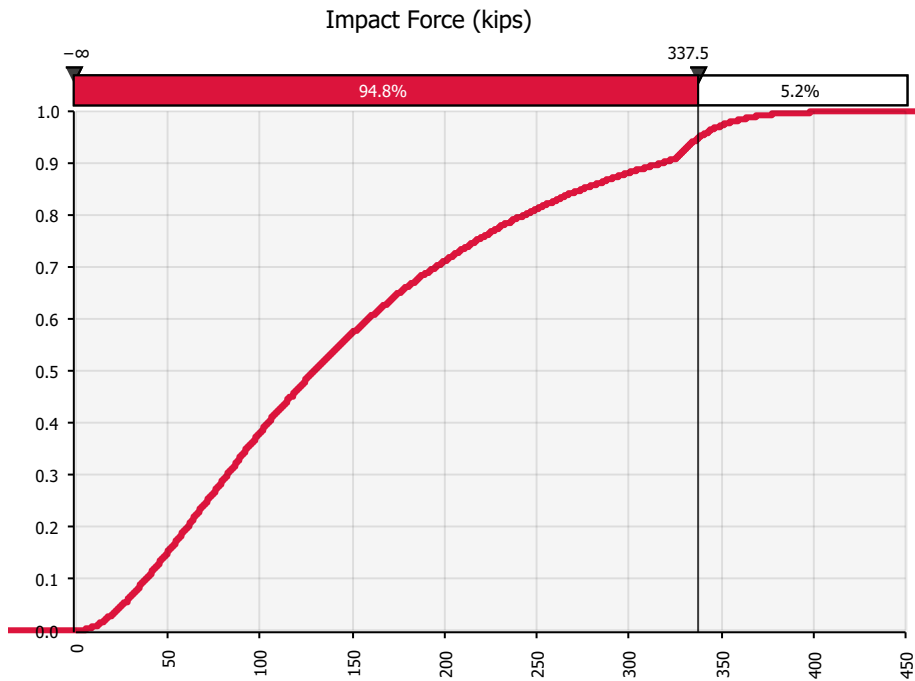


Figure D.9. Cumulative Probability Distribution for Impact Forces

D.3.4.3. For a PBIA, the simplest way to determine the return period is to use percentiles for the distribution of annual impact forces. Percentiles are defined as the percentage of annual impact force that occurs at or below that impact force. The resulting percentiles can be used to determine the probability of exceedance, P(E), which is the converse of the percentile such that both should add up to unity. The return period, RT, can be determined by using the equation:

$$RT = 1/(1-\text{Percentile (in decimal)})$$

$$= 1/P(E)$$

7.4.6.4. The values for this PBIA example are shown in Table D.8.

Table D.8
Percentiles for Impact Load

50%	129.17
55%	142.99
60%	158.87
65%	175.08
70%	194.91
75%	216.76
80%	242.82
90%	317.24
95%	338.17
97.5%	351.55
99.33%	367.60
99.999%	505.12

D.3.5. Design of Upper Guide Wall for Barge Impact.

D.3.5.1. Based on the criteria for return period discussed in Chapter 2 of this manual, return periods for the impact design for the upper guide wall are selected in Table D.9. These return periods were selected for this design due to trying to meet the performance requirements set for the design events in Chapter 2.

Table D.9
Design Force for Upper Guide Wall

Event Loading	Design Return Period (years)
Usual	2 years
Unusual	150 years
Extreme	1000 years

D.3.5.2. These impact forces selected do not include the load factors for each of the design cases as discussed in Chapter 2. A summary table without and with the load factors included for the design of the wall are shown in Table D.10 and D.11.

Table D.10
Unfactored Design Impact Force for Upper Guide Wall

Event Loading	Design Return Period (years)	Impact Force (kips)
Usual	2 years	129
Unusual	150 years	367
Extreme	1000 years	505

Table D.11
Factored Design Impact Force for Upper Guide Wall

Event Loading	Design Return Period (years)	Impact Force (kips)
Usual	2 years	284
Unusual	150 years	587
Extreme	1000 years	606

D.3.6. Historical PBIA Results and Return Periods for USACE Navigation Projects

The values from both deterministic and PBIA with the associated return periods are shown for projects discussed in Appendices C and D. These values are presented for historical purposes and represent the state-of-the-practice design values based on guidance available at the time of design.

Table D.12
Historical Design Forces for USACE projects

Project/Type of Structure and Location	No. of Barges	Weight	ERDC Model Test	Load Cases					
				Usual		Unusual		Extreme	
				Kips	R.P.	Kips	R.P.	Kips	R.P.
Olmsted Locks and Dam									
OLM Upper River Wall - floating	15	30000	yes	600	1	900	50	1000	1000
OLM Upper Middle Wall - floating	15	30000	no	300	1	600	50	800	1000
OLM Lower Wall - rigid & floating	15	30000	no	300	1	450	50	500	1000
TG Tainter Gate Pier	15	30000	no			625			
TG at EL 314(HFA-89)(not used)	15	30000	no			1460	6fts/45 degree	2210	6fts/0 degree
TG at lower pier	15	30000	no					1791	4fts/0
								1588	4fts/45
Marnet Lock	9	18000	Yes						
MAR Upper Guide Wall - Loss of Power	9	18000							
MAR Condition only) Fdn	9	18000		0	0	250	200	1060	1000
MAR Beam	9	18000		0	0	195	150	943	500
MAR Upper Guard Wall Fdn	9	18000		370	5	640	200	810	1000
MAR Beam	9	18000		350	5	600	150	710	500
Winfield Lock	9	18000	Yes						
Upper Guard Wall Beam	9	18000		610	2	810	50	920	500
Cell	9	18000		680	5	840	100	950	1000
Kentucky Lock									
Upper Land Wall - floating	15	30000	No	290	1	510	50	590	1000
Existing Lower Wall - temp. str.	15	30000		400					
Cofferdam Cell - temp. str.	15	30000		500					
Chickamauga Lock	15	30000	No						
Upper River Wall	15	30000		250		700		900	
Upper Middle Wall	15	30000		125		350		450	
Lower Wall	15	30000		125		350		450	
US Bullnose	15	30000						2000	
DS Bullnose	15	30000						1000	
UMR&IWW	15	30000							
Upper Guide Wall	15	30000	No	330		500		700	
Lower Guide Wall	15	30000		165		250		350	
End Cell - Upper	15	30000				1400		1950	
Lower	15	30000				700		1000	
Upper Ohio (EDM) Locks	12	20400	No						
UO Upper	12	20400		500		730		1100	
UO Lower	12	20400		250		375		550	
UO Upper Cell	12	20400				1600		2500	
UO Lower Cell	12	20400				800		1250	
UO Chamber Walls	12	20400				80		125	
R.C. Byrd L&D	15	30000							
RCB Upstream Guide Wall Fdn	15	30000		370		640		810	
RCB Beam	15	30000		350		600		710	
RCB Upstream Guard Wall	15	30000		680	5	840	100	950	1000
McAlpine L&D	15	30000							
MLP Approach Walls Normal to Wall	15	30000		300		450		500	
MLP Parallel to Wall	15	30000		135		203		225	
MLP Nose Cell	15	30000				1400		1950	
Charleroi									
CHR Upper Guide Wall - 5 fps	9	18000		1122		1666		1870	
CHR Lower Guide Wall - 1.5 fps	9	18000		336		498		560	

Appendix E

Rigid Wall Historical Model

E.1. Technical Background.

E.1.1. Rigid Wall Model – Generation II Barge Impact Model (Historical ONLY). Barge impact is an important load case in defining the wall dimensions in either preliminary or advanced designs. The method presented in ETL 1110-2-563 was based on the direct results from the full-scale experiments conducted by USACE from 1997 to 2000 as discussed in Appendix B. The data used to derive the empirical correlation was limited to flotilla velocities up to 3.4 fps longitudinal to the wall, for impact angles up to 21.1 degrees, and for linear momentum normal to the wall between 650 and 1,025 k-sec. The empirical equation developed estimates the impact load normal to the structure and **is only shown** here for historical purposes and for comparison to the newer FEM-based empirical models defined in Chapter 4 for approach walls. The difference in both models is highlighted in the examples below.

E.1.2. Based on the results (Patev 2000) and processing of the experiments (Arroyo 2000), an empirical equation was developed to equate the maximum impact force normal to the wall, F_m , to the linear momentum of the flotilla as it impacts the wall. Figure E.1 shows the data required for the empirical equation. The results from the empirical equation also compare well with a derivation of the mechanical model for the impact of a rigid flotilla on a rigid wall.

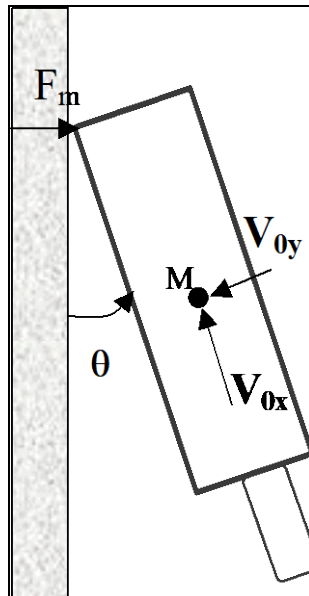


Figure E.1. Data Requirements for Empirical Model

E.1.3. However, based on field observations and limitation of the field data, the values from the empirical equation are limited to an F_m of less than 800 kips. The designer should be careful to show the impact values of the maximum impact force that exceeds 800 kips. This limitation is imposed because the equation does not account for the effects of lashing failures or deck buckling of the plates under higher impact loads.

E.1.4. The empirical equation is defined as:

$$F_m = 0.435 \cdot m \cdot (V_{0x} \cdot \sin \theta + V_{0y} \cdot \cos \theta)$$

$$F_m \leq 800 \text{ kips}$$

where,

m = mass in kip - sec²/ft

where $m = \frac{2W}{g}$ where W = weight of barge train in short tons (including towboat) and

2 is the conversion factor from short tons to kips

$$g = 32.2 \text{ ft/sec}^2$$

V_{0x} = initial longitudinal velocity of barge in x - direction (ft/sec)

V_{0y} = initial transverse velocity of barge in y - direction (ft/sec)

θ = approach angle (degrees)

E.2. Design Parameters.

E.2.1. Deterministic Example. This example is for the design of a rigid approach wall for a new lock on the Ohio River. Based on present traffic predictions and navigation model testing at ERDC, a 15-barge tow and input parameters selected for the usual, unusual, and extreme load cases. **Bold values** are the calculation of the force using the empirical model defined in Chapter 4.

E.2.1.1. Usual load case:

$$V_{0x} = 2 \text{ ft/sec}$$

$$V_{0y} = 0.01 \text{ ft/sec}$$

$$\theta = 10 \text{ degrees}$$

$$W_{\text{barge}} = 30,000 \text{ short tons}$$

$$(F_w)_{\text{max}} = 0.435 \cdot (30,000 \cdot 2 / 32.2) \cdot (2 \cdot \sin(10) + 0.01 \cdot \cos(10)) = 289.72 \text{ kips}$$

From empirical equation defined in Chapter 4, **F = 249.29 kips**

E.2.1.2. Unusual load case:

$$V_{0x} = 4 \text{ ft/sec}$$

$$V_{0y} = 0.03 \text{ ft/sec}$$

$$\theta = 20 \text{ degrees}$$

$$W_{\text{barge}} = 30,000 \text{ short tons}$$

$$(F_w)_{\text{max}} = 0.435 \cdot (30,000 \cdot 2 / 32.2) \cdot (4 \cdot \sin(20) + 0.03 \cdot \cos(20)) = 1,132.68 \text{ kips } (>800 \text{ kips max})$$

From empirical equation defined in Chapter 4, **F = 467.57 kips**

E.2.1.3. Extreme load case:

$$V_{0x} = 6 \text{ ft/sec}$$

$$V_{0y} = 0.05 \text{ ft/sec}$$

$$\theta = 30 \text{ degrees}$$

$$W_{\text{barge}} = 30,000 \text{ short tons}$$

$$(F_w)_{\text{max}} = 0.435 * (30,000 * 2 / 32.2) * (6 * \sin(30) + 0.1 * \cos(30)) = 2,466.78 \text{ kips } (>800 \text{ kips max})$$

From empirical equation defined in Chapter 4, **F = 721.39 kips**

E.2.2. Probabilistic Example.

E.2.2.1. This example is for the design of a rigid approach wall for a new lock on the Ohio River. Based on present traffic predictions and navigation model testing at ERDC, a 15-barge tow and input parameters selected for probabilistic analysis are shown in Table E.1.

Table E.1
Input Parameters for Probabilistic Example

Parameter	Distribution	E(x)	$\sigma(x)$	Min(x)	Max(x)
Velocity – x (ft/sec)	Lognormal	2	1	0.1	7
Velocity – y (ft/sec)	Lognormal	0.01	0.001	0.001	0.05
Angle (degs)	Lognormal	10	4	1	30
Weight – entire flotilla (short tons)	Constant	30,000	-	-	-

E.2.2.2. The probabilistic model run is made using Monte Carlo Simulations for 50,000 iterations, and the results for the usual (2 year), unusual (150 year), and extreme (1000 year) load cases are shown in Table E.2.

Table E.2
Design Load Cases from Probabilistic Calculations

Load Case	Force (kips)	Force (kips) – Empirical Model in Chapter 4
Usual – 2 year	398	306
Unusual – 150 year	1,130*	445
Extreme – 1000 year	1,467*	510

(Note that * reflects loads that are greater than 800 kips limitation of this model.)

E.2.2.3. Also, notice the significant difference in the extreme load case for the deterministic calculation compared to Table E.2. This is due to the true frequency of the extreme load in the probabilistic calculations. Deterministic calculations using this historical empirical model typically overestimates for forces in the unusual and extreme events since calibration was not made to nonlinear events above 800 kips.

Appendix F

Damage Model – Coastal and Inland Riverine Floodwalls

F.1. General.

F.1.1. This appendix documents the finite element (FE) modeling efforts pertaining to damage assessments for barge impacts on typical USACE floodwalls. Two reinforced concrete (R/C) floodwall structures are identified and modeled for these purposes. One floodwall is a coastal T-wall, whereas the second is a riverine I-wall with embedded steel sheet piling. The overall FE models for both walls incorporate a nonlinear concrete material model and nonlinear steel material model. Since damage and failure in the vertical portions of each reinforced concrete wall are of primary focus, simplified foundation modeling techniques are employed.

F.1.2. The T-wall and I-wall FE models are each integrated with a high-resolution FE model of a fully loaded jumbo hopper barge (see Chapter 3). The integrated model is then used for purposes of conducting dynamic barge-wall impact simulations. Computed results from quasi-static lateral load simulations (i.e., “pushover” analyses) are also reported for the T-wall and I-wall configurations.

F.1.3. Results from the dynamic impact simulations and static pushover simulations are then compared to identify and characterize differences. For the representative set of simulated barge impact conditions and wall configurations, flexural patterns of damage are primarily observed. Thus, the results obtained suggest that conservative wall designs are likely to be produced by the combination of dynamically computed peak impact loads and statically computed wall capacities.

F.1.4. This appendix content is organized such that:

F.1.4.1. Section F.2 contains documentation of a nonlinear material model capable of representing concrete damage and failure for use in modeling the T-wall and I-wall configurations.

F.1.4.2. Section F.3 provides FE model details for the T-wall configuration.

F.1.4.3. Section F.4 discusses results from dynamic barge-wall impact simulations and quasi-static pushover simulations for the T-wall configuration. Comparisons between observed damage modes associated with the dynamic and static approaches are emphasized.

F.1.4.4. Section F.5 provides FE model details for the I-wall configuration.

F.1.4.5. Section F.6 discusses results from dynamic and quasi-static pushover simulations for the I-wall configuration. This discussion focuses on comparisons of the damage modes associated with the dynamic and static approaches.

F.2. Nonlinear Concrete Material Model.

F.2.1. Overview.

F.2.1.1. Concrete floodwalls may be subjected to barge impacts over a variety of different operational conditions. However, such structures are particularly at risk during flood stage conditions. To assess failure modes of concrete wall structures under barge impacts, FE simulation techniques and a nonlinear concrete material model are integrated together. In prior studies (Murray 2007, Murray et al., 2007), the accuracy of the LS-DYNA (LSTC 2016) concrete material model `MAT_CSCM` was comprehensively evaluated.

F.2.1.2. This “continuous cap surface model” was evaluated for applications involving the simulation of vehicle impacts against concrete structures. Concrete strain rates arising during vessel impacts on floodwalls are only about an order of magnitude smaller than those arising during vehicle impacts. Therefore, the `MAT_CSCM` model is utilized herein for simulating vessel impacts against concrete floodwalls.

F.2.2. Verification of the Material Model. In Consolazio and Han (2018), the accuracy of this material model was verified under varying loading conditions. Verification was carried out for both unreinforced (plain concrete) and R/C structural members. For example, simulations (using LS-DYNA) were conducted on a single solid element under uniaxial tension and compression. Then, the agreement between computed versus theoretical results were shown.

F.2.2.1. A 6 in. diameter, 12 in. long concrete cylinder was also utilized in simulating uniaxial tension and compression loading. Material properties identical to those of the single element were utilized. Subsequently, simulations were conducted on both unreinforced and R/C beam models. Results obtained from transverse loading of the R/C beam model were verified against manually constructed moment-curvature relationships.

F.2.2.2. Reinforced Concrete Slab Model. To facilitate damage assessments of floodwalls during barge impacts, modeling of R/C slab behavior (two-way flexure) is required. This is accomplished by coupling together concrete (modeled as solid elements) and a grid of embedded mild steel reinforcement (modeled as beams).

F.2.2.2.1. The accuracy of the `MAT_CSCM` material model is assessed when combined with use of a rebar coupling technique (`CONSTRAINED_BEAM_IN_SOLID`, or CBIS). Specifically, simulation of a R/C slab is conducted, and results are compared to a yield line analysis. Two-way inelastic flexural behavior is considered in both types of analysis (FE, yield line). Such behavior is expected to occur throughout the stems of R/C floodwalls subjected to barge impact loads.

F.2.2.2.2. For model verification purposes, a square slab (Figure F.1) is modeled with dimensions of 240 in. x 240 in. x 8 in. (thick). Reinforcing bars (No. 4, 0.5 in. diameter) are embedded in the slab at a spacing of 9 in. on center in both directions. As noted above, the `CONSTRAINED_BEAM_IN_SOLID` method is used to couple rebar (beam) and concrete slab (solid) elements together. The concrete material model `MAT_CSCM` is defined for concrete with a compressive strength of 5 ksi. A maximum aggregate size of 0.75 in. is specified.

F.2.2.2.3. An elastic, perfectly plastic stress-strain relationship is used for the steel reinforcement. Contact (compression-only) boundary conditions are modeled using concrete strips that support the four edges of the slab. Linearly increasing uniform pressure load is applied to the top surface of the slab.

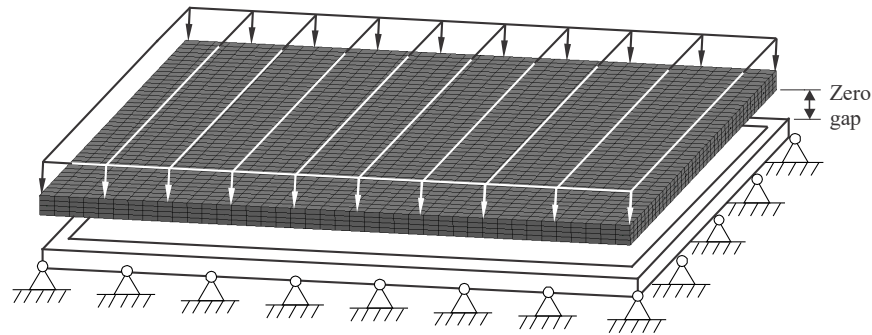


Figure F.1. Boundary Conditions and Loading Applied to Reinforced Concrete Slab Model

F.2.2.2.4. For LS-DYNA models utilizing the concrete material model `MAT_CSCM`, sustained damage can be indicated (visually rendered) by plotting a damage index plot. The colorized fringes (LS-DYNA color contours) range from 0 (undamaged; shown as blue) to 1 (fully damaged; shown as red). As shown in Figure F.2 (adapted from Murray 2007), before an element reaches maximum strength, the damage index (fringe level) equals 0.

F.2.2.2.5. Values of 0, in this context, signify that full residual material capacity is available, and no damage has occurred. After an element reaches maximum strength, damage starts to accumulate, and the available residual material capacity gradually reduces. When no further residual capacity is available, the damage index (fringe level) equals 1, indicating a completely damaged material state.

F.2.2.2.6. The `MAT_CSCM` material model permits erosion of elements (element deletion) to simulate concrete crushing. Erosion occurs after the damage index exceeds 0.99 and the maximum principal strain exceeds a critical threshold. Simulation of the slab under two-way flexure is conducted with the element erosion feature active. Slab deformations at the ultimate (failure) load condition are shown in Figure F.3 using colorized plots of damage index.

F.2.2.2.7. Force-displacement data from the simulation is shown in Figure F.4. To independently verify the accuracy of the FEA results, an ultimate-strength yield line analysis is also conducted for the slab. Ultimate capacities obtained from the FE simulations and from yield line analysis indicate good agreement (Figure F.4), differing by less than 3%.

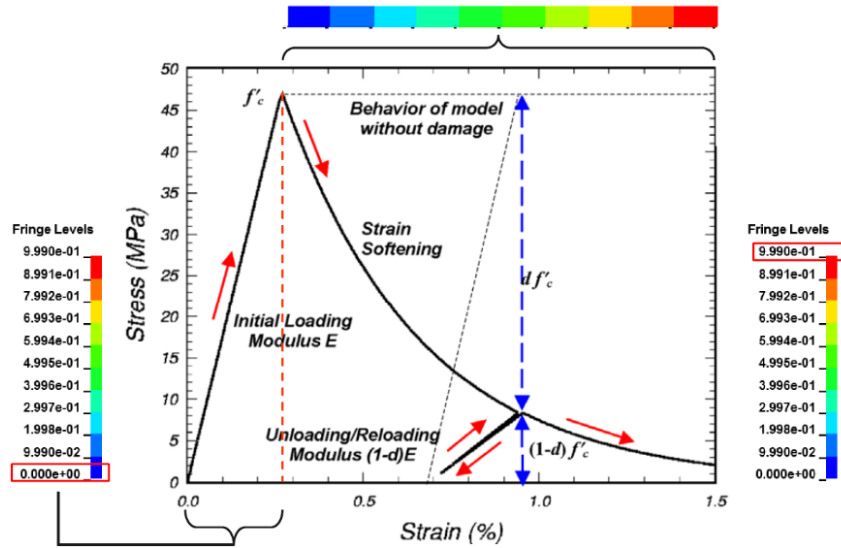


Figure F.2. Damage Index as Reported by the MAT_CSCM Material Model (Adapted from Murray 2007)

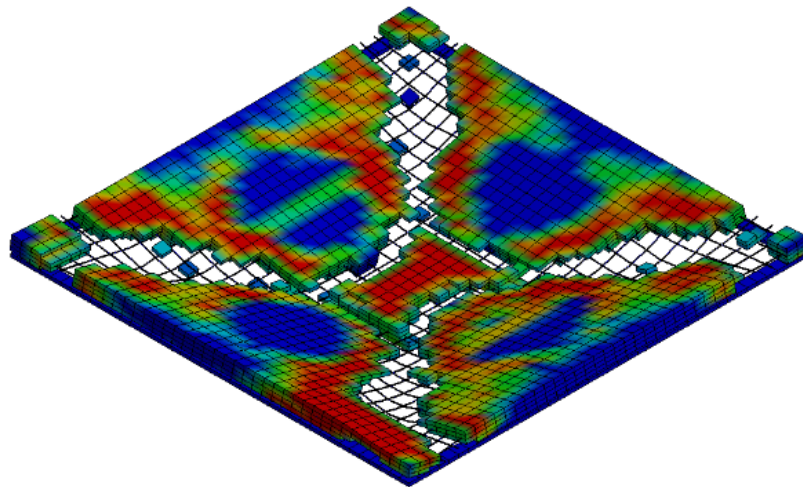


Figure F.3. Deformations at Failure of Slab Model with Damage Index Indicated Using Color (Blue = 0, or Undamaged; Red = 1, or Fully Damaged)

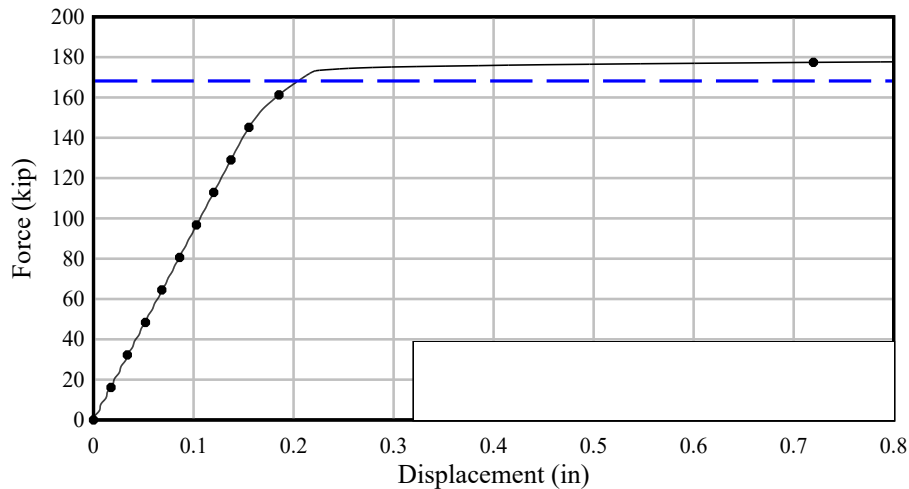


Figure F.4. Comparison of Slab Finite Element Results and Yield Line Analysis Results

F.3. Modeling of Coastal R/C T-Wall.

F.3.1. Overview.

F.3.1.1. Using structural drawings of a coastal R/C T-wall near Port Arthur, Texas (see Consolazio and Han 2018), a floodwall FE model is developed. The FE model is composed of both structural and simplified soil components. Structural components of the T-wall include a concrete stem, steel reinforcement (rebar), and a concrete footing. Soil components include backfill soil on the land side of the floodwall (see Consolazio and Han 2018 for a detailed treatment of the soil resistance modeling).

F.3.1.2. The coastal R/C T-wall is constructed as an array of 24-ft-long monoliths. Three such monoliths, with appropriate boundary conditions (discussed later), are modeled for purposes of conducting barge impact simulations. In addition, a 72-ft continuous monolith is modeled and subjected to various forms of impact loading.

F.3.2. Structural Components of the T-Wall Monolith.

F.3.2.1. The concrete stem and footing (Figure F.5) are modeled using 8-node solid elements. Solid element sizes vary at different locations (Figure F.5b). To represent concrete damage and failure under barge impact loading, the vertical stem of the floodwall is modeled using the concrete material model `MAT_CSCM`. A compressive strength of 4 ksi is specified along with a maximum aggregate size of 0.75 in. Failure of the horizontal footing is not anticipated to occur during impact loading. Therefore, a linear-elastic material model (without steel reinforcement) is utilized for the footing.

F.3.2.2. Modeling of steel reinforcement (rebar) in the vertical stem includes vertical rebar, longitudinal rebar, and top-of-wall stirrups. These three forms of reinforcement are embedded into the solid mesh of the concrete stem. All steel reinforcement bars are modeled using beam elements. An elastic, perfectly plastic stress-strain relationship is employed in the material model of the steel reinforcement. The constraint command `CONSTRAINED_BEAM_IN_SOLID` (CBIS) couples the steel reinforcement beam elements to the surrounding concrete solid elements.

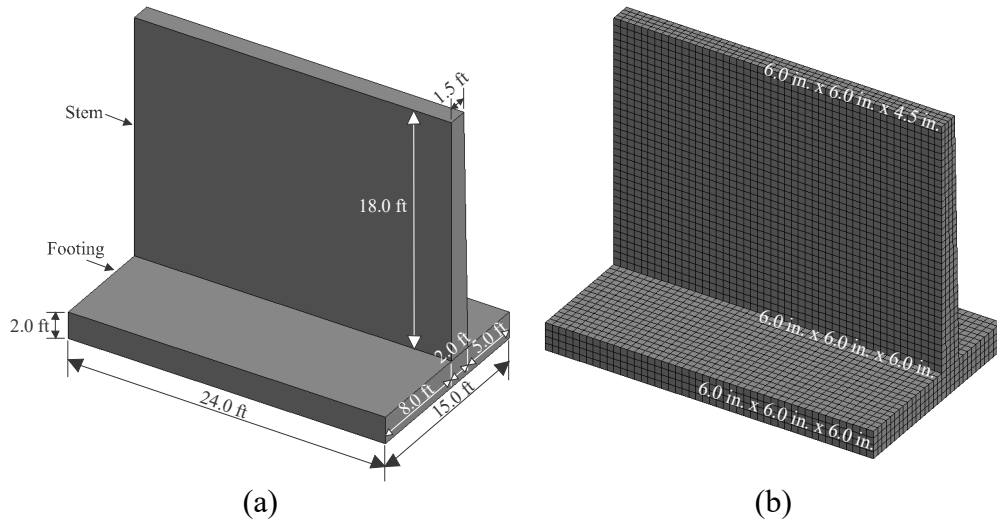


Figure F.5. Finite Element Model of a 24-ft R/C T-Wall Monolith: (a) Without Element Mesh Shown; (b) With Element Mesh Shown

F.3.3. Soil Resistance Modeling. To represent backfill soil resistance in the model, soil springs are placed on the land side, as shown in Figure F.6. Lateral stiffness of the backfill soil is quantified using software separate from LS-DYNA. Parameters of the backfill are taken to be the same as those utilized in Consolazio et al. (2014). Lateral stiffnesses are computed using FB-MultiPier (BSI, 2016). See Consolazio and Han (2018) for additional details concerning the soil resistance modeling.

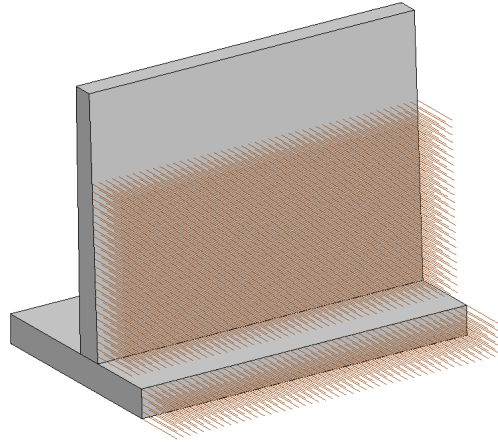


Figure F.6. R/C T-Wall 24-ft Monolith FE Model with Lateral Backfill Soil Springs
(Note: Floodwall Mesh Not Shown for Clarity)

F.3.4. Boundary Conditions. Simplified boundary conditions are defined along the bottom surfaces of the footings (Figure F.7). Vertical displacements are restrained, and transverse displacements are left active (free). Longitudinal (along-wall) displacements at the bottom surface of the central monolith are left free as well. However, those on the bottom surfaces of the upstream and downstream monoliths are fixed. In this way, boundary conditions on the bottom surfaces approximate the resistance of additional monoliths present in the physical structure (but not directly included in the model).

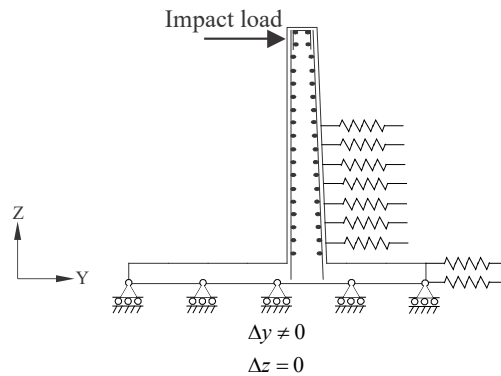


Figure F.7. Sectional View of Boundary Conditions on Floodwall Monoliths

F.3.5. Contact Between Barge Model and T-Wall Model.

F.3.5.1. To characterize barge impact loads, the barge model (Chapter 3) is merged together with the R/C T-wall FE model. Contact detection is defined between the deformable bow of the barge model and the impacted surface of the floodwall. Solid element erosion is activated for the concrete elements that represent the floodwall stem. Consequently, the barge-to-wall contact surface is continuously updated to approximate the evolution of structural concrete damage during impact.

F.3.5.2. Static and dynamic coefficients of friction of 0.50 and 0.45, respectively, are assigned to the barge-to-floodwall stem (i.e., steel-to-concrete) contact interfaces. Additional contact detection is defined between the deformable barge bow and the beam elements representing the steel reinforcing bars. Static and dynamic coefficients of friction of 0.55 and 0.45, respectively, are assigned to the barge-to-rebar (i.e., steel-to-steel) contact interfaces.

F.4. Coastal R/C T-Wall Damage Case Studies.

F.4.1. Overview. To characterize damage phenomena of coastal R/C T-walls under barge impact loading, barge and coastal R/C T-wall FE models are utilized in impact simulations. It is expected that floodwalls may be at risk for barge impacts during flood stage conditions. Therefore, flood stage hydrostatic pressure load is applied to the wall before simulating barge impact. The peak dynamic barge impact force in excess of hydrostatic (EOH) load is defined to distinguish impact from hydrodynamic loads. Values of EOH force are quantified along with wall responses (e.g., extent of damage) as part of the dynamic simulations.

F.4.1.1. Complementary static analyses are conducted to determine static peak EOH force. In the following, comparisons between damage modes (obtained from dynamic versus static simulations) demonstrate that wall capacities computed using traditional static approaches are conservative. In other words, traditional static approaches yield relatively smaller capacities in comparison to corresponding capacities associated with dynamic response. Therefore, comparing statically computed wall capacities to dynamically computed peak impact loads constitutes a conservative design approach.

F.4.1.2. Wall damage patterns are influenced by the manner in which loads are applied (direction, rate) and the configuration of the floodwall structure. Thus, damage patterns of floodwalls under barge impact loading, and walls subjected to quasi-static loading are both investigated. Wall deformations and concrete damage index plots are also assessed. Two typical failure modes—local flexural failure and global flexural failure—generally occur in concrete walls under the application of normal (perpendicular) loading. To reach either failure mode, a corresponding failure capacity must be reached or exceeded.

F.4.1.3. T-Wall Configurations Considered.

F.4.1.3.1. To consider variations of floodwall configuration (e.g., length of monolith) and interaction conditions between adjacent monoliths, two distinct floodwall configurations are investigated. The two configurations are divided into case studies referred to as case study I and case study II.

F.4.1.3.2. In case study I, three 24-ft-long floodwall monoliths are separated by gaps. In this way, each monolith has nearly independent response when one of the monoliths is subjected to barge impact load. In case study II, a continuous floodwall with a 72-ft length (i.e., the length of three integrally/continuously joined 24-ft monoliths) is investigated. A relatively severe barge impact condition (30° impact angle, 5 ft/sec impact speed) is selected to quantify the peak dynamic EOH force. The peak dynamic EOH force is then compared to the corresponding peak static EOH force. EOH forces are resolved in the direction normal (perpendicular) to the wall.

F.4.2. Modeling Assumptions.

F.4.2.1. Barges striking near the top of a floodwall have the potential to generate maximum loads during flood stage conditions. As such, in the FE models, the top elevation of the barge headlog is aligned with the top elevation of floodwall (Figure F.8). In the fully loaded (2,000 short tons) condition, a hopper barge drafts such that the water surface is approximately 4 ft below the top of the barge headlog. Correspondingly, hydrostatic loading is applied to each wall model starting at an elevation 4 ft below the top of the wall. For all cases investigated, hydrostatic pressure is applied to the wall prior to barge-related lateral loads.

F.4.2.2. For the longitudinal (along-wall) impact location, a representative location at mid-length of the monolith is selected (Figure F.9). Simulated barge impact speeds include a baseline speed of 5 ft/sec. A lower level speed of 3.0 ft/sec and an upper level speed of 7.0 ft/sec are also considered. In each impact case, a fully loaded jumbo hopper barge weighing 2,000 short tons is modeled. A summary of key modeling assumptions is listed below:

F.4.2.2.1. Lengths of floodwall monolith/wall: 24 ft and 72 ft;

F.4.2.2.2. Impact location: at mid-length of wall;

F.4.2.2.3. Impact angles: 15°, 30°, and 45°;

F.4.2.2.4. Impact speeds: 3 ft/sec, 5 ft/sec, and 7 ft/sec;

F.4.2.2.5. Weight of impacting barge: 2,000 short tons (i.e., fully loaded jumbo hopper barge).

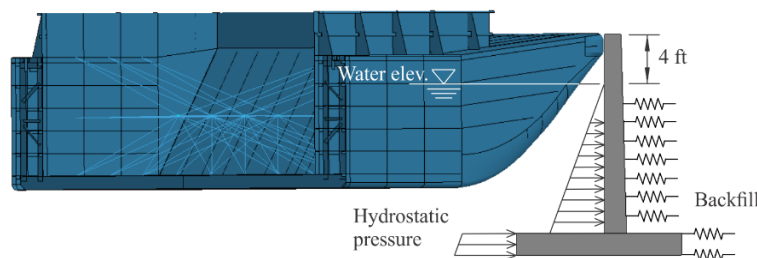


Figure F.8. Vertical Impact Location at Top of Floodwall and Hydrostatic Pressure Distribution

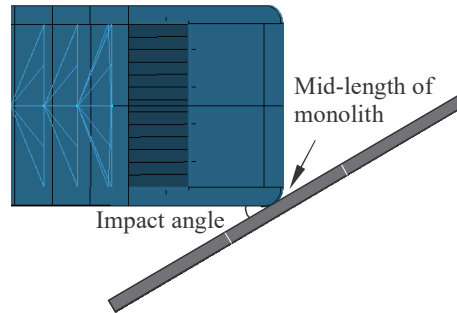


Figure F.9. Longitudinal Impact Location at Mid-Length of Monolith

F.4.3. Case Study I: Three Floodwall Monoliths (Independent Response). An impact simulation is conducted using a single barge model impacting the floodwall model. Each monolith is separated by large 2-in. gaps to bring about independent response (Figure F.10). An impact angle of 30° and impact speed of 5 ft/sec are assigned to the barge. See Consolazio and Han (2018) for additional details.

F.4.3.1. A quasi-static pushover simulation is also conducted. Displacements are slowly (quasi-statically) applied to the wall model (Figure F.11) by applying prescribed velocity to a rigid block that remains in contact with the wall. The block is modeled with an area that approximates the contact area of the barge headlog during the dynamic impact simulations. Considerations are made to ensure that the wall response remains approximately static in nature. The prescribed velocity applied to the block is selected to be 20 times slower than the mean wall velocity obtained from dynamic simulation ($\bar{v}_{wall} \div 20$ in Figure F.11).

F.4.3.2. Contact detection between the rigid block and wall surface is defined so that force applied by the block to the wall can be quantified. Since hydrostatic load is present during the simulation, the contact force computed from the simulation is EOH. That is, the EOH force is computed so as to facilitate comparisons to the dynamic barge impact results.

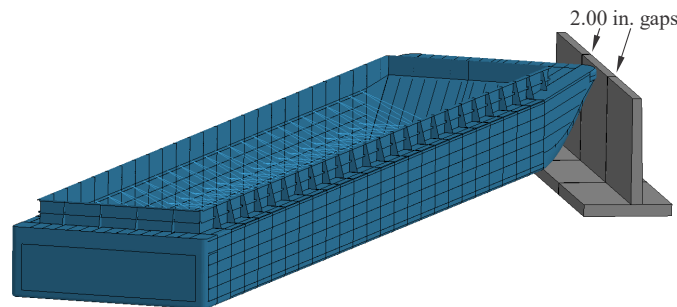


Figure F.10. Model of 30° Barge Impact at 5 ft/sec on Coastal R/C T-Wall with Three Monoliths

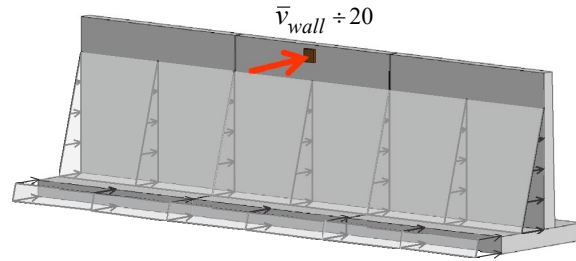


Figure F.11. Quasi-Static Simulation of Coastal R/C T-Wall with Three Monoliths

F.4.3.3. At peak dynamic EOH force, the middle (impacted) monolith is severely damaged and exhibits a global (i.e., full-length) flexural failure near mid-height (Figure F.12a). Localized flexural failure also occurs near the impact location. For the quasi-static analysis, a global flexural failure at approximately mid-height of the wall occurs. Flexural failure at this elevation in the wall stem is caused by a significant reduction in vertical rebar cross-sectional area. Also, soil resistance acting on the lower portion of the non-impact (i.e., flood-protected) side of the wall contributes to the damage state.

F.4.3.4. As is evident in Figure F.12, the pattern of wall damage under dynamic loading is somewhat more distributed than in the static case. In the static case, wall collapse is governed by the formation of essentially one plastic hinge line across the entire width of the monolith. Importantly, the static wall resistance forces (Figure F.13) never exceed the dynamic values. As such, statically computed capacity (maximum resistance force) is shown to be conservative (i.e., smaller than the dynamically computed resistance). See Consolazio and Han (2018) for additional comparisons, including those based on sensitivity studies.

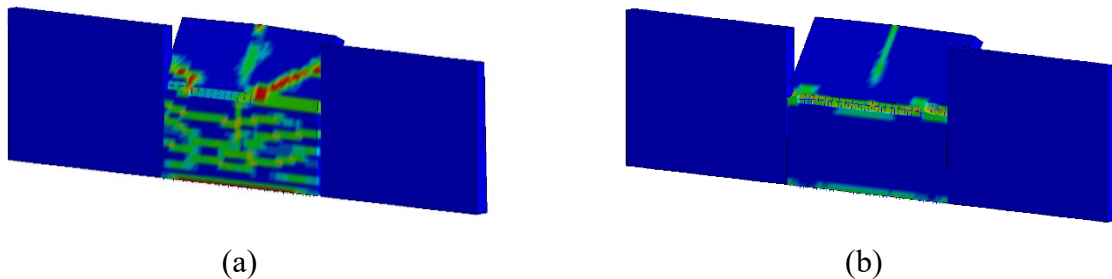


Figure F.12. Damage States Associated with Dynamic and Static Peak EOH Forces (Displacement Scale Factor = 20; Footing Not Shown): (a) Dynamic; (b) Quasi-Static

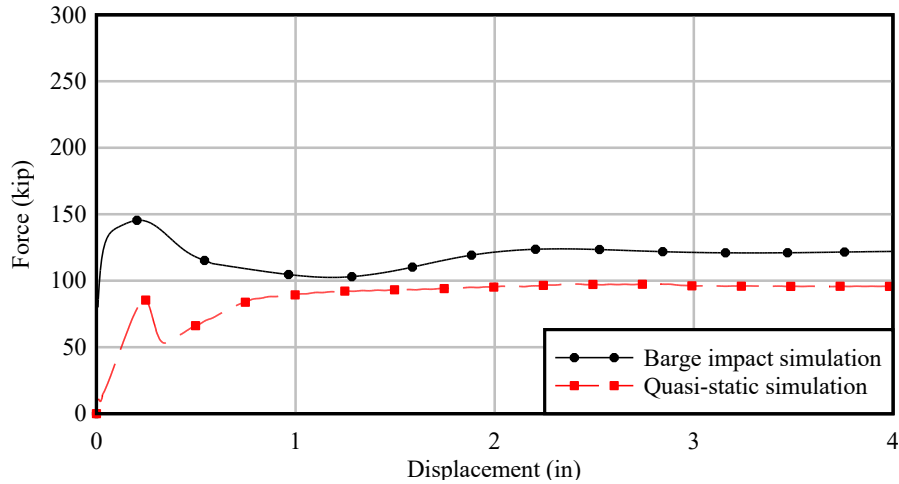


Figure F.13. Comparison of Wall Resistance Forces from Barge Impact Simulation and Quasi-Static Pushover Simulation

F.4.4. Case Study II: Continuous Floodwall. An impact simulation (Figure F.14) is conducted between a continuous 72-ft T-wall and a single barge model. The barge impacts the wall at 30° with an impact speed of 5 ft/sec. A quasi-static pushover simulation is also conducted (Figure F.15). Here, displacements are slowly applied to the wall model by applying prescribed velocity to a rigid block. Considerations are made to ensure that the wall response remains approximately static in nature. The prescribed velocity applied to the block is selected to be 20 times slower than the mean wall velocity obtained from dynamic simulation ($\bar{v}_{wall} \div 20$ in Figure F.15).

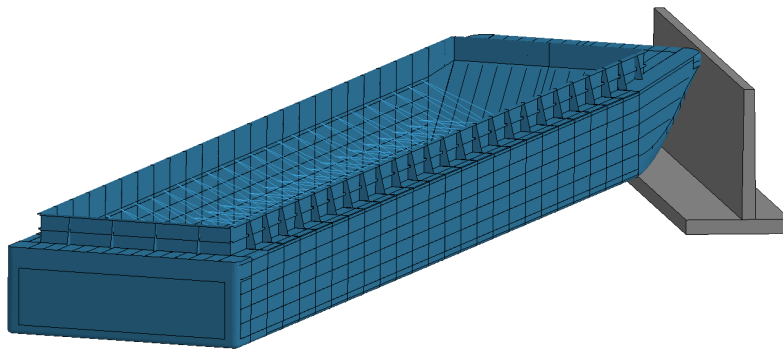


Figure F.14. Model of 30° Barge Impact at 5 ft/sec on Continuous Coastal R/C T-Wall

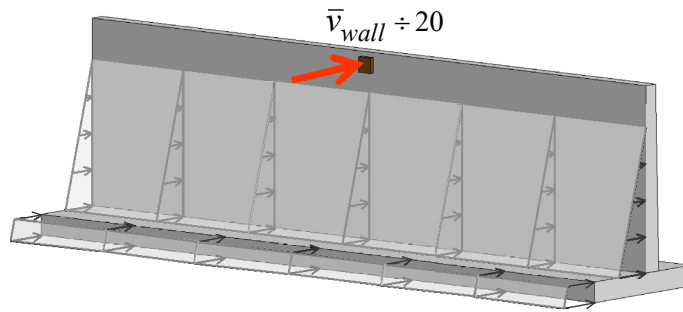


Figure F.15. Quasi-Static Simulation of Continuous Coastal R/C T-Wall

F.4.4.1. An additional simulation is conducted to determine whether observed differences in dynamic and static damage patterns are attributable to load rate. In particular, a simplified fast rate dynamic pushover simulation is conducted (Figure F.16). A prescribed velocity is again imposed on a rigid block that remains in contact with the wall throughout the simulation. However, to incorporate dynamic (inertial) effects, prescribed velocity is set equal to the mean wall velocity (\bar{v}_{wall}) associated with the dynamic impact simulation.

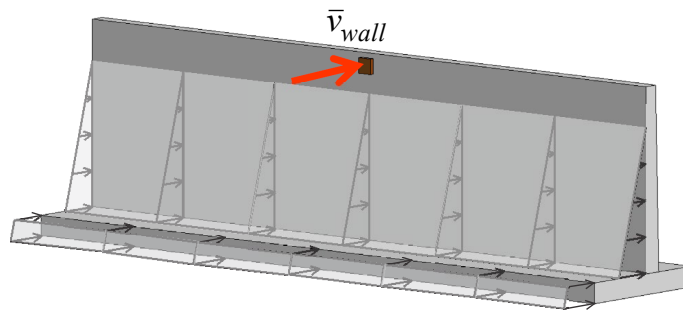


Figure F.16. Dynamic Pushover Simulation of Continuous Coastal R/C T-Wall

F.4.4.2. In Figure F.17, damage plots are shown for the dynamic barge impact simulation, dynamic pushover simulation, and quasi-static pushover simulation. In contrast to the three monolith T-wall configuration described above, the continuous wall consistently exhibits a much more distributed pattern of damage. Localized flexural failure occurs near the impact location. Damage states shown are associated with the corresponding peak EOH forces.

F.4.4.3. Under dynamic loading on the continuous wall, the patterns of wall damage are relatively more distributed than in the static case. In the static case, damage tends to be concentrated in a relatively small number of flexural failure bands. Importantly, the static wall resistance forces (Figure F.18) never exceed the dynamic values. As such, statically computed capacity is shown to be conservative (i.e., smaller than the dynamically computed resistance). See Consolazio and Han (2018) for additional details.

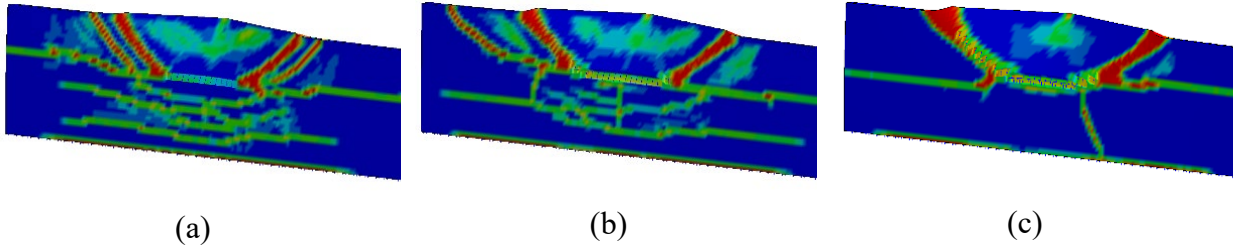


Figure F.17. Damage States Associated with Dynamic and Static Peak EOH Forces (Displacement Scale Factor = 20; Footing Not Shown): (a) Barge Impact; (b) Dynamic Pushover; (c) Quasi-Static

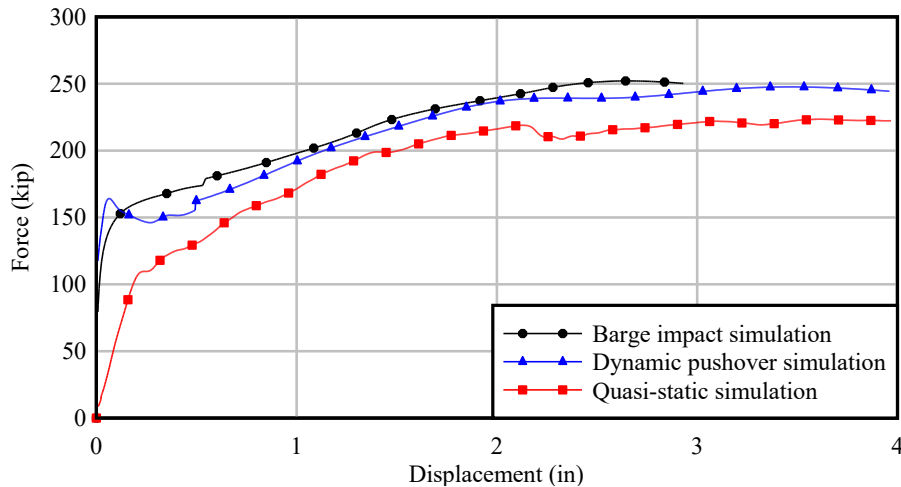


Figure F.18. Comparison of Wall Resistance Forces from Barge Impact Simulation, Dynamic Pushover Simulation, and Quasi-Static Pushover Simulation

F.5. Modeling of Riverine R/C Sheet Pile I-Wall.

F.5.1. Overview. An FE model of a riverine R/C + sheet pile I-wall at Pigeon Creek in Evansville, Indiana, is discussed in the following. The riverine R/C + sheet pile (denoted R/C+SP) I-wall includes not only steel reinforcing bars, but also embedded steel sheet piling. The FE model includes both structural and soil resistance components and is based on as-built drawings. Excerpts of the as-built drawings are provided in Consolazio and Han (2018).

F.5.2. Structural Components of the I-Wall Monolith. A 21-ft-long concrete floodwall monolith FE model is developed using 8-node solid elements. Element sizes vary at different locations along the wall (Figure F.19). Concrete is modeled using the LS-DYNA nonlinear concrete material model `MAT_CSCM`. A compressive strength of 4 ksi is assigned, along with a maximum aggregate size of 0.75 in.

F.5.2.1. Modeling of steel reinforcement in the floodwall monolith includes vertical and longitudinal reinforcing bars. Reinforcement is embedded into the solid model of the concrete monolith. All steel reinforcement bars are modeled using beam elements. An elastic, perfectly plastic stress-strain relationship is employed in the material model of the steel reinforcement. The constraint command `CONSTRAINED_BEAM_IN_SOLID` (CBIS) is used to couple the steel reinforcement beam elements to the surrounding solid concrete elements.

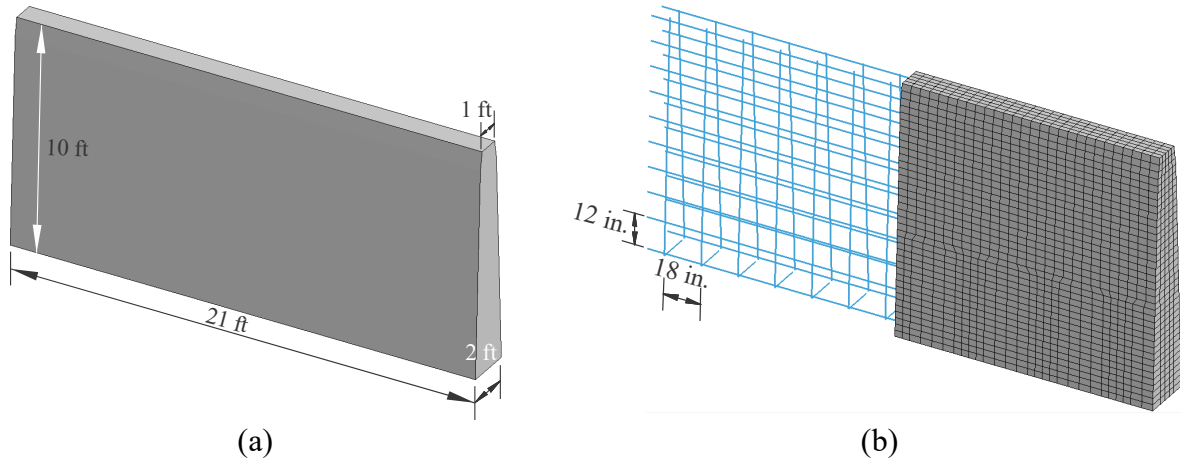


Figure F.19. Finite Element Model of 21-ft-Long Floodwall Monolith:
 (a) Without Element Mesh Shown; (b) With Mesh and Reinforcement Shown

F.5.2.2. Steel Sheet Piling. Steel sheet piling is embedded into the I-wall concrete monolith. Cross-sectional geometry, dimensions, and material properties of the sheet piling correspond to type Z-27. An FE mesh of the shell represents the piling geometry (Figure F.20). Industry standard specifications (ASTM A328/A328M-13a, 2013) are assumed and an elastic, plastic material model is adopted (see Consolazio and Han 2018). Sheet piling segments are installed in a staggered-pair configuration. Stagger spacing is 3 ft, corresponding to the width of a pair of Z sections. Bond between concrete and steel sheet piling (Figure F.21) is modeled using nodal merging.

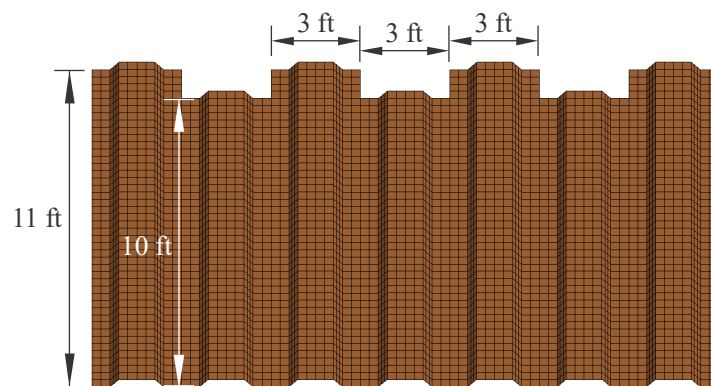


Figure F.20. Finite Element Model of Staggered Sheet Piling for Single Monolith

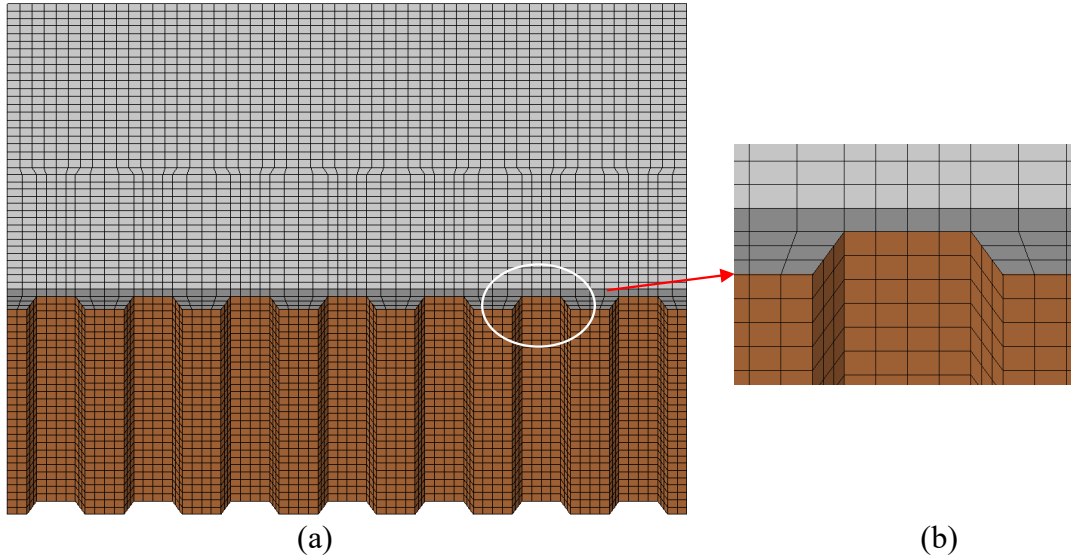


Figure F.21. Nodal Merging Method Used for Concrete-to-Sheet Piling Connection:
 (a) Single Monolith Model; (b) Mesh Details

F.5.3. Soil Resistance Modeling.

F.5.3.1. Nonlinear soil springs are attached to concrete floodwall nodes and sheet pile nodes at 6-in. vertical spacings. Soil elements include p-x and p-y springs in the horizontal directions for lateral resistance (Figure F.22a). T-z and q z springs in the vertical direction provide skin friction and pile tip bearing resistance (Figure F.22b). Both horizontal and vertical soil resistance phenomena are considered. A three-monolith configuration is shown in Figure F.23. Note that the three-monolith configuration is modeled such that the concrete stems are separated by gaps (e.g., 0.25 in.), whereas the sheet piling is continuous.

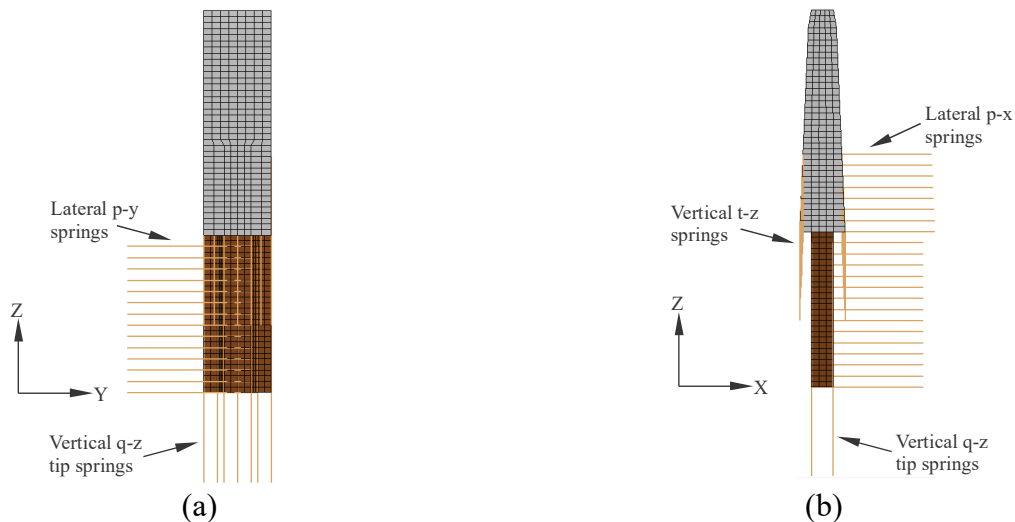


Figure F.22. 3-ft Longitudinal Slice of Floodwall Model with Soil Springs Included:
 (a) Longitudinal View; (b) Side View

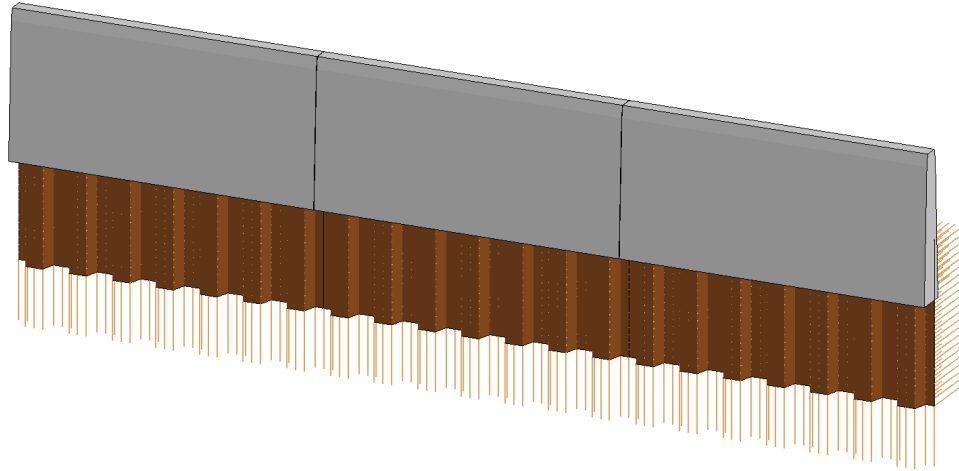


Figure F.23. Floodwall Model with Three Monoliths
(Some Soil Springs Not Shown for Clarity)

F.5.3.2. For all soil resistance springs, nonlinear force-deformation curves are calculated using separate software (FB MultiPier; BSI, 2016). Nonlinear resistance relationships are then extracted for integration into the LS-DYNA model. See Consolazio and Han (2018) for a detailed treatment of the soil resistance modeling, including through-depth selection of soil resistance parameters.

F.5.4. Contact Between Barge Model and I-Wall Model.

F.5.4.1. To quantify barge impact loads on the I-wall, the barge model (see Chapter 3) is merged together with the floodwall FE model. Contact detection is defined between the deformable bow of the barge and the impacted surface of the floodwall. Solid element erosion at failure is activated for the concrete elements representing the floodwall.

F.5.4.2. Static and dynamic coefficients of friction of 0.50 and 0.45, respectively, are assigned to the barge-to-floodwall monolith (i.e., steel-to-concrete) contact interfaces. Additional contact detection is defined between the deformable barge bow and the beam elements representing the steel reinforcing bars. Static and dynamic coefficients of friction of 0.55 and 0.45, respectively, are assigned to the barge-to-rebar (i.e., steel-to-steel) contact interfaces.

F.6. Riverine R/C Sheet Pile I-Wall Damage Case Studies.

F.6.1. Overview. To characterize damage phenomena under barge impact loading, barge and coastal R/C I-wall FE models are utilized in impact simulations. Hydrostatic pressure is considered and is applied to the wall before applying barge impact loads. The dynamic peak EOH force (defined above in section F.4) is utilized to distinguish impact load from hydrodynamic load. EOH loads are quantified along with wall responses (e.g., extent of damage). Typical failure modes found to occur in I-walls under normal (perpendicular) loading are local flexural failure and global flexural failure.

F.6.1.1. Complementary static analyses are conducted to quantify the static EOH force. Also, damage modes obtained from dynamic and static simulations are compared. Results demonstrate that static wall capacities are conservative relative to those computed from dynamic analysis. Therefore, comparing statically computed wall capacities to dynamically computed peak impact loads constitutes a conservative design approach.

F.6.1.2. I-Wall Configurations Considered. To consider variations of floodwall configuration (e.g., length of monolith) and interaction conditions between adjacent monoliths, two distinct floodwall configurations are investigated. The two configurations are divided into case studies referred to as case study I and case study II. In case study I, three 21-ft-long floodwall monoliths are separated by gaps (0.25 in.). As a result, the concrete monoliths respond semi-independently to barge impact load. Recall that individual concrete monoliths are still connected by continuous sheet piling. In case study II, a continuous concrete floodwall with a 63-ft length (i.e., the length of three integrally joined 21-ft monoliths) is investigated.

F.6.2. Modeling Assumptions.

F.6.2.1. Barges striking near the top of a floodwall have the potential to generate maximum loads during flood stage conditions. In the FE models, the top elevation of the barge headlog is aligned with the top elevation of the floodwall (Figure F.24). A fully loaded hopper barge drafts at a depth such that the water surface is approximately 4 ft below the top elevation of the barge headlog. Correspondingly, hydrostatic loading is applied to each wall model starting at an elevation 4 ft below the top of the wall.

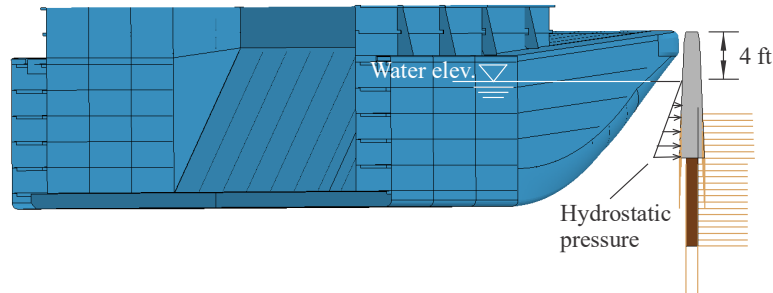


Figure F.24. Vertical Impact Location at Top of Floodwall and Hydrostatic Pressure Distribution

F.6.2.2. For the longitudinal (along-wall) impact location, a representative location at mid-length of the monolith is selected (Figure F.25). Simulated barge impact speeds include a baseline speed (5 ft/sec). Also, a lower level speed of 3.0 ft/sec and an upper level speed of 7.0 ft/sec are considered. For all cases investigated, hydrostatic pressure is applied to the wall before conducting barge impact simulations or imposing quasi-static loading. In each impact case, a fully loaded jumbo hopper barge weighing 2,000 short tons is modeled. A summary of key modeling assumptions includes:

F.6.2.2.1. Lengths of floodwall monolith/wall: 21 ft and 63 ft;

F.6.2.2.2. Impact location: at mid-length of wall;

F.6.2.2.3. Impact angles: 15°, 30°, and 45°;

F.6.2.2.4. Impact speeds: 3 ft/sec, 5 ft/sec, and 7 ft/sec;

F.6.2.2.5. Weight of impacting barge: 2,000 short tons (i.e., fully loaded jumbo hopper barge).

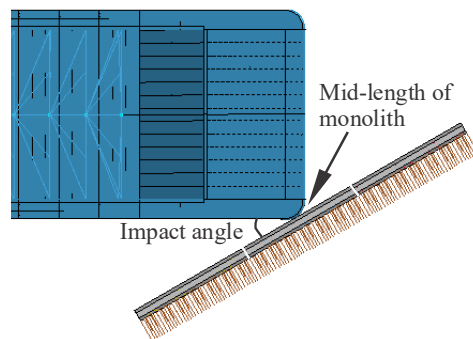


Figure F.25. Longitudinal Impact Location at Mid-Length of Monolith

F.6.3. Case Study I: Three Floodwall Monoliths (Semi-Independent Response). An impact simulation is conducted using a single barge model impacting the floodwall model. Each monolith is separated by 0.25-in. gaps so as to bring about semi-independent response (Figure F.26). An impact angle of 30° and impact speed of 5 ft/sec are assigned to the barge. See Consolazio and Han (2018) for additional details.

F.6.3.1. A quasi-static pushover simulation is also conducted. Displacements are slowly (quasi-statically) applied to the wall model (Figure F.27) by applying prescribed velocity to a rigid block, which remains in contact with the wall. The block is modeled with an area that approximates the contact area of the barge headlog during the dynamic impact simulations. Considerations are made to ensure that the wall response remains approximately static in nature. The prescribed velocity applied to the block is selected to be 20 times slower than the mean wall velocity obtained from dynamic simulation ($\bar{v}_{wall} \div 20$ in Figure F.27).

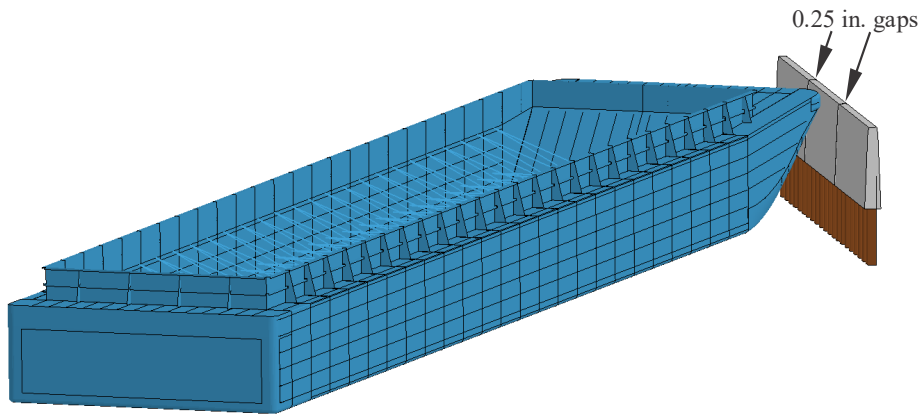


Figure F.26. Model of 30° Barge Impact at 5 ft/sec on Riverine R/C+SP I-Wall with Three Monoliths

F.6.3.2. Contact detection between the rigid block and wall surface is defined so that force applied by the block to the wall can be quantified. Since hydrostatic load is present during the simulation, the contact force computed from the simulation is EOH. That is, the EOH force is computed so as to facilitate comparisons to the dynamic barge impact results.

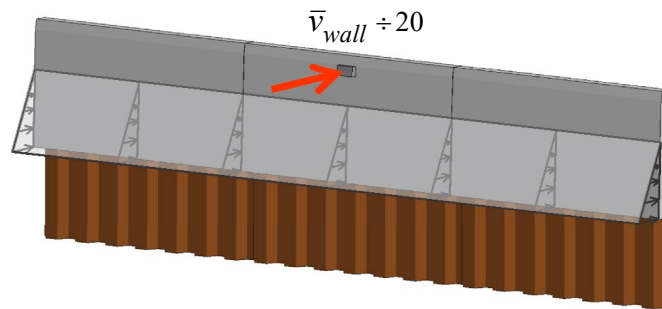


Figure F.27. Quasi-Static Simulation of Riverine R/C+SP I-Wall with Three Monoliths

F.6.3.3. In Figure F.28, a visual comparison is provided of damage from dynamic barge impact simulation and from quasi-static simulation. The damage states shown are those associated with the corresponding peak EOH forces for each case and are qualitatively similar. Of note, the static wall resistance forces (Figure F.29) never exceed the dynamic values. As such, statically computed capacity (maximum resistance force) is shown to be conservative (i.e., smaller than the dynamically computed resistance). See Consolazio and Han (2018) for additional comparisons.

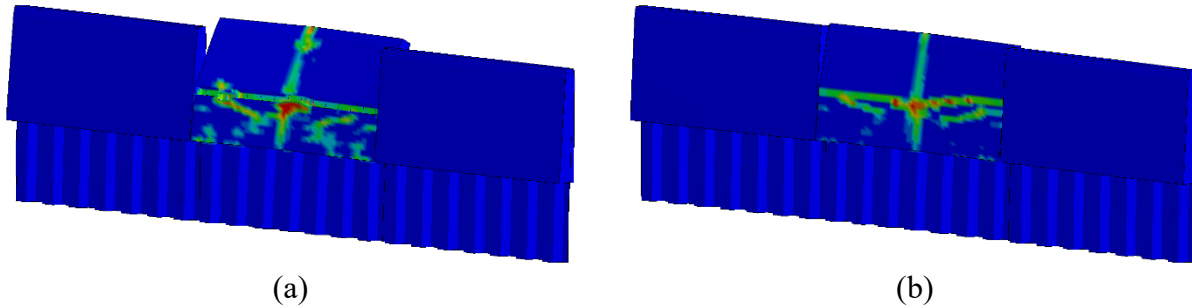


Figure F.28. Damage States Associated with Dynamic and Static Peak EOH Forces (Displacement Scale Factor = 20): (a) Barge Impact; (b) Quasi-Static

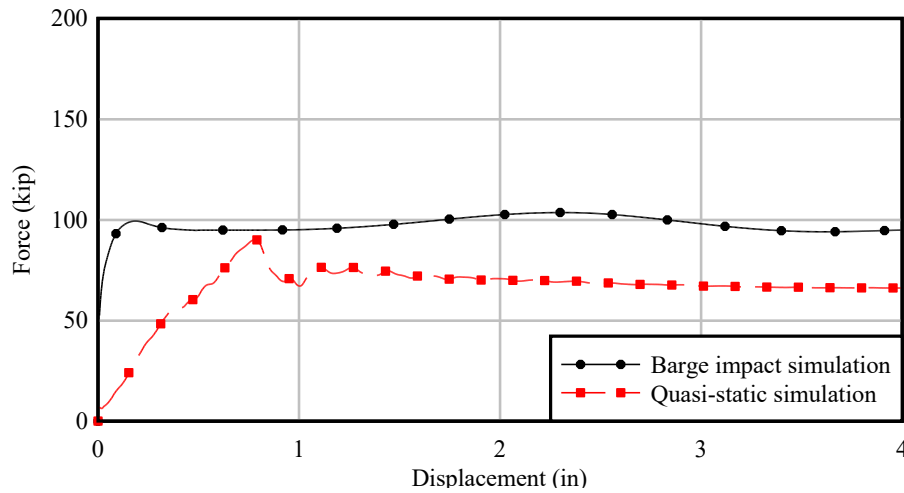


Figure F.29. Comparison of Wall Resistance Forces from Barge Impact Simulation and Quasi-Static Pushover Simulation

F.6.4. Case Study II: Continuous Floodwall. An impact simulation (Figure F.30) is conducted between a continuous I-wall and a single barge model. The barge impacts the wall at 30°, with an impact speed of 5 ft/sec. A quasi-static pushover simulation is conducted (Figure F.31). Here, displacements are slowly applied to the wall model by applying prescribed velocity to a rigid block. Considerations are made to ensure that the wall response remains approximately static in nature. The prescribed velocity applied to the block is selected to be 20 times slower than the mean wall velocity obtained from dynamic simulation ($\bar{v}_{wall} \div 20$ in Figure F.31).

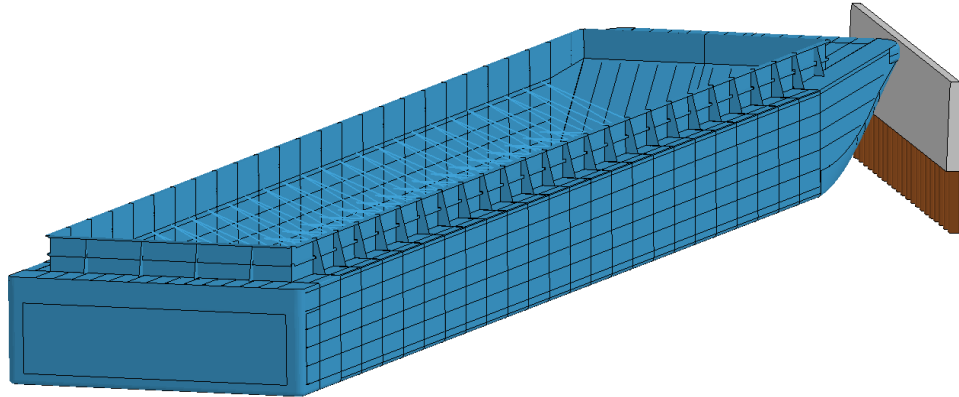


Figure F.30. Model of 30° Barge Impact at 5 ft/sec on Continuous Riverine R/C+SP I-Wall

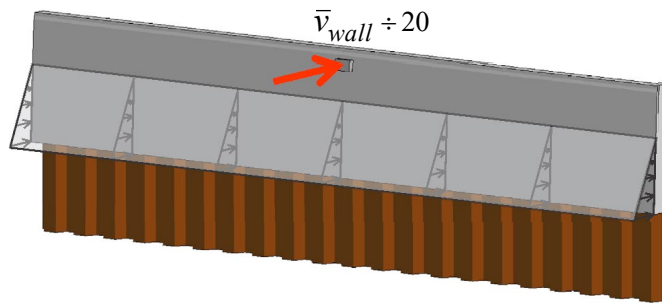


Figure F.31. Quasi-Static Simulation of Continuous Riverine R/C+SP I-Wall

F.6.4.1. An additional simulation is conducted to determine whether observed differences in dynamic and static damage patterns are attributable to load rate. In particular, a simplified fast rate dynamic pushover simulation is conducted (Figure F.32). A prescribed velocity is again imposed on a rigid block that remains in contact with the wall throughout the simulation. However, to incorporate dynamic (inertial) effects, prescribed velocity is set equal to the mean wall velocity (\bar{v}_{wall}) associated with the dynamic impact simulation.

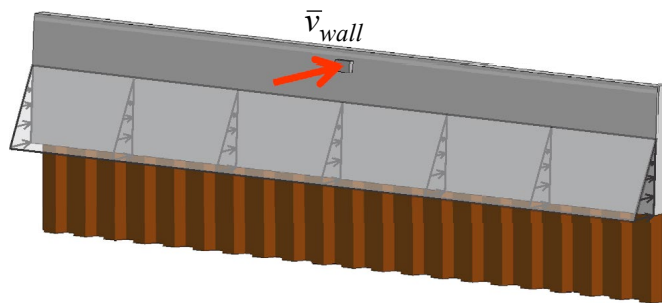


Figure F.32. Dynamic Pushover Simulation of Continuous Riverine R/C+SP I-Wall

F.6.4.2. In Figure F.33, damage index plots are shown for the dynamic barge impact simulation, dynamic pushover simulation, and quasi-static pushover simulation. In contrast to the three-monolith I-wall configuration described above, the continuous wall consistently exhibits a much more distributed pattern of damage. In addition, for the continuous wall, localized flexural failure occurs near the impact location. Damage states shown are associated with the corresponding peak EOH forces.

F.6.4.3. Under dynamic loading on the continuous wall, the patterns of wall damage are relatively more distributed than in the static case. In the static case, damage tends to be concentrated in a relatively small number of flexural failure bands. As before, the static wall resistance forces (Figure F.34) never exceed the dynamic barge impact simulation values. As such, statically computed capacity is shown to be conservative (i.e., smaller than the dynamically computed resistance). See Consolazio and Han (2018) for additional details.

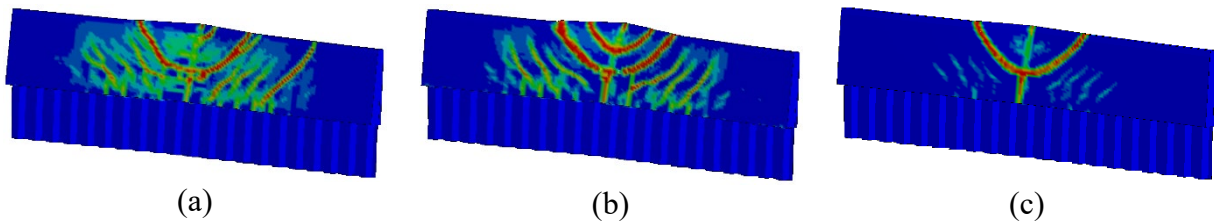


Figure F.33. Damage States Associated with Dynamic and Static Peak EOH Forces (Displacement Scale Factor = 20; Footing Not Shown):
 (a) Barge Impact; (b) Dynamic Pushover; (c) Quasi-Static

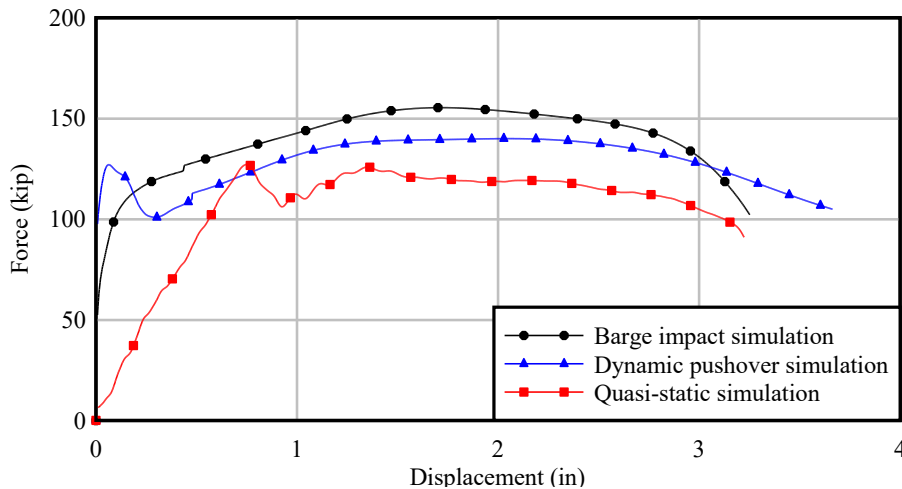


Figure F.34. Comparison of Wall Resistance Forces from Barge Impact Simulation, Dynamic Pushover Simulation, and Quasi-Static Pushover Simulation

Appendix G

Hurricane and Storm Damage Risk Reduction Systems

G.1. General.

G.1.1. This appendix presents a framework for probabilistic barge impact analysis (PBIA) and is not considered guidance but shows the application how to develop guidelines for critical structures subjected to hurricane and mesoscale wind environments. The framework incorporates findings from previous forensic, experimental, and numerical modeling investigations. This appendix also documents the application of the PBIA framework in forming recommendations for barge impact forces on hurricane floodwalls. In particular, recommendations are made for design-level impact forces on Hurricane and Storm Damage Risk Reduction Systems (HSDRRS) located throughout New Orleans, Louisiana. Specific to Appendix G are impacts between single barges driven by hurricane conditions, such as extreme winds and floodwalls.

G.1.2. Included here are brief reviews of structural configurations and FE models of two representative types of floodwalls located throughout New Orleans. See Chapter 3 for details pertaining to modeling of impacting barges. This appendix also provides the components of the PBIA framework. Subsequently, the framework is utilized to probabilistically assess barge impact loads on floodwalls in a hurricane environment. Outcomes of the assessment include recommended load magnitudes and wall overstress factors for usual, unusual, and extreme conditions.

G.1.3. Scope. The material in this appendix has been organized into the following sections:

G.1.3.1. Section G.2 documents the structural configurations for two representative types of hurricane floodwalls.

G.1.3.2. Section G.3 provides FE model details for the two types of floodwalls.

G.1.3.3. Section G.4 discusses an overview of the PBIA framework, as well as details regarding each major framework component.

G.1.3.4. Section G.5 then carries out the application of the PBIA, with focus on wind-driven impacts between single barges and two representative floodwall FE models.

G.1.3.5. Section G.6 provides recommendations for the design of HSDRRS systems, including design forces, overstress factors, and associated return periods.

G.2. Characterization of Representative Floodwall Structural Configurations and Lateral Load Responses.

G.2.1. Overview. Hurricane events such as Hurricane Katrina (2005) led to scenarios where wind-driven barges impacted floodwall structures shown in Figure G.1. Such impacts

contributed, in part, to widespread damage (via flooding) to the city of New Orleans. Investigation of the probability of floodwall failure due to barge impact is therefore necessary. Such investigation necessitates identification of typical section profiles from among common floodwall configurations. With focus on HSDRRS infrastructure prevalent throughout New Orleans, two types of floodwalls were identified in Davidson et al. (2020).

G.2.1.1. In New Orleans, floodwalls are generally associated with either the Task Force Hope Hurricane Protection Office (HPO), or the USACE New Orleans District (MVN) Protection and Restoration Office (PRO). Accordingly, two structural configurations are selected for investigation (and discussed later) to reflect the majority of hurricane protection floodwalls in New Orleans.



(a)



(b)

Figure G.1. Aberrant Barge Impacts on New Orleans Area Floodwalls During Hurricane Katrina: (a) Bow-Wall Collision; (b) Bow-Wall Collision with Extensive Wall Damage

G.2.1.2. Finite element (FE) models of the selected sections are subsequently developed for conducting pushover analyses using structural analysis software (STAAD.Pro). A consistent set of FE models is also developed for simulation using FB-MultiPier and LS-DYNA. These models are used to simulate wide-ranging dynamic barge impact scenarios, as detailed in Getter et al. (2015). For all analyses documented in the following, hydrostatic loads are applied to each wall type (HPO and PRO) that are representative of storm event conditions.

G.2.1.3. Identification of typical floodwall sections and associated lateral load analyses serve several purposes. First, representative estimates are established for lateral load capacities of impacted floodwalls. Next, required data are provided for empirically estimating maximum loads for a wide range of impact scenarios (discussed later). Finally, comparisons are facilitated between the demands that arise due to impact loads and corresponding floodwall resistance.

G.2.2. HPO Configuration. The HPO structural configuration is selected from a 20-mi length of T-walls, positioned along the Lake Pontchartrain and Vicinity (LPV-145) Reach in St. Bernard Parish (i.e., in the eastern portions of New Orleans). The selected configuration is shown in Figure G.2. This configuration is representative of floodwalls with top elevations that vary from 28.9 ft up to 32.1 ft. Footing bottom elevations range from 17.1 ft to 17.5 ft.

G.2.2.1. The reinforced concrete (R/C) structure has an 11-ft stem height, a 14-ft footing width, and a 50 ft length. Compressive strength of the concrete, f'_c , is 4 ksi. The T-wall configuration is supported by three rows of steel h-piles (24 total HP 14x73 piles with yield strength, F_y , of 36 ksi). Accounting for 2:1 batter, the piles extend 92.5 ft away from the footing bottom. Representative soil profile and boring data are detailed in Getter et al. (2015) and Consolazio et al. (2010).

G.2.2.2. Loads applied to the HPO floodwall for purposes of conducting pushover analysis include self-weight, buoyancy, and lateral load. The lateral load is incrementally increased in magnitude and is applied at the top of the wall. Lateral load is distributed over a 2-ft wide by 2-ft tall area at the monolith center shown in Figure G.2b. Hydrostatic pressure load is associated with the 100-year water surface elevation, and extends to the wall top, 8.4 ft above the still water level (SWL) elevation.

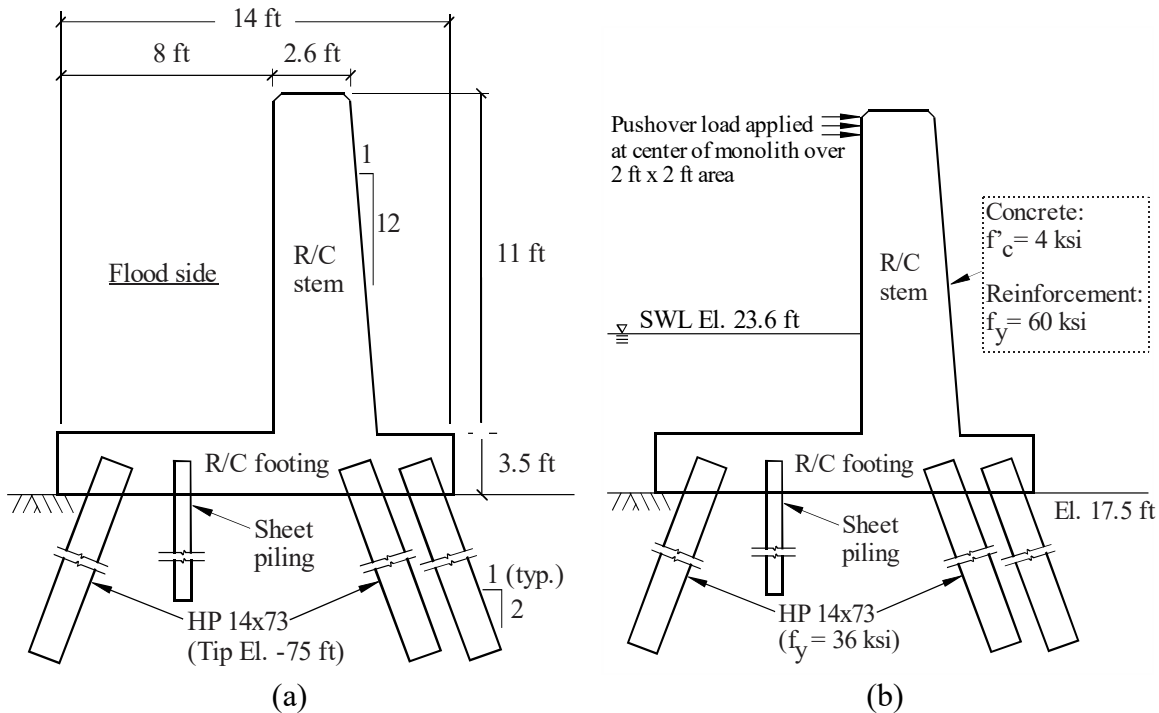


Figure G.2. Typical HPO Floodwall Configuration: (a) Members and Dimensions; (b) Constitutive Properties and Pushover Loading

G.2.3. PRO Configuration. PRO floodwalls located throughout New Orleans are categorized herein as being T-walls positioned atop earthen levees. The selected structural configuration corresponds to PRO projects distributed throughout south-central portions of New Orleans. Specifically, the floodwall shown in Figure G.3, is selected from along the West Bank and Vicinity (WBV-4.2) Belle Chasse Highway to Hero Canal project. This location is on the west side of Algiers Canal in New Orleans (Davidson et al., 2020 provide additional details).

G.2.3.1. The configuration in Figure G.3a is representative of R/C (f'_c of 4 ksi) T-walls with top elevations from 8.5 ft to 14 ft. Corresponding stem heights range between 3.9 ft to 4.9 ft. The footing is 9 ft wide and 27 ft long and is founded on two rows of 14-in. square prestressed concrete piles. All piles (6 per row, each with f'_c of 5 ksi) are battered (2:1) and tipped at an elevation of -50 ft. See Getter et al. (2015) and Consolazio et al. (2010) for detailed treatments of soil profile and boring data.

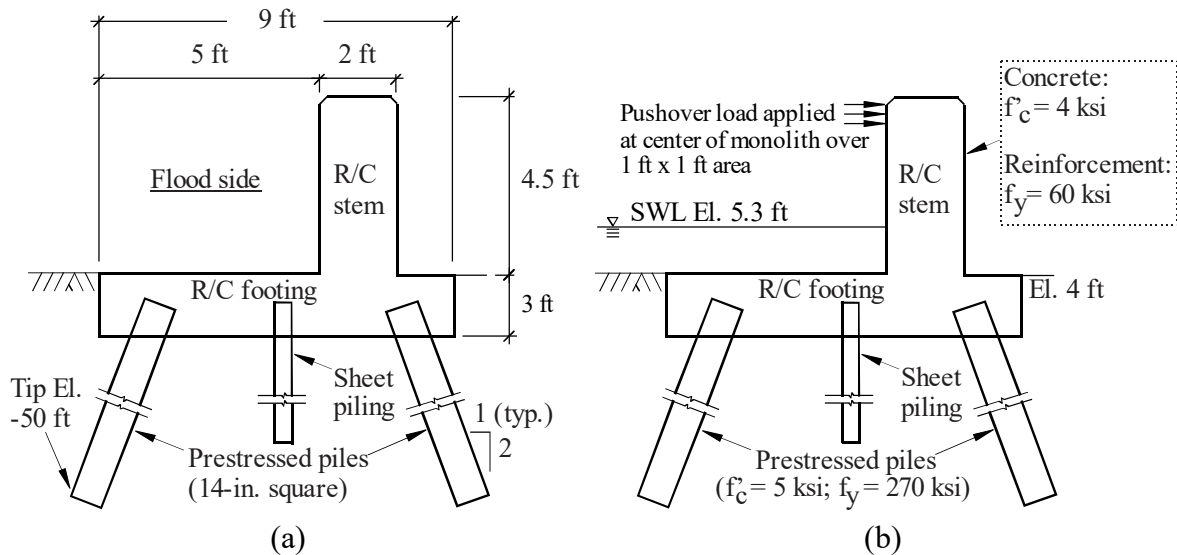


Figure G.3. Typical PRO Floodwall Configuration: (a) Members and Dimensions; (b) Constitutive Properties and Pushover Loading

G.2.3.2. Lateral load is incrementally increased on the PRO floodwall in Figure G.3b model. Load is distributed over a 1-ft by 1-ft area, positioned concentrically (lengthwise) at the wall top. This smaller distribution area (compared to that of the HPO wall) is selected given the relatively short wall stem height. The PRO wall geometry would permit only limited portions of a barge bow to make contact with the wall stem. Self-weight, buoyancy, and hydrostatic loads are applied simultaneously with lateral load. Hydrostatic load is associated with water at the top of the wall (3.2 ft above the SWL elevation).

G.3. Finite Element Modeling of HPO and PRO Floodwalls.

G.3.1. Overview.

G.3.1.1. Delineations of element types making up the HPO and PRO floodwall FE models are given in Figure G.4. Forensic analysis following Hurricane Katrina (2005) indicated that catastrophic wall failures (global collapse) occurred primarily due to inadequate soil resistance, not structural failure (Bae 2008). Therefore, floodwall structural members (wall stems, footings, and piles) are modeled as linear elastic, while nonlinearity is incorporated into the modeling of soil resistance.

G.3.1.2. Floodwall R/C footings and wall stems are modeled primarily using shell elements. However, the topmost portions of the wall stems are modeled with solid elements. Solid elements are better able to represent the physical contact geometry in barge impact simulations (see Getter et al., 2015). For all analyses, piles (with pinned-head fixity) are modeled using frame elements. Soil resistance is modeled using distributed nonlinear springs spaced vertically at 4-ft vertical intervals. Empirical force-deformation relationships assigned to lateral (p - y), skin friction (t - z), and compression-only end bearing (q - z) springs are detailed in Consolazio et al. (2010).

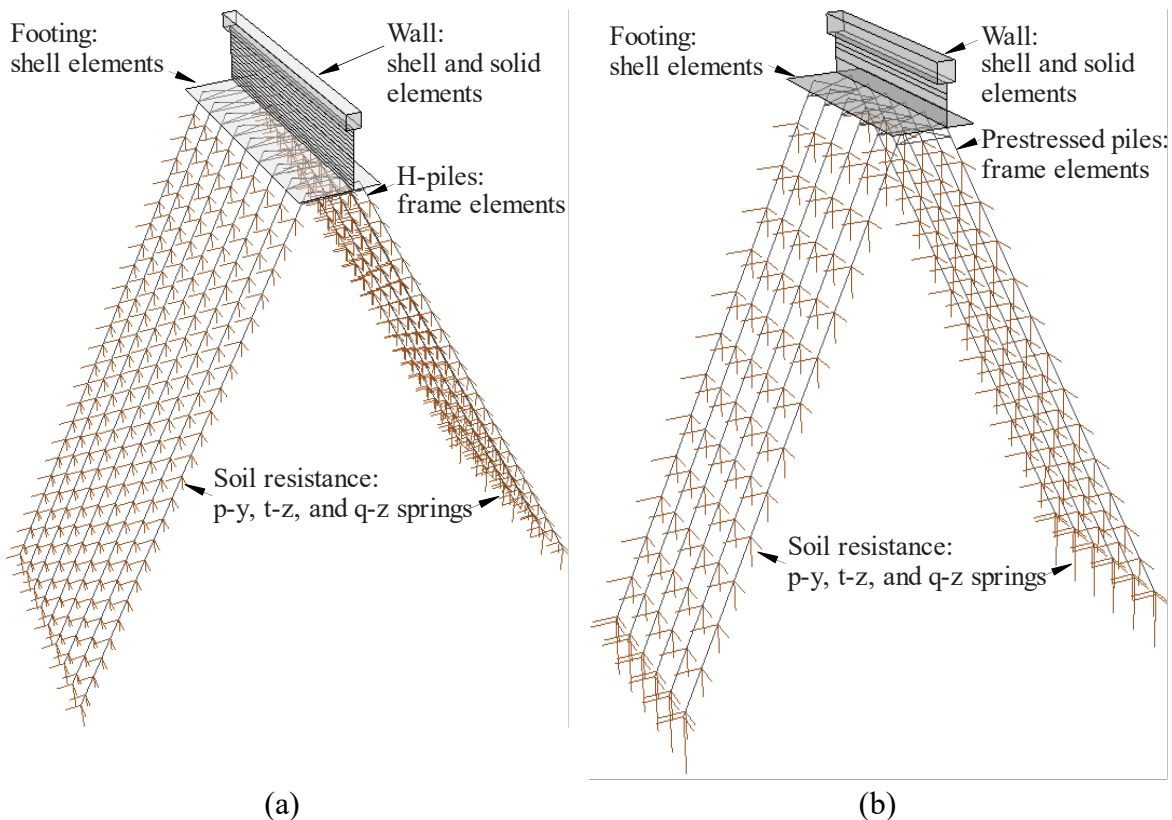


Figure G.4. Finite Element Models of Floodwalls (Not to Relative Scale): (a) HPO; (b) PRO

G.3.2. Lateral Load Responses of HPO and PRO Floodwalls. Using the STAAD.Pro software package, pushover analyses are performed on HPO and PRO floodwall FE models. Such analyses provide estimates of ultimate lateral load capacities for representative floodwall configurations. Lateral loads that produce floodwall damage are considered to be of secondary importance relative to those associated with floodwall collapse.

G.3.2.1. In this context, floodwall damage is defined as localized (non-catastrophic) failure near the immediate area of applied lateral load. Floodwall collapse is defined as widespread, permanent displacement along the wall monolith (e.g., wall overturning). Emphasis is placed on identifying lateral loads that cause complete loss of floodwall function (leading to uncontrolled release of water).

G.3.2.2. Collapse Limit States Due to Impact Loading. Table G.1 lists and Figure G.5 plots excerpted results from the pushover analyses. Results include lateral loads applied to the HPO (Figure G.2b) and PRO (Figure G.3b) FE models, and horizontal displacements at top-center wall locations. Also listed are corresponding limit states. These consist of: pile bearing (i.e., plunging), pile pullout in tension, and development of ultimate internal moment at the base of the wall stem.

Table G.1
HPO and PRO Floodwall Limit States, Pushover Loads, and Horizontal Deflections

Limit state	HPO		PRO	
	Load (kip)	Horizontal deflection (in.)	Load (kip)	Horizontal deflection (in.)
Pile plunging	920	1.2	305	1.29
Pile pullout	1070	1.8	420	1.75
Stem moment capacity	3122	5.3	249	1.07

G.3.2.2.1. Given the relatively soft underlying soil, all piles in a row reach the plunging limit state at approximately the same lateral load. A similar phenomenon is observed with regards to pile pullout. Accordingly, the plunging and pullout limit states align with that of a catastrophic collapse condition.

G.3.2.2.2. In contrast, maximum section moments at the wall stem bases are found to develop in relatively localized regions. Such regions would be located, for example, beneath the lateral load application areas indicated in Figure G.2b and Figure G.3b. It is assumed that localization of this type is aligned with a damage (as opposed to collapse) limit state. As such, additional capacity of the stem-footing interface would remain available through load redistribution under increased lateral loading.

G.3.2.2.3. The controlling failure mechanism for both the HPO and PRO floodwalls is attributed to pile plunging. Corresponding lateral loads are 920 kip and 305 kip, respectively. Due to simultaneity of plunging across the affected pile rows, widespread permanent displacements (Figure G.5) are computed. Such displacements are attributed to the onset of pile plunging (approximately 1.3 in. for both the HPO and PRO floodwalls). Lateral loads that cause pile plunging are therefore considered, as discussed later, in formulating design guideline recommendations.

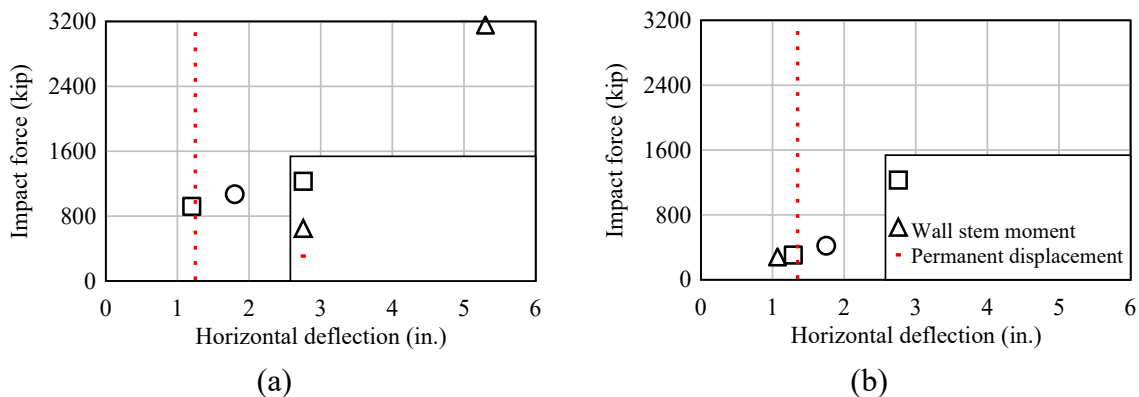


Figure G.5. Pushover Analysis Loads and Deflections Corresponding to Floodwall Limit States: (a) HPO; (b) PRO

G.4. Probabilistic Barge Impact Analysis. Primary outcomes of the floodwall investigations are recommended HSDRRS design guidelines for load cases, load magnitudes, and overstress factors. These recommendations apply to floodwalls impacted by aberrant barges in a hurricane environment. Recommended design impact loads are primarily based on the PBIA (originally proposed in Patev 2000). PBIA employs a Monte Carlo probabilistic simulation approach for accumulating cumulative distribution functions (CDFs) of aberrant barge impact force. CDFs of impact force allow direct estimation of probability of exceedance when deciding on recommended design loads.

G.4.1. Overview.

G.4.1.1. The PBIA framework (Figure G.6) utilizes a multi-step process for sampling values of barge impact velocity. A CDF of sustained wind speed is sampled from and then empirically related to resulting barge velocity. Next, barge orientation parameters are sampled: barge-floodwall impact angle, and initial barge impact location (bow or stern). Together, the sampled values of barge impact velocity, angle, and initial impact location constitute one realization of an impact scenario.

G.4.1.2. For each realization, the sampled values (velocity, orientation, location) are empirically related to a single maximum barge impact force. HPO and PRO floodwalls are each treated separately. The probabilistically determined impact force is then cataloged. This process is repeated many times to form a CDF of impact force. Thereafter, the CDF can be used in relating impact force to return period. Individual components of the PBIA framework are presented below.

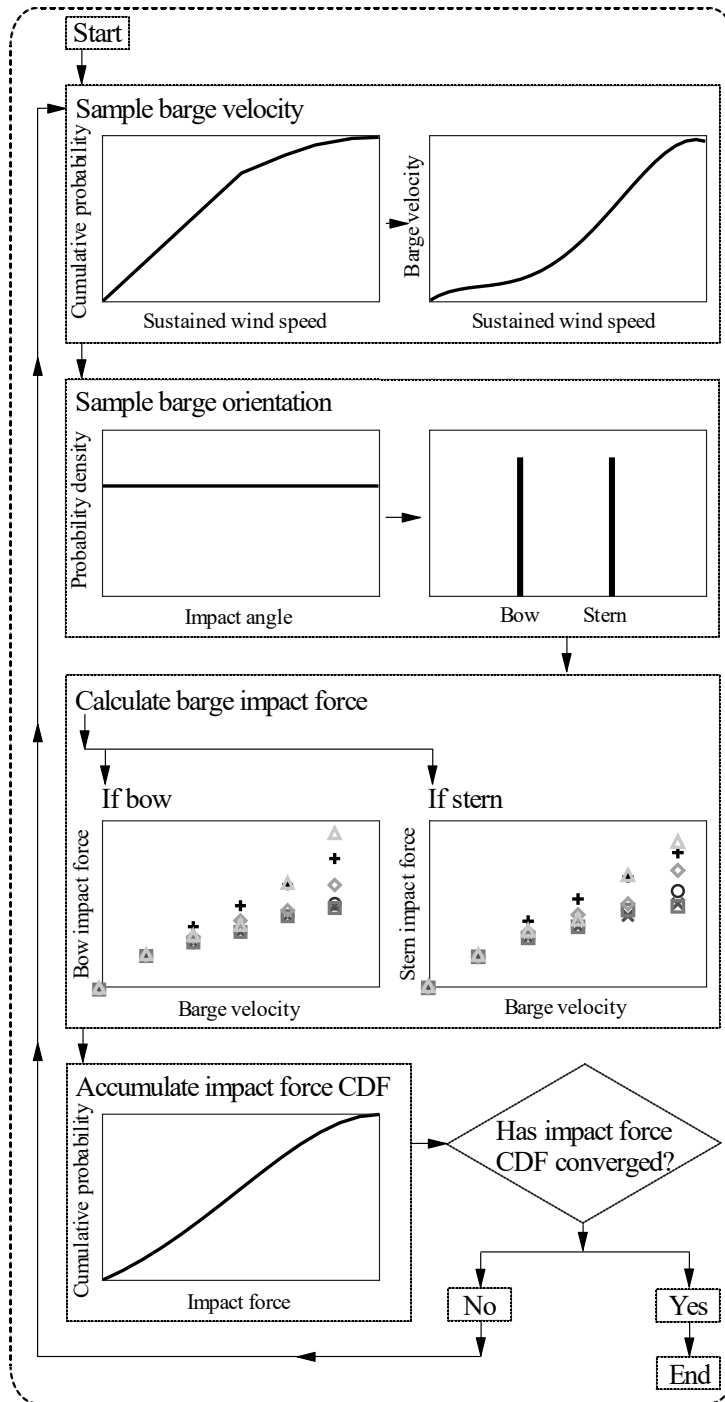


Figure G.6. Probabilistic Barge Impact Analysis (PBIA) of Hurricane Floodwalls

G.4.2. Impact Velocity. The probabilistic approach for sampling impact velocities (Figure G.7a) is formed using a database of sustained hurricane wind speeds and return periods. The HURISK database (originally developed by NOAA 1987) is drawn on to pair sustained wind speeds and return periods. Specifically, sustained 1-minute duration wind speeds are paired with “on average” return periods. The data utilized correspond to hurricane intensities (or categories) that could be expected within 85 mi of New Orleans.

G.4.2.1. It is assumed that short-duration (e.g., 3 sec) wind gusts are not able to appreciably propel empty open-hopper barges. Even when empty, such barges are partially submerged and possess bare steel (empty) weights of 285 tons. Since short duration gusts are assumed to not affect barge speed, only sustained wind speeds are utilized. A sustained wind speed CDF (Figure G.7a) therefore serves as the primary forcing function for obtaining barge impact velocities (Figure G.7b).

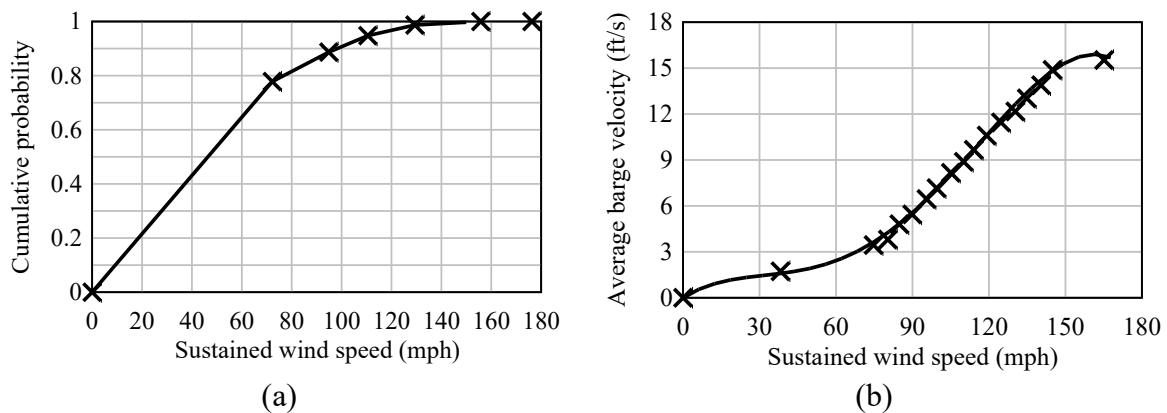


Figure G.7. Probabilistic Determination of Aberrant Barge Velocity: (a) CDF of Sustained Hurricane Wind Speed; (b) Average Barge Velocity versus Sustained Wind Speed

G.4.2.2. Sustained Wind Speed Versus Aberrant Barge Velocity. An investigation by Patev et al. (2010) of sustained wind speed versus aberrant barge velocity is summarized here. Reduced scale (1:25) experiments and multiple-scale computational fluid dynamics (CFD) simulations were carried out on model barges. Over a wide range of conditions, the barge models were positioned in close proximity to floodwalls.

G.4.2.2.1. A total of 378 physical tests were conducted in the Coastal Engineering Basin at the United States Naval Academy in Annapolis, Maryland. Test parameters varied with respect to wind, water, and barge orientation. Variations of wind included: none, sustained and uniform, sustained but non-uniform. Variations of water included: depth, calmness, uniform waves, and non-uniform waves. Variations of barge orientation included: varying relative angles between barge and wall (parallel through perpendicular).

G.4.2.2.2. To model a levee floodwall, a stiffened panel was rigidly mounted in the coastal basin. The levee floodwall was oriented perpendicular to both the basin floor and the wave maker. It was not feasible to model the changes in base elevation approaching the levee. A photograph of the stiffened wall, as arranged in the coastal basin, is presented in Figure G.8. Barge motions were measured using overhead video, a barge-mounted accelerometer, and an ultrasonic distance sensor.

G.4.2.2.3. Additional data were gathered using wave gauges mounted close to the wall, and a single force gauge mounted on the wall (Figure G.9). For each test, barge velocity was measured just prior to floodwall impact and paired with the sustained wind speed. Despite the comprehensive nature of the experiments, practical limitations precluded tests of wind speeds in excess of 80 mph. Similarly precluded were non-uniform base elevations near the floodwall and wave crests parallel to the floodwall.



Figure G.8. Experimental Levee Floodwall, Shown with Wave Gauges and Force Gauge in Place and 1-ft by 1-ft Grid on Floor of Coastal Basin



Figure G.9. Barge Model Resting Broadside Against Model Levee Floodwall, and Weight Pan for Constant Force Pulling

G.4.2.2.4. A concurrent numerical study was conducted (see Patev et al., 2010) to overcome the practical limitations encountered during physical testing. The numerical study was also utilized to quantify total impedance of water (added mass, radiation damping, and viscous damping). Initial CFD simulations were conducted at model scale (1:25) and compared to experimental measurements to validate the numerical modeling approach. Subsequently, CFD simulations were carried out at full scale for Category I, III, and V hurricane wind speeds.

G.4.2.2.5. The full-scale simulations allowed for barge motions to be computed in response to variations of wind, waves, and currents. Results from the CFD simulations led to development of an empirical polynomial regression equation (recall Figure G.7b):

$$V_B = -1.37 \times 10^{-7} \cdot V_W^4 + 4.06 \times 10^{-5} \cdot V_W^3 - 3.04 \times 10^{-3} \cdot V_W^2 + 1.06 \times 10^{-1} \cdot V_W \quad (\text{G.1})$$

where V_B is the wind-driven barge velocity (ft/s) and V_W is the sustained wind velocity (mph). Regarding impedance characterization, a theoretical approach for predicting added mass was developed. The recommended approach indicated good agreement with experimental results (for the in-common test conditions associated with a Category I hurricane event).

G.4.3. Barge Orientation Relative to Wall. A uniform probability distribution function (PDF) is defined for sampling relative barge-floodwall orientation angles just prior to impact (Figure G.10a). Geographical Information System analysis of representative width navigable waterways throughout New Orleans is presented in Davidson et al. (2020). Results indicated that such waterways would not permit barge-floodwall orientation angles greater than approximately 75° (where 90° signifies head-on impact).

G.4.3.1. Further, it is assumed that perfectly side-on barge impacts (i.e., 0° angle) are extremely unlikely to occur. Consequently, 0° impacts are excluded from the PBI framework. Impact angles included in the uniform PDF thus range from 1° to 75° .

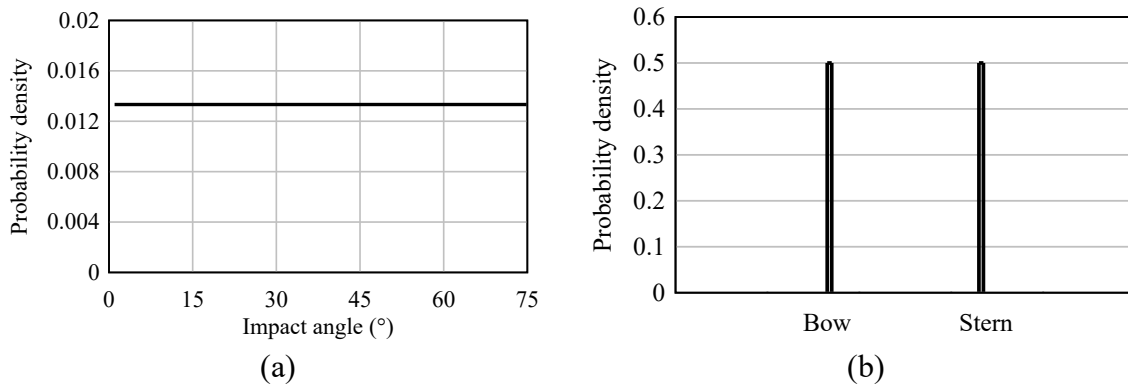


Figure G.10. Probabilistic Determination of Barge Impact Orientation: (a) PDF of Impact Angle; (b) Probability Mass Function (PMF) of Bow or Stern Impact

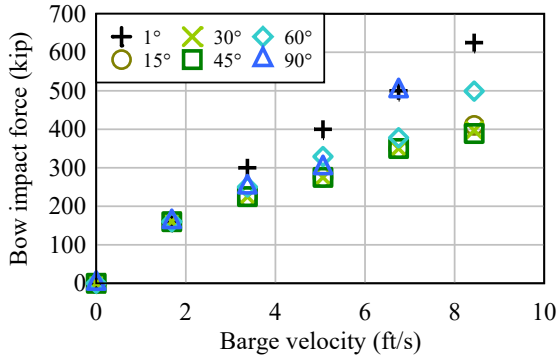
G.4.3.2. Determining whether a barge impacts a floodwall at either the bow or stern also requires consideration. It is assumed that the bow and stern barge-ends possess equal likelihood of making initial contact on impacted floodwalls. This assumption is reflected in the bow-stern PMF, Figure G.10b. Distinguishing bow impacts from stern impacts is necessary because impact forces differ for these two cases (Getter et al., 2015). The impact angle PDF (Figure G.10a) and the bow-stern PMF (Figure G.10b) are both incorporated into the barge orientation sampling process.

G.4.4. Aberrant Barge Impact Force. Empirical relationships are formed for relating sampled values of barge impact velocity and orientation to maximum impact force. Such relationships are formulated using both dynamic barge-wall impact simulations and results reported in the literature. In particular, two-parameter regression relationships (with independent variables of impact velocity and impact angle) are developed. The relationships are applicable to bow impacts and stern impacts on HPO (Figure G.11a–b) and PRO (Figure G.11c–d) floodwalls.

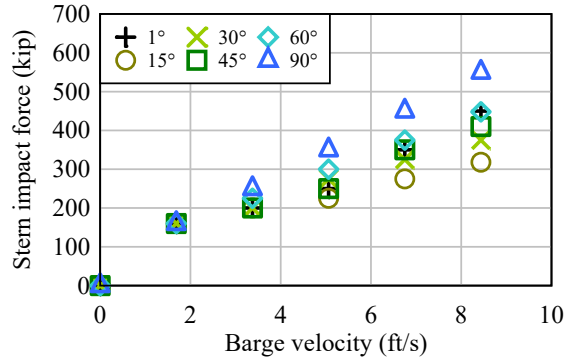
G.4.4.1. To compute peak impact forces, the HPO and PRO floodwall FE models are integrated together with single-barge FE models. Once integrated, dynamic contact-impact analyses are performed. In Figure G.12, an example integrated model for simulating impact between a barge and the PRO floodwall is shown. Integrated models incorporate contact definitions, frictional parameters, and buoyancy effects consistent with documentation provided in Chapter 3.

G.4.4.2. Barge stress and deformation results from a typical bow impact are shown in Figure G.13. It is noteworthy that even considering the small draft and shallow rake angle, the barge does not ride over the wall. Instead, a large indentation forms in the contact area, including some limited tearing of the corner hull plate. Yielding of the steel barge components is limited to an area within approximately 3.5 ft of the contact region. Similar results were observed for stern impacts (Consolazio et al., 2010), but with less damage to the barge.

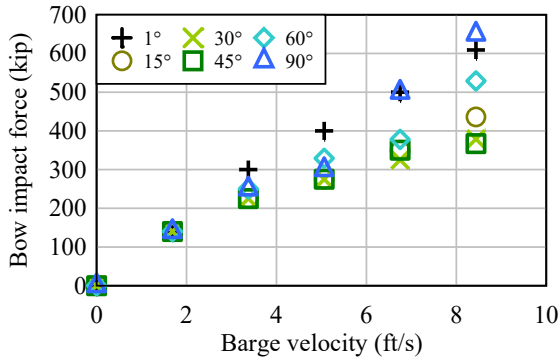
G.4.4.3. Forces plotted in Figure G.11 are bounded by the maximum reported in Getter et al., 2015, which is 625 kip. This value corresponds to a barge impact velocity (normal to wall) of 8.5 ft/s and impact angle of 1°. For sampled impact velocities and angles that do not fall on the values depicted in Figure G.11, interpolation is utilized. Forces obtained from Figure G.11 (as part of PBIA) are accumulated to form CDFs for both HPO and PRO floodwalls.



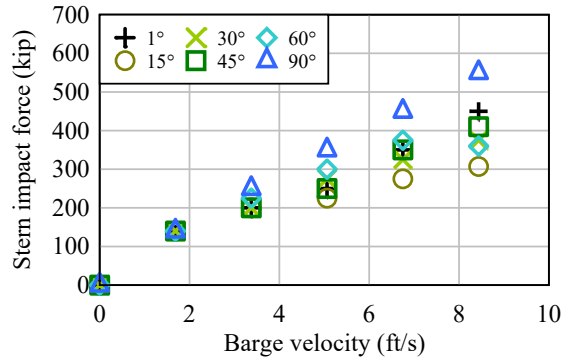
(a)



(b)



(c)



(d)

Figure G.11. Maximum Barge Impact Force Versus Velocity and Angle: (a) Bow-HPO Wall; (b) Stern-HPO Wall; (c) Bow-PRO Wall; (d) Stern-PRO Wall

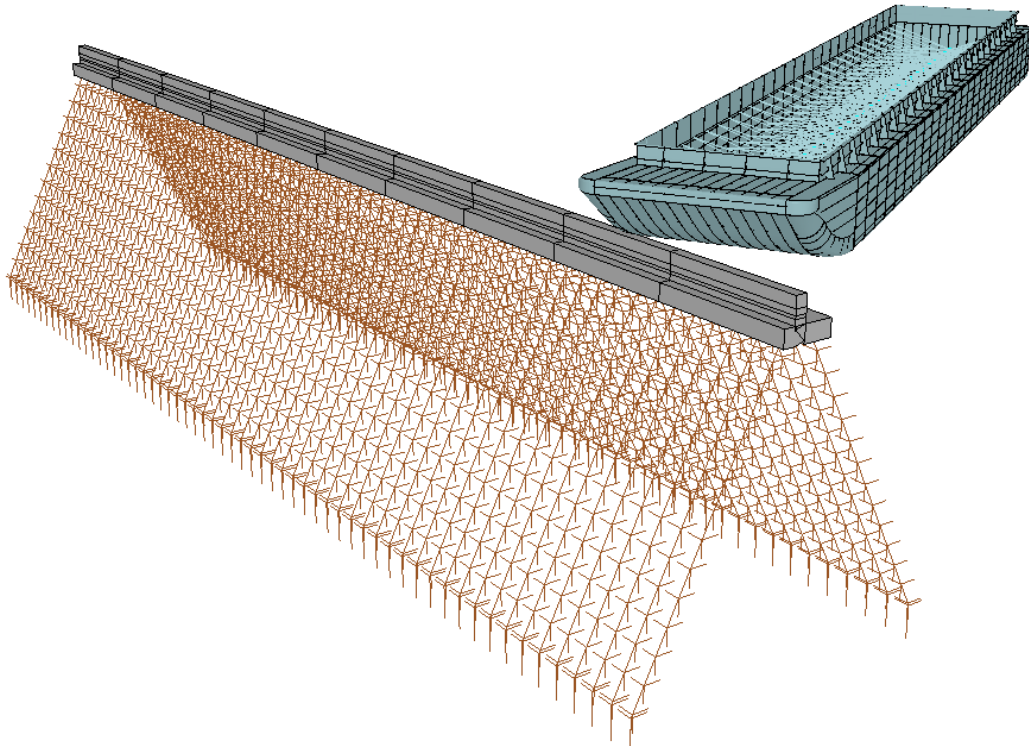


Figure G.12. Combined FE Model of Impacting Barge and PRO Wall

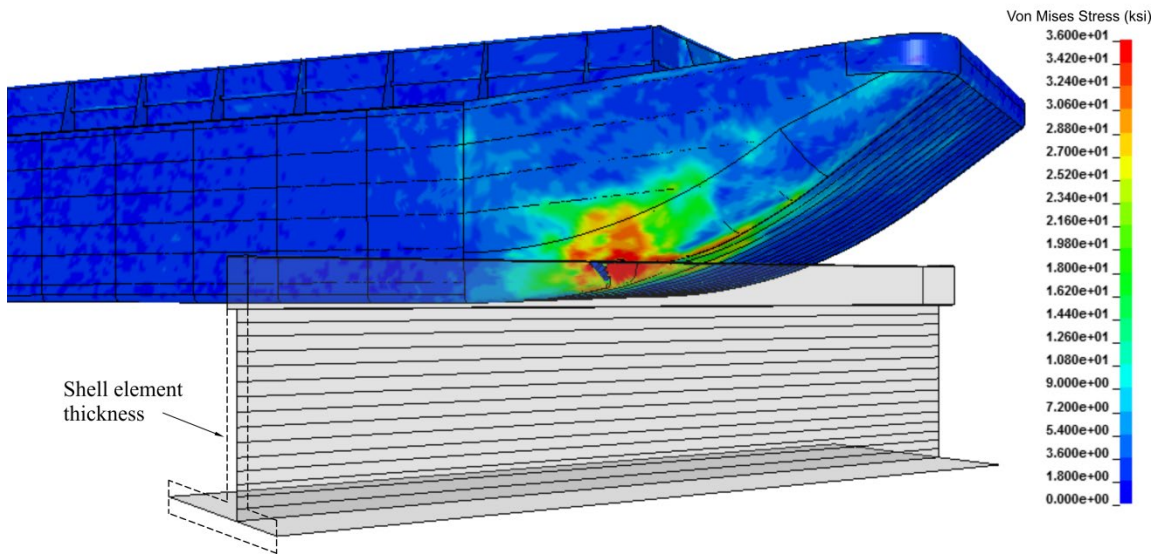


Figure G.13. Bow Impact on HPO Wall. Contour of Von Mises Stress (ksi) Showing Bow Deformation and Tearing of Outside Hull Plates

G.5. Application of Probabilistic Barge Impact Analysis to HPO and PRO Floodwalls. The PBIA framework is applied with respect to barge impacts on HPO and PRO floodwalls. Approximately 50,000 realizations (each) are required to reach convergence of the respective CDFs of maximum impact force. Nonetheless, 100,000 realizations are selected to preclude convergence issues. Impact force CDFs are combined with barge aberrancy rates to produce return periods as discussed below.

G.5.1. Probability of Hurricane-Induced Barge Aberrancy. Forensic analysis of the New Orleans barge inventory (Davidson et al., 2020) revealed a prevalence of empty open-hopper barges. The analysis also enabled the probability of hurricane-induced barge aberrancy to be estimated. High-resolution aerials of the area just prior to and immediately following the hurricane event were examined. Barges that were identified as having broken loose from moorings or offload facilities were cataloged as aberrant.

G.5.1.1. Barges were also categorized as aberrant if observed to reach locations where barges were previously not located. Aberrant barges were further divided into two sub-categories, as listed in Table G.2. Sub-categorization was based qualitatively on proximity (near, distant) to offload facilities and local raft mooring areas.

Table G.2
Barge Aberrancy Caused by Hurricane Katrina in 2005

Proximity to offload/local mooring facilities	Number of aberrant barges	Percentage of all New Orleans barges
Near	270	10.1%
Distant	68	2.5%
Total	338	12.7%

G.5.1.2. Of 338 aberrant barges identified via forensic analysis, 68 were categorized as distant from pre-hurricane mooring areas or offload facilities. Also, these 68 barges were generally observed to be located (post-hurricane) either on levees or against floodwalls. To estimate aberrancy, the total number of barges present prior to Hurricane Katrina (2,668) was compared to the number of aberrant distant barges (68). This yielded a probability of aberrancy of 2.5%. However, not all of the 68 aberrant barges were positioned against floodwalls. Therefore, the floor of the calculated aberrancy rate (2%) was utilized in developing return periods.

G.5.2. Return Periods of Aberrant Barge Impact Forces.

G.5.2.1. PBIA (recall Figure G.6) carries with it the premise that all statistical realizations are tantamount to imminent barge-floodwall impact. Return periods of impact force obtained under this unconditional premise are therefore combined with the probability of barge aberrancy (2%). This process yields conditional estimates of impact force return periods (Figure G.14).

G.5.2.2. For example, a 180-kip force on an HPO floodwall produces an unconditional annual probability of exceedance of 0.5 (Table G.3). This corresponds to an unconditional return period of approximately two years (Figure G.14a). In contrast, the conditional probability is 2% of the unconditional exceedance value, or $(0.02 \cdot 0.5) = 0.01$ (Table G.3). This produces a conditional return period of 100 years (Figure G.14a).

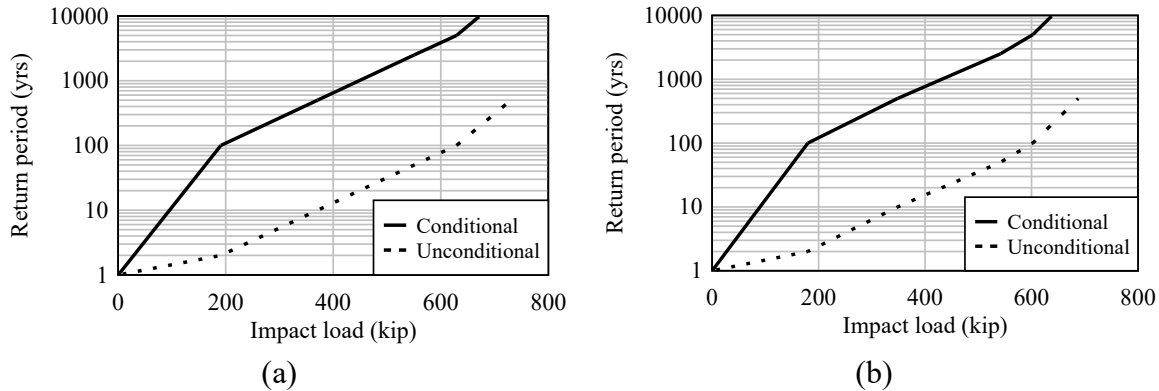


Figure G.14. Barge Impact Force Versus Return Period for Floodwalls: (a) HPO; (b) PRO

Table G.3
Barge Impact Force Versus Return Period for HPO and PRO Floodwalls

HPO load (kip)	PRO load (kip)	Unconditional probability	Conditional probability	Return period (yr)
0	0	0	0	0
190	180	0.5	0.01	100
370	349	0.1	0.002	500
550	543	0.02	0.0004	2,500
630	602	0.01	0.0002	5,000
730	687	0.002	0.00004	25,000

G.6. Recommendations for Floodwall Design. HSDRRS design guidelines, as specified in section 5.0 of USACE (2007), were developed without explicit consideration for aberrant barge impact loading. The guidelines presented here thus represent an update in several ways. Dedicated aberrant barge impact load cases, load magnitudes, and overstress factors are introduced. Acceptable probabilities (return periods) of impacted floodwall collapse are established. Consequently, the risks to population, property, infrastructure, and conservation areas of New Orleans are reduced.

G.6.1. Assumptions and Limitations.

G.6.1.1. Recommendations given below are formulated by characterizing loads that arise due to first-strike impacts of single, empty open-hopper barges. Such impacts are assumed to occur on HPO and PRO floodwalls and are driven by a hurricane environment.

Recommendations are derived from impact loads occurring at or near the center of floodwall monoliths. Primary emphasis is on collapse limit states (e.g., pile plunging) of the impacted floodwalls with secondary emphasis on damage limit states.

G.6.1.2. Recommended design loads, to which return periods are attributed, are based on aberrancy data collected from Hurricane Katrina, a Category 3 storm. For more or less intense hurricane events, aberrancy rates would be estimated to be greater or lesser in magnitude, respectively.

G.6.2. Load Cases and Magnitudes. Four candidate load cases are considered in the design guidelines. This approach is consistent with the load case listings and associated return periods defined in EC 1110-2-6066 (USACE 2011). The four cases consist of: usual, unusual, and extreme (I and II). Relative to forces that are probabilistically determined for HPO and PRO floodwalls, forces recommended for use in design are increased by 20% in Table G.4. This increase reflects uncertainties in physical testing, numerical modeling (including pushover analyses of typical configurations), and the PBIA framework.

G.6.2.1. The usual load case in Table G.4 connotes a return period of two years, commensurate with normal conditions (not hurricane conditions). Consequently, the usual load case is excluded from further consideration. The unusual load case is tied to the 100-year level of protection and is applicable to hurricane conditions. It is also typical of the return periods included in previous HSDRRS design provisions (USACE 2007).

G.6.2.2. The extreme load case is subdivided into extreme I and extreme II. This subdivision ensures resiliency of HPO and PRO floodwalls under variations of extreme-event loadings. Specifically, the extreme I load case includes a 500-year impact load. In contrast, the extreme II load case simultaneously combines a 100-year impact load and 100-year wave load. Both extreme-event load cases require pushover analysis.

Table G.4
Load Cases and Impact Forces Recommended for Design of HPO and PRO Floodwalls to Resist Aberrant Barge Impact Loads

Load case	Return period (yr)	HPO		PRO	
		Probabilistic impact force (kip)	Recommended impact force (kip)	Probabilistic impact force (kip)	Recommended impact force (kip)
Usual	2	N/A	N/A	N/A	N/A
Unusual	100	190	225	180	215
Extreme I	500	370	450	349	420
Extreme II	100	190	225	180	215

G.6.3. Allowable Overstress Factors. Allowable overstress factors are listed in Table G.5 for aberrant barge impact design of floodwalls. Here, the usual load case is again recognized as not applicable. Note that allowable overstress factors of 0% (no permitted overstress) are recommended for extreme I and extreme II. Not permitting overstress factors for the extreme load cases is an artifact of requiring pushover analysis. Stated alternatively, pushover analyses are intended to facilitate comparisons of design impact loads to floodwall collapse limit loads.

Table G.5
Overstress Factors Recommended for Design of HPO and PRO Floodwalls to Resist Aberrant Barge Impact Loads

Load case	Recommended allowable overstress factors			
	HPO foundation	HPO wall	PRO foundation	PRO wall
Usual	N/A	N/A	N/A	N/A
Unusual	33%	50%	33%	50%
Extreme I	0%	0%	0%	0%
Extreme II	0%	0%	0%	0%

Appendix H

Flexible Timber Guide Walls

H.1. General.

H.1.1. This appendix presents a method for empirically assessing barge impact loads on flexible timber guide wall structures. This example was developed specific for an MVN project and may not be applicable to all timber guide walls in the USACE inventory. Additional DFEM modeling of similar structure across the inventory would be required to develop a generic impact guidance for all timber guide walls. Oblique (i.e., glancing blow) flotilla-wall collisions are focused on, and an empirical load prediction model is presented that facilitates impact-resistant design. The associated empirical equations incorporate dependency on the momentum of the lead row of an impacting barge flotilla. Also, the relative flotilla-wall orientation (i.e., impact angle) is considered in the load calculation process

H.1.2. This appendix also includes a brief review of finite element (FE) model components for flexible timber guide walls (modeling of barge flotillas is discussed in Chapter 3). It also provides summaries of simulated (oblique) collision forces, which are utilized to develop empirical load prediction equations. Derivation of the load prediction equations is additionally provided, where the derivation is based on curve fitting of peak values of simulated collision forces. Bilinear curve fits are formulated to relate normal-to-wall impact force to the lead-row momentum of the impacting flotilla, as well as the impact angle.

H.1.3. Scope. The appendix content is organized such that:

H.1.3.1. Section H.2 contains a brief review of major FE model components for flexible timber guide walls.

H.1.3.2. Section H.3 documents the empirical load prediction model, including listings of simulated values of peak collision forces and the curve fit procedure.

H.2. Flexible Timber Guide Wall Modeling.

H.2.1. Overview. During flotilla-wall collisions, the dynamic characteristics of the flotilla and impacted wall structure both influence the generation of impact forces. Component descriptions and FE modeling techniques attributed to barge flotillas are provided in Chapter 3. Modeling considerations for flexible timber guide walls are briefly revisited below in section H.2.3 (see Consolazio and Wilkes 2013 for a detailed treatment of the modeling effort).

H.2.2. Background.

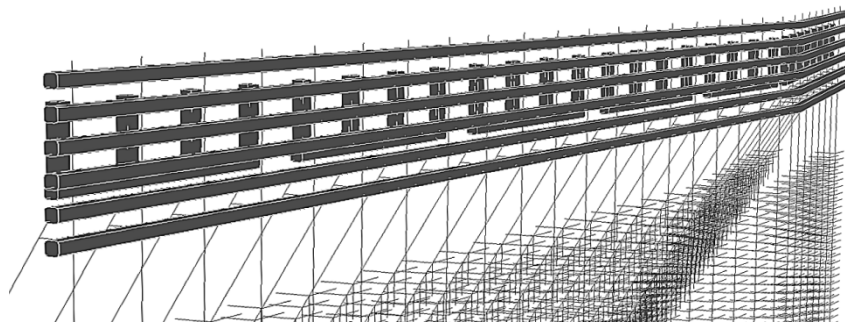
H.2.2.1. Flexible timber guide wall structures are used by USACE as components of broader navigational control structures on a large number of inland waterways. Of particular interest is determination of magnitudes of impact forces that are generated during shallow-angle barge impacts. Flexible timber guide walls are much less stiff than are impacting barges or flotillas. As such, impact behavior differs significantly from impacts on rigid or semi-flexible

concrete walls (see Chapter 4). Therefore, methods described in Chapter 4 may be of limited value when quantifying design loads for flexible timber guide walls.

H.2.2.2. As such, characterization of design-relevant barge impact loads on a typical flexible timber guide wall is described. For FE modeling purposes, a guide wall of the Catfish Point control structure 2 (Figure H.1) in Louisiana is selected. The structure of interest is constructed using plumb and battered timber piles and fiberglass reinforced plastic wale beams connected with steel bolts. It is anticipated that impact loads quantified for this wall are representative of similarly constructed flexible timber guide walls. Also, data from impact simulations on this flexible timber guide wall complement data provided elsewhere for stiffer concrete walls (see Chapter 4).



(a)



(b)

Figure H.1. Catfish Point Flexible Timber Guide Wall Control Structure 2:
(a) Site Photo; (b) Finite Element Model (Piles and Soil Springs Rendered as Lines)

H.2.3. Structural Components of the Flexible Timber Guide Wall.

H.2.3.1. The FE model consists primarily of piles, wales, thrust blocks, and various connection components. Of interest is quantifying conservative impact loads that are representative of forces on structures of similar configuration and construction. To ensure conservatism, all structural components are assigned linear elastic material properties, and failure is not modeled. Material parameter values are obtained from relevant literature and are detailed in Consolazio and Wilkes (2013).

H.2.3.2. Geometry and structural configuration information are taken from site plans of the Catfish Point Control Structure: North and South Guide Walls Replacement. Plan excerpts are provided in Consolazio and Wilkes (2013). The modeled section of the project site includes a 100-ft-long wall and a 38.5-ft end flare (angled at 15°). A plan view of the wall is provided in Figure H.2. As oriented, barge flotillas impacting the structure approach from left to right.

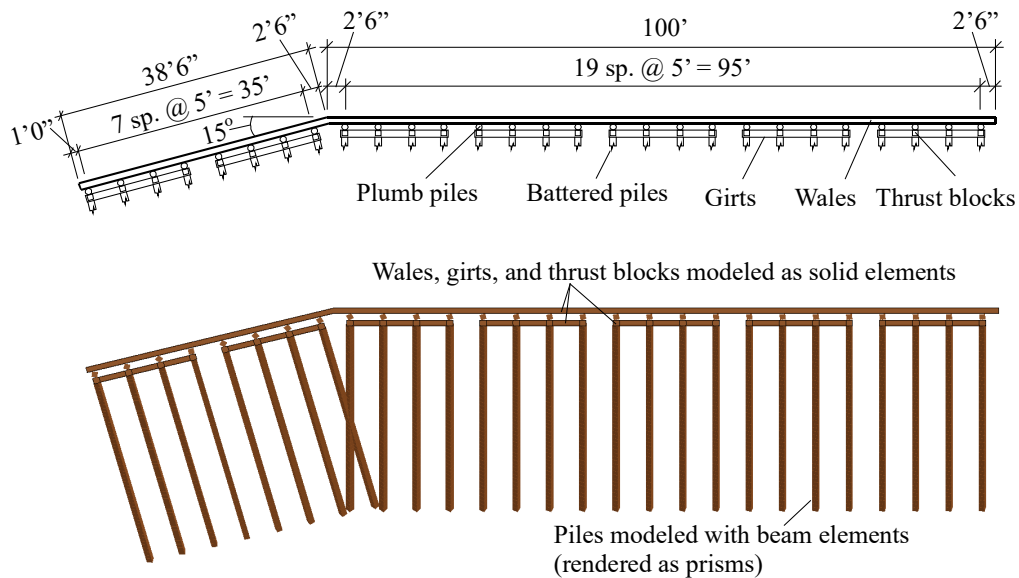


Figure H.2. Plan View and Geometry of Flexible Timber Guide Wall (Schematic Diagram and Rendering of the Corresponding FE Model)

H.2.4. Modeling of Piles, Wales, and Thrust Blocks. The wall is composed of timber piles (plumb, battered), horizontal wales and girts, vertical thrust blocks, and steel bolts (Figure H.3). In both the flare and the primary wall, each set of four-pile groups is tied together. Pile groups are tied with a horizontal girt on the back side of the wall. In Figure H.3a, battered piles are shown extending away from the impact face.

H.2.4.1. The wall utilizes 12-in. diameter circular timber piles to generate lateral resistance to impact loads. Plumb and battered piles are both modeled using resultant beam elements. Consequently, beam elements (and nodes) are positioned along the centerlines of the piles. Nodes to which the pile elements connect are evenly spaced at vertical intervals of 1 ft (Figure H.3b). Beam section stiffness is specified by assigning a cross-sectional area, moments of inertia, and an elastic modulus of 1,600 ksi.

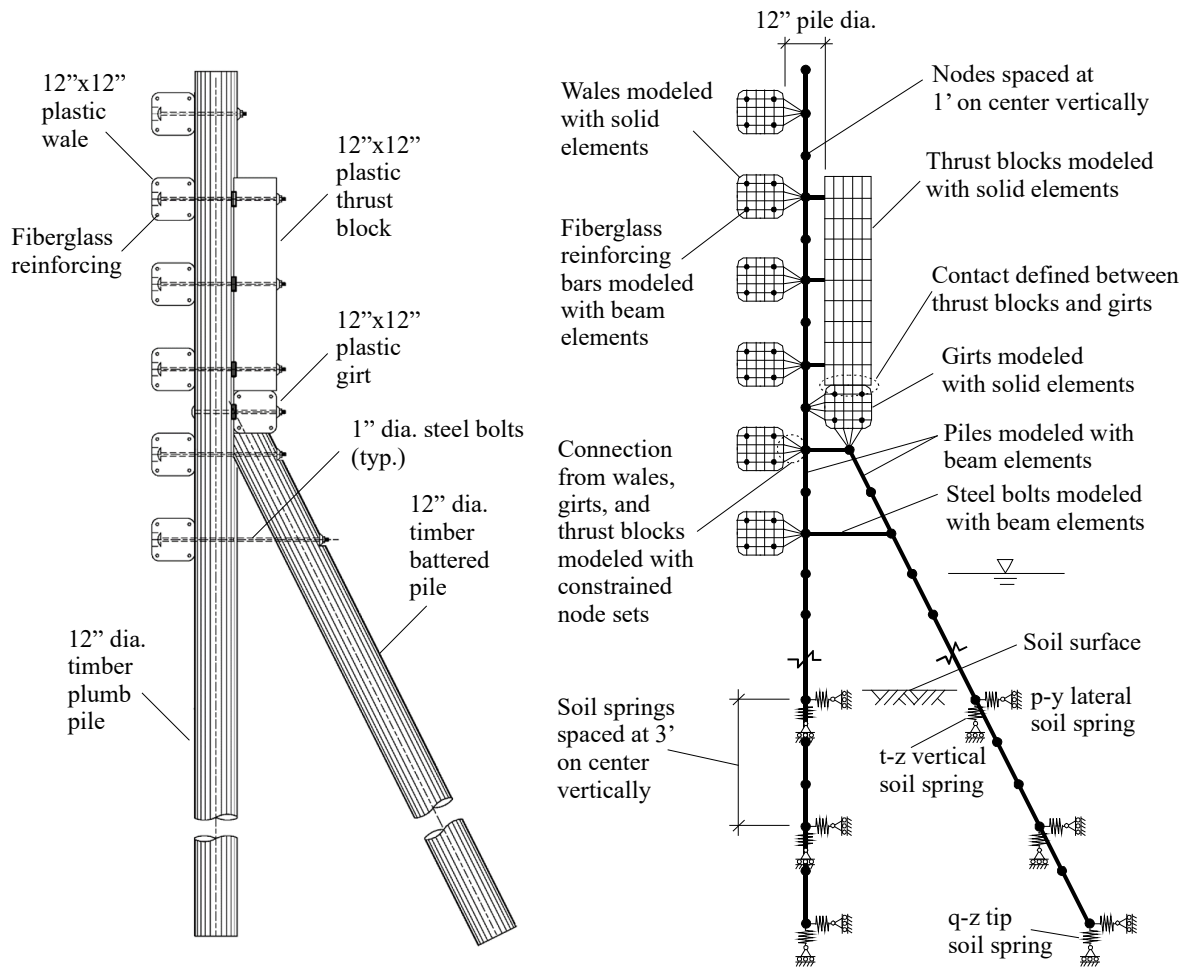


Figure H.3. Flexible Timber Guide Wall: (a) Structural Components; (b) Finite Element Model

H.2.4.2. Fiberglass-reinforced recycled plastic beams form the impact face of the wall, the thrust blocks, and the girts on the non-impact side. Wales, girts, and thrust blocks are 12 in. x 12 in. recycled plastic with four 1.25 in. diameter embedded fiberglass reinforcing bars. In the FE model (Figure H.3b), all recycled plastic components are modeled using solid 8-node brick elements. The majority of these elements measure 2.4 in. x 2.4 in. x 6 in. The 6 in. dimension is oriented along the longitudinal axis of each member.

H.2.4.3. Embedded fiberglass reinforcing bars are modeled as resultant beam elements, each 6 in. long (additional details are provided in Consolazio and Wilkes, 2013). In total, approximately 54,000 solid recycled plastic elements and 8,600 fiberglass beam elements are used in the wall FE model. Because fiberglass reinforcing bar elements share common nodes with the surrounding solid recycled plastic elements, composite action is represented. Stated alternatively, strain compatibility is enforced at the interface between the two materials.

H.2.5. Soil Resistance Modeling. As detailed in Consolazio and Wilkes (2013), representative soil profiles (layerings) are established based on conditions at the project site. Soil parameters are approximated with the intent of producing conservative estimates of barge impact forces. Soil layer parameters are used to compute force-displacement curves for vertical and lateral soil springs. These springs are, in turn, attached to timber pile elements (Figure H.4).

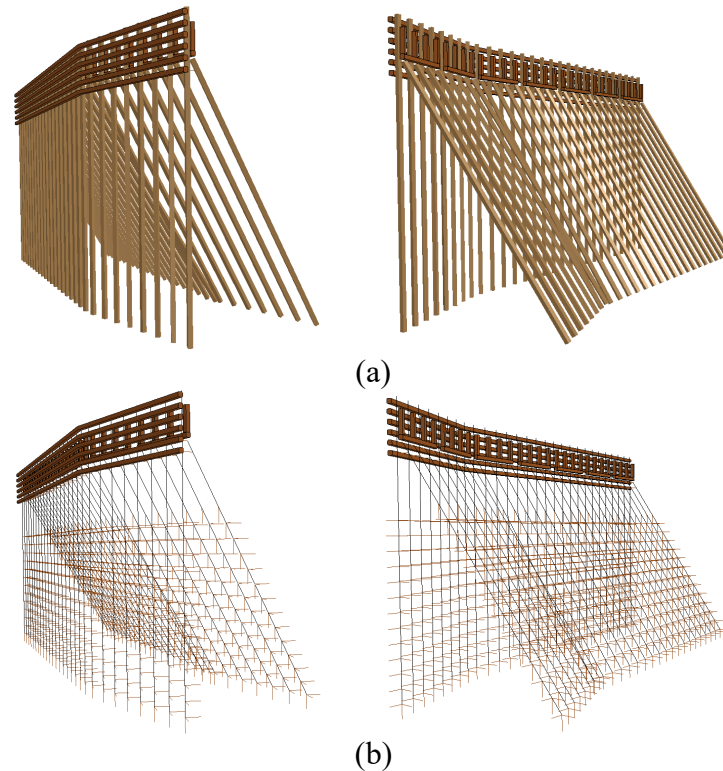


Figure H.4. Isometric Views of the Flexible Timber Guide Wall FE Model: (a) Without Soil Spring Elements; with Piles Rendered as “Prisms” of Appropriate Diameter; (b) With Soil Springs and Pile Elements Rendered as Lines

H.2.5.1. In Figure H.4a, pile elements are illustrated with beam prisms to provide a sense of physical pile diameter and geometry. In Figure H.4b, pile elements are instead indicated simply as lines (although the cross-sectional properties still represent the physical diameter). Figure H.4b also indicates nonlinear soil spring elements, representing lateral and vertical soil stiffnesses. Soil spring elements are attached to the pile nodes at 3 ft vertical spacings.

H.2.5.2. Lateral soil resistances, in perpendicular directions, at each pile node are represented by separate p-y and p-x springs. Vertical soil resistance at each node is represented by either a t-z (skin) spring or a compression-only q-z (tip) spring. The software package FB-MultiPier (BSI 2013) is used to convert soil layer parameters into corresponding nonlinear force-displacement relationships. Soil layerings considered, and properties assigned to the nonlinear soil resistance springs, are detailed in Consolazio and Wilkes (2013).

H.2.6. Modeling of Contact.

H.2.6.1. To quantify impact loads, the flexible timber guide wall structural model is integrated together with various barge flotilla models. For example, impact between a 2x2 flotilla and the flexible timber guide wall is shown in Figure H.5. Integrated barge and wall models incorporate contact detection, friction, buoyancy, and lashing modeling, consistent with documentation provided in Chapter 3. Using integrated barge and wall models, 30 impact simulations are conducted.

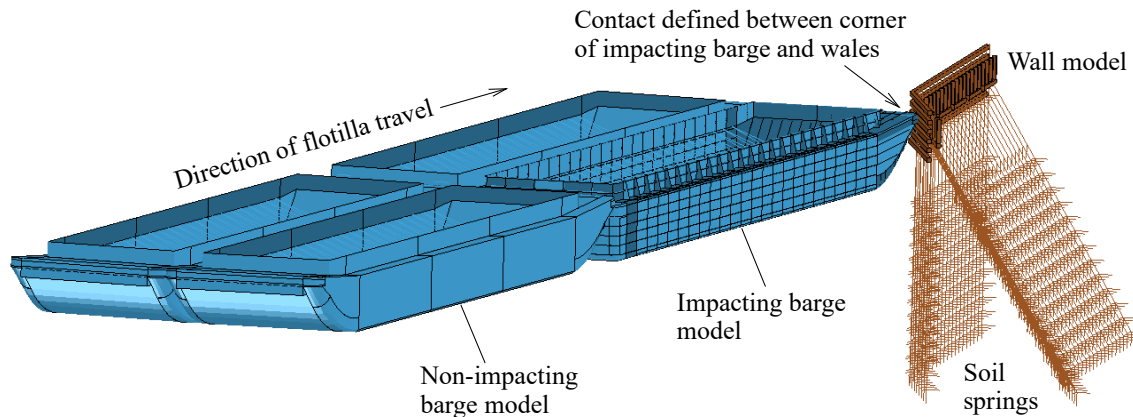


Figure H.5. Definition of Contact between Barge Flotilla Model and Flexible Timber Guide Wall Model

H.2.6.2. During impact simulation, the barge contacts only the outer surfaces (solid-element faces) of the wales (Figure H.5). Therefore, contact is detected only between the exterior faces of the wales (recall Figure H.3b) and starboard corner barge nodes. Static and dynamic coefficients of friction between the steel barge and recycled plastic wales are 0.30 and 0.20, respectively. See Chapter 3 for additional details regarding flotilla modeling.

H.3. Empirical Load Prediction Model.

H.3.1. Introduction. To quantify barge impact loads, the flexible timber guide wall model is integrated with six different barge flotilla configurations. In total, 30 dynamic impact simulations are conducted (Table H.1) to develop empirical load prediction equations.

Table H.1
Peak Force Results for Flotilla Collisions on Flexible Timber Guide Walls

Flotilla Size	Impact Speed	Impact Angle On Flare	Impact Angle On Wall	Impact Location	Peak Impact Force (kip)
1 x 1	2 FPS	25°	-	Flare	76
1 x 1	4 FPS	-	15°	Wall	133
1 x 1	4 FPS	15°	-	Flare	124
1 x 2	2 FPS	15°	-	Flare	68
1 x 2	4 FPS	-	15°	Wall	148
1 x 2	4 FPS	25°	-	Flare	214
1 x 3	2 FPS	15°	-	Flare	71
1 x 3	2 FPS	-	15°	Wall	85
1 x 3	2 FPS	25°	-	Flare	135
1 x 3	4 FPS	-	15°	Wall	132
1 x 3	4 FPS	15°	-	Flare	146
1 x 3	4 FPS	25°	-	Flare	191
2 x 1	2 FPS	15°	-	Flare	83
2 x 1	2 FPS	25°	-	Flare	147
2 x 1	2 FPS	25°	-	Flare	172
2 x 1	4 FPS	-	15°	Wall	167
2 x 1	4 FPS	15°	-	Flare	192
2 x 1	4 FPS	25°	-	Flare	255
2 x 2	2 FPS	15°	-	Flare	100
2 x 2	2 FPS	25°	-	Flare	163
2 x 2	2 FPS	25°	-	Flare	187
2 x 2	4 FPS	-	15°	Wall	176
2 x 2	4 FPS	15°	-	Flare	211
2 x 2	4 FPS	25°	-	Flare	312
2 x 2	4 FPS	25°	-	Flare	333
2 x 2	6 FPS	15°	-	Flare	248
2 x 2	6 FPS	-	15°	Wall	250
2 x 2	6 FPS	15°	-	Flare	267
2 x 3	2 FPS	-	15°	Wall	119
2 x 3	6 FPS	-	15°	Wall	247

H.3.2. Collision Conditions.

H.3.2.1. Two distinct impact locations on the flexible timber guide wall model are simulated. The first location is on the flare (end-treatment) at the fourth pile line from the flare-to-wall connection (Figure H.6a). The second location is on the primary wall at the first pile line from the flare-to-wall connection (Figure H.6b). Impacts on the flare are conducted at 15° and 25°, whereas impacts on the primary wall are conducted only at 15°. Approximately twice as many impacts are conducted on the flare because a wider range of impact angles are considered feasible.

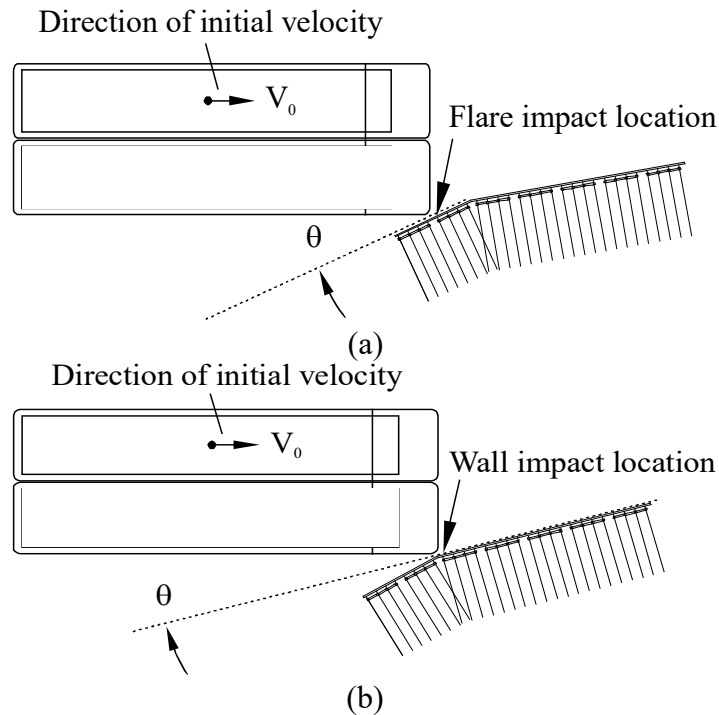


Figure H.6. Impact Locations on Flexible Timber Guide Wall Model:
 (a) Flare Impact at Fourth Pile Line from the Flare-to-Wall Connection;
 (b) Wall Impact at First Pile Line from the Flare-to-Wall Connection

H.3.2.2. The flare impact point is expected to be somewhat stiffer than the wall impact point. During a flare impact, the barge moves toward the geometrically stiffened region where the flare and wall join together (Figure H.6a). In the wall impact case (Figure H.6b), the barge moves away from this area, resulting in a gradual reduction of stiffness. Due to the differences of stiffness, high-momentum impacts on the flare typically generate larger forces than wall impacts. This further motivates conducting a greater number of flare impacts, so as to produce conservatism in the empirical load prediction model.

H.3.3. Peak Impact Forces on Flexible Timber Guide Walls. Figure H.7 plots peak (normal) impact forces (from Table H.1) for the 30 impact simulations. Forces are plotted against the momentum of only the lead row of the impacting flotilla, and normal to the wall. For comparisons of total momentum versus lead-row momentum, as well as results from sensitivity studies, see Consolazio and Wilkes (2013). Variations in the number of flotilla rows, number of flotilla columns, and soil resistance are investigated therein. For conservatism, results from the sensitivity studies are not included in development of the empirical load prediction model formulated below.

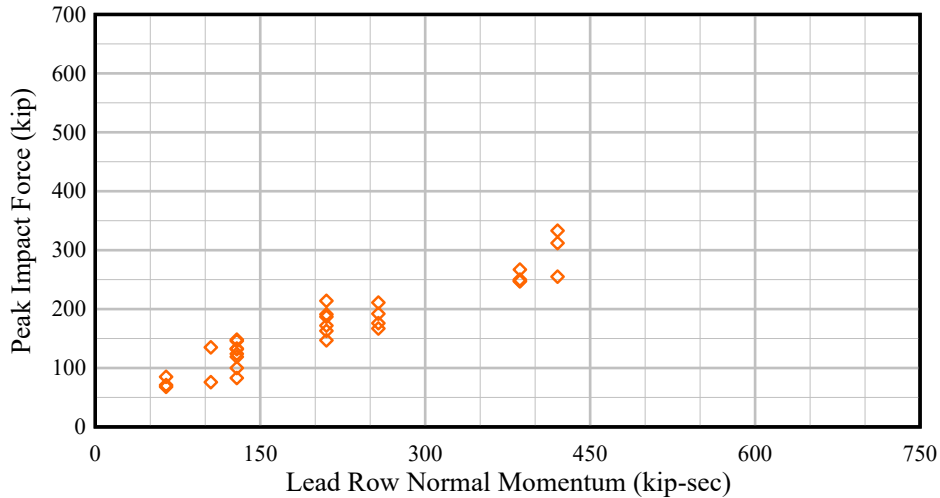


Figure H.7. Peak Force Results for Flotilla Collisions on Flexible Timber Guide Walls (30 Cases)

H.3.4. Empirical Load Prediction Model. Examination of peak forces (Figure H.7) reveals an approximately linear relationship between impact force and flotilla lead-row momentum. A single-segment linear relationship fitted to the data would not, however, pass through the origin. Consequently, and to maintain consistency with empirical models presented elsewhere in this manual, a two-segment bilinear functional form is selected instead. A bilinear fit enables low and moderate to high levels of momentum to be distinguished and ensures that the curve passes through the origin (Figure H.8).

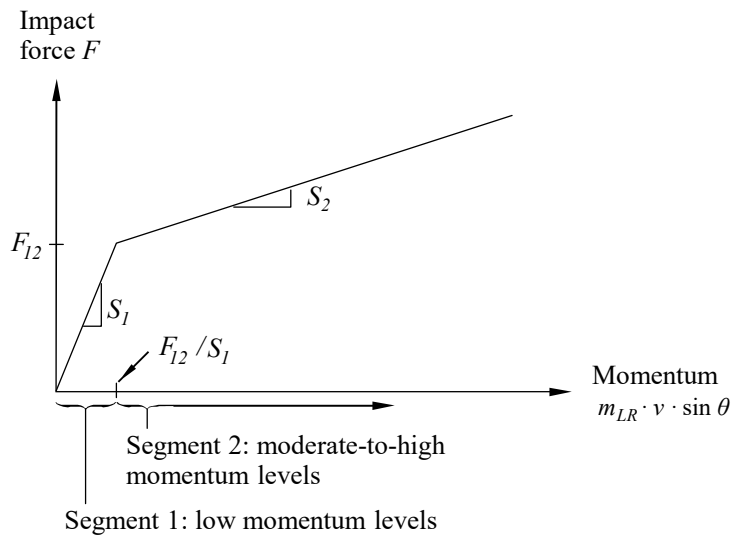


Figure H.8. General Form of Unified Bilinear Curve Fit Used for Flexible Timber Guide Walls

H.3.4.1. The above considerations lead to the following bilinear functional form for predicting peak normal-to-wall impact force, F :

$$F = \begin{cases} S_1 \cdot (m_{LR} \cdot v \cdot \sin \theta) & \text{if } m_{LR} \cdot v \cdot \sin \theta \leq (F_{12}/S_1) \\ F_{12} + S_2(m_{LR} \cdot v \cdot \sin \theta - (F_{12}/S_1)) & \text{otherwise} \end{cases} \quad (\text{H.1})$$

H.3.4.2. Upon solving for the parameters F_{12} , S_1 , and S_2 that best fit the data shown in Figure H.7—using the same type of error minimization process that was described in Chapter 4 for concrete walls—the following load prediction model is established for flexible timber guide walls:

$$F = \begin{cases} 1.156 \cdot m_{LR} \cdot v \cdot \sin \theta & \text{if } m_{LR} \cdot v \cdot \sin \theta \leq 88 \text{ kip-sec} \\ 101 + 0.553 \cdot (m_{LR} \cdot v \cdot \sin \theta - 88) & \text{otherwise} \end{cases} \quad (\text{H.2})$$

where F is the impact force normal to the wall in units of kip. Lead-row barge flotilla momentum normal to the wall is $m_{LR} \cdot v \cdot \sin \theta$ in units of kip-sec.

H.3.4.3. Confidence bounds are also established at confidence levels of 1-standard deviation (84.1%) and 2-standard deviations (97.7%) from the mean. Functionally, these bounds are given by:

$$F_{84.1\%} = \begin{cases} 1.317 \cdot m_{LR} \cdot v \cdot \sin \theta & \text{if } m_{LR} \cdot v \cdot \sin \theta \leq 88 \text{ kip-sec} \\ 116 + 0.633 \cdot (m_{LR} \cdot v \cdot \sin \theta - 88) & \text{otherwise} \end{cases} \quad (\text{H.3})$$

and:

$$F_{97.7\%} = \begin{cases} 1.488 \cdot m_{LR} \cdot v \cdot \sin \theta & \text{if } m_{LR} \cdot v \cdot \sin \theta \leq 88 \text{ kip-sec} \\ 130 + 0.711 \cdot (m_{LR} \cdot v \cdot \sin \theta - 88) & \text{otherwise} \end{cases} \quad (\text{H.4})$$

H.3.4.4. In Figure H.9, the mean-value load prediction model, Equation H.2, is compared to impact simulation force data (Table H.1). Reasonable agreement is observed.

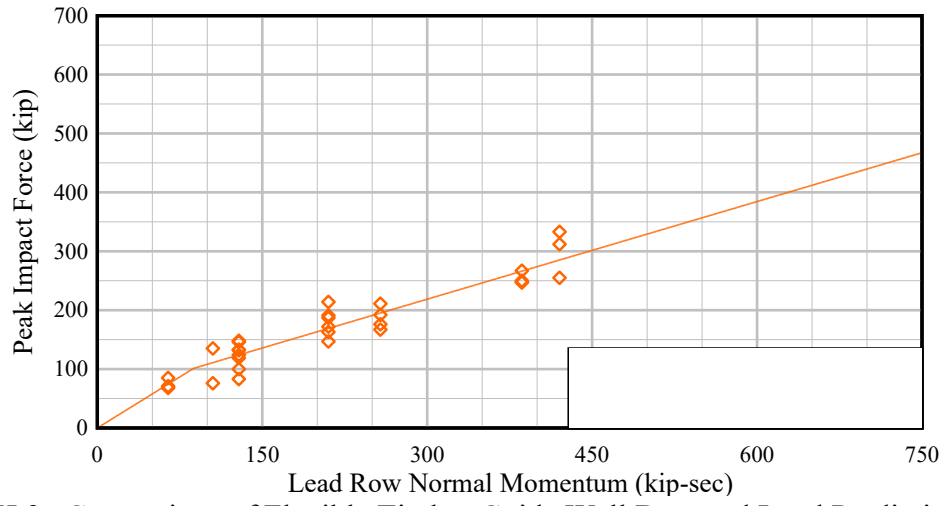


Figure H.9. Comparison of Flexible Timber Guide Wall Data and Load Prediction Model

Appendix I

Lock Dewatering Structures

I.1. Lock Dewatering Structures.

I.1.1. This section was developed to assist designers with methods on how to estimate the barge impact loads on lock dewatering structures such as bulkheads, center posts structures, and Poiree dams. The methods presented reflect the impact loads that are accidental (i.e., loss of control or loss of power of a maintenance barge) and not from an aberrant barge breaking loose from a flotilla, entering the lock approach, and colliding with the lock dewatering structure.

I.1.2. The examples presented utilize both finite element model (FEM) calculations to estimate the stiffness (i.e., force-deflection curve) for a lock dewatering structure and the low-order dynamic method presented in Chapter 5 of this EM. The FEM is also used to examine the combined stress ratio (CSR) (i.e., utilization ratio) defined in ACI-360 for the critical members in the structure where the CSR limit is greater than 1.

I.2. Center Post Dewatering Structure.

I.2.1. Introduction.

I.2.1.1. Several projects on the McCellan-Kerr Arkansas River Navigation System (MKARNS) utilize a removable center post and lock dewatering bulkheads for the maintenance closure system. The center post anchorage at several projects have failed due to corrosion at the anchors. The corrosion was likely aggravated by the presence of dissimilar metals as a result of a change during construction of the existing anchorages.

I.2.1.2. In 2016, a preliminary Architect-Engineer design was submitted to Little Rock District (SWL) for the Murray L&D Bulkhead Center Post. The scope of the project was to design a replacement anchorage for the center post. As part of the preliminary AE calculations, an impact load of 5 kip/ft was included in the design that is more in line with ice loads, not barge impact. This resulted in a substantially larger anchorage, where extensive modifications would be required. Additionally, SWL designers had concerns about constructability of the replacement anchorage and requested assistance from HQUSACE on the design.

I.2.1.3. SWL submitted a memorandum to HQUSACE that requested the anchorages “be repaired to satisfy the original design criteria or be designed to withstand a more credible impact load.” The basis for this request is that SWL does not experience ice loading consistent with many other projects in USACE. SWL also notes that EM 1110-2-2107 requires a load of “5,000 lbs/ft applied uniformly over a 2-ft depth across hydraulic steel structure members exposed to ice,” but that barge impact loads and application are not provided for dewatering structures.

I.2.1.4. The SWL memo also states that many entities have interpreted EM 1110-2-2107 such that lock dewatering structures must be designed for barge impact loads of 5 kips/ft. The memorandum prompted a follow-up call between HQUSACE, SWL, and the USACE Inland Navigation Design Center (INDC) where the INDC offered assistance in conducting a barge impact analysis on the existing structure to determine the estimated forces into the anchorage given the current crane barges in the SWL maintenance fleet. The analysis discussed below will be used to inform future designs for barge impact forces on replacement anchorages at the MKARNS projects.

I.2.2. Purpose of Barge Impact Analysis.

I.2.2.1. The purpose of this barge impact analysis is to determine how the center post structure will react under an accidental barge impact load from a maintenance vessel. The structural response is used to determine an estimated design impact load that a working barge would exert on the structure during an accidental barge impact. The estimated design impact load is used to develop a capacity curve for the structure as a function of the design loading and combined stress ratio. The capacity curve and anchorage loads are applicable for this center post type along the MKARNS system, give the loading conditions described in this report.

I.2.2.2. The existing center post for the dewatering bulkheads was modeled as a simple 3D beam and node FEM. All structural elements are composed of beam elements that connect at nodes within the structural model and plate elements to represent the skin plate. The software used to create the analysis model is Bentley STAAD.Pro. The INDC and SWL both agreed to use STAAD.Pro to perform the analysis due to the SWL internal knowledge of the software package and the availability under the Bentley license agreement for all districts.

I.2.3. Structural Layout and Nodal Placement.

I.2.3.1. STAAD.PRO creates beam elements such that the neutral axis of the member will create a straight line between the start and the end node. As such, the nodes along the vertical plate girders are located along the neutral axis of each girder. The origin of the structure is located at the pin where the vertical girder sits in the center post anchorage. The pin serves as a reference point for checking the dimensions for all of the member nodes. A top and a side view of the center post were drawn in Microstation to determine the optimal node locations for input in STAAD.Pro. Figure I.1 shows an elevation view of the structure.

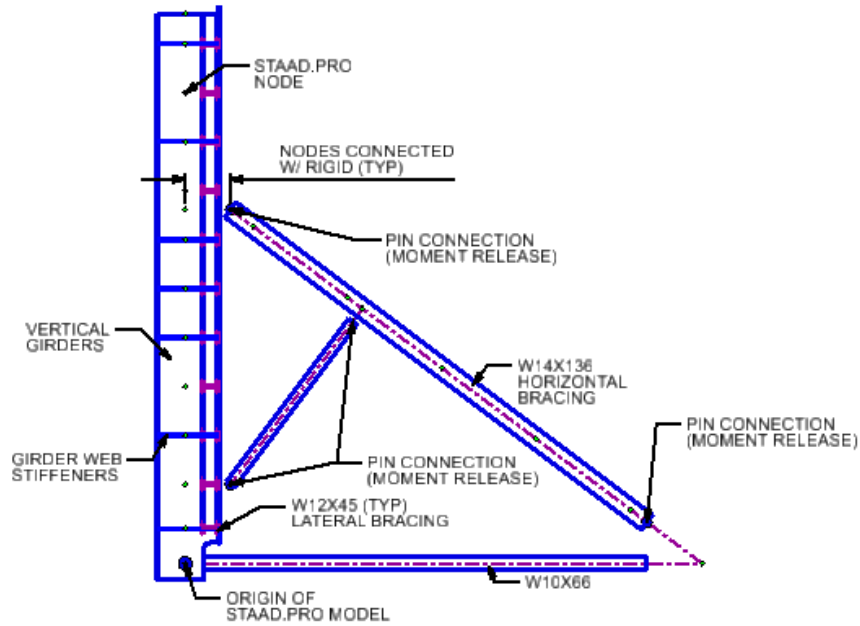


Figure I.1. Sideview of Bulkhead Center Post with Nodes for STAAD.Pro Identified

I.2.3.2. The horizontal bracing is connected to the vertical girders using a master/slave node command. This connects each of the bracing start nodes (Node 38 and Node 16) to the respective nodes on the vertical girders (Node 32 and Node 10) using a rigid member that allows for full force transfers and also accounts for the eccentricities between the members. Figure I.2 highlights the master/slave nodes for the top bracing with the master node being on the vertical girder and the slave node being on the bracing.

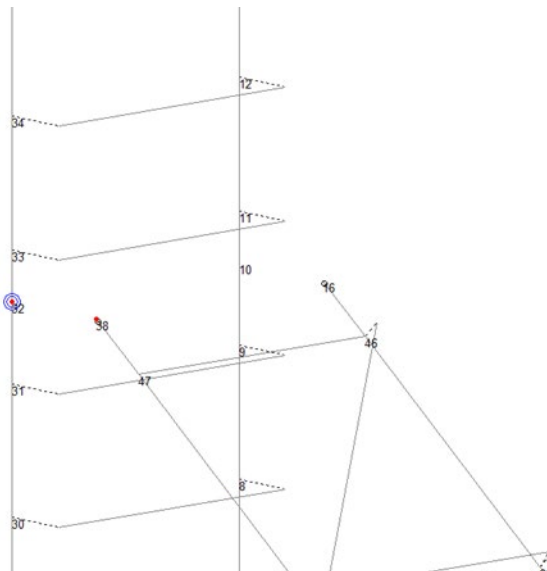


Figure I.2. Highlighted Master (Node 32)/Slave Node (Node 38) for the Connection of the Horizontal Bracing on the Left Vertical Girder

I.2.3.3. There are two different support types in the model, and they are placed at the pin connection at the bottom of the vertical girders, Nodes 1 and 21, and the back of the bottom/back of the horizontal braces, Nodes 19 and 41. The support at the bottoms of the vertical girders is pinned, while the support at the back of the bracing is fixed, as it is embedded into the concrete lock sill.

I.2.3.4. The skin plate that connects the vertical girders was modeled on a grid of nodes that is 13.65 in. lock side of the centerline of the vertical girders. The skin plate was then modeled between these nodes using plate elements with the same thickness as the skin plate. These nodes are then connected to the nodes on the centerline of the vertical girders using the master/slave node command explained earlier. The final beam and node layout for the structure with the support nodes can be seen in Figure I.3.

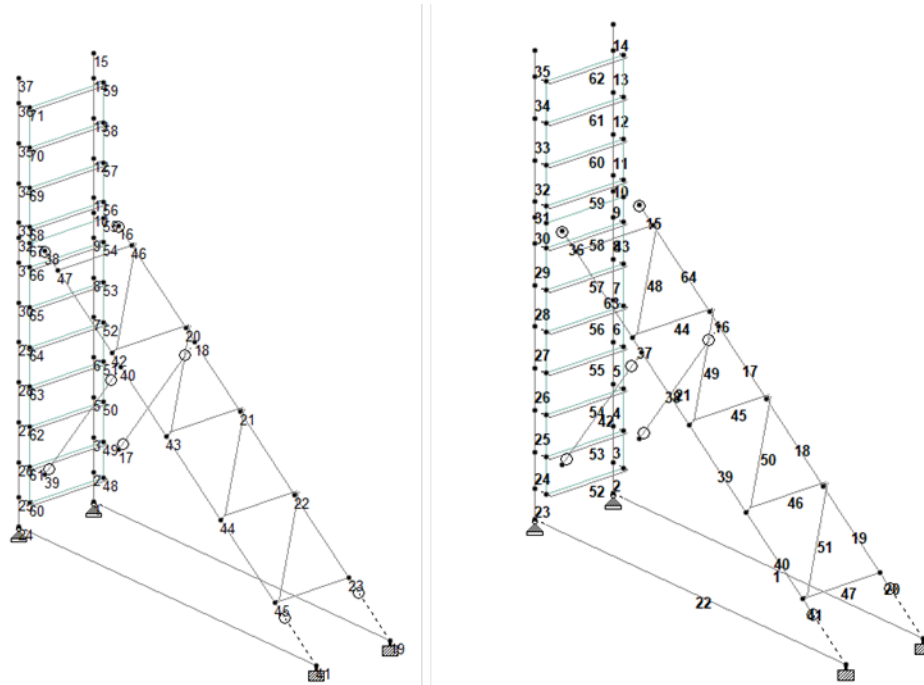


Figure I.3. (Left) Layout of Structural in STAAD.Pro Model with the Node Numbers Shown; (Right) Layout of the Structural Elements in STAAD.Pro with the Beam Numbers Shown

I.2.3.5. Member Properties.

I.2.3.5.1. All of the structural members that make up the center post are specified as ASTM A36 Gr. 36 steel, as specified on the drawings. The members themselves are almost all typical steel shapes that are preloaded into STAAD.Pro, with only a few notable exceptions. Several of the members that make up the horizontal bracing are older steel shapes that needed to be loaded into the model. They are available in member tables that can be found in the STAAD.Pro database and then loaded into the model separately.

I.2.3.5.2. The only member that needed to be custom created in the software was the vertical plate girders. This done by using the User Table Manager function, which allows the user to create custom shapes such as plate girders. Figure I.4 below shows the input screen for this feature with the properties for the vertical girders included. The member properties that STAAD.Pro calculated were checked in Mathcad to ensure they were accurate, the capacity of the vertical girder. Table I.1 summarizes the steel shapes used for each of the beam elements in the STAAD.Pro model.

Table I.1
Overview of Structural Beam Elements in STAAD.Pro

Staad.Pro Beam Descriptions			
Section	Material	Beams	Designation
W12x45	ASTM A36	52 to 62	Horizontal Vertical Girder Bracing
W8x20	ASTM A36	21, 42	Lower Support Strut
W10x66	ASTM A36	1, 22,	Bottom Horizontal Beam
W14x136	ASTM A36	15 to 20, 36 to 41, 63 to 64	Horizontal Support Strut
ST5x12.7	ASTM A36	44 to 46, 48 to 51,	Horizontal Bracing for Struts
C12x20	ASTM A36	43, 47,	Horizontal Bracing for Struts
Vertical Plate Girder	ASTM A36	2 to 14, 23 to 35	Vertical Plate Girder

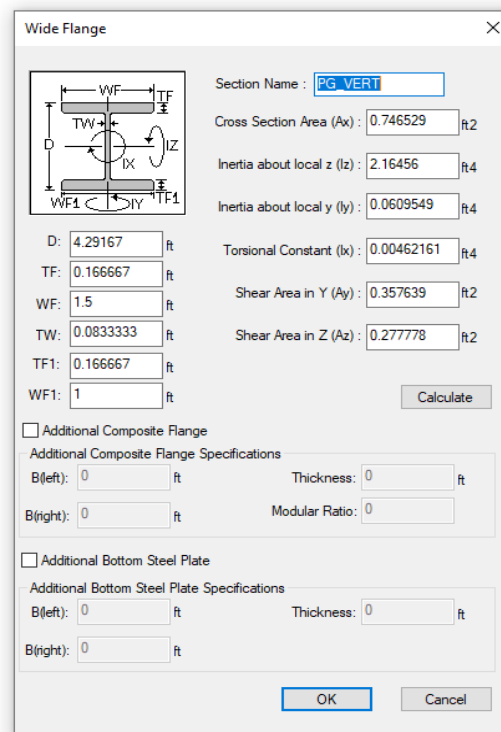


Figure I.4. Input Screen for Creating the Custom Plate Girder in STAAD.Pro

I.2.3.5.3. Several of the members are connected using pins. These connections do not allow transfer of moment between the members, as shown in Figure I.3. By default, STAAD.Pro treats all nodes as rigid connections, so moment releases were added at the end nodes of each member where pin connections are located. Several members connect with each other at locations other than at the intersection of their centerlines.

I.2.3.5.4. Offsets were used to manually displace the start or end node of a member in these instances. These offsets are shown as dotted lines in the software. All of the members labeled as Horizontal Vertical Girder Bracing and Horizontal Bracing for Struts in Table I.1 utilize this offset. To test the sensitivity of the offsets in the model, a second model was created that used master/slave nodes rather than offsets to connect members that did not connect on their centerlines. The results of this second model showed that for many of these members, the difference between the two models was less than 0.5%, which adds validity to the original model that utilized member offsets.

I.2.3.5.5. The cross bracing that connects the horizontal bracing was rotated to appropriately align the cross-bracing flanges with the horizontal bracing flange. This was done in STAAD.Pro by adjusting the beta angle for these members to 36.87 degrees. The angle used in the rotation was measured from the Microstation model of the center post. Figure I.5 shows a rendered model of the center post.

I.2.3.5.6. The plate elements that represent the skin plate use the same ASTM A36 material that is used by the beam elements. The skin plate thickness transitions from 1/2 in. below where the bottom bracing attaches to the vertical beam, and 9/16 in. above this point. The plate elements used to represent the skin plate also are 1/2 in. thick below this point, and 9/16 in. thick above this point in the structure. Figure I.5 shows the final layout of the beam and plate elements in the STAAD.Pro model.

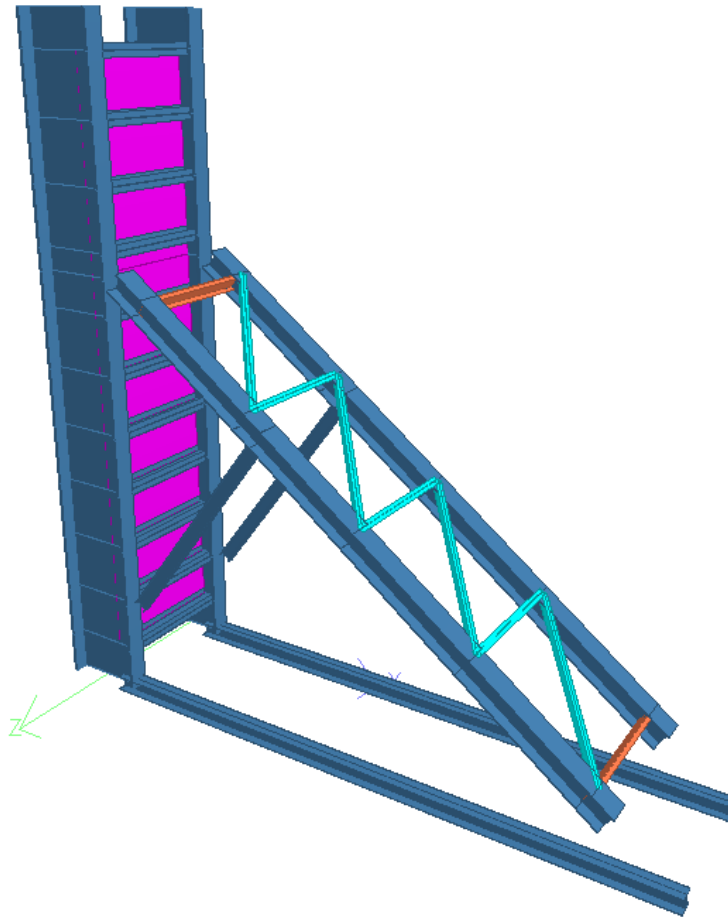


Figure I.5. Analysis Model of the Center Post Created in STAAD.Pro

I.2.3.5.7. The asymmetry on the back horizontal causes a rotation in the structure. The result of this rotation is that the support reactions are different on each of the vertical girder bases. When the diagonal braces that make the structure asymmetric are removed, the forces on each side of the structure are symmetric, as expected.

I.2.3.6. STAAD.Pro Steel Design Checks.

I.2.3.6.1. The steel design feature within STAAD.Pro was used to determine if a structural member met American Institute of Steel Construction (AISC) 360-16 Allowable Strength Design (ASD) strength requirements under the design loadings. Per EM 1110-2-2107, “capacities of HSS members will be consistent with the current edition of the American Institute of Steel Construction (AISC) Steel Construction Manual, 14th ed. ...” (pg 3-1) and “repairs to existing HSS that were originally designed using ASD may be designed using AISC-ASD procedures ...” (pg 1-1). AISC 360-16 was used for better compatibility with the latest version of STAAD.Pro.

I.2.3.6.2. However, preliminary STAAD.Pro runs were completed utilizing both versions of AISC with negligible differences in results. Note that hand calculations were completed utilizing AISC, 14th edition. The unbraced lengths for the beam elements, as described in the preceding paragraphs, were assigned as necessary to the structure. Note that unless otherwise specified in the program, STAAD.Pro considers an element's unbraced length to be equal to its length in the model.

I.2.3.6.3. For example, the W14x136 members that comprise the back bracing of the structure are split by nodes to allow connection at the horizontal bracing for struts (ST5 x 12.7). STAAD.Pro defaults to assume that the member's length is consistent with the node-to-node length and is braced in each axis. The W14x136 is braced in its weak axis at each strut, so the appropriate unbraced lengths were assigned using the appropriate steel design parameters.

I.2.3.6.4. A summary of the design parameters in the model are presented below:

- Unbraced length in the Z axis changed for W14x136 members to account for bracing only at end pins and where 8WF20 frames into member.
- Unbraced length in the X axis changed for W14x136 members to account for bracing only at end pins and where 8WF20 frames into member.
- Unbraced lengths in the Y axis for sections of W14x136 where 8WF20 members connect to horizontal support strut.
- Unbraced length in the Z axis changed for all sections of the vertical girders to account for being braced only at its base, and where W14x136 and the 8WF136 frame into vertical girder.
- Unbraced length in the X axis changed for all sections of the vertical girders to account for being braced only at its base, and where W14x136 and the 8WF136 frame into vertical girder.

I.2.3.6.5. A hand calculation was performed in Mathcad to verify the accuracy of the model calculations for a section of the vertical girder, the ST 5x12.7, and a section of the W14x136 horizontal support strut. The combined loading from these calculations was compared to the utilization ratios calculated in the model and the check was within 0.1% of each other.

I.2.3.7. Model Limitations. The following limitations apply to this STAAD.Pro model:

I.2.3.7.1. The web stiffeners on the vertical girders, and the vertical plates against which the bulkheads bear, were not included in the model. This will result in a conservative analysis of the vertical girders.

I.2.3.7.2. The skin plate was included in the model to capture the stiffness of the structure. When the skin plate was added to the model, it dramatically increased the stiffness of the center post, but only in one direction. When a load was applied to the vertical girders, a torsional force would be created due to each side of the member deflecting at a different rate. This torsion would not exist as the hydrostatic load on the girders would be applied to the members close to its downstream flange, which, unlike the model, is where STAAD.Pro applies the load on the centroid of the member.

I.2.3.7.3. The purpose of the model is to determine the force transfer to the anchorage. Failure of the pin connections are not considered as part of this analysis.

I.2.3.8. Loadings on the STAAD.Pro Model.

I.2.3.8.1. The loads applied to the structure include the following:

- Hydrostatic load from the water on the river side of the structure.
- Impact load that is representative of a floating plant impacting the center post.
- Dead load equal to the self-weight of the structural elements.

I.2.3.8.2. The draft depth of the barge is 6 ft above the waterline and includes a 2-ft headlog. If a barge accidentally impacts the center post, it would do so over this 2-ft section. All barge impact loads are applied over a 2-ft-long section of the vertical girders. This impact load is applied symmetrically to both vertical girders or unsymmetrically to only one of them, depending on the STAAD.Pro model.

I.2.3.8.3. The hydrostatic load on the structure is applied to the vertical plate girders on the face of the center post with an equal load being applied to both of these members. The dead load (self-weight) on the structure is different than what was represented in the model due to a number of elements in the structure not being included. The self-weight of the structure as shown on the contract drawings is 53 kips, while the self-weight of the model is 49.91 kips. This difference however will have minimal effects on the analysis results.

I.2.3.8.4. The load combinations applied to the structure are unfactored combinations of the hydrostatic load, self-weight, and the impact loads. Unfactored load combinations were used, and the structure was to be checked using AISC and ASD strength requirements; requirements from EM 1110-2-2107 were also considered. Figure I.6 shows a free-body diagram of the system with the loads applied to the vertical girders as well as the pool elevation in relation to the impact load. This pool elevation was initially chosen as it would produce the largest resultant loads on the center post anchorage.

**Table I.2
Summary of Design Models Used with Their Corresponding Loads, Water Elevations, and the Purpose of Each of the Models**

Model File Name	Loads Considered	Pool Elevations	Purpose of Model
Symmetric Impact Analysis	<ol style="list-style-type: none"> 1) Hydrostatic load 2) Dead load 3) Positive impact load applied to both vertical girders 4) Negative impact load applied to both vertical girders 	30' 6"	<ol style="list-style-type: none"> 1) Determine the center post response under symmetric impact loads, nodal displacements used to determine equivalent impact load 2) Combined stress ratio for each member not considered for this model
Unsymmetric Impact Analysis	<ol style="list-style-type: none"> 1) Hydrostatic load 2) Dead load 3) Positive impact load applied to right vertical girder 4) Negative impact load applied to right vertical girder 	30' 6"	<ol style="list-style-type: none"> 1) Determine the center post response under unsymmetric impact loads, nodal displacements used to determine equivalent impact load 2) Combined stress ratio for each member not considered for this model
Symmetric Design Impact with Lowering Water Elevations	<ol style="list-style-type: none"> 1) Hydrostatic load 2) Dead load 3) Symmetric design impact load applied to both vertical girders 	30' 6" 30' 0" 28' 0" 24' 9" 23' 5"	<ol style="list-style-type: none"> 1) Determine utilization of structural members under design impact loads when barge impacts both vertical girders symmetrically 2) Creation of a capacity curve for the structure at differing water elevations 3) Calculation of center post anchorage loads at differing water elevations
Unsymmetric Design Impact with Lowering Water Elevations	<ol style="list-style-type: none"> 1) Hydrostatic load 2) Dead load 3) Unsymmetric design impact load applied to right vertical girder 	30' 6" 30' 0" 28' 0" 24' 9" 23' 5" 21' 6" 18' 3" 15' 0" 11' 9"	<ol style="list-style-type: none"> 1) Determine utilization of structural members under design impact load when barge impacts only the right vertical girder 2) Creation of a capacity curve for the structure at differing water elevations 3) Calculation of center post anchorage loads at differing water elevations

I.2.3.10. Overview of Analysis of Structure Stiffness.

I.2.3.10.1. The estimate for the structure stiffness (force-deflection) was performed by manually adding increasing impact loads to the structure to determine the structures response for each of these loads. This differs from a true pushover analysis where incremental loads are applied to the structure until plastic hinges form, as a result of a member yielding in tension. The top node on the right vertical girder was monitored to determine its deflection as a result of these loads. A table comparing these deflections with the applied impact loads is presented in Table I.3.

I.2.3.10.2. The right girder was selected for monitoring because during the unsymmetric impact case, it produces the largest utilization ratios for the structural members. This is due to the asymmetry of the horizontal support strut, will force all of the load into one side of the strut. A total of three different magnitudes of impact loads were analyzed:

- A negative magnitude impact load to determine the response of the structure as it moves from a deformed position (top of the vertical girders are deflecting toward the chamber) back toward a vertical position.
- An impact magnitude of zero to determine the steady state deflection of the structure.
- A positive impact load to determine the deflection of the structure during barge impact.

I.2.3.10.3. Additional impact magnitudes were not required as the structure deflection had a linear relationship to the applied impact load. This was determined when additional impact magnitudes were applied to the structure. These loads were subsequently taken out for clarity when this linear relation was determined. This linear relationship is logical because the model is part of an elastic analysis and Table I.3 shows the deflections of the top nodes from both the symmetric and unsymmetric impact loads in the analysis. The impact load shown in the table is the total impact load applied to the structure.

Table I.3
Loads Added to the Model for the Pushover Analysis

(Each of the impact loads were combined with the hydrostatic and dead loads to determine the structural response under different impact magnitudes.)

	Node	Load Case	Deflection X-Axis (in)	Load (kip)
Unsymmetric Impact Results	15	64:HS+9.0IM	1.65	541.5
		66:HS-4.0IM	-0.745	-240.7
		67:HS+D	-0.008	0
	37	64:HS+9.0IM	0.071	541.5
		66:HS-4.0IM	-0.012	-240.7
		67:HS+D	0.014	0
Symmetric Impact Results	15	65:HS+9IM	1.707	1083
		66:HS-4.0IM	-0.77	-481.3
		67:HS+D	-0.008	0
	37	65:HS+9IM	1.775	1083
		66:HS-4.0IM	-0.769	-481.3
		67:HS+D	0.014	0

I.2.3.11. Estimate of Design Barge Impact Load.

I.2.3.11.1. This section estimates the barge impact load based on the SWL requirements for a crane deck barge that impacts the center post during a lock dewatering. This impact occurs either by the crane barge losing its stability, the spuds fail, and the barge rotates and impacts the dewatering structure; or an impact occurs due to pilot error or loss of power when the barge rotates forward and impacts the dewatering structure.

I.2.3.11.2. The equivalent impact load is calculated using the low-order dynamic model (LODM) that was developed for USACE by University of Florida. This LODM uses a simplified dynamic multiple degree-of-freedom model that solves the equations of motion for a barge in contact with a structural element such as approach wall. The model solves for either a flexible or a rigid structure and includes the masses for both the barge and impacted structure in this case the lock dewatering structure. The LODM accounts for both damping and a dynamic coefficient of friction during the impact as well as the stiffness (force vs. deflection) of the impacted structure. The output from the LODM solves for the maximum impact force and displacement of the structure as well as the time history of the resulting impact.

I.2.3.11.3. The input parameters selected for the lock dewatering structure LODM are as follows:

- Flexible wall option was used.
- Barge Column and Rows – 1. A single crane deck barge was modeled.
- Barge Weight – 4,088 short tons. This is based on drawings for the crane deck barge supplied by SWL with a working draft of 6 ft.
- Impact Speed. One ft/sec was assumed at impact to the center post. This value was selected due to close proximity of vessel to center post structure and the potential for aberrant conditions that might occur.
- Impact Angle – 30 degs. This was the maximum angle possible for the impact. Sensitivities to lower angles were analyzed and the results indicated these produced lower forces so 30 degs was felt conservative for this capacity analysis.
- Wall Weight – 100 kips. This was the total weight calculated from the STAAD model for steel components (center post and stoplogs) contributing to the impact. The maximum impact force from the LODM is not sensitive to the weight of the wall but the wall displacements from LODM will be slightly different.
- Dynamic Coefficient of Friction – 0.45. This was selected based on recommendations in the University of Florida (UF) LODM report.
- Time End – 5 sec. This was anticipated to be the longest value needed for the time history analysis.
- Time Sample – 0.01 sec. This is a time step for convergence of the model results.
- Wall Damping Ration – 0.05. This was selected based on recommendations in the UF LODM report.
- Wall Stiffness. The wall stiffness comes from the output of the STAAD pushover model presented in Table I.3 The maximum value both positive and negative are used to define a linear curve in the LODM analysis.
- Hydrodynamic Added Mass. Not include in this LODM analysis due to the short duration of the impact loads.

I.2.3.11.4. Based on the above inputs to the LODM and load cases defined in Table I.3 above, the symmetric load case calculated a maximum force is 304.8 kips with a maximum center post displacement of 0.609 in. These time histories for force and displacement are shown in Figure I.8 and Figure I.9. Note that the force goes to zero at 0.36 seconds, but the center post structure continues to vibrate with positive and negative displacement cycles to the end of the of the selected model time (5 secs).

I.2.3.11.5. For the unsymmetric load case in Table I.3, the maximum impact force was 248 kips with a displacement of 0.769 in. These time histories are shown in Figure I.9 and Figure I.10. Likewise, for the symmetric load without and with lower hydrostatic head, the maximum impact force was 303 and 284 kips respectively with a displacement of 0.61 and 0.42 in., respectively, and are shown in Figure I.7 and Figure I.8 and in Figure I.11 and Figure I.12.

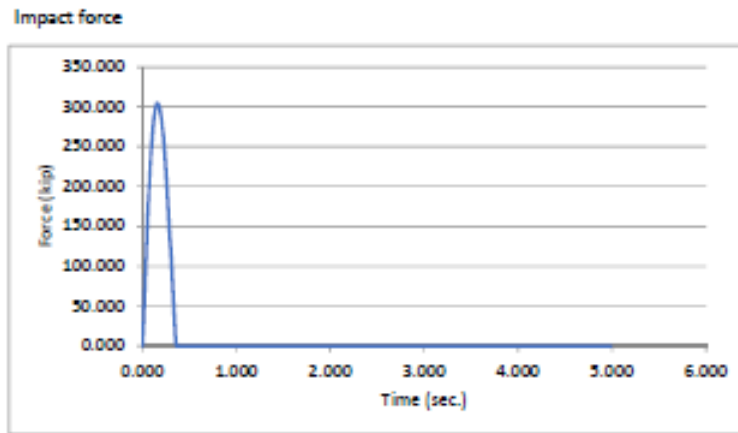


Figure I.7. LODM Impact Force Time History – Symmetric Load Case

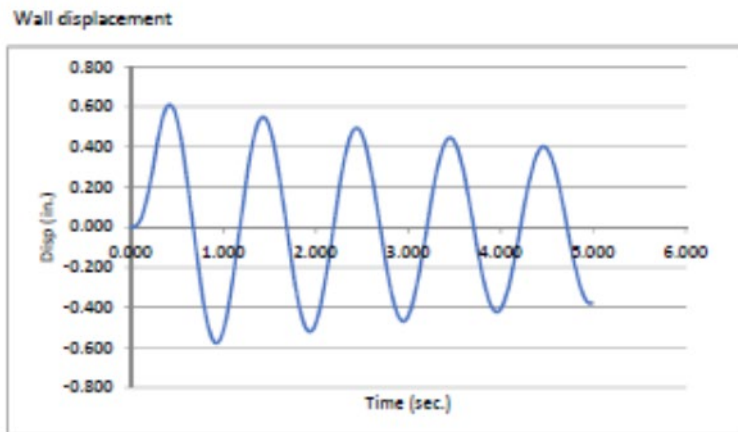


Figure I.8. LODM Displacement Time History – Symmetric Load Case

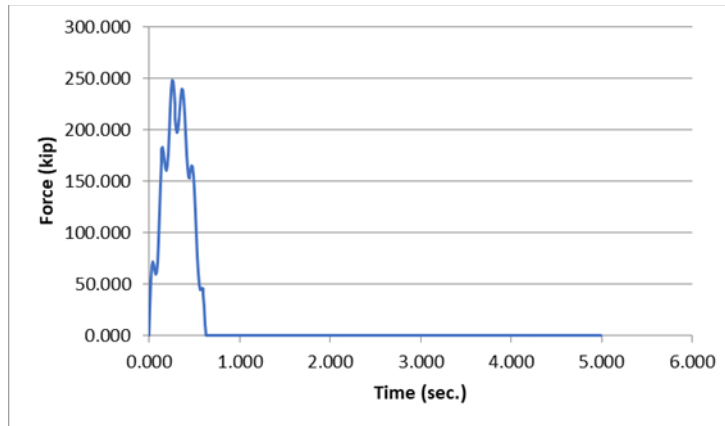


Figure I.9. LODM Impact Force Time History – Unsymmetric Load Case

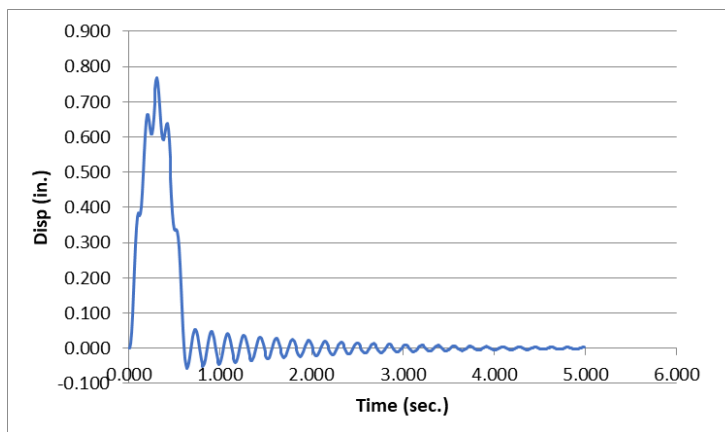


Figure I.10. LODM Displacement Time History – Unsymmetric Load Case

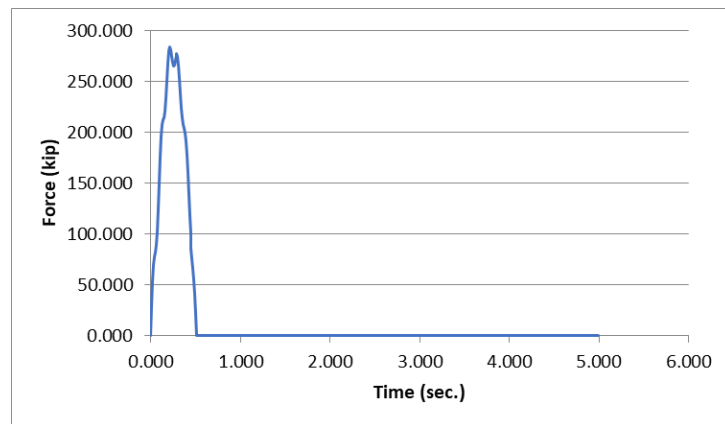


Figure I.11. LODM Impact Force Time History – Symmetrical and Lower HS Load Case

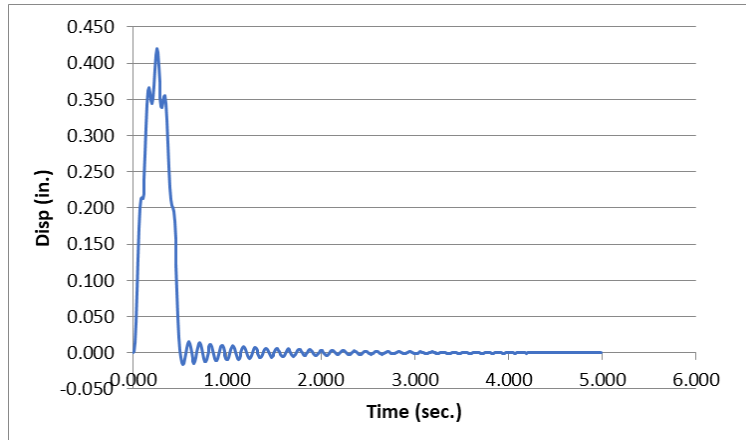


Figure I.12. LODM Displacement Time History – Symmetric and Lower HS Load Case

I.2.3.12. Capacity Curve of the Center Post.

I.2.3.12.1. The symmetric and unsymmetric impact loads, determined in the previous section, were applied to the STAAD.Pro models as part of an unfactored load cases that includes the hydrostatic load and dead load on the structure. The results from this analysis were then used to determine if the structure met the AISC 360-16, ASD strength requirements. In both cases, the structure had members that no longer met this strength requirement.

I.2.3.12.2. A capacity curve for the structure was created by varying the pool elevation outside of the lock chamber, while the chamber is dewatered. This in turn would lower the location where the barge would impact the structure and decrease the hydrostatic load on the structure. The analysis considered multiple pool elevations, and the member with the highest utilization ratio in STAAD.Pro was graphed against the corresponding pool elevation for that load case. This was completed for both a symmetric with lower head and an unsymmetric barge impact load. The utilization ratios were checked using Mathcad to ensure the accuracy of the calculations in STAAD.Pro and these ratios were less than 2% difference.

I.2.3.12.3. The capacity curve was created so that the combined stress ratio could be determined at different pool elevations. This will ensure that it can be used at multiple projects along the MKARNS, as each project has different pool elevations.

I.2.3.12.4. During the unsymmetric impact loads the impact load was only applied to the right vertical girder. Under symmetric loading this load was applied to both girders. The summary information is shown in Table I.4 and Table I.5. The plots of the utilization ratio with water elevation are shown in Figure I.13 and Figure I.14.

Table I.4

Summary of Data from STAAD.Pro

(Used to create the capacity curve of the structure based on the member with highest utilization ratio under symmetric barge impact loads.)

Utilization Ratios Under Symmetric Barge Impact							
Head Differential (ft)	Axial Compression (kip)	Mx (kip*in)	My (kip*ft)	Calculated Utilization	Staad.Utilization	Element	Member
30.5	731.55	15.638	145.902	1.026	1.023	40	W14x136
30	705.77	14.34	140.7	0.989	0.986	40	W14x136
28	609.75	9.535	121.34	0.854	0.829	40	W14x136
24.75	474.46	2.73	94.1	0.663	0.662	40	W14x136
23.5	431.75	0.52	-85.53	0.603	0.602	40	W14x136

Capacity Curve of Dewatering Centerpost Under Symmetric Loading

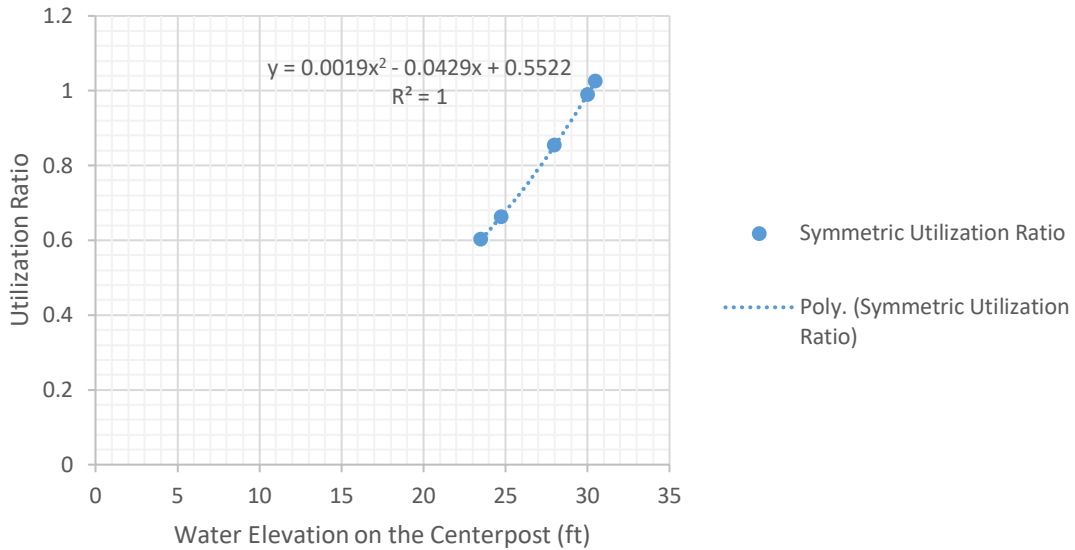


Figure I.13. Capacity of the Structure Graphed Against the Water Elevation Outside of Lock Chamber Under Symmetric Barge Impact Loads

Table I.5

Summary of Data from STAAD.Pro

(Used to create the capacity curve of the structure based on the member with highest utilization ratio under unsymmetric barge impact loads.)

Utilization Ratios Under Unsymmetric Barge Impact						
Head Differential (ft)	Axial Compression (kip)	Mx (kip*in)	My (kip*ft)	Calculated Utilization	Element	Member
30.5	42.239	9	4.67	1.736	48	ST 5x12.7
30	44.28	8.806	4.588	1.699	48	ST 5x12.7
28	40.63	8.057	4.26	1.559	48	ST 5x12.7
24.75	35.205	6.904	3.779	1.35	48	ST 5x12.7
23.5	33.347	6.481	3.61	1.279	48	ST 5x12.7
21.5	30.46	5.809	3.349	1.167	48	ST 5x12.7
18.25	26.132	4.805	2.95	0.999	48	ST 5x12.7
15	22.11	4.056	2.57	0.847	48	ST 5x12.7
11.75	18.25	3.44	2.23	0.703	48	ST 5x12.7

Capacity Curve of Dewatering Centerpost Under Unsymmetric Loading

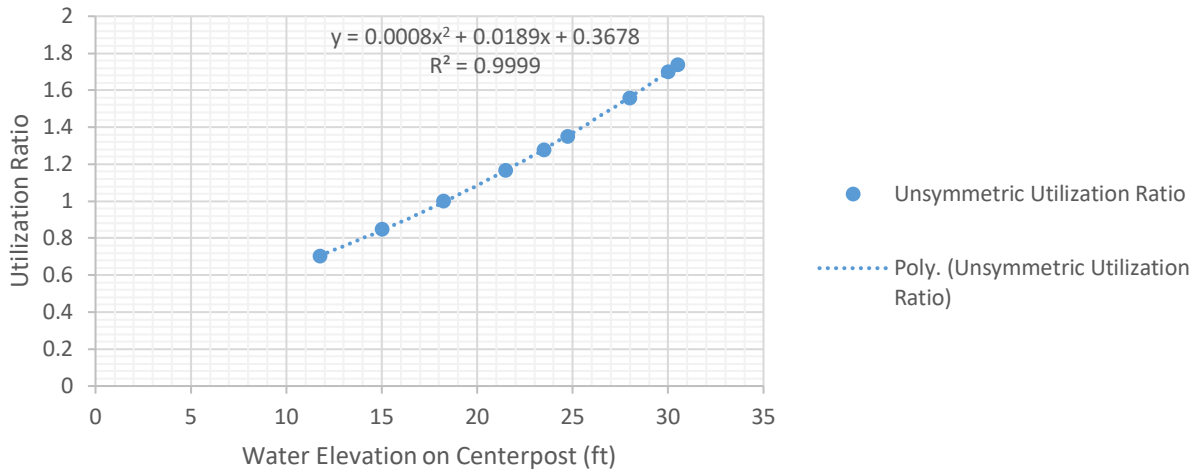


Figure I.14. Capacity of the Structure Graphed Against the Water Elevation Outside of Lock Chamber Under Symmetric Barge Impact Loads

I.2.3.12.5. The member with the largest utilization ratio, in the Symmetric Design Impact with Lower Water Elevations model, was a section of the W14x136 horizontal support strut. Within this model, a member would no longer meet AISC 360-16, ASD strength requirements when a head differential of slightly more than 30 ft is applied to the structure.

I.2.3.12.6. Within the unsymmetric barge impact model, the member that had the largest utilization ratio was a diagonal truss bracing section of ST 5x12.7. For the Unsymmetric Design Impact with Lowering Water Elevations model, this section would no longer meet AISC 360-16, ASD strength requirements when a head differential greater than 18 ft is applied to the structure.

I.2.3.13. Forces Acting on Center Post Anchorage.

I.2.3.13.1. The analysis described in the section above focuses on the maximum loading applied to the center post in order to determine an equivalent impact load. This loading scenario is specific to this project and may not be appropriate for all closures structures on the MKARNS system, as the differential loading for a dewatered chamber varies between each project. In order to help inform future anchorage replacement designs, the force transmitted to the anchorage was plotted against the corresponding head differential for the Unsymmetric Design Impact with Lowering Water Elevations model and the Symmetric Design Impact with Lower Water Elevations model.

I.2.3.13.2. The function provided at each plot is fit based on the data points from the analysis as shown in Figure I.13 and Figure I.14. Each function can be used as a guide in order to determine the required design forces. It should be noted that this function should be used only as a guide and is not a replacement for checking the utilization ratios per the latest AISC code and USACE guidance for future designs. Connections are also critical and should be checked to insure their capacity to transfer load is not exceeded.

I.2.3.13.3. The maximum considered design load for the anchorage should not exceed what the structure is able to withstand or use a water level that is not realistic for a particular lock. When using the unsymmetric load graphs, the largest load considered should correspond to a water elevation not greater than 18 ft. For the symmetric barge impact graphs, the largest considered load should be when the water elevation is 30 ft.

I.2.3.13.4. Differential hydrostatic forces during normal dewatering conditions are considered in this analysis but note that the hydrostatic loading presented in this analysis did not consider the maximum allowable hydrostatic loading on the lock walls, nor did it consider historical flood out elevations provided to SWL Operations. Lock wall stability needs to be checked as define in EM 1110-2-2100, or the most recent guidance, prior to dewatering each chamber. Appropriate flood out elevations should be set once an analysis has been conducted that meets all criteria as designated. Due to the possibility of barges impacting the structure symmetrically on both vertical girders, as well as an unsymmetrically and only hit one girder, any new design must consider at both scenarios.

I.2.3.14. Conclusions. In summary, the purpose of the analysis of the center post structure was do determine if the center post can withstand an accidental impact, specifically from a floating plant barge. The estimated design impact load calculated in section I.2.3.5 is the probable magnitude of the maximum impact, based on an extreme scenario where the chamber is fully dewatered and the pool elevation is such that it would result in a barge impact at the very top of the structure.

I.2.3.15. Recommendations.

I.2.3.15.1. Based on typical water levels on the MKARNS and the elevations of the lock sills, all of the upper sills have a head differential that is greater than the 18 ft. This head

differential is greater than what the center post is able to withstand based on AISC 360-16, ASD strength requirements, when the lock is dewatered and the center post is impacted.

I.2.3.15.2. As such, mitigation measures should be put in place that will decrease the potential for loss of life in the event of an accidental impact. One example measure would be requiring the floating plant to be moored at end of the lock that had the lower water elevation on the center post. This would lower the chance for a catastrophic failure in the event of an accidental impact on the center post. Another potential mitigation measure would be requiring that all personnel be out of the dewatered chamber during activities that raise the risk of an accidental impact to the center post. One such activity would be when the floating plant is being moved into a new location near the dewatering structure.

I.2.4. Bulkhead Dewatering Structure.

I.2.4.1. Introduction.

I.2.4.1.1. As the USACE navigation infrastructure continues to age, corrective maintenance is being performed on more frequent intervals to keep lock downtime to a minimum. With increased corrective maintenance, there is an increasing possibility of floating plants impacting the hydraulic steel structures used to dewater navigation locks. These accidental impact loads are highly dependent on the site conditions at each project site. These factors include the geometry of the lock, the barge/floating plant that impacts the dewatering structures, and the dewatering structures themselves.

I.2.4.1.2. The geometry of the lock and the geometry of the barge/floating plant must be looked at simultaneously as they are used to determine several factors regarding how the barge is able to impact the structure. These factors are listed below:

- Velocity of the maintenance barge at impact to the bulkhead structure.
- The angle the maintenance barge will make with the dewatering structure at impact.
- The mass of the maintenance barge impacting the structure as well as the mass of the structure.
- The location of the impact on the dewatering structure and how far from the lock wall this impact can take place.

I.2.4.1.3. The dewatering structure that is impacted also plays a key role in determining the potential impact magnitude. This is because the stiffer the structure the larger the impact load that can be transferred into the structure. So, for example, a structure that deflects 2 in. under a load on 400 kips will have a larger impact load applied to it than a structure that deflects 2 in. under a load of 200 kips.

I.2.4.1.4. As part of this chapter, it is recommended that additional case studies, using similar analytical methods presented in this section, need to be made to determine a set guidance for calculating these impact loads during the design for new dewatering structures. The following sections outline the process used to calculate a probable impact load on a 110 ft bulkhead structure used on the Montgomery Point L&D.

I.2.4.2. Purpose of the Analysis.

I.2.4.2.1. To calculate the structural response under barge impact loads a STAAD.Pro model of the structure was created. This analysis model can then be used to determine how the structure will respond under several different load magnitudes and at several different locations along its length. Each location was looked at individually as the structure would not behave uniformly along its length.

I.2.4.2.2. The existing bulkhead structural needed to be modeled with as much accuracy as was practical. A similar project described in section I.2.3 on a center post dewatering structure was recently completed by a team from the Inland Navigation Design Center (INDC) using the structural analysis software STAAD.Pro, so it was decided to use this program for this example.

I.2.4.2.3. The process is similar to the example in section I.2.3 where the estimated design impact load from an accidental barge impact is calculated and applied to the structure being designed. STAAD.pro could performed a code check on the members to ensure the structure could withstand an accidental barge impact during dewatering. The response of the structure under the applied load could also be compared to the anticipated deflection at the impact point to verify calculations used to determine a probable impact magnitude. Finally, the support reactions on the bulkhead slots that are calculated from the probable impact loads can be used to design the bulkhead slots.

I.2.4.3. Structural Model in STAAD.Pro.

I.2.4.3.1. The STAAD.pro model of the 110 ft dewatering bulkheads was originally created INDC as part of the design for the new bulkhead slots that were to be cut into the lock walls at Montgomery Lock. Much of the model is composed of beam elements as the existing bulkhead uses rolled shapes for many of its structural members. In several areas of the model plate elements are also used to represent several components such as the full depth diaphragm plates, the skin plate, and the built-up end section of the bulkheads.

I.2.4.3.2. After careful review of the FEM developed by INDC for Montgomery Lock, it was determined that several changes needed to be made to the model to increase the model's accuracy and to ensure a code check could be run on the bulkhead after the new impact magnitudes were calculated.

I.2.4.3.3. These changes are outlined below:

- Changed the members within the model that were defined as prismatic T-sections to a custom T-section shape defined using the User Table Manager feature. This change was necessary because the program is unable to perform a code check of a member if it is defined as a prismatic shape but can when the member is created using a user defined table.

- Corrected the locations for two of the full depth diaphragm plates in the model. This included moving the diaphragm plates that are closest to the bearing blocks, one cross section further toward the center of the bulkhead. An additional pair of diaphragm plates were added, one cross section off the centerline of the bulkhead, as this pair of diaphragms were missing in the original model.

- Altered the end support nodes so that they only provide support in the direction of flow and are only present on the nodes on the dry side of the bulkhead.

- Changed the member properties from a buoyant weight of the steel to the 50 ksi steel properties that are preloaded into STAAD.Pro.

- Changed the self-weight load case so the total load of the structure within STAAD.Pro would equal the structures self-weight printed on its as-built drawings.

- Changing model design parameters so that the model beam elements are checked using ASD rather than Load Resistance Factored Design, as well as changing design unbraced lengths for several of the members.

I.2.4.3.4. The final STAAD.Pro model of the Bulkhead is shown in Figure I.15. The figure shows the model with the beam and plate elements filled.

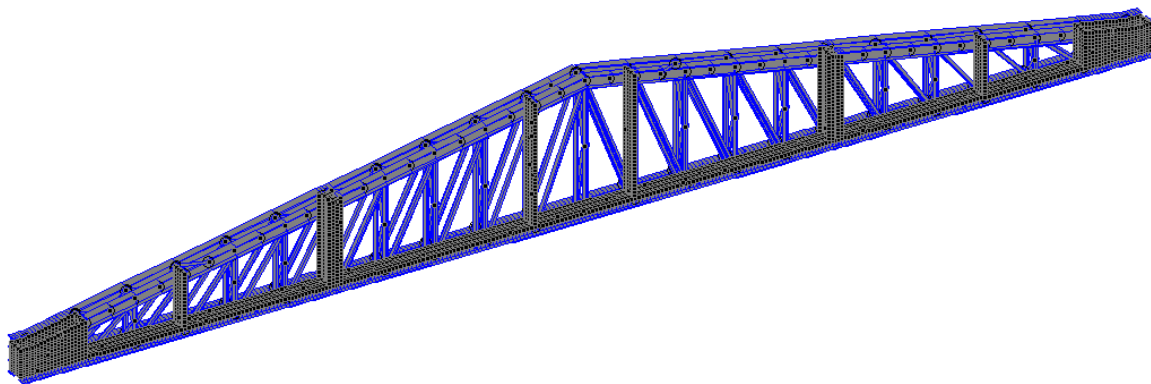


Figure I.15. STAAD.Pro Model of the 110-ft Bulkheads at the Montgomery Point L&D, with the Models Beam and Plate Elements Filled

I.2.4.3.5. It is also important to note that this lock utilizes two different bulkheads, one for 52-ft head, and the other for 30-ft head closures. The only difference between the two bulkheads is their height. Where the 52-ft bulkhead is 2 ft 9 in. from the top contact to its bottom contact, and the 30-ft bulkhead is 3 ft 0 in. The 52-ft bulkhead was the one modeled in STAAD.Pro as it would be stiffer than the 30-ft bulkhead, which would allow for a larger impact magnitude.

I.2.4.4. Model Limitations. As with any complex FEM that is created within STAAD.Pro, the model must be presented with several limitations in the model.

I.2.4.4.1. The gusset plates used to connect many of the structural members were not included in the model. Instead, the members that used these connections had a moment release on their ends to simulate the fact that the gusset plates would not transfer moments in these connections.

I.2.4.4.2. The skin plate on the dry side of the bulkhead was modeled on the centerline of the I-beams that make up this side of the bulkhead. On the actual bulkhead, the skin plate is connected to the tension flange of the I-beams; this change should have minimal effects on the structural model.

I.2.4.4.3. The model ends at the contact bearing blocks that bear against the bulkhead slots on each lock wall. This will create some isolated stress concentrations at the ends of the bulkhead but as the system response is linear, its effects on the overall structural response will be minimal.

I.2.4.5. STAAD.Pro Design Checks.

I.2.4.5.1. The steel design feature within STAAD.Pro was used to determine if a structural member meets AISC 360-16 strength requirements under the design loadings. This code was used rather than AISC 360-10, as was requested in EM 1110-2-2107, due to technical issues within STAAD.Pro. If the AISC 360-10 code was selected in STAAD.Pro, an error message would appear when the user tried to analyze the model.

I.2.4.5.2. This error caused the program to stop the analysis and made it impossible to view the analysis results. The unbraced lengths for the beam elements, as described in the proceeding paragraphs, were assigned as necessary to the structure. Note that unless otherwise specified within the program, STAAD.Pro considers an element's unbraced length to be equal to that element's length within the model.

I.2.4.5.3. The members that needed to have this change were several of the roller I-beams on the wet side of the bulkhead, and many of the horizontal T-shapes that were only braced in only one direction with the diagonal cross braces. The altered lengths and the members these were applied to can be seen in the code check section of the STAAD.Pro outputs.

I.2.4.6. Loadings on the Model.

I.2.4.6.1. The only loads that were applied to the structure were hydrostatic loads, impact loads and the self-weight of the structural elements. The impact loads were applied either on the centerline of the bulkhead (mid-span) at 1/4 span or 3/8 span. These locations are shown in the Figure I.16 through Figure I.18. In all cases, the impact loads used in the model were point loads applied to the nodes on the top and bottom of the bulkhead. All the load combinations used in the design were unfactored to try and replicate the structures response under each of the incremental impact loads.

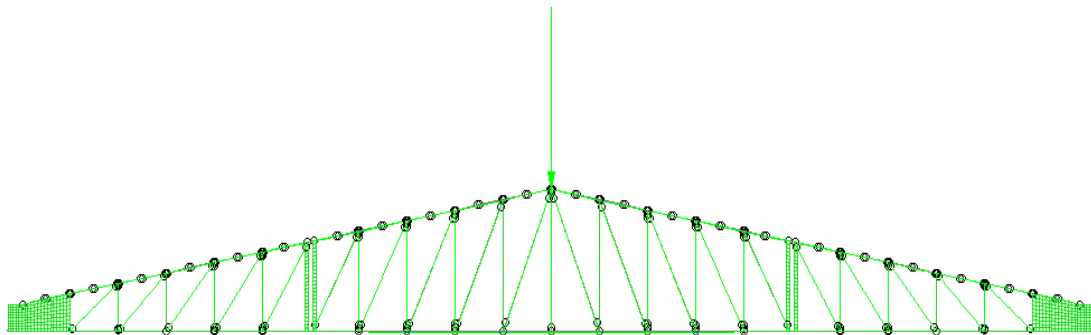


Figure I.16. Impact Locations for When the Barge Impacts the Bulkhead at Mid-Span

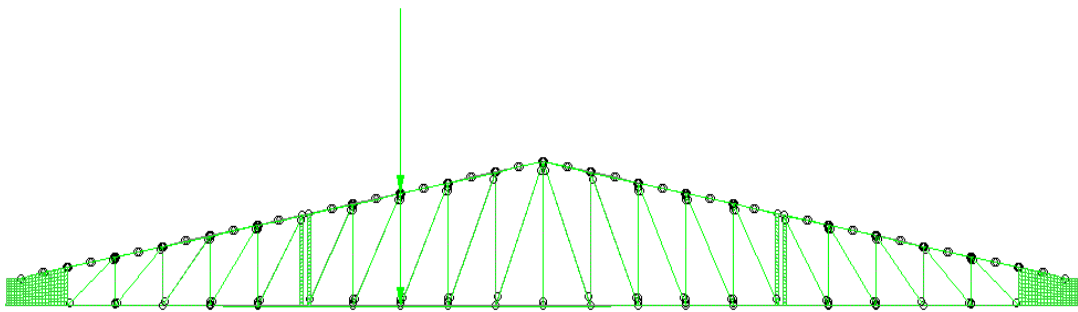


Figure I.17. Impact Locations for When the Barge Impacts the Bulkhead at 3/8 Span

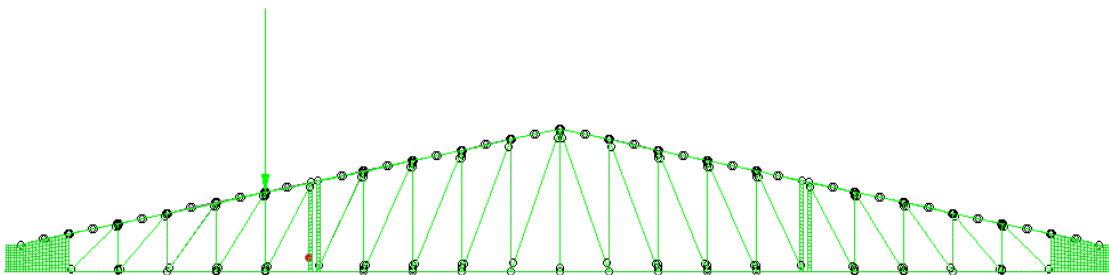


Figure I.18. Impact Location for When the Barge Impacts the Bulkhead at 1/4 Span

I.2.4.6.2. The 1/4 span location was the furthest point to the lock wall where a floating plant in the Little Rock district fleet would be able to impact the bulkheads. The midpoint location was selected as it would likely product the largest impact magnitude while it was assumed it would also create the largest combined stress ratio in the structural members. The 3/8 span location was selected due to it being at halfway between the 1/4 and the 1/2 span locations. It is important to note as well that due to the symmetry of the model, it was necessary to only apply the impact loads to the one side of the structure. Applying the loads on the opposite side would produce mirrored results in the structure.

I.2.4.7. Overview of Structural Response Calculations.

I.2.4.7.1. To determine the structural response or stiffness of the structure under potential barge impacts, incremental loads were applied to the structure at the three locations mentioned in section I.2.4.6 (1/4 span, 3/8 span, and at midpoint of the span). As the model is linear elastic in nature, there was only a need to have three data points to determine the structures response. As such, the impact magnitudes applied to the structure were the same at each location and are shown below:

- 400 kips. This load was used as an upper bound assumption for what a barge impact would be on the structure.
- 0 kips. This was used to determine a steady states reaction of the structure when only the self-weight of the structure was considered.
- -100 kips. This reverse load was used to determine how the structure would react after it had been impacted.

I.2.4.7.2. The response of the structure determined by its deflection into the lock chamber was then graphed compared to the applied load. The graphs at each of the three locations are shown in Figure I.19 through Figure I.21.

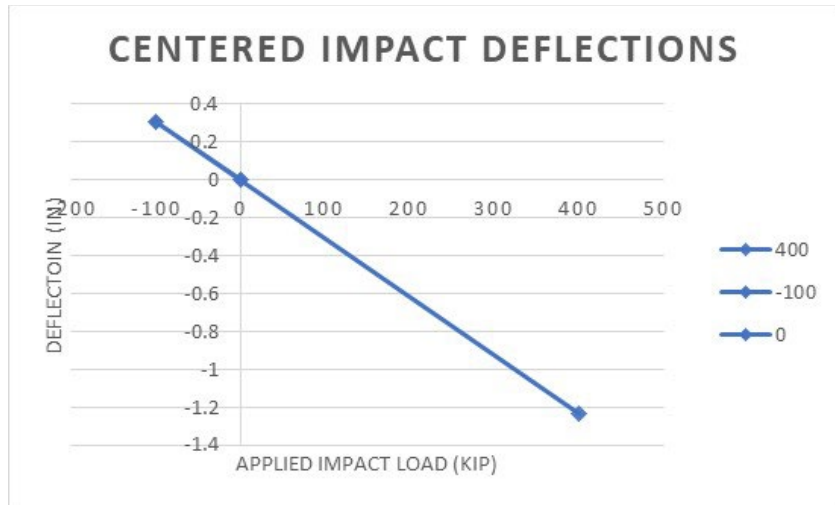


Figure I.19. Graph of the Incremental Impact Loads at the Midpoint of the Bulkhead; Negative Deflections are Considered Toward the Dry Side of the Bulkhead

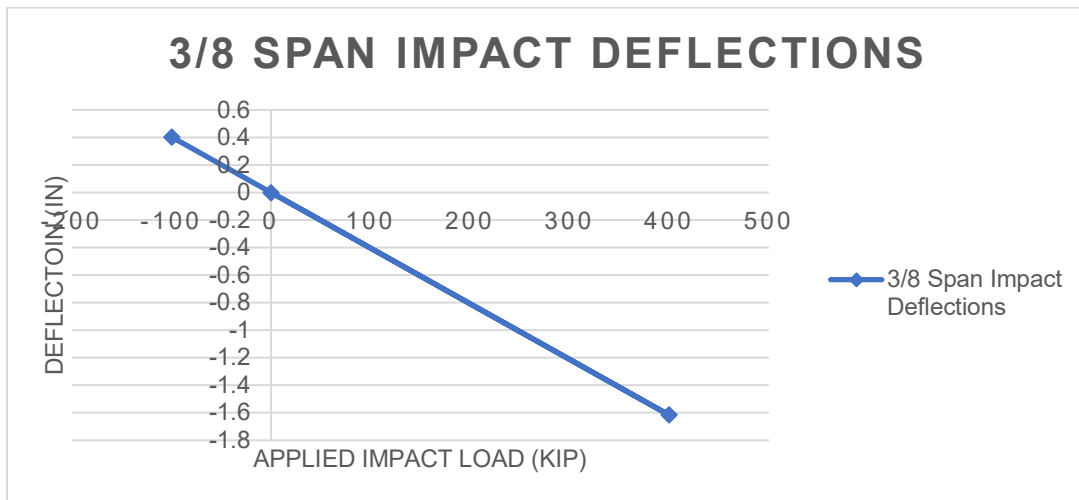


Figure I.20. Graph of the Incremental Impact Loads at the 3/8 Span of the Bulkhead; Negative Deflections are Considered Toward the Dry Side of the Bulkhead

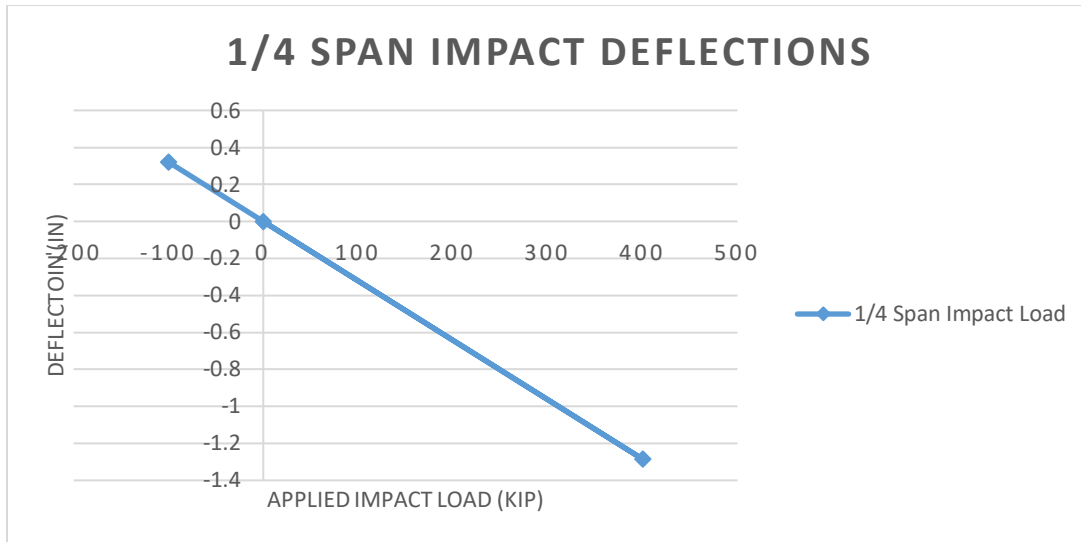


Figure I.21. Graph of the Incremental Impact Loads at the 1/4 Span of the Bulkhead; Negative Deflections are Considered Toward the Dry Side of the Bulkhead

I.2.4.8. Estimated Barge Impact Loads – Low-Order Dynamic Model

I.2.4.8.1. This section estimates the barge impact load based on a crane deck barge that impacts the bulkhead during a lock dewatering. This impact occurs either by the crane barge losing its stability, the spuds fail, and the barge rotates and impacts the dewatering structure; or an impact occurs due to pilot error or loss of power when the barge rotates forward and impacts the dewatering structure.

I.2.4.8.2. The equivalent impact load is calculated using the low-order dynamic model (LODM) that was developed for USACE by University of Florida. This LODM uses a simplified dynamic multiple degree-of-freedom model that solves the equations of motion for a barge in contact with a structural element such as approach wall. The model solves for either a flexible or a rigid structure and includes the masses for both the barge and impacted structure, in this case the lock dewatering structure.

I.2.4.8.3. The LODM accounts for both damping and a dynamic coefficient of friction during the impact as well as the stiffness (force vs. deflection) of the impacted structure. The output from the LODM solves for the maximum impact force and displacement of the structure as well as the time history of the resulting impact.

I.2.4.8.4. The input parameters selected for the bulkhead structure LODM are as follows:

- Flexible wall option was used.
- Barge column and rows – 1. A single crane deck barge was modeled.

- Barge Weight – See Table I.6. This is based on information for three different deck barges used in the Southwest Division fleet. The working draft of the crane barge is assumed to be 6 ft.

- Impact Speed – 1 ft/sec was assumed at impact into three locations in the bulkhead. These locations were mid-span, 3/8 span, and 1/4 span.

- Impact Angle – See Table I.7. This was the maximum angle possible for the impact based on lock geometry and the three crane barge sizes.

- Wall Weight – 37 kips. This was the total weight calculated from the STAAD.Pro model for steel bulkhead components contributing to the impact.

- Dynamic Coefficient of Friction – 0.45. This was selected based on recommendations in the UF LODM report.

- Time End – 5 sec. This was anticipated to be the longest value needed for the time history analysis.

- Time Sample – 0.01 sec. This is a time step for convergence of the model results.

- Wall Damping Ration – 0.05. This was selected based on recommendations in the UF LODM report.

- Wall Stiffness. The wall stiffness comes from the output of the STAAD pushover model presented in section I.2.4.7. The maximum value both positive and negative are used to define a linear curve in the LODM analysis.

- Hydrodynamic Added Mass. Not include in this LODM analysis due to the short duration of the impact loads.

I.2.4.8.5. The barge impact forces result from LODM for the three barges and impact locations are 141, 137, and 196 kips. The results with the maximum forces and mean estimates of force are shown in Table I.8. These barge impact forces are now used back in the STAAD.Pro model statically to estimate what the combined stress or utilization factors would be for the bulkhead structure.

Table I.6
Barge Weights

Beam (ft)	Length (ft)	Draft (ft)	Weight, tons
35	195	6	1,280
50	200	6	1,875
84	255	6	4,016

Table I.7
Impact Angles for Deck Barges

Beam (ft)	Length (ft)	1/4 span (27.5 ft) (degs)	3/8 span (41.25 ft) (degs)	Mid-span (55 ft) (degs)
35	195	25	30	35
50	200	15	25	30
84	255	15	20	25

Table I.8
Peak Barge Impact Forces

Beam (ft)	Length (ft)	1/4 span (27.5 ft) (kips)	3/8 span (41.25 ft) (kips)	Mid-span (55 ft) (kips)
35	195	141	137.4	187.8
50	200	137.4	133	180.8
84	255	141.1	136	196.6
Max		141.1	137.4	196.6
Mean		139.8	135.5	188.4

I.2.4.9. STAAD.Pro Model Results.

I.2.4.9.1. The calculated impact loads at the three locations are then applied to the model in unfactored load combinations with the impact load and the self-weight of the structural members. The model is then checked to determine if the beam elements can still meet combined loading requirements as determined in AISC 360-16 using allowable stress design.

I.2.4.9.2. From the STAAD.Pro model, the largest utilization ratio (combined stress ratio in AISC) was calculated as 0.799 on one of the double angles that make up a diagonal brace on the wet side of the bulkhead. This value is less than the maximum allowable value of 1 from AISC 360-16, showing that the structure can withstand the calculated load from an accidental barge impact. Using the loads from the STAAD.Pro model, the utilization ratio on this member was verified in a Mathcad calculation and the difference was less than 1%.

I.2.4.9.3. Additionally, the resultant forces on the bulkhead slots were also determined so they can be used in the design of the new bulkhead slots for the lock. The loads on each of the supports that make up the connection between the bulkhead and the slots in the lock wall are not uniform, so it is necessary to design the slots for the maximum observed point load from any of these supports, as well as the total load into the lock wall from the bulkhead. The support nodes on the left and the right side of the bulkhead are shown in Figure I.22. The resultant loads into the lock wall from the bulkhead slots are shown in Table I.9 and Table I.10.

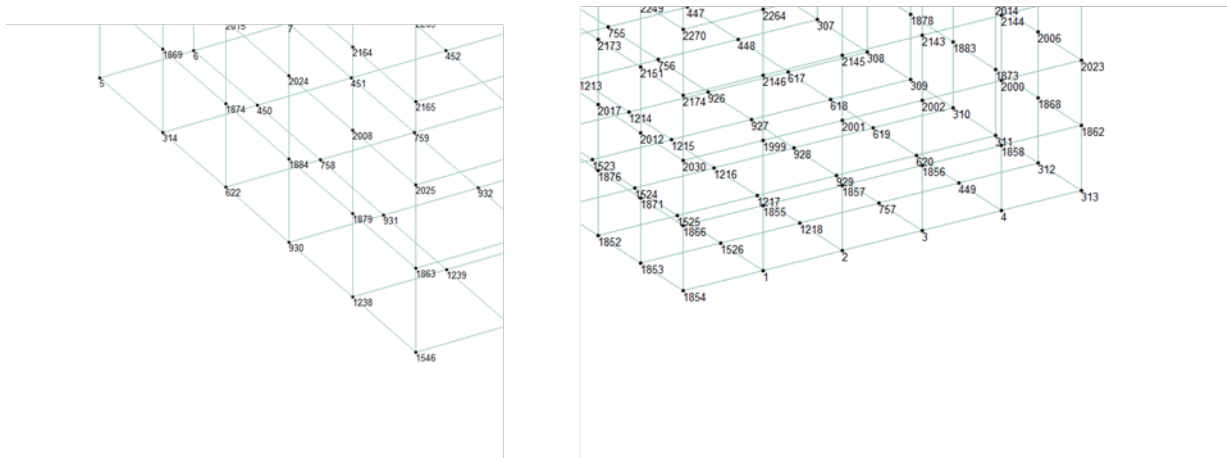


Figure I.22. Support Nodes on the Corner of the STAAD.Pro Model Where the Bulkhead Will Bear Against the Bulkhead Slots Cut Into the Lock Wall

Table I.9
Support Reactions on the Bulkhead Slots from Each of the Design Impact Load Cases
(The X axis is vertical in the model and the Y axis is the direction of flow.)

Load Case	Side of the Bulkhead	FX	FY
		(kip)	(kip)
18:1/2 SPAN DEAD+IMPACT	Right Side of Bulkhead	-26.430	15.734
		-22.914	11.086
		-22.959	11.169
		-26.550	16.035
		-166.863	22.558
		-166.010	21.718
	Left Side of Bulkhead	166.861	22.555
		26.554	16.036
		22.963	11.170
		22.919	11.087
		26.434	15.735
		166.009	21.716
19:3/8 SPAN DEAD+IMPACT	Right Side of Bulkhead	-21.039	11.199
		-18.318	7.853
		-18.351	7.943
		-21.128	11.523
		-132.160	16.110
		-131.581	15.219
	Left Side of Bulkhead	232.970	29.764
		36.979	23.064
		31.921	16.074
		31.861	15.965
		36.816	22.671
		231.864	28.714
20:1/4 SPAN DEAD+IMPACT	Right Side of Bulkhead	-8.813	4.098
		-7.719	2.886
		-7.733	2.969
		-8.844	4.395
		-54.809	6.101
		-54.714	5.277
	Left Side of Bulkhead	182.089	24.828
		28.804	19.735
		24.773	13.822
		24.724	13.725
		28.675	19.385
		181.281	23.880

Table I.10
Summary of Loads on Each Side of the Bulkhead from the Design Impact Load Cases

Summary of Horizontal Loads on the Bulkhead		
Load Case	Right Side Load (kip)	Left Side Load (kip)
18:1/2 SPAN DEAD+IMPACT	98.300	98.299
19:3/8 SPAN DEAD+IMPACT	69.847	136.252
20:1/4 SPAN DEAD+IMPACT	25.726	115.375

I.2.5. Conclusions

I.2.5.1. The methods and results from this example show that using both STAAD.Pro and the LODM can yield valuable insight to accidental barge impacts to dewatering structures. Both examples show that using the 5 kip/ft impact load prescribed in EM 1110-2-2107 for hydraulic steel structures is very conservative for accidental impacts during maintenance conditions. However, consideration should be given to follow similar methods to examine each bulkhead structure, as each structure has differences. The differences in estimated impact loads are likely due to several factors, including the angle the barge can impact the structure as well as the stiffness of the structure itself.

I.2.5.2. These broad differences at this point make it difficult to pinpoint one magnitude for an accidental impact load that could be used across multiple structures. Instead, it is proposed that during an analysis of an existing dewatering structure or during the design of a new one, the design engineers perform a similar analysis to what was done on this dewatering structure. This includes the development of a finite element analysis model to determine the structure's response under barge impact loads and estimating the forces due to impact from the LODM specific to barge fleet characteristics and lock geometry. Lastly, this calculated impact load should be inserted back into the finite element analysis model for the purposes of designing and analyzing the structure and determining which, if any, members are critical to failure of the dewatering structure.

I.2.5.3. Lastly, it is important to mention that the results of the bulkhead structure example under the calculated impact loads that none of the structural members reached a critical level of loading under AISC. In contrast, the center post dewatering example had multiple members that would no longer meet loading requirements under certain water elevations combined with the impact load. These differences clearly highlight that different types of dewatering structures are present at USACE lock facilities.